Study of crystal-hosted melt inclusions at Santorini (Greece), with implications for magma genesis and plumbing system processes

Taya Therese Flaherty

UNIVERSITÉ CLERMONT AUVERGNE

Collegium des Sciences Fondamentales

ÉCOLE DOCTORALE DES SCIENCES FONDAMENTALES

THÈSE

Présentée pour obtenir le grade de

DOCTEUR D'UNIVERSITÉ

Spécialité : Structure et évolution de la Terre et des autres planètes

Par

Taya Therese FLAHERTY

M.Sc. Géologie (Michigan Technological University), M.Sc. Sciences de la Terre - Magmas et Volcans (Université Clermont Auvergne), B.Sc. Géologie (University of Pittsburgh)

Study of crystal-hosted melt inclusions at Santorini (Greece), with implications for magma genesis and plumbing system processes

Étude des inclusions magmatiques du Santorin (Grèce) : implications pour la genèse des magmas et les processus magmatiques

Soutenue publiquement le 16 janvier 2020 devant la commission d'examen :

Ralf Gertisser (Rapporteur)	Keele University, Royaume-Uni
Luca Caricchi (Rapporteur)	Université de Genève, Suisse
Lorella Francalanci (Examinateur)	Université de Florence, Italie
Lucia Gurioli (Examinateur)	Université Clermont Auvergne, France
Muriel Laubier (Examinateur)	Université Clermont Auvergne, France
Tim Druitt (Directeur de thèse)	Université Clermont Auvergne, France
Pierre Schiano (Directeur de thèse)	Université Clermont Auvergne, France

Laboratoire Magmas et Volcans, Université Clermont Auvergne, CNRS UMR 6524, OPGC-IRD | 6 avenue Blaise Pascal, Campus de Cézeaux, 63170 Aubière

Abstract

Many arc volcanoes are capable of producing devastating caldera-forming eruptions. Santorini Volcano (South Aegean Volcanic Arc, southern Aegean Sea, Greece) is an arc volcano responsible for numerous such eruptions over its >0.65 My history, the most recent being the Late Bronze Age (LBA) eruption. However, there are a number of unresolved questions relating to the Santorini volcanic system including the nature of the primary magmas of Santorini and how they change with time, differentiation processes and the relationship between mafic and silicic magmas, the origins of long-term geochemical trends in magma composition, and what changes occur in the plumbing system during the build-up to a large caldera-forming eruption. In this thesis, I present a large set of high-resolution crystal-hosted melt inclusion (MI) and groundmass glass data to address these questions relating to the nature of magma genesis and differentiation at Santorini.

The dataset includes many olivine-hosted MIs of primitive basaltic composition, which are rare as whole rocks on Santorini and in the volcanic arc in general. These MIs show there is a range in the incompatible trace element chemistry of the most primitive basaltic melts at Santorini. Primitive MIs have typical subduction zone geochemical signatures and vary between incompatible-poor and incompatible-rich types, which we refer to as low Nb and high Nb primitive melt types, respectively. The primitive MIs range in La/Yb from 1.5 (flat, tholeiitic-like) in the low Nb type to 3.2 (inclined, calc-alkaline-like) in the high Nb type. We back-calculate primary melt compositions using different methods and find that the primary melts parental to the low Nb and high Nb MIs have respectively low Nb and high Nb characteristics. The low Nb and high Nb type primitive melts cannot be related by fractional crystallization but are instead related by different degrees of partial melting of the mantle. We derived the degree of mantle partial melting (F) using the petrogenetic modelling software PRIMACALC2 (F = 6% for high Nb primary melt; F= 8% for low Nb primary melt) and carrying out mantle melting models (F = 18% for high Nb primary melt; F = 22% for low Nb primary melt). The two approaches differ in F but agree that a different degree of melting can explain the compositional variation between the two endmember Nb melt types. The predominant metasomatic signature in the primary melts is from melting of sediment in the subducted slab; there is very little evidence for slab-derived aqueous fluids. There may be some influence from residual rutile in the slab, but this does not

dominate the different Nb groupings. There is no consistent temporal change in the primary basaltic melts with time, suggesting that the two different endmember primary melts have been available for ascent into the crust over much of the history of the volcano. We conclude that at least two mantle source domains exist below Santorini: a source giving way to low Nb primary melts (characterized by higher sediment melt signatures and a higher degree of partial melting) and one giving rise to high Nb primary melt (characterized by a smaller, yet still prominent, sediment melt signature and associated with a few percent less melting). The absence of a strong slab-derived aqueous fluid component, coupled with the presence of arc tholeiitic compositions and regional extension around the volcanic field, suggests there could be a role of decompression melting beneath Santorini.

We related primitive parental melts to Santorini magmas of intermediate and silicic composition to shed light on the processes of magma differentiation. MI and groundmass glasses form lineages that can be subdivided into the different Nb series, with each series exhibiting two distinct stages of differentiation on log-log variation plots: Stage 1 from basalt to basaltic andesite, and Stage 2 from basaltic andesite to rhyodacite. While Stage 2 can be modelled by fractional crystallization (FC) using reasonable values of bulk solid-melt partition coefficient (D), Stage 1 cannot. Stage 1, and to a large extent both stages, can be modelled satisfactorily from the respective parental compositions using assimilation fractional crystallization (AFC) with r (ratio of mass of contaminant to mass of magma crystallized) values of 0.15-0.5 and a silicic contaminant with ratios of incompatible elements to Th that are similar to, or lower than those of silicic melts of the magmatic series themselves. Stage 2 can be similarly modelled by AFC, but also by almost pure FC using reasonable Ds. There are many possible contaminant compositions, but they can be narrowed down based on a mean solution distribution and geological reasoning. One possibility is that the contaminant is a highly evolved, low-fraction silicic melt, which appears from published whole rock Sr isotopic data to be variably radiogenic. This melt may be present interstitially, or as veins and dykes, in the variably mushy plutonic products and crustal rocks making up the Santorini magmatic system. Mantle-derived basaltic melts may encounter and interact with this contaminant during ascent to the surface.

Santorini magmas of intermediate to silicic composition exhibit a well-documented decrease in incompatible element content (including K, Rb, Zr, La, Nb) with time since

530 ka. We show that the individual trends making up the temporal variation can be explained by AFC differentiation from the different endmember parental magmas. It follows that the temporal decrease in incompatible elements is parent-related, as previously suggested but not proven. Given that low and high Nb basaltic melts have been generated throughout the history of Santorini in different mantle source domains, the temporal change in incompatibles must be due to an increase *in the proportion* of low Nb primary melt relative to high Nb primary melt with time. This could be due to a growing influence of crustal rifting and extension in the region, possibly associated with an increasing degree of decompression melting relative to fluid-flux melting.

We have also investigated the evolution of the magmatic plumbing system of Santorini during the build-up to a major caldera-forming eruption. During the 80 ky period prior to the Late Bronze Age (LBA) eruption, the magmatic system was fed by the two Nb type primary endmember melts. Anomalously high Ba magmas erupted between 20 and 3.6 ka, and present within the LBA eruption products, may record a third mantle-derived melt endmember or low Nb melt contaminated by Ba-rich crustal rocks or minerals. The LBA rhyodacitic magma is not related by differentiation to the high-Ba magmas in any simple way, since it does not lie on the high Ba liquid line of descent (LLD) given by the MIs and glasses. However, some high Ba MIs form a band between the high Ba LLD and the rhyodacite, suggesting interactions between these two magma batches prior to eruption. In the Kameni volcanism following the LBA eruption, the high Ba component is no longer observed. Some geochemical evidence reveals a growing role of cryptic amphibole in the magmatic system from 55 ka onwards prior to the LBA eruption, suggesting the possible development of a crustal amphibole 'sponge' during this period. We observe that trends of some interplinian MIs and glasses form tight subparallel trends, whereas those associated with the large silicic eruptions are more scattered. We speculate that this may be indicative of growing, increasingly heterogeneous and mushy magmatic systems during the build-up periods to large silicic eruptions, associated with a greater degree of crystal scavenging and inheritance.

Résumé

Un grand nombre de volcans d'arc sont capables de produire des éruptions caldériques. Le volcan de Santorin (*South Aegean Volcanic Arc*, l'Égée-Méridionale, Grèce) est un volcan d'arc responsable de plusieurs éruptions de ce type au cours de ses 0,65 Ma d'activité, et dont l'éruption de l'Âge de Bronze Tardif (éruption *Late Bronze Age*, LBA) est la plus récente. Pourtant, de nombreuses questions sur le système volcanique de Santorin restent non résolues telles que la nature des magmas primaires et la manière dont leurs compositions changent au cours du temps, l'origine des magmas intermédiaires et acides, les raisons des tendances géochimiques des magmas acides observées sur le long terme, et la nature des changements se produisant dans le système magmatique dans la période précédant une grande éruption caldérique. Dans cette thèse, je présente un large ensemble de données de haute précision sur les inclusions vitreuses et les verres matriciels, afin de répondre aux questions relatives à la genèse et l'évolution des magmas du Santorin.

Notre échantillonnage est composé de nombreuses inclusions vitreuses piégées dans des cristaux d'olivine dont les compositions basaltiques primitives sont rarement représentées par les roches totales du Santorin et plus généralement de l'ensemble de l'arc volcanique. Ces inclusions vitreuses révèlent qu'il existe une gamme de teneurs en éléments en traces incompatibles dans les magmas basaltiques les plus primitifs du Santorin. Les inclusions primitives présentent une signature géochimique typique des magmas de zone de subduction. La gamme des compositions varie d'appauvri à enrichi en éléments incompatibles, appelés type *low Nb* et type *high Nb*. Les rapports La/Yb des inclusions vitreuses primitives sont compris entre 1,5 (plat, de genre tholéitique) dans le type *low Nb* et 3,2 (incliné, de genre calco-alcalin) dans le type *high Nb*. Nous avons calculé les compositions des liquides magmatiques primaires en utilisant différentes méthodes et nous avons mis en évidence que les liquides primaires parentaux des magmas de types *low Nb* et *high Nb* sont respectivement appauvris et enrichis en éléments incompatibles. Les différents types de magmas primitifs ne peuvent pas être expliqués par la cristallisation fractionnée de l'un de ces magmas, mais sont plutôt associés à différents degrés de fusion partielle du manteau. Nous avons déterminé les degrés de fusion partielle (F) du manteau en utilisant le logiciel de modélisation petro-génétique PRIMACALC2 (F = 6% pour les liquides silicatés primaires *high Nb,* F = 8% pour les liquides silicatés primaires *low Nb*) et en effectuant

des modèles de fusion partielle du manteau (F = 18% pour les liquides silicatés primaires *high Nb*, F = 22% pour les liquides silicatés primaires *low Nb*). Les valeurs de F obtenues à partir de ces deux approches diffèrent. Cependant, les résultats obtenus montrent qu'une différence dans le degré de fusion partielle du manteau peut expliquer la gamme des compositions observée entre les différents types de magmas primitifs. La signature métasomatique prédominante dans les liquides primaires provient de la fusion partielle des sédiments de la plaque plongeante. Il y a peu de preuves de l'influence de fluides aqueux provenant de la plaque plongeante. Il y a peut-être une influence du rutile résiduel, mais celle-ci ne domine pas l'origine des différentes séries. Il n'existe aucune tendance temporelle cohérente dans les magmas basaltiques parentaux au cours du temps, ce qui suggère que les différents types de magmas primaires sont restés disponibles pour l'ascension dans la croûte durant la plupart de l'histoire du volcanisme du Santorin. Nous concluons qu'il existe au moins deux sources dans le manteau qui donnent naissance aux types *low Nb* (caractérisé par une signature plus importante de sédiments fondus et un degré de fusion partielle du manteau plus élevé) et *high Nb* (caractérisé par une signature plus faible, mais toujours prononcée, de sédiments fondus, associée à un degré de fusion partielle du manteau moins élevé). L'absence de la signature d'un fluide aqueux provenant de plaque plongeante, couplée à la présence des compositions tholéitiques et de l'extension tectonique régionale autour du volcan, suggèrent un rôle important de la fusion partielle du manteau par décompression au-dessous du Santorin.

Nous avons relié les magmas primitifs parentaux du Santorin aux magmas intermédiaires et acides pour identifier les processus d'évolution magmatique. Les inclusions vitreuses et les verres matriciels constituent des lignées qui peuvent être subdivisées en différentes séries basées sur leurs teneurs en Nb. Chaque série montre deux étapes distinctes d'évolution sur les graphiques de variation log-log : Etape 1 de basalte à andésite basaltique, et Etape 2 d'andésite basaltique à rhyodacite. L'Etape 2 peut être modélisée par cristallisation fractionnée, mais l'Etape 1 ne le peut pas. L'Etape 1, voire les deux étapes, peut être modélisée par un processus de cristallisation fractionnée et assimilation, avec une valeur de r (rapport de la masse de contaminant sur la masse de magma cristallisé) comprise entre 0.15 et 0.5 et un contaminant acide dont les rapports entre les éléments incompatibles et le Th sont inférieurs ou égaux à ceux des séries magmatiques acides. L'Etape 2 peut être modélisée par cristallisation fractionnée et assimilation, mais aussi par simple cristallisation fractionnée, en

utilisant des coefficients de partage (Ds) réalistes. Une myriade de compositions contaminantes sont possibles, mais les possibilités peuvent être réduites en se basant sur la distribution statistique des solutions moyennes et sur le raisonnement géologique. Une des possibilités est que le contaminant est un magma liquide très évolué, avec une faible fraction de liquide siliceux, qui apparait avoir des compositions isotopiques en Sr très variables, d'après les données publiées de roches totales. Ce liquide magmatique peut être présent interstitiellement ou, comme des veines ou des dykes, dans le système magmatique variablement cristallin du Santorin. Les magmas basaltiques parentaux d'origine mantellique peuvent rencontrer et interagir avec ce contaminant lors de l'ascension vers la surface.

Il a jusque-là été très documenté dans la littérature que les magmas intermédiaires à acides du Santorin montrent une diminution des teneurs en éléments incompatibles (e.g. K, Rb, Zr, La, Nb) corrélée avec le temps et ce depuis 530 ka. Les tendances individuelles qui s'inscrivent dans l'évolution temporelle générale peuvent être expliquées par la différenciation des magmas basaltiques parentaux par cristallisation fractionnée et assimilation. Il en découle que la diminution des teneurs en éléments incompatibles au cours du temps est directement liée aux magmas parentaux, comme suggéré auparavant mais non prouvé. Etant donné que les magmas basaltiques *low Nb* et *high Nb* ont été générés tout au long de l'histoire de Santorin à partir des différents domaines du manteau, la diminution de la teneur en éléments incompatibles au cours du temps doit être causée par une augmentation *de la proportion* de liquide silicaté primaire *low Nb* par rapport à celle de liquide silicaté primaire *high Nb* au cours de temps. Ceci peut être dû à une influence croissante de l'extension crustale régionale.

Nous nous sommes également intéressés à l'évolution du système magmatique du Santorin pendant la période précédant l'éruption LBA. Au cours des 80 ka précédant l'éruption, le système magmatique était approvisionné par des liquides magmatiques primaires de compositions extrêmes en Nb. Des magmas anormalement riches en Ba mis en place entre 20 et 3.6 ka, et présents dans les produits de l'éruption LBA, peuvent attester de l'existence d'un troisième pôle mantellique ou peuvent représenter des magmas de séries *low Nb* contaminés par des roches ou minéraux crustaux riches en Ba. Le magma de composition rhyodacitique n'est pas le simple produit de la différenciation de magmas riches en Ba, puisque les deux magmas ont des tendances géochimiques différentes. Par contre, quelques inclusions vitreuses ayant piégé du

magma riche en Ba forment une bande entre les groupes de magmas riches en Ba et ceux de composition rhyodacitique. Cela suggère une interaction entre les magmas de ces deux compositions avant l'éruption LBA. Dans le volcanisme moderne « Kameni » qui a suivi l'éruption LBA, le pôle représentant le magma riche en Ba n'est plus observé. Il y a quelques indications qui montrent un rôle croissant d'une amphibole « cryptique » dans le système magmatique à partir de 55 ka avant l'éruption LBA, suggérant le développement d'une « éponge » crustale d'amphibole pendant cette période. Les tendances décrites pour quelques éruptions « interpliniennes » forment des tendances subparallèles rapprochées, alors que les tendances associées aux grandes éruptions acides « Pliniennes » sont plus dispersées. L'hypothèse la plus probable est que la dispersion des données est liée à la croissance du système magmatique pendant les périodes précédant les grandes éruptions acides, et ce associé à un taux de piégeage et d'héritage des cristaux plus important.

Acknowledgements

I would first like to thank my day-to-day supervisor Tim Druitt for his guidance, direction, insightful discussions and for keeping me from panicking when things were tough. I also thank Pierre Schiano for his helpful discussions and sharing his expertise on melt inclusions and geochemistry. I thank Olgeir Sigmarsson for discussions and feedback on geochemical approaches, and Lorella Francalanci for providing key samples, welcoming us to her lab in Florence and for sharing her geochemical expertise.

On the practical side of things, I would like to thank Jean-Luc Devidal for countless hours of assistance on the microprobe and Jean-Marc Hénot for assistance on the SEM. Many thanks to Nicolas Cluzel for help and advice for melt inclusion preparation and homogenization. Thanks to Claire Fonquernie for advice and training on rock crushing and mineral separation techniques. Thank you to Estelle Rose-Koga for allowing for and coordinating the use of the Vernasdky heating stage. Thanks to Muriel Laubier for helpful discussions about melt inclusions. Thank you also to Isabelle Roche, Audrey Chazal and Nathalie Elaydi for administrative help.

I have gained so many great friends, labmates and officemates during these past years in Clermont-Ferrand, of whom there are too many to name, but I have to say that they all made Clermont feel like a real home to me. Thank you to my great friend and former roommate JM, you are truly one of the kindest souls I have ever met. Thanks for all the discussions about both academia and life, and for helping me to come out of my shell. To SV: you were my inseparable sidekick during the M2R in Clermont, but the saga didn't end there—the terrible twosome continued on! Thank you for all the great memories, discussions and support through these past years. Thank you, MG, for all the time spent in the melt inclusion lab and the office, for discussions, polishing for countless hours (sometimes to silly music) and for being there when I needed someone to talk to. Thank you, PF, for being a great officemate and friend, for rainy day road trips to Gerzat and for lots of laughter. Thanks to CI and PF for great memories and lots of fun together. Thank you to MM for your friendship and mentorship, for unforgettable moments in Santorini and Clermont—it was great to have another US American friend in France! Thank you DN for discussions about geochemistry, melt inclusions and modelling, as well as some great times outside the lab such as playing board games! Thank you to AW for real talk and many nice moments shared together!

Thanks to LT for being a great friend and for many memories, such as falling through the frozen pond in Jardin Lecoq. Thank you SdS for wonderful memories both in Florence and in Clermont. Thank you BQ for your friendship and help and support with administrative and visa matters. Thanks to DF, AH and LM for your kind friendship during these last years and also for a really memorable time in Washington D.C.

I also want to thank my support network outside of the academic setting. At home in Pittsburgh, I give a special thank you to my siblings Devon, Daragh, Manny, Garrick, Jill, Revere and Jason and to my friends JC, LM, KZ, NR, JR, SB, SN, SH, MH and so many others who have always been there supporting me from so far away. I also must thank my medical doctor, Dr. M, for helping me survive the last several years, as it seems as though I have never been so frequently sick as I have been in France.

To Quentin: Thank you for your unconditional love and support during these last years. Thanks for all the practical things as well, from help with visa problems to helping to improve my French.

Lastly, I must thank my parents for their support of my endeavors so far away from home. I would like to take a little extra space to talk about my father, who unfortunately passed away during the final year of my PhD, and my mother who gave up everything else to take care of him for more than five years. My father, as a judge and a scholar, gave me a strong moral character and taught me to question the world around me. These qualities have allowed me to excel in my academic journey. He also taught me to see the beauty in the world and to choose to always be kind and optimistic. These traits have come to define my personality and outlook on life, and I am extremely grateful for this. Dad: It has been a hard year without you, and I'll miss you very much, always. My mother taught me dedication, inspired me to dream big and encouraged me to never give up. I adopted her adventurous spirit. She provided moral and financial support through the years to help me to get me where I am. Mom: I could never have done it without you.

This doctoral research project was financed through the LabEx Centre Clermontois de Recherche sur le Volcanisme (ClerVolc).

For my mother and late father

Linet M. Flaherty and John P. Flaherty Jr.

Table of Contents

List of Appended Papers

There are two papers appended to the thesis, following the References:

1. Flaherty et al. (2018)
2. Schiavi et al. (2018)

Electronic Supplementary Information

There are also electronic supplementary files associated with this thesis. These files include:

1. **Thesis.pdf** - An electronic copy of this thesis
2. **Melt inclusion and groundmass data.xlsx** - Data tables with all melt inclusions and groundmass analyses
3. **MI correction spreadsheet.xlsx** - A spreadsheet containing an example melt inclusion correction calculation, which was used in this thesis to correct all olivine-hosted melt inclusions.
4. **Whole rock database.xlsx** - A compilation of published whole rock data currently available for Santorini assembled by the author
5. **D calculator.xlsx** A spreadsheet used to calculate Ds for different compositions based on available partitioning coefficients from the literature.

List of Figures

List of Tables

Introduction

Arc volcanoes pose a significant hazard to populations and environment worldwide. Eruptions at arc environments may range from phreatic steam explosions to devastating ignimbrite-forming eruptions, with effects on local, regional or even global scales. Large populations live near active volcanoes around the world, as volcanic soil often provides fertile land for agricultural development. Arc volcanoes in general are considerably dangerous, as they tend to be more water-rich, and thus more explosive, than volcanoes in other tectonic settings. Notable destructive arc volcanic eruptions in recent modern history include Mount St. Helens (USA) in 1980 and Mt. Pinatubo (USA) in 1991. While some arc volcanoes are nearly continuously active, such as Mt. Etna (Italy), Stromboli (Italy) and Sakurajima (Japan), others may be dormant for many years. Large caldera-forming eruptions in particular are low-frequency, high-impact events that are capable of a high level of catastrophe and have produced some of the most voluminous explosive eruptions preserved in the geologic record, many occurring in arc settings (Mason et al. 2004; Self 2006; Cashman and Giordano 2014). We need to study arc volcanoes so that we can understand signs of unrest, interpret signals correctly and mitigate risks to populations. A large part of understanding a volcano's eruptive behavior comes from studying its plumbing system and the processes that drive magma genesis, differentiation and transport through the crust.

Santorini is one such arc volcano which is located in the southern Aegean Sea along the South Aegean Volcanic Arc. Santorini has a long (>0.65 My) history of explosive eruptions, one of the most recent being the Late Bronze Age (LBA) eruption which discharged 48-86 km^3 (DRE) of magma (Bond and Sparks 1976; Druitt et al. 1999; Druitt 2014; Johnston et al. 2014). I use Santorini Volcano as a natural volcanic laboratory to study key questions about processes occurring in this continental arc magmatic system from magma genesis in the mantle to eruption at the surface.

Santorini as an excellent laboratory volcano

Santorini provides excellent exposures of eruption products from its >0.65 My history. The caldera cliffs have allowed a detailed stratigraphic history to be assembled. Detailed studies have already been undertaken on tephrostratigraphy and on both absolute and relative dating of products (Huijsmans 1985; Friedrich et al. 1990; Druitt et al. 1999; Vespa et al. 2006; Satow 2012; Fabbro et al. 2013; Satow et al. 2015;

Athanassas et al. 2016). The eruptive history, for both major explosive eruptions and minor units of the volcano, is therefore well documented.

The remarkable exposure and detailed understanding of the stratigraphy of the volcanic products have been accompanied by numerous studies on the mineralogy, componentry, petrology and geochemistry of the erupted products (Nicholls 1971; Bond and Sparks 1976; Puchelt 1978; Barton et al. 1983; Heiken and McCoy 1984; Huijsmans 1985; Barton and Huijsmans 1986; Sigurdsson et al. 1990; Sparks and Wilson 1990; Francalanci et al. 1998; Tarney et al. 1998; Druitt et al. 1999; Mortazavi and Sparks 2004; Vespa et al. 2006; Druitt 2014; Simmons et al. 2016; Pantazidis et al. 2019). Textural studies have been carried out, notably on lavas and enclaves (Higgins 1996; Holness et al. 2005; Martin et al. 2006; Jerram and Martin 2008; Simmons et al. 2017; Myers et al. 2018). Several studies using mass-balance geochemical modelling, U-Th-Ra isotopic disequilibria and other techniques have been carried out to understand magma genesis and differentiation (Nicholls 1971, 1978; Mann 1983; Huijsmans 1985; Pyle et al. 1988; Zellmer 1998; Druitt et al. 1999; Zellmer et al. 2000, 2005; Vaggelli et al. 2009; Bailey et al. 2009; Baziotis et al. 2018). Melt inclusion volatile barometry has progressed our understanding of volatile behavior at Santorini, and have allowed us to better constrain magma storage depths (Vaggelli and Francalanci 1998; Michaud et al. 2000; Vaggelli et al. 2009; Druitt et al. 2016). Experimental petrology and phase equilibria have also furthered our understanding of the plumbing system (Cottrell et al. 1999; Cadoux et al. 2014; Andújar et al. 2015, 2016). Diffusion chronometry studies have refined the timescales of magmatic processes preceding some of the largest eruptions at Santorini, showing that large melt-rich magma chambers are assembled rapidly prior to eruption (Druitt et al. 2012; Fabbro et al. 2017; Flaherty et al. 2018).

Multibeam bathymetry mapping and seafloor exploration of the caldera basin have led to new discoveries about the history of the volcano, its underwater topography and its eruptions (Nomikou et al. 2014, 2016; Hooft et al. 2017). Remote sensing and GIS studies have also played a part in our understanding of the volcano (Pyle and Elliott 2006; Marsellos et al. 2016; Oikonomidis and Pavlides 2017; Pasqualon et al. 2017). Modern geophysical methods and seismic imaging, including recent high-resolution tomography, have allowed us to effectively image the crust below the volcano (Papazachos et al. 2000; Johnston et al. 2014; Nomikou et al. 2016, 2018; Hooft et al.

2019). Continued monitoring and long-term eruption predictions are essential for risk management at the volcano (Papadopoulos and Orfanogiannaki 2005; Parks et al. 2012, 2015; Rizzo et al. 2015; Papageorgiou et al. 2019).

Fundamental questions and approach

These previous studies of Santorini provide a wealth of information, and an excellent geological context, for addressing fundamental questions related to an explosive arc volcano. Despite the many studies previously carried out at Santorini, there are still a number of issues that remain poorly understood. The aim of this thesis is to address the following fundamental questions:

- What is the nature of primary magmas at Santorini, and how do they change in space and time?
- What are the origins of more evolved magmas?
- What are the origins of long-term geochemical trends in silicic magmas?
- What happens in the plumbing system of a volcano during the build-up period to a large caldera-forming eruption?
- With new insight, how does the Santorini magmatic system operate physically?

One of the biggest obstacles in the way of resolving these questions lies with the inherent nature of using whole rock analyses, which are the type of analyses on which most geochemical studies at Santorini are based. Whole rock analyses can provide highly useful information about a volcanic system; however, it must be recognized that whole rocks (1) represent the end product of a potentially long suite of open-system differentiation processes of the parental magma, (2) rarely preserve early- or deep-formed magma compositions, especially in arc settings where mantle-derived magmas must traverse thick crustal sections to reach the surface, and (3) may be contaminated by xenocrysts, contain recycled antecryst populations, or represent mixtures of magmas. Also, combining different datasets of whole rock analyses may bring about even more issues, including, but not limited to, the variability in data quality, the reliability of sampling methodology, and differences of analytical methods.

In order to navigate around these problems, and to address the scientific questions outlined above, I have carried out a melt inclusion (MI) study on mafic, intermediate and silicic magma compositions throughout the eruptive history of Santorini. MIs are small pockets of silicate melt that become trapped in a mineral during its growth from

a magma. Once fully encased by the growing crystal, an isolated MI acts as a closed system and thus avoids changes to its composition that would typically occur during open system differentiation of a magma (crystal fractionation, degassing, etc.). Therefore, MIs provide the best representations of real melt compositions and provide 'snapshots' of melt evolution, potentially recording the early-formed mantle-derived melts. In addition, I have also analyzed interstitial groundmass (GM) glasses of the products, which are the final composition of the melt upon eruption, after all differentiation processes have occurred.

In this thesis, I present a large, high-precision MI and GM dataset on mafic through silicic melt compositions and use these data for better understanding the generation and differentiation of magmas at Santorini. There are several important factors to note that bring originality to this thesis. Firstly, this dataset provides a large number of mafic MIs, including a subset of "primitive" (i.e. early formed, relatively unmodified mantle-derived melt) compositions, from many units throughout the >0.65 My eruptive history of Santorini. This allows for the study of the nature of parental magmas feeding the Santorini magmatic system, and to identify long-term temporal trends. This is the first study to examine primitive melt compositions at Santorini with tight, time-stratigraphic control. Secondly, this thesis ultimately provides a single dataset of MIs that have been prepared to the same standards and analyzed on the same instruments, ensuring a reliable, high-quality dataset to evaluate extremely small geochemical variations. Lastly, a part of this thesis has resulted in the compilation of all existing (1,100+) whole rock data analyses (major elements, trace elements and isotopes) from the literature that is made available, and has in fact already been shared, among current and future Santorini researchers. In this thesis, the findings from the MIs are linked in with a quality-sorted version of this whole rock database in order to integrate our discoveries with previous work and to expand our coverage to a greater number of eruptions.

It should be noted that the thesis plans evolved quite a lot during the course of the last three years. While a melt inclusion study was always intended to be a major part of this thesis, we had originally intended to pair melt inclusion trace elements with isotope geochemistry. In the original proposal, it was planned to carry out a U-Th disequilibria study on basaltic rocks in order to better understand the nature of basaltic reservoirs below Santorini. After our first field mission in October-November 2016, we realized

that we were not able to sample a sufficient number of basalts to be successful in this endeavor. We soon after turned our attentions to Sr isotopes and planned for a collaboration with Lorella Francalanci at the University of Florence to carry out Sr isotope microdrilling in plagioclase zones next to the melt inclusions to link trace element chemistry with Sr isotopes; however, due to a fire in their laboratory, we were ultimately not able to realize this work. Lastly, at the start of the last year of the thesis, we planned to analyze Sr isotopes of single MI-hosting primitive olivine crystals via dissolution to better understand the isotopic compositions of primitive Santorini melts. Samples were prepared and analyzed via scanning electron microscopy (SEM) to identify the most primitive olivines; however, due to unfortunate circumstances in my personal life and having run out of time, this was also not able to be realized. Therefore, this thesis is now entirely focused on trace element chemistry of melt inclusions in mafic, intermediate and silicic products from Santorini.

Outline of the thesis

The thesis is subdivided into seven chapters, with two introductory chapters (Chapters 1 and 2), a methodology chapter (Chapter 3), three results chapters (Chapters 4, 5 and 6) and a final conclusion chapter, with perspectives and suggestions for future work (Chapter 7). Chapter 4 and 5 are written as papers, while Chapter 6 is work in progress.

Chapter 1 is an introductory chapter reviewing important aspects of subduction zones and arc magmatism, as well as discussing the role of melt inclusions as a key tool in their study. The processes involved in the generation of subduction zone magmas will be summarized, with a particular emphasis on the origins of geochemical heterogeneity of arc magmas. Some basic geochemical concepts used later on in the thesis will be introduced.

In Chapter 2, I first present the geologic history and setting of the South Aegean Volcanic Arc before describing the local setting and eruptive history of Santorini Volcano. I review previous studies carried out on understanding the generation and differentiation of Santorini parental magmas, and I indicate how this study fits into prior work done on these topics.

Chapter 3 is a review of the methodologies used in this thesis. It discusses sample preparation, analytical methods and data correction procedures in detail. Melt inclusions in many cases require a suite of corrections before the analytical data can be

used. There are many different approaches used in the literature for the correction of melt inclusions, and in this chapter, I also justify the correction scheme that we have adopted, based on the needs of this thesis. These methodologies are necessarily repeated in the publication-style manuscripts of Chapters 4 and 5.

In Chapter 4, I present olivine-hosted melt inclusion data and focus on the least-evolved, "primitive" melt inclusions to ultimately study the nature of the mantle-derived primary melts and to examine temporal trends. Several methods are used to back-calculate primary melt compositions (i.e. the unmodified mantle melts that ultimately feed the Santorini magmatic system) from the primitive melt endmembers, and the geochemistry is used to evaluate how different subduction components influence their chemistry and variation. I also discuss the variation of primitive magmas in the context of time.

With the nature of the primary melts now better understood, I then focus on the relationship between the parental basalts and the silicic magmas of Santorini in Chapter 5. I carry out mass balance geochemical modelling to find out what crustal processes best reproduce the different lineages seen in the geochemical data. The high-resolution melt inclusion dataset allows us to observe data trends in detail, allowing for precise modelling of different lineages. The melt inclusion data are then linked with previously published whole rock data to investigate the origins of a previously observed but unexplained temporal trend in magma composition at Santorini.

In Chapter 6, the window of time is narrowed down to the last 80 ka of the eruptive history of Santorini to examine the build-up period to the large, caldera-forming Late Bronze Age (LBA) eruption of Santorini. This chapter is still work in progress owing to the tight 3-year limit to the thesis. In this chapter, we investigate a change in behavior in the system at ~55 ka, principally seen in the geochemistry of magmas. The most notable changes are indications of amphibole fractionation and the appearance of an anomalously high Ba magma component. We discuss possible explanations for these changes and how they may play a role in the build-up to the LBA eruption. Additionally, we speculate on a relationship between the increased scatter of MI and GM compositions and higher degrees of mixing and interaction among magma batches in a growing, increasingly heterogeneous, mushy plumbing system preceding the LBA eruption.

Chapter 7 brings together the results from Chapters 4, 5 and 6. I discuss the implications of these results for the model of the Santorini plumbing system, and then present some perspectives and suggestions for future work.

There are also two publications that accompany this thesis. The first paper (Flaherty et al. 2018) was published during the course of the thesis and combines results of my Master's research on the timescales of magma chamber assembly prior to the Late Bronze Age (LBA) eruption of Santorini with other data to give a comprehensive view of the sequence and timescales of pre-eruptive events in the magmatic system. The second paper (Schiavi et al. 2018) is a technique development study for improving dissolved H_2O quantification in glasses using Raman spectroscopy, led by Federica Schiavi at the Laboratoire Magmas et Volcans (LMV). We used Raman spectroscopy H_2O data gathered for some melt inclusions in this thesis, which had previously been analyzed by secondary ion mass spectrometry (SIMS) in Druitt et al. (2016), to show that the calibration gives comparable H_2O results to the SIMS-analyzed melt inclusions therefore confirming that the calibration works on natural glasses.

Roles of authors

Each result chapter of this thesis (Chapters 4, 5 and 6) is written in the format of an article manuscript, and in some cases, there have been input from colleagues; therefore, it is necessary to identify the roles of different contributors. In Chapter 4, the author list and order has been determined as T. Flaherty, T. Druitt, P. Schiano, O. Sigmarsson and L. Francalanci. The work and writing were done by T. Flaherty under the supervision of T. Druitt, with further guidance, in-depth discussions and suggestions for improvement by P. Schiano, O. Sigmarsson and L. Francalanci. In Chapter 5, the final author list has not been determined; however, the work and writing were completed by T. Flaherty under the supervision of T. Druitt, with some helpful discussions and suggestions from P. Schiano and O. Sigmarsson. Chapter 6, a work in progress, was written co-jointly by T. Flaherty and T. Druitt. Data acquisition, methods, results and some interpretation and subsequent discussion were completed by T. Flaherty, while T. Druitt also contributed a major part to the introduction, interpretation, discussion and preliminary model.

Chapter 1: Subduction zone magmatism and contribution of melt inclusion studies

1.1 Introduction

Arc volcanoes threaten large numbers of human populations and their livelihoods across the world. Scientists must study arc volcanoes in order to more accurately interpret signs of unrest, so as to ultimately mitigate the risks to the populations living around them. A significant component of understanding the behavior of a volcano comes from detailing its plumbing system and the processes that drive magma genesis, differentiation and transport through the crust. It is for this reason that many scientists dedicate their lives to the study of subduction zones, i.e. the tectonic setting that gives rise to arc volcanoes, and the relationship among subduction processes, arc magma chemistry and eruptive behavior.

Subduction, the process of recycling oceanic lithosphere back to the mantle at convergent plate boundaries, is a key concept in plate tectonic theory (Tatsumi and Eggins 1995; Stern 2002; Tatsumi 2005; Zheng 2019). At these convergent plate boundaries, the denser of two lithospheres sinks into the mantle (Figure 1.1). Generally speaking, two converging oceanic plates give rise to island arcs (e.g. the Aleutian Arc, Izu-Bonin-Mariana Arc), whereas continental arcs form where oceanic crust subducts beneath continental lithosphere (e.g. the Andean Volcanic Belt, the Cascades Volcanic Arc) (Winter 2013). While similar in many ways, the two type of arcs can differ greatly in their behavior and the types of magmas erupted (Pearce 1982).

Subduction zones and their magmatic systems are studied in many ways, including seismic tomography, gravity, electrical conductivity, surface heat flow and measurements of tectonic stress fields (Tatsumi and Eggins 1995). Experimental petrology is used to recreate different pressure-temperature (P-T) conditions in the crust and mantle. Lastly, the chemistry of erupted products and mass balance chemical modelling using major elements, trace elements and isotopic data enable us to reconstruct physical processes occurring from magma genesis to eruption (Allègre et al. 1977; Minster et al. 1977; Rollinson 1993; Janoušek et al. 2016).

It is necessary to understand the processes that occur during subduction before arc magmatism can be put into any meaningful context. It is also necessary to know what

is recycled along with oceanic lithosphere, such as oceanic crust and sediments, and what effects the subduction of each of these components brings to the geochemical signature associated with subduction-related magmas. This chapter will first discuss the features of subduction zones before focusing on the genesis of subduction zone magmas.

1.2 Subduction zone dynamics

1.2.1 Subduction zone geometry

Land features associated with subduction zones

The main features associate with a subduction zone include a trench, forearc region, magmatic arc (i.e. the volcanic or magmatic front) and back-arc basin (Figure 1.1) (Stern 2002). The trench is a surface expression of the collision zone where one plate overrides another. The forearc region exists between the trench and volcanic arc. An accretionary wedge of scraped-off rocks and sediments can occur near the trench in the forearc zone. Subduction-generated volcanism occurs at the volcanic front, which forms an arc more or less parallel to the trench. The backarc region exists behind the volcanic front, is often a site of extension and may experience magmatism due to decompression melting in a similar manner to mid-ocean ridge settings. Back-arc regions often develop basins and can be the sites of rift magmatism (Figure 1.1) (Taylor & Karner 1983).

Mantle wedge dynamics

The mantle wedge is the asthenosphere that lies between the subducting slab and the crust above and is a dynamic zone where arc primary magmas are generated (Figure 1.1) (van Keken 2003; Wiens et al. 2008; Zheng 2019). Due to viscous coupling between the slab and adjacent asthenospheric mantle, the subduction of oceanic lithosphere into the mantle induces convection in the mantle wedge (i.e. corner flow or trench parallel flow) between the slab and overriding crust (Alvarez 1982; Russo and Silver 1994; Peyton et al. 2001; Long and Silver 2008). The convecting mantle wedge is heterogeneous in temperature and behaves as a viscous fluid (Tatsumi and Eggins 1995).

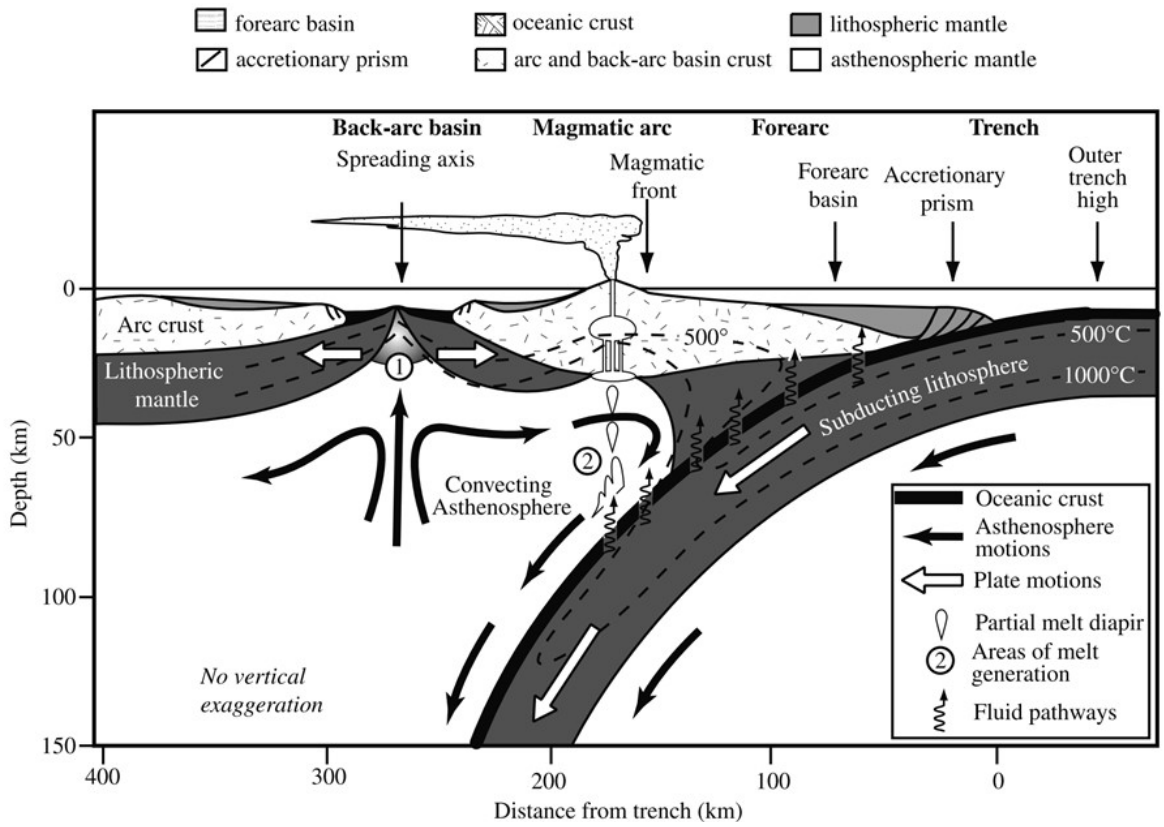

Figure 1.1: Cross-section through a subduction zone, highlighting important features discussed in the text. From Stern (2002).

Coupling between the plates and convective corner flow develops a stress gradient in the mantle wedge, where compression is located towards the trench and extension forms in the backarc region (Tsunakawa 1986; Tatsumi and Tsunakawa 1992). In the extensional regime of backarc settings, asthenospheric upwelling and decompression melting can occur, similar to mid-ocean ridge type processes (Figure 1.1) (McKenzie 1969; Toksöz and Bird 1977; Taylor and Martinez 2003; Pearce and Stern 2006).

Slab architecture and geometry

Generally speaking, subducting oceanic plates consist of (1) a top layer of subducted sediments (typically 200 to 700 m thick, potentially several kilometers) (Plank and Langmuir 1998), (2) a middle layer of oceanic crust (5 to 7 km of gabbro and basalt formed at fast spreading ridges, or <5 km of gabbros in peridotite formed at slow spreading ridges) (Ildefonse et al. 2007) and (3) up to ~100 km of lithospheric mantle (depleted peridotite), which all then descend into the asthenospheric mantle (Poli and Schmidt 2002; Spandler and Pirard 2013). The slab can be different ages, temperatures, thicknesses, mineralogies and buoyancies. These and other factors, such

as slab dip, the age of the slab, the rate of convergence, mantle wedge thickness and composition also play roles in what is erupted at the surface.

Mafic rocks in the subducting slab typically metamorphose into eclogitic gneiss, which are dense and impermeable, while sediments and serpentinite tend to become schistose. Due to rheological differences, there is typically a mélange zone (i.e. a "subduction channel") of rocks and fluids which are broken up and deformed (Spandler et al. 2008; Spandler and Pirard 2013). Sediments that overly the oceanic crust can be scraped off into the accretionary wedge; however, a lot of sediments, if not most, is subducted (Clift et al. 2009).

Both the down-going slab and its accumulated sediments contain a large amount of water. As the slab descends, it encounters higher pressures and temperatures, which initiate dehydration. Three main stages of dehydration are expected at different P-T conditions during subduction: (1) serpentine dehydration at ~600°C, (2) amphibole and/or chlorite breakdown and dehydration at 3.5 GPa (110 km depth) at the amphibolite-eclogite transition and (3) phlogopite (or other hydrous minerals such as lawsonite and phengite) breakdown at ~6.0 GPa or ~200 GPa (Tatsumi and Eggins 1995; Spandler et al. 2003).

High-pressure mélange rocks form from the mixing of different components (sediments, altered oceanic crust, ultramafics) at the interface between the slab and mantle. A mixture ascends upwards probably as partially molten diapirs to the mantle source of arc primary magmas (Tatsumi and Eggins 1995; Nielsen and Marschall 2017; Codillo et al. 2018). The introduction of subduction components (hydrous melt, supercritical fluid, etc.) into the mantle wedge alters the chemical and physical conditions of the peridotite, lowering the solidus of the mantle peridotite and promoting hydrous flux melting.

Slab rollback

A common occurrence in many volcanic arcs is oceanward (opposite direction to subducting plate motion) trench migration due to slab rollback (Elsasser 1971; Garfunkel et al. 1986; Stegman et al. 2006) as a consequence of trench-slab anchoring, mantle flow dynamics and differential plate motions and/or speeds. Slab rollback can contribute to the formation of backarc regions by inducing trench migration, therefore causing extension in the overriding plate.

Slab tearing and breakoff

Slab tears, windows and complete breakoff can also occur after a slab has entered the mantle and becomes segmented in some way, which has been observed in subduction zones around the world (Wortel and Spakman 2000; Miller et al. 2006; Rosenbaum et al. 2008). Slab tearing can occur due to different rates of collision and rollback across the subduction zone (Govers and Wortel 2005; Rosenbaum et al. 2008). Slab tearing can influence and change the dynamics of asthenospheric mantle flow below the subduction zone and therefore have an effect on subduction zone magmatism.

1.3 Petrology and geochemistry of arc magmas

1.3.1 General geochemistry concepts

Major elements, trace elements and isotopes are the main geochemical tools for investigating arc volcanism. Major elements are typically reported as major element oxides. Trace elements are generally defined as elements which make up < 0.1 wt. % of a rock (Rollinson 1993). They generally enter minerals within a rock by substituting major elements. Although they are present in very small quantities, they constitute a powerful tool to understand igneous rocks. An element can be described as compatible or incompatible in a rock or mineral based on whether it is of a suitable charge and/or size to be included in a solid phase, or whether it is more likely to be rejected from the solid phase and rest in the melt. The partition coefficient k_D, is a measure of compatibility and for a given trace element is defined as $k_D = C_{mineral}/C_{melt}$. If $k_D > 1$, a trace element is compatible and is welcomed into a crystal structure. If $k_D < 1$, a trace element has a charge and/or size that makes it unsuitable to be included in a crystal structure and it is thus referred to as incompatible. If $k_D = 1$, there is an equal abundance of the trace element partitioned between the mineral and melt.

Since a rock is made of many minerals and trace elements may differentially partition into a rock's mineral constituents, a bulk partition coefficient (D) is often used when talking about a rock rather than a mineral. This takes into account the abundance of different minerals in the rock and the compatibility of a trace element into each of these minerals. Partition coefficients are determined by studying natural systems or experimentally. Essentially one measures abundances in a mineral and in a neighboring glassy matrix. Controls on compatibility and thus trace element

abundances include composition (the most important control), temperature, oxygen fugacity, etc. (Rollinson, 1993).

There are several groups of trace elements that exhibit similar behavior. Rare earth elements (REEs; a.k.a. lanthanides) are very useful to igneous geochemists. They are generally trivalent, with some exceptions such as Eu and Ce, which can exist in other valence states as well. The REEs can be further subdivided into light rare earth elements (LREEs), middle rare earth elements (MREEs) and heavy rare earth elements (HREEs). Although the rare earth elements have very similar overall characteristics, these further subdivisions are able to be fractionated from one another, which can provide clues about processes and crystallizing phases in the history of a magmatic suite. Incompatible elements can also be subdivided based on their ionic potential. Large ion lithophile elements (LILEs) are elements with a large radius but low charge. High field strength elements (HFSEs) have small ionic radii but high charge. Elements with lower ionic radii and lower ionic charges tend to be more compatible. LILES are fluid-mobile, meaning they will preferentially enter a fluid phase if present, while HFSEs are generally fluid-immobile. Some elements may be either HFSE or LILE depending their valence state (i.e. their behavior is redox-controlled) (Keppler 2017).

Separate differentiation trends emerge in arc settings based on whether there is an iron-depletion (calc-alkaline) or enrichment (tholeiitic) trend (Miyashiro 1974; Chin et al. 2018). One hypothesis is that tholeiitic magmas are associated with dryer, less oxidized mantle sources and/or lower pressure melting, while calc-alkaline magmas are derived from a more hydrated, more oxidized mantle source (due to oxidized nature of slab input) and/or higher pressure melting (Grove and Baker 1984; Sisson and Grove 1993b; Chin et al. 2018). Other hypotheses for the origin of the different magma series are related to assimilation and the degree of 'thermal maturation' of a system (Myers et al. 1985; Hora et al. 2009). Magmas that remain stagnant in the crust for longer periods of time undergo more interaction with the crust and modification that leads to calc-alkaline trends and magmas with a shorter overall residence time in the crust, coming through the crust in periods of higher average flux, would be more prone to have a tholeiitic character (Myers et al. 1985). This model suggests difference in the character of volcanic output, even from adjacent systems, could be due to the degree of thermal maturation rather than crustal thickness. Hora et al. (2009) also argues that Fe-enrichment and tholeiitic vs. calc-alkaline magmatic character depends on thermal

maturation and flux, with differing transport rates and overall throughput of magmas through the crustal plumbing system playing a role in their resulting composition.

Miyashiro (1974) proposed calc-alkaline and tholeiitic fields on the basis of a plot of FeO*/MgO versus SiO_2. The equation used by Miyashiro for the dividing line between the calc-alkaline and tholeiitic series is:

$$SiO_2 \text{ (wt \%)} = 6.4 \times (FeO^*/MgO) + 42.8 \qquad \text{(Equation 1.1)}$$

where calc-alkaline and tholeiitic trends fall above and below this line, respectively. Magma series can be differentiated on a ternary AFM diagram plotting which plots alkalis ($Na_2O + K_2O$), FeO^T and MgO (Irvine and Baragar 1971).

1.3.2 Overview of petrology of arc magmas

1.3.3 Geochemistry of arc magmas

Arc magmas have a typical geochemical signature that distinguishes them from other tectonic settings. In general, high field strength elements (HFSEs; e.g. Nb, Ta, Zr, Hf) are characteristically depleted relative to large ion lithophile elements (LILEs) and rare earth elements (REEs), which is not seen in MORB and OIB signatures. This has been interpreted two main ways: (1) as a HFSE-bearing residual phase such as rutile or sphene in the mantle wedge that keeps the HFSE (Hermann and Rubatto 2009; Skora and Blundy 2010), or (2) that the HFSEs are conservative and reflect the composition of the mantle wedge, while the LILE and REEs are selectively enriched from a "subduction component" (Pearce 1983; McCulloch and Gamble 1991; Pearce and Peate 1995). The subduction component has higher LILE/HFSE and LREE/HFSE ratios than found in mantle-derived melts from OIB settings, MORB settings, etc. There have been recent studies that suggest HFSE mobilities may approach those of LILEs and LREEs at high enough pressures and fluid solute contents (Brenan et al. 1995; Stalder et al. 1998; Kessel et al. 2005).

1.4 The generation of arc magmas

1.4.1 What are the sources of arc magma geochemical signatures?

There are three main sources of arc magma heterogeneity: (1) Mantle heterogeneity, i.e. the composition of the mantle wedge before subduction, (2) the contribution from the subducted slab via aqueous fluids, sediment melts or supercritical fluids and (3) differentiation processes as mantle melts ascend through the crust (fractional crystallization, assimilation, mixing).

1.4.2 Mantle wedge compositions

There are many different types of mantle reservoirs proposed. The depleted mantle (DM or DMM) is an incompatible element depleted source that is the typical source for mid-ocean ridge basalts (MORB), the most voluminous basalt type erupted on Earth (Salters and Stracke 2004; Workman and Hart 2005). Enriched mantle (EM), HIMU (high-μ), FOZO (focus zone) and C (common component) are other reservoirs mentioned and are often associated with oceanic island basalts (OIB), i.e. those formed in ocean basins but not along plate boundaries and tend to have high incompatible element ratios. These reservoirs, or mixtures of these reservoirs, manifest as different basalt types when erupted at the surface.

While MORB is the most voluminous basalt type, different types of MORBs are proposed. Normal (N-MORB) is statistically the most common MORB erupted (Gale et al. 2013). This type of MORB is depleted in incompatible elements, depleted in LREEs, low in total alkalis and has non-radiogenic Sr & Pb (though it has radiogenic Nd), and is typically associated with "normal" oceanic ridges (Sun et al. 1979; Tarney et al. 1980; Cohen and O'Nions 1982). Enriched MORB (E-MORB) and depleted MORB (D-MORB) also exist but are less common and can be thought of more like endmembers of a spectrum of MORB compositions (Gale et al. 2013). MORB has elevated abundances of incompatible elements and slightly different Sr & Nd isotopes (though Pb ratio may be much higher) than MORB. E-MORB can resemble OIB; however, E-MORB is less alkali-rich and follows a different iron-enrichment pattern during differentiation.

A large percentage of the mantle (up to 80%) is thought to be processed at mid-ocean ridges and thus has a DMM composition, thus this composition probably makes up a large proportion of the volume of at least the upper mantle below subduction zones. Many models argue mantle wedges are a depleted MORB composition, which is thought to make up a large part of the upper mantle (e.g. Allègre 1982); however, there can be mixing of DMM with other reservoirs or mantle components, so the composition of the mantle below subduction zones can be very heterogeneous, and incompatible element enriched regions are thought to exist in some shallow parts of the mantle (Cousens et al. 1995). Furthermore, prior episodes of subduction can deplete the mantle even further. When assessing the geochemistry of subduction zone magmas, it is necessary to investigate this, as it is a common source of arc magma heterogeneity.

1.4.3 Slab components

Contribution from the slab to the mantle wedge may range from aqueous fluids to variably hydrous granitic melts to supercritical fluids at high pressures (Kessel et al. 2005). Collectively, the different types of contributions from the slab are referred to as the "slab component" to arc magmas. In this thesis, the term "compatibility" describes solid-melt element partitioning, while "mobility" describes the degree to which an element readily enters an aqueous fluid phase.

Incompatible elements may differ in their mobility in aqueous fluids as a function of their ionic potential, ranging from highly fluid mobile (e.g. Cs, Rb, Ba, Sr, Pb, U) to less fluid mobile (e.g. Th, La, Nd), to virtually fluid-immobile (e.g. Sm, Dy, Yb, Lu) (Hawkesworth et al. 1993; Kessel et al. 2005; Spandler and Pirard 2013; Keppler 2017). In the case of hydrous melts, the behaviors of certain elements change due to compounding effects of mobility in fluids and incompatibility in melts (e.g. LREE and Th which are less fluid mobile, but rather incompatible, readily enter hydrous melts). Elements that are both incompatible and non-mobile due to their high ionic potential (e.g. Nb, Ta, Ti, Zr, Hf, HREE) are considered to be 'conservative' or non-mobile in aqueous fluids and incompatible when dealing with hydrous melts (Tatsumi et al. 1986; Keppler 2017), although their relative immobilities and incompatibilities can change with temperature and pressure conditions of the slab (Manning 2004; Kessel et al. 2005).

Slab-derived aqueous fluids

Dehydration of sediments or the slab (leaving an eclogitic residue) produces aqueous fluids which can ascend into the mantle wedge, induce flux melting and impart a characteristic geochemical signature in the primary mantle melts that subsequently form. Serpentinite in the down-going slab is expected to be a big contributor of fluids released by the slab into the mantle wedge (Ulmer and Trommsdorff 1995). A typical 'aqueous fluid signature' could be described as the following: High fluid-mobile to fluid-immobile incompatible elements (Ba/Th, Ba/Nb, Ba/La, U/Th, Sr/Ce, Pb/Ce, Pb/U, etc.) and high $^{238}U/^{230}Th$ disequilibrium (Ayers 1998; Kessel et al. 2005; Wehrmann et al. 2014). Ba, U, Pb and Sr are particularly mobile, even at low temperatures (Kessel et al. 2005). Th and LREEs are less fluid-mobile (i.e. may become mobile at higher temperatures) and the MREEs and HREEs are virtually fluid-immobile (Kessel et al. 2005; Wehrmann et al. 2014). High fluid-mobile to fluid-immobile element ratios are associated with high hydrous fluid flux, which occurs due to high amounts of hydrous flux melting. Lower ratios of these elements may suggest lower melting and/or other types of metasomatic agents.

Slab-derived sediment melts

Sediment metasomatism of the mantle wedge can occur via the dehydration and/or melting of subducting sediments (Johnson and Plank 2000). High Th/La Th/Nb, Th/Nd, Rb/Nb, etc. are common proxies for sediment melts (Elliott et al. 1997; Johnson and Plank 2000; Plank 2005; Keppler 2017). Plank and Langmuir (1998) indicate that there is generally some correlation between the chemistry of subducted sediments and that of the arc basalts formed by partial melting of metasomatized mantle. Some notable examples where the geochemistry of arc magmas can be explained by sediment melts include the Aleutians (George et al. 2003), the Tonga-Kermadec Arc (George et al. 2005), Arigin Island in the Mariana Arc (Elliott 2003) and the Aegean Arc (Francalanci et al. 2005b; Vaggelli et al. 2009; Bailey et al. 2009; Francalanci and Zellmer 2019).

^{10}Be is formed from spallation of atmospheric O and N and readily is incorporated into sediments (Hawkesworth et al. 1993). Boron is highly concentrated in sediments and can also be used to study the subducted sediment component; it is somewhat analogous to using ^{10}Be, as it is very concentrated in sea water and thus is absorbed into sediments (Morris et al. 1990). ^{10}Be can be used as a tracer of subducted sediment in island arcs

(Tera et al. 1986; Morris and Tera 1989). Pelagic sediments have very high Ba (e.g. Ba/Ta, Ba/Rb, Ba/Th, Ba/La; Boström et al. 1973; Hole et al. 1984) and negative Ce anomalies, which could be translated into a geochemical signal in arc magmas.

Slab-derived supercritical fluids

There is also the possibility of supercritical fluids, which can mobilize almost all incompatible elements (Kessel et al. 2005). In contrast to a hydrous melt which may only contain a few weight H_2O, a supercritical fluid is composed of both a melt and fluid in significant amounts (each being between ~30-70%) coexisting at pressures and temperatures that surpass a critical point (Kawamoto et al. 2012; Ni et al. 2017). Some authors have tried to constrain the pressure-temperature conditions for the existence of supercritical fluids, but there are still many uncertainties about not only the conditions of formation but also the inherent properties of such supercritical fluids themselves (Ni et al. 2017).

Other possibilities

At special or extreme conditions, melting of the subducting basaltic oceanic crust itself can occur and generate adakitic melts (Defant and Drummond 1990; Drummond et al. 1996; Martin et al. 2005; Castillo 2012). Adakites by their original geochemical definitions are silica-rich magmas and have distinctively high Sr/Y and La/Yb (Defant and Drummond 1990, 1993). There is, however, controversy over whether there can be other sources of adakitic magmatic signatures (Castillo 2012).

1.4.4 Origin of the Nb-Ta anomaly

A negative Nb-Ta anomaly is also characteristic of subduction zones. There are several hypotheses for the origin of this anomaly. Keppler (1996) and Kessel et al. (2005) suggest poor solubility of Nb and Ta in aqueous fluids causes low abundance of Nb and Ta in arc magmas. Rutile, however, is commonly found as an accessory phase in metamorphic rocks, and it can accommodate HFSEs in high concentrations, especially Nb and Ta. Therefore, the existence of rutile in residual subducted eclogite or sediments is commonly used to explain the depletion of Nb and Ta seen in arc magmas (Rudnick et al. 2000). Nb and Ta are compatible in rutile, with partition coefficients in the range of 100-500 (Foley et al. 2000). Nb and Ta are considered to be two of the most fluid-immobile elements, so Nb/Ta ratios in subduction zones should reflect, and

be controlled only by, the metasomatized mantle wedge composition (Münker et al. 2004).

1.5 Differentiation of arc magmas

1.5.1 The nature of continental crust

Continental lithosphere includes both the continental crust and the lithospheric mantle, i.e. the non-convecting part of the upper mantle. Lithospheric mantle is denser than the asthenosphere and is typically zoned from lherzolite to harzburgite (Irifune 1993; Davies 1999; Stern 2002). The continental crust is zoned and can be subdivided into upper and lower crust. The upper crust typically contains shallow level of sedimentary and volcanic rocks underlain by felsic to mafic igneous intrusives and low- to medium grade metamorphic rocks (e.g. gneisses, schists, amphibolites and marbles) towards the upper-lower crust boundary (Wedepohl 1995). The lower crust is expected to mostly contain felsic to mafic high-grade metamorphic rocks such as granulites (Rudnick and Fountain 1995; Wedepohl 1995). The Mohorovičić discontinuity (i.e. Moho) is defined as the boundary between the crust and mantle. The subcontinental, upper mantle lithosphere sits between the continental crust and asthenospheric mantle (Griffin et al. 1999). The lithosphere thins in sites of extension and rifting, where decompression melting induces adiabatic rise of asthenospheric mantle.

1.5.2 Overview of transcrustal magma storage systems

Melts that are produced in the mantle ascend through the mantle wedge in a diapiric fashion and into the crust, where they are stored, differentiated, and further transported until they reach the surface and erupt at an arc volcano. The plumbing system of arc volcanoes differ in their forms due to many factors. Most plumbing systems can be divided into deep plumbing systems and shallow plumbing systems (Tibaldi 2015).

1.5.3 Deep crustal differentiation

Generally speaking, magma differentiation occurs in two very broad regions in subduction zone settings: (1) at the base of the crust, in 'MASH zones' (Hildreth and Moorbath 1988) or 'deep crustal hot zones' (Annen et al. 2006) and (2) in upper crustal magma reservoirs that go on to feed volcanoes. The Melting, Assimilation, Storage and

Homogenization (MASH) model (Hildreth and Moorbath 1988) states there is a mixing zone at the base of the lower crust where melts differentiate based on density with more silicic magmas rising to the top while mafic-ultramafic residuals/cumulates remain at the base of the crust or sink back into the mantle (Hildreth and Moorbath 1988; Saleeby 2003). Another proposal is the existence of a deep crustal hot zone (Annen et al. 2006; Klaver et al. 2018) where basaltic sills are injected and crystallize; basalt differentiation can be accompanied by simultaneous partial melting of the crust, but this is not necessary.

High alumina basalts (Al_2O_3 > 16.5 wt%) are commonly found in arc settings and usually have SiO_2 < 54 wt% and <6-7 wt% MgO (Crawford et al. 1987; Sisson and Grove 1993a). It is proposed that most high-Al basalts are not primary and are in fact differentiated basalts (Sisson and Grove 1993a). Primary magmas can stall at the base of the crust where the reach a density equilibrium and fractionate an olivine ± clinopyroxene (without plagioclase, in the presence of H_2O) assemblage to create differentiated high Al basalts that ascend into the crust (Sisson and Grove 1993a; Kay and Kay 1994).

Silicic magmas produced in the lower crust can then potentially make themselves available for transfer to the upper crust where they can form pre-eruptive reservoirs.

1.5.4 Upper crustal magma differentiation and storage

Sizable upper crustal magma reservoirs are built incrementally over long periods of time through periodic additions of new melt batches, probably emplaced horizontally as sills at the base of a pre-existing magma reservoir, over time amassing in a stack-like fashion (Annen 2009). Upper crustal magma reservoirs can lose heat to the surrounding rock and crystallize if not sustained by a continual heat source; therefore, the frequency and volume (i.e. flux) of new incoming magma batches govern the nature, mobility and eruptibility of a magma reservoir.

The crystal mush paradigm, which can explain how large magmatic systems are maintained over geologically long timescales, acts as a very important linkage between plutonism and volcanism (Bachmann and Bergantz 2008; Dufek and Bachmann 2010; Huber et al. 2010; Cooper and Kent 2014). Magmas stored in near-solidus conditions may be defrosted and remobilized by new magmatic intrusions or gas fluxes which cause interstitial melt to be extracted from crystal mush (Bachmann and Bergantz

2008; Cooper and Kent 2014; Menand et al. 2015). Melts can then (in variable ways; Kennedy et al. 2018) accumulate to form large eruptible volumes, sometimes over durations of months to decades (Druitt et al. 2012; Gualda and Sutton 2016; Flaherty et al. 2018). Melt-rich lenses form in a reservoir providing the reservoir is sufficiently porous to allow melt to assemble (Solano et al. 2012) and are probably transient features, supported by thermodynamic arguments and geophysical evidence showing a global lack of large melt-rich reservoirs below active volcanoes.

1.5.5 Origins of voluminous intermediate magmas

In island arcs, the average composition of the crust is basaltic (Debari and Sleep 1991). The average composition of the continental crust on the other hand is andesitic (Taylor and McLennan 1985; Rudnick and Gao 2003) due to the more silicic rocks such as granites found in the upper crust. Basalts can often be a rare or absent composition erupted at arc volcanoes due to the long passage through the continental crust. Primary or near-primary melts are therefore hard to find. Intermediate (andesite to dacite) compositions are ubiquitous among arc volcanoes around the world, in both continental and oceanic settings. Magmas of andesitic composition are often erupted in large volumes as well. So, there is a debate on how and where large volumes of intermediate to silicic magmas are generated in the crust.

A common proposal is that mafic magmas evolve by fractional crystallization to produce andesites (Bowen 1919; Gill 1981; Greene et al. 2006; Jagoutz 2010). This entails that mafic cumulates form as evolved melts are extracted from a crystallizing magma (Greene et al. 2006; Müntener and Ulmer 2006; Jagoutz 2010). There is both field and geophysical evidence for large mafic cumulates at the base of arc crust that support this mechanism of andesite genesis.

Another proposition is the partial melting of crustal material. Ascending mantle-derived basaltic melts may either underplate the crust or intrude the crust in the form of dykes. In the case of underplating, the transfer of heat and volatiles could be sufficient to partially melt the lower crust, depending on temperatures and periodicity (Petford and Gallagher 2001). Partial melting of mafic crust can produce andesitic melts (Petford and Atherton 1996), although some models (Dufek and Bergantz 2005) show that it is difficult to produce large amounts of hydrous magmas through partial melting of the crust.

Lastly, another proposition is the mixing of mafic and silicic endmembers to produce intermediate magmas. Magmas of all compositions can coexist in the same magmatic system over time but also in space (e.g. quenched mafic enclaves can occur in rhyolites, for example). Mafic and felsic magmas can cohabit the same space or be in proximity—leading to the possibility of mixing. Mixing between felsic and mafic magmas would result in an intermediate andesitic composition. In this case, an argument must be made for the origin of a felsic endmember. It could be a fractionated melt, or a rhyolite produced through partial melting of crust. At the base of continental arc crust, mantle-derived basaltic melts may interact with granitic melts in order to form andesite (Hildreth and Moorbath 1988).

Disequilibrium textures and mixed crystal populations are commonly observed in andesites, and these are indicators that they may mainly result from mixing processes (Anderson 1976; Eichelberger 1978). Using a compilation of melt inclusion data from the literature on arc volcanoes, Reubi and Blundy (2009) show that andesitic melts are in fact uncommon at arc volcanoes. While this could in part be due to a bias stemming from the melt inclusion approach, it provides an argument that mixing and homogenization play a large role in producing andesite bulk rock compositions.

Deep-formed silicic melts in MASH zones or deep crustal hot zones could then go on to mix with basalts or less evolved magmas to generate large volumes of hybridized andesites (Reubi and Blundy 2009). It is a matter of debate how silicic melt batches leave the lower crustal MASH or hot zone; it could be sporadic, regular, or could match the rate of mantle melt input into the lower crust. Klaver et al. (2018) suggests the felsic mixing endmember could be formed through a peritectic melt reaction where partial melting of wehrlite (ol + cpx) cumulates forms amphibole, and the amount of amphibole formed controls the silica content of the resulting melts.

1.6 Melt inclusions in the study of arc magma genesis

1.6.1 Traditional role of whole rock analyses

Whole rock analyses have traditionally been a standard for studying rock geochemistry. Whole rocks can be analyzed for major elements, trace elements and isotopic compositions. However, with the recognition that magmas can carry a 'crystal cargo' that could potentially include minerals from many different sources (Bachmann

and Bergantz 2004; Davidson et al. 2007b; Ganne et al. 2018), some researchers are turning to other means to obtain the best representation of real melt compositions. Melt inclusions have become a widely used tool in recent studies.

1.6.2 What are melt inclusions?

Melt inclusions are small pockets of melt which are trapped within crystals (Figure 1.2) (Lowenstern 1995). They provide snapshots of melt composition over the course of the magma evolution, whereas whole rock and matrix glass analyses represent only end products of potentially long cycles of magma mixing, crystal fractionation and contamination by antecrystic and xenocrystic debris (Roedder 1984; Sobolev 1994).

Melt inclusions can be used in a number of ways to learn about arc magmatic systems. Olivine-hosted melt inclusions are useful for many reasons. Firstly, due to olivine's early appearance during the crystallization of mafic magmas, the melt trapped by this phase at depth can be relatively unmodified (i.e. primitive) and can give information about the source of primary magmas that is often lost during further chemical differentiation. Secondly, olivine crystals contain very small amounts of elements that are often of interest (i.e. incompatible trace elements) within the melt inclusion, which means that diffusion of elements into the host mineral will be negligible; thus, original

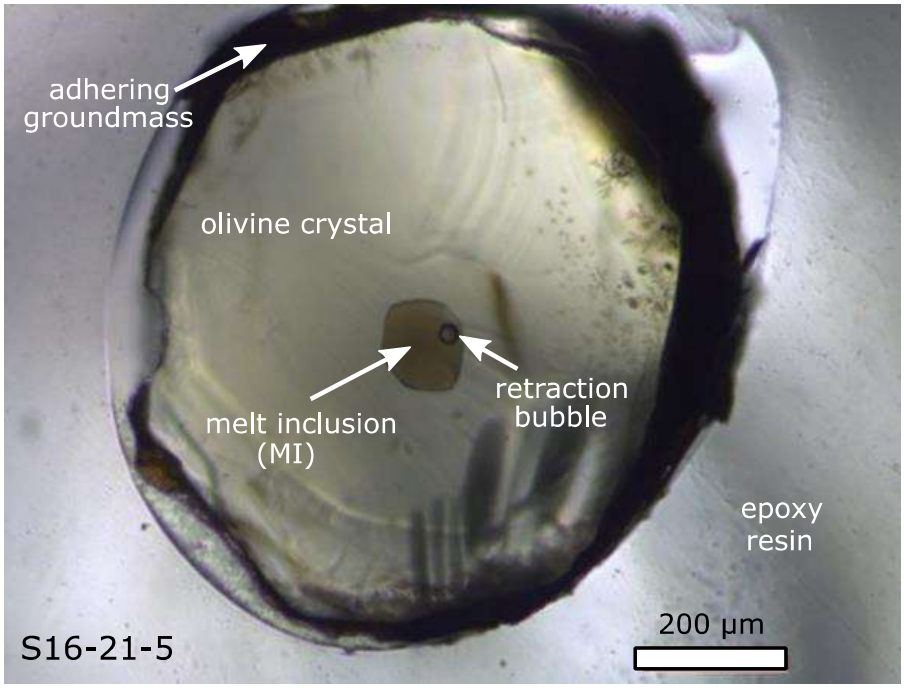

Figure 1.2: A glassy melt inclusion in an olivine host crystal.

melt compositions are more likely to be retained (Qin et al. 1992). For these reasons, olivine-hosted melt inclusions are widely used; however, other minerals can also be used to learn about magmatic systems. Plagioclase-hosted inclusions can record a wide range of melt compositions due to its ubiquity in magmas of different stages of evolution. Calcic plagioclase crystals may trap mafic compositions, but due to their later appearance compared to olivine, are not likely to contain primitive melt inclusions.

Primary melt inclusions are those trapped during crystal growth, while secondary inclusions are trapped after original crystal growth has terminated (for instance, melt trapped along fractures in the crystal) (Roedder 1984). At the time of trapping, most melt inclusions are incorporated as a silicate liquid, but they can undergo various phase changes depending on cooling conditions (Roedder 1984). If cooling is fast enough that quenching is effectively achieved, an inclusion will remain glassy; however, if cooling is slow, the inclusion may partially or even completely crystallize. Also, if originally glassy inclusions are subjected to high temperatures for extended periods of time, they may devitrify. Vapor phases and fluids (such as a saline liquid) may also "unmix" from the inclusion during cooling.

Silicate hosts of melt inclusions are incompressible (Roedder 1984); thus, a melt inclusion theoretically acts as an isochoric system in which volume does not vary (Lowenstern 1995). Consequently, silicate melts have a high $\Delta P/\Delta T$ (generally around 0.5-1.5 MPa/°C), meaning that pressure changes rapidly with small temperature changes inside the inclusion (Lowenstern 1995). During cooling and depressurization, a melt may become saturated with a volatile phase and form a bubble ("retraction bubble" or "shrinkage bubble") (Figure 1.2), which is compressible and changes the thermodynamic properties of the inclusion. Eventually the inclusion will pass through the glass transition temperature. Melt inclusions can fracture and leak ("decrepitate") after entrapment (Tait 1992). If temperature is held constant, the internal pressure of the melt inclusion remains approximately that of entrapment; therefore, during isothermal decompression, a large pressure gradient can be formed between the inclusion and the crystal surface.

1.6.3 Post-entrapment modifications

Melt inclusions are subject to a number of post-entrapment modifications, including crystallization on the inclusion walls during cooling (because crystallization is favored at the phase boundary between olivine and melt, rather than nucleating a free daughter crystal) and diffusive re-equilibration. A large number of studies outlining correction procedures to overcome the difficulties surrounding melt inclusions have led to an increased confidence that melt inclusions are in fact reliable recordkeepers of geochemical information, and as such melt inclusions have gained much popularity. Other processes include crystallization of daughter minerals in the interior of the melt inclusion, devitrification of originally glassy melt inclusions held at high temperatures, and chemical alteration by fluids. Crystallized and devitrified inclusions can be experimentally reheated, then quenched to return back to a homogeneous glass. Melting of olivine during melt inclusion homogenization experiments is not uncommon (Danyushevsky et al. 2000).

1.6.4 Justification of using melt inclusions as faithful recorders of melt composition

It is recognized that crystals growing from magma are immediately surrounded by 'boundary layers' where differential diffusion rates of elements at the crystal interface cause short-scale compositional gradients not representative of the melt (Watson et al. 1982). As melt inclusions are trapped at the crystal-melt boundary, there is a concern that melt inclusions do not actually represent real melt compositions. However, several studies (Lowenstern and Mahood 1991; Bacon et al. 1992; Dunbar and Hervig 1992) have demonstrated that melt inclusions do indeed reflect real melt compositions and are little affected by boundary layer effects. Anderson (1974) concluded that boundary layer effects are absent in melt inclusions larger than 25 μm in diameter; this is not far from the minimum inclusion size for current analytical techniques (e.g. EMPA, LA-ICP-MS), thus the boundary layer effect is likely not to be a problem.

There is also a question of bias. Bias may come from the natural system, considering that many stages of melt composition may be missing, and this may influence interpretation of the data. Sampling bias can arise due to a number of stages in the sample preparation stage, such as choosing only certain minerals or only selecting melt inclusions of certain properties (for example, choosing large inclusions over small

ones, or glassy inclusions over crystallized ones). Care must be taken to identify and potential biases and to address them in data interpretation.

Chapter 2: The Aegean Arc and the Santorini magmatic system

2.1 The Aegean Arc

2.1.1 Development and tectonics

The Aegean region (Figure 2.1) is related to subduction zone activity with a complex and tectonic stress regime that heavily influences volcanic activity along the arc. In order to provide a context for investigating and understanding the geochemistry of Santorini magmas, the local and regional tectonics and geodynamics of the Eastern Mediterranean and how the subduction zone geometry and processes influence the magmatism at Santorini and other active volcanic centers along the arc will first be discussed.

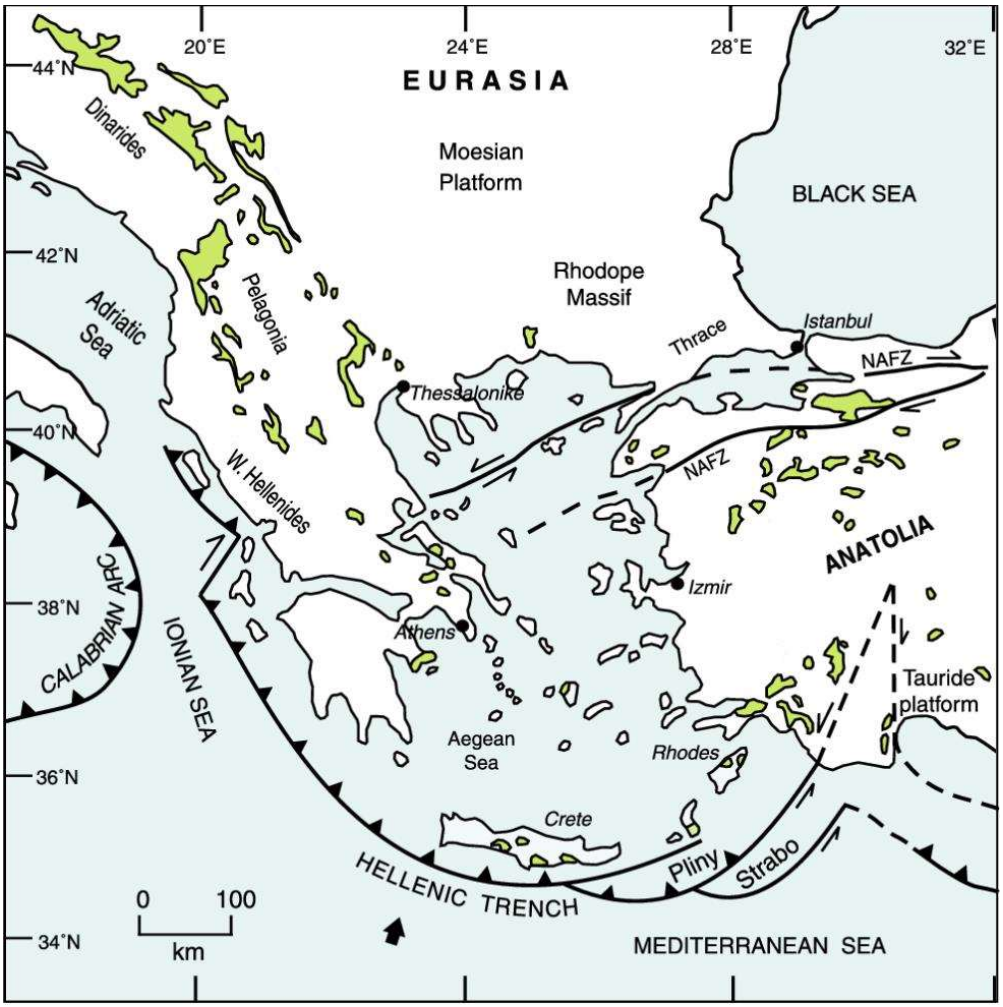

Figure 2.1: Map of Greece and the Aegean region, showing some of the main structural features discussed in the text. Ophiolites are shown in green. NAFZ = North Anatolian Fault Zone. Modified from Ghikas et al. (2010).

The Eastern Mediterranean Sea represents the last remains of the Tethys Ocean, which mostly disappeared as the African and Eurasian plates collided and subduction commenced. Northward subduction of Tethyan crust during the Jurassic led to the creation of the Hellenide Complex (located in modern-day southwestern mainland Greece; Figure 2.1), which was formed due to the accretion of different terranes onto the Eurasian mainland and consists mainly of stacked nappes (van Hinsbergen et al. 2005). After continental collision was underway, the volcanic arc shifted southward starting around the Miocene and the forearc (e.g. Crete) was uplifted (ten Veen and Kleinspehn 2002; Le Pichon et al. 2002; van Hinsbergen et al. 2005; Ring et al. 2010; Klaver et al. 2015). Continued northward subduction of the Tethyan oceanic crust has produced island arc volcanism at the southern border with Eurasia ever since the Oligocene, and the volcanic front has shifted southward over time until it reached its current position today (Vougioukalakis et al. 2019).

Back-arc extension in both the Tyrrhenian and Aegean Seas is due to slab rollback in the Neogene, and the slab rollback is responsible for extension, rotation and slab segmentation all along the length of the Mediterranean (Le Pichon and Angelier 1979). The Tethyan subduction zone was split into two branches due to rotation of microplates within the Eurasian crust (Robertson and Grasso 1995), creating two separate subduction zones: the Aeolian Arc to the west and the Aegean Arc to the east; both having volcanism starting in the Pliocene.

Following a period of roll-back induced alkaline volcanism, modern tholeiitic to calc-alkaline volcanism along the Aegean Arc began around 4.7 Ma (Francalanci et al. 2005b; Fytikas and Vougioukalakis 2005; Pe-Piper and Piper 2005; Francalanci and Zellmer 2019; Vougioukalakis et al. 2019). The Aegean region has had an extensional regime since the Pliocene due to slab rollback (Mercier 1981; Papadopoulos et al. 1986; Wortel and Spakman 2000; Özbakır et al. 2013). The subduction angle ranges from 10° to 30°, generally increasing towards the east (Kalogeropoulos and Paritsis 1990; Jackson 1994; Papazachos 2019).

The Aegean Arc can be subdivided into six main structural features: (1) the Mediterranean ridge formed by flexing of subducting sea floor, (2) the Hellenic trench, (3) the outer, non-volcanic Cretan arc, (4) the fore-arc basin Sea of Crete, (5) the active Aegean volcanic arc and (6) the extensional back-arc basin comprising the Northern Aegean Sea (Biju-Duval et al. 1974; Mitropolous et al. 1987). A large accumulation of

sediment (~8 km) covers the Hellenic trench, which is thicker than most other arc trenches (Clift and Vannucchi 2004; Woelki et al. 2018). It is believed that a thick layer of sediment is subducted (Le Pichon and Angelier 1981).

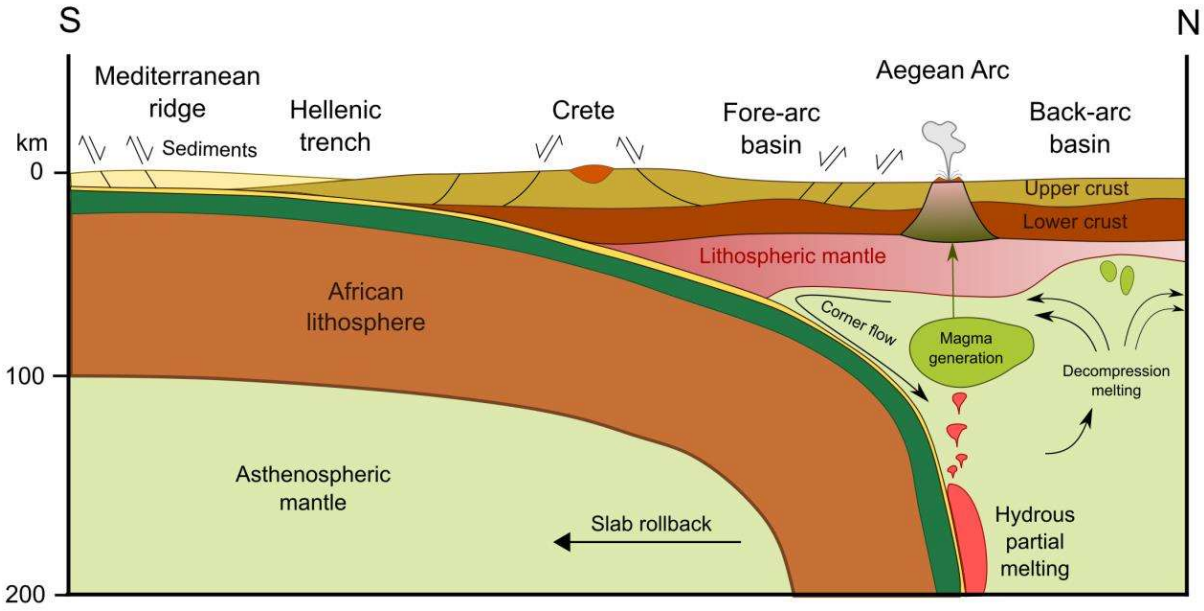

Figure 2.2: South-to-north cross-section across the southern Aegean Sea, from the plate boundary to the Aegean Arc. Figure after Dilek and Altunkaynak (2009).

There are many active volcanic centers or fields along the arc, which Francalanci and Zellmer (2019) split into five volcanic fields (west to east): (1) Susaki volcanic field, (2) Aegina-Poros-Methana volcanic field, (3) Milos volcanic field, (4) Christiana-Santorini-Kolumbo volcanic field and (5) Kos-Nisyros-Yali volcanic field. These volcanic centers are part of the Cyclades Island group and lie on the Cycladic Massif, a metamorphic complex that formed ~60 Ma during the Miocene. The Tripolitza unit is a metamorphosed carbonate that makes up one of the nappes of the Hellenide Complex, which underlies and makes up much of the arc basement. Santorini's basement, which is exposed in several places, consists of Tripolitza marbles and related schists, phyllites and quartzite. On the nearby island of Ios are orthogneisses which underly the Tripolitza (Thomson et al. 2009) and therefore may form the lower crust of Santorini (Druitt et al. 1999; Kilias et al. 2013).

2.1.2 Sub-Aegean Mantle

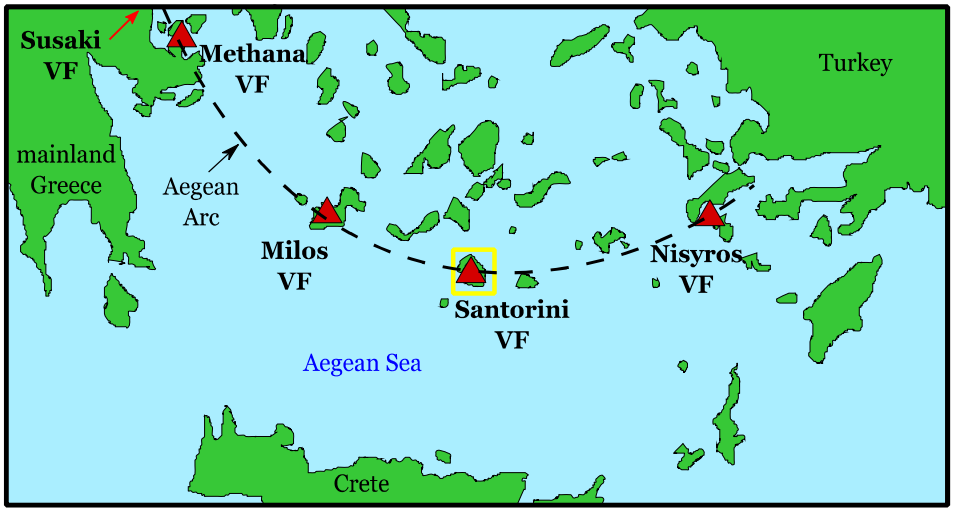

Figure 2.3: The Aegean Arc. The arc consists of five major volcanic fields. Susaki volcanic field is located north of Methana and is slightly out of the figure.

The mantle source below many arc volcanoes is probably depleted MORB mantle (DMM) composition, similar to many arcs (White and Dupré 1986; Ellam and Hawkesworth 1988). Several studies agree that a DMM composition is likely below Santorini and the Aegean Arc (Francalanci et al. 2005b; Klaver et al. 2016; Francalanci and Zellmer 2019; Papazachos 2019). The arc shows an along-arc systematic variation of isotopic compositions, with decreasing Sr and Pb isotope ratios and generally increasing Nd isotope ratios from west to east, which has been correlated to sediment melt input to the mantle wedge (Francalanci et al. 2005b; Klaver et al. 2015, 2016; Francalanci and Zellmer 2019).

Nisyros has geochemical characteristics associated with more of an ocean island basalt (OIB) source, which could be attributed to slab tearing and infiltration of more enriched sub-slab mantle (Klaver et al. 2016). Evidence from several sources points to the existence of slab tearing in the Aegean-Anatolian region, with most of the extent of the interior of the tear positioned under western Anatolia (Figure 2.4) (Barka and Reilinger 1997; Biryol et al. 2011; Özbakır et al. 2013; Klaver et al. 2016). The tearing results in two "branches" of the down-going slab: (1) an Aegean branch to the west and (2) Cyprus branch to the east (Jolivet et al. 2013). The Pliny-Strabo trench region is a large shear zone that may be a surface expression of this tear (Figure 2.1) (Özbakır et

al. 2013). Tomographic studies (Biryol et al. 2011) show a rise of hotter mantle above the tear, and the influence of the rising mantle can be seen in the geochemistry of the volcanoes overlying the slab tear (e.g. Nisyros) (Klaver et al. 2016). Volcanism in western Anatolia during the last ~12 Ma has been alkaline in character, attributed to an OIB-like enriched mantle (Dilek and Altunkaynak 2009). Klaver et al. (2016) showed that Aegean volcanoes of Nisyros and Santorini, despite being ~100 km and ~250 km (respectively) away from the edge of the slab tear, are influenced in their geochemistry by infiltrating of tear-derived subslab enriched mantle with ~10% of subslab mantle contributing to primary magmas of Nisyros.

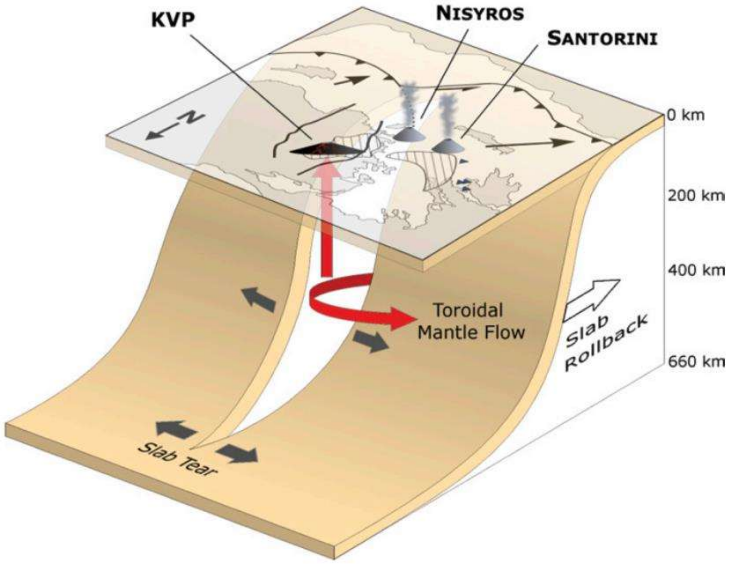

Figure 2.4: Model of the Aegean slab tear. From Klaver et al. (2016). KVP = the Kula volcanic province, a predominantly alkaline volcanic field located in western Turkey.

2.1.3 Physical and geochemical along-arc variations

The Aegean Arc shows physical and geochemical along-arc variation in terms of its subduction geometry, crustal thickness and geochemistry (Francalanci et al. 2005b; Francalanci and Zellmer 2019; Papazachos 2019). The thickness of the continental crust is variable, with the western and eastern sections of the arc having thicker crust (32-34 km) and the central section having thinner (23-26 km) crust (Makris 1977; Papazachos 2019). The arc lies ~150 km above the Benioff zone, though it is deeper (>190 km) in the middle of the arc (Keller 1982; Papadopoulos 1982). Slab rollback since the Pliocene has created an extensional regime, which is greatest towards the

center of the arc (Mercier 1981; Papadopoulos et al. 1986; Wortel and Spakman 2000; Özbakır et al. 2013; Francalanci and Zellmer 2019).

Bailey et al. (2009) argued on the basis of certain diagrams (e.g. from Pearce and Parkinson 1993 and Pearce and Peate 1995) that Santorini sub-arc, pre-metasomatized mantle could be considered a transitional tectonic setting between oceanic and continental arcs and has probably not undergone an earlier melting episode.

Enrichments from different subduction components change along the arc. Overall the Aegean Arc has low Ba/La ratios and plot near the lower limit for island arc basalts (Wilson 1989).

2.2 Santorini volcano

Santorini Volcano (Figure 2.5) is a circular island archipelago located in the southern Aegean Sea towards the center of the Aegean Arc. The outer islands of Thera, Therasia and Aspronisi surround the central islands of Palea Kameni and Nea Kameni. The present physiography of the island group is mainly a result of several hundreds of thousands of years of explosive volcanism, effusive shield-building periods and caldera collapses (Druitt and Francaviglia 1992). The composite, flooded caldera measures 10 x 6 km and consists of several underwater basins surrounding the Kameni islands. The regional extensional regime influences the behavior of the volcano, as most eruptive vents align along volcano-tectonic lineaments, which are surface expressions of faults oriented NE-SW due to the regional stress regime (Figure 2.5) (Francalanci et al. 2005b).

Santorini lies on 25 km of extended continental crust (reduced from an original ~50 km), with the upper crust constituting the top 0-15 km and the lower crust as the bottom 15-25 km (Tirel et al. 2004; Karagianni et al. 2005; Konstantinou 2010). Konstantinou (2010) correlates seismic wave velocities in the upper crust to represent quartzite or granitic gneiss, and the lower crust to correspond to diabase or mafic granulite.

Prior to the onset of volcanism, an island primarily consisting of phyllites and crystalline limestones existed (part of the Cycladic Massif metamorphic complex) which outcrop in several places in the southeastern part of the main Thera island (Skarpelis and Liati 1990; Kilias et al. 1998). Mount Profitis Ilias and Gavrillos Ridge

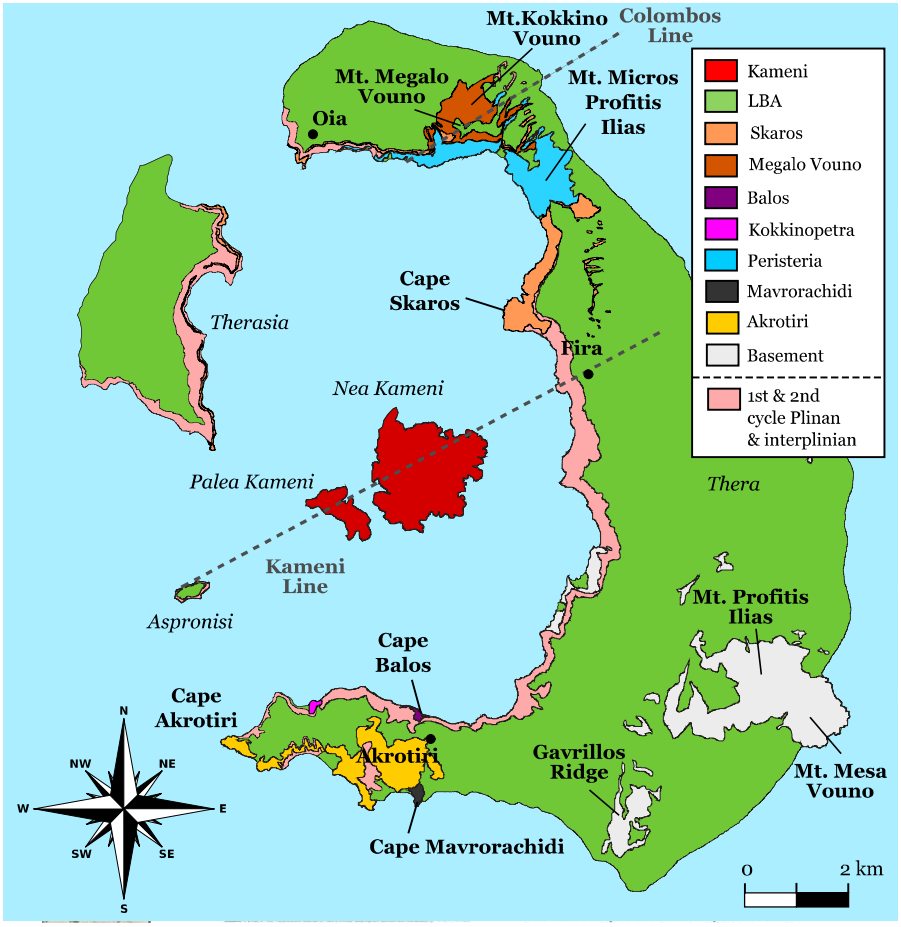

Figure 2.5: Geologic map of Santorini (based on that of Druitt et al. 1999) highlighting volumetrically prominent units as well as those relevant to this study. First and second cycle Plinian and interplinian units not already shown (e.g. Late Bronze Age eruption; LBA) are grouped together as one map unit, as the layers are numerous and thin and would be difficult to show. Approximate locations of each sample from this study are marked with white stars and the respective sample names. Numerous past eruption vents align long the Kameni Line and Colombos Line, which are parallel to regional faults and thought to be surface expressions of basement faults.

in the south of Santorini represent parts of this old pre-volcanic island (Druitt et al. 1999). The basement rocks of the pre-volcanic island include metapelites and limestones; the metapelites were metamorphosed to blueschist facies which then subsequently underwent retrograde metamorphism to greenschist facies (Druitt et al. 1999; Elburg et al. 2014). Skarpelis et al. (1992) drilled into the basement at Megalochori in southern Thera and reported the mineralogy of a granite they encountered at ~255 m depth (approximately near sea level), consisting of alkali feldspar (microcline), plagioclase, quartz, biotite, hornblende and other accessory phases such as magnetite and zircon. The granite was dated at 7-9 Ma.

2.3 Volcanic evolution

Quaternary volcanism began at Santorini ≥650 ka in the form of submarine centers, followed by the establishment of subaerial eruptive centers on the Akrotiri peninsula and Peristeria stratovolcano to the north, which existed 650 to 430 ka (Figure 2.6) (Druitt et al. 1999). Since 360 ka, volcanic activity has involved infrequent, major Plinian eruptions alternating with numerous, minor interplinian eruptions and/or shield-building stages (Druitt et al. 1999; Vespa et al. 2006). Two explosive cycles are recognized—the first from 360 to 172 ka, and the second from 172 to 3.6 ka (Figure 2.6). The two cycles follow a similar pattern: a transition from dominantly intermediate to dominantly silicic explosive eruptions, with the large silicic eruptions causing caldera collapse.

The most recent volcanism (<3.6 ka) has been centered on the Kameni islands and could be considered to be the start of a new explosive cycle (Figure 2.6). The volcanism has built up a submarine-to-subaerial, 470-m-high, ~4 km^3 edifice in the center of the caldera basin (Nomikou et al. 2014, 2019). The most recent volcanic activity was a minor effusive eruption in AD 1950 on Nea Kameni (Georgalas 1953; Pyle and Elliott 2006).

During a period of unrest in 2011-12, seismic activity was centered just north of Nea Kameni at a depth of approximately 4 km (Parks et al. 2015). This is consistent with previous Nea Kameni magma chamber depth estimates (Barton and Huijsmans 1986; Delibasis et al. 1990; Druitt et al. 2016). The seismicity was also accompanied by uplift across the caldera. This period of unrest has been interpreted to have been caused by an intrusion of magma (perhaps occurring in two pulses) to a shallow reservoir below Santorini (Parks et al. 2015). The 2011-12 unrest was the first major volcanic unrest observed since the last eruption in 1950, although the crisis period ultimately ended with no eruption and seismicity has been relatively low ever since.

2.3.1 Early volcanism (650-350 ka)

The earliest volcanic products found on Santorini are submarine tuffs, which were erupted between 1.6 to 2.0 Ma (in the uppermost Pliocene) (Ferrara et al. 1980; Seidenkrantz and Friedrich 1993). Other volcanic centers along the Aegean arc have similar timeframes for early volcanism (Ferrara et al. 1980; Fytikas et al. 1986;

Vougioukalakis et al. 2019). The oldest known subaerial effusive volcanism was centered on and near the modern-day Akrotiri Peninsula (Figure 2.5; 2.6) (Early lavas and tuffs of Akrotiri; >650-550 ka) (Davis et al. 1998; Druitt et al. 1999). These eruptions produced amphibole-bearing silicic lavas and tuffs containing abundant mafic enclaves (Mortazavi and Sparks 2004; Kitsopoulos 2007). To the north was the formation of a stratovolcano complex called Peristeria Volcano (530-430 ka) (Figure 2.5) (Druitt et al. 1999). The lavas were mainly basalts to andesites, although tuffs and olivine-bearing scoria layers can be found within the deposits. Dykes cut through the strata; some can be traced to individual lava flows, while the stratigraphic age of others are ambiguous. Several periods of Strombolian eruptions led to the establishment of cinder cones on the southern peninsula (Cinder cones of Akrotiri; 450-340 ka) overlapping in age with Peristeria Volcano (Davis et al. 1998; Druitt et al. 1999). The cinder cones (Balos, Kokkinopetra, Mavrorachidi) erupted basalt and represent some of the least evolved magmas on Santorini (Figure 2.5; 2.6) (Baziotis et al. 2018).

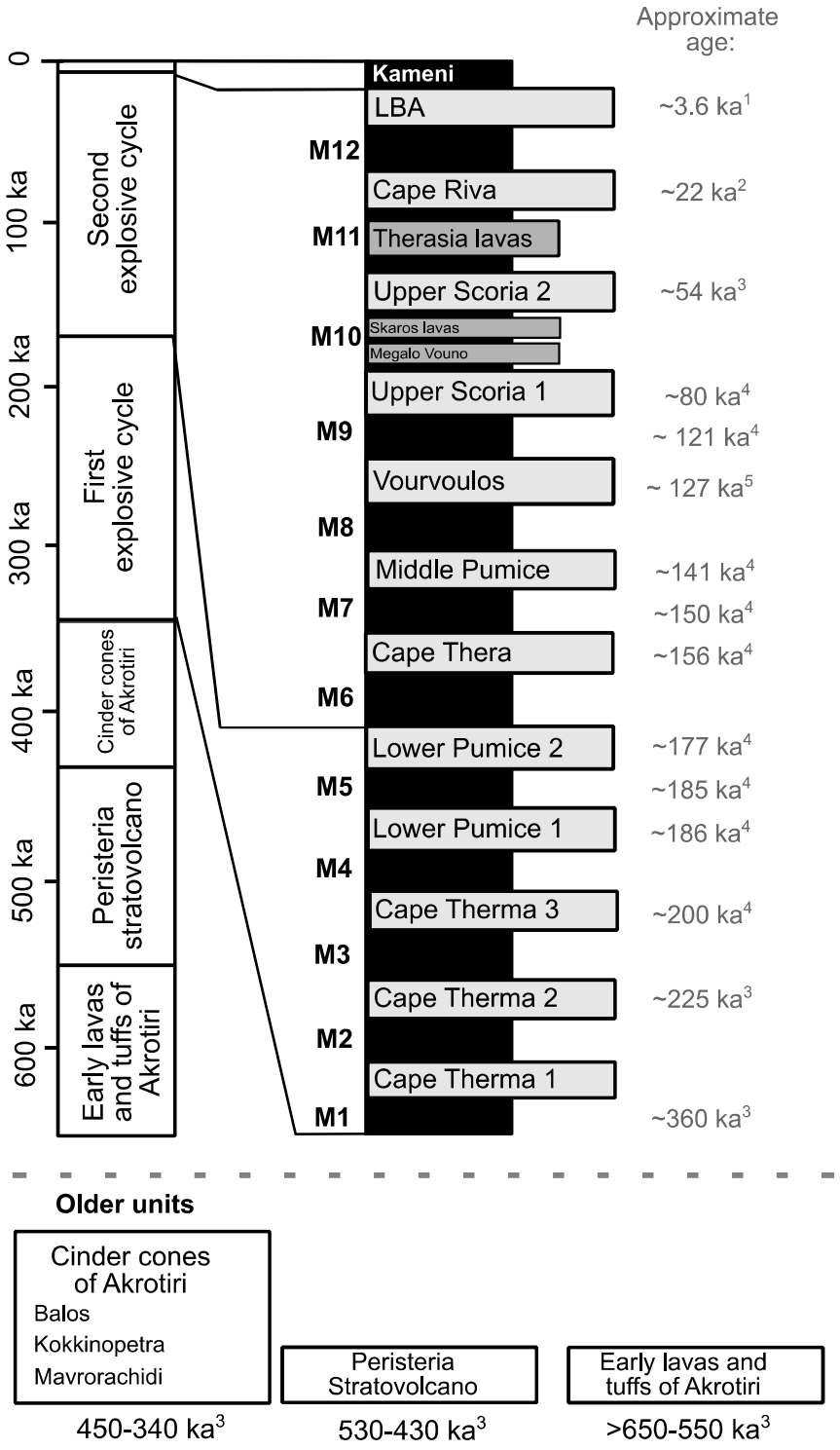

Figure 2.6: A broad overview of the Santorini eruptive history, with the left approximately to scale, using dates from Druitt et al. (1999) and, on the right, the sequence (not to scale) of twelve identified Plinian eruptions (wide grey rectangles) since 360 ka. Plinian eruptions are separated by interplinian periods (smaller black rectangles) M1 through M12. Subdivisions follow Druitt et al. (1999) and Vespa et al. (2006). Older units are summarized below the stratigraphic columns. References for ages: (1) Friedrich et al. (2006); (2) Ramsey et al. (2015); (3) Druitt et al. (1999); (4) Wulf et al. (2020); (5) Satow et al. (2015).

2.3.2 First (360-180 ka) and second (180 ka-3.6 ka) eruptive cycles

There have been 12 recognized Plinian eruptions since ~360 ka (Figure 2.6) (Druitt et al. 1999; Vespa et al. 2006). Interplinian periods between the Plinian eruptions are named M1 to M12 according to their chronological order (Figure 2.6) and may be further subdivided into individual eruption units either with proper names or stratigraphic descriptors (see Vespa et al. (2006) for stratigraphy of the interplinian eruptions).

The first explosive cycle (360-172 ka) began with a succession of dominantly intermediate Plinian eruptions interspersed with interplinian periods of sub-Plinian or effusive activity and terminated with the pair of dominantly silicic Plinian eruptions Lower Pumice 1 and Lower Pumice 2. The second explosive cycle (172 ka-3.6 ka) also began with mostly intermediate Plinian eruptions interspersed with interplinian periods of sub-Plinian or effusive activity and terminated with the pair of dominantly silicic Plinian eruptions Cape Riva and Late Bronze Age eruptions. The most recent volcanism (<3.6 ka) has been centered at the Kameni islands, with the most recent activity being a minor effusive eruption in AD 1950 on Nea Kameni (Pyle and Elliott 2006).

The LBA eruption took place in a flooded caldera setting, most likely with a central island (Druitt and Francaviglia 1992). The eruption occurred in four main phases, preceded by subplinian 'precursory' explosions which laid down a relatively thin deposit of lapilli and ash (Heiken and McCoy 1984). Four eruptive stages (phases 1-4) have been recognized. Phase 1 was a plinian eruption originating from a centrally located subaerial vent, which laid down a reversely-graded, poorly stratified, compositionally-zoned pumice fall deposit (Bond and Sparks 1976; Druitt et al. 1999). The eruption switched from plinian to phreatomagmatic due to vent migration into the flooded caldera (Druitt et al. 1999; Druitt 2014). Phase 2 consisted of pyroclastic surges with some pumice-fall layers. During phase 3, a massive tuff was deposited from relatively cool pyroclastic flows. Phase 4 consisted of hot pyroclastic flows which covered the islands in ignimbrite up to 60 m thick (Bond and Sparks 1976; Druitt et al. 1999). Over the course of the eruption, a total of 48-86 km^3 of magma and commutated lithic debris was erupted (Druitt and McCoy 2019).

2.3.3 Kameni volcanism (< 3.6 ka)

Following the LBA eruption, the volcano returned to typical interplinian activity involving minor effusive activity and small explosive eruptions (Higgins 1996; Druitt et al. 1999). This volcanism has led to the creation of two post-caldera islands: Palea Kameni and Nea Kameni. Palea Kameni was the first island to break the surface in 197 BC and was the site of active volcanism until 726 AD. Nea Kameni appeared later and was the site of active dacitic volcanism between 1570-1950, subdivided into about 10 eruptive episodes (Barton and Huijsmans 1986; Druitt et al. 1999; Martin et al. 2006). Despite the relatively restricted compositional homogeneity, there are several different populations of mafic enclaves co-erupted with the lavas over time (Holness et al. 2005; Martin et al. 2006).

2.4 Mineralogy of Santorini volcanics

Santorini eruption products range from basalt to rhyodacite in composition, with rare rhyolites (Figure 2.7). Santorini basalts contain olivine, plagioclase, clinopyroxene and minor magnetite (Figure 2.7). Basaltic andesites and andesites contain plagioclase, clinopyroxene, olivine, magnetite and sometimes olivine and/or orthopyroxene. Dacites and rhyodacites contain plagioclase, clinopyroxene, orthopyroxene, magnetite, ilmenite, apatite and pyrrhotite (Figure 2.7).

Basalts and basaltic andesites typically contain olivine of $Fo_{72\text{-}80}$ composition (Mann 1983); however, higher Fo olivine has been documented. Highly forsteritic olivine up to Fo_{96} is reported in Kameni magmatic enclaves (Martin et al. 2006). Olivine cores in Skaros can reach up to Fo_{90} (Russell 1999). The M12 interplinian scoria contains forsteritic olivine up to Fo_{90} as well (Vaggelli et al. 2009). Some of the cinder cones on Santorini have produced olivine up to Fo_{85} (Davis et al. 1998). In contrast, in more evolved and particularly in magmas of the most tholeiitic character at Santorini, fayalitic olivine can appear (e.g. $Fo_{38\text{-}39}$ olivine in Vourvoulous eruption and Fo_{34} olivine in the Middle Pumice eruption; Druitt et al. 1999). Some mafic to intermediate magmatic enclaves and minor scoria clast components in silicic products contain olivine, such as those found in the Lower Pumice 2, Cape Riva, LBA and Kameni eruptions (Boyle 1994; Druitt et al. 1999; Holness et al. 2005; Gertisser et al. 2009; Druitt 2014). In some of these cases, olivine in may be cumulitic (e.g. some olivines in enclaves from the Kameni eruptions; Francalanci et al. 1998).

Orthopyroxene is a common phase in Santorini magmas found in more evolved units, usually andesitic to rhyodacitic magmas. It occurs as ferroenstatite (or hypersthene in older classification systems) (Mann 1983; Druitt et al. 1999) with compositions of $En_{29-47}Fs_{43-47}Wo_3$ (Druitt et al. 1999). Clinopyroxene is found in almost all units from Santorini and is typically classified as augite with compositions of $En_{36-44}Fs_{15-24}Wo_{40-44}$ (Druitt et al. 1999).

Amphibole occurs in abundance in silicic magmas and quenches mafic enclaves from the Early Akrotiri centers; however, it is rarely seen in products from the last 360 ka. The only other known occurrences of amphibole in Santorini rocks are in Lower Pumice 2 (Druitt et al. 1999; Gertisser et al. 2009) and a crystal-rich pumice component of the LBA eruption (Boyle 1994; Druitt et al. 1999; Druitt 2014). There is some trace element evidence for cryptic amphibole in some Santorini magmas younger than 54 ka (e.g. flat trend in Y, decreasing Dy/Yb with differentiation) (Francalanci et al. 2005b; Klaver et al. 2016) (Chapter 6).

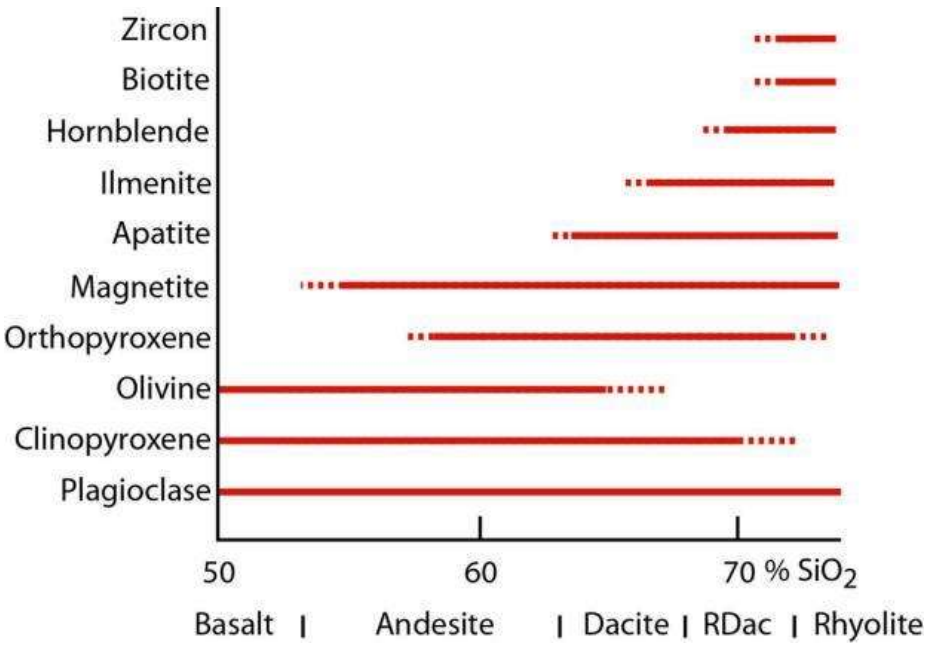

Figure 2.7: Typical mineralogies of magmas at Santorini. RDac = rhyodacite. After Druitt et al. (1999).

The main Fe-Ti oxide phases in Santorini are magnetite and ilmenite (Figure 2.7) (Druitt et al. 1999; Druitt 2014). Spinel inclusions have been observed in some olivine crystals (typically those which are more magnesian) and are particularly abundant in

olivine crystals from Balos (Gartzos et al. 1998), Kokkinopetra and M12 scoria (Vaggelli et al. 2009) products.

Apatite inclusions occur primarily within plagioclase, magnetite and pyroxene crystals in units of more evolved compositions (Figure 2.7) (Druitt et al. 1999). Biotite occurs in the most evolved Akrotiri products. Zircon has been reported in silicic magmas of the Early Akrotiri, Lower Pumice 2 (Druitt 1999) and LBA (Schmitt et al. 2016) eruptions.

2.5 Chemistry and petrology of Santorini magmas

At Santorini, low-K, high-Al basalts evolve into medium- to high-K dacites and rhyodacites. Products span from mildly tholeiitic to calc-alkaline in character. Major and trace element diagrams are shown below. Major element diagrams (Figure 2.8) show that the data falls on relatively tight trends, apart from early Akrotiri volcanics (not shown), which often plot separately from the rest of the data due to their fundamental chemical differences compared to the other series. TiO_2 generally increases with SiO_2 until it reaches a peak around 58-60 wt % SiO_2, after which it decreases, consistent with Fe-Ti oxide (magnetite and ilmenite) crystallization in more evolved magmas (Figure 2.8f).

2.6 Magma genesis: Previous studies on basalts

Basalts are more common at Santorini than at other volcanoes along the Aegean Arc (Mitropolous et al. 1987; Francalanci et al. 2005b). However, basalts are still relatively rare at Santorini compared to other compositions erupted at the volcano, and most basalts have significantly evolved by the time they reach the surface. Basaltic andesite is more common than basalt. Mafic magmas in the range of basalt to basaltic andesite are erupted in the forms of lava flows, scoria falls, mafic enclaves and minor mafic scoria clasts. Mafic magmas appear intermittently throughout the history of the volcano. Several andesites have been shown to be hybrids between mafic and silicic magmas (Fabbro et al. 2013).

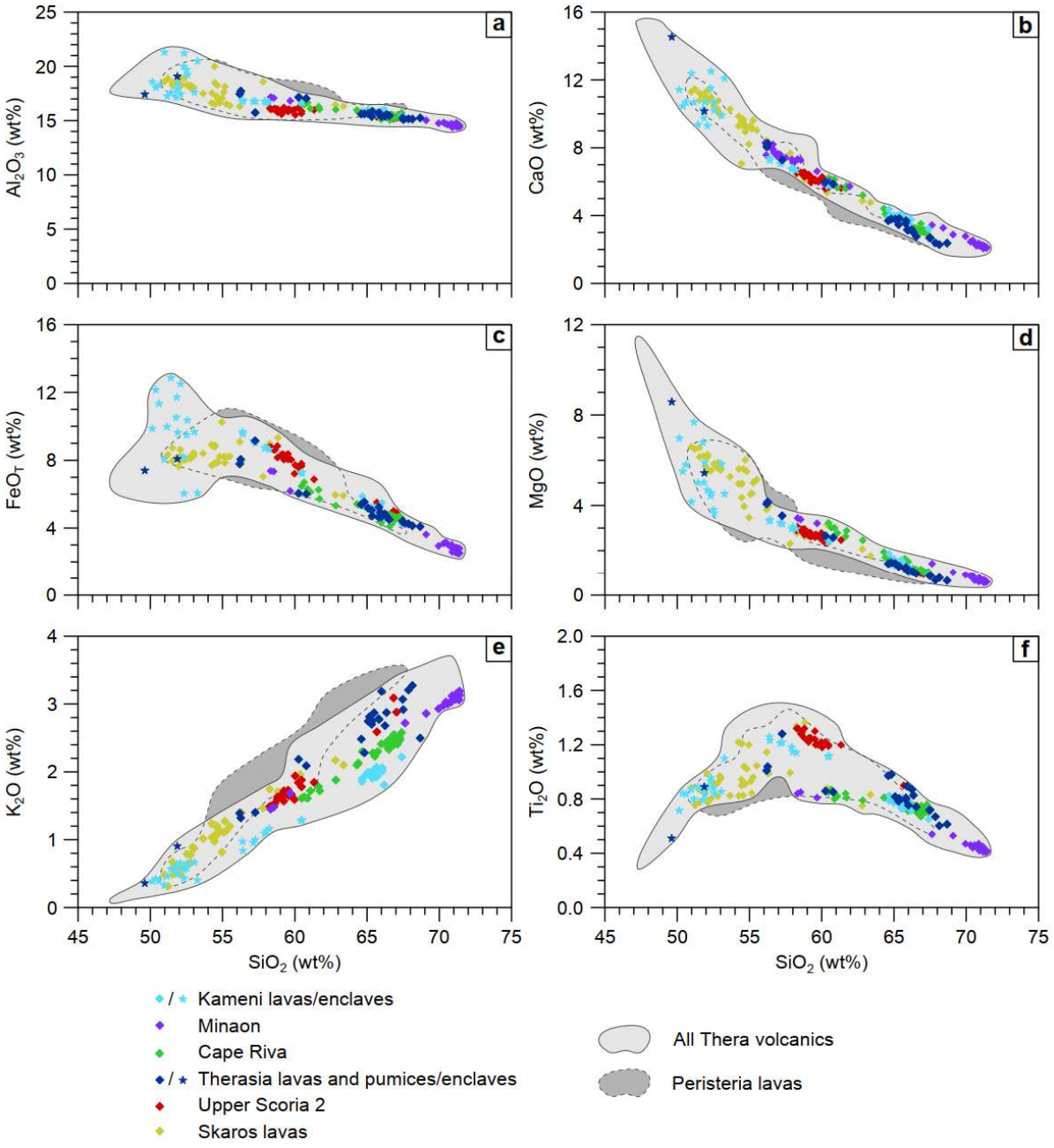

Figure 2.8: Major element variation diagrams for Santorini magmas (from Fabbro 2014). FeO_T is the total iron (FeO + Fe_2O_3) converted to FeO.

Santorini basalts have been the focus of a number of studies (Nicholls 1978; Tarney et al. 1998; Vaggelli et al. 2009; Bailey et al. 2009; Baziotis et al. 2018) and have been included in a number of more general studies on the volcano (Nicholls 1971; Huijsmans 1985; Huijsmans and Barton 1989; Druitt et al. 1999, 2016). Compared to other compositions erupted at the volcano, basalts are relatively rare, and most basalts have significantly evolved by the time they reach the surface, the most mafic whole rock having ~6 wt. % MgO. Nicholls (1978) estimated that primary mantle melts (9-12 wt%

MgO) at Santorini ascend into the crust and differentiate at the Moho or lower crust, producing differentiated basalts and leaving behind mafic to ultramafic cumulates. Baziotis et al. (2018) estimated a primary mantle melt composition and the conditions of mantle melting starting with a whole rock analysis from the basaltic Balos cinder cone.

Tarney et al. (1998) identified an incompatible element (e.g. Nb, Zr) 'enriched' calc-alkaline trend and incompatible 'depleted' tholeiitic trend in Santorini products, and attributed at least some of the variation to mantle source variations. The study of Bailey et al. (2009) on the dykes and lavas in the northern caldera walls showed there was a range in incompatible elements in basaltic to basaltic andesite magmas and subdivided this range into different basalt groups. Vaggelli et al. (2009) studied primitive olivine-hosted melt inclusions from a single scoria fall in the M12 interplinian period.

Partial melting of the sub-Aegean mantle wedge generates basaltic melts that feed Santorini. Bailey et al. (2009) calculated mantle melting percentages of 30-32% for different basalt groups using the modelling methods of Pearce and Parkinson (1993) but admitted that other experimental studies (e.g. Plank and Langmuir 1998) would suggest lower estimates of around 10-25%. The most primitive basalts on Santorini are about 50 wt % SiO_2 and up to 7 wt % MgO (Druitt et al. 1999). Nicholls (1978) proposes that Santorini primitive basaltic melts could have undergone fractionation of 6-12 wt% olivine, 4 wt% clinopyroxene and 0.5 wt% Cr-spinel before storage in the crust. Basalts tend to lack a negative Eu anomaly (Mann 1983), thus the extent of plagioclase crystallization is thought to be limited. Though there is a slightly lower level of HREE in some patterns of the Aegean volcanoes, there is not sufficient evidence to say there is residual garnet in the source (Mitropolous et al. 1987). A slight enrichment of LREE over HREE could be obtained if there were low degrees of melting of a garnet-bearing lherzolite source but could also be explained by addition of a LREE-rich sediment-derived component (Bailey et al. 2009).

Santorini basalts show the lowest Ba/La values of the arc, suggesting very little involvement of slab-derived aqueous fluid over much of the history of Santorini (Francalanci et al. 2005b). However, Zellmer et al. (2000) argue that ^{238}U excesses indicate slab-derived fluids were involved at least in the young Kameni volcanics, and that the fluid was introduced >180 ky before the Kameni eruptions. Mortazavi and

Sparks (2004) highlight the role of hydrous mafic magmas in the generation of the older Akrotiri calc-alkaline volcanics.

In the past, the composition of subducting sediments for Santorini has been relatively unconstrained. Klaver et al. (2015) investigated the compositions of Eastern Mediterranean Sea (EMS) sediment compositions brought to the surface in Deep Sea Drilling Project (DSDP) and Ocean Drilling Program (ODP) expeditions. They analyzed the chemistry of 45 sediment samples and determined the provenances of the components making up the sediments based on trace element geochemistry, noting that the four main sediment sources were Nile sediments, Saharan dust, Tethyan ophiolite belt and Mediterranean volcanics. Their modelling shows that EMS sediments can explain the trace element signatures of volcanic rocks from many Aegean centers, with the exception of Nisyros, which requires a unique mantle source component.

Zellmer et al. (2000) used a GLOSS composition (i.e. GLObal Subducting Sediment; Plank and Langmuir (1998) of a terrigenous sediment component for subducted sediment in their modelling, which was the most reasonable composition available to them at the time. This suggested that there is a small addition of sediments to the mantle as sediment melts. Other studies agree that the mantle wedge is metasomatized primarily by sediment melts (Francalanci et al. 2005b; Vaggelli et al. 2009; Bailey et al. 2009; Francalanci and Zellmer 2019) (Chapter 4). Bailey et al. (2009) suggest the contamination of the sub-Santorini mantle by bulk sediment addition or high-temperature melting of terrigenous or pelagic sediments.

2.7 Differentiation of Santorini magmas

Results from previous mass balance geochemical modelling (Nicholls 1971, 1978; Mann 1983; Huijsmans 1985; Druitt 1999), and experimental petrology (Cadoux et al. 2014; Andújar et al. 2015, 2016), indicate that Santorini magmas undergo multiple stages of evolution from their parent magmas. Geochemical modelling shows that parental basalts must crystallize between 10-60 % to form basaltic andesite and 60-80% to form andesite (Nicholls 1978; Mann 1983; Huijsmans 1985; Druitt et al. 1999). Experiments by Andújar et al. (2015) also agree with these values of 60-80% crystallization (olivine, cpx, plagioclase, Ti-magnetite and opx ± pigeonite and ilmenite) to produce andesite

from basalt. Silicic melts then ascend upward and fractionate to more silicic liquids in the upper crust (Cadoux et al. 2014; Andújar et al. 2016; Flaherty et al. 2018).

Some authors have suggested that assimilation also occurs based on isotopic data. Variations in $^{87}Sr/^{86}Sr$ and $^{143}Nd/^{144}Nd$ show clear divergence from the mantle correlation line (Druitt et al. 1999), which suggests contamination either by continental crust (DePaolo and Wasserburg 1976) or by subducted sediment in the mantle wedge (Ben Othman et al. 1989). A positive correlation between $^{87}Sr/^{86}Sr$ and SiO_2 has been observed in Santorini magmas by Druitt et al. (1999) and Bailey et al. (2009). Previous studies using assimilation-fractional crystallization (AFC) models of trace elements and isotopes (Barton et al. 1983; Druitt et al. 1999) argue that AFC could better explain geochemical trends than fractional crystallization alone. Questions still remain, however, about the nature of assimilation, where it occurs and what is the contaminant.

2.8 Temporal trends

Temporal changes in incompatible trace elements, such as K, have been observed along the arc at different volcanic centers (Francalanci and Zellmer 2019). Santorini is one such center along the arc to experience a temporal decrease in K and other incompatible elements (Figure 2.9) (Huijsmans et al. 1988; Druitt et al. 1999; Francalanci et al. 2005b; Fabbro et al. 2013; Francalanci and Zellmer 2019). As the magmas become progressively depleted in incompatible elements with respect to SiO_2 since 530 ka (i.e., excluding the Early Akrotiri magmas), fanning trends are created (Huijsmans 1985; Druitt et al. 1999; Francalanci et al. 2005b; Fabbro et al. 2013). Bailey et al. (2009) also recognized fanning trends in trace element data of northern Santorini lavas and dykes; however, time information was not available, and it is not clear if and how the mafic compositions relate to more silicic products of the volcano. The temporal decrease is most evident in K_2O but is also prominent in many incompatible trace elements (e.g. Rb, Zr, Nb, Hf).

The decrease in incompatible elements with respect to SiO_2 over time is most clear in intermediate and silicic products from published whole rock data (Figure 2.9); however, the resolution of the whole rock database is not high enough to determine whether the different trends also extend into mafic compositions. Thus, the source of this decrease is not yet understood. One possibility is that the decrease is due to a

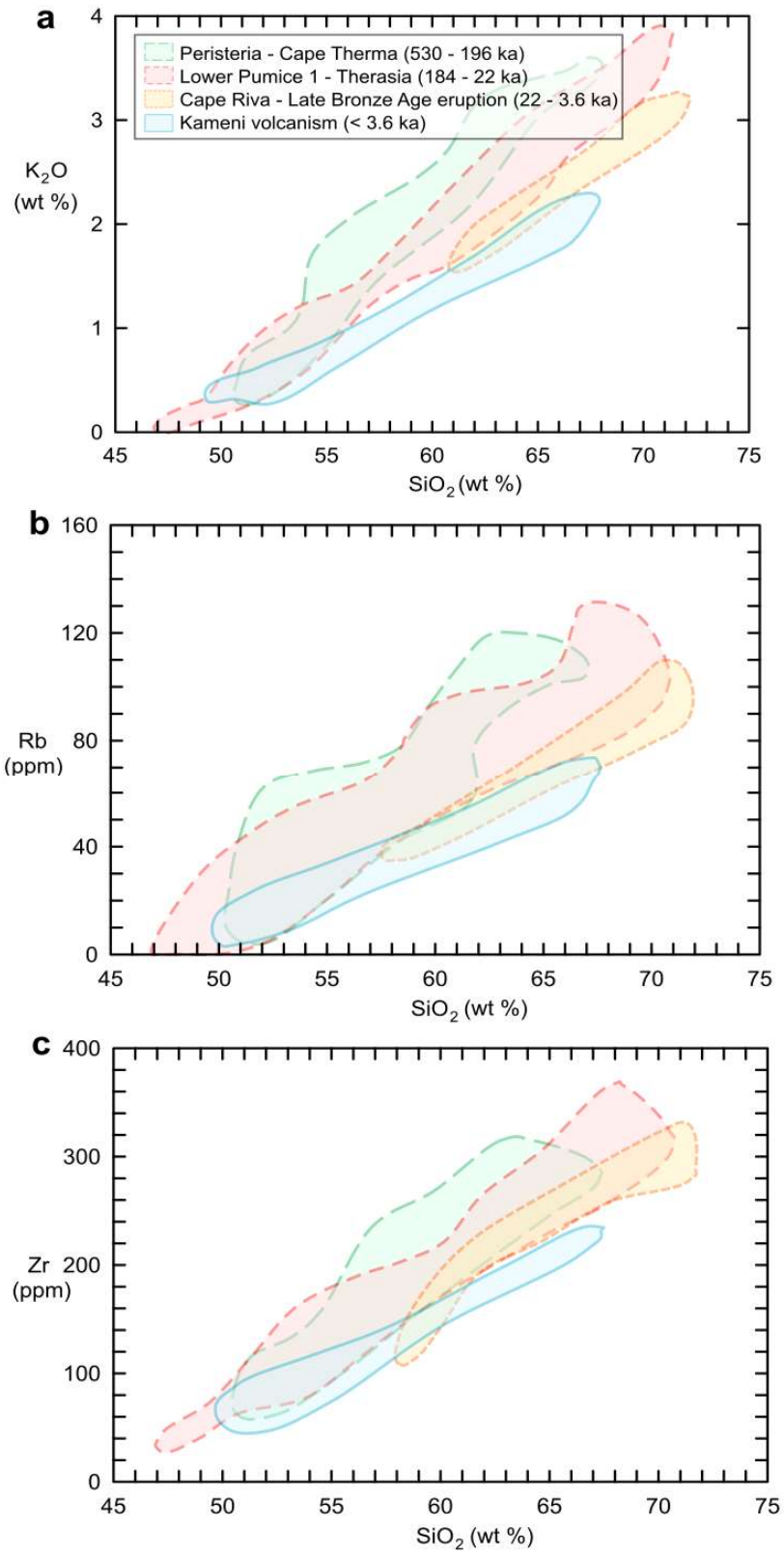

Figure 2.9: Temporal decrease of selected incompatible elements with respect to silica over time. Different discrete "jumps" in the decrease of incompatible elements can be distinguished by plotting the whole rock fields for different time periods. Peristeria to Cape Therma 3 are the highest in incompatible element concentrations, while the most recent Kameni magmas are the lowest. Figure adapted from Fabbro et al. (2013).

temporal change in the degree of melting and/or degree of metasomatism of the mantle source (Huijsmans et al. 1988). Some authors have indeed proposed that an increased influence from extension-related decompression melting over time could explain the decrease in incompatible elements (Francalanci et al. 2005b; Francalanci and Zellmer 2019). Another possibility is that the temporal decrease in incompatibles could be linked to the degree of crustal contamination, as the crust is enriched in incompatible elements; thus, a decrease in assimilation over time could in theory also explain the temporal change (Druitt et al. 1999).

2.9 The transcrustal magmatic system of Santorini

The plumbing system below Santorini caldera (Figure 2.10) has provided likely near-constant passage for hundreds of km^3 of magma over its >0.5 Ma history, and as such it should be underlain by an extensive pluton zoned from gabbro to granodiorite (Druitt et al. 1999, 2016). Melt inclusion volatile barometry suggest basalts (6.5-7.5 wt % MgO with up to 4 wt % H_2O; Druitt et al. 2016) intrude at or around the interface between upper and lower crust, producing a mushy zone at between 8-15 km. Silicic melts are transferred into the upper crust, where they intrude as sills at the base of mushy silicic plutons. Plinian storage regions form between 4-8 km, while interplinian reservoirs may form even shallower (Druitt et al. 2016).

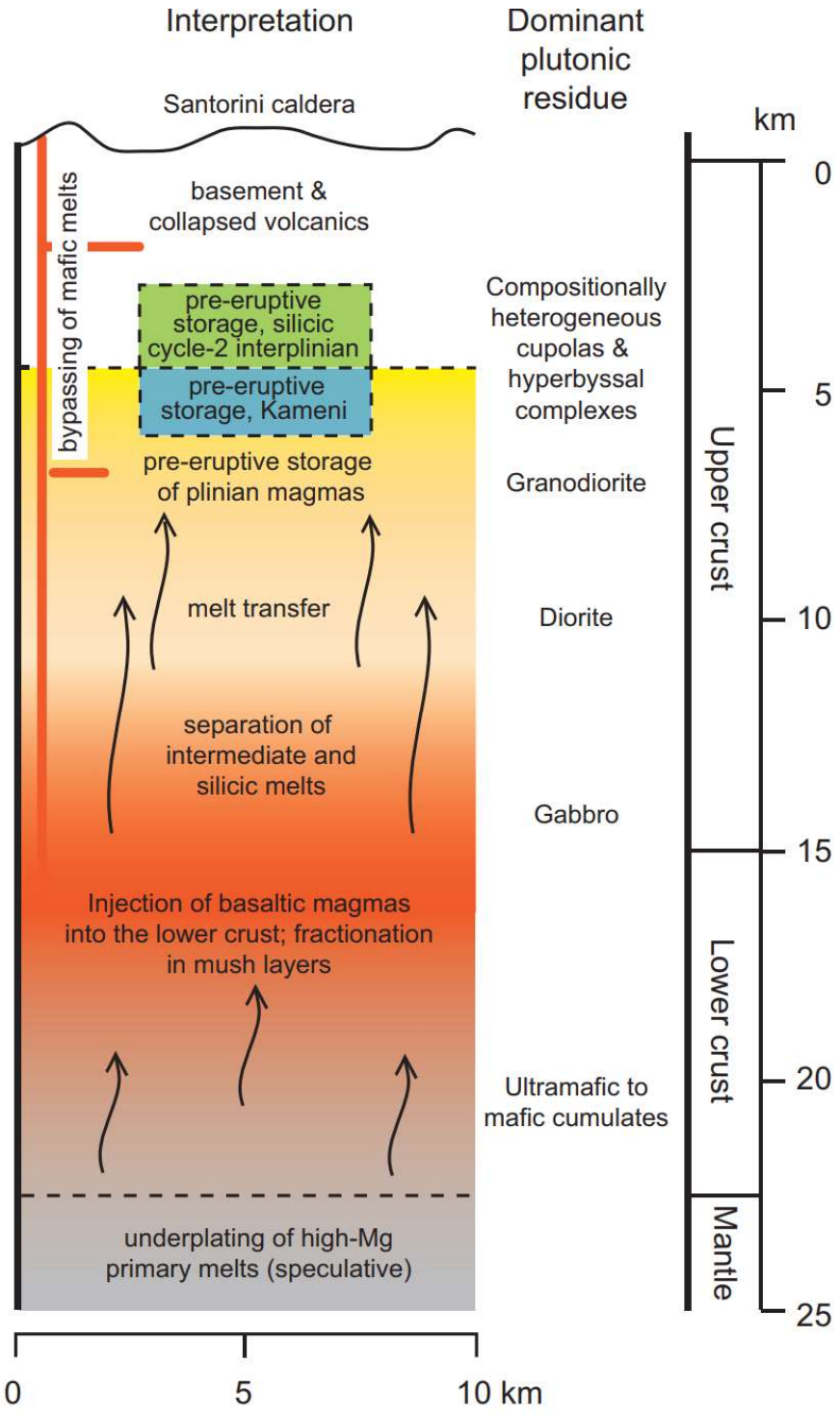

Figure 2.10: Model of the plumbing system of Santorini (from Druitt et al. 2016, 2019).

Chapter 3: Sampling and analytical methods

3.1 Field sampling

Fieldwork was undertaken in October 2016 to sample olivine-bearing mafic units from the last 20-50 ka of Santorini history that were missing from the in-house collection at the Laboratoire Magmas et Volcans (LMV). A second field mission took place in April 2018 with the main goal of sampling older, geochemically distinct units of Santorini. Where possible, small glassy scoria were collected, as they were more likely to have quenched upon eruption and therefore cooled quickly enough to avoid crystallized melt inclusions and H_2O loss from inclusions.

Some samples studied in this thesis were taken from a pre-existing collection housed in the LMV. Some melt inclusions that were already mounted in indium for the study of Druitt et al. (2016) were also used.

3.2 Sample preparation

3.2.1 Melt inclusion (MI) preparation

Selected samples were crushed with a jaw crusher housed at the LMV, then sieved into various size fractions depending on the sample. The fractions typically used were 100 to 250 µm, 250 to 500 µm, and/or 500 µm to 1 mm. Each size fraction was further divided into magnetic and non-magnetic fractions using a hand magnet. In ideal cases, the non-magnetic fraction contained the crystals of interest; however, sometimes if crystals were coated in groundmass, the magnetic fraction was also kept and exploited if needed. Crystals larger than 500 µm were usually picked by hand under a binocular microscope, while smaller crystals sometimes required the use of a Frantz magnetic separation machine to isolate.

A textural control was implemented during melt inclusion (MI) selection to ensure having accurate and representative melt compositions. Primary MIs were preferred, i.e. those which preserve melts at the time of crystal entrapment and are not formed due to secondary processes such as dissolution and recrystallization. Where possible, glass-coated crystals were chosen, and euhedral crystals were preferred where they were present. Crystals were inspected under an optical microscope with 20 to 50x magnification to search for indications of melt leakage and decrepitation, as well as to

identify fractures, melt tubes or other connections to the surface. MIs that had passed these textural controls, and which furthermore had a large enough size (at least 20 µm diameter of analyzable area, not including the bubble) were selected.

Crystals were mounted on glass slides with crystal bond and polished until it was possible to see into the crystals and identify MIs. If MIs were glassy and crystal-free (an exception made for spinel, which can exist prior to the MI and provide a nucleation site for the MI to form), crystals were mounted in brass cylinders filled with epoxy resin, then polished using a sequence of silicon carbide (1200 & 2400 grade) and diamond (6, 3 and ¼ µm grades) polishing mats until the MI was exposed at the surface and well-polished.

3.2.2 Homogenization

If inclusions were crystallized, it was necessary to reheat the MIs and quench them to glass in an experimental process known as homogenization or reheating. Homogenization experiments are needed for samples from relatively slowly-cooled scoriae, lavas and magmatic enclaves, where MIs are expected to be partially or wholly crystallized.

For homogenization, an apparatus called a Vernadsky-type heating stage was used (Figure 3.1). The Vernadsky heating stage was developed by Sobolev et al. (1980) and has since been used in many laboratories. The setup includes a small heating device, upon which a disk-shaped sapphire sample holder sits, which supports a MI-bearing crystal (Figure 3.1). A quartz window on top of the heating stage allows an observer to monitor and track changes in the MI during the experimental runs. A petrographic microscope is used to monitor the MIs at 10x to 20x magnification.

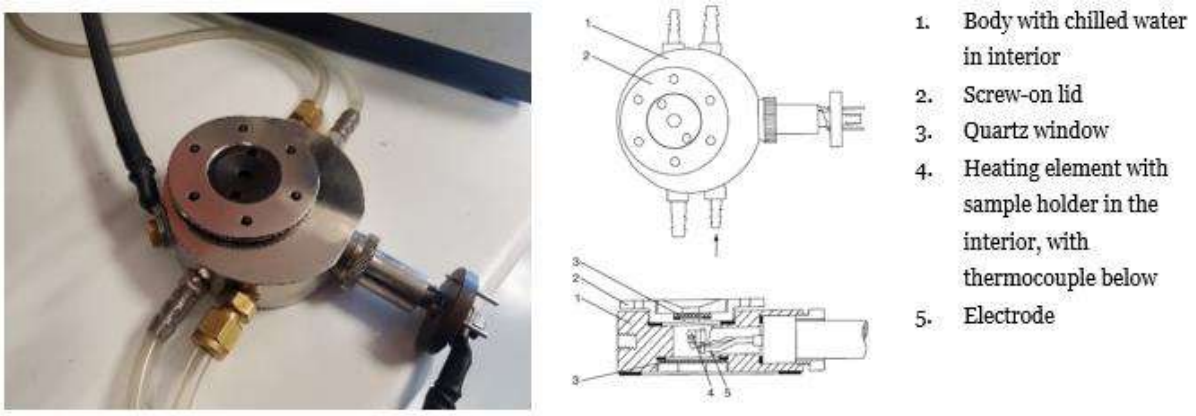

Figure 3.1: The Vernadsky-type heating stage. Left: Vernadsky-type heating stage located at the Laboratoire Magmas et Volcans. Center and right: Description of heating stage from Schiano (2003).

Crystals were polished lightly on two parallel sides using a 2400 grade silicon carbide mat and 6 μm diamond mat, such that the free crystal sits flat on the sapphire disk and that the observer can see the MI clearly. Care was taken not to polish too close to the MI, as close proximity to the surface can increase the chance of decrepitation of the MI.

Each reheating experiment was performed at 1 atm and low oxygen fugacities (fO_2), typically between 10^{-18} to 10^{-20} atm. The low fO_2 is principally used to prevent oxidation of olivine, which can make it too difficult to see the MI clearly through the homogenization experiment and can affect olivine stability (Nitsan 1974). However, it is important to note that imposing fO_2 risks changing the redox conditions of the MI, as fO_2 can re-equilibrate quickly (Bucholz et al. 2013). A Pt-Pt_{90}-Rh_{10} thermocouple is attached to the sample holder to track the temperature. The oxygen fugacity is controlled by running He through a furnace at 680-700°C containing a zirconium rod. As the helium passes over the zirconium, the zirconium removes oxygen from the air, allowing the low oxygen fugacities to be obtained. The helium flux was set at about 20 mL/min.

A speck of gold or silver, with a precisely known melting temperature (1064°C for gold) can be placed on top of the crystal and used to determine the difference in temperature (the actual temperature and that read by the thermocouple which is displayed by the thermometer).

During the course of an experiment, the temperature is increased by gradually increasing the voltage (V) supplied to the heating stage. As the voltage increases, the

intensity (I) also increases (nonlinearly); however, the intensity exhibits a linear correlation with the apparent temperature from the thermometer (TA). Using a metal such as gold or silver and recording the melting temperature from the thermometer allows for the determination of a function that gives the real temperature (TR) from the apparent temperature.

The MI-bearing crystal is heated incrementally until the MI melts completely, then it is quenched. The quenching process happens very quickly (dropping to below the glass transition temperature usually within 1 to 2 seconds) due to two factors: (1) cooling of the surrounding of the heating stage by chilled water (~15°C) and (2) the notably high thermal conductivity of helium.

In ideal cases where the MI is volatile-saturated, the homogenization temperature (i.e. the temperature at which a single phase of homogenous melt is achieved) should be close to the temperature of entrapment. However, the bubble does not always disappear due to the difference between the pressure of entrapment and the 1 atm at which the experiments are performed. Where the bubble does not disappear, or where the MI is volatile-undersaturated, the minimum entrapment temperature can be estimated from the temperature at which all daughter minerals have melted.

Chen et al. (2011) determined heating rates and maximum high-temperature dwell times to minimize the probability of water loss from MIs during homogenization experiments. A fast heating rate (100-200 K/min) was used to heat the MI until near homogenization. At higher temperatures, as the homogenization temperature was being approached, the heating rate was decreased to ~50 K/min or less to record any phase changes and the homogenization temperature. Both the overall duration of the experiments and the high-temperature (above ~1100°C, where water loss could potentially start immediately) dwell time, were kept short to avoid water loss as well. The overall experiment duration was kept shorter than 20 minutes (except for two experiments), while the high temperature dwell time was kept as short as possible (just enough to reach the point of complete melting of all crystals, and then 30 to 60 s to allow the melt to homogenize before quenching). The same heating stage was used as in Chen et al. (2011).

While this thesis does not focus on volatiles, the experimental conditions remained within the limits given by Chen et al. (2011) for negligible water loss (Figure 3.2); thus, it can be assumed that homogenized melt inclusions have not lost a significant amount

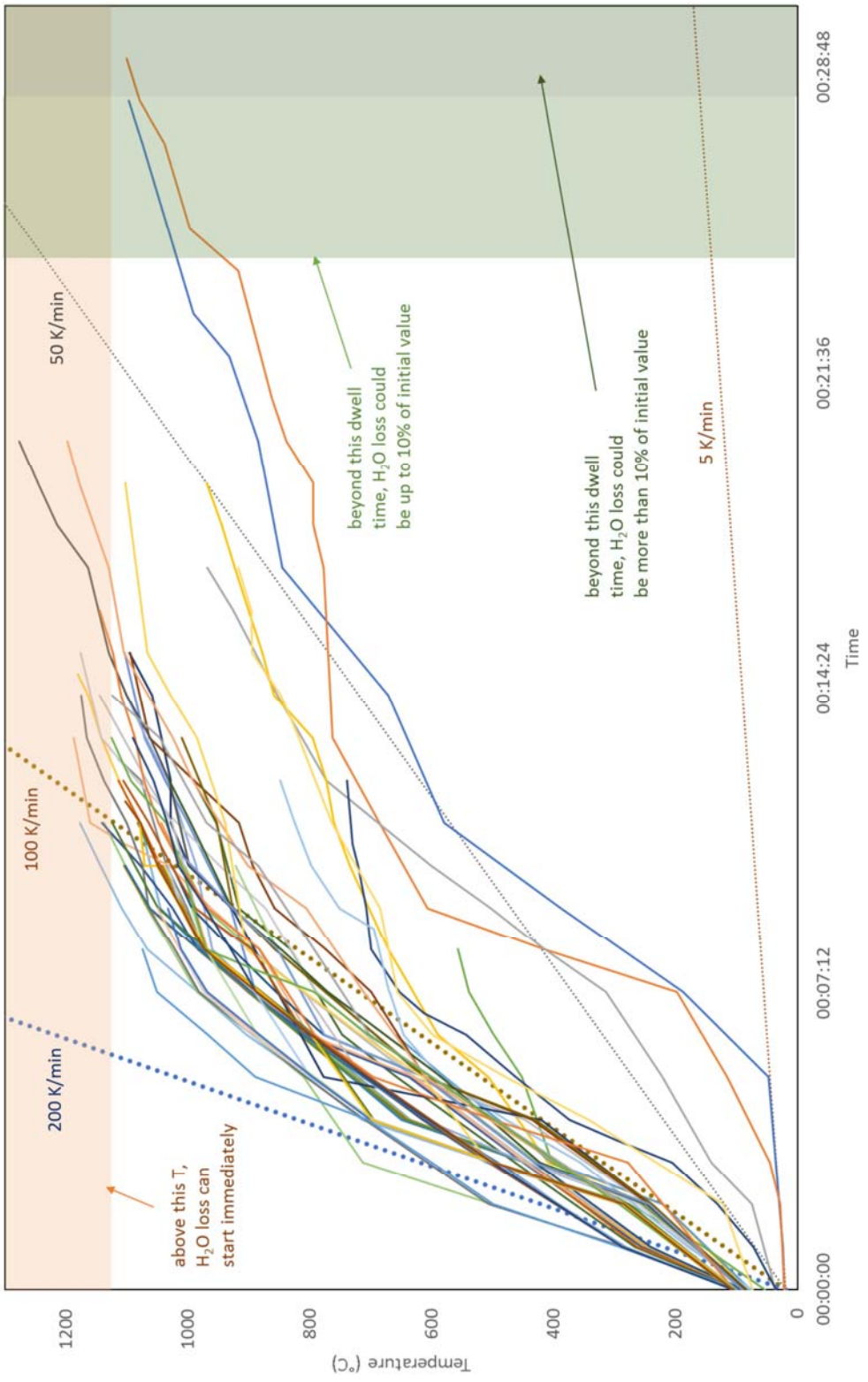

Figure 3.2: Experimental heating rates (T in °C on *y*-axis, time in hh:mm:ss format on x-axis) for homogenized samples. Fields indicating experimental conditions favorable for water loss taken from Chen et al. (2011).

of water. Whether or not there was natural loss and/or re-equilibration of water contents within the inclusion prior to eruption, however, is difficult to determine.

Models of Bucholz et al. (2013) show that full fO_2 re-equilibration can occur on the order of hours to several days at high temperatures (>1000°C) and can be comparable to the timescales of H_2O re-equilibration. As we have respected the conditions of Chen et al. (2011) for preserving the initial H_2O content of MIs, we argue that fO_2 re-equilibration by homogenization has also been minimal. We cannot, however, rule out that MIs have not re-equilibrated prior to eruption. Re-equilibration of fO_2 can affect the $Fe^{2+}/\Sigma Fe$, which is a factor in correcting MI compositions and will be discussed later in this chapter.

3.2.3 Groundmass glass preparation

Groundmass glasses were also prepared, using the same general technique as for melt inclusions. Small lapilli, preferably vesicular and glassy in appearance, were chosen and mounted in brass cylinders filled with epoxy resin. The cylinders were polished very lightly using the same sequence of polishing mats as for MIs until they were visibly well-polished under reflected light.

3.3 Analytical methods

3.3.1 Microprobe for major elements and volatiles in melt inclusions

A CAMECA SX-100 electron microprobe (EMP) with 15 kV accelerating voltage housed at the Laboratoire Magmas et Volcans (LMV) was used to analyze major element compositions and volatile elements (Cl, S, F) of melt inclusions and matrix glasses.

Melt inclusions (MIs) and groundmass glasses (adhering and far field glass; ranging from fully glassy to microlite-rich) were analyzed for major elements with a defocused (10 to 20 µm spot size) electron beam at 4 to 8 nA beam current. Diffraction crystals and counting times for each element are given in Table 3.1. A defocused beam size was needed to avoid Na depletion, which is an interaction of an oxidizing electron beam with the hydrous silicate glass, causing Na to migrate. In addition to a defocused beam, Na was analyzed first for a counting time of 10s to minimize low Na counts, which were

seen to be unaffected in the first ~10s but then rapidly decreased for longer durations (Figure 3.3). Major element analysis was always performed before any other analyses involving electron beam interaction (before volatiles, capturing a backscattered electron image of the whole crystal, etc.).

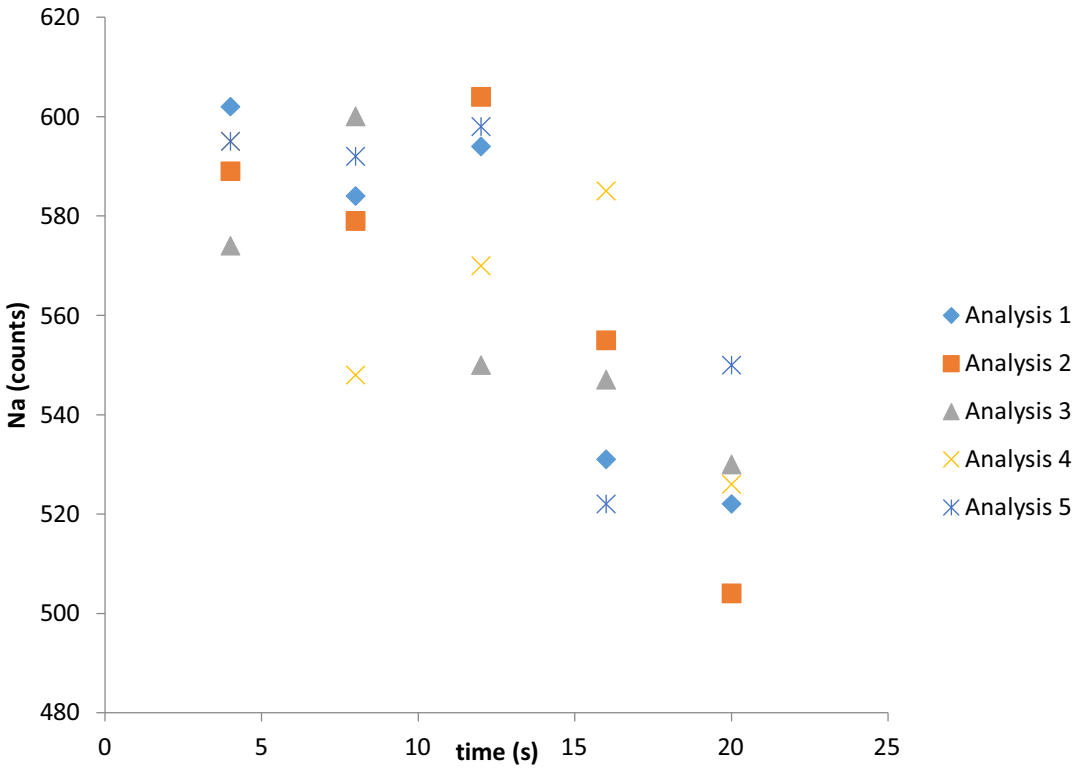

Figure 3.3: Na loss as a function of time. Na counts were recorded every 4 s for five spot analyses (10 μm diameter) in different locations within one large plagioclase-hosted melt inclusion. Na counts drop after ~10 s.

The basaltic glass standard A99 was used to calibrate the silicate glasses for major elements (Table 3.2). Depending on the size of the MI, between one and four major element analyses were taken. Where more than one analysis was taken, the compositions were averaged and checked for compositional homogeneity. Analytical error on analyses were converted to 2σ standard deviation and compared with 2σ standard deviation resulting from averaging. The maximum value between the two was kept as the 2σ standard deviation.

Table 3.1: Summary table of microprobe analysis conditions, different crystal types and counting times.

			Diffraction crystals			
Analysis type	**Beam size**	**Beam current**	**TAP**	**TAP**	**LPET**	**LiF**
Major elements	10-20 µm	4-8 nA	Na (10 s) Mg (20 s)	Si (10 s) Al (20 s)	K (40 s) Ca (10 s) Ti (10 s) P (10 s)	Fe (40 s) Mn (30 s)

Table 3.2: Analysis of glass standard A99 at the LMV compared to published values. Published values of the A99 glass standard (USNM; Jarosewich et al. 1979) compared with example average values analyzed by EMPA at the LMV. 2σ represents standard deviation on the mean of 10 analyses.

	A99 (USNM)	**A99 (LMV)** Mean (n=10)	2σ
SiO_2	50.94	50.86	0.46
TiO_2	4.06	4.18	0.13
Al_2O_3	12.49	12.60	0.16
FeO^T	13.3	13.28	0.55
MnO	0.15	0.19	0.14
MgO	5.08	5.01	0.15
CaO	9.3	9.16	0.15
Na_2O	2.66	2.76	0.22
K_2O	0.82	0.86	0.04
P_2O_5	0.38	0.48	0.10
Total	99.18	99.49	

3.3.2 Host mineral analysis with microprobe

Backscatter electron (BSE) imagery was used to judge where to analyze the host mineral in equilibrium with each melt inclusion. Minerals were measured with a focused (in reality: ~1 µm) beam size and 15 nA beam current.

3.3.3 LA-ICP-MS analysis

Trace elements were analyzed by laser ablation induced coupled plasma mass spectroscopy (LA-ICP-MS) at the LMV. The LA-ICP-MS consists of a Resonetics ArF excimer (193 nm wavelength) laser (model: RESOlution M-50E) coupled to a Thermo Element XR ICP-MS.

The elements (isotope of each element) analyzed include: ^{6}Li, ^{7}Li, ^{9}Be, ^{29}Si, ^{43}Ca, ^{44}Ca, ^{45}Sc, ^{47}Ti, ^{51}V, ^{53}Cr, ^{59}Co, ^{60}Ni, ^{65}Cu, ^{66}Zn, ^{71}Ga, ^{72}Ge, ^{75}As, ^{85}Rb, ^{88}Sr, ^{89}Y, ^{90}Zr, ^{93}Nb, ^{95}Mo, ^{115}In, ^{133}Cs, ^{137}Ba, ^{139}La, ^{140}Ce, ^{141}Pr, ^{146}Nd, ^{147}Sm, ^{153}Eu, ^{157}Gd, ^{159}Tb, ^{163}Dy, ^{165}Ho, ^{166}Er, ^{169}Tm, ^{172}Yb, ^{175}Lu, ^{178}Hf, ^{181}Ta, ^{208}Pb, ^{232}Th and ^{238}U. Glass NIST612 (rhyolite) was used as a reference standard for melt inclusion analysis, while NIST610 (rhyodacite) and/or BCR2 (basalt) were used as external standards. Average analyses of internal and external standards are given in Table 3.3. Cs values were rejected from any melt inclusions analyzed in previously made indium mounts (i.e. for Druitt et al. 2016), as there was clear Cs contamination from the SIMS Cs+ ion beam and/or Cs in indium which had entered into small cracks or pits on the surface of the inclusion.

A single analysis contains 30 s of background signal collection followed by 90-100 s of sample analysis with a 15-33 µm beam size, and results in a time-resolved signal to be treated with a data reduction software in order to obtain elemental abundances. GLITTER software was used to reduce the data and obtain trace element concentrations. Analyses are given in a supplementary electronic file. Detection limits are given in Table 3.4.

Since signals vary with time for many reasons (e.g. increasing depth of laser pit), to compare measurements it is necessary to work in terms of ratios. The determination of trace element concentrations is based on conversion of absolute intensities to concentrations via normalization of a known internal standard. The calculation is as follows:

$$C_i^{sample} = C_{IS}^{sample} \times \frac{I_i^{sample}}{I_{IS}^{sample}} \times \frac{C_i^{ref}}{C_{IS}^{ref}} \times \frac{I_{IS}^{ref}}{I_i^{ref}} \qquad \text{(Equation 3.1)}$$

(where C = concentration in ppm, I = intensity in counts per second or cps, IS = internal standard, ref = reference standard). ^{44}Ca was used as an internal reference isotope. CaO (wt%) values previously determined by microprobe were used as input for internal standards.

Table 3.3: Averages analyses of glass reference standards. NIST612 was used as an internal reference standard, while NIST 610 and BCR were used as external standards.

	NIST 612				NIST 610				BCR			
	Average (ppm)		Detection Limit		Average (ppm)		Detection Limit		Average (ppm)		Detection Limit	
	n=10	2σ	n=10	2σ	n=5	2σ	n=5	2σ	n=10	2σ	n=10	2σ
Li	40.79	1.97	0.67	0.85	462.44	12.75	0.62	0.16	9.09	0.71	1.43	0.81
Be	37.55	0.47	0.09	0.10	423.85	4.54	0.09	0.05	2.10	0.24	0.21	0.10
Si	339000	18900	659	578	389000	82900	650	200	320000	83000	1000	500
Ca	85100	850	224	198	80500	1600	200	30	51000	1100	400	200
Sc	40.40	1.20	0.29	0.30	461.48	36.03	0.23	0.07	32.74	1.40	0.48	0.20
V	39.08	0.68	0.18	0.08	445.31	12.40	0.17	0.03	443.86	21.74	0.26	0.06
Cr	36.57	3.25	4.51	9.67	378.46	27.00	2.69	0.56	17.62	3.14	16.00	17.48
Co	35.44	0.57	0.22	0.11	403.46	6.59	0.21	0.12	38.20	1.49	0.28	0.08
Ni	38.80	1.82	1.41	1.43	439.87	31.24	1.24	1.37	11.73	4.05	3.11	1.30
Cu	37.74	1.75	0.38	0.25	429.96	9.86	0.35	0.18	18.80	1.75	0.62	0.23
Zn	38.33	2.23	2.41	7.29	422.95	17.26	1.20	0.52	159.10	9.23	8.61	9.30
Ga	36.66	0.99	0.08	0.05	420.01	32.42	0.08	0.03	23.05	0.77	0.15	0.06
Ge	35.60	2.27	1.39	0.77	375.13	55.29	1.29	0.18	4.04	2.01	2.17	0.67
As	36.36	1.65	0.38	0.80	333.62	40.50	0.33	0.15	1.27	0.66	0.83	0.48
Rb	31.48	0.55	0.07	0.09	422.96	29.89	0.06	0.04	47.67	1.80	0.14	0.07
Sr	78.66	1.19	0.06	0.04	516.10	32.10	0.06	0.01	335.40	9.39	0.11	0.05
Y	38.38	0.37	0.02	0.03	457.15	15.12	0.02	0.02	31.22	0.89	0.05	0.03
Zr	37.97	0.31	0.24	0.56	427.90	25.36	0.21	0.39	167.42	5.28	0.87	0.58
Nb	39.52	1.29	0.01	0.02	466.43	44.64	0.01	0.00	11.74	0.59	0.02	0.01
Mo	37.99	1.36	0.09	0.09	415.64	9.34	0.07	0.02	267.64	18.28	0.16	0.07
In	40.95	4.27	0.02	0.01	505.03	27.40	0.02	0.00	0.11	0.03	0.03	0.01
Cs	42.20	1.21	0.05	0.06	364.69	26.37	0.05	0.04	1.15	0.10	0.10	0.05
Ba	39.61	1.36	0.12	0.10	433.04	32.67	0.10	0.04	661.82	19.55	0.21	0.09
La	35.91	0.48	0.01	0.01	437.56	48.61	0.01	0.01	23.57	0.41	0.02	0.01
Ce	38.52	0.47	0.01	0.01	451.38	26.39	0.01	0.02	50.57	1.33	0.02	0.01
Pr	37.50	0.89	0.01	0.00	439.15	25.40	0.01	0.01	6.28	0.24	0.01	0.01
Nd	35.55	1.17	0.03	0.04	421.04	45.15	0.02	0.03	27.11	1.10	0.08	0.05
Sm	37.84	0.76	0.03	0.03	438.83	49.27	0.02	0.03	6.30	0.25	0.07	0.03
Eu	35.21	0.80	0.01	0.01	442.02	72.23	0.01	0.01	1.83	0.07	0.02	0.01
Gd	37.01	0.79	0.04	0.03	424.40	67.66	0.04	0.05	6.02	0.22	0.10	0.05
Tb	36.70	1.89	0.00	0.00	436.54	60.91	0.00	0.00	0.93	0.04	0.01	0.00
Dy	35.68	0.51	0.02	0.02	425.47	48.29	0.02	0.02	5.95	0.27	0.06	0.03
Ho	38.05	0.75	0.00	0.00	454.19	48.30	0.00	0.01	1.19	0.05	0.01	0.00
Er	37.98	0.37	0.02	0.03	436.00	37.15	0.01	0.01	3.39	0.13	0.06	0.04
Tm	37.12	0.79	0.00	0.00	442.25	27.32	0.00	0.00	0.48	0.03	0.01	0.00
Yb	39.18	0.54	0.02	0.02	442.60	50.61	0.02	0.01	3.16	0.15	0.04	0.02
Lu	36.91	0.33	0.00	0.00	445.60	33.83	0.00	0.00	0.46	0.03	0.01	0.00
Hf	35.71	2.18	0.01	0.02	402.30	74.21	0.02	0.03	4.51	0.27	0.06	0.04
Ta	38.66	2.18	0.01	0.00	468.75	18.79	0.01	0.00	0.69	0.07	0.01	0.00
Pb	38.60	0.77	0.03	0.02	428.01	50.48	0.02	0.01	10.66	0.48	0.04	0.01
Th	37.40	0.97	0.00	0.00	453.04	53.96	0.00	0.00	5.50	0.17	0.01	0.00
U	37.64	1.07	0.00	0.00	472.88	41.07	0.00	0.00	1.65	0.09	0.00	0.00

Table 3.4: Average detection limits for trace elements for mafic and silicic melt inclusions.

	Mafic melt inclusions (basalt to andesite) Detection limit		**Silicic melt inclusions (dacite to rhyolite)** Detection limit	
	n=35	2σ	n=20	2σ
Li	1.33	1.92	0.59	0.67
Be	0.27	0.39	0.16	0.18
Si	1140	1732	790	902
Ca	364	507	316	354
Sc	0.39	0.60	0.37	0.43
V	0.32	0.45	0.29	0.32
Cr	5.04	7.16	6.82	6.79
Co	0.25	0.44	0.21	0.24
Ni	3.70	6.26	3.97	4.14
Cu	0.40	0.60	0.44	0.50
Zn	1.95	2.79	2.34	2.70
Ga	0.16	0.24	0.16	0.17
Ge	2.47	3.46	2.31	2.64
As	0.63	0.95	0.41	0.47
Rb	0.18	0.26	0.10	0.11
Sr	0.13	0.19	0.08	0.09
Y	0.05	0.08	0.03	0.03
Zr	1.00	1.46	0.45	0.48
Nb	0.02	0.02	0.01	0.01
Mo	0.13	0.19	0.12	0.12
In	0.03	0.05	0.03	0.03
Cs	0.14	0.22	0.07	0.07
Ba	0.26	0.40	0.18	0.19
La	0.03	0.04	0.02	0.02
Ce	0.03	0.05	0.02	0.02
Pr	0.02	0.02	0.01	0.01
Nd	0.10	0.17	0.05	0.05
Sm	0.08	0.14	0.07	0.10
Eu	0.03	0.05	0.02	0.02
Gd	0.15	0.21	0.09	0.10
Tb	0.01	0.02	0.01	0.01
Dy	0.07	0.11	0.04	0.05
Ho	0.01	0.02	0.01	0.01
Er	0.07	0.12	0.03	0.04
Tm	0.01	0.02	0.01	0.01
Yb	0.06	0.09	0.03	0.04
Lu	0.01	0.01	0.01	0.01
Hf	0.07	0.11	0.04	0.04
Ta	0.02	0.03	0.01	0.01
Pb	0.07	0.16	0.08	0.12
Th	<0.00	0.01	<0.00	0.01
U	<0.00	0.01	<0.00	<0.00

3.4 Corrections for post-entrapment changes to melt inclusions

At the time of trapping, most MIs are incorporated as a silicate liquid, but they can undergo various phase changes depending on cooling conditions (Roedder 1984). If cooling is fast enough that quenching is effectively achieved, a MI will remain glassy; however, if cooling is slow, the MI may partially or even completely crystallize. Also, if originally glassy MIa are subjected to high temperatures for extended periods of time, they may devitrify. Vapor phases and fluids (such as a saline liquid) may also "unmix" from the MI during cooling.

3.4.1 Correction for Fe and Mg in olivine post-entrapment crystallization

Post-entrapment crystallization (PEC) of olivine on the walls of the MI is expected to occur upon cooling (Roedder 1984; Kress and Ghiorso 2004). This operates as fractional crystallization of concentric shells of the host mineral on the MI walls and can reach values of up to ~15 wt % olivine crystallized within the inclusion (Sobolev and Chaussidon 1996). PEC changes the composition of the trapped melt in the MI, as compatible major and trace elements are partitioned from the trapped melt into the crystal shell forming on the MI wall. This increases the concentration of incompatible elements in the remaining trapped melt. A correction to reverse this process is necessary to obtain the original composition of the trapped melt.

During PEC, the composition of olivine crystallized on the MI walls is governed by equilibrium olivine-melt partitioning rules. The forsterite (Fo) content of the crystallized olivine follows Fe^{2+}/Mg partitioning rules, which have been studied by many authors. The Fe^{2+}/Mg ratio is usually expressed as FeO/MgO, and the partition coefficient (k_D) of FeO/MgO between olivine and the melt is used to express equilibrium between olivine-melt pairs:

$$k_{D_{ol-l}}^{FeO/MgO} = \frac{\left(\frac{FeO}{MgO}\right)_{ol}}{\left(\frac{FeO}{MgO}\right)_{liq}} \qquad \text{(Equation 3.2)}$$

While an average of $k_{D_{ol-li}}^{Fe-M} = 0.3$ is used ubiquitously in the literature (Roeder and Emslie 1970), some authors have studied the effects of temperature, pressure, H_2O

content and other melt components on k_D values and have found them to vary quite significantly.

Choosing a k_D from the literature depends on the purpose (Falloon et al. 2007) and available data. One of the simplest methods is to adopt the Roeder and Emslie (1970) value, 0.30 ± 0.04, which is independent of pressure, temperature and melt composition, but to do so is to acknowledge that there could be an error on the resulting calculations since subsequent experiments show k_Ds can range by at least ± 0.1 (Toplis 2005). However, many parameterizations require values that are difficult to constrain by independent methods and therefore can incorporate circular arguments.

The method used here is a compromise between these difficulties. Definitive post-entrapment crystallization calculations will use the k_D of Roeder and Emslie (1970). Each MI is corrected in the following manner. First, the olivine entrapment temperature is estimated using a T- and P-independent formulation from Putirka (2008; Eq 13). The temperature is also calculated with the Beattie (1993) thermometer, assuming a realistic pressure, for comparative purposes. The two thermometers often give very similar results. The ferric-ferrous iron ratio for the MI is then calculated with the equation of Kress and Carmichael (1991), the temperature coming from Putirka (2008; Eq 13), the fO_2 set at the QFM buffer and the pressure set to 100 MPa. The fO_2 buffer was chosen based on oxygen fugacities determined for basalts from Andújar et al. (2015) and pressures from melt inclusion volatile barometry by Druitt et al. (2016). The MI composition is recalculated dry and with FeO and Fe_2O_3.

The k_D for the uncorrected MI and its host olivine is then calculated. If the k_D is lower than 0.30, equilibrium olivine addition is simulated in 0.01 wt % increments, recalculating the melt composition and equilibrium olivine composition at each step, until the resulting calculated k_D is equal to 0.30. The total wt % olivine added back to the melt is taken to be the amount of post-entrapment crystallization (PEC).

If the k_D is higher than 0.30, this means that olivine was probably melted back into the MIs during homogenization. We use the same approach as olivine addition but in reverse for olivine removal for the MI until the resulting k_D is equal to 0.30. This approach is not strictly appropriate, as host olivine should be added back instead of a calculated equilibrium olivine composition, but tests show that there is generally not a large difference whether a calculated equilibrium olivine composition is added back

stepwise or if the host olivine is added back into the MI in bulk. We will change the algorithm to add back bulk olivine for the final publication.

Details on calculating equilibrium olivine and adding back to melt inclusion

The method to calculate equilibrium olivine is detailed step-by-step below. First, an expression was derived to be able to calculate olivine Fo content in terms of an FeO/MgO ratio of an olivine. Fo is the forsterite content of the olivine and n represents molar proportion.

$$\mathrm{Fo} = \left(\frac{n_{MgO}}{n_{MgO}+n_{FeO}}\right)_{ol} \qquad \text{(Equation 3.3)}$$

This expression can be inverted to result in an equation with an FeO/MgO term:

$$\frac{1}{\mathrm{Fo}} = \frac{n_{MgO}+n_{FeO}}{n_{MgO}} = \frac{n_{MgO}}{n_{MgO}} + \frac{n_{FeO}}{n_{MgO}} = 1 + \frac{n_{FeO}}{n_{MgO}} \qquad \text{(Equation 3.4)}$$

and can be solved algebraically for Fo:

$$\mathrm{Fo} = \frac{1}{1+\left(\frac{n_{FeO}}{n_{MgO}}\right)_{ol}} \qquad \text{(Equation 3.5)}$$

Next, the definition of the $k_{D\,FeO-MgO}^{ol-melt}$ was used to derive an expression to determine the olivine FeO/MgO ratio given a known melt FeO/MgO ratio:

$$k_{D\,FeO-MgO}^{ol-melt} = \frac{\left(\frac{FeO}{MgO}\right)_{ol}}{\left(\frac{FeO}{MgO}\right)_{melt}} \qquad \text{(Equation 3.6)}$$

$$\left(\frac{FeO}{MgO}\right)_{ol} = k_{D\,FeO-M}^{ol-melt} \times \left(\frac{FeO}{MgO}\right)_{melt} \qquad \text{(Equation 3.7)}$$

Multiplying both sides of the above equations by $\frac{M_{MgO}}{M_{FeO}}$ (where M represents molar mass) gives the desired function:

$$\left(\frac{n_{FeO}}{n_{MgO}}\right)_{ol} = Kk_{D\,FeO-MgO}^{ol-melt} \times \left(\frac{FeO}{MgO}\right)_{melt} \times \frac{M_{MgO}}{M_{FeO}} \qquad \text{(Equation 3.8)}$$

which allows the determination of the FeO/MgO for an olivine in equilibrium with any given melt composition. The above expression for the FeO/MgO ratio of olivine can be substituted into the previously derived equation for forsterite content to give:

$$\mathrm{Fo} = \frac{1}{1+\left[k_{D\,FeO-MgO}^{ol-melt} \times \left(\frac{FeO}{MgO}\right)_{melt} \times \frac{M_{MgO}}{M_{FeO}}\right]} \qquad \text{(Equation 3.9)}$$

which allows one to calculate the forsterite content of olivine in equilibrium with any given melt composition. The two above equations are key for the following steps.

Next, an equilibrium olivine composition in weight percent oxides was derived from the Fo content. This calculation generates the equilibrium composition of an ideal olivine [$(Mg,Fe^{2+})_2SiO_4$)], i.e. all elements other than Mg, Fe^{2+} and Si are treated as perfectly incompatible. In reality, this is not the case as some Ti, Al, Fe^{3+} and other elements are typically taken in by olivine in very small amounts. However, the effects of these elements are quite small and thus this calculation should be a good approximation.

First it was necessary to find molar proportions of Mg, Fe^{2+} and Si in the equilibrium olivine in terms of a known value; e.g. FeO/MgO ratio of olivine, which can be obtained using an above equation. To do this, stoichiometry must be considered. The olivine formula $(Mg^{2+}Fe^{2+})_2SiO_4$ gives the following number of moles of each constituent:

$$n_{Fe^{2+}} + n_{Mg} = 2 \qquad n_{Si} = 1 \qquad n_{O_2} = 2 \quad \text{(Equation 3.10a, b, c)}$$

Algebraic rearrangement allows the derivation of expression for the molar proportions of each individual constituent given the iron-magnesium ratio of the olivine.

$$n_{Fe^{2+}} + n_{Mg} = 2 \qquad \text{(Equation 3.11)}$$

Multiplying each side by 1/Mg gives:

$$\frac{n_{Fe}}{n_{Mg}} + \frac{n_{Mg}}{n_{Mg}} = \frac{2}{n_{Mg}} \qquad \text{(Equation 3.12)}$$

reducing to:

$$\frac{n_{Fe}}{n_{Mg}} + 1 = \frac{2}{n_{Mg}} \qquad \text{(Equation 3.13)}$$

Multiplying each side then by n_{Mg} gives:

$$n_{Mg}\left(\frac{n_{Fe}}{n_{Mg}}+1\right)=2 \qquad \text{(Equation 3.14)}$$

solved for n_{Mg} to give:

$$n_{Mg}=\frac{2}{\left(\frac{n_{Fe}}{n_{Mg}}+1\right)} \qquad \text{(Equation 3.15)}$$

With the above expression, the molar proportion of Mg can be determined given the $(FeO/MgO)_{ol}$ calculated with Equation 3.7. It follows that $n_{Fe2+} = 2 - n_{Mg}$, and $n_{Si} = 1$. These molar proportions can then be easily converted to weight percent oxides, giving an ideal composition of olivine in equilibrium with a melt composition and can be added into the melt using the mass-conserving mixing formula:

$$(\text{new wt \% oxide})_{melt} = [1 - (\text{step size}/100)]*(\text{old wt \% oxide})_{melt} + (\text{step size}/100)*(\text{wt \% oxide})_{olivine}$$

(Equation 3.16)

and the incompatible elements are diluted at a rate of:

$$(\text{new wt \% oxide})_{melt} = (\text{old wt \% oxide})_{melt} - (\text{old wt \% oxide})_{melt}*(\text{step size}/100)$$

(Equation 3.17)

A user-friendly spreadsheet is made available as a supplementary electronic file.

3.4.2 Diffusional re-equilibration correction

Iron loss, i.e. the re-equilibration of the Fe^{2+} of MIs with external surroundings (olivine host and/or external melt), is a common phenomenon for olivine-hosted inclusions and has been described many times in the literature (Qin et al. 1992; Danyushevsky et al. 2000; Cottrell et al. 2002). Olivine crystallizing on the walls of a MI will be more Fe-rich than the host olivine, and the crystallizing olivine will take out more Mg than Fe^{2+} from the melt according to partitioning rules, leading to a depletion in the melt of Mg and enrichment in Fe^{2+} over the course of post-entrapment crystallization. This results in Mg diffusing into the MI and Fe diffusing out in order to equilibrate the sharp gradient. At high temperatures, Fe-Mg diffusion can occur rapidly. In small crystals with relatively large MIs, re-equilibration can also occur quickly (Qin et al. 1992).

Fe loss can be recognized as it causes a negative correlation between the Fo content of the olivine host and the total FeO of the melt (Danyushevsky et al. 2002). If the apparent olivine-MI k_D is higher than 0.3, this could be a sign of melting of excess host olivine into the MI during experimental homogenization or the use of an incorrect ferric-ferrous iron ratio in the correction procedure. Iron loss can occur when a MI is subjected to high enough temperatures for diffusion of iron to begin. Since the trapped melt is higher in Fe than its more magnesian olivine host, iron (Fe^{2+}) will diffuse into the host in an attempt to reach equilibrium, resulting in a loss of Fe from the MI over time.

The problem of diffusional Fe loss has been discussed in the past (Danyushevsky et al. 2000; Gaetani and Watson 2000; Kent 2008) and corrections have been undertaken in many studies, but there is no standard correction. It is suggested to estimate an initial FeO, and the best way to do this is to plot the FeO of groundmass and whole rock data and extrapolate the FeO value of the MI with suspected iron loss back to the FeO trend. However, these types of corrections are only possible when sufficient other data (whole rock and groundmass analyses) exist.

When Fe diffusion is not accounted for, the PEC correction can lead to erroneous melt compositions in FeO, MgO and Al_2O_3. We did not globally correct for Fe loss because it appears to vary for the samples studied and it was not always possible to compare with whole rock and groundmass data to make an accurate assumption of initial FeO. We avoid the Fe loss problem in this paper by (1) focusing mainly on trace elements, (2) only presenting data for major elements TiO_2, K_2O and CaO (which are relatively little affected) and (3) evaluating Fe loss on an individual MI basis if we later want to use FeO and MgO.

3.4.3 Correction for compatible trace elements in olivine

Compatible elements are taken in by olivine crystallizing on the walls of the MI; therefore, the measured compatible elements in the MI need to be corrected for this crystallization.

Prior to trace element correction, the amount of PEC was determined for each MI during Fe-Mg correction. The amount of PEC is required to perform the trace element correction.

First, olivine-melt k_Ds were determined from a subset of MIs for which trace element data were obtained for both the MI and adjacent olivine composition. Simply taking the measured trace element data for olivine and MIs would not be appropriate, as more compatible elements will be partitioned into the olivine crystallizing on the MI walls, therefore depleting the MI in that element. Instead, the original MI concentration was determined by applying a reverse fractional crystallization simulation using the equation:

$$C_0^{MI} = \frac{C_{liq}^{MI}}{F_C^{kD-1}} \qquad \text{(Equation 3.18)}$$

where C_0^{MI} is the original MI composition, C_{liq}^{MI} is the MI composition, F_C is the fraction crystallized (F_C = 1 - %PEC/100) and a nominal value is entered for the k_D. An equilibrium olivine composition is then generated by multiplying C_0^{MI} by the k_D. Then, the k_D is changed until this equilibrium olivine calculation matches the measured host composition adjacent to the MI. The k_D that renders the calculated host olivine identical to the actual host composition was taken to be the real k_D.

However, not all MI-adjacent olivine trace element compositions could be measured. It was necessary to assess which k_Ds appeared to change with Fo content and which remained relatively constant. Where k_Ds changed with Fo content, a function was fit to the correlation and was used to determine the k_D for each MI. Where the k_Ds were not a strong function of Fo, an average of the values was taken. The results of the k_D calculations and dependencies will be discussed in the following chapter.

The trace elements were then corrected for all the olivine-melt pairs with unknown k_Ds with the above equation, but this time using the known or calculated k_D value.

3.4.4 Corrections for melt inclusions of other phases

During PEC in plagioclase-hosted MIs, Ca is preferentially depleted from the melt as a more Na-rich rim forms around the inclusion; however, due to complicated dependencies on pressure and temperature on the composition of the crystallizing plagioclase, a correction procedure is not as straightforward as for olivine. As there is no way to easily quantify the amount of PEC, plagioclase MIs were not corrected for major or trace elements (for the moment). Melt inclusions in pyroxenes were also not corrected; however, these make up a very small percentage of the MIs in our dataset.

3.4.5 Note about Sr values

We observed that Sr was sometimes abnormally low (sometimes at ~ 0 ppm in MIs). We do not know the origin of these low Sr values. We sometimes report and plot Sr in thesis, but we do not place emphasis or base conclusions on the Sr contents due to the unknown origin of these abnormally low Sr values.

Chapter 4: Multiple mantle source domains beneath Santorini Caldera

Authors: T. Flaherty[1], T. Druitt[1], P. Schiano[1], O. Sigmarsson[1], L. Francalanci[2]

[1]Laboratoire Magmas et Volcans, Université Clermont-Auvergne, CNRS, Clermont Ferrand, France

[2]Dipartimento di Scienze della Terra, Università degli studi di Firenze, Italy

Abstract

Santorini Volcano (Greece) is situated in an extensional basin toward the center of the South Aegean Volcanic Arc. Basalts are more common at Santorini than at other volcanic centers along the volcanic arc, allowing the opportunity to study primitive basaltic melts feeding an arc volcano capable of large explosive eruptions as well as effusive activity. We investigate the nature of primitive melts at Santorini with a new dataset of olivine-hosted melt inclusions covering units from throughout the >0.65 Ma history of the volcanic field. A clear range in incompatible trace elements exists in the most primitive melts, with high-Nb (more calc-alkaline) and low-Nb (more tholeiitic) endmembers recognized by previous studies. Production of these melts can be modelled by different degrees of partial melting of a depleted-MORB-like mantle metasomatized mainly by slab-derived sediment melts with possibly different residual mineralogies. The lack of evidence for a major role of slab-derived aqueous fluids suggests that basalt genesis in the mantle wedge beneath Santorini could be driven at least partly by decompression melting. The different endmember primitive melts have been erupted repeatedly over the history of the volcano, sometimes together within a relatively short (< 10 ky) time period, suggesting that at least two long-lived mantle source domains feed basaltic magmas to Santorini.

Keywords: Santorini; subduction zones; arc magmas; melt inclusions; trace elements.

4.1 Introduction

Arc volcanoes, i.e. those formed above subduction zones, can be particularly explosive compared to those in other tectonic settings (Gill 1981; Sisson and Grove 1993a; Plank et al. 2013). Since large populations live on or near volcanically active continental margins, it is critical to study continental arc volcanism with the goal of minimizing associated risks. Understanding the generation and differentiation of subduction zone magmas allows us to decipher the deep physical and chemical processes that culminate in volcanic eruptions at the surface.

Arc magmas show a higher degree of compositional diversity than those in other settings (Ducea et al. 2015; Turner and Langmuir 2015), which can help trace the processes that result in magma genesis. Most of the diversity in arc magmas can be attributed to petrological processes (crystallization, magma mixing, crustal melting, assimilation, etc.), modifying primary melts transported through the crust; however, primitive arc magmas (i.e. magmas derived from mantle melting that are relatively unaltered by crustal processes) have been observed to vary on a range of spatial and temporal scales before modification by crustal processes. The heterogeneity of primitive arc magmas can be explained by the variability in the compositions of the mantle wedge and down-going slab, and the relative contributions from each to magma production (Gill 1981; Pearce and Peate 1995; Kessel et al. 2005; Keppler 2017). Subducting slabs release aqueous fluids, hydrous melts and/or supercritical fluids into the mantle wedge, which then induce flux melting by lowering the solidus of peridotite (Arculus 1994; Gaetani and Grove 1998; Katz et al. 2003; Kessel et al. 2005; Grove et al. 2012; Zellmer et al. 2015). These primary mantle melts and associated heat drive magmatism in the overlying arc crust.

Separate differentiation trends emerge in arc settings based on whether there is an iron-depletion (calc-alkaline) or iron-enrichment (tholeiitic) trend (Miyashiro 1974; Chin et al. 2018). One hypothesis is that tholeiitic magmas are associated with dry, less oxidized mantle sources and/or lower pressure melting, while calc-alkaline magmas are derived from more hydrated, more oxidized mantle sources (due to the oxidized nature of slab input) and/or higher pressure melting (Grove and Baker 1984; Sisson and Grove 1993a; Chin et al. 2018). While calc-alkaline magmas are almost unique to subduction zones, tholeiites also appear in other settings, most commonly in mid-ocean ridge or back-arc settings (Presnall et al. 1979), or in shield-building stages of

hot spot volcanoes such as Hawaii or Réunion, where tholeiites are erupted in large volume (Moore and Clague 1992). A range of primitive melts have been reported for arc volcanoes around the world. The Cascades, for example, erupt basalts akin to Oceanic Island Basalt (OIB; alkaline magmas typically associated with oceanic intraplate volcanoes), arc tholeiite and calc-alkaline magmas, which are attributed to variable mantle parental domains with subduction slab contributions for the more calc-alkaline magmas (Hughes 1990; Leeman et al. 1990; Bacon et al. 1997; Mullen et al. 2017; Pitcher and Kent 2019; Wanke et al. 2019). Other notable cases of variable primitive melts include the Andes (Watt et al. 2013; Weller and Stern 2018), the Mexican Volcanic Belt (Wallace and Carmichael 1999) and the Kurile Island Arc (Bindeman and Bailey 1999). Increasing discovery of ranges of primitive melt types below arcs around the world, especially using olivine-hosted melt inclusion studies, attests to complex mantle and subduction zone processes below arc volcanoes.

The South Aegean Volcanic Arc (Figure 4.1a) shows a wide variation of primitive and evolved magmas (Mitropolous et al. 1987; Huijsmans et al. 1988; Druitt et al. 1999; Francalanci et al. 2005b; Klaver et al. 2016; Francalanci and Zellmer 2019). Basalts are more common at Santorini than at other volcanic centers along the Aegean Arc, partly due to its location in an extensional basin near the center of the arc (Figure 4.1a). It lies on ~25 km of thinned continental crust, which allows basalts to reach the surface relatively easily (Francalanci et al. 2005b; Francalanci and Zellmer 2019).

The frequency of basaltic eruptions in the eruptive record at Santorini, combined with excellent exposure, allows us in the present paper to use olivine-hosted melt inclusions to investigate the nature and origin of the primary basaltic melts feeding Santorini, and how they vary over time. Olivine-hosted inclusions provide samples of primitive melts, which, unlike whole rocks, are not potentially contaminated with antecrysts or xenocrysts. We present a full chrono-stratigraphic context of the volcano in this study, having sampled many key major and minor units throughout the entire volcanic history, and show that Santorini magmas are fed from at least two compositionally distinct mantle source domains.

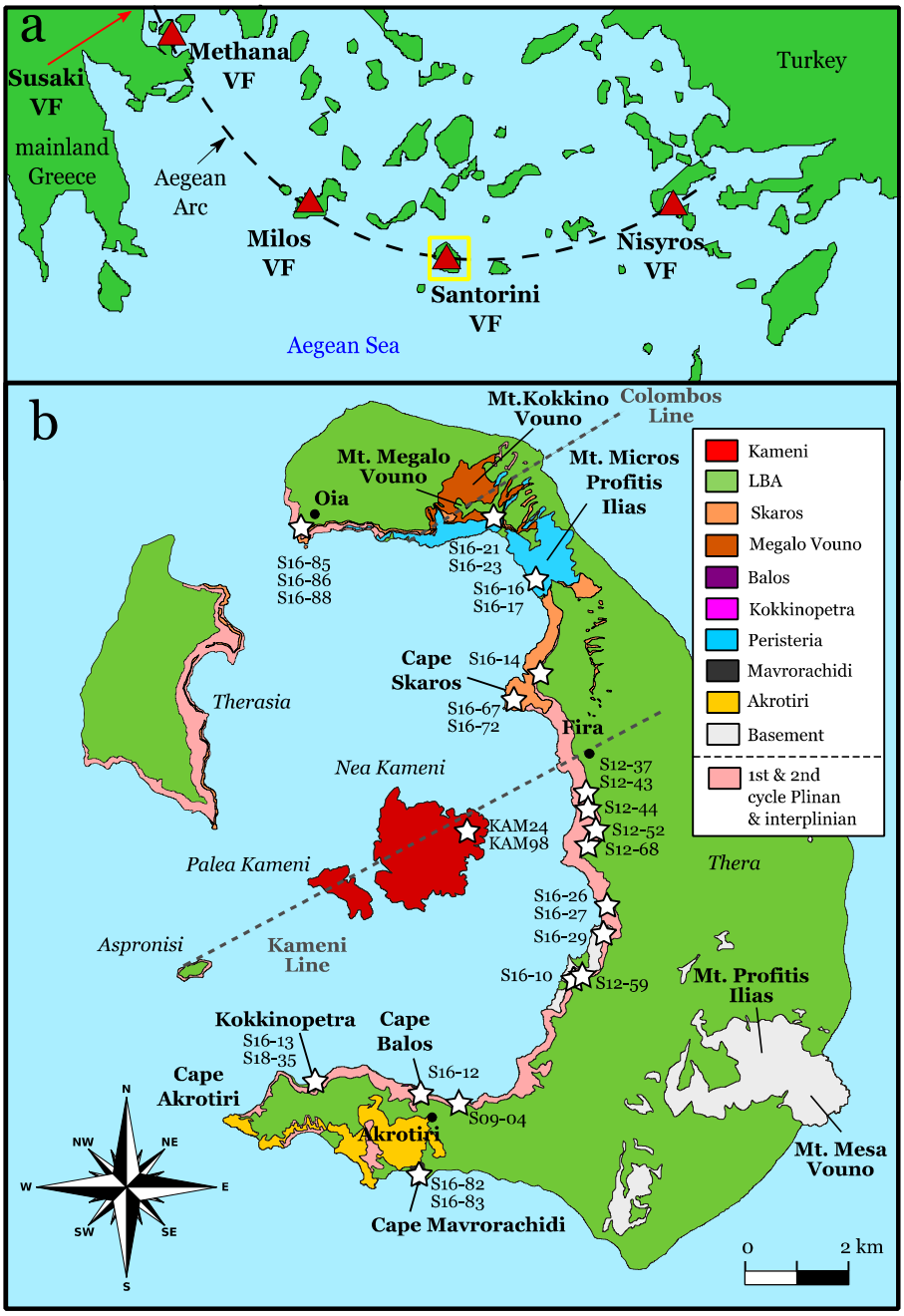

Figure 4.1: (a) Map of the southern Aegean Sea showing the main volcanic centers of the Aegean Arc. (b) Geologic map of Santorini (based on that of Druitt et al. 1999) highlighting the exposures of pre-volcanic basement, the volumetrically prominent volcanic units and the units relevant to this study. First and second cycle Plinian and interplinian units not already shown (e.g. LBA eruption) are grouped together as one map unit, as the layers are numerous and thin and would be difficult to show. Approximate locations of each sample from this study are marked with white stars and the respective sample names. Numerous past eruption vents align long the Kameni Line and Colombos Line, which are parallel to regional faults and thought to be surface expressions of basement faults.

4.2 Geologic context

Modern tholeiitic to calc-alkaline volcanism along the Aegean Arc began around 4.7 Ma (Fytikas and Vougioukalakis 2005; Vougioukalakis et al. 2019), due to subduction of the African plate (~ 1 cm yr^{-1} to the NE) below the Aegean microplate (moving ~3.5 cm yr^{-1} to the SW) (Kahle et al. 1998; McClusky et al. 2000; Papazachos 2019). The Benioff zone lies about ~150 km below the arc, although it is deeper (>190 km) in the center of the arc (Keller 1982; Papadopoulos 1982). The mantle below the Aegean Arc is believed to be of a depleted MORB mantle (DMM) composition (Francalanci et al. 2005b; Francalanci and Zellmer 2019; Papazachos 2019). The thickness of the continental crust is variable, with the western and eastern sections of the arc having thicker crust (32-34 km) and the central section having thinner (23-26 km) crust (Makris 1977; Papazachos 2019). The lithospheric extension, which is greatest towards the center of the arc, is thought to be accompanied by decompression melting (Francalanci and Zellmer 2019). This may obscure signatures of calc-alkaline fluid-flux melting, as melts of more MORB-like or back-arc-basin-like tholeiitic character should be expected with decompression melting (Stolper and Newman 1994; Sinton et al. 2003; Pearce and Stern 2006; Bézos et al. 2009). The arc hosts several volcanic fields (Figure 4.1a), one of the most explosive centers being Santorini Volcano, whose last major explosive eruption was in the Late Bronze Age and resulted in a caldera collapse and local, regional and global impacts on human populations and the environment (Bond and Sparks 1976; Sigurdsson et al. 1990; Antonopoulos 1992; Pyle 1997; Druitt et al. 1999; Eastwood et al. 2002; Friedrich and Sigalas 2009; Druitt 2014; Cadoux et al. 2015; Athanassas et al. 2018).

Santorini is located in the center of the island arc (Figure 4.1a,b). Volcanism there began ~650 ka in the form of submarine centers, lava domes and tuffs on the modern-day Akrotiri peninsula (Figure 4.1b). This was followed by establishment of Peristeria stratovolcano in the north between 530-430 ka and semi-contemporaneous cinder cones of Balos, Kokkinopetra and Mavrorachidi in the south from ~520-350 ka (Druitt et al. 1999) (Figure 4.1b).

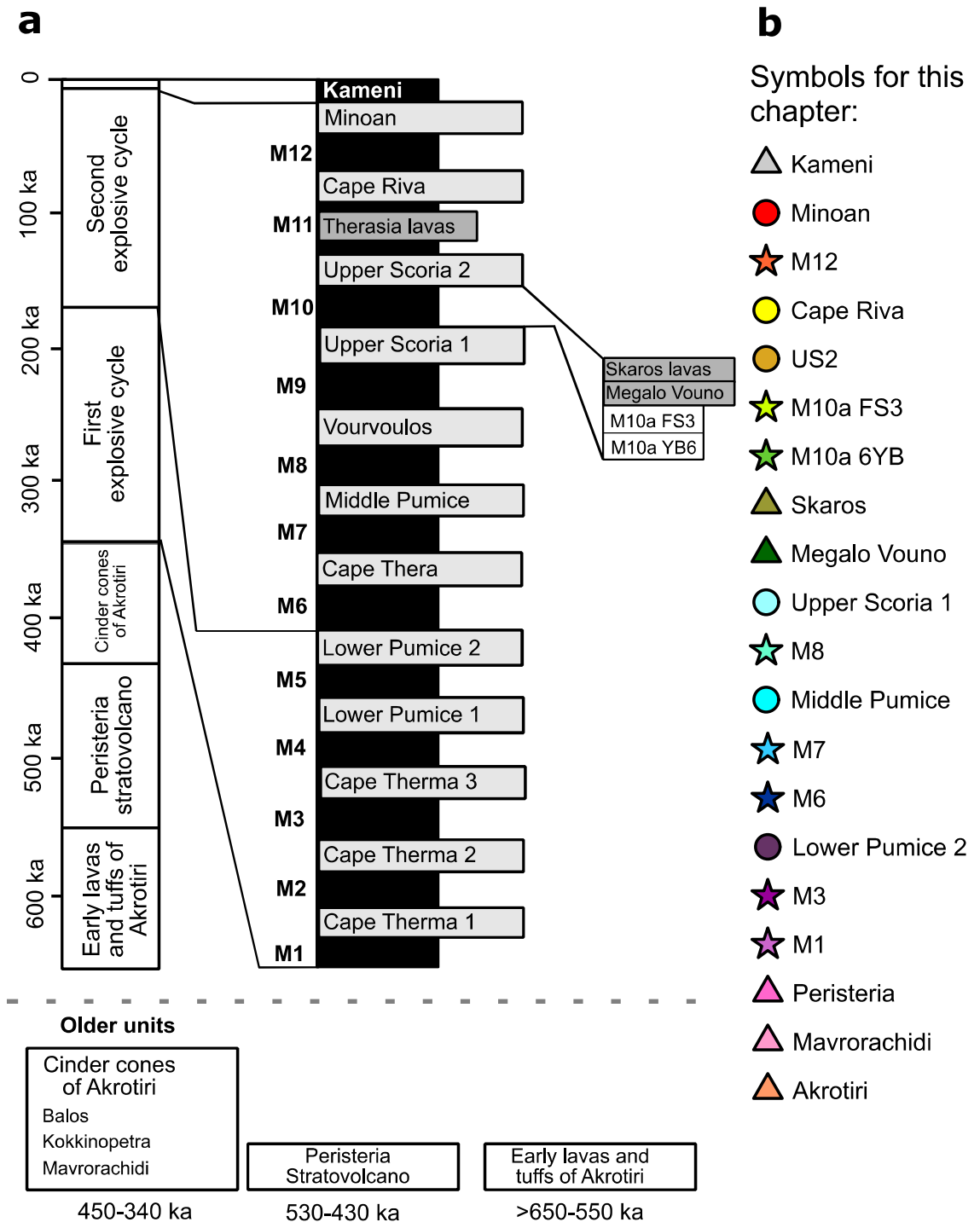

Figure 4.2: Santorini eruptions and symbols used in this chapter. (a) A broad overview of the Santorini eruptive history, with the left approximately to scale, using dates from Druitt et al. (1999) and, on the right, the sequence (not to scale) of twelve identified Plinian eruptions (wide grey rectangles) since 360 ka. Plinian eruptions are separated by interplinian periods (smaller black rectangles) M1 through M12. Subdivisions follow Druitt et al. (1999) and Vespa et al. (2006). Older units are summarized below the stratigraphic columns. (b) Symbols shown are those used in geochemical diagrams to follow in this chapter.

Since 360 ka, major Plinian eruptions have alternated with interplinian periods characterized by intracaldera edifice construction and relatively minor explosive activity (Druitt et al. 1999; Vespa et al. 2006) (Figure 4.2a). The twelve identified Plinian eruptions are given names, whereas interplinian periods are designated as 'M' (for 'minor') plus their number in the stratigraphic sequence (Druitt et al. 1999; Vespa et al. 2006) (Figure 4.2a). Two general eruptive cycles are recognized—the first from 360 to 172 ka, and the second from 172 to 3.6 ka (Druitt et al. 1999; Gertisser et al. 2009). The two cycles follow a similar pattern: a transition from dominantly intermediate to dominantly silicic explosive eruptions, with the large silicic eruptions (Lower Pumice 1 and Lower Pumice 2 of cycle 1; Cape Riva and Late Bronze Age eruption of cycle 2) resulting in caldera collapse (Figure 4.2a) (Druitt et al. 1999).

The most recent volcanism (<3.6 ka) has built up the present-day 400-m-high Kameni intracaldera edifice (Figure 4.1b), the last eruption of which was a minor effusive eruption in 1950 (Georgalas 1953; Pyle and Elliott 2006; Nomikou et al. 2014). In 2011-12 there was a period of unrest involving increased seismicity and inflation centered to the north of Nea Kameni, which has since been attributed to magmatic intrusion below the volcano (Parks et al. 2015).

Santorini eruptive products range from basalt to rhyodacite in composition and from mildly arc (low-K) tholeiitic to calc-alkaline in character (Huijsmans et al. 1988; Tarney et al. 1998; Druitt et al. 1999; Bailey et al. 2009). A multi-level transcrustal plumbing system has been envisaged beneath the 10 x 6 km caldera where basalts with up to 2 to 4 wt % H_2O intrude at or around the interface between upper and lower crust, producing a mush in which more evolved melts are generated. These evolved melts can then be transferred upwards to feed upper crustal magma reservoirs (Cadoux et al. 2014; Andújar et al. 2015; Druitt et al. 2016; Flaherty et al. 2018).

Santorini basalts have been the focus of a number of studies (Nicholls 1978; Tarney et al. 1998; Vaggelli et al. 2009; Bailey et al. 2009; Baziotis et al. 2018) and have been included in a number of more general studies on the volcano (Nicholls 1971; Huijsmans 1985; Huijsmans and Barton 1989; Druitt et al. 1999, 2016). Compared to other compositions erupted at the volcano, basalts are relatively rare, and most have significantly evolved by the time they reach the surface; the most mafic whole rock at Santorini has ~6 wt. % MgO. Nicholls (1978) estimated that primary mantle melts (9-12 wt% MgO) ascend into the crust and differentiate at the Moho or in the lower crust

below Santorini, producing differentiated basalts and leaving behind mafic to ultramafic cumulates. Baziotis et al. (2018) estimated a primary mantle-melt composition and the conditions of mantle melting starting with a whole rock analysis from the basaltic Balos cinder cone (Figure 4.1b).

Previous studies have suggested that different magmatic series exist at Santorini based on geochemical grounds. Tarney et al. (1998) identified an incompatible element (e.g. Nb, Zr) 'enriched' calc-alkaline trend and incompatible 'depleted' tholeiitic trend in Santorini products, and attributed at least some of the variation to mantle source variations. The study of Bailey et al. (2009) on the dykes and lavas of the northern caldera walls showed that there was a range in incompatible elements in basaltic to basaltic andesite magmas. Vaggelli et al. (2009) studied olivine-bearing melt inclusions from a single scoria fall of the M12 interplinian period. None of these studies on basalts, however, placed the different primary magmas in detailed stratigraphic context, nor did they address how their availability beneath the volcano has varied through time.

4.3 Methods

Samples of Santorini mafic products were collected during two sampling missions, focusing on olivine-bearing scoria in order to have the best chance of finding glassy melt inclusions (MI) (Figure 4.1b; Table 4.1). The main types of samples in this study are scoria (with glassy to variably microcrystalline matrix), lava, and mafic enclaves in silicic pumice. All scoria samples were collected from airfall layers so as to maximize chances of rapid post-eruptive cooling, preserving fully glassy MIs. The samples have typical mineral assemblages of Santorini basalts: olivine + pyroxene (dominantly cpx) + plagioclase + Fe-Ti oxides. Magnetite appears as free crystals and inclusions in other phases. Ilmenite is sometimes present in the groundmass, often with skeletal growth patterns, suggesting late-stage crystallization. A list of samples and short descriptions is given in Table 4.1.

The samples were crushed with a jaw crusher and sieved into various size fractions. Fractions were magnetically separated, then MI-bearing crystals were hand-picked under a binocular microscope. A visual textural control was applied during MI selection, where crystals were inspected to identify fractures, melt splays, melt tubes or other connections to the surface of the crystal to avoid erroneous melt compositions.

Inclusions that displayed signs of alteration were rejected. A further selection requirement was that the MIs had to have at least 20 x 20 μm of analysable area, not including the bubble.

If MIs were crystallized or devitrified, it was necessary to remelt them, then quench to a homogenous glass, using a Vernadsky-type heating stage. The stage includes a small heating device, upon which a disk-shaped transparent sample holder sits. The sapphire disk supports a free MI-bearing crystal, polished lightly on two parallel sides so that

Table 4.1: Samples used in the present study with descriptions. *Samples provided by L. Francalanci.

Eruption	Samples	Sample description
LBA	S19-01	Cauliform mafic scoria, large single clast
	S94-01	Cauliform mafic scoria, small single clast
	S94-07	Cauliform mafic scoria, small single clast
	S94-09	Cauliform mafic scoria, small single clast
Kameni	KAM24*	Type "B1" mafic enclave with cumulitic texture
	KAM98*	Type "A" mafic enclave with cumulitic texture
M12	S16-14	Bulk sample of small vesicular mafic scoria
Cape Riva	S16-85	Bulk sample of vesicular mafic scoria
	S16-86	Bulk sample of vesicular mafic scoria
	S16-88	Bulk sample of vesicular mafic scoria
US2	S09-44	Bulk sample of vesicular mafic scoria
M10a FS3	S12-43	Bulk sample of scoria
M10a 6YB	S12-37	Bulk sample of scoria
Skaros	S16-67	Bulk sample of scoria
	S16-72	Massive lava, one clast
Megalo Vouno	S16-21	Bulk sample of scoria
	S16-23	Bulk sample of scoria
Upper Scoria 1	S09-04	Bulk sample of scoria
M8	S12-68	N/A (MIs from previous study)
Middle Pumice	S12-59	N/A (MIs from previous study)
M7	S12-44	N/A (MIs from previous study)
M6	S12-52	N/A (MIs from previous study)
Lower Pumice 2	S16-10	Bulk sample of cauliform mafic enclaves
M3	S16-29	Bulk sample of scoria
M1	S16-26	Bulk sample of scoria
Peristeria	S16-16	Bulk sample of scoria
Mavrorachidi	S16-82	Bulk sample of scoria
	S16-83	Bulk sample of scoria
Akrotiri	S18-11	Vesicular mafic enclave from Akrotiri lava

the free crystal sits flat on the disk and that the observer can see clearly inside the crystal. A quartz window on top of the heating stage allows an observer to monitor and track changes in the MI during experimental runs under a petrographic microscope at 10-20x magnification.

Each reheating experiment was performed at 1 atmosphere pressure and at low oxygen fugacities, typically between 10^{-18} to 10^{-20} atm. A Pt-Pt_{90}-Rh_{10} thermocouple is attached to the sample holder to track the temperature. The oxygen fugacity is controlled by running helium through a 680-700°C furnace containing a zirconium rod. As the helium passes over the zirconium, the zirconium removes oxygen from the air, allowing the low oxygen fugacities to be obtained. The helium flux is set at about 20 mL/min. During the course of an experiment, the temperature is increased by gradually increasing the voltage supplied to the heating stage. The MI-bearing crystal is heated incrementally until the MI melts completely. The MI is then quenched by cutting the power to the furnace. The quenching process happens very quickly (dropping to below solidus temperature usually within 1 to 2 seconds) due to two factors: (1) cooling of the surrounding of the heating stage by chilled water (~15°C) and (2) the high thermal conductivity of helium.

Selected MI-bearing crystals (e.g. Figure 4.3a) were mounted in epoxy in small brass cylinders and polished using a sequence of silicon carbide (1200 & 2400 grade) and diamond polishing mats (6, 3 and ¼ µm grades) until the MI was exposed at the surface and was visibly well-polished under reflected light.

A CAMECA SX-100 electron microprobe (EMP) with 15 kV accelerating voltage housed at the Laboratoire Magmas et Volcans (LMV) was used to analyze major element compositions of the MIs using a defocused (10 to 20 µm spot size) electron beam at 4 to 8 nA beam current in order to avoid Na depletion (Nielsen and Sigurdsson 1981). Sodium was analyzed first for a counting time of 10s to minimize low Na counts, which were seen to be unaffected in the first ~10s but then rapidly decreased for longer durations. Major element analysis was always performed before any other analyses involving electron beam interaction (e.g., backscattered electron imagery). Depending on the size of the MI, between one and four spot analyses were taken. Where more than one analysis was taken, the compositions were averaged and checked for compositional homogeneity. Analytical errors on analyses were converted to 2σ standard deviation and compared with 2σ standard deviation resulting from averaging. The larger value

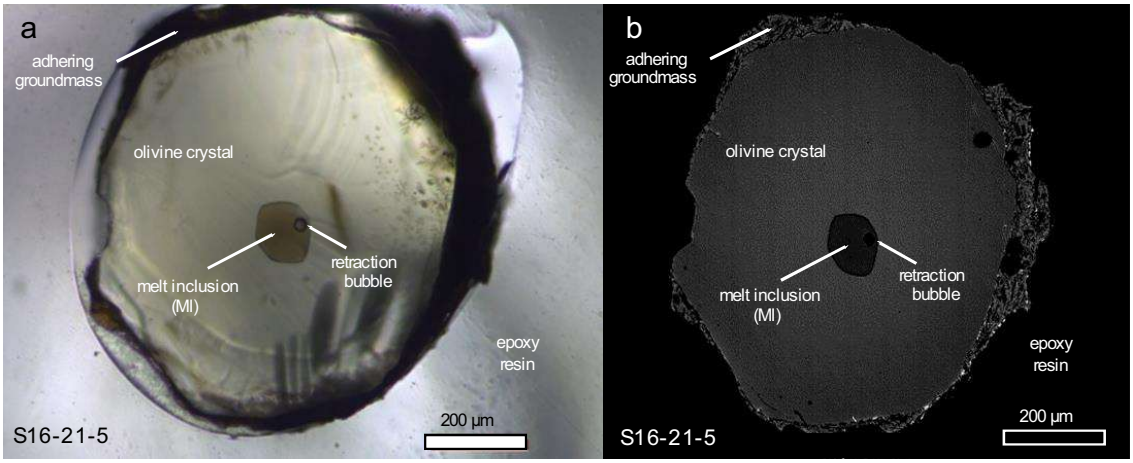

Figure 4.3: Melt inclusion in an olivine host. (a) S16-21-5 photograph, transmitted light. (b) S16-21-5 backscatter electron (BSE) image.

between the two was kept as the 2σ standard deviation. Backscatter electron (BSE) imagery was used to judge where to analyze the host mineral in equilibrium with each melt inclusion (Figure 4.3b). Minerals were measured for major elements via EMPA with a focused (in reality: ~1 µm) beam size and 15 nA beam current.

Trace elements were analyzed by laser ablation induced coupled plasma mass spectroscopy (LA-ICP-MS) at the LMV. The LA-ICP-MS set-up consists of a Resonetics ArF excimer (193 nm wavelength) laser (model: RESOlution M-50E) coupled to a Thermo Element XR ICP-MS. NIST612 and/or NIST610 glasses were used as reference standards, while BCR2 was used as an external standard. Cesium values were rejected from any melt inclusions analyzed in previously made indium mounts (Druitt et al. 2016 MI volatile study), as there was clear Cs contamination from the SIMS Cs+ ion beam and/or Cs in indium which had entered into small cracks or pits on the surface of the inclusion. A single LA-ICP-MS analysis contains 30 s of background signal collection followed by 90-100 s of sample analysis, and results in a time-resolved signal. GLITTER software was used to reduce the data and calibrate with standards to obtain trace element concentrations.

The olivine-hosted MIs are corrected for post-entrapment crystallization (PEC) (Roedder 1984; Kress and Ghiorso 2004). This process operates as fractional crystallization of concentric shells of the host olivine on the MI walls and can reach values of up to ~15 wt % of olivine crystallized (Sobolev and Chaussidon 1996).

First, the olivine entrapment temperature is estimated using a T- and P-independent formulation from Putirka (2008; Eq 13). The ferric-ferrous ratio for the MI is then calculated with the equation of Kress and Carmichael (1991), the temperature coming from Putirka (2008; Eq 13), the fO_2 set as the QFM buffer (a realistic oxygen fugacity buffer based on literature; e.g. Andújar et al. 2015), and at a pressure of 100 MPa. The MI composition was recalculated dry with both ferric and ferrous iron.

The partition coefficient k_D for the uncorrected MI and its host olivine was then calculated. All olivine-hosted MIs are corrected so that their corrected kD is 0.30, no matter if they are in the Roedder & Emslie (1970) range of 0.30 ± 0.03 or not. When the microprobe analytical error is taken into account, there is an 18 to 141 % error on the kD, with a 37 % average error (n=96). In fact, 51% of total ol-hosted MIs may have kDs that fall in the 0.30 ± 0.03 range. If the k_D was lower than 0.30, equilibrium olivine was added in 0.01 wt % increments, recalculating the melt composition and equilibrium olivine composition at each step, until the resulting calculated k_D was equal to 0.30 (Roedder & Emslie 1970). The total wt % olivine added back to the melt was taken to be the amount of PEC.

Trace elements were also corrected for PEC, since trace elements are also affected by wall crystallization. The original MI concentration was determined by applying reverse fractional crystallization using the Rayleigh fractionation equation:

$$C_0^{MI} = \frac{C_{liq}^{MI}}{F^{k_D-1}} \qquad \text{(Eq. 4.1)}$$

where C_0^{MI} is the original MI composition, C_{liq}^{MI} is the measured and corrected MI composition, F in this case is the fraction crystallized (F = %PEC/100) and a nominal value is entered for the k_D. An equilibrium olivine composition is then generated by multiplying C_0^{MI} by the k_D. Then, the k_D is changed until this equilibrium olivine calculation matches the measured host composition adjacent to the melt inclusion. The k_D that renders the calculated host olivine identical to the actual host composition was taken to be the real k_D. A summary of olivine-melt k_Ds is given in

Table **4.2**.

If the k_D is higher than 0.30, this means that olivine was probably melted back into the MIs during homogenization. We use the same approach as olivine addition but in reverse for olivine removal for the MI until the resulting k_D is equal to 0.30. This

approach is not strictly appropriate, as host olivine should be added back instead of a calculated equilibrium olivine composition, but tests show that there is generally not a large difference whether a calculated equilibrium olivine composition is added back stepwise or if the host olivine is added back into the MI in bulk. Of 126 olivine-hosted melt inclusions, 79 homogenized inclusions showed negative PEC indicating olivine resorption. The average PEC for these 79 MIs is -3.7 % PEC. We observe that at -3.7 % PEC, there is almost no difference between adding back host olivine in bulk than the standard procedure we carried out. At larger olivine resorption, PEC increased when adding back bulk olivine rather than equilibrium olivine. The MI with the most suspected resorbed olivine PEC changed by a factor of ~1.67 when adding back host olivine rather than equilibrium olivine. This would have a negligible effect on incompatible elements such as Nb.

The effects of changing pressure and oxygen fugacity were also explored and were found to have a minimal effect on the final trace element calculation. The effects of changing these parameters were tested on four representative melt inclusions, varying in their uncorrected k_D from 0.25 to 0.54. Lowering the pressure to 50 MPa decreases the PEC by up to 10%, while increasing the pressure to 200 and 400 MPa increases the PEC by up to 40%. Increasing the oxygen buffer from QFM to NNO and NNO+1 can increase or decrease the PEC and can potentially have a large effect on the PEC, as the PEC can vary, either positively or negatively, from 0 to ~260%. In some cases, the PEC of an unhomogenized MI can become negative by increasing the fO_2. These changes have a negligible effect on incompatible elements such as Nb (increase by 0 to 4%) but will more strongly affect major elements and compatible elements.

The problem of diffusional Fe loss has been discussed by previous authors (Danyushevsky et al. 2000; Gaetani and Watson 2000; Kent 2008), but there is no standard correction model. Furthermore, a reliable correction is only possible when whole rock or groundmass analyses allow extrapolation back to an assumed FeO differentiation trend. When Fe diffusion is not accounted for, the PEC correction can lead to melt FeO, MgO and Al_2O_3 contents that are erroneous. We did not globally correct for Fe loss because it appears to vary for the samples studied, and it was not always possible to compare with whole rock and groundmass data to make an accurate assumption of initial FeO. We avoid the Fe loss problem in this paper by (1) focusing mainly on trace elements, (2) only presenting data for major oxides TiO_2, K_2O and CaO,

which will not be greatly influenced by the Fe-loss effect, and (3) evaluating Fe loss on an MI-by-MI basis if we want to estimate FeO and MgO in primary melts.

Table 4.2: Calculated olivine-melt k_Ds. Olivine-melt k_Ds are included from Laubier et al. (2014) for comparison. k_D represents the olivine-melt partition coefficient and n represents the number of individual k_D determinations that are averaged to give the reported average k_D. /

	This study			Laubier et al. (2014)	
Element	Average k_D	Standard Deviation (2σ)	n	Average k_D	Standard Deviation (2σ)
Sc	0.20	0.13	22	0.25	0.11
V	0.02	0.01	22	0.013 to 0.090 (fO2-dep)	0.003 to 0.029 (fO2-dep)
Cr	1.9	1.8	10		
Co	9.8	12.4	22	5.21	1.50
Ni	22.3	11.6	15	22.29	9.12
Cu	0.36	1.1	22		
Zn	1.8	1.2	21		
Ga	0.005	0.001	7		
Rb	0.0004	0.0006	6		
Sr	0.00008	0.0001	7	0.0005	0.0003
Y	0.003	0.002	12	0.0131	0.0153
Zr	0.0003	0.0007	8		
Nb	0.0006	0.0006	11		
Ba	0.00009	0.00005	2		
La	0.0001	0.0003	3		
Ce	0.0001	0.0002	6		
Pr	0.0001	0.0003	4		
Nd	0.0003	0.0004	2		
Sm	0.002	0.003	3		
Eu	0.0003	-	1		
Gd	0.0005	0.0001	2	0.0013	0.0011
Tb	0.001	0.001	5		
Dy	0.002	0.0005	4		
Ho	0.003	0.002	5		
Er	0.005	0.002	5		
Tm	0.008	0.005	5		
Yb	0.01	0.009	7	0.0267	0.0141
Lu	0.02	0.01	5		
Hf	0.0002	0.0001	2		
Ta	0.005	-	1		
Pb	0.02	0.04	2		

Th	0.0001	0.0001	5	
U	0.0001	0.0001	5	

4.4 Results

4.4.1 Olivine-hosted melt inclusions

The forsterite content (Fo; molar MgO/[MgO+FeO]) of the olivine zones hosting the MIs range between Fo_{70} and Fo_{88}, but most are below Fo_{85}; Ni contents range from 0.02 to 0.30 wt %. Normal, reverse and multiple zoning is observed in olivines. Zone boundaries typically appeared diffuse rather than sharp. Some olivine rims are in equilibrium with the host groundmass. Spinel crystals are observed in some olivines. They are (magnesio)chromite to hercynite in composition with observed Cr# (molar Cr/[Cr+Al]) ranging from 0.17 to 0.70 and Mg# (molar Mg/[Mg+Fe^{2+}]) from 0.22 to 0.63. Sulfides were also present in some melt inclusions. Wavelength dispersive spectroscopy (WDS) spectra of a sulfide exposed in KAM24-T09 showed prominent peaks in S, Fe, Cu and Ni. One glassy MI (S09-44-7) hosted in a magnesian (Mg# = 81) clinopyroxene was also included in the dataset.

Major elements are plotted against SiO_2 in Figure 4.4. K_2O increases with SiO_2, CaO decreases with SiO_2 and TiO_2 increases up to 52-55 wt% SiO_2 before decreasing (Figure 4.4). The MI data are in agreement with the fields of Santorini whole-rock samples taken from the literature (Figure 4.4). Melt inclusions reach up to 7.0 wt % MgO. This is not as high as the 9-12 wt% MgO calculated by Nicholls (1978) for primary melts. Even the least evolved MIs have undergone some differentiation.

Thorium is expected to have nearly perfectly incompatible behavior for Santorini magmas as shown by Mann (1983); therefore, we use Th as an index of differentiation. Compatible trace elements are plotted in Figure 4.5. Ni decreases with differentiation due to olivine, spinel and clinopyroxene crystallization, Sc decreases more gradually due to pyroxene crystallization and Sr decreases mainly by plagioclase crystallization. Vanadium, a redox-sensitive element, is slightly scattered but the MIs show a clear range.

Selected incompatible elements are plotted in Figure 4.6. Some elements such as U and Rb form tight trends with Th that pass through the origin. Others such as Nb, Zr, Ba

and Nd form distinct subparallel trends with similar slopes which, when back-extrapolated, intersect the y-axis.

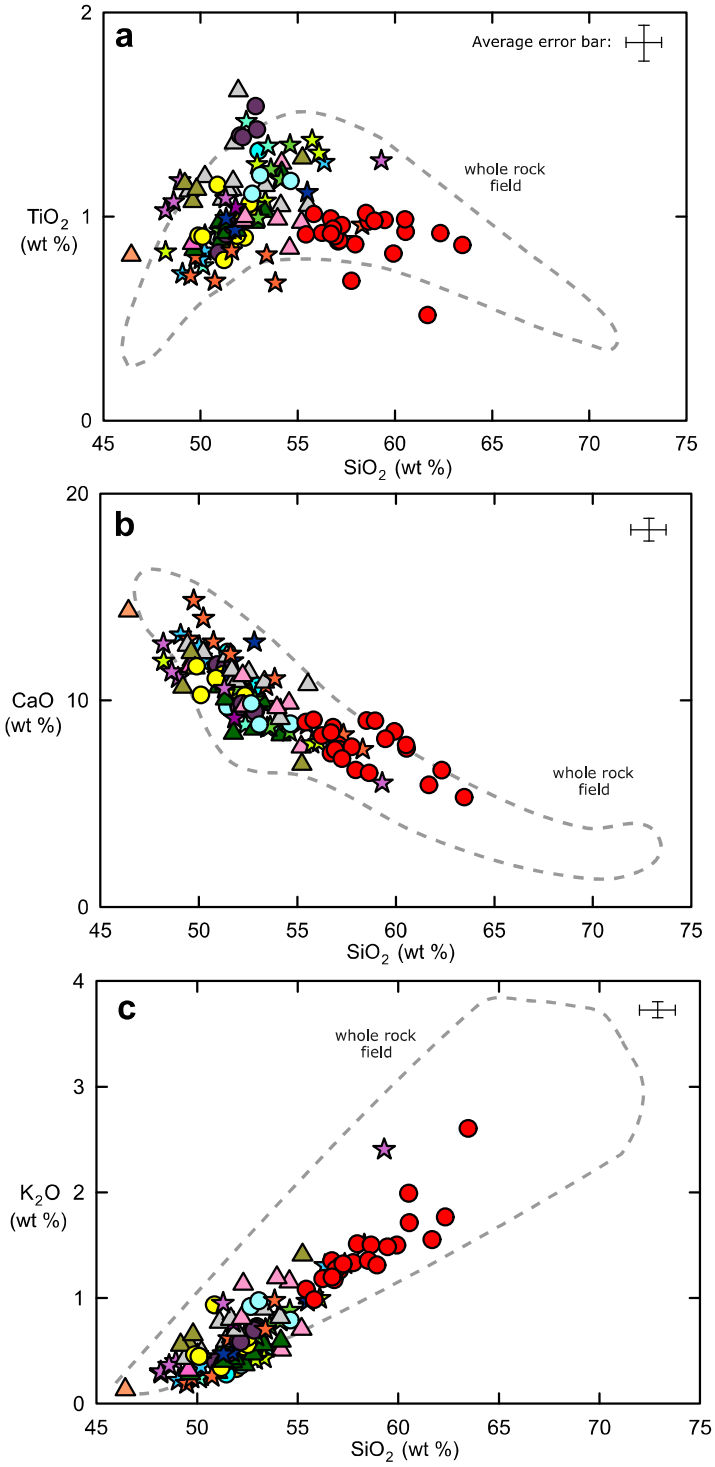

Figure 4.4: Selected major elements vs SiO_2 for melt inclusions. MIs are recalculated to 100% anhydrous and corrected. The grey dashed area represents the field of whole rock data from the author's unpublished database. Error bars represent either 2σ analytical uncertainty or 2σ standard deviation on the average of analyses for each inclusion, i.e. a maximum error estimate. Symbols as in Figure 4.2b.

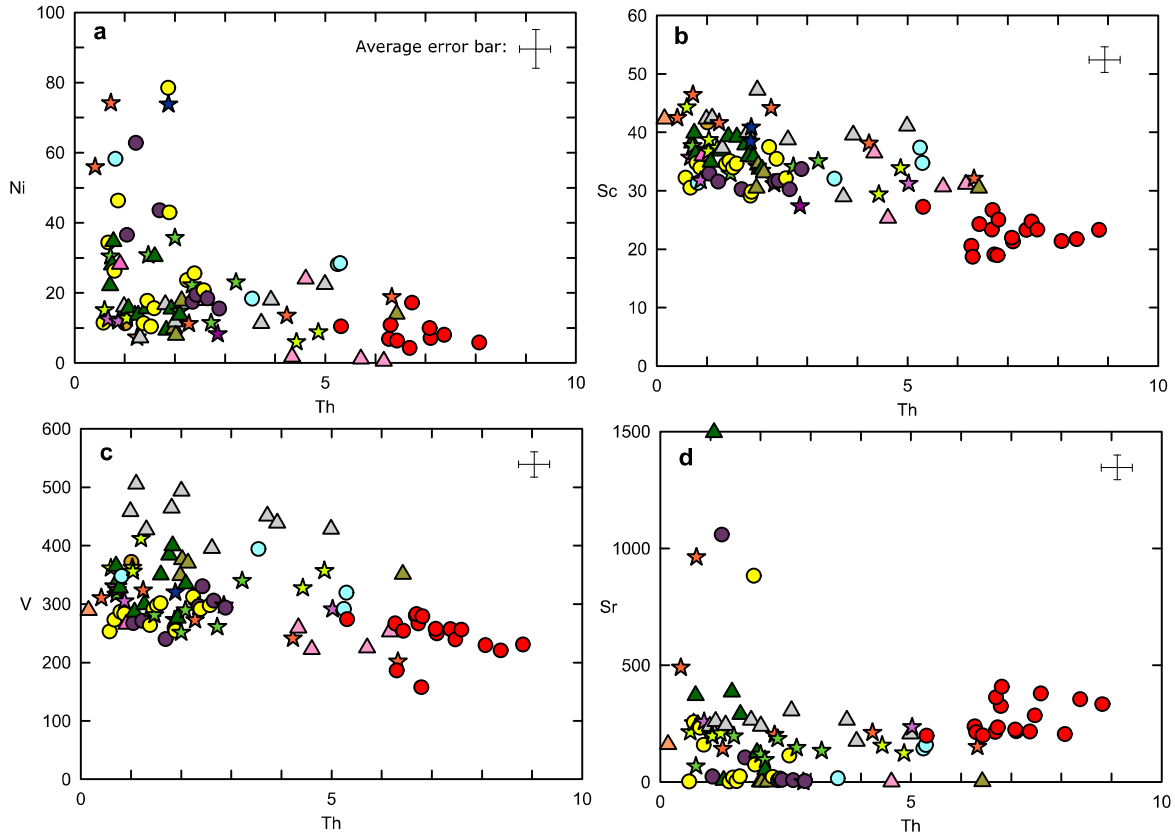

Figure 4.5: Selected compatible trace elements vs Th. Trace elements are in ppm. Error bars represent 2σ analytical uncertainty. Symbols as in Figure 4.2b. Note that some Sr values are abnormally low (see Section 3.4.5).

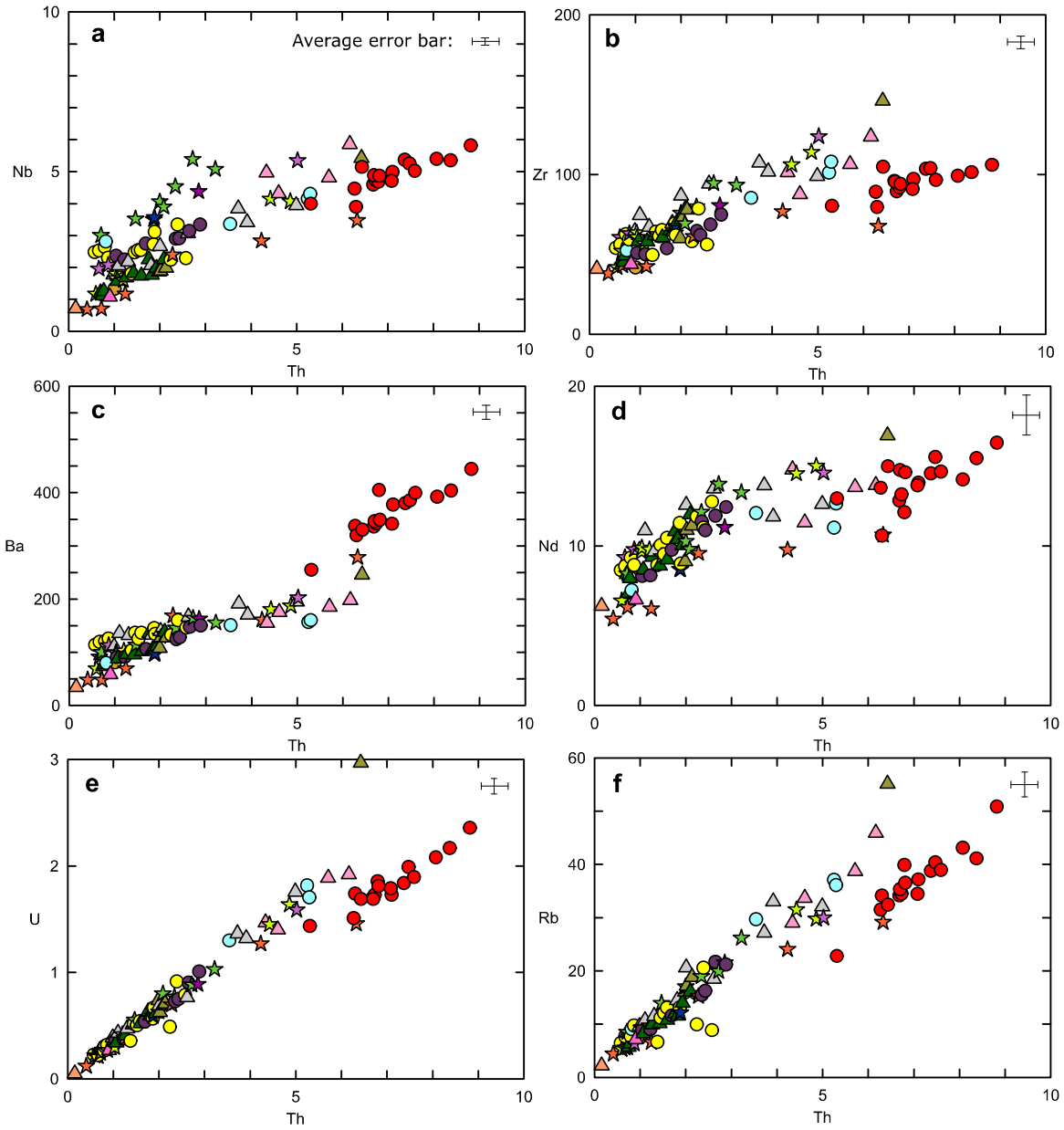

Figure 4.6: Selected incompatible elements vs Th. Trace elements are in ppm. Error bars represent 2σ analytical uncertainty. Symbols as in Figure 4.2b.

4.4.2 Identifying primitive melts

Melts are commonly considered to be primitive if they are in equilibrium with mantle olivine (Fo_{86-91}). Such melts have Mg# $\geq$ 70 (Metrich and Clocchiatti 1996; Kohut et al. 2006). The Fo content of the olivine can also be used as a measure. The Fo content of host olivine is plotted against MI Th content in Figure 4.7, where there is a general trend of decreasing Fo with Th, which is to be expected as melts differentiate. The Fo contents of most olivine hosts are lower than those of mantle olivine. MI-bearing olivines in unit M12 (Figure 4.2a) are uniformly Fo-rich despite a range in Th, possibly due to late-stage diffusional Fe-Mg re-equilibration of the olivine (Dohmen et al. 2007; Gordeychik et al. 2018).

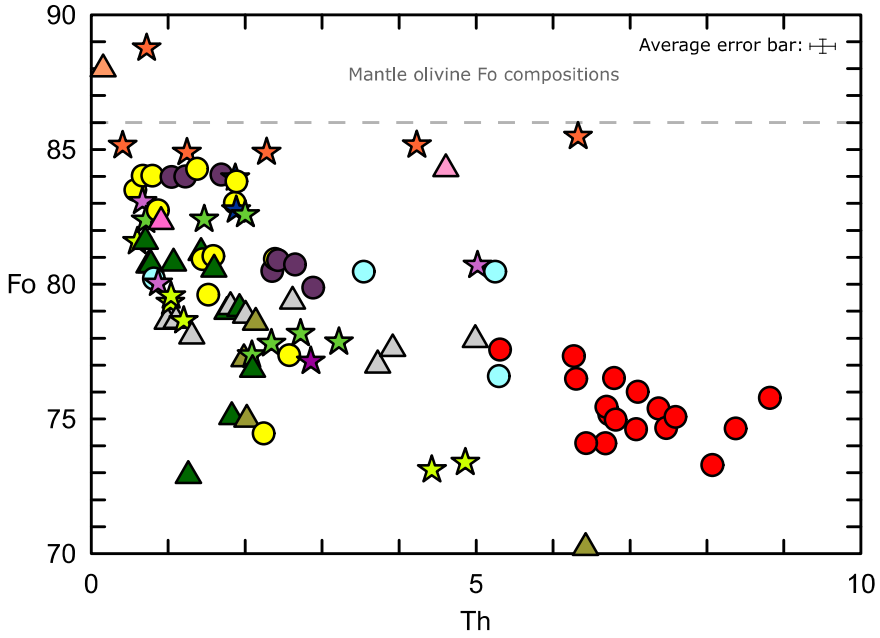

Figure 4.7: Forsterite (Fo) content of olivine zone hosting melt inclusions versus Th content of the melt inclusion. Th is given in ppm. Error bars represent 2σ analytical uncertainty. Symbols as in Figure 4.2b.

Given the large range of olivine host compositions, we define our primitive MIs as those with <1 ppm Th, and the rest of this paper concerns these MIs.

Spider diagrams are plotted for those MIs with <1 ppm Th in Figure 4.8. Trace element spectra show geochemical signatures typical of arc volcanism (Pearce and Peate 1995; Codillo et al. 2018; Zheng 2019). There is a prominent depletion in Nb and Ta, and an enrichment in Pb. Large ion lithophile elements (LILE) are enriched relative to high

field strength elements (HFSE), and light rare earth elements (LREE) are enriched relative to heavy rare earth elements (HREE) (Figure 4.8a,b). No Eu anomaly is observed (Figure 4.8b). LILE and HFSE contents correlate positively but are sometimes decoupled.

4.5 Discussion

4.5.1 Nature of primitive melts

The primitive (<1 ppm Th) melts exhibit a clear range in incompatible trace elements contents. Since Nb shows the greatest variation, we follow Bailey et al. (2009) in recognizing two endmember melt types, low Nb and high Nb, with a continuum between the highest and lowest Nb endmembers. The lowest Nb endmember (e.g. S16-14-9) shows the lowest concentrations of HFSE, but also of LILE, and the REE spectrum is nearly flat with La/Yb as low as 1.8. This is reminiscent of tholeiitic magmas such as MORB. On the other hand, the highest Nb endmember (e.g. S12-37 1-3) is higher in incompatible elements, both HSFE and LILE, and the REE spectra are more fractionated with La/Yb as high as 3.2. This is more of a calc-alkaline signature, where more fluid-mobile LREE are enriched over the less fluid-mobile HREE.

To illustrate the elemental differences, selected primitive MIs are plotted on a spider diagram normalized to the lowest Nb MIs in Figure 4.9. The high Nb melts are not only enriched in Nb and Ta but are also enriched in other incompatible elements including the LILE compared to the low Nb melts.

The ratios V/Sc and V/Yb can be useful proxies for fO_2 in basaltic melts (Aeolus Lee et al. 2005; Laubier et al. 2014). V and Sc have similar behavior during mantle melting and are unlikely to be modified by crustal contamination. The solid-melt partitioning of V is redox-sensitive because of its multiple valence states (Canil 1997, 2002; Li and Lee 2004; Mallmann and O'Neill 2009); the partition coefficient of V decreases at higher fO_2 (Mallmann and O'Neill 2009; Laubier et al. 2014) so a higher V/Sc would be expected for more oxidizing conditions, assuming no cpx fractionation. V/Yb is also used as an fO_2 proxy and may be a more reliable than V/Sc if there has been cpx fractionation (Laubier et al. 2014). The V/Sc ratio for our primitive MIs varies from 7 to 11 (Figure 4.10), indicating either a range in fO2 of the primitive melts or cpx fractionation. Certain units have similar V/Sc ratios and form groupings, but there is

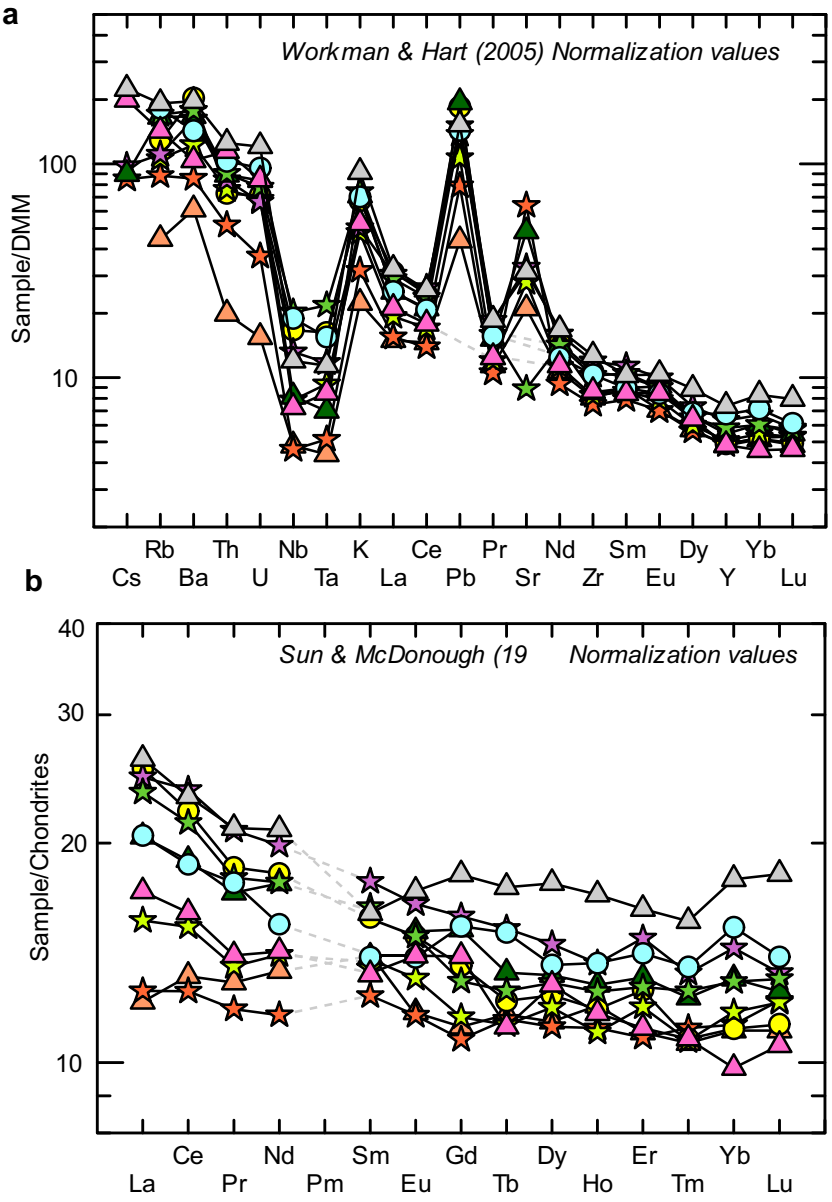

Figure 4.8: Spider diagram and REE spectra for selected primitive (<1 ppm Th) melt inclusions. (a) The extended spider diagram is based on the ordering of Sun and McDonough (1989) with some slight modifications. Normalization values are from Workman and Hart (2005) for depleted MORB mantle (DMM). (b) The REE spectrum ordering is based on increasing atomic number. Normalization values are from Sun and McDonough (1989) for chondrite composition. Samples included in both diagrams are the lowest Th sample for each unit that contains a primitive melt inclusion. The samples shown are: S16-88-3a, S12-37 1-3, S12-43 7-1, KAM24-T08, S16-26-5, S16-16-1, S09-04-6, S16-21-2, S16-14-9 and S18-11-1a. Symbols as in Figure 4.2b. Dashed lines = no data available for an element for a given sample.

Table 4.3: Selected primitive (< 1 ppm Th) melt inclusions. Those included are the lowest Th sample for each unit that contains a near-primary melts. FeO^T = FeO total. bdl = Below detection limit.

Sample name	S16-14-9	S18-11-1a	S16-16-1	S12-437-1	S16-21-2	KAM24-T08	S16-26-5	S16-88-3a	S09-04-6	S12-371-3
Fo (olivine)	85	88	82	82	82	79	83	83	80	82
SiO_2	49.5	46.4	49.6	48.2	51.1	51.6	48.2	51.5	51.4	51.0
TiO_2	0.71	0.81	0.87	0.83	0.89	1.13	1.03	0.85	0.91	0.93
Al_2O_3	19.9	18.6	18.8	18.8	17.9	23.2	22.1	19.4	18.5	19.0
FeO^T	7.8	8.4	9.5	10.3	9.6	4.9	7.5	7.8	9.8	8.5
MnO	0.14	0.15	0.21	0.28	0.15	0.03	0.09	0.21	0.21	0.14
MgO	6.5	8.8	6.6	6.8	6.3	2.4	5.3	5.8	5.9	5.8
CaO	13.0	14.3	11.6	11.9	10.8	11.5	12.7	11.1	9.7	11.2
Na_2O	2.2	2.1	2.3	2.5	2.7	4.4	2.6	2.7	2.8	2.8
K_2O	0.19	0.13	0.32	0.29	0.43	0.55	0.30	0.40	0.42	0.44
P_2O_5	0.02	0.09	0.11		0.12	0.17	0.04	0.10	0.20	
Sum	99.9	99.9	99.9	99.9	99.9	99.9	99.9	99.9	99.9	99.9
Li	7.6	bdl	4.0	4.1	4.4	5.2	4.6	4.0	bdl	6.0
Be	0.50	bdl	0.37	0.23	0.55	0.92	0.52	0.42	bdl	0.56
Sc	42	42	36	44	38	42	36	32	31	38
V	310	289	266	361	365	458	330	253	348	316
Cr	70	211	29	28	36	12	13	56	bdl	38
Co	33	70	34	33	34	16	25	28	50	31
Ni	56	342	28	15	22	16	12	12	58	30
Cu	596	75	90	34	210	43	59	0	bdl	12
Zn	75	117	2.5	102	119	49	96	76	89	82
Ga	18	15	7.6	19	18	24	20	17	19	18
Ge	3.5	bdl	1.6	2.6	2.4	bdl	2.6	2.1	9.6	4.4
As	0.47	0.76	bdl	0.51	0.50	bdl	0.55	0.57		0.58
Rb	4.4	2.2	7.1	5.3	8.3	9.6	5.5	6.5	9.1	8.5
Sr	489	161	bdl	214	370	239	252	2	bdl	68
Y	16	16	16	17	18	25	21	16	22	19
Zr	38	41	44	42	43	64	61	54	53	52
Nb	0.69	0.71	1.1	1.2	1.2	1.8	2.0	2.5	2.8	3.0
Mo	0.48	bdl	0.76	0.54	0.46	0.52	0.80	0.41	0.47	0.79
Cs	0.11	bdl	0.26	x	0.11	0.29	0.12	bdl	bdl	x
Ba	48	34	59	69	94	111	91	114	80	100
La	3.0	2.9	4.1	3.7	4.8	6.2	5.8	6.0	4.9	5.6
Ce	7.7	8.0	9.8	9.4	12	14	14.49	14	11	13
Pr	1.1	1.2	1.3	1.3	1.6	2.0	2.0	1.8	1.7	1.7
Nd	5.4	6.2	6.6	6.6	8.2	9.7	9.3	8.5	7.2	8.3
Sm	1.9	2.1	2.0	2.1	2.1	2.5	2.7	2.4	2.1	2.5
Eu	0.67	0.68	0.81	0.76	0.88	1.00	0.96	0.86	0.81	0.86
Gd	2.2	2.3	2.9	2.4	3.1	3.7	3.3	2.8	3.2	2.7
Tb	0.43	0.44	0.42	0.42	0.50	0.65	0.57	0.45	0.56	0.47
Dy	2.8	2.9	3.2	3.0	3.3	4.5	3.7	3.1	3.5	3.3
Ho	0.63	0.68	0.66	0.62	0.72	0.96	0.77	0.67	0.77	0.71
Er	1.8	1.8	1.8	2.0	2.2	2.7	2.5	2.1	2.3	2.1
Tm	0.28	0.27	0.27	0.27	0.31	0.40	0.34	0.27	0.34	0.32
Yb	1.9	1.9	1.7	2.0	2.2	3.0	2.4	1.9	2.6	2.2
Lu	0.31	0.28	0.27	0.31	0.32	0.46	0.34	0.29	0.35	0.33
Hf	1.2	1.3	1.3	1.2	1.3	1.8	1.8	1.5	1.4	1.5
Ta	0.05	0.04	0.08	0.09	0.07	0.11	0.11	0.16	0.15	0.21
Pb	1.4	0.8	bdl	1.9	3.5	2.7	2.5	3.3	2.6	2.7
Th	0.41	0.16	0.91	0.60	0.70	0.99	0.67	0.57	0.81	0.71
U	0.12	0.05	0.27	0.22	0.27	0.39	0.21	0.23	0.31	0.25

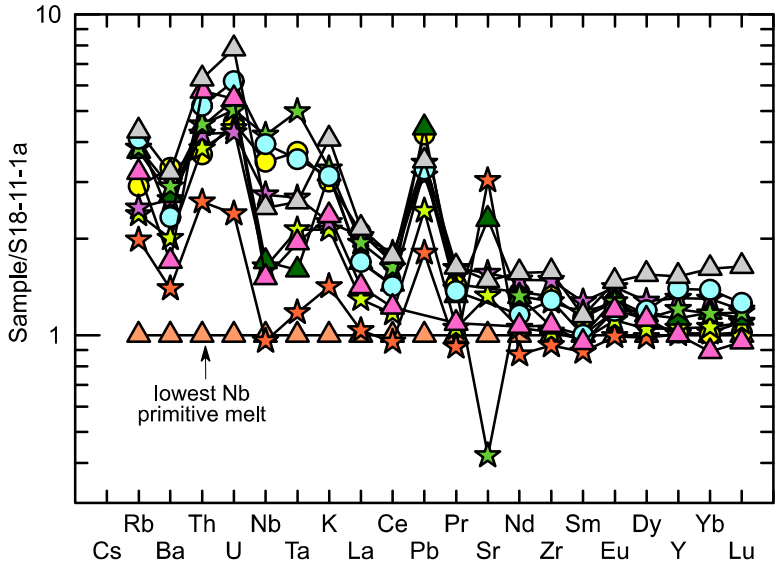

Figure 4.9: Selected primitive (<1 ppm Th) melt inclusions normalized to the lowest Nb, most tholeiitic primitive melt inclusion to illustrate elemental variation. Symbols as in Figure 4.2b. Sr data may not be reliable (see Section 3.4.5).

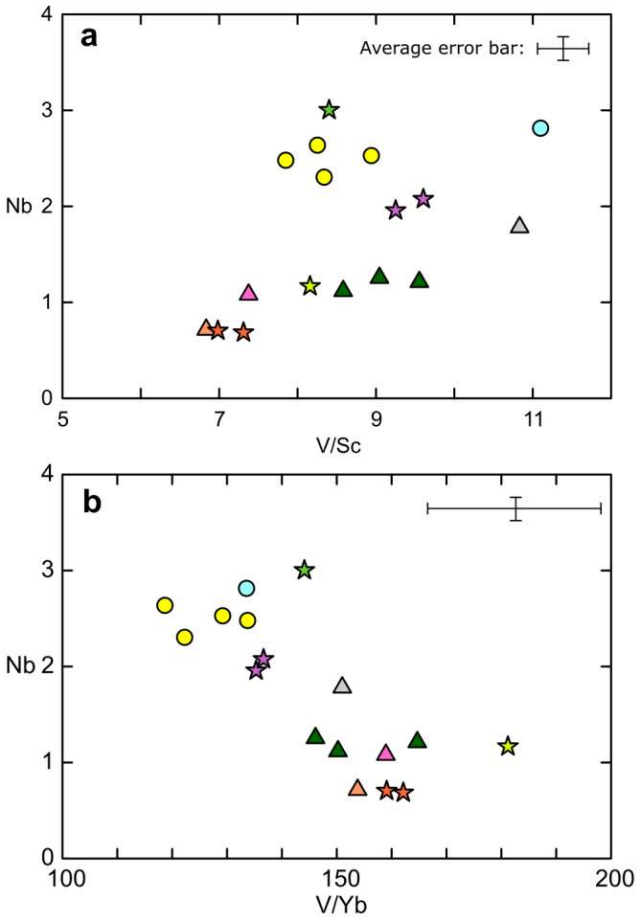

Figure 4.10: Nb vs. V/Sc and Nb vs. V/Yb. These element ratios involving compatible and incompatible elements can serve as fO_2 proxies (Aeolus Lee et al. 2005; Laubier et al. 2014). Error bars represent 2σ analytical uncertainty. Symbols as in Figure 4.2b.

no clear relationship between V/Sc and melt Nb type. Y/Yb ranges from 118 to 181 and shows a negative correlation with Nb for the primitive melts.

Our data confirm previous findings, based on whole rock studies, of two endmember parental basalts on Santorini: a more tholeiitic low-Nb type, and a more calc-alkaline high Nb type (Tarney et al. 1998; Vaggelli et al. 2009; Bailey et al. 2009).

4.5.2 Origin of the primitive melts

We now address the origins of the low Nb and high Nb primitive melts at Santorini. We first try to model the derivation of the highest Nb primitive melt from the lowest Nb one by fractional crystallization of an olivine-spinel assemblage (model not shown). This failed to produce the incompatible elements of the highest Nb melt. The different primitive melts are not due to different degrees of fractional crystallization of a common parent; they therefore must be generated by different conditions of partial melting of the mantle wedge or slab contributions.

4.5.3 Estimation of the mantle melt compositions

We use three approaches to calculate approximate primary melt compositions for the low and high Nb primitive melts as starting compositions using (1) an olivine-only fractionation model, (2) software PRIMACALC2 using the same input conditions as in Baziotis et al. (2018) and (3) carrying out a simple model of mantle partial melting until primary melt compositions are reached.

Method 1: Olivine-only fractionation model

The simplest method to back-calculate to a primary melt is to implement an olivine-only fractionation model and to add back equilibrium olivine until the melt is in equilibrium with mantle olivine compositions ($Fo_{86\text{-}91}$, 2000-4000 ppm Ni) assuming a lherzolite mantle lithology (Tatsumi and Ishizaka 1982; Danyushevsky et al. 2000; Korenaga and Kelemen 2000; Herzberg et al. 2007; Schmidt and Jagoutz 2017). The back-calculation only concerns major elements, but trace elements of the resulting primary melts can be calculated using the starting composition, olivine-melt k_Ds (

Table **4.2**) and the amount (wt%) of olivine needed to be added back.

Two olivine-only fractionation major element models were carried out, one for each primitive MI endmember: S16-14-9 (low Nb) and S12-37 1-3 (high Nb). These MIs do

not show evidence for Fe loss, as even their uncorrected FeO/MgO k_Ds (0.26 and 0.33, respectively) fall within the 0.30 ± 0.04 accepted in the literature for equilibrium partitioning (Roeder and Emslie 1970; Ford et al. 1983; Kent 2008); therefore, using major elements in this case was not a problem. The models followed the same calculation procedure as the MI correction scheme outlined in the methods section, except that equilibrium olivine was added to the MIs until the melt was in equilibrium with Fo_{91} olivine (Tatsumi and Eggins 1995). The results are given in

Table **4.5**. The models required addition of 15-22 wt % olivine, resulting in melts with 12-14 wt % MgO, in agreement with a previous calculation by Nicholls (1978), who used a similar approach but different starting composition.

Method 2: PRIMACALC2

Olivine-only fractionation may not be realistic, as pyroxene and spinel may saturate early as a primary melt crystallizes along its cotectic (Grove and Baker 1984; Grove et al. 2003; Tatsumi and Suzuki 2009; Nandedkar et al. 2014). Indeed the presence of a MI with ~ 1 ppm Th in a cpx of sample S09-44-7 shows that cpx crystallizes early. Various modelling programs have been made available for primary melt back-calculations involving the fractionation of multiple phases, such as Petrolog3 (Danyushevsky and Plechov 2011), alphaMELTS (Antoshechkina and Asimow 2016) and PRIMACALC2.00 (Kimura and Ariskin 2014). PRIMACALC2 is a software (Kimura et al. 2010; Kimura and Ariskin 2014) using COMAGMAT3.72 (Ariskin and Barmina 2004) to calculate primary mantle melt compositions from major element basalt compositions according to mass balance models, and PRIMELT2 (Herzberg and Asimow 2008) to estimate the physical conditions of mantle melt generation such as the pressure, temperature and degree of mantle melting. PRIMACALC2 considers H_2O effects and a range of fractionating minerals, and it runs in a Microsoft Excel worksheet with the full assumptions and calculation details of the PRIMACALC2 program explained by Kimura and Ariskin (2014). PRIMACALC2 has already been used by Baziotis et al. (2018) on a basalt from Santorini (Balos cinder cone).

We have carried out two PRIMACALC2 models, one for each Nb type endmember, using the input conditions given in Baziotis et al. (2018) (see Table 4.4 for all input

Table 4.4: Input conditions for the COMAGMAT 3.72 code, used by the PRIMACALC 2 model. The code used for each input parameter in our calculations is given, with a short explanation for each code. The present study uses the same input conditions as Baziotis et al. (2018). Some input cells are not used in the version of COMAGMAT 3.72 adapted for PRIMACALC2 modelling, and thus do not require user input ('*Unused*'). Some values are left at default values, and it is suggested by the authors of the software not to change them.

PRIMACALC2 Input	Code used	Explanation
CRYSTALIZATION MODE	FRC	Fractional crystallization is used as the crystallization mode instead of equilibrium crystallization or other options.
PRESSURE_CONDITION	ISO	Isobaric crystallization is chosen instead of increasing pressure or decompression crystallization.
SET_SET P_MAX P [kbar]	2	For the "ISO" pressure condition, this is the 'actual' pressure for the starting composition used.
SET_MAX P_STEP P [kbar]	11	For the "ISO" pressure condition, this is the maximum pressure to be used in calculations.
SET_NUL/ MIN P [kbar]	0	For the "ISO" pressure condition, this value should be set to 0.
MINERAL_CHEMISTRY	*Unused*	-
LOW-Ca_Px_MODEL	OPX	This code chooses an orthopyroxene model instead of a pigeonite model for low-Ca pyroxene.
NUMBER OF COMPOSITION	*Unused*	-
OXYGEN_SYSTEM	OPE	An 'open system' is used, which gives the option to use an oxygen buffer. It is also possible to put 'CLO' for 'closed system' and use a Fe^{2+}/FeO^* ratio.
OXYGEN_BUFFER_CONDI	CON	This indicates a constant oxygen fugacity route. It is also possible to choose 'VAR', which changes the oxygen fugacity during crystallization.
INIT_OXYGEN_BUFFER	QFM	For 'OPE' and 'CON', the desired oxygen buffer is chosen here (QFM, NNO, IW or HM).
LOG_UNIT_SHIFT_OXBUFFER	2	This sets the oxygen buffer log shift. Here the oxygen buffer is set at QFM+2.
FINAL_OXYGEN_BUFFER (VAR)	*Unused*	-
XSTALLIZATION_INCRIM.[%]	1	Default value; suggested not to change.
XSTALLIZATION_RANGE_MAX	75	Default value; suggested not to change.
TEMP_CONVERGENCE	0.5	Default value; suggested not to change.
PHASE_COMP[mol%]	0.25	Default value; suggested not to change.
H2O_IN_PRIMARY_MELT[wt.%]	1	This is the assumed initial H_2O content in the primary melt.
OUTPUT_FILE_NAME	00000001	Default value; suggested not to change.
MAJOR_COMP	#####	This is a cell containing results of a calculation and is referenced in final output table. This cell should not be changed.
TRACE_COMP (DUMMY)	*Unused*	-

parameters), although we explored a range of assumed H_2O as well. In the results, we will refer to the modelling results using 1 wt% H_2O assumed in the primary melt, used by Baziotis et al. (2018) as initial input conditions. The low Nb and high Nb near-primary endmembers again have different primary melt predecessors and the incompatible-rich and incompatible-poor nature of each near-primary melt is preserved.

From PRIMACALC2, we also estimated the pressure, temperature and degree of melting in the mantle for the two Nb types (Table 4.5). T_{Dry} is the temperature estimated from a T-MgO_{melt} relationship as part of the PRIMELT2 calculation, which is a calculation based on anhydrous experiments (Herzberg et al. 2007). T_{Wet} is calculated by taking T_{Dry} and adding a parameterization from Katz et al. (2003) that allows for the calculation of melting conditions in the presence of a hydrous mantle. F_{Dry} and F_{Wet} are the degrees of partial melting associated with anhydrous and hydrous conditions, respectively.

Method 3: Trace element partial melting model

Lastly, we performed a partial melting model of a lherzolite mantle until the composition of the partial melt reached that of a primary melt, but only for conservative elements (i.e. those which are neither added by slab-derived aqueous fluids or hydrous melts, nor retained in the source; we choose Yb and explain why below). This approach (1) allows an estimation of the degree of melting but also (2) shows which elements are affected by subduction components (although it does not result in a quantitative primary melt composition).

We carry out a simple batch melting model for the source mantle, assuming a depleted MORB-like mantle (DMM; Workman and Hart 2005 with some values supplemented

Table 4.5 (next page): Results from olivine-only fractionation models and PRIMACALC2 models for Nb type near-primary endmembers. Models are shown for 1 wt% H2O assumed in the primary melt, following conditions used by Baziotis et al. (2018), but we also report model results for elevated H2O contents as well in the table. For S16-14-9, the PRIMACALC2 model could not converge above ~2 wt% H2O, and for S12-37 1-3, the PRIMACALC model could not converge above ~3 wt% H2O. Major oxides given in wt %, trace elements given in ppm. P (GPa), T (dry and wet; °C), F (dry and wet; %) are the pressure, temperature and degree of melting conditions of the source mantle (all variables are output of PRIMACALC2). Symbols as in Figure 4.2b.

	Low Nb			High Nb		
	S16-14-9			S12-37 1-3		
	Olivine-only	PRIMACALC2 (at 1 wt% H2O)	PRIMACALC2 (at 2 wt% H2O)	Olivine-only	PRIMACALC2 (at 1 wt% H2O)	PRIMACALC2 (at 3 wt% H2O)
SiO2	48.2	46.09	45.61	48.9	47.51	44.50
TiO2	0.60	0.43	0.46	0.74	0.57	0.62
Al2O3	17.0	15.7	15.3	15.2	17.9	15.3
FeO_T	8.2	10.5	11.9	9.14	8.7	12.82
MnO	0.12	0.08	0.08	0.11	0.12	0.13
MgO	12.5	14.00	13.56	14.0	11.26	13.14
CaO	11.08	11.27	11.40	9.00	11.60	11.83
Na2O	1.87	1.47	1.45	2.26	1.98	1.53
K2O	0.16	0.10	0.11	0.35	0.22	0.20
P2O5	-	0.20	0.20	-	-	-
SUM		100	100		100	100
Rb	3.6	2.21	2.28	6.81	4.38	4.15
Ba	39.3	25.5	25.82	80	55.4	51.66
Th	0.33	0.20	0.21	0.57	0.36	0.34
U	0.096	0.06	0.06	0.19	0.13	0.12
Nb	0.56	0.34	0.35	2.4	1.53	1.47
Ta	0.04	0.02	0.03	0.16	0.11	0.10
K	1326	1185	1210	2884	2846	2673
La	2.42	1.63	1.68	4.45	3.15	3.09
Ce	6.26	4.21	4.39	10.4	7.35	7.44
Pb	1.16	0.94	0.91	2.17	1.94	1.74
Pr	0.91	0.64	0.67	1.36	1.00	1.04
Sr	400	524	481	54.4	91	80
Nd	4.43	3.16	3.36	6.60	4.89	5.34
Sm	1.54	1.15	1.25	2.00	1.54	1.81
Zr	31.0	20.4	21.56	41.9	28.3	29.48
Hf	0.95	0.68	0.75	1.22	0.90	1.04
Eu	0.55	0.42	0.46	0.69	0.54	0.65
Gd	1.80	1.39	1.54	2.12	1.67	2.06
Tb	0.35	0.27	0.30	0.37	0.30	0.37
Dy	2.32	1.80	2.01	2.61	2.08	2.60
Y	13.2	10.3	11.4	15.5	12.4	15.36
Ho	0.51	0.40	0.44	0.56	0.45	0.56
Er	1.46	1.12	1.24	1.68	1.32	1.63
Tm	0.23	0.18	0.19	0.25	0.20	0.24
Yb	1.56	1.17	1.29	1.76	1.36	1.62
Lu	0.25	0.19	0.20	0.26	0.20	0.24
Ni	4057	135	110	3442	68	45
P (GPa)		2.3	2.4		1.8	2.7
T dry (°C)		1436	1431		1349	1301
T wet (°C)		1436	1431		1349	1102
F dry (%)		8	7		6	0
F wet (%)		5	5		1	0

from Salters and Stracke 2004 and bulk partition coefficients (D) from Workman and Hart 2005 (Figure 4.11). Partial melting of DMM is modelled until the Yb content of the modelled melt reaches that of the primary melt determined with PRIMACALC2, as Yb is unlikely to be modified by slab input as long as there is no garnet involvement (Pearce and Peate 1995). Similar approaches have been used in the past (e.g. Zellmer et al. 2000). There is no strong evidence for garnet as a fractionating or residual phase in magma genesis at Santorini due to relatively high Sc, Y and Yb, as well as the absence of strongly fractionated REE patterns. In fact, Santorini has the least fractionated REE patterns of the Aegean Arc, and the range of La/Yb ratios at Santorini are consistent with addition of a LREE-rich slab-derived sediment component to the source rather than garnet involvement during mantle melting (Mitropolous et al. 1987; Francalanci et al. 2005b; Bailey et al. 2009; Francalanci and Zellmer 2019). In the slab-sediment dehydration and melting experiments of Johnson and Plank (2000), Yb was shown to be lightly to strongly immobile (i.e., preferring to stay in sediment residue) both in sediment-derived aqueous fluids ($D^{Yb}_{sediment-aq\ fluid}$ ~1-3) and melts ($D^{Yb}_{sediment-melt}$ ~2-10). Yb should also not be hugely modified by a deep fractionating mineral assemblage, such as olivine ($k^{Yb}_{D_{olivine-bas}}$ < 0.03; Laubier et al. 2014), spinel ($k^{Yb}_{D_{spinel-basalt}}$ < 0.01; McKenzie and O'Nions 1991), cpx ($k^{Yb}_{D_{cpx-basal}}$ < 0.5, rarely up to 1; Laubier et al. 2014) and plagioclase ($k^{Yb}_{D_{plagioclase-basalt}}$ < 0.003; Laubier et al. 2014). Also, bulk D_{Yb} generally seems to increase with increasing differentiation, and here we are focusing on deep differentiation and very early cpx compositions. With these hypotheses, Yb should act as a relatively neutral element only significantly modified by the degree of partial melting. We therefore assume that the Yb content of the mantle will not have been greatly affected by metasomatism by slab-derived components or deep fractionation.

Two partial melting models were carried out, each aiming at reproducing the Yb for one of each Nb endmember type primary melt. The partial melting models are shown in Figure 4.11. The low Nb series required a higher degree (F = 23%) of partial melting than the high Nb series (F = 18%). This slight difference may well be within error, but it shows that, given identical input conditions, variable partial melting is a possible explanation for the low Nb and high Nb melt types.

Other than Yb, the incompatible elements that match well are Y, Zr, Hf, MREE and HREE. The Ds of Workman and Hart (2005) do not account for rutile, which may

explain the Nb and Ta variations, since these elements are shown to be retained if rutile is a residual phase in the dehydrating or melting slab component. The other elements (LILE, LREE and Th) are elevated with respect to the partial melting models, and were probably mostly added by a subduction component, as discussed in detail below.

Comparing methods estimating primary melt compositions and melting conditions

We first compare the results of the methods in terms of the resulting primary melt compositions they give. While the olivine-only fractionation model is simple, it may not really reflect the fractionating assemblage. The best fit PRIMACALC2 model

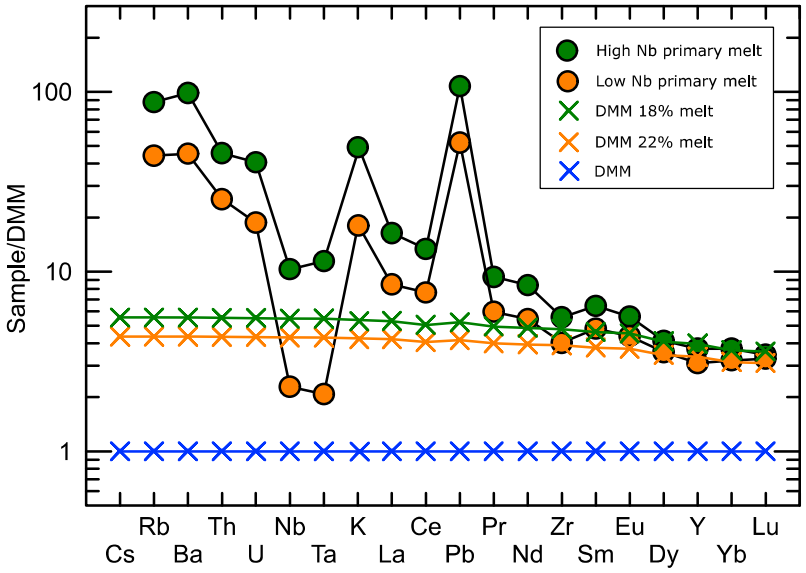

Figure 4.11: Partial melting model. The high Nb and low Nb primary melts are the PRIMACALC2 modelling results assuming 1 wt% H2O assumed in the primary melt. Samples normalized to depleted MORB mantle (DMM) values of Workman and Hart (2005) with some values (such as Cs) supplemented from Salters and Stracke (2004). Symbols as in Figure 4.2b. Sr is not presented (see Section 3.4.5 about abnormally low Sr contents).

requires that primary melts also crystallize plagioclase, clinopyroxene and magnetite in addition to olivine before the primitive MI compositions are reached. The primitive MIs lack Eu anomalies, which argues against significant plagioclase crystallization; therefore, plagioclase may actually be suppressed by the water content of the primitive melts. The primitive nature of the cpx-bearing melt inclusion S09-44-7 (~ 1 ppm Th), however, shows that cpx can indeed begin to crystallize quite early. In any case, both the olivine-only fractionation and PRIMACALC2 models give slightly different primary melts with the incompatible-rich and incompatible-poor natures of the two Nb type endmembers. The low Nb type primitive MIs have a low Nb primary melt predecessor, and vice versa for the high Nb MIs.

As cpx and magnetite may crystallize before the trapping of primitive melt inclusions, we may not be able to use the ratio V/Sc or V/Yb as proxies for fO_2. Since we see clear evidence for early forming cpx, we do not rely on V/Sc for an fO_2 proxy (Aeolus Lee et al. 2005; Laubier et al. 2014). However, we do not have such clear evidence that magnetite is actually crystallizing before the primitive MIs—it is only suggested by the PRIMACALC2 results. Therefore, we may possibly be able to use V/Yb as an fO_2 proxy (Laubier et al. 2014). In fact, what we see in V/Yb, is that the high-Nb primitive melt inclusions which are anticipated to be the most calc-alkaline, have the lowest V, and vice versa for the low-Nb primitive melt inclusions; therefore, V/Yb trends are opposite of what we expect (Figure 4.10). Crystallization of magnetite could render the V/Yb oxygen fugacity proxy unusable, and in theory could actually potentially reverse the fO_2-V/Yb relationship as our more calc-alkaline would be crystallizing magnetite causing a depletion in V relative to Yb, which could produce the correlations that we see (Figure 4.10); however, this requires further investigation.

Baziotis et al. (2018) also used PRIMACALC2 for calculating a primary basalt composition, using a Santorini basalt from Balos cinder cone. It was not possible in the present study to analyze MIs from Balos, as they were found to be altered, but our groundmass analyses suggest it belongs to the high Nb type or is intermediate between low and high Nb types. The Balos primary basalt calculated by Baziotis et al. (2018) indeed lies between our low and high Nb type primary melts.

We now compare the methods in terms of the degree of mantle melting they infer. Our Method 2 (PRIMACALC2) gives lower melting estimates (F < 6-8 %) than Method 3 (F = 18-23 %). These values are comparable to those published previously by Zellmer et al. (2000) (15-20%) and Baziotis et al. (2018) (18%), but are lower than those estimated by Bailey et al. (2009) using the model of Pearce and Parkinson (1993) (30-32 %), although those authors admitted that 10-25% was probably more realistic. In both of our methods, and in the study of Bailey et al. (2009), however, the amount of melting required to generate the low Nb primary melt is a few percent higher than that required to generate the high Nb melt. Although these slight differences may be within error of the methods, they show that a different degree of mantle melting is a possible explanation for the different Nb primary melts at Santorini.

PRIMACALC2 provides estimates of the temperature and pressure of melting: 1310-1436°C (T_{Dry}) or 1111-1436°C (T_{Wet}) and 2.2-2.3 GPa for low Nb primary melt, and 1349-

1425°C (T_{Dry}) or 1227-1349 (T_{Wet}) and 1.7-2.5 GPa for the high Nb primary melt. We note that the upper temperature estimates are quite high. Previous estimates for the Aegean Arc lie around 1280°C (Syracuse et al. 2010). The P and T conditions of the primary basalt by Baziotis et al. (2018) also fall between the low and high Nb type primary melt P and T estimates from PRIMACALC2. The pressure and temperature ranges of mantle melting conditions, as well as the degree of melting, are reasonable and comparable with those at other volcanoes around the world such as the NE Japan Arc and the Tonga-Kermadec Arc (Syracuse et al. 2010; Baziotis et al. 2018). The range of pressures and temperatures lie approximately within the field of stability of spinel lherzolite (O'Neill 1981; Klemme and O'Neill 2000; Batanova and Savelieva 2009), which is consistent with the absence of plagioclase or garnet in the source mantle inferred on geochemical grounds (e.g. absence of Eu anomaly, low degree of REE fractionation easily explained by addition of LREE-rich sediment).

Finally, we note there is the possibility that the different endmember primary melts come from the same degree of melting of two different mantle sources, but that those two mantle sources had undergone different degrees of previous melting in the past. For example, a heterogeneous mantle might arise from juxtaposition of deeper, undepleted mantle with shallower, depleted mantle near an asthenospheric upwelling or slab tear (Francalanci et al. 2005b; Klaver et al. 2016; Papazachos 2019). This is difficult to test, but we present it as a possibility although Bailey et al. (2009) used the Nb-Yb diagram of Pearce and Parkinson (1993) to argue that the mantle source below Santorini has not undergone previous melting.

4.5.4 Subduction-derived fluids and melts

Figure 4.11 showed that the two endmember primary melts derive from mantle domains with different trace element compositions, and that both of those domains differ markedly from the depleted mantle MORB (DMM) composition, notably by enrichment in incompatible elements. We now consider the origin of those enrichments. We will move forward with two hypotheses: that the range of primary melts are a result of (1) a combination of different degrees of mantle wedge partial melting and different degrees of input of slab-derived components, or (2) different degrees of input of slab-derived components alone.

4.5.5 The nature of the subduction component at Santorini

Possible contributions from the subducting slab to the mantle wedge (and hence as chemical components to the magmas) include (1) aqueous fluids released from the dehydrating oceanic crust, and (2) variably hydrous silicic melts generated by melting of subducted oceanic sediments, both of which are (3) supercritical fluids at high pressures (Bureau and Keppler 1999; Ferrando et al. 2005; Kessel et al. 2005). We will refer to these consistently as slab-derived aqueous fluids, slab-derived sediment melts, and slab-derived supercritical fluids. We use "compatibility" to describe solid-melt partitioning and "mobility" to describe the degree to which an element readily enters an aqueous fluid phase. Hence, an incompatible element preferentially partitions into a melt phase rather than a solid phase, and a fluid-mobile element readily partitions into an aqueous fluid, whereas a fluid-immobile element does not.

Incompatible elements may differ in the extent to which they partition into slab-derived aqueous fluids as a function of their ionic potential, ranging from highly fluid-mobile (e.g. Cs, Rb, Ba, Sr, Pb, U) to less fluid-mobile (e.g. Th, La, Nd) to essentially fluid-immobile (e.g. Sm, Dy, Yb, Lu & HFSE) (Hawkesworth et al. 1991; Kessel et al. 2005; Spandler and Pirard 2013; Keppler 2017). In the case of slab-derived hydrous sediment melts, the behaviors of certain elements change due to compounding effects of mobility in fluids and incompatibility in melts (e.g. LREE and Th which are not fluid-mobile, but are incompatible and thus partition readily into hydrous melts). Elements that are both fluid-immobile and incompatible due to their high ionic potential (e.g. Nb, Ta, Ti, Zr, Hf, HREE) and/or high compatibility in rutile, which can be present in the slab and remain as a residual phase, are considered to be 'conservative' in both cases of aqueous fluids and hydrous melts (Tatsumi et al. 1986; Keppler 1996). The relative immobilities and incompatibilities of these traditionally 'conservative' elements, however, can change with temperature and pressure conditions of the slab (Manning 2004; Kessel et al. 2005). In the case of supercritical fluids, experiments have shown that almost all incompatible elements partition into a supercritical fluid phase at extreme temperature and pressure conditions (Kessel et al. 2005; Chen et al. 2018).

It is difficult, even impossible, to estimate the compositions of slab-derived aqueous fluids, as there are too many unknowns. We do, however, have access to an extensive database of analyses of Eastern Mediterranean oceanic sediments (Klaver et al. 2015)

and compositions like the Global Subducting Sediment (GLOSS) (Plank and Langmuir 1998) that we can use to test the possibility of subducted sediment involvement in mantle metasomatism, which serves as a good starting point. Thus, we address the nature of the principal subduction component in the following way. We first compare the trace element spectra of typical depleted mantle (DMM), the different Nb type primary melts, and Eastern Mediterranean sediments in order to see if the shapes of the sediment spectra match that of the subduction component seen in the primary melts. Then we look at some trace element ratios typically used as proxies for slab-derived aqueous fluids and sediment melts to qualitatively evaluate the possible contributions of each.

The elevated LILE, LREE and Th in the primitive melts with respect to the partial melting models probably represent elements added by a subduction component. These are elements that are typically carried in sediment melts (in particular, Th and LREE such as La), but which do not partition strongly into aqueous fluids (Kessel et al. 2005; Keppler 2017). In Figure 4.12, we have taken the mantle partial melting models and

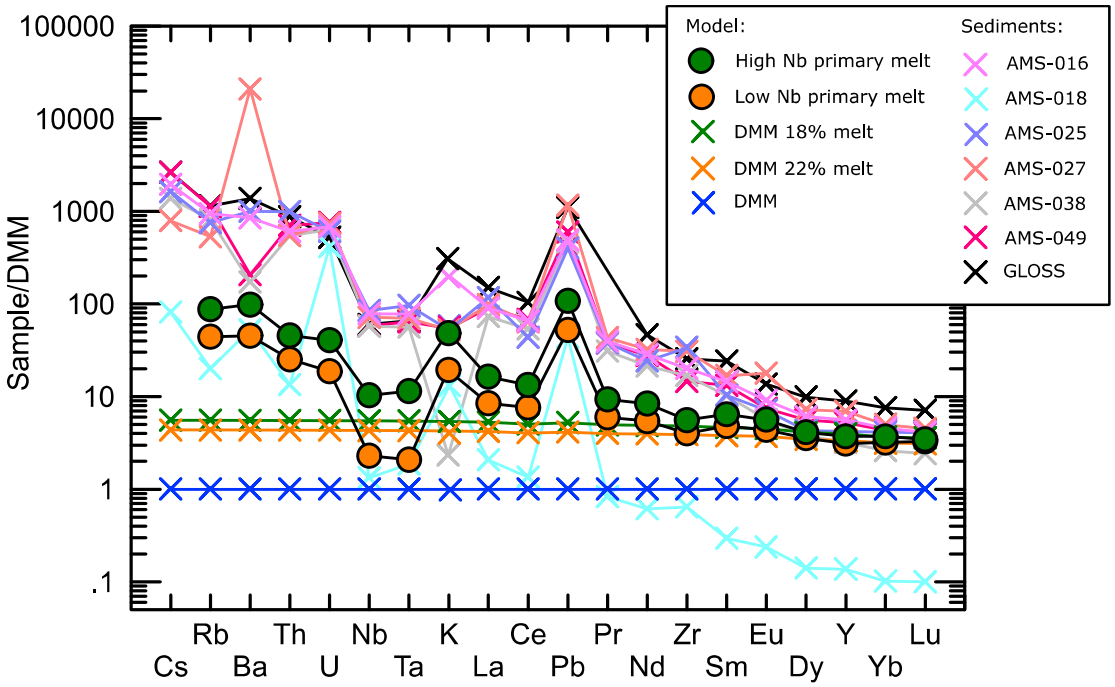

Figure 4.12: Spider diagram showing lowest and highest Nb primitive melts compared with a range of different Eastern Mediterranean Sediments (EMS; Klaver et al. 2015 and the Global Subduction Sediment composition (GLOSS; Plank and Langmuir 1998).

added some representative Eastern Mediterranean Sediments from the study of Klaver et al. (2015) as well as the average Global Subducting Sediment (GLOSS) composition of Plank and Langmuir (1998) for comparison. We see that while partial melting explains the right-hand part of the element spectra, the slab-derived sediments could explain the elements on the left that are enriched beyond the mantle partial melting models. The subducted sediments are rich in LILE, LREE, Th, Pb and Sr (not shown). Some also show a positive spike in K. Judging qualitatively, it is possible that a combination of partial melting and slab-derived sediment melts can produce the primary melt trace element spectra that form the left-hand part of the spectra. A similar conclusion was reached by Zellmer et al. (2000) based on trace element spectra comparing a Santorini melt model to GLOSS sediment composition.We now plot trace element ratios for our primitive (<1 ppm Th) MI in Figure 4.13a, Figure 4.13b and Figure 4.13c. The high and low Nb primary melt compositions calculated from PRIMACALC2 are shown as colored boxes. Eastern Mediterranean and GLOSS sediment compositions are also plotted, with some notable sediments at different ends of the compositional spectrum labelled. In each plot, the ratio on the vertical axis is a proxy of slab-derived aqueous fluids, and that on the horizontal axis is a proxy of slab-derived sediment melt.

The U/Th ratio is a common proxy for slab-derived aqueous fluid. It is low at Santorini (Figure 13a), and variations in other common aqueous fluid proxies such as Ba/Th (similar to Ba/La, Ba/Rb, Rb/Th and Pb/U; not shown) are small (Figure 13b, c). However, Ba can also be enriched in sediments and their melts (Boström et al. 1973; Kessel et al. 2005). Low, constant U/Th and a variation in Ba/Th suggests that slab-derived sediment melt, not aqueous fluid, dominates the mantle metasomatism signature. Those MIs with higher aqueous fluid proxies are generally of the higher Nb, more calc-alkaline type (Figure 13a, b, c).

Figure 4.13 (next page): Ratio-ratio diagrams illustrating variations in primitive melts due to differing slab components. The depleted MORB mantle (DMM) estimations are from Salters and Stracke (2004) and Workman and Hart (2005). Eastern Mediterranean Sediments (EMS) from Klaver et al. (2015) are also plotted for comparison. Symbols as in Figure 4.2b unless noted otherwise in the figure.

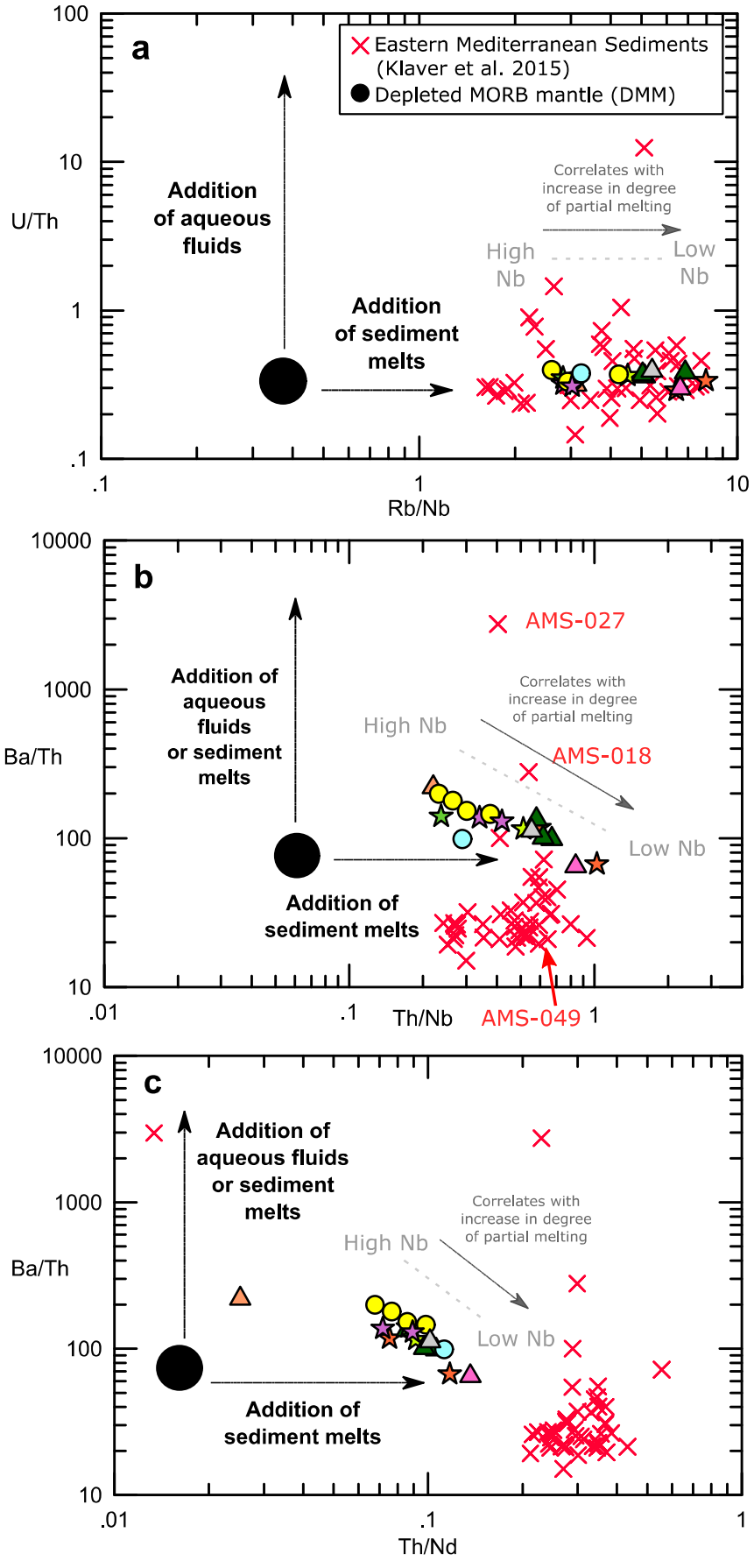
a
Eastern Mediterranean Sediments
(Klaver et al. 2015)
Depleted MORB mantle (DMM)
Addition
of aqueous
fluids
Addition
of sediment
melts
Correlates with
increase in degree
of partial melting
High
Nb
Low
Nb
U/Th
Rb/Nb
100
10
1
.1
.1
1
10
b
AMS-027
Addition of
aqueous
fluids
or sediment
melts
Correlates with
increase in degree
of partial melting
High Nb
AMS-018
Low Nb
Addition of
sediment melts
Ba/Th
Th/Nb
AMS-049
10000
1000
100
10
.01
.1
1
c
Addition of
aqueous fluids
or sediment
melts
Correlates with
increase in degree
of partial melting
High Nb
Low Nb
Addition of
sediment melts
Ba/Th
Th/Nd
10000
1000
100
10
.01
.1
1

On a diagram of Ba/Th versus Th/Nd (Figure 13c), Ba/Th for the higher Nb series is higher than DMM and must come from the slab. The only sediment plotted with high Ba/Th is AMS-027, which is an undescribed Nile River Fan sediment (Klaver et al. 2015). The other sediments cannot provide the means to elevate Ba/Th in the high Nb series. The same is seen for Ba/Rb (not shown). Either the higher Ba/Th and Ba/Rb are brought in the hydrous sediment melt, or involvement of a specific type of slab-derived sediment with high Ba/Th (like AMS-027) is needed to explain the high Nb magmas.

High Th/La Th/Nb, Rb/Nb, etc. are common proxies for slab-derived sediment melts (Johnson and Plank 2000; Plank 2005; Keppler 2017). Sediment melt proxies such as Rb/Nb, Th/Nb and Th/Nd vary more than those for fluid proxies (Figure 13 a,b,c). The melts with higher values of these ratios tend to be the lower Nb, more tholeiitic ones (e.g. M12, Megalo Vouno) (Figure 13 a,b,c).

Our conclusion that the principal slab-derived component in Santorini basalts is subducted sediment is in agreement with previous studies (Zellmer et al. 2000; Francalanci et al. 2005b; Vaggelli et al. 2009; Bailey et al. 2009; Francalanci and Zellmer 2019). Bulk sediment addition to the mantle wedge is probably not realistic and sediments are probably rather added into the mantle wedge as hydrous partial melts (Johnson and Plank 2000; Bailey et al. 2009). Previous studies have also ruled out a large slab-derived aqueous fluid contribution (Francalanci et al. 2005b; Francalanci and Zellmer 2019). A low degree of U-Th disequilibrium has been attributed to fluid addition to the mantle (Zellmer et al. 2000; Zellmer and Turner 2007) but could also be alternatively explained by the introduction of altered oceanic crust (O. Sigmarsson, personal comm.). The ArcBasaltSimulator5 results from Baziotis et al. (2018), which agree with seismic observations, suggest that the pressure and temperature of the slab surface are 4.4 GPa and 800°C which may be conducive to a production of a supercritical fluid, although conditions under which a supercritical fluid can form are not well understood (Hermann et al. 2006; Zheng et al. 2011; Kawamoto et al. 2012; Ni et al. 2017).

4.5.6 Is there a rutile effect on the different Nb groups?

Rutile is a common mineral in subducting slabs and can retain Nb, Ta and other HFSE, thus controlling their behavior during subduction (Brenan et al. 1994; Pearce and Peate 1995; Schmidt et al. 2004, 2009). Nb-Ta anomalies are present for both Nb endmember primary melts and cannot be explained by partial melting (Figure 4.11) suggesting rutile is likely present in the residue left behind by the sediment melts. An alternative possibility to explain the variation of Nb (and Ta) of primitive melts could be that the variation of these elements is solely, or at least principally, controlled by residual rutile in the slab sediments that give rise to the melts that metasomatize the mantle. We now explore the importance of rutile on the Nb variation of our primitive melts.

Figure 4.14 shows a spider diagram with elements reordered according to relative enrichment of incompatible elements with respect to DMM, in a way similar to an ordering of McCulloch and Gamble (1991) but based rather on enrichment of our own data with respect to depleted MORB mantle (DMM). Of all the elements, Nb and Ta show the greatest variation, possibly due to variable residual rutile. It is clear that the most enriched elements on the left of the diagram (LILE and LREE) are derived from sediment melts. Therefore, the relative enrichment towards the left could be a first-order estimation of the order of element partitioning into sediment melts. Nb and Ta can be affected by rutile, but also can be partitioned into sediment melts (depending a number of factors including the amount of residual rutile, degree of sediment melting, etc.); therefore these elements are placed at the left-hand side because there are multiple effects that could contribute to their variation.

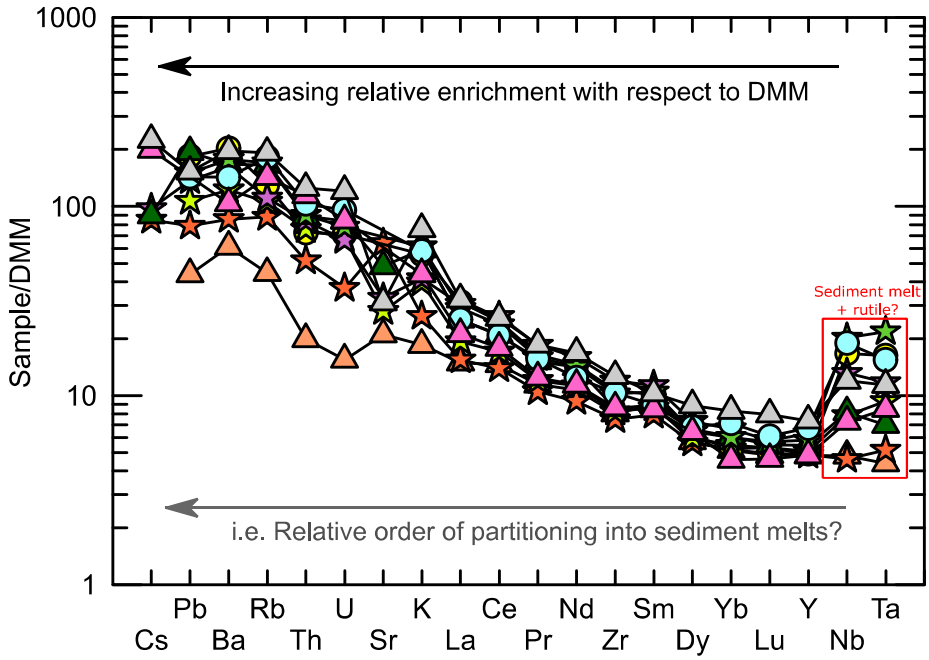

Figure 4.14: Re-ordered spider diagrams for selected primitive melt inclusions. Elements are arranged in order of relative enrichment with respect to DMM, apart from Nb and Ta, which are quite variable and may have multiple effects from both residual rutile and enrichment in sediment melts. Those included are the lowest Th sample for each unit that contains a near-primary melts. The samples shown are: S16-88-3a, S12-37 1-3, S12-43 7-1, KAM24-T08, S16-26-5, S16-16-1, S09-04-6, S16-21-2, S16-14-9 and S18-11-1a. Symbols as in Figure 4.2b.

In the case where Nb and Ta are partly or wholly controlled by residual rutile, a smaller and larger amount of rutile would give the high and low Nb series, respectively. The effect would be amplified by the degree of sediment melt addition to the different domains of the mantle. Nb enrichment is, however, generally coupled with the enrichment of other incompatible elements for the different series; therefore, we argue that the Nb series are not controlled solely by the presence of rutile in the residue. Coupling of Nb enrichment with that of other incompatible elements which are not partitioned into rutile (such as Ba, La, REE, etc.) is an argument in favor of partial melting and sediment melt addition dominating the trace element spectra with Nb included. Nb will be enriched by partial melting and can also enter sediment melts (Kessel et al. 2005; Chen et al. 2018). This is well-illustrated in Figure 4.15. Nb/U can be used as an indicator of a residual rutile effect and/or indicator of the character of the metasomatizing agent, while Ba/Th cannot be affected by residual rutile in the source due to the non-partitioning of these two latter elements into rutile

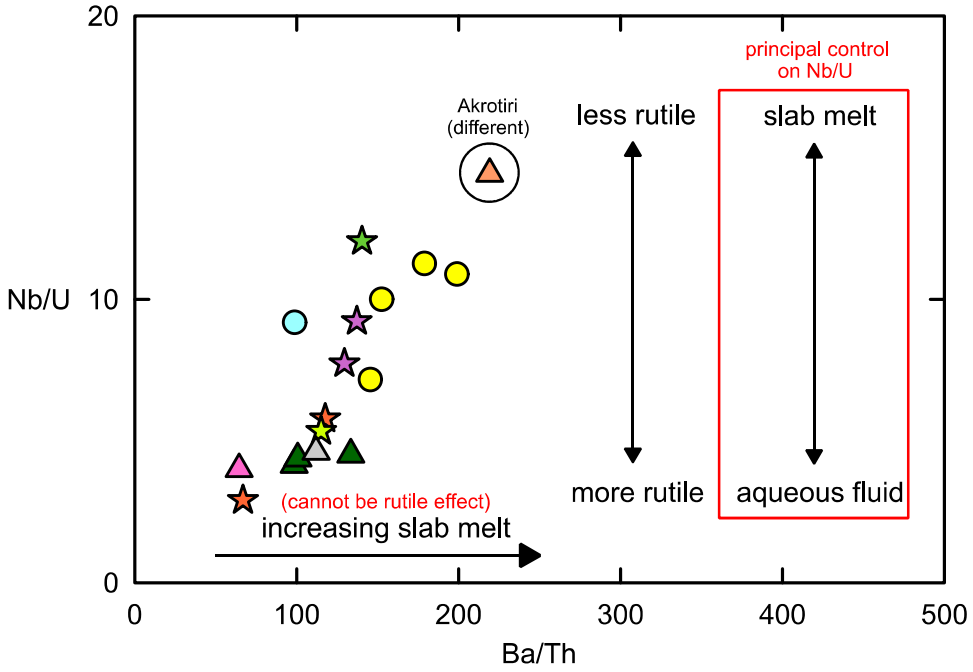

Figure 4.15: Nb/U vs Ba/Th for primitive (< 1 ppm Th) melt inclusions. A good linear positive correlation between these element ratios shows the correlated behavior of Nb and Ba. This suggests that Nb/U (a proxy for rutile and/or metasomatizing agent) is principally controlled by the slab melt rather than rutile, and Nb is not principally controlled by rutile. Symbols as in Figure 4.2b.

(Klemme et al. 2005). A good correlation of these two ratios indicate that the behavior of Nb and Ba are linked, and that slab melt has a dominant control on Nb.

We cannot rule out, however, that the influence of rutile may vary between the Nb groups. There might be some effect on the composition of Nb, Ta and the HFSE by rutile, which could explain why a minor decoupling of Nb with some other elements exists (e.g. Cape Riva and Kameni MIs for example are not the highest in Nb but are highest in Ba; Figure 4.8a).

4.5.7 Different mantle source domains

We argue for at least two mantle source domains below Santorini: a low Nb mantle melt source and a high Nb mantle melt source. The low Nb source is characterized by a higher degree of mantle wedge partial melting and is associated with a higher slab-derived sediment melt signature (possibly with more residual rutile in the sediment), leading to primary melts with an incompatible-poor, more tholeiitic character. The high Nb source is characterized by a few percent less of partial melting and a smaller,

yet still prominent, sediment melt input (possibly with less residual rutile in the sediment) resulting in incompatible-enriched primary melts of more calc-alkaline character. A small slab-derived aqueous fluid signature may be present in the high Nb source.

Three features of Santorini magmatism are suggestive of a possible role of decompression melting in the mantle beneath Santorini: (1) the absence of a strong slab-derived aqueous fluid geochemical signature, (2) the existence of arc-tholeiitic compositions with relatively flat REE patterns (e.g. Figure 4.8b), and (3) strong regional crustal extension. The possible importance of decompression melting beneath Santorini has also been emphasized by previous authors (Francalanci et al. 2005b; Francalanci and Zellmer 2019). It can occur in extensional back-arcs in a similar way to mid-ocean ridge settings, where upwelling of asthenospheric mantle causes partial melting; however, in back-arc settings, basalts may fall anywhere between N-type MORB and typical calc-alkaline basalts (Presnall et al. 1979; Saunders and Tarney 1984), as indeed observed at Santorini.

4.5.8 Variations in time and space

Our new data enable us to document how the different primitive basaltic melts vary in availability with respect to time at Santorini. When the Nb contents of the primitive melts (<1 ppm Th) are plotted against time/stratigraphy, no systematic trend is evident (Figure 4.16). This is reinforced if we include the whole rock data of Bailey et al. (2009) from two distinct time periods (Peristeria and Skaros volcanoes), and back-extrapolate to ~ 1 ppm Th. The combined data clearly suggest that both Nb melt types have been available throughout the 650 ky history of the volcano. Indeed, in some cases, both extremes of the Nb type spectrum have been erupted within a very short time period, such as in the M10 interplinian period (within a 10-20 ky period).

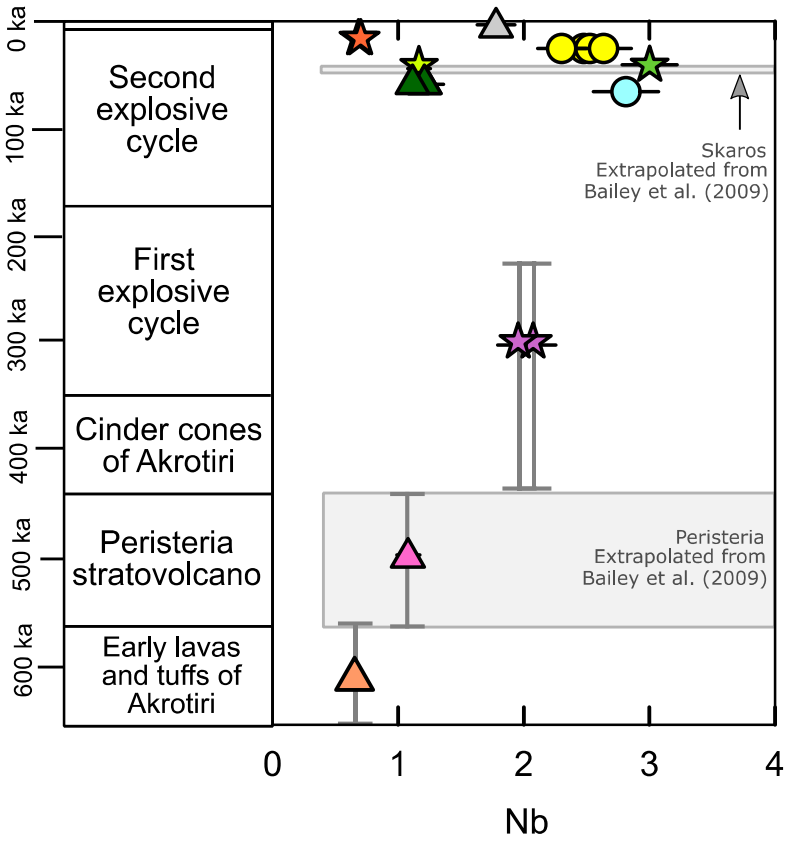

Figure 4.16: Variation of Nb in primitive (<1 ppm Th) melt inclusions over time. Whole rock data for Skaros and Peristeria mafic lavas and dykes from Bailey et al. (2009) extrapolated to ~1 ppm Th are represented by grey boxes. Melt inclusion data and extrapolated whole rock data show there is no systematic variation or patterns of Nb with time. In some cases, different Nb-type extremes are erupted within a short (~ 10 ka) period of time, such as during the M10 interplinian period. Symbols as in Figure 4.2b.

Now, it is important in this context to consider the possibility of crystal inheritance. Do the primitive MIs in Figure 13 (and their host olivines) really belong to their host magma (with the stratigraphic age plotted), or are some recycled from earlier units? Recycling of crystals in magmas is commonly invoked (Blundy and Shimizu 1991; Francalanci et al. 2005a; Jerram and Martin 2008). In Figure 4.17, we plot MI compositions, plus associated groundmass glasses (see Chapter 5), in several individual eruption units of our sample set. In most cases it is clear that the groundmass glasses lie on the same trends as the MIs, showing that the MIs and their host olivines are indeed genetically related to the host interstitial melt, and are not recycled. Although we cannot rule out any crystal inheritance at all, the data suggest that it is probably not common enough to invalidate the conclusions of the previous paragraph.

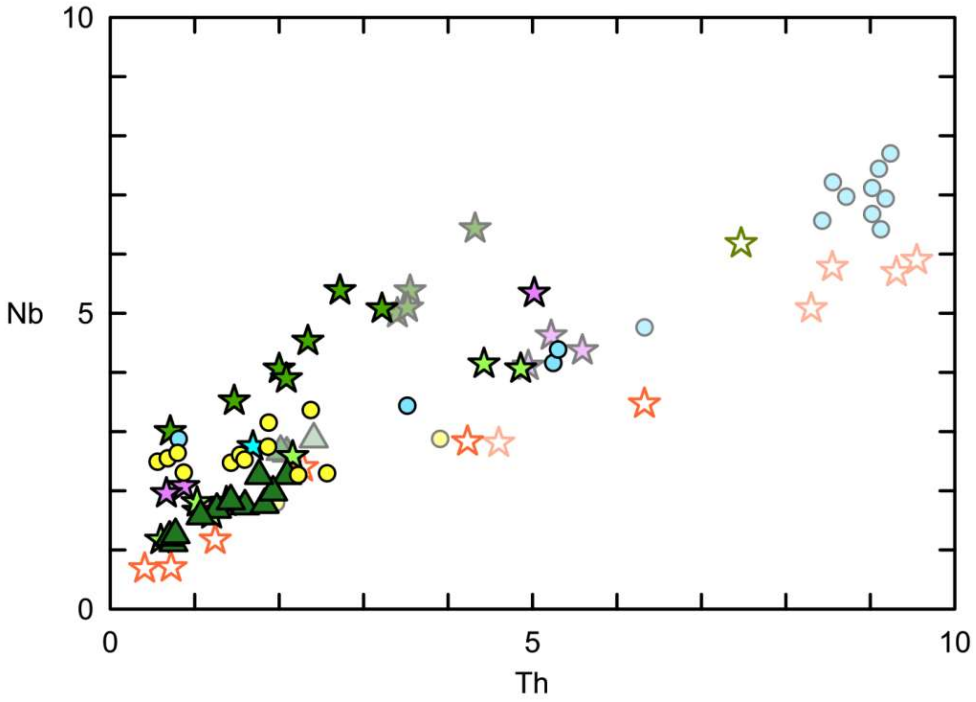

Figure 4.17: Nb vs Th for example data trends of different eruptions; M10-YB6 (green stars) and M12 (orange stars). Melt inclusions are opaque while groundmass glasses (unpublished data) are slightly transparent. It is clear the melt inclusions and groundmass data form straight subparallel trends; therefore, the melt inclusions and groundmass melts are cogenetic. Symbols as in Figure 4.2b.

It is hard to say whether there is any systematic spatial variation in primary melt types at Santorini, as the vent locations for all the eruption units studied are not precisely known. The caldera has a large surface area of >40 km^2, and is underlain by a 25-km-thick crustal column; yielding a large volume to work with. However, seeing that calculated vent locations generally repeat along defined volcanotectonic lineaments (Druitt et al. 1999) (Figure 4.1b), magma bodies feeding eruptions along those lineaments are probably in close proximity to one another. There is no evidence to support that different lineaments are associated with different magma series. For example, while Peristeria and Megalo Vouno are both on or near the Colombos Line (Figure 4.1b), Peristeria has a medium Nb primitive melt (evolving into medium to high Nb compositions; not shown here) and Megalo Vouno primitive and more evolved melts are all low Nb compositions.

4.5.9 Model for the plumbing system

A model for the plumbing system of Santorini is proposed in Figure 4.18. Our data suggest that there are at least two mantle source domains beneath Santorini: a low-Nb domain (2.2-2.3 GPa) associated with higher degrees of mantle melting and a high Nb domain (1.7-2.5 GPa) with a few percent less melting. Both domains are have been metasomatized predominantly by slab-derived sediment melts, with the low Nb domain carrying a slightly higher sediment melt signature. The sediment melts may leave behind varying amounts of residual rutile.

These domains have existed throughout the history of Santorini and have been tapped closely in time. The two endmember primary melts are concluded to have been available simultaneously throughout most of the history of the volcano, consistent with previous studies (e.g. Bailey et al. 2009).

The primary melts enter the crust and differentiate at the Moho or in the lower crust, producing the primitive basaltic melts trapped as melt inclusions in olivines (and more rarely in cpx), and leaving behind mafic to ultramafic cumulates of olivine and clinopyroxene. The primitive melts then differentiate by fractional crystallization, accompanied by some crustal assimilation (Mann 1983; Druitt et al. 1999; Bailey et al. 2009) in transcrustal magma reservoirs, generating the low-pressure fractionation trends that are studied in the next chapter.

4.6 Conclusions

1. Olivine-hosted MI data show there is a range in incompatible trace element chemistry in the least-evolved magmas of Santorini. The olivines studied range from Fo_{70} to Fo_{88}. Not all olivine-hosted MIs are primitive. We define our primitive MIs as those with < 1 ppm Th. The primitive MIs have typical subduction zone geochemical signatures, with LILE enriched over HFSE, LREE enriched over HREE and prominent negative Nb-Ta anomalies and positive Pb anomalies

2. The primitive MIs vary between incompatible-poor and incompatible-rich types. Since Nb shows the greatest variation, we call these low Nb and high Nb primitive melt types, respectively, following Bailey et al. (2009). The primitive MIs range in La/Yb from 1.5 (flat and tholeiitic-like) in the low Nb type to 3.2 (inclined and calc-alkaline-like) in the high Nb type.

3. The low Nb and high Nb type primitive melts cannot be related by fractional crystallization.

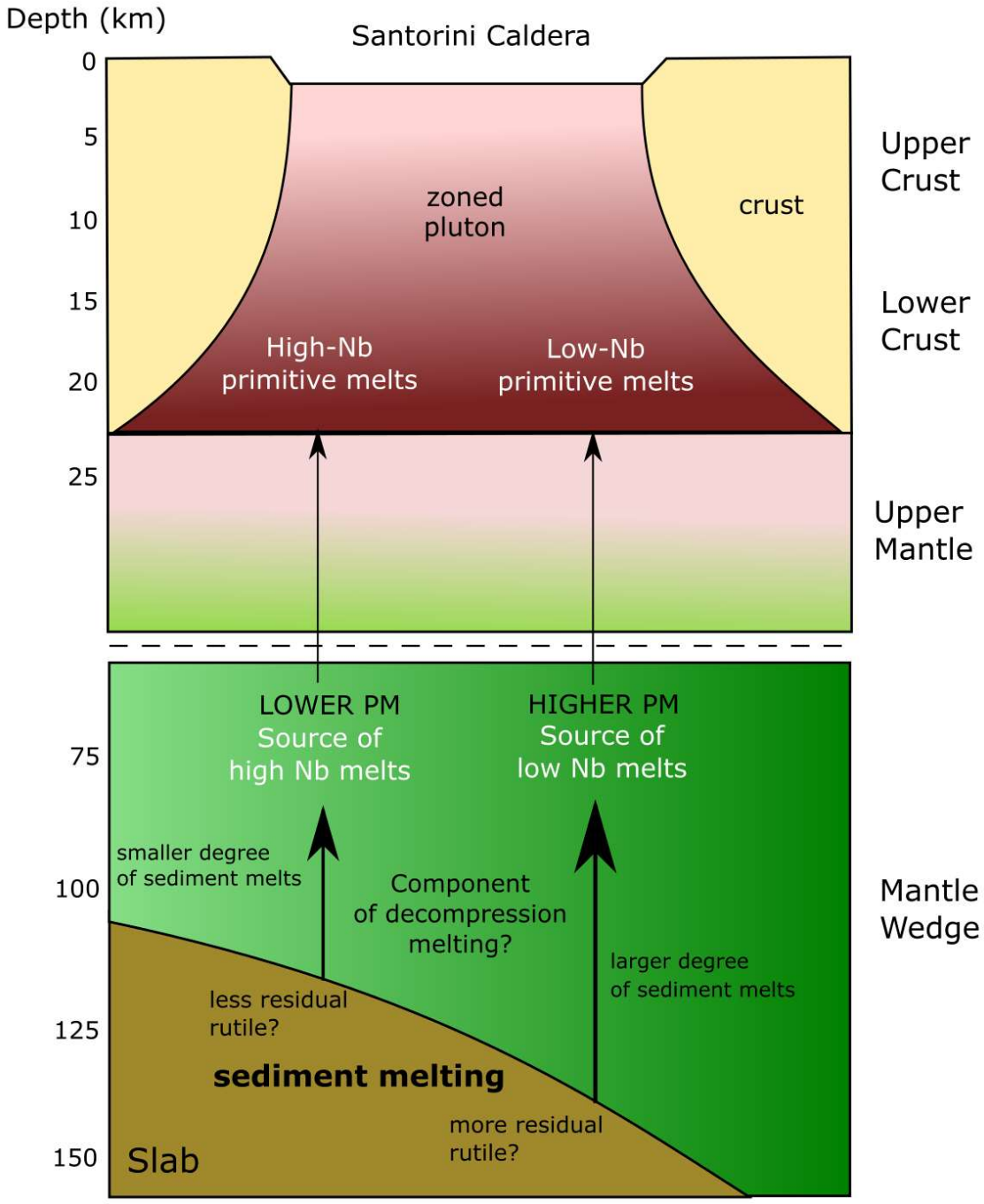

Figure 4.18: Model of the plumbing system of Santorini. Different amounts of sediment melts, possibly with different amounts of residual rutile in each case, metasomatize the mantle wedge above the subducting slab. A region of lower degrees of partial melting (PM) is produced by smaller amounts of sediment melt addition, which creates high-Nb primary melts that in turn give rise to the high Nb series. A region of a higher degree of sediment melt addition produces higher degrees of melting that give rise to the low Nb series. The different Nb-type primitive melts then enter the crust and differentiate within in the multi-level zoned pluton by fractional crystallization or assimilation fractional crystallization processes.

4. Using PRIMACALC2 and mantle melting models, we derived a range of degree of melting (F) of the mantle to produce the different endmember primary melt types. PRIMACALC2 gives lower melting estimates (6% for high Nb primary melt; 8% for low Nb primary melt) than our mantle melting model (18% for high Nb primary melt; 22% for low Nb primary melt). The degree of melting between the two melt types probably differs by a few percent. PRIMACALC2 gives conditions for mantle melting of 2.3 GPa for low Nb primary melt and 1.8 GPa for high Nb primary melt.

5. The predominant metasomatic signature in the primary melts is from slab-derived sediment melting. There is very little effect from slab-derived aqueous fluids. The low Nb melts carry a higher sediment melt signature than the high Nb melts. There may be some influence from residual rutile, but this does not dominate the different Nb groupings. The different primary melts are mainly a result of different degrees of partial melting of a mantle wedge metasomatized by slab-derived sediment melts.

6. The two different endmember primary melts have been available for ascent into the crust over much of the >650 ky history of the volcano. This conclusion is in line with those of other authors (e.g. Vaggelli et al. 2009; Bailey et al. 2009).

7. The absence of a strong slab-derived aqueous fluid component, coupled with regional extension around the volcanic field and the presence of arc tholeiitic compositions, could possibly be related to increasing role of decompression melting at Santorini.

Chapter 5: Differentiation of magmas, plumbing system processes and temporal trends revealed by crystal-hosted melt inclusions

Abstract

Santorini volcano (Greece) is situated in an extensional basin toward the center of the South Aegean Volcanic Arc. There is a well-documented temporal decrease seen in many incompatible elements with respect to silica in evolved magmas at the volcano; however, the cause of this decrease is not well understood. To investigate this temporal trend, we have analysed major elements ± trace elements of 130 olivine- and 190 plagioclase-hosted melt inclusions and 295 groundmass glasses from volcanic units of the last <530 ka at Santorini. Santorini melt inclusions and groundmass glasses define geochemical trends on variation plots that can be split into low Nb and high Nb series based on the parental basaltic melts described in Chapter 4. It is useful to also distinguish a medium Nb series. Each series exhibits two distinct stages of differentiation on log-log variation plots: Stage 1 from basalt to basaltic andesite, and Stage 2 from basaltic andesite to rhyodacite. The two stages cannot be modelled together by FC as this requires unreasonably high Ds for most incompatible elements. While Stage 2 can be modelled by FC using reasonable Ds, Stage 1 cannot. Stage 1, and to a large extend both stages, can be modelled satisfactorily from the respective parental compositions using AFC with r values of 0.2-0.5 and a silicic contaminant with ratios of incompatible elements to Th that are similar to, or lower than those of silicic melts of the magmatic series themselves. Stage 2 can be similarly modelled by AFC, but also by almost pure FC using reasonable D values. There are many possible best-fit contaminants, but they can be narrowed down based on mean-solution distribution and geological reasoning. One possibility is that the contaminant is a highly evolved, low fraction silicic melt, which appears from published whole rock Sr isotopic data to be variably radiogenic. It may be present interstitially, or as veins and dykes, in the variably mushy plutonic products making up the Santorini crustal magmatic system. Mantle-derived basaltic parent melts encounter and interact with this contaminant during ascent to the surface. Melt inclusion and groundmass trends on K_2O versus SiO_2 have the same origin as those on Nb vs Th, which are explained by AFC

differentiation from different primitive parental magmas. It follows that the well-known temporal decrease in K_2O (and other incompatible elements) at Santorini over time since 530 ka is also parent-related, as previously suggested but not proven. Given that low and high Nb basaltic melts have been generated throughout the history of Santorini in different mantle source domains (Chapter 4), the temporal change in incompatibles must be due to an increase *in the proportion* of low Nb primary melt relative to high Nb primary melt with time. This could be due to a growing influence of crustal rifting and extension in the region, with possibly increasing decompression melting over fluid-flux melting over time.

Keywords: Santorini; arc volcanism; incompatible elements; magma differentiation

5.1 Introduction

Arc volcanoes threaten human populations and their livelihoods. It is necessary to better understand the behavior of arc volcanoes in order to interpret signs of unrest and mitigate hazards. Santorini Volcano (South Aegean Volcanic Arc, Greece) is an active arc volcano responsible for at least twelve Plinian eruptions over the last 360 ky, the most recent being the 48-86 km^3 (dense-rock equivalent) Late Bronze Age (LBA) eruption. Santorini has had small-scale historical eruptions, the last in 1950, and a seismic crisis in 2011-2012. Erupted magma compositions have been diverse throughout the history of Santorini with several distinct geochemical lineages, the origins of which are not yet well understood. Understanding the origins of geochemical diversity at Santorini would provide information on the magmatic processes driving eruptions there.

Arc magma compositions evolve through complex processes of generation, then differentiation, of mantle-derived melts (Ducea et al. 2015; Turner and Langmuir 2015; Janoušek et al. 2016). In continental arc settings like the Aegean, subduction of oceanic crust and lithosphere releases slab-derived aqueous fluids and sediment melts into the asthenospheric wedge above the subducting slab, which lower the solidus of mantle peridotite and cause partial melting (Gaetani and Grove 1998; Katz et al. 2003; Kessel et al. 2005; Grove et al. 2012; Zellmer et al. 2015). The chemistry of the primary arc melts thus produced depends on the types and proportions of slab-derived aqueous fluids and sediment melts that metasomatize the mantle wedge, as well as the composition of the mantle itself. Mantle-derived melts then evolve and differentiate as they ascend through the arc crust. Crystallization, magma mixing, assimilation of foreign material, and combinations of these, are commonly invoked to explain different geochemical series of arc magmas (Eichelberger 1978; DePaolo 1981; Rollinson 1993; Albarède 2009; Reubi and Blundy 2009; Janoušek et al. 2016). Two fundamental questions related to arc magmatism are: (1) What can geochemical variations tell us about physical processes occurring in the magmatic system, and (2) as continental arc volcanoes often have a full range of compositions from basalt to rhyolite, what is the relationship between mafic and silicic magmas?

Santorini has been the subject of several geochemical and petrological studies (e.g. Mann 1983; Huijsmans 1985; Zellmer et al. 2000; Vaggelli et al. 2009; Bailey et al.

2009; Gertisser et al. 2009; Cadoux et al. 2014; Andújar et al. 2015, 2016; Baziotis et al. 2018), but questions remain about what petrological processes govern the differentiation of its magmas. While many whole rock studies have been carried out there, whole rocks are mixtures of crystal and melt, and can be hard to interpret if some of the crystals are inherited and/or the melts are themselves mixtures (Kent 2008; Reubi and Blundy 2009). Crystal-hosted melt inclusions, on the other hand, provide snapshots of pure magmatic melts at different stages of their evolution. This paper uses melt inclusions and groundmass glasses, all analyzed by the same electron microprobe and ICP-MS instruments, to generate a database of internally consistent, high-quality melt compositions in order to investigate the relationships between mafic, intermediate and silicic magmas at Santorini. We use melt inclusions hosted in olivine, plagioclase and pyroxene, collected from many different chrono-stratigraphic levels, to trace the evolution of melts from basalt to rhyodacite. We then use this new high-precision dataset to carry out geochemical modelling to explain the compositional data trends. We also use the data to explain a well-documented decrease in incompatible element contents of Santorini intermediate and silicic magmas through time, over the last half million years of the volcano's history (Druitt et al. 1999). To this end we build on previous studies of primitive basaltic melts at Santorini (Bailey et al. 2009; Chapter 4) and exploit a database of previously published whole rock analyses.

5.1.1 Volcanological context

Santorini lies on the South Aegean Volcanic Arc, a continental island arc formed by subduction of the African oceanic plate below the Aegean continental microplate. The arc extends across the southern Aegean, from mainland Greece to the Anatolian Peninsula (Figure 5.1a). It hosts several active volcanic fields (Francalanci and Zellmer 2019). The arc lies about 150 km above the Benioff zone, more (>190 km) in the center of the arc (Keller 1982; Papadopoulos 1982). The thickness of the continental crust is variable, with the western and eastern sections of the arc having thicker crust (32-34 km), and the central section having thinner (23-26 km) crust (Makris 1977; Papazachos 2019). The angle of subduction varies from 10° to 30°, increasing from west to east (Kalogeropoulos and Paritsis 1990; Jackson 1994; Papazachos 2019). Slab rollback since

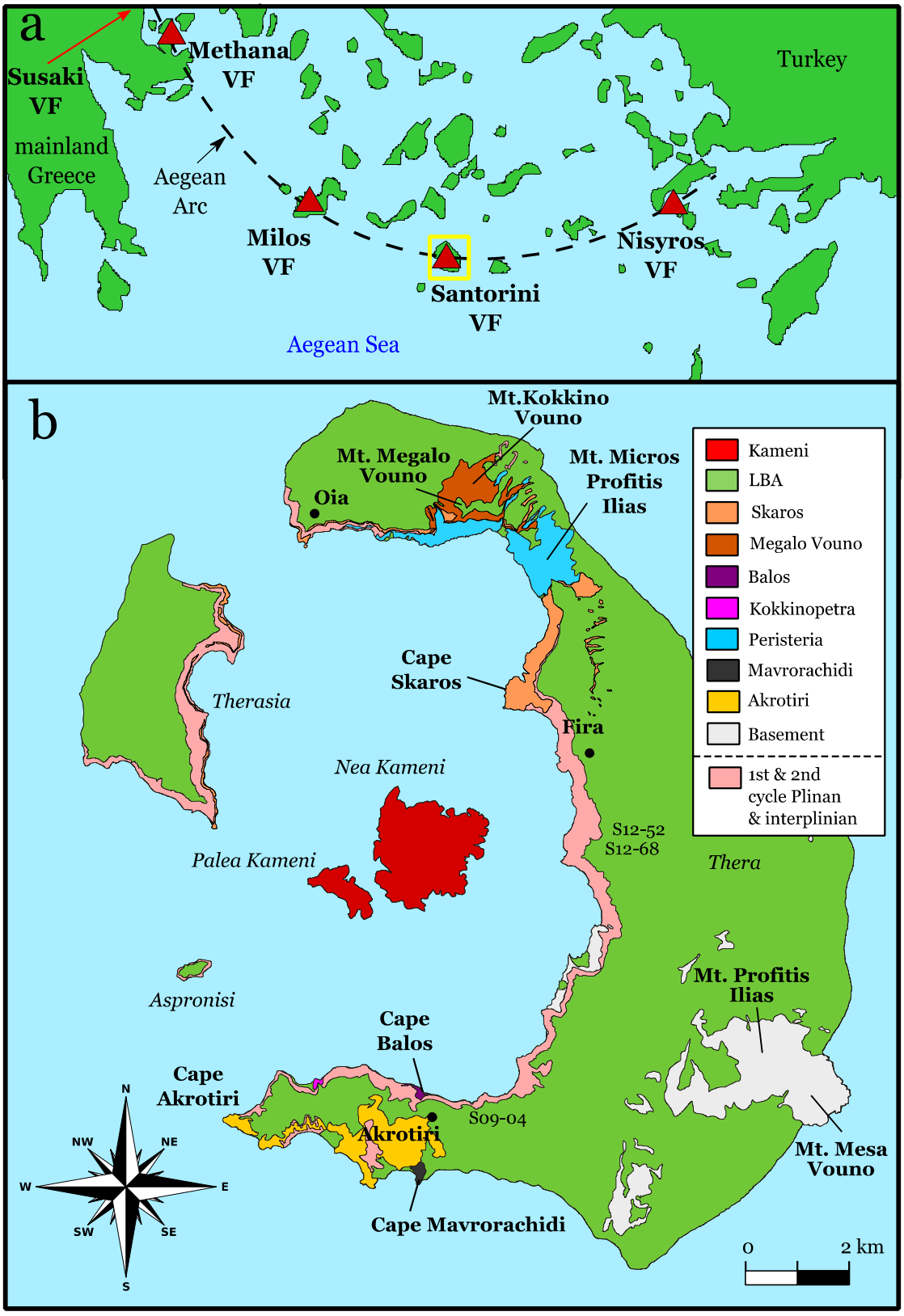

Figure 5.1: (a) Map of the southern Aegean Sea showing the main volcanic centers of the Aegean Arc. (b) A simplified geologic map of Santorini (based on that of Druitt et al. 1999). First and second cycle Plinian and interplinian units not already shown (e.g. LBA) are grouped together as one map unit, as the layers are numerous and thin and would be difficult to show.

the Pliocene has created an extensional regime, which is greatest towards the center of the arc (Mercier 1981; Papadopoulos et al. 1986; Wortel and Spakman 2000; Özbakır et al. 2013; Francalanci and Zellmer 2019). The thinner crust of the central arc allows basalts to reach the surface more easily than elsewhere along the arc (Francalanci et al. 2005a; Francalanci and Zellmer 2019; Papazachos 2019).

Santorini Volcano is located at the center of the arc, underlain by 23 km of extended continental crust (Figure 5.1a, b). It lies in a NE-SW-trending rift zone, called the Santorini-Amorgos Rift, with Plio-Quaternary sedimentary fills up to 800 m thick (Klaver et al. 2016; Nomikou et al. 2018). Rifting began 3.8-5.3 My ago in the Pliocene and is proceeding at about 2.5 mm/y (Nomikou et al. 2018).

The present circular physiography of the island group is the result of over half a million years of volcanism and caldera collapse (Druitt and Francaviglia 1992). The composite, flooded caldera measures 10 x 6 km and consists of several underwater basins surrounding the central Kameni islands (Figure 5.1b) (Druitt 2014). Prior to the onset of volcanism, an island consisting of schists and limestones existed (part of the Cycladic Massif metamorphic complex) (Figure 5.1b) (Skarpelis and Liati 1990; Kilias et al. 1998). Products of the earliest known volcanism are preserved on the modern-day Akrotiri Peninsula (Early lavas and tuffs of Akrotiri; 650-580 ka) (Davis et al. 1998; Druitt et al. 1999). These eruptions produced amphibole-bearing silicic lavas and tuffs containing abundant mafic magmatic enclaves. In the north, a stratovolcano complex called Peristeria Volcano was constructed between 530 and 430 ka (Druitt et al. 1999). The Peristeria lavas are mainly basalts to andesites, although tuffs and olivine-bearing scoria layers also occur. Dykes cut through the Peristeria lavas and were studied by Bailey et al. (2009). Several periods of Strombolian eruptions led to the establishment of cinder cones in the southern part of the volcanic field (Cinder cones of Akrotiri; 520-350 ka), broadly simultaneously with Peristeria (Davis et al. 1998; Druitt et al. 1999). The cinder cones erupted some of the least evolved basalts on Santorini (Baziotis et al. 2018).

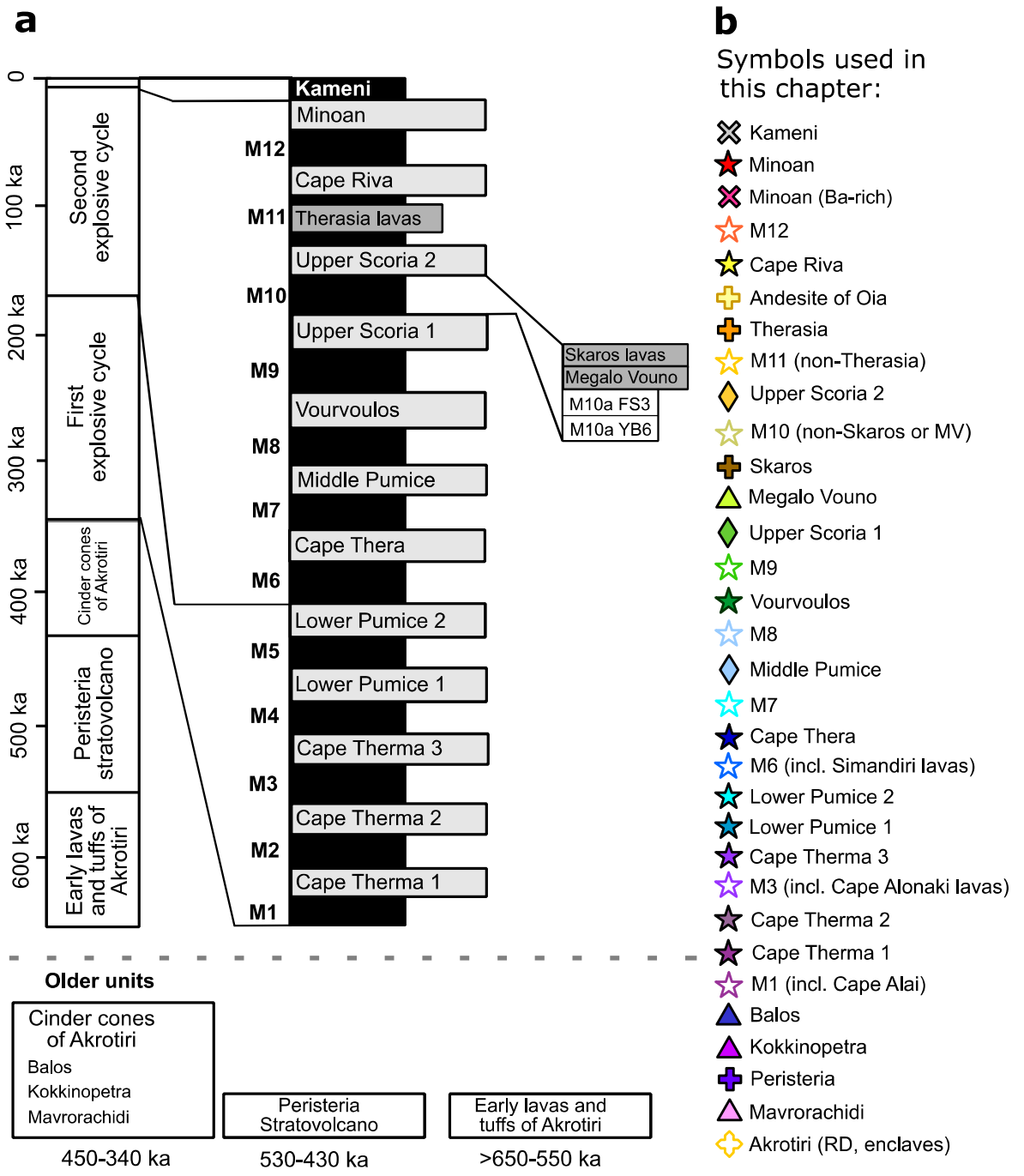

Figure 5.2: Santorini eruptions and symbols used in this chapter. (a) A broad overview of the Santorini eruptive history, with the left approximately to scale, using dates from Druitt et al. (1999) and, on the right, the sequence (not to scale) of twelve identified Plinian eruptions (wide grey rectangles) since 360 ka. Plinian eruptions are separated by interplinian periods (smaller black rectangles) M1 through M12. Older units are summarized below the stratigraphic columns. Subdivisions follow Druitt et al. (1999) and Vespa et al. (2006). (b) Symbols shown are those used in geochemical diagrams to follow in this chapter.

Since ~360 ka, the activity has been characterized by at least twelve large Plinian eruptions alternating with 'interplinian' periods of minor explosive eruptions and shield-building (Figure 5.2a) (Druitt et al. 1999; Vespa et al. 2006). The interplinian periods are labelled M1 to M12 in chronological order and are subdivided into individual eruptive units (Figure 5.2a; Vespa et al. 2006). Two explosive cycles are recognized in the last 360 ky—the first from 360 to 172 ka, and the second from 172 to 3.6 ka. Each cycle involves the transition from dominantly intermediate to dominantly silicic eruptions and terminates with large silicic eruptions and caldera collapse. The first cycle (360-172 ka) began with a succession of dominantly intermediate eruptions (Cape Thermas 1 and 3; also, a small silicic Plinian eruption Cape Therma 2), and terminated with caldera-forming silicic eruptions Lower Pumice 1 and Lower Pumice 2. The second cycle (172-3.6 ka) began with mostly intermediate explosive eruptions (Cape Thera, Middle Pumice, Vourvoulos, Upper Scoria 1, Upper Scoria 2), and terminated with the silicic caldera-forming Cape Riva and Late Bronze Age eruptions, the last-mentioned 3600 years ago. The most recent volcanism (<3600 y) has been centred on the 400-m-high Kameni intracaldera edifice, the subaerial summits of which form the islands of Nea Kameni and Palaea Kameni (Figure 5.1b). Nine historical eruptions of mafic-enclave-bearing dacitic magma are known to have occurred from Kameni, the last in 1950 (Pyle and Elliott 2006). The Kameni eruptions may mark the beginning of a third explosive cycle (Figure 5.2a).

5.1.2 Geochemistry and petrology of Santorini magmas

The mantle of the Aegean region most likely has a depleted MORB mantle (DMM) composition (Francalanci et al. 2005b; Francalanci and Zellmer 2019; Papazachos 2019). Beneath the island arc the mantle wedge has been metasomatized, mainly by hydrous sediment melt addition from the down-going slab (Francalanci et al. 2005b; Vaggelli et al. 2009; Francalanci and Zellmer 2019; Chapter 4). The arc shows along-arc systematic variations of isotopic compositions, with decreasing $^{87}Sr/^{86}Sr$, $^{207}Pb/^{204}Pb$, $^{208}Pb/^{204}Pb$ and generally increasing $^{143}Nd/^{144}Nd$ from west to east, correlated with slab-derived sediment melt input to the mantle wedge (Francalanci et al. 2005b; Klaver et al. 2015, 2016; Francalanci and Zellmer 2019; Papazachos 2019). Most magmas erupted along the arc are calc-alkaline to high-K calc-alkaline, although tholeiitic magmas also occur at Santorini (Francalanci and Zellmer 2019). Three features of Santorini magmatism are suggestive of a role of decompression melting in

the mantle wedge: (1) the absence of a strong slab-derived aqueous fluid geochemical signature (Chapter 4), (2) the existence of arc-tholeiitic compositions with relatively flat REE patterns (Chapter 4), and (3) strong regional crustal extension (Nomikou et al. 2018).

Santorini eruption products range from basaltic to rhyodacitic, with rare rhyolites. Low-K, high-Al basalts evolve into medium- to high-K dacites and rhyodacites. Products span from mildly tholeiitic to calc-alkaline in character. Basaltic lavas and scoria have olivine, plagioclase, cpx and minor magnetite. Olivine can contain Cr-rich spinel inclusions (Vaggelli et al. 2009; Chapter 4), indicating that spinel forms before, or at the same time as, olivine (Kamenetsky 2001). Basaltic andesites and andesites contain plagioclase, cpx, olivine, magnetite and sometimes opx. Ilmenite and opx often are found as interstitial groundmass phases and probably form late at low temperatures (Andújar et al. 2015). Dacites and rhyodacites contain plagioclase, cpx, opx, magnetite, ilmenite, apatite and pyrrhotite. Fayalitic olivine is present in some dacites of more tholeiitic character (e.g. Vourvoulos). There are no major phases that appear at the surface that incorporate K, Rb and Ba in large amounts, such as potassium feldspar or amphibole (exceptions for amphibole are the 650-530 ka Akrotiri products, and rarely in mafic enclaves associated with LBA and Lower Pumice 2 eruptions). There is some trace element evidence for cryptic amphibole (e.g. flat trend in Y, decreasing Dy/Yb with differentiation; Francalanci et al. 2005b; Klaver et al. 2016; Chapter 6).

The plumbing system below Santorini has provided passage for hundreds of km^3 of magma over the >0.65 My history of the volcano, which is probably underlain by a thick pluton zoned upwards from ultramafic to gabbro, diorite and granodiorite (Druitt et al. 1999, 2016). Primary mantle melts with up to 14 wt% MgO ascend into the crust and differentiate in the Moho or lower crust, producing differentiated basalts and leaving behind ultramafic and mafic cumulates (Nicholls 1978; Chapter 4). Primary basaltic melts beneath Santorini are generated in the mantle wedge in two or more distinct mantle domains (Chapter 4): a low Nb, tholeiitic endmember melt and a high-Nb calc-alkaline endmember melt. The low Nb melt is probably generated by a few percent higher degree of melting of the mantle, which is metasomatized by sediment melts, than the high Nb melt (Bailey et al. 2009; Chapter 4). Phase equilibria experiments and melt inclusion volatile barometry suggest that basalt differentiates to

basaltic andesite in the lower- to mid-crust (≥15 km), while basaltic andesite differentiates to silicic magmas in the upper crust (<8 km) (Cadoux et al. 2014; Andújar et al. 2015, 2016; Druitt et al. 2016). Geochemical modelling shows that basalts must crystallize by 10 to 60 % in order to generate basaltic andesite, and 60 to 80% to form andesite (Nicholls 1971, 1978; Mann 1983; Huijsmans 1985; Druitt et al. 1999). The phase-equilibria experiments of Andújar et al. (2015) also suggest that 60 to 80% crystallization (olivine, cpx, plagioclase, Ti-magnetite and opx ± pigeonite and ilmenite) is required to produce andesite from basalt.

Some authors have also suggested, based on isotopic data, that crustal assimilation occurs. Variations in $^{87}Sr/^{86}Sr$ and $^{143}Nd/^{144}Nd$ show clear divergence from the mantle correlation line (Druitt et al. 1999), due either to crustal contamination (DePaolo and Wasserburg 1976) or to contamination by slab-derived sediments in the mantle wedge (Ben Othman et al. 1989). However, a positive correlation between $^{87}Sr/^{86}Sr$ and SiO_2 has been observed in the general magma suite by Druitt et al. (1999), and in basalts by Bailey et al. (2009), suggesting crustal contamination. Assimilation-fractional crystallization (AFC) models of trace elements and isotopes (Barton et al. 1983; Druitt et al. 1999) suggest that AFC can better explain the observed geochemical trends than fractional crystallization alone. Questions still remain, however, about the nature of the contaminant and where the contamination occurs. Magma mixing also occurs at Santorini, forming hybrid andesites (Fabbro et al. 2013).

A notable, but poorly understood, feature of Santorini magmatism is the temporal decrease in K and other incompatible elements (e.g., Rb, Zr, Nb, LREE) clearly displayed by intermediate to silicic compositions with time since about 530 ka (Peristeria Volcano) (Huijsmans et al. 1988; Druitt et al. 1999; Francalanci et al. 2005b; Fabbro et al. 2013; Francalanci and Zellmer 2019) (Figure 5.3). As Santorini magmas become progressively depleted in incompatibles over time with respect to SiO_2, from Peristeria to Kameni, different trends are created (Huijsmans 1985; Druitt et al. 1999; Francalanci et al. 2005b; Bailey et al. 2009; Fabbro et al. 2013) (Figure 5.3). Note that the early 650-530 ka Akrotiri products do not conform to this trend and are assigned to a different geochemical series not considered in this paper (Mortazavi and Sparks 2004). Temporal changes in incompatible trace elements have also been observed at other volcanic centers of the Aegean arc, although less well defined (Francalanci and Zellmer 2019).

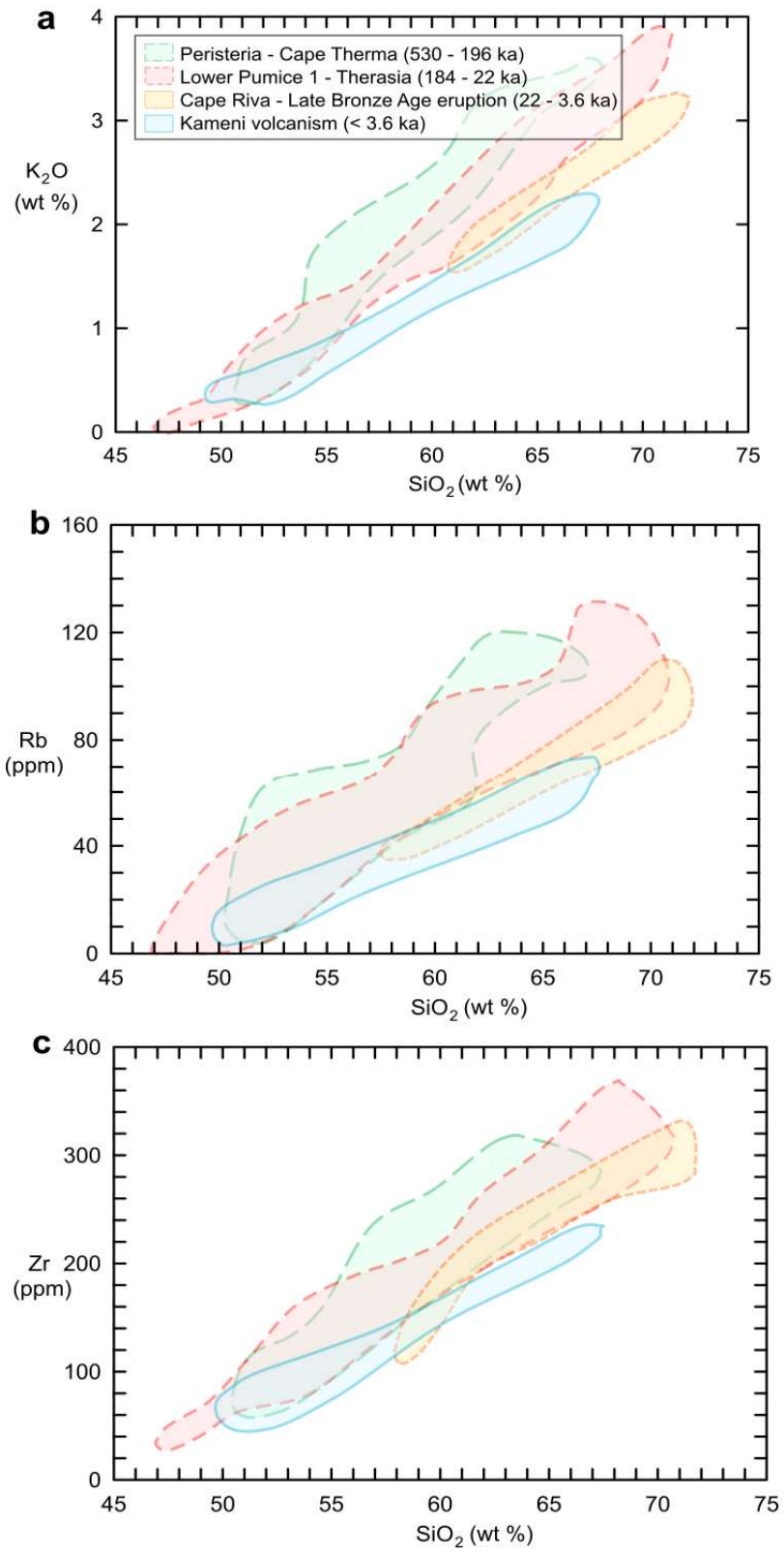

Figure 5.3: Temporal decrease of selected incompatible elements with respect to silica over time. Different discrete "jumps" in the decrease of incompatible elements can be distinguished by plotting the whole rock fields for different time periods. Peristeria to Cape Therma 3 are the highest in incompatible element concentrations, while the most recent Kameni magmas are the lowest. Figure adapted from Fabbro et al. (2013).

This decrease in incompatibles with respect to SiO_2 is very clear in silicic products from the whole rock database (Figure 5.3); however, the resolution of the whole rock database is not good enough to assess whether the different time-varying trends extend back to basaltic compositions, or if the time-variation is only present in the more evolved products. Thus, the source of the incompatible decrease is not yet understood.

One possibility is that it relates to a temporal change in the degree of melting or degree of metasomatism of the mantle wedge (Huijsmans and Barton 1989; Francalanci et al. 2005b; Fabbro et al. 2013). Another is a time-increasing influence of extension-related decompression melting (Francalanci et al. 2005b; Francalanci and Zellmer 2019). A temporal decrease in the degree of crustal contamination with time is also a possibility, since the continental crust is enriched in incompatible elements relative to basalt (Druitt et al. 1999). Other possibilities were discussed by Huijsmans and Barton (1989).

Armed with (1) abundant chrono-stratigraphically controlled melt inclusions, including many primitive basaltic ones, (2) an internally consistent, high-quality analytical database analysed on the same instruments, and (3) knowledge of the nature, origin and time-variation of Santorini primary melts (Chapter 4), we now re-evaluate the genesis of the different magmatic series at Santorini and place better constraints on the origin of the decrease in incompatibles with time with respect to silica (Figure 5.3).

5.2 Methodology

5.2.1 Melt inclusion and groundmass glass preparation

Crystal-hosted melt inclusions (MIs) and groundmass glasses were prepared from different units from the stratigraphy of Santorini. Where possible, small glassy scoria were collected, as they were more likely to have quenched upon eruption and cooled quickly enough to avoid MI and groundmass crystallization. Some samples, already mounted in Indium mounts, were taken from the study of Druitt et al. (2016). Selected samples were crushed with a jaw crusher, then sieved into various size fractions depending on the sample. The fractions typically used were 100 to 250 μm, 250 to 500 μm, and/or 500 μm to 1 mm. Each fraction was further divided into magnetic and non-

magnetic fractions using a hand magnet. In ideal cases, the non-magnetic fraction contained the crystals of interest; however, sometimes if crystals were coated in groundmass, the magnetic fraction was also kept and exploited if needed. Crystals greater than 500 μm in size were usually picked by hand under a binocular microscope, while smaller ones sometimes required the use of a Frantz magnetic separation machine to isolate. A total of 320 MIs were analyzed, hosted in olivine (n=130), plagioclase (n=190), clinopyroxene (n=12) and orthopyroxene (n=1), along with 295 groundmass glasses.

A textural control was implemented during MI selection to ensure having accurate and representative melt compositions. Where possible, glass-coated crystals were chosen, and euhedral crystals were preferred where present. Crystals were inspected under an optical microscope with 20 to 50x magnification to search for evidence of melt leakage and decrepitation, as well as to identify fractures, melt tubes or other connections to the surface. Melt inclusions that had passed these textural controls, and which furthermore had a large enough size (i.e. having at least 20 μm diameter of analyzable area, not including the bubble) were selected. Primary MIs were preferred, but in some cases non-primary MIs were accepted, as they could provide some information about melt differentiation.

Crystals were mounted on glass slides with crystal bond and polished until it was possible to see into the crystals and identify MIs. If MIs were glassy and crystal-free (an exception was made for spinel, which can exist prior to MI entrapment and provide a nucleation site for the inclusion to form), crystals were mounted in brass cylinders, filled with epoxy resin, and polished using a sequence of silicon carbide (1200 & 2400 grade) and diamond (6, 3 and ¼ μm grades) polishing mats until the MI was exposed at the surface and well-polished. Groundmass glass was mounted in epoxy and resin in brass cylinders in a similar manner to the MIs. It was necessary to polish lightly so that the groundmass glass did not break in the process.

If the MIs are crystallized, it is necessary to reheat the inclusions and quench them to glass. Reheating is needed for samples from relatively slowly cooled scoriae, lavas and magmatic enclaves, where MIs are partially or wholly crystallized. The details of the reheating process are outlined in Chapter 3.

5.2.2 Analytical methods

A CAMECA SX-100 electron microprobe with 15 kV accelerating voltage housed at the LMV was used to analyze major element compositions of MIs and glasses using a defocused (10 to 20 μm spot size) electron beam at 4 to 8 nA beam current. A defocused beam size was needed to avoid Na depletion under the effect of the electron beam (e.g. Nielsen and Sigurdsson 1981). Na was analyzed first for a counting time of 10s to minimize low Na counts, which were seen to be unaffected in the first ~10s, but then rapidly decreased for longer durations. Major element analysis was always performed before any backscattered electron imagery. The glass standard A99 was used to calibrate the silicate glasses for major elements. Depending on the size of the MI, between one and four major element analyses were taken. Where more than one analysis was taken, the compositions were averaged and checked for compositional homogeneity. Analytical errors on analyses were converted to 2σ standard deviation and compared with 2σ standard deviation resulting from averaging. The maximum value between the two was kept as the 2σ standard deviation.

Backscatter electron (BSE) imagery was used to judge where to analyze the host mineral in equilibrium with each melt inclusion. Minerals were measured for major elements via EMPA with a focused (in reality: ~1 μm) beam size and 15 nA beam current.

Trace elements were analyzed by laser ablation induced coupled plasma mass spectroscopy (LA-ICP-MS) at the LMV. The LA-ICP-MS set-up consists of a Resonetics ArF excimer (193 nm wavelength) laser (model: RESOlution M-50E) coupled to a Thermo Element XR ICP-MS. The elements (isotope of each element) analyzed include: ^{6}Li, ^{7}Li, ^{9}Be, ^{29}Si, ^{43}Ca, ^{44}Ca, ^{45}Sc, ^{47}Ti, ^{51}V, ^{53}Cr, ^{59}Co, ^{60}Ni, ^{65}Cu, ^{66}Zn, ^{71}Ga, ^{72}Ge, ^{75}As, ^{85}Rb, ^{88}Sr, ^{89}Y, ^{90}Zr, ^{93}Nb, ^{95}Mo, ^{115}In, ^{133}Cs, ^{137}Ba, ^{139}La, ^{140}Ce, ^{141}Pr, ^{146}Nd, ^{147}Sm, ^{153}Eu, ^{157}Gd, ^{159}Tb, ^{163}Dy, ^{165}Ho, ^{166}Er, ^{169}Tm, ^{172}Yb, ^{175}Lu, ^{178}Hf, ^{181}Ta, ^{208}Pb, ^{232}Th and ^{238}U. Glasses NIST612 and/or NIST610 were used as reference standards, while BCR2 was used as an external standard. CaO was used as an internal standard. A single analysis contains 30 s of background signal collection followed by 90-100 s of sample analysis, and results in a time-resolved signal to be treated with a data reduction software in order to obtain elemental abundances. GLITTER software was used to reduce the data and obtain trace element concentrations. Note: Cs values were rejected

from any melt inclusions analyzed in previously made indium mounts (Druitt et al. 2016), as there was clear Cs contamination from the SIMS Cs^+ ion beam and/or Cs in indium which had entered into small cracks or pits on the surface of the inclusion.

5.2.3 Post-entrapment correction of melt inclusions

It is often necessary to correct MI compositions to reverse effects of post-entrapment evolution, notably post-entrapment crystallization and diffusional re-equilibration (Roedder 1984; Danyushevsky et al. 2000; Kress and Ghiorso 2004). Post-entrapment crystallization (PEC) of the host mineral on the walls of an inclusion is expected to occur upon cooling (Roedder 1984; Kress and Ghiorso 2004). This process operates as fractional crystallization of concentric shells of the host mineral on the inclusion walls and, for olivine, can reach values of up to ~15 wt % olivine crystallized (Sobolev and Chaussidon 1996). PEC changes the composition of the trapped melt in the inclusion, as compatible major and trace elements are partitioned from the melt into the crystal shell, increasing the concentration of incompatible elements in the remaining trapped melt. The correction procedure for olivine is described in Chapter 3. We do not correct for pyroxene or plagioclase because it is not as straightforward as for olivine, and no simple methods exist. We focus particularly on incompatible elements, which are not very much affected by PEC.

5.2.4 Units studied in this paper

Most Santorini magmas fall within consistent bands on geochemical diagrams, but there are two anomalous cases : (1) early (>650-530 ka) Akrotiri lavas and tuffs (and associated mafic enclaves), which are amphibole-bearing and more radiogenic than most Santorini magmas (Mortazavi and Sparks 2004), and (2) a radiogenic, Ba-rich volumetrically minor component associated with the LBA eruption (Druitt 2014). Both of these groups have geochemical characteristics that set them apart from the majority of Santorini magmas, and they are both excluded from this chapter. The magmas discussed in this paper include all those from Peristeria Volcano (530-430 ka) to Kameni Volcano (<3.6 ka), except the LBA Ba-rich component, which is discussed in Chapter 6.

5.2.5 Whole rock database

One of our goals after modelling is to carry over any new insights to whole rock data, for which there is a large number of analyses and significantly better coverage of the history of the volcano; thus, in order to do this, whole rock database was assembled. Details on this whole rock database are given in Appendix 1.

5.3 Results

The range of mineral compositions adjacent to MIs are Fo_{69-89} for olivine, An_{33-93} for plagioclase, Mg# (molar Mg/[Mg+Fe]) 62-81 for cpx and Mg# 62-65 for opx. Crystals range from euhedral to anhedral, and some may have been fractured during the rock crushing process. Many olivine-hosted MIs were not in equilibrium with the host crystal prior to the PEC correction.

Selected major elements versus SiO_2 are plotted for MIs and groundmass glasses in Figure 5.4. Compositions vary from 48 to 75 wt. % SiO_2, ranging from basalt to rhyolite. We do not plot MgO or FeO, because of possible errors for olivine-hosted MIs caused by Fe loss and the PEC correction. TiO_2 increases with SiO_2 to a maximum around 60 wt% SiO_2, before decreasing (Figure 5.4). CaO versus SiO_2 produces a curvilinear trend (Figure 5.4). K_2O increases with SiO_2, demonstrating incompatible behavior (Figure 5.4). We plot CaO/Al_2O_3 versus MgO to seek incoming of plagioclase and clinopyroxene in Figure 5.4, but it is not very clear.

When plotting trace elements, we use Th as an index of differentiation rather than SiO_2 because (1) Th is a highly incompatible element in Santorini magmas (Mann 1983), and (2) it was measured on the same ICP-MS as the other trace elements, whereas SiO_2 and other major elements were measured on the electron microprobe.

Compatible elements versus Th are plotted in Figure 5.5. Compatible elements can be affected by post-entrapment crystallization, which is corrected for in olivine-hosted MIs, but not for MIs hosted in other minerals as discussed earlier. Ni and Co decrease rapidly with Th and level off at low values in evolved melts. Sc decreases more steadily. Sr peaks very early and sharply before steadily decreasing.

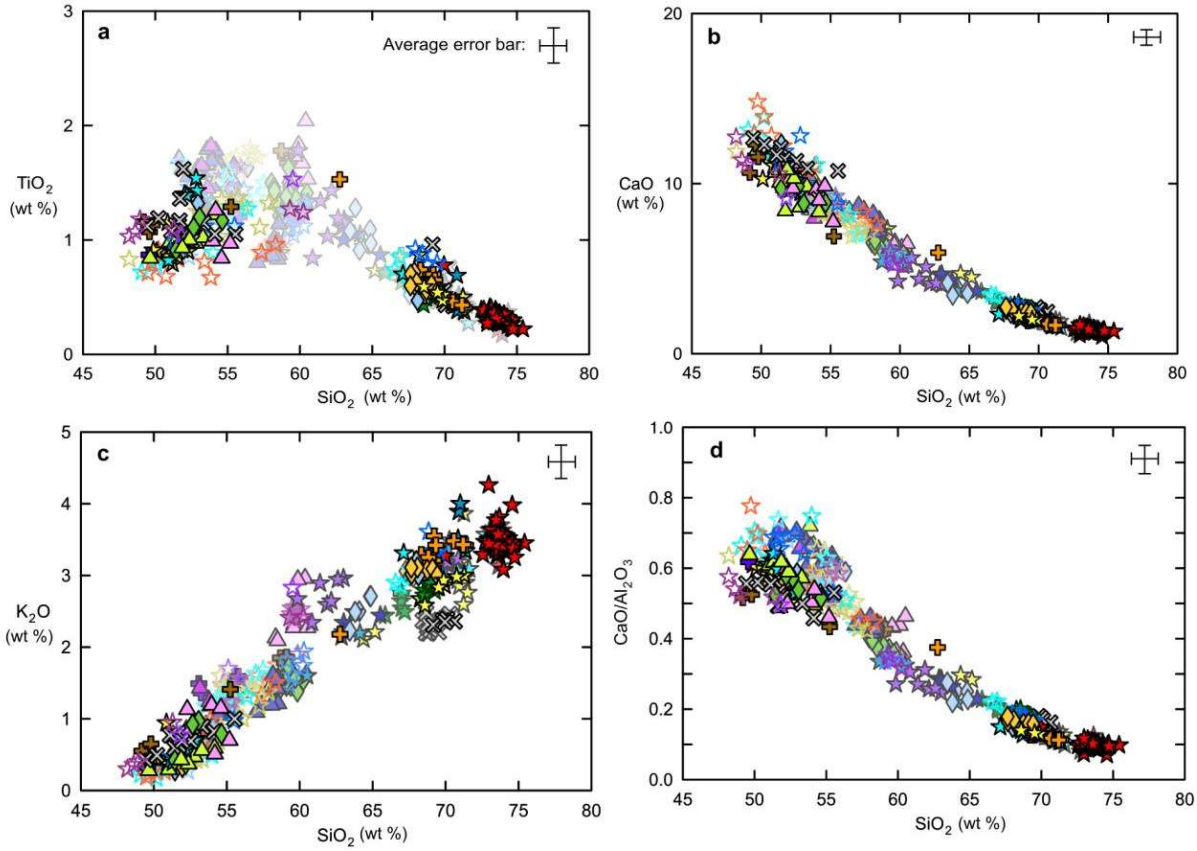

Figure 5.4: Major element oxides vs. SiO_2. Melt inclusion symbols are opaque while groundmass glass are at 70% opacity. Oxides are in wt %. See Figure 5.2b for symbols.

Figure 5.6 shows typical large ion lithophile elements (LILE) elements (Rb, U, Cs, Ce, Pb, Ba) versus Th. Rb and U form very tight trends with Th, demonstrating their strongly coupled geochemical behavior. The trends pass through the origin. Cs also forms a relatively tight trend, but there is more scatter. The other LILE shown here (Pb and Ba) all show more variation, and do not extrapolate back to the origin; instead, they intersect the y-axis due to the presence of higher concentrations of these elements in the primary basaltic melts (Chapter 4). Figure 5.7 shows rare earth elements (REE; light REE or LREE: La, Nd, Pr, Sm; middle REE or MREE to heavy REE or HREE: Dy, Yb) versus Th. The REEs form bands that widen with increasing atomic number. The REEs also intersect the *y*-axis. Figure 5.8 shows high field strength elements (HSFE; Nb, Zr, Hf, Y) versus Th. Zr forms a tight, thin band versus Th. Nb, Hf and Y show more variation. All HFSE have non-negligible concentrations in primary basaltic melts and intersect the y-axis at values greater than zero.

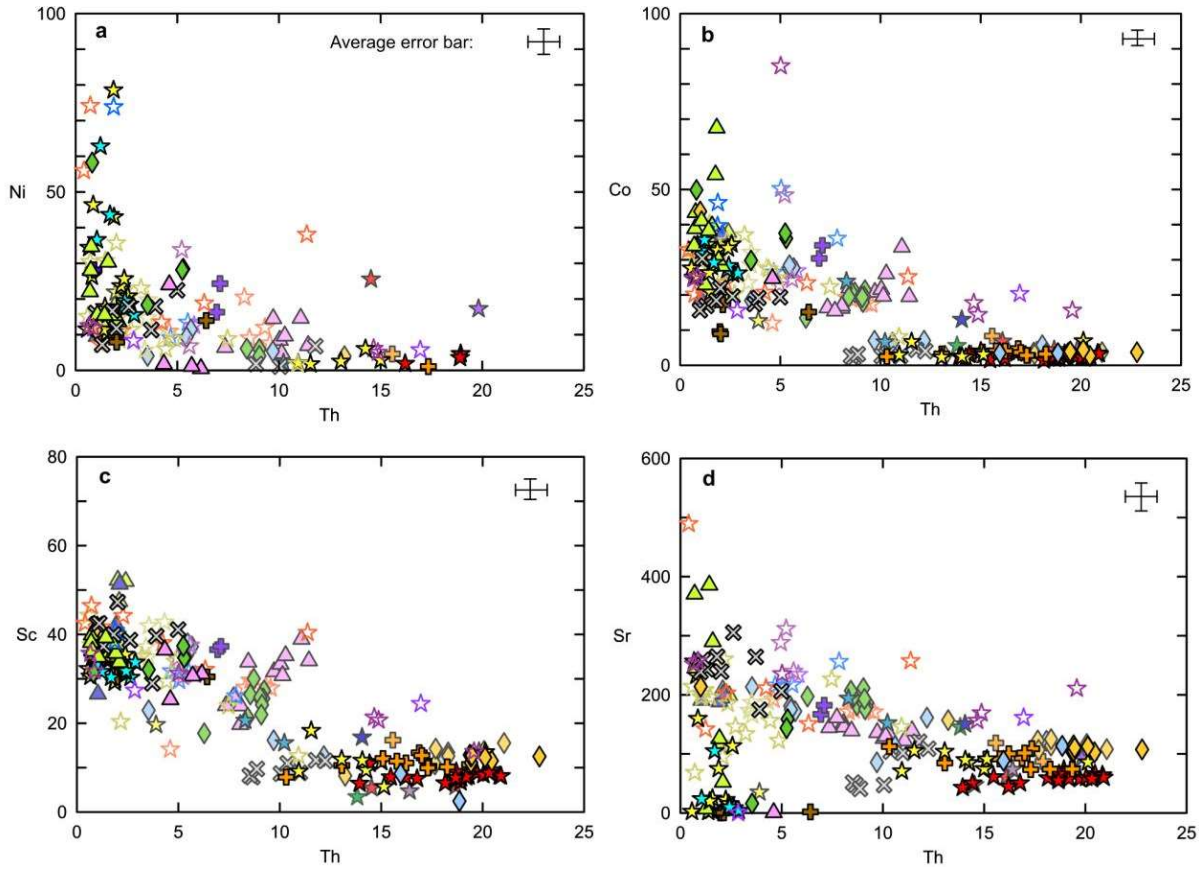

Figure 5.5: Compatible trace elements vs. Th. Melt inclusion symbols are opaque while groundmass glass are at 70% opacity. Trace elements are in ppm. See Figure 5.2b for symbols.

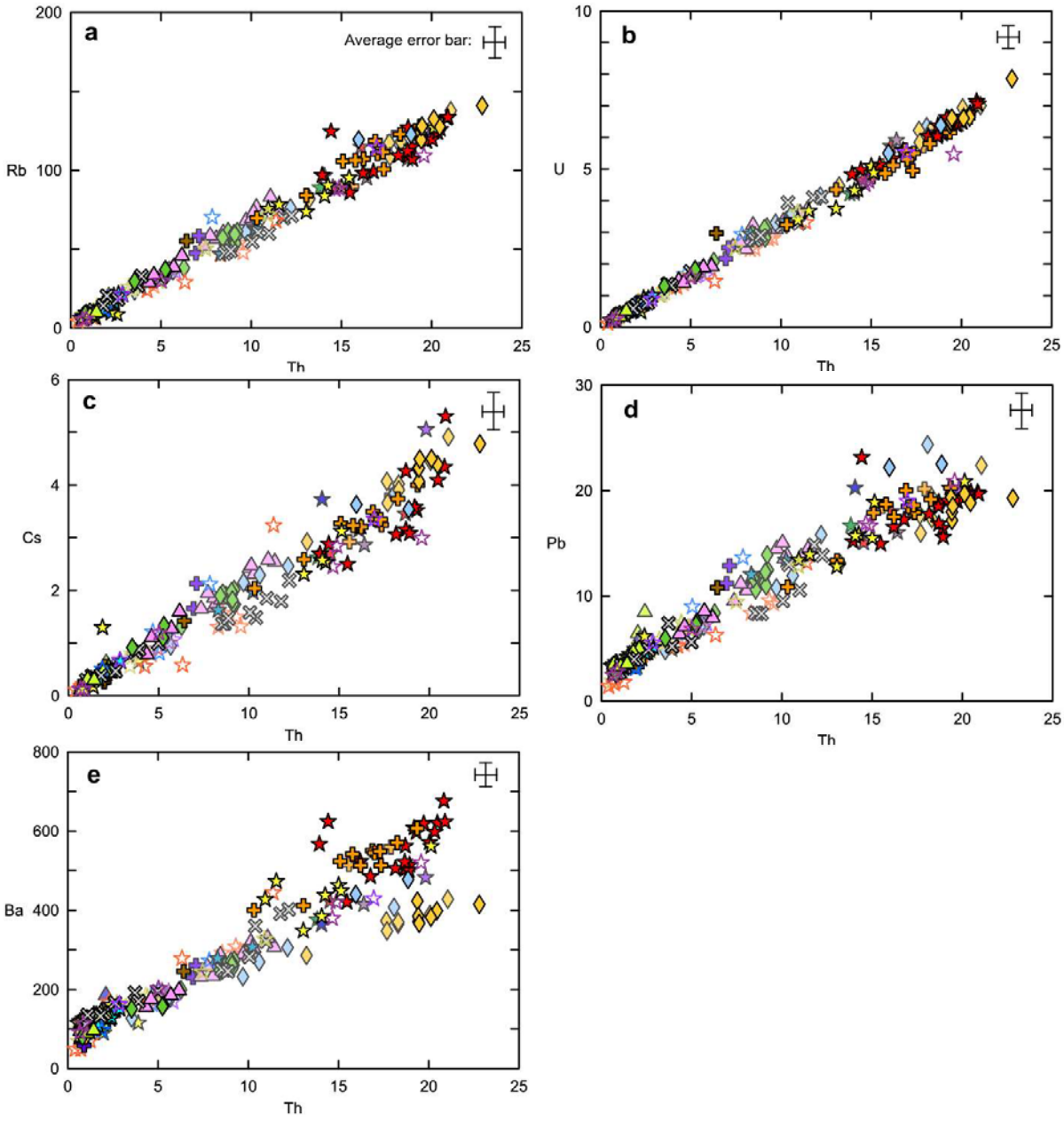

Figure 5.6: Incompatible large ion lithophile elements (LILE) vs Th. MI data are opaque and groundmass data are at 70% opacity. Trace elements are in ppm. See Figure 5.2b for symbols.

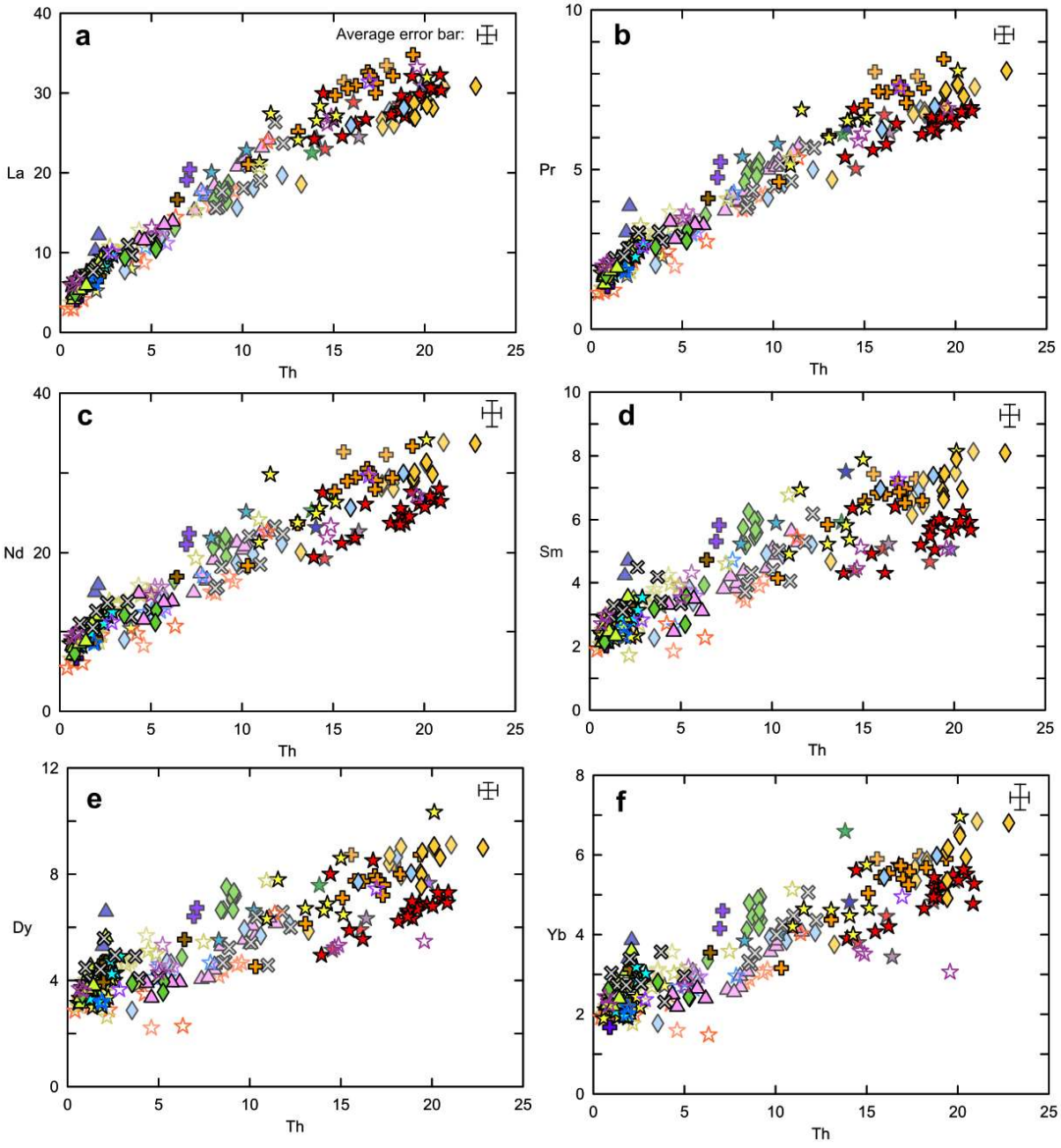

Figure 5.7: Incompatible rare earth elements (REE) vs Th. MI data are opaque and groundmass data are at 70% opacity. Trace elements are in ppm. See Figure 5.2b for symbols.

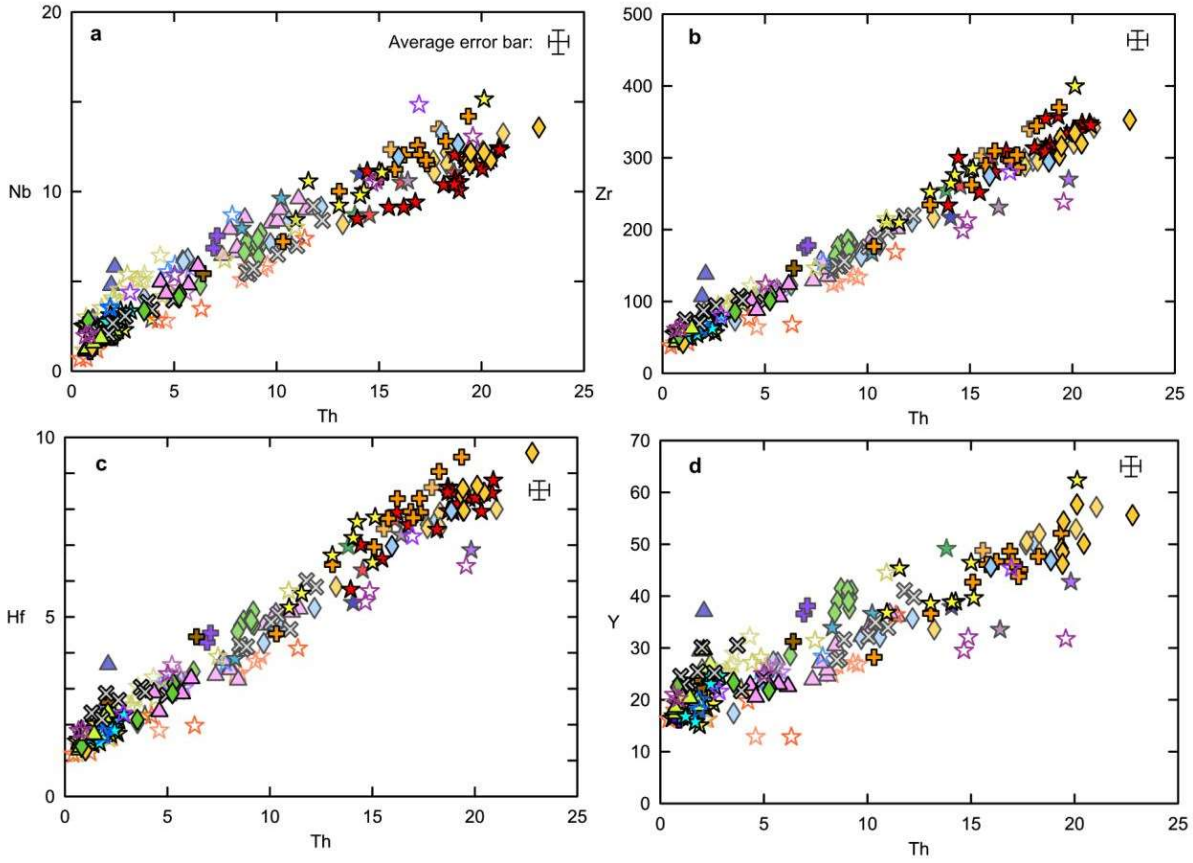

Figure 5.8: Incompatible high field strength elements (HFSE) vs Th. MI data are opaque, groundmass data at 40% opacity. Trace elements are in ppm. See Figure 5.2b for symbols.

A pronounced compositional gap is present in the MI data and also (but less so) in groundmass data. The compositional gap is present in MI data for both major elements (~56 to 66 wt% SiO_2) (Figure 5.4) and trace elements (~ 7-12 ppm Th) (Figures 5.5, 5.6, 5.7, 5.8) with just a few inclusions falling in the gap. Histograms plotted for MIs for SiO_2 contents reveal the depth of the compositional gap (Figure 5.9a). A similar histogram for groundmass glasses also reveals a gap, although less pronounced than that for the MIs (Figure 5.9b). We will infer later that these gaps are probably in part artefacts of sampling and MI preservation. Histograms for Fo content of MI-hosting olivines and An contents of MI-hosting plagioclase are also included (Figure 5.9c,d).

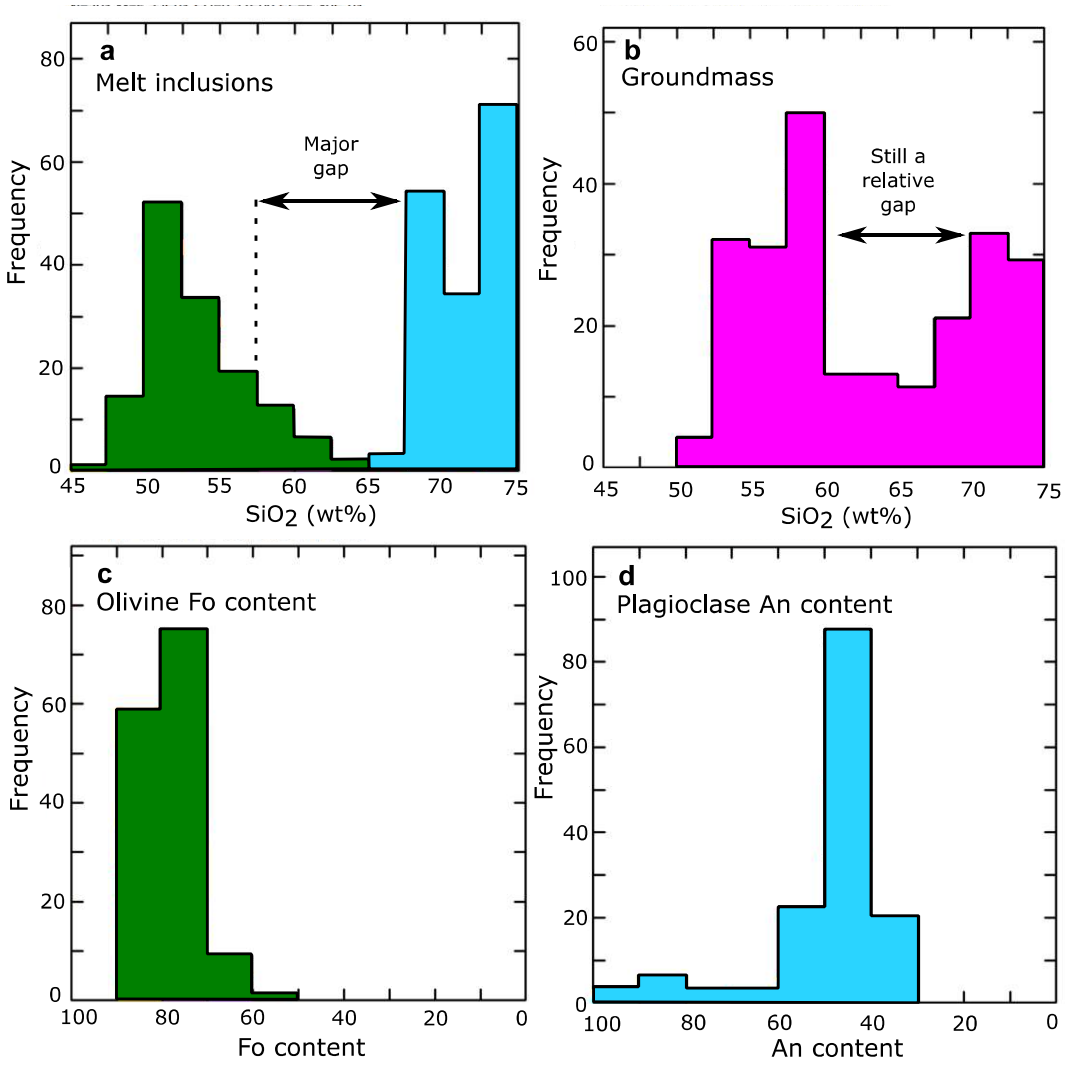

Figure 5.9: Histograms for (a) melt inclusion data for SiO_2 (wt %), (b) groundmass glass data for SiO_2 (wt %), (c) compositions of MI-hosting olivine zones (Fo content) and (d) compositions of MI-hosting plagioclase zones (An content). Green = olivine or olivine-hosted melt inclusions, blue = plagioclase or plagioclase-hosted melt inclusions, pink = groundmass.

5.4 Fractional crystallization (FC) modelling

We now use geochemical modelling to understand the processes behind the differentiation of Santorini magmas. To ease visibility during modelling, the MI and groundmass glass data were divided into different subparallel Nb series (low, high, and an intermediate 'medium' group – see Chapter 4), following an approach similar to that of Bailey et al. (2009) (Figure 5.10). The data were divided into groups of approximately equal size on a Nb-SiO_2 diagram, and then slight modifications were made. For example, in some cases where data from individual eruptions straddled the

low-medium or medium-high dividing lines, the individual eruptions were kept in the same grouping; therefore, there is some overlap among the groups.

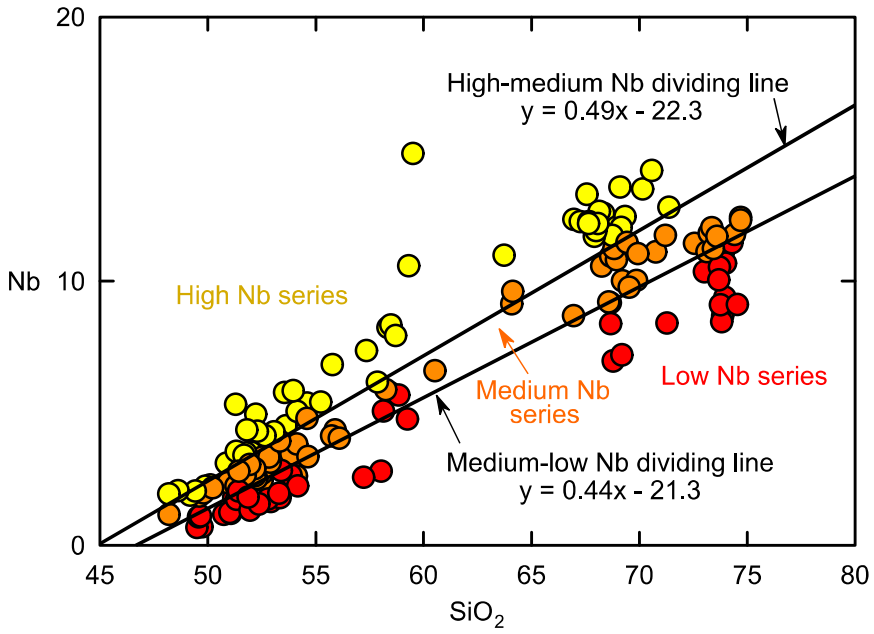

Figure 5.10: Nb groups divided on the basis of Nb vs SiO_2. Equations are given for the division lines. Some points lie out of their respective Nb fields, as some Nb types were changed slightly to produce best possible fits on diagrams to be shown later.

We first attempt to model the data by simple fractional crystallization (FC). Fractional crystallization has already been shown to play an important role in magma differentiation at Santorini (e.g. Nicholls 1971; Mann 1983; Druitt et al. 1999). Some of the clearest evidence for FC can be gathered from major element diagrams, such as with FeO^T (FeO and Fe_2O_3 recalculated as total FeO) and MgO (compatible in ferromagnesian phases and Fe-Ti oxides; not shown), CaO and Al_2O_3 (compatible in plagioclase and pyroxenes), TiO_2 (Figure 5.4; peaks due to crystallization of Fe-Ti oxides) and P_2O_5 (peaks due to apatite crystallization; not shown) with respect to SiO_2. K_2O (Figure 5.4) increases linearly, owing to it highly incompatible nature in <530 ka Santorini magmas where there are no observed phases (e.g., sanidine, biotite) that incorporate it in significant amounts. Compatible trace elements in ferromagnesian phases (Ni, Co, Sc etc.) and plagioclase (Sr) also show that FC is a key process. Compatible-incompatible element diagrams (e.g., Ni-Th, Co-Th, Sc-Th; Figure 5.5) produce curved, hyperbolic trends rather than straight lines, arguing for FC and against significant mixing. Lastly, observed modal mineralogy in natural products

changes with the degree of evolution of the magmas in a way (described earlier) that is consistent with FC (Mann 1983). Fragments of gabbro and diorite discharged during some eruptions may be cumulates resulting from FC (Druitt et al. 1999; Whitley et al. 2018).

Before we can start modelling, it is necessary to discuss the choice of parents, crystallizing assemblages, and bulk distribution coefficients (D) used in the modelling.

Choice of parental melts

We choose a low Nb type primitive melt (from M12 scoria; S16-14-9) and a high Nb type primitive melt (from M10 YB6; S12-37 1-3) from Chapter 4 as parents, whose trace element spectra are shown in Figure 5.11. We prefer to use real melt compositions as opposed to invented or back-calculated parent compositions, since we know that these are real melts in the system, that they are among the most primitive observed, and that each type has erupted multiple times over the history of the volcano (Chapter 4).

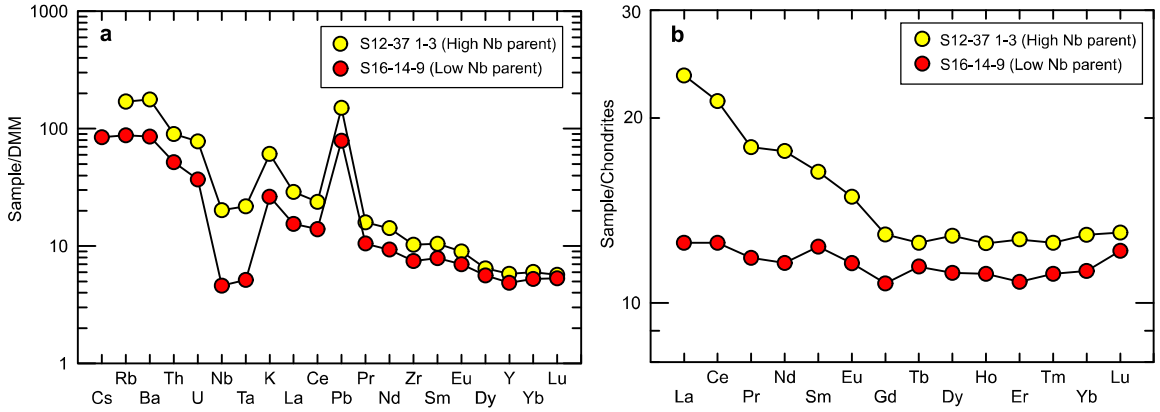

Figure 5.11: Trace element spectra of Nb type endmember parental melts used for modelling. (a) Extended trace element diagram with samples normalized to depleted MORB mantle (DMM). Order is slightly modified from Sun and McDonough (1989), normalization values from Workman and Hart (2005) with some values from Salters and Stracke (2004). (b) REE spectra with samples normalized to chondrites. Order (slightly modified) and normalization values from Sun and McDonough (1989).

Due to the large initial range of certain elements (e.g. Nb, Ba, etc.), and sensitivity of FC models to the starting composition, different parents are needed to explain the data. Models using only one 'average' parent consistently fail to model the spread of the data (models not shown); the two endmember parent compositions are needed. We stress

that we have no constraints as to whether in reality there are two primary magmas at Santorini, or whether there is a range spanning the two endmembers. In our FC models, we model low Nb data series from the low Nb parent and high Nb data series from the high Nb parent. Remaining data are included in the 'medium' Nb series.

Choice of crystallizing assemblage and determination of reasonable Ds

Melt composition influences element partitioning (Rollinson 1993) and, as a result, Ds change during differentiation. However, variable Ds are difficult to model. We will focus mainly on the initial trends coming off the parent magmas, and so use constant Ds corresponding to a basalt to basaltic andesite crystallizing assemblage. Appendix 2 discusses the choice of crystallizing assemblages and the calculation of Ds, and only a summary is provided here.

The chosen assemblage for basalt-to-andesite crystallization is 0.15 ol + 0.3 cpx + 0.5 plag + 0.05 mag. Similar assemblages have been used in previous geochemical modelling at Santorini (e.g. Mann 1983), and they agree with observed modal mineralogies and experimental petrology studies (Andújar et al. 2015). Amphibole is absent as a phenocryst phase is most <530 ka magmas at Santorini, and geochemical proxies for amphibole (Y, MREE) provide no evidence for it until the period leading up to the LBA eruption (see Chapter 6). We created a spreadsheet with mineral-melt k_Ds for the relevant mineral phases from 84 literature sources (Appendix 2). The k_Ds were entered into a table, and organized by mineral and melt composition, keeping reported ranges and standard deviations attached. Only k_Ds for subalkaline melts were included, unless there were few to no k_Ds available for a particular composition (for example, most k_D data for amphibole-basalt are for alkali basalt). An average D (D_{avg}) was calculated using the average k_D for each mineral for the given melt compositional range. Similarly, the minimum (D_{min}) and maximum (D_{max}) Ds were calculated using minimum and maximum k_Ds respectively, for each mineral and melt composition, including error margins on individual k_Ds. Therefore, the minimum and maximum are real limits given by the current k_D literature.

The calculated average Ds represent reasonable values; thus, we use these average Ds in the FC modelling. Table 5.1 gives a summary table of these 'reasonable' Ds, but a full table of Ds is given in Table A2.2 in Appendix 2. We have modified D_{Th}, however, to be taken as 0.001 to approximate perfectly incompatibility (D=0) in the FC modelling. We

also report the ranges of possible Ds, for both anhydrous and hydrous assemblages, calculated from the literature in Table A2.2 to show the limits of the variability of Ds, and we refer to these ranges below when discussing the feasibility of FC models.

Table 5.1: Reasonable (average) Ds used in FC and AFC modelling for mafic to intermediate differentiation with an anhydrous crystallizing assemblage. See text and Appendix 2 for full explanation and refer to Table A2.2 for full detailed table of Ds and possible ranges calculated from the literature.

Rb	Sr	Y	Zr	Nb	K	Ba	La	Nd	Sm	Dy	Yb	Hf	Ta	Pb	Th	U
0.07	1	0.3	0.1	0.1	0.09	0.2	0.1	0.2	0.2	0.3	0.3	0.1	0.1	0.2	0.001	0.1

For the remainder of this chapter, a D will be referred to as "reasonable" if it resides in the range of possible Ds in Table A2.2. Conversely, a D will be referred to as "unreasonable" if it is near the minimum or maximum values of the possible range or exceeds it.

5.4.1 One-stage fractional crystallization

Fractional crystallization models for highly incompatible elements versus Th are shown in Figure 5.12 on log-log plots. All models are taken to 95% crystallization, at 5% increments represented by dots along the model path. The advantage of using log-log plots is that FC gives straight line liquid lines of decent, where the slope of the line can be used to derive the bulk D, assuming that Th behaves totally incompatibly (D=0) and can thus be related to F. We now briefly describe how to derive the bulk D from the slope of a log-log plot based on the approach of Allègre et al. (1977), which was also used in Mann (1983).

The Rayleigh fractionation equation:

$$C_L^i = C_0^i F^{(D^i - 1)} \qquad \text{(Equation 5.1)}$$

describes the evolution of a magma of trace element *i* with differentiation by fractional

Figure 5.12 (next page): Fractional crystallization (FC) models using realistic (average) Ds for a mafic to intermediate crystallizing assemblage. D_{Th} is set to 0.001 to approximate perfect incompatibility. The remainder of Ds used can be found in Table A2.2. All models are taken to 95% crystallization, with each dot along the model representing 5% crystallization increments. "High" refers to the high-Nb series model derived from a high Nb parent and "Low" refers to the low Nb series model derived from a low-Nb parent. Major element oxides in wt %, trace elements are in ppm.

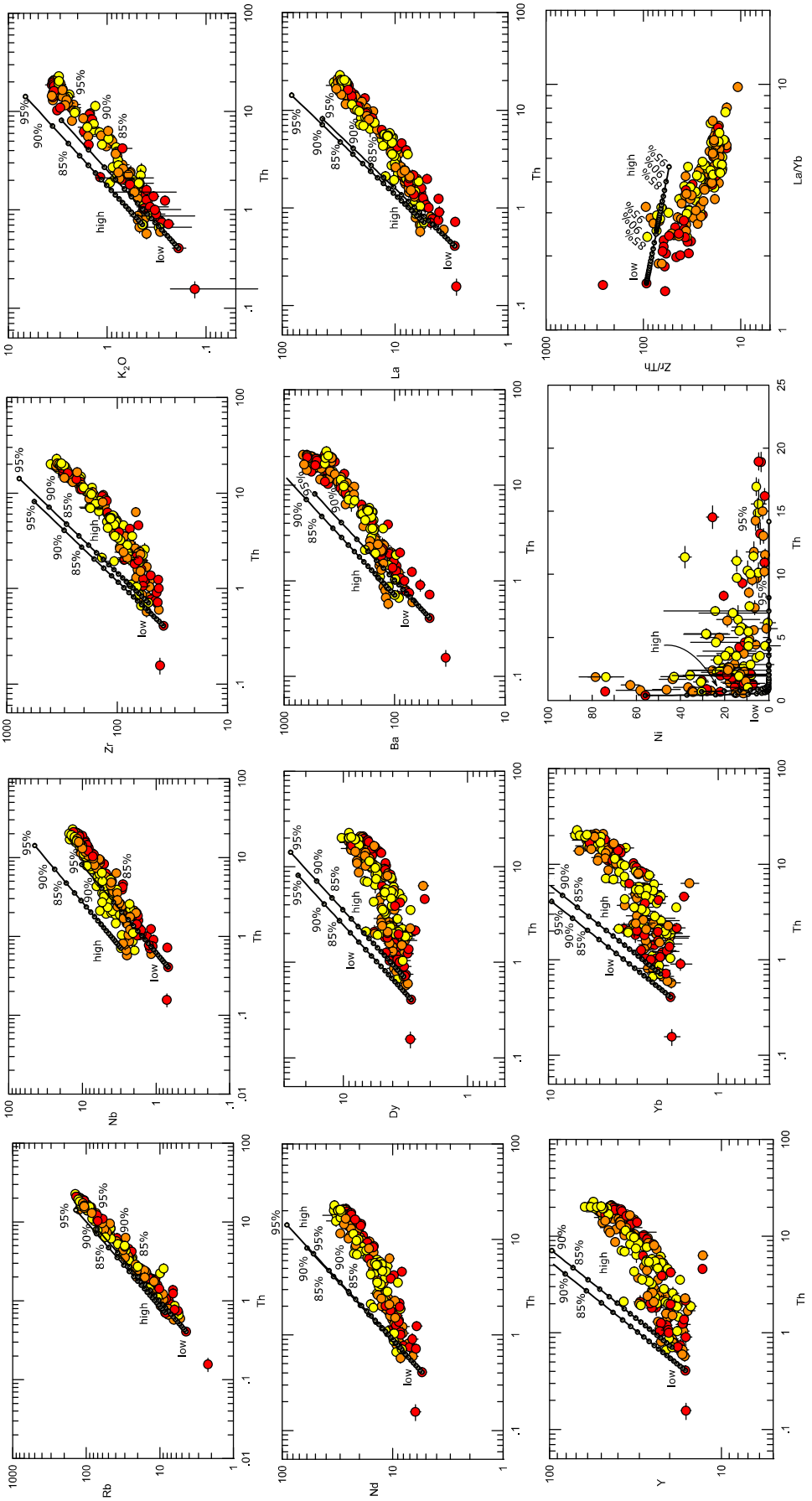
K2O
Zr
La
Zr/Th
Rb
Nb
Ba
Ni
Nd
Dy
Yb
La/Yb
Y
Th
high
low
95%
90%
85%

crystallization, where C_L^i is the concentration of trace element i in the evolving liquid, C_0^i is the concentration of trace element i in the initial liquid, F is the weight fraction of residual liquid and D^i is the bulk partition coefficient of trace element i. If a highly incompatible element (H) is taken into the equation, where $D_H \ll 1$, then:

$$F \approx \frac{C_0^H}{C_L^H} \qquad \text{(Equation 5.2)}$$

If we choose Th to be the highly incompatible element in Equation 5.2, then:

$$F = \frac{C_0^{Th}}{C_L^{Th}} \qquad \text{(Equation 5.3)}$$

On a log-log plot of trace element i against Th, the Rayleigh fractional crystallization becomes:

$$\log\left(C_L^i\right) = \left(D^i - 1\right)\log\left(\frac{C_0^{Th}}{C_L^{Th}}\right) + \log(C_0^i) \qquad \text{(Equation 5.4)}$$

which can be expanded to:

$$log\left(C_L^i\right) = \log(C_0^i) + (D^i - 1)\left(\log\left(C_0^{Th}\right)\right) + (D^i - 1)\left(\log\left(C_L^{Th}\right)\right) \qquad \text{(Equation 5.5)}$$

and can be rearranged in a way that is in the form of the equation of a line on a log-log plot:

$$log\left(C_L^i\right) = \log(C_0^i) + \left(1 - D^i\right)\left(\log\left(C_0^{Th} \cdot \ C_L^{Th}\right)\right) \qquad \text{(Equation 5.6)}$$

where the slope m is equal to (1-D^i) and can be determined graphically by:

$$m = \frac{\Delta \log y}{\Delta \log x} \text{ or } \frac{\log y_2 - \log y_1}{\log x_2 - \log x_1} \qquad \text{(Equation 5.7)}$$

While the FC models can closely model Rb (also U; not shown) using a reasonable D, they cannot model the other incompatible elements. The FC models for most incompatible elements fail because the Ds needed to reproduce the data trends are consistently too low. There is a constant need for higher Ds for elements that are normally rather incompatible during differentiation in the basalt to basaltic andesite compositional range.

In Figure 5.13, the Ds were modified until the models fit the data trends, but this required Ds that are at their maximum experimental values, or are even outside of them. Even the initial trends coming off the basaltic parents require anomalously high

Ds (more the Ds expected of andesitic melts) for most incompatible elements. For example, there are no observed mineral phases in <530 ka Santorini magmas that take in significant Rb or K (sanidine or mica), yet the Ds required to model K need to be higher than expected. K and Rb typically behave similarly, but here they are fractionated from one another with different Ds. Another problem is that the forced FC models do not capture the shapes of the data trends between basalt and andesite. For example, on the plot of Zr versus Th (Figure 5.13) the data trend is concave-upwards, yet the model lines are straight. While the forced FC model can reproduce the data trends approximately, they do not do so in detail.

Lastly, models are taken up to 95% crystallization (equivalent to two stages of 80% crystallization), yet they do not model the whole length of the data trends. While admittedly we have focused on modelling just the basalt to basaltic andesite compositional range, there are some cases where tight trends indicate that Ds will not change with differentiation (e.g. U-Th), and yet this is still the case. Therefore, several steps of fractional crystallization would be needed to explain the most evolved magmas.

Figure 5.13 (next page): Fractional crystallization (FC) models using forced Ds to orient FC models toward the data trends. D_{Th} is set to 0.001 to approximate perfect incompatibility. All models are taken to 95% crystallization, with each dot along the model representing 5% crystallization increments. "High" refers to the high-Nb series model derived from a high-Nb parent and "Low" refers to the low-Nb series model derived from a low-Nb parent. Major element oxides in wt %, trace elements are in ppm.

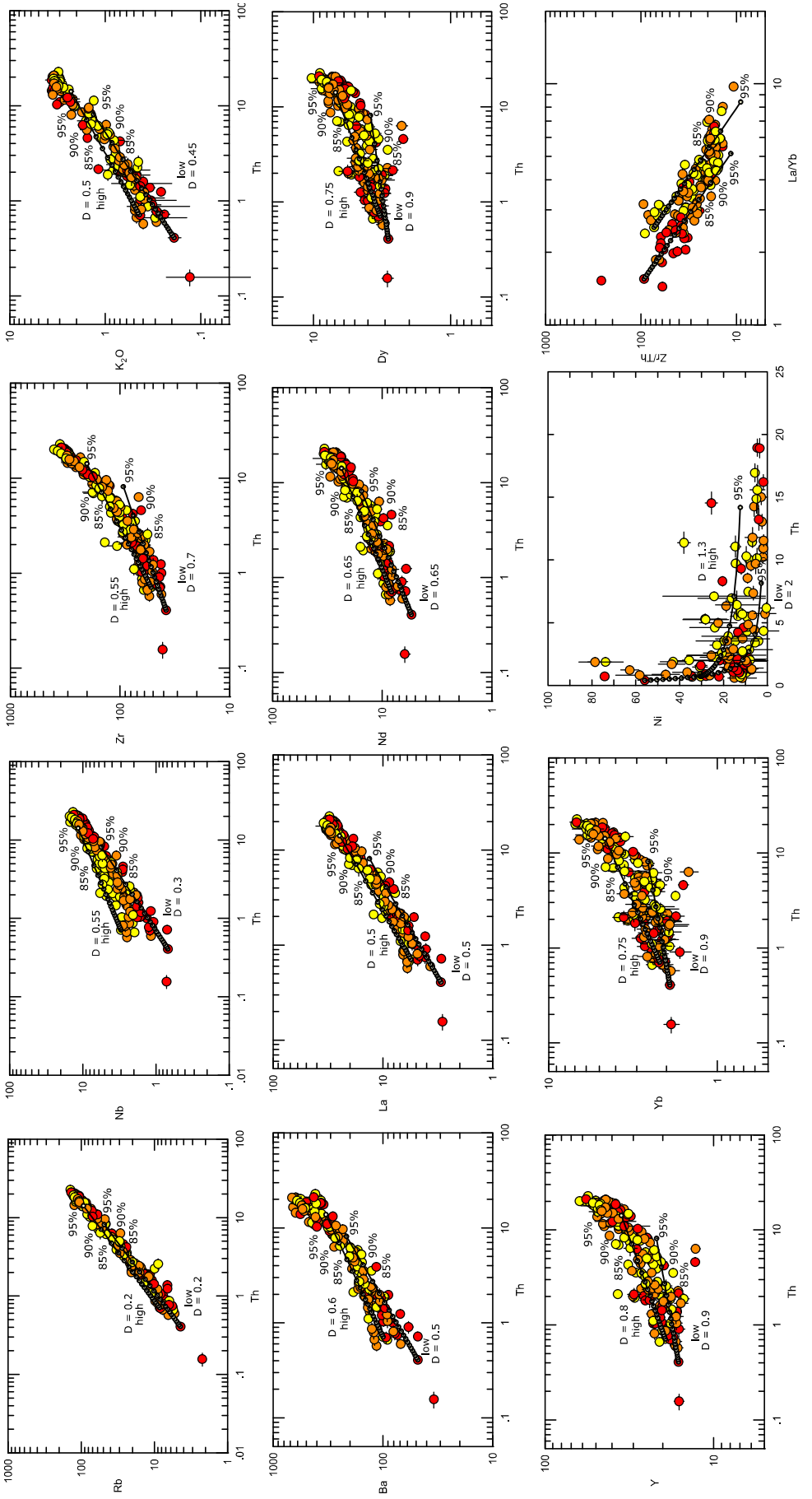
K2O
D = 0.5
high
low
D = 0.45
Zr
D = 0.55
high
low
D = 0.7
Dy
D = 0.75
high
low
D = 0.9
Zr/Th
La/Yb
Nb
D = 0.55
high
low
D = 0.3
Nd
D = 0.65
high
low
D = 0.65
Ni
D = 1.3
high
low
D = 2
Rb
D = 0.2
high
low
D = 0.2
La
D = 0.5
high
low
D = 0.5
Yb
D = 0.75
high
low
D = 0.9
Ba
D = 0.6
high
low
D = 0.5
Y
D = 0.8
high
low
D = 0.9
Th
95%
90%
85%

5.4.2 Two-stage fractional crystallization

Simple one-stage FC from a primitive parent cannot explain the observed data trends; however, previous workers have successfully modelled Santorini magmas by FC in the past using reasonable Ds (e.g. Mann 1983) What explains this discrepancy? Recall that our new MI dataset contains a large number of primitive basaltic compositions (Chapter 4); hence, the basalt to basaltic andesite range is now heavily populated. This allows us to see trend features that were not previously evident using whole rock data.

One thing that is noticeable on the log-log plots of many of the incompatible elements is that there are changes of slopes in the data trends between ~1 and 5 ppm Th (Figures 5.12, 5.13). This change in slope separates the data series into a Stage 1 (basalt to basaltic andesite), and a Stage 2 (basaltic andesite to rhyodacite) (Figure 5.14).

We therefore investigated a two-stage model of FC. Best-fit regression lines were assigned by eye to each stage, and the slopes (equal to 1-D) were determined manually (Figure 5.14). The results show that in each case Stage 1 requires a large D, whereas Stage 2 generally requires a smaller D that is similar to the (reasonable) D determined for each element by Mann (1983). The one-stage FC models of Mann (1983) worked because he and other workers did not have such a large, high-precision dataset of low-Th basaltic samples as us; he was only modelling Stage 2.

So what is Stage 1? Simple FC fails to explain Stage 1 because such high Ds are impossible for many of the elements modelled. We show in Table 5.2 that even by changing the mineral assemblage, we cannot approach the Ds that are needed in Figure 5.14. We note also that more than 90 % crystallization would be required to generate melts across the range of stage 1 (from ~1 to 5 ppm Th).

Figure 5.14 (next page): Multiple stage FC models, with estimated Ds. Derivation of Ds for different stages (determined by the change in slope, indicated as a range by a grey band from ~1-5 ppm Th) was done for each stage by determining the slope by eye and implementing the method of Allègre et al. (1977) to get the D from the slope. Stage 1 covers basalt to basaltic andesite compositions, and Stage 2 covers basaltic andesite to rhyolite compositions.

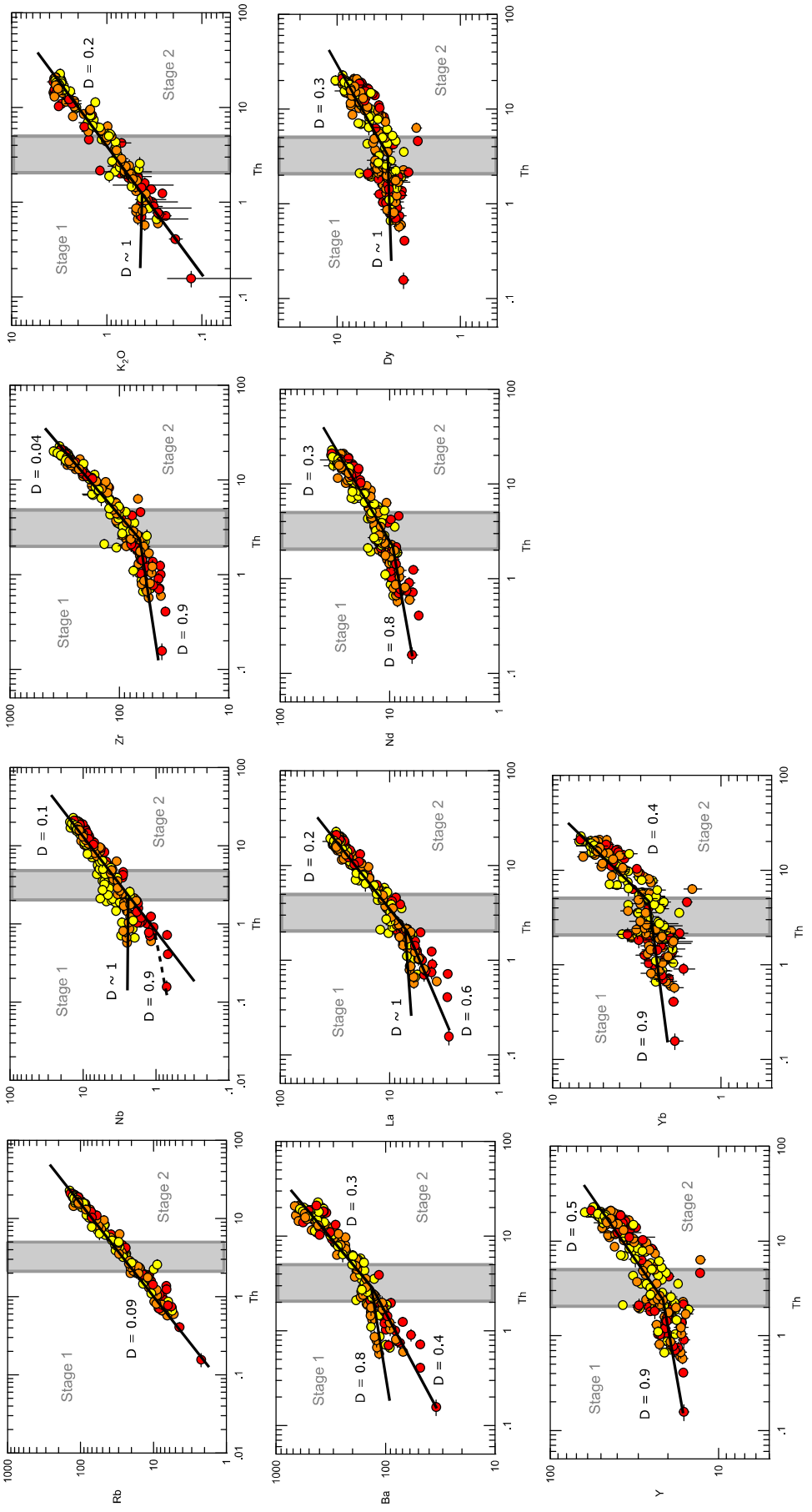
Rb
Stage 1
Stage 2
D = 0.09
Nb
D = 0.1
D ~ 1
D = 0.9
Zr
D = 0.04
D = 0.9
K2O
D = 0.2
D ~ 1
Ba
D = 0.8
D = 0.4
La
D = 0.2
D ~ 1
D = 0.6
Nd
D = 0.3
D = 0.8
Dy
D = 0.3
D ~ 1
Y
D = 0.5
D = 0.9
Yb
D = 0.4
D = 0.9
Th

Table 5.2: Ds calculated for different mineral assemblages to show that such high Ds for the Stage 1 portion of the data trends cannot be achieved with reasonable assemblages.

	Mineral assemblages using mafic-intermediate Ds			
Avg Ds	**0. 95 ol + 0.05 sp**	**0.15 ol + 0.3 cpx + 0. 55 plag**	**0.1 ol + 0.2 cpx + 0.15 amph + 0.5 plag + 0.05 mag**	**0.1 ol + 0.4 cpx + 0.35 amph + 0.1 plag + 0.05 mag**
D_{Rb}	0.007	0.07	0.1	0.2
D_{Nb}	0.03	0.09	0.2	0.3
D_{Zr}	0.06	0.1	0.2	0.3
D_{K2O}	0.006	0.1	0.3	0.4
D_{Ba}	0.0009	0.2	0.4	0.6
D_{La}	0.004	0.1	0.1	0.2
D_{Nd}	0.003	0.1	0.2	0.4
D_{Dy}	0.006	0.2	0.4	0.8
D_{Y}	0.009	0.4	0.5	0.9
D_{Yb}	0.02	0.3	0.4	0.7

It appears from the above that simple FC from a primitive melt composition (either one-stage or two-stage) cannot fully explain the observed data trends, and that an additional process is required.

5.5 Assimilation fractional crystallization (AFC)

We now try to model the data trends by a combination of FC and assimilation (assimilation fractional crystallization, AFC) using the equation of DePaolo (1981):

$$\frac{C_L}{C_0} = F^{-z} + \left(\frac{r}{r-1}\right)\frac{C_\alpha}{zC_0}(1 - F^{-z}) \qquad \text{(Equation 5.8)}$$

where F is the fraction of melt left during cooling of the magma, r is the ratio of mass assimilated over mass crystallized (m_a/m_c), z is expressed by $z = (r + D - 1)/(r - 1)$ and C_L, Co and Ca are the concentrations of an element in the resulting liquid, parent magma and assimilant, respectively. These equations involve a parameter r, with is the ratio of mass assimilated to mass crystallized. The contaminant in AFC could be a melt, or a rock that is then melted by the heat of the magma.

The same parents were used in the AFC modelling as in the FC modelling. The Ds were kept to reasonable values, the same as for the one-stage FC modelling in Figure 5.12 (see Table 5.1). We tried three approaches for AFC modelling: (1) using an empirical approach with a hypothetical contaminant, (2) using a best-fit parameter to look at a range of possible contaminants, and (3) finding a mean solution.

Inspection of the FC models of Figure 5.12 reveals that any contaminant must have ratios of incompatible elements to Th that either lie on or below the data trend in order to 'pull' the FC vectors down onto those data trends. This constraint was used as the starting point for AFC modelling.

Method 1. Empirical modelling

As a first attempt, we fitted the models by eye using a value for r of 0.15, as deduced by Druitt et al. (1999), and by trial and error arrived at an assimilant with a suitable composition that we assumed was a silicic melt with 20 ppm Th (see Table 5.3 for the contaminant composition). The resulting models are shown in Figure 5.15, with the contaminant as a green dot. Generally, these models worked well using reasonable D values and captured the curved data trends in a way that pure FC could not, including stage 1. The models simulate not only the basalt to basaltic andesite range, but the entire compositional range for most incompatible elements. They explain the progressive steepening of the data trends, because basalts with low Th are more sensitive to contamination by a Th-rich melt than andesites and dacites with higher Th. Moreover, the F required to produce the entire compositional range is about 80 %, much less than the pure FC models. The contaminant that worked best has a composition with low Zr/Th, low MREE/Th and low HREE/Th ratios compared to erupted Santorini melts.

Figure 5.15 (next page): Empirical AFC models using an invented contaminant composition. "High" refers to the high-Nb series model derived from a high-Nb parent and "Low" refers to the low-Nb series model derived from a low-Nb parent. The grey band refers to the range of Th (~1-5 ppm) over which element trends have a change in slope.

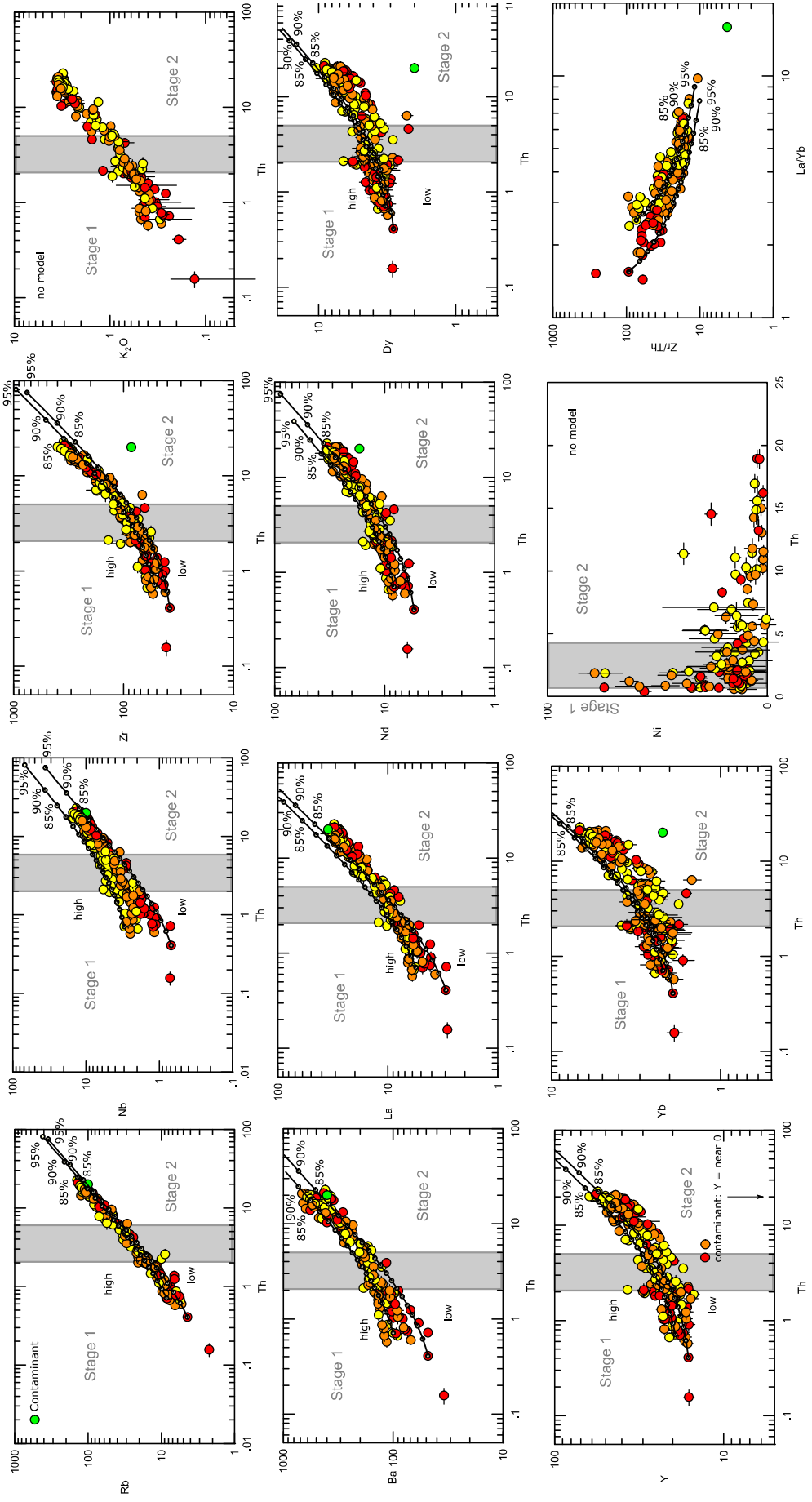
Contaminant
Stage 1
Stage 2
high
low
no model
contaminant: Y = near 0
Rb
Nb
Zr
K2O
Ba
La
Nd
Dy
Ni
Yb
Y
Zr/Th
La/Yb
Th
95%
90%
85%

Table 5.3: Element values and ratios of contaminant use in empirical modelling.

Elements (ppm)	Ba	Rb	Zr	Nb	Y	La	Nd	Sm	Dy	Yb	Ta	Pb	Th	U
Contaminant	400	100	80	10	0.05	35	18	3.1	2.7	2.2	1.0	18	23	7.0
Ratios	**Ba/Th**	**Rb/Th**	**Zr/Th**	**Nb/Th**	**U/Th**	**Nd/Th**	**Y/Th**	**Yb/Th**	**La/Th**	**La/Yb**				
Contaminant	17	4.3	3.5	0.4	0.3	0.8	0.002	0.1	1.5	16				

Since the solutions shown in Figure 5.15 are far from unique, we developed a more rigorous approach to the modelling in order to investigate the possible range of solutions.

Method 2. Examining the range of solutions in a table using a best-fit parameter

A least-squares method for quantifying the model fit was programmed for different input parameters into the AFC equation (see Appendix 2 for details, equations and assumptions involved in this method). We vary three contaminant parameters: the element/Th ratio, r and Th. Th contents for the contaminant were limited to 10-50 ppm, as justified in Appendix 2. The output of the least-squares method gives a fit parameter that represents the sum of squared differences (SSD) between the model and actual data at each real data point. We built a spreadsheet in which, when different ranges of these input parameters were defined, a color-coded table (see Table A2.3 for an example) would show where the best relative fits occurred within the desired ranges of input parameters. This allowed us to find sets of parameters that would lead to good solutions (i.e. small SSDs). The possible range of solutions was then investigated using the spreadsheet as a tool with the aim of "mapping" all of the best possible solutions for each contaminant element/Th ratio (see Appendix 2 for more details). By exploring different contaminant element pair ratios at different contaminant Th and r values, we learnt the following about modelling parameters.

1. AFC models fail when r = 0 (or very small values) and Th = 0 (or very small values).
2. For a given contaminant element/Th ratio, the r-Th pairs giving best solutions are tightly correlated, showing a hyperbolic pattern in the best-fit spreadsheet. (Shown in Table A2.3).

3. For many elements, the majority of the best-fit solutions appeared at high contaminant element/Th ratios, close to (or below) those of the data trends themselves.
4. A wide range of contaminant element/Th ratio, r and contaminant Th values give good solutions. It is therefore impossible to narrow down the possibilities of what the best-fit contaminant can be.

The majority of solutions on the spreadsheet focused around higher contaminant element/Th ratios (e.g. most green squares, i.e. best fits, are located at higher ratios in Table A2.3) lying on or near the data trend itself. These approximate an almost pure mixing scenario; however pure mixing is clearly ruled out by the curved data trends on compatible-incompatible plots (e.g., Ni-Th; Figure 5.15), as already mentioned.

While this approach improves our understanding of what the range of possible solutions are, it does not help us to narrow down a particular best solution. On the contrary, it shows that without further constraints, there is a very wide range of possible contaminants.

Method 3. AFC modelling with a mean solution as contaminant composition

As a last approach, we determine the mean of possible solutions, i.e., a mean contaminant element/Th ratio, contaminant Th content and r for each element. We select key element ratios U/Th, Rb/Th, Zr/Th, Nd/Th, Ba/Th and Nd/Th. We then plotted solutions of a range of ratios, Th and r in the spreadsheet comparing relative fits. Then we identified the lowest 2% of solutions using conditional formatting and calculated the mean, minimum and maximum element/Th ratios, Th and r from these lowest 2% of solutions. These were then used to estimate a mean contaminant chemical composition and r values (Table 5.4). This is not a unique solution or real composition but represents **an average of all possible solutions**.

Table 5.4: Results for (a) contaminant element/Th ratios, (b) contaminant Th, (c) r values and (d) element concentrations from Method 3, i.e. the mean solution approach.

(a) Contaminant element/Th ratios:

	Low Nb			High Nb		
	Avg	Min	Max	Avg	Min	Max
U/Th	0.315	0.312	0.318	0.3264	0.316	0.328
Rb/Th	5.4	4.2	5.6	6.1	4.3	6.3
Nb/Th	0.56	0.4	0.65	0.48	0.2	0.55
Zr/Th	5.4	0	9	10.5	0	14
Ba/Th	26	16	32	22.6	22.2	23
Nd/Th	0.57	0	1.25	1.4	0	1.6

(b) Contaminant Th:

	Low Nb			High Nb		
	Avg	Min	Max	Avg	Min	Max
From U/Th	28	10	50	26	10	50
From Rb/Th	26	10	50	29	10	50
From Nb/Th	22	10	50	32		
From Zr/Th	25	10	50	32	10	50
From Ba/Th	19	10	40	45	36	50
From Nd/Th	20	10	38	33	10	50
	Avg (+/-)	**24 (+26/-14)**		**Avg (+/-)**	**33 (+17/-23)**	

(c) r:

	Low Nb			High Nb		
	Avg	Min	Max	Avg	Min	Max
From U/Th	0.25	0.1	0.9	0.24	0.1	0.5
From Rb/Th	0.30	0.1	0.6	0.35	0.1	0.7
From Nb/Th	0.17	0.1	0.7	0.43	0.1	0.7
From Zr/Th	0.20	0.1	0.4	0.55	0.1	0.9
From Ba/Th	0.14	0.1	0.4	0.85	0.7	0.9
From Nd/Th	0.16	0.1	0.4	0.43	0.1	0.9
	Avg (+/-)	**0.19 (+0.71/-0.09)**		**Avg (+/-)**	**0.52 (+0.38/-0.42)**	

(d) Contaminant element concentrations

Low Nb		High Nb	
U	8 (+8/-5)	**U**	11 (+5/-8)
Rb	135 (+145/-93)	**Rb**	213 (+102/-170)
Nb	14 (+18/-10)	**Nb**	17 (+10/-15)
Zr	135 (+315/-135)	**Zr**	369 (+331/-369)
Ba	653 (+947/-493)	**Ba**	792 (+358/-570)
Nd	14 (+48/-14)	**Nd**	40 (+40/-40)
Th	24 (+26/-14)	**Th**	33 (+17/-23)

5.6 Discussion of modelling

The above modelling shows that neither one-stage, nor two-stage, pure FC can explain the low and high Nb differentiation series observed at Santorini, and that an AFC process is required. While AFC has been proposed previously at Santorini (Barton et al. 1983; Briqueu et al. 1986; Druitt et al. 1999; Zellmer et al. 2000; Bailey et al. 2009), our new database of MI compositions allows us to extend modelling to more primitive compositions than before, and hence to generate more convincing data fits.

5.6.1 Nature of the contaminant(s)

While our AFC models have a wide variety of possible solutions, the contaminant needs to have the same, or lower, incompatible trace element contents as the data series themselves. The mean solution composition given in Table 5.4 is that of an intermediate to silicic melt (10-50 ppm Th), the composition of which is the same (within the bounds of the very large uncertainties) for the low and high Nb series. Since the range of Th was imposed during modelling, we can only say that this is one possible solution for the contaminant composition. Estimated r values are 0.2 for the low Nb series and 0.5 for the high Nb series, although the uncertainty is probably quite high and it is possible the uncertainties overlap; therefore, for the moment, we cannot say if the different Nb series actually require different r values.

There are many potential contaminants at Santorini, including lower crustal amphibolites or granulites and upper crustal granitoids, metapelites, limestones, metavolcanics or hydrothermal systems (Barton et al. 1983; Briqueu et al. 1986; Wyers 1987; Druitt et al. 1999; Konstantinou 2010). Identifying a single contaminant is neither possible nor geologically realistic. However, Santorini magmas are neither silica-oversaturated, nor are they peraluminous, both of which can be markers of contamination by metapelites (Hawkesworth and Vollmer 1979; Blum et al. 1987). Neither are typical indications of limestone assimilation (diopsidic cpx, nepheline and/or high $\delta^{18}O$) observed (Daly 1933; Taylor Jr 1980; Druitt et al. 1999; Iacono Marziano et al. 2008). Druitt et al. (1999) ruled out Naxos basement, Miocene granitoids from neighboring islands and both average upper and lower crust from Barton et al. (1983), primarily on the basis of Sr, and argued that a contaminant with lower Sr than these were needed. Briqueu et al. (1986) carried out successful AFC modelling based on a Santorini metavolcanic rock, though this was followed up by Druitt et al. (1999) who argued that trace element and isotope AFC models could be carried out successfully, but there was a problem with SiO_2.

The AFC modelling presented in this paper is consistent with a mean contaminant with low incompatible element contents in order to pull the pure FC models down towards the data series (Figure 5.15). We stress that this mean is almost certainly some sort of very crude average of a range of different contaminants, both in the upper and lower crust. However, we wish to present an interesting possibility. In Table 5.5 we compare

our contaminants (empirical, mean for low Nb series, and mean for high Nb series) with a number of highly evolved silicic melts found in different contexts: rhyolite of the 650-550 ka Akrotiri series of Santorini, high-silica rhyolite from Milos Volcano, high silica rhyolite from the Bishop Tuff (California), and average Sierra Nevada aplite. In all cases these highly evolved melts present valid, geologically reasonable candidates for our calculated mean contaminants at Santorini. They all have low incompatible element contents due to their highly evolved nature. This raises the possibility that there exist below Santorini regions of mushy rock containing highly evolved interstitial melts (or dykes of aplite) through which ascending basalts ascend and by which they are contaminated. Those melts may be present in near-solidus plutonic mushes and/or in partially molten septa of basement rock. Interaction of magmas with such highly evolved near-solidus melts is one possible mechanism for explaining the AFC trends at Santorini.

Table 5.5: Contaminants and some highly evolved silicic compositions from our dataset and from the literature. There are many similarities between the given contaminants and different types of highly evolved, low fraction silicic melts such as high silica rhyolites and aplites.

	Ba	Rb	Zr	Y	Nb	La	Sm	Dy	Yb	Ta	Pb	Th	U
Empirical contaminant	400	100	80	low	10	35	3.1	2.7	2.2	1.0	18	23	7
Mean contaminant (low Nb)	653	135	135		14							24	8
Mean contaminant (high Nb)	792	213	369		17							33	11
Akrotiri rhyolite[1]	905-980	105-115	85-95	16	10-11	34-38	2-3	2-3	1-3	0.9-1.0	18-19	22-26	6-8
High-silica rhyolite (Milos)[2]	400-550	90-150	50-60	20-40	-	20-30	2.4	-	2-4	-	-	10-20	2-5
High-silica rhyolite (Bishop Tuff)[3]	0-400	100-200	80-150	10-25	low	15-60	3-4	1-4	1-3	0.8-2	-	10-20	3-7
Aplite (Sierra Nevada)[4]	0-700	100-400	0-100	0-40	0-7	5-45	0.1-5	0.05-3	0.1-4	0.2-0.8	20-40	20-60	5-30

[1]The author's data; [2]Fytikas et al. (1986); [3]Hildreth (1979); [4]Glazner et al. (2008)

Can we place any constraints on the degree of variability of the contaminant based on our trace element data? Figure 5.16 shows the lineages of MIs and glasses from a number of individual eruptions, grouped into (1) small interplinian eruptions and (2) large Plinian eruptions (Figure 5.16). The interplinian lineages form subparallel vectors with different degrees of Nb enrichment related to the Nb content of the basaltic parents (see Chapter 4) and are suggestive of fairly constant contaminant. The Plinian lineages, on the other hand, scatter more widely and depart from the subparallel trends, suggesting a greater degree of variability in the contamination process associated with large eruptions, perhaps due to the presence of a larger volume and greater chemical variability of melt-bearing mushes in the magmatic system immediately prior to, and immediately after, large eruptions. This scattering of MI compositions prior to large eruptions is examined in Chapter 6 in the case of the LBA eruption.

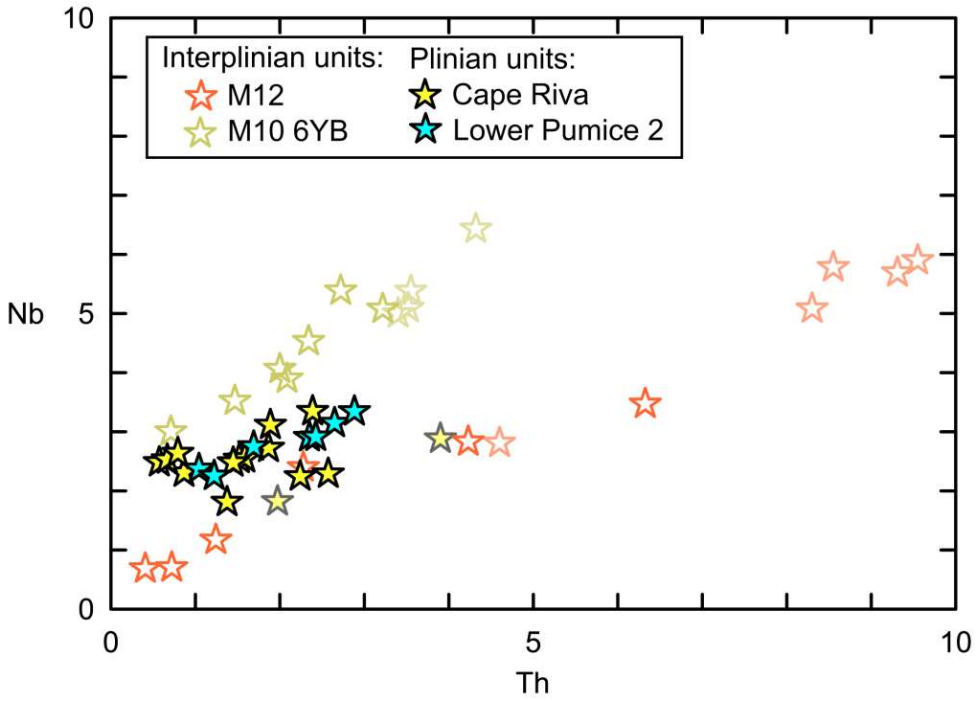

Figure 5.16: Lineages of melt inclusions (100% opaque) and glasses (70% transparent) from a number of individual eruptions of two different types, interplinian and Plinian, to show differences in behavior and scatter. Small interplinian eruptions M10 6YB and M12 and large Plinian eruptions Cape Riva and Lower Pumice 2 are shown as examples of the two different eruption types. Interplinian eruptions form subparallel vectors and tight trends, whereas the Plinian eruptions do not follow the subparallel trends and are more variable, especially for the Cape Riva eruption.

Isotopic composition of the contaminant(s)?

In order to further constrain the nature of the contaminant(s), we have compiled and plotted on $^{87}Sr/^{86}Sr$ versus SiO_2 (Figure 5.17) published Sr isotopic data for Santorini whole rocks, which we have separated into stratigraphic groups (Figure 5.17). If the data are all plotted together, without discriminating between stratigraphic groups, the overall trend shows a positive increase in radiogenic Sr with SiO_2, suggesting contamination (AFC) by radiogenic crust as a general process and indeed this conclusion has been drawn by a number of authors (Druitt et al. 1999; Zellmer et al. 2000; Bailey et al. 2009). However, when split into individual eruption units, different trends emerge. First, there exists a range of $^{87}Sr/^{86}Sr$ values (0.7035-0.7045) at low SiO_2 contents that probably correspond to the different primitive melts (Bailey et al. 2009) (Figure 5.17). Second, some units exhibit clearly inclined, radiogenic AFC trends (Peristeria 3; Upper Scoria 2; possibly Peristeria 1) while others do not (Lower Pumice 2; Skaros) (Figure 5.17).

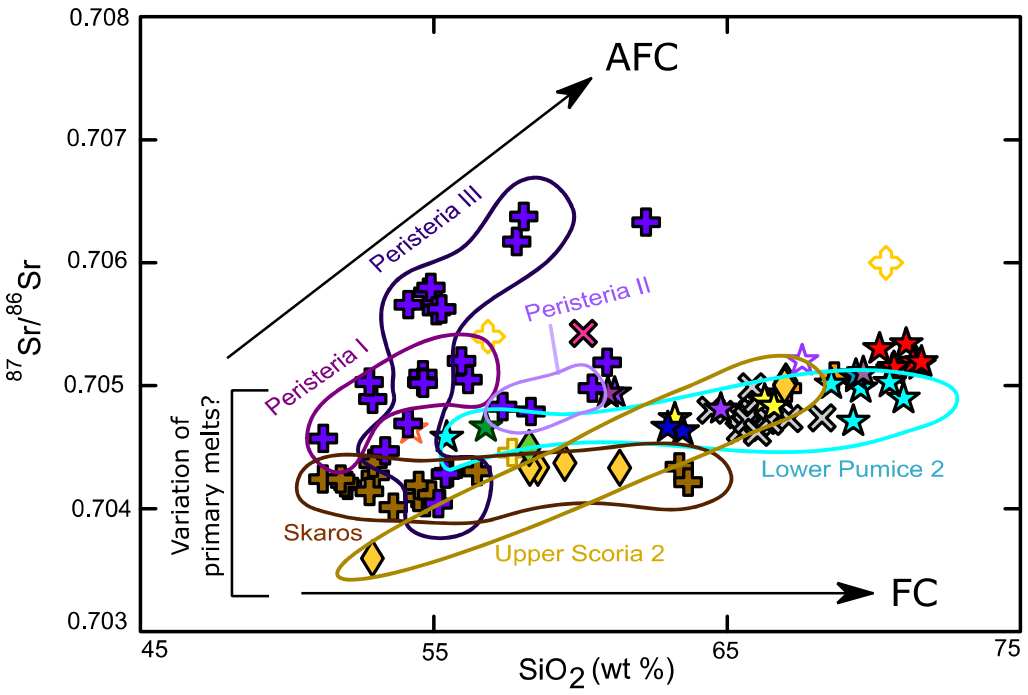

Figure 5.17: $^{87}Sr/^{86}Sr$ vs SiO_2 for all available whole rock data from the literature (from the author's unpublished whole rock database), divided by unit with our symbology. Peristeria data are subdivided into phases I, II and III based on sampling information given in the literature sources. Other units with sufficient data to suggest a general trend are highlighted.

Now since our trace element modelling suggests that AFC is the general rule as Santorini, and that pure FC is not tenable, Figure 5.17 suggests that contaminant(s) vary widely in their Sr isotopic ratios, from ~0.704 in Skaros, >0.705 in Upper Scoria 2, and >0.7065 in Peristeria 3. We infer that the contaminant(s) of the AFC trends are variably radiogenic, and that this is consistent with the existence beneath Santorini of a range of different interstitial melts derived from plutonic mushes and partially molten basement lithologies.

Where and when does assimilation occur?

Hot primitive basaltic magmas would assimilate crustal materials more easily than cooler, more differentiated magmas (DePaolo 1981; Marsh 1989; Spera 2001); therefore, one could argue that assimilation is more likely to take place at lower crustal levels where temperatures are greater. Indeed, it has been proposed that many magmatic systems are underlain by a deep-crustal MASH (Mixing Assimilation Storage Homogenization) zone (Hildreth and Moorbath 1988), also referred to as the "deep crustal hot zone" (Annen et al. 2006), where basalts are contaminated. On the other hand, the clear evidence for radiogenic contaminants suggests that the upper crust is also involved, as concluded by previous authors (Druitt et al. 1999; Zellmer et al. 2000). Bailey et al. (2009) noted that Sr and Pb isotopes tend to increase sharply in Santorini whole rocks in the basaltic range of SiO_2 contents. Our new MI and glass trace element data and AFC modelling agree that AFC begins at the very earliest stages of differentiation, from basalt to basaltic andesite (Stage 1). It is possible that at least part of this contamination takes place in the deep crust, although more multi-isotopic data are required to tell.

While the AFC models appear to model the entire compositional range (Figure 5.15), Stage 2 can also be modelled reasonably well by pure FC (Figure 5.14), as shown previously by Mann (1983). So, another possibility is that while AFC generates Stage 1 (basalt to basaltic andesite), purer FC generates Stage 2 (basaltic andesite to rhyodacite). More work is required to distinguish between (1) continuous AFC throughout the compositional range, and (2) or initial AFC followed by purer FC. One problem is that Stage 1 trace elements are much more sensitive to contamination than Stage 2 trace elements, so that while the difference between AFC and FC trends is very marked in Stage 1, it is less so in Stage 2. This is why more isotopic data are required:

some existing Sr isotope trends increasing with silica suggest that continuous AFC is more likely, but other trends appear flat and are thus not consistent with continuous AFC (Figure 5.17).

Volume constraint concerns alleviated with AFC modelling

An AFC model requires smaller volumes of primary basalt entering the magmatic system compared to a multi-stage FC model, and perhaps makes more sense geologically. Pure fractional crystallization would require multiple stages of storage and FC in a multi-level crustal plumbing system, and the mantle input of primary basalt would need to be very high to explain large silicic eruptions such as the LBA eruption (48-86 km^3 of rhyodacitic magma). AFC models, on the other hand, require as little as 40% using a mean solution-like assimilant and up to 80% crystallization for an invented contaminant similar to a highly evolved silicic melt from a parental basaltic melt to model the entire liquid line of descent, which is more reasonable.

5.7 Origin of the compositional gap

Recent studies have drawn attention to the existence of compositional gaps in MI data from some volcanoes and have taken this as evidence that most andesites are hybrids produced by the mixing of basaltic and silicic endmembers (Reubi and Blundy 2009). Our MI data for Santorini indeed show a compositional gap in the range 58-66 wt% SiO_2, which is not observed in the whole rock data (Figure 5.9a). Indeed, a less well-defined gap also exists in our data for groundmass glasses (Figure 5.9b). On the other hand many features of Santorini magmas (curved trends on compatible-incompatible plots, peaks in TiO_2 versus SiO_2; Figures 5.4, 5.5) are strongly indicative of an FC (in detail AFC), not mixing, origin of most andesites at Santorini (Mann 1983; Druitt et al. 1999).

The paucity of andesitic MIs in our dataset may be in large part an artefact (Figure 5.9a). Most of our MIs are hosted by olivine (which crystallizes only in basalt-basaltic andesite range) and sodic An_{30-60} plagioclase (since MIs in calcic $An_{>60}$ plagioclase are often complexly shaped and rarely analyzable) (Figure 5.9c,d). Hence there is a bias in our data towards more mafic and more silicic MIs. The smaller gap in groundmass melts may be a sampling artefact (Figure 5.9b). However, another possibility is that the gaps are real and have a physical origin. For example, fractional crystallization is

increasingly believed to take place in mush columns, where the evolved melts are squeezed out and segregated by gravitational compaction (e.g. Jackson et al. 2019). Perhaps this process somehow results in a paucity of crystal growth and MI entrapment in the andesitic melt composition range? Certainly we do not consider the plots of Figure 5.9 to be unambiguous evidence for andesite production through mixing, although this does occur as a subordinate process at Santorini (Fabbro et al. 2017).

5.8 Origins of temporal trends at Santorini

We now address the origin of the well-documented temporal decrease of incompatible elements (K, Rb, Zr, Nb, LREE) with respect to silica at Santorini, described earlier (Huijsmans 1985; Huijsmans et al. 1988; Druitt et al. 1999; Francalanci et al. 2005b; Fabbro et al. 2013) (Figure 5.3). What new insights can our new high-precision trace element data provide?

In Figure 5.18 we show how the low, medium and high Nb groupings of our MI and glass data (Figure 5.10) map onto plots of Nb-Th and K_2O-SiO_2. The three groups (Figure 5.18a) map well onto Nb vs Th (Figure 5.18b), which we have shown to be modelled well by AFC from the different parental magmas—the high Nb group requiring a high Nb parent, the low Nb group requiring a low Nb parent. They also map quite well onto K_2O vs SiO_2 (Figure 5.18c), on which a decrease in K_2O over time is clear in the whole-rock dataset (Figure 5.3). Note that in mapping from one plot to another the three groups become somewhat scattered, showing that other secondary processes are also at play.

Figure 5.18 allows us to show that the Nb vs Th and K_2O vs SiO_2 trends have a common origin. Since the different Nb groups can be modelled by AFC from different Nb parents on Nb vs Th, then trends on K2O vs SiO_2 must also be due to AFC from the same parents. So, the well-known temporal decrease in incompatibles (with respect to SiO_2) over time is related to a change in the composition of parental magmas with time.

In order to reinforce this, we have plotted in Figure 5.19 the incompatible element contents of all samples (MI and glasses of this study; previously published whole rock data) in the 58-60 wt% SiO_2 range as a function of stratigraphic height at Santorini

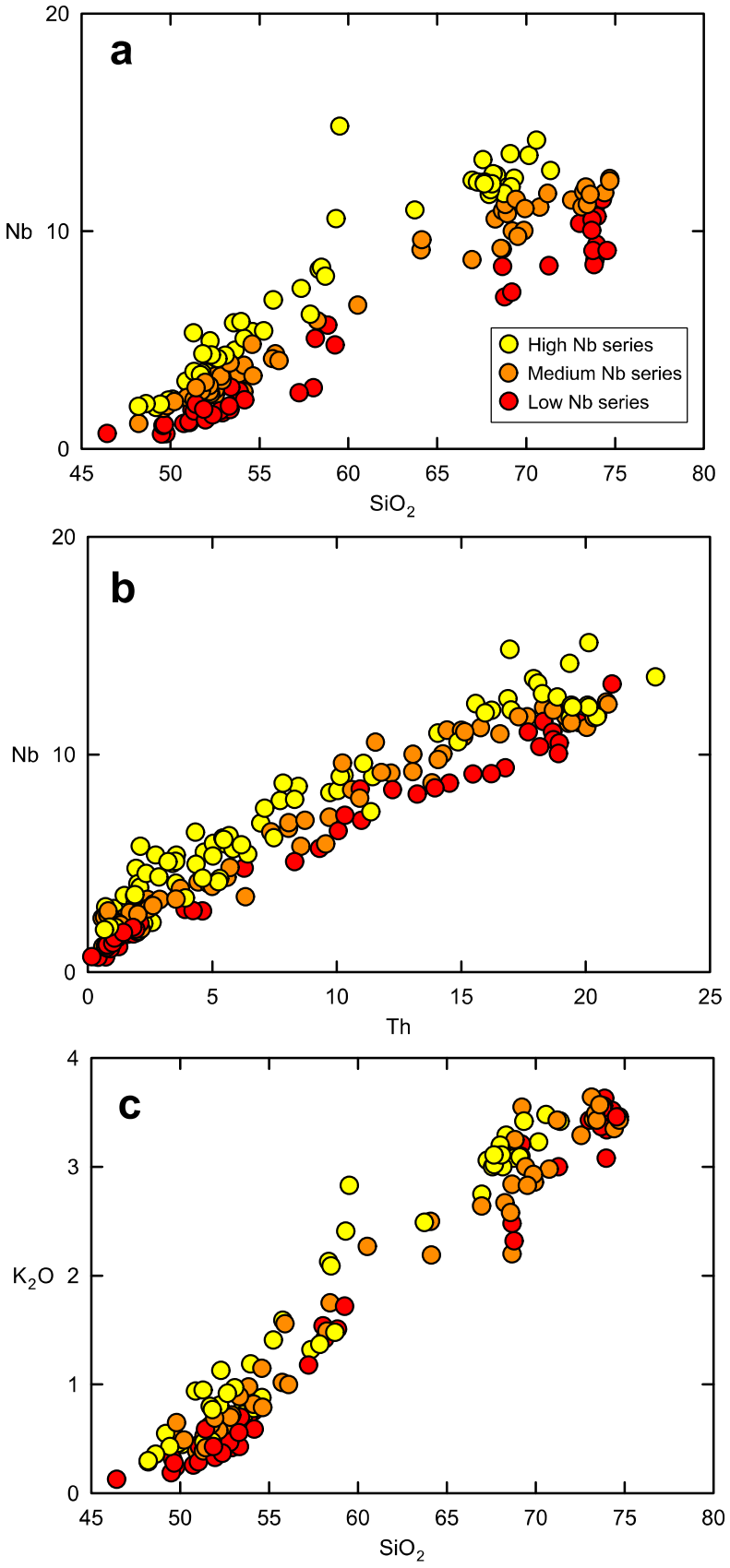

Figure 5.18: Nb groups can be mapped onto Nb vs Th and onto K_2O vs SiO_2.

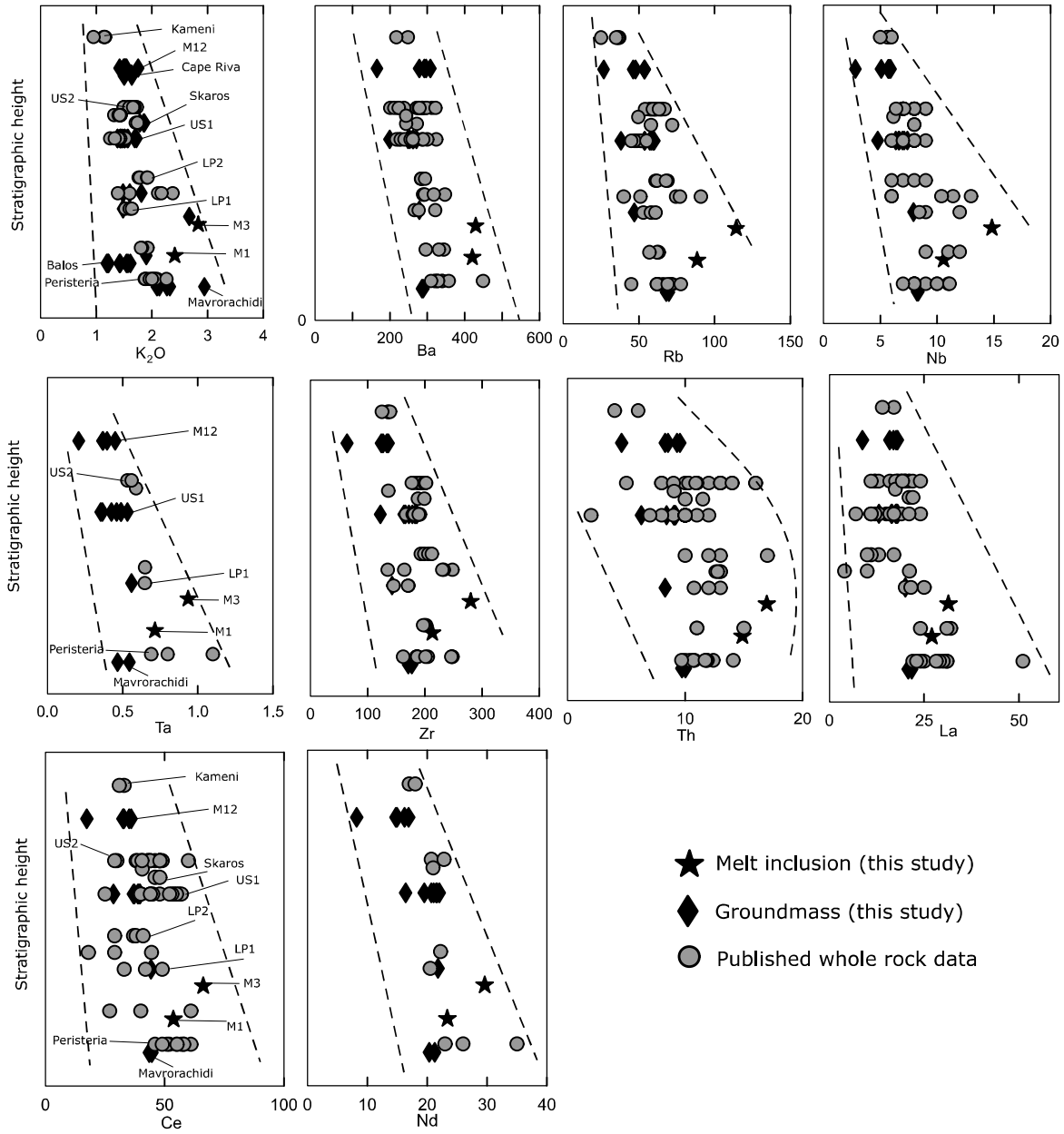

Figure 5.19: Temporal trends for key elements for the 58-60 wt% SiO_2 range. Data include melt inclusions and groundmass (from this study) and whole rock data and data from the author's unpublished database. The whole rock data has been quality-sorted and includes: Post-2000 published data, the dataset published in Druitt et al. (1999), the dataset published in Huijsmans (1985) and some key pre-2000 datasets. Some key units are labelled for reference. We add dashed lines to help guide the reader's eye.

since 530 ka, (excluding the high-Ba LBA magmas of Druitt 2014). The drop in all incompatible elements (e.g., K, Ba, Rb, Nb, Ta, Zr, Th, La, Ce, Nd) with time in MIs, glasses and whole rocks is clear from these plots. It is also possible to repeat this exercise with other silica windows, but the trend is less clear.

While previous authors have speculated that the temporal evolution in composition is due to changing basaltic parent (Huijsmans 1985; Huijsmans et al. 1988; Druitt et al. 1999; Francalanci et al. 2005b; Fabbro et al. 2013) our new data allow us to show this unambiguously. The findings of Chapter 4 also allow us to be more specific about the processes involved. In Chapter 4 we showed that there is not in fact any temporal variation in primary melts below Santorini. Both low Nb and high Nb primary melts have been erupted throughout the history of the volcano (also suggested by Bailey et al. 2009) and have been erupted together in time intervals as short as ~10 ka. Moreover, we presented evidence that inheritance of crystals (and their MIs) is not a predominant factor. Therefore, the decrease in incompatibles over time is *not* due to a change in the primary magmas over time. The observations can be explained, however, if the *relative proportions* of the low Nb and high Nb primary magmas ascending into the crust from the mantle change with time. Specifically, this would require an increasing proportion of the low Nb melt over time. As the different primary melts enter the crust, they mix in different proportions, and the composition of that *average primary melt* changes with time in a way to produce intermediate and silicic differentiates that became increasingly incompatible-depleted. At times, however, the individual primary melts penetrate the crust and are erupted (as during the M10 interplinian period), but the large volumes of magma of the Plinian eruptions 'see' some average parent whose composition changes with time.

We conclude, then, that the two mantle source regions beneath Santorini (Chapter 4) have persisted over at least the last half a million years, but that the mantle domain involving a higher degree of melting (low Nb melt; Chapter 4) has been increasingly tapped at the expense of the other (high Nb melt). One possibility is that this is the result of an increasing importance of decompression melting (over subduction fluid flux melting) with time as rifting and extension across the volcanic field takes place (Francalanci et al. 2005b; Francalanci and Zellmer 2019).

5.9 Implications for magmatic plumbing system

Figure 5.20 summarizes some aspects of the crustal magmatic system beneath Santorini inferred in this and the preceding chapter. Primary basaltic melts are extracted from at least two mantle source domains, probably created by different degrees of partial melting induced possibly by variable amounts of decompression melting and addition of slab-derived sediment. These two domains (and their

respective melts) have both existed for the last half a million years, but with an increasing proportion of melt extraction from the higher partial melt domain, perhaps due to increasing effects of decompression melting resulting from crustal extension.

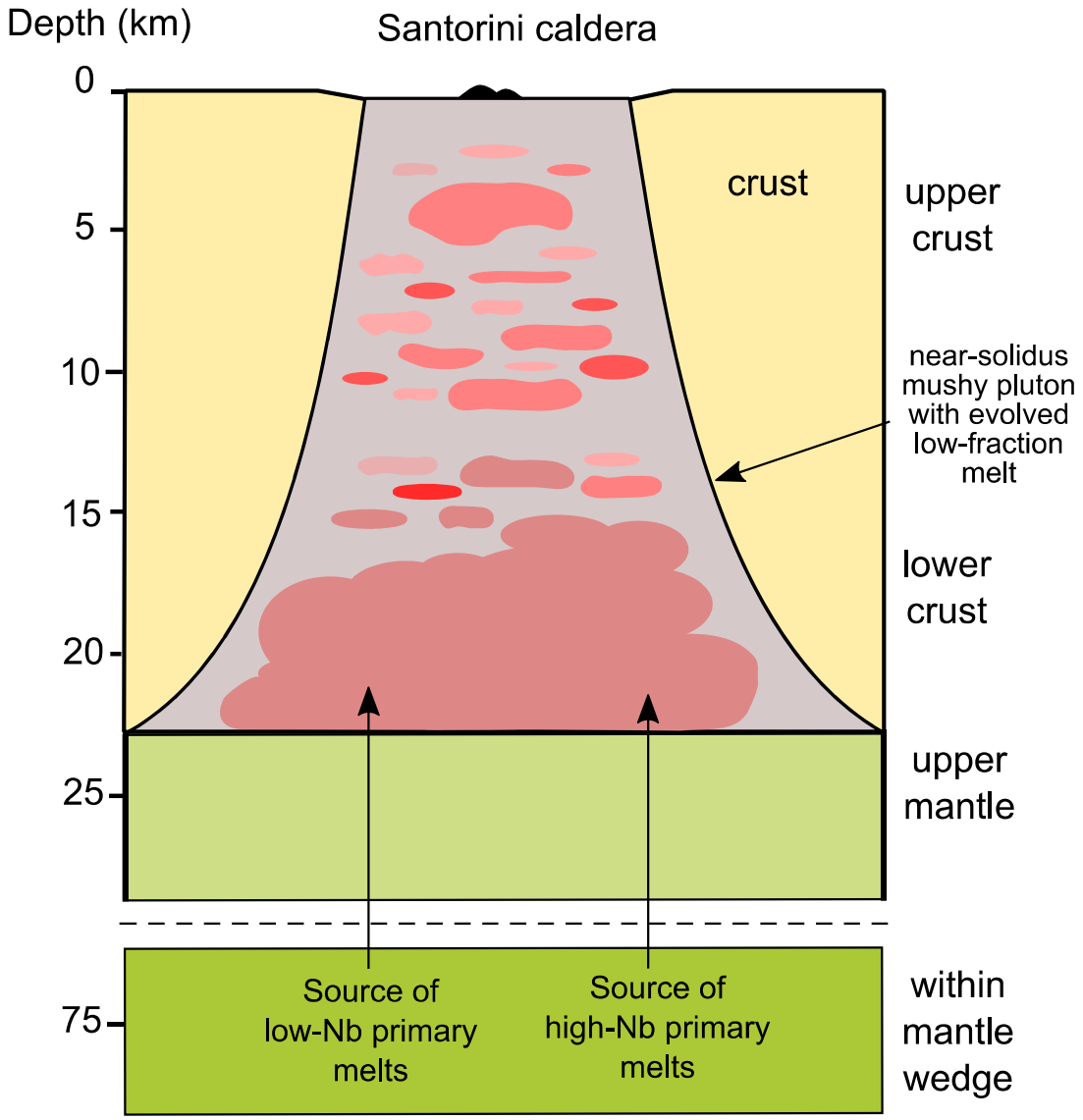

Figure 5.20: Simple model of the magmatic system. Parental magmas of different incompatible element chemistry (ranging from low to high Nb type endmembers) derived from different mantle sources enter the lower crust. The parental basalts interact with a pervasive, low fraction melt and differentiate by AFC in the mushy pluton.

As these primary basaltic melts ascend through the 25-km thick crust, and the thick sub-caldera pluton, they evolve by fractional crystallization to intermediate and silicic derivatives. They are also contaminated by melts derived either from the crust, the pluton, or both, which possibly have the characteristics of low-fraction silicic melts. We envisage that the variably mushy crust and pluton interacts with, and contaminates, the ascending magmas, generating AFC-like geochemical trends. The contaminant could be variably evolved and variably radiogenic, so long as it has an approximately constant incompatible/Th ratio. Contamination may occur at all levels in the crust or may be more pronounced in a lower crust MASH zone.

5.10 Conclusions

The main conclusions of this study are as follows:

1. Santorini melt inclusions and groundmass glasses define trends on geochemical variation plots that can be split into low Nb and high Nb series based on parental basaltic melts from Chapter 4. It is useful to also distinguish a medium Nb series.
2. Each series exhibits two distinct stages of differentiation on log-log variation plots: Stage 1 from basalt to basaltic andesite, and Stage 2 from basaltic andesite to rhyodacite.
3. The two stages cannot be modelled together by one-stage FC, as this requires unreasonably high Ds for most incompatible elements. While Stage 2 can be modelled by FC using reasonable Ds (as done by previous authors, such as Mann 1983), Stage 1 cannot.
4. Stage 1, and to a large extent both stages, can be modelled satisfactorily from the respective parental compositions using AFC with r values of 0.15-0.5 and a silicic contaminant with ratios of incompatible elements to Th that are similar to, or lower than those of silicic melts of the magmatic series themselves. Stage 2 can be similarly modelled by AFC, but also by almost pure FC using reasonable D values.
5. Statistical modelling shows that there are many possible contaminant compositions, but they can be narrowed down based on a mean solution distribution and geological reasoning. One possibility is that the contaminant is a highly evolved, low-fraction silicic melt, which appears from published whole rock Sr isotopic data to be variably radiogenic.

6. We speculate that a low-fraction silicic melt may be present interstitially, or as veins and dykes, in the variably mushy plutonic products making up the Santorini crustal magmatic system. Mantle-derived basaltic parent melts might encounter and interact with this contaminant during ascent to the surface.
7. Melt inclusion and groundmass trends on K_2O versus SiO_2 have the same origin as those on Nb versus Th, which are explained by AFC differentiation from different primitive parental magmas. It follows that the well-known temporal decrease in K2O (and other incompatible elements) at Santorini over time since 530 ka is also parent-related, as previously suggested but not proven.
8. Given that low and high Nb basaltic melts have been generated throughout the history of Santorini in different mantle source domains (Chapter 4), the temporal change in incompatibles must be due to an increase *in the proportion* of low Nb primary melt relative to high Nb primary melt with time. This could be due to a growing influence of crustal rifting and extension in the region, and an associated increase of decompression melting over fluid-flux melting.

Chapter 6: Build-up to a large silicic eruption at Santorini Volcano

6.1 Introduction

This final chapter is a progress report on a study of the implications of our melt inclusion and glass data for the build-up to the large caldera-forming eruption of the late Bronze Age. Our aim is to integrate these data into existing models of the Late Bronze Age (LBA) eruption based on other data, including whole rock chemistry and petrology (Druitt et al. 1999), melt inclusion volatile barometry (Druitt et al. 2016), experimental petrology (Cottrell et al. 1999; Cadoux et al. 2014; Andújar et al. 2015, 2016), and diffusion chronometry (Druitt et al. 2012; Fabbro et al. 2017; Flaherty et al. 2018). However, having run out of time, we present just a short summary of our ongoing findings and some tentative conclusions. This chapter was written with a contribution from T. Druitt

Large explosive caldera-forming eruptions at arc volcanoes are low-frequency, but high-impact, events. The processes that occur during the build-up periods to such eruptions are still poorly understood. It is necessary to understand these processes if ever the need arises to interpret geophysical signals of volcanic unrest corresponding to this scale of activity. In this chapter, we focus on two aspects of the build-up period up to the LBA eruption: (1) the geochemical evidence for the involvement of amphibole in magma genesis which is otherwise generally absent from the products of the last 530 ky at Santotini, and (2) the presence within the magmatic system of a suite of Ba-enriched magmas which are anomalous in terms of their geochemistry with respect to other magmas of the volcano. We present melt inclusion data from olivine, plagioclase and pyroxenes, as well as groundmass glass data, from a range of eruptions from 80 ka to the present-day. This period includes the products of the volcano from the long build-up period to the eruption, but also those of the present-day post-LBA Kameni Volcano. The study builds on the conclusions of the previous chapters, which have been clearly stated and will not be repeated here.

6.1.1 The 80 ky of Santorini activity leading up to the LBA eruption and post-LBA intracaldera Kameni volcanism

The regional context of Santorini, its volcanic history and the chemistry/petrology of its magmas have been described in detail in previous chapters. We identify the onset of build-up to the LBA eruption at about 80 ka (Figure 6.1), since it is from thereon that geochemical signatures related to the LBA eruption begin to become detectable, as will become apparent later. We now describe the eruptions of that period and their products. We also include the post-LBA intracaldera Kameni volcanism.

The ~80 ka **Upper Scoria 1 eruption** was a primarily silicic andesitic in composition and generated a scoria fall deposit overlain by base surge and scoria flow deposits (Druitt et al. 1999).

The **M10 interplinian period** included the construction of the 300-m-high (above present-day sea level) Skaros lava shield, but also weak explosive activity before (pre-Skaros; M10a) and after (post-Skaros; M10b) (Druitt et al. 1999; Vespa et al. 2006). M10a consists mainly of scoria and ash fall layers ranging from basaltic andesite to andesite in composition (Vespa et al. 2006). The Skaros shield volcano constituted 12 km^3 of ~30 mainly basaltic andesite to andesite lavas that filled a pre-existing caldera (Huijsmans 1985; Briqueu et al. 1986; Huijsmans and Barton 1989; Druitt et al. 1999). M10b (excluding Megalo Vouno) is thinner than M10a, and consists of scoria, pumice and ash layers (Vespa et al. 2006). Megalo Vouno and Kokkino Vouno cinder cones are mostly basalt to basaltic andesite in composition (Druitt et al. 1999; Vespa et al. 2006).

The **Upper Scoria 2 eruption** occurred around 54 ka. It had an initial Plinian phase that discharged dacitic magma, followed by pyroclastic surges and scoria flows that discharged silicic andesite magma (Druitt et al. 1999).

The **M11 interplinian period** is divided into M11a (pre-Therasia lavas) and M11b (post-Therasia lavas). Formation of the Therasia dome complex was the major event occurring in the M11 interplinian period, creating a 200-m-thick sequence of predominantly rhyodacitic or dacitic lava flows (with two andesitic flows at the top of the sequence) containing mafic inclusions and erupted between 45 and 25 ka (Fabbro et al. 2013). The small-volume Andesite of Oia was also erupted within this time period. M11 pyroclastic deposits consist mainly of silicic pumice fallout.

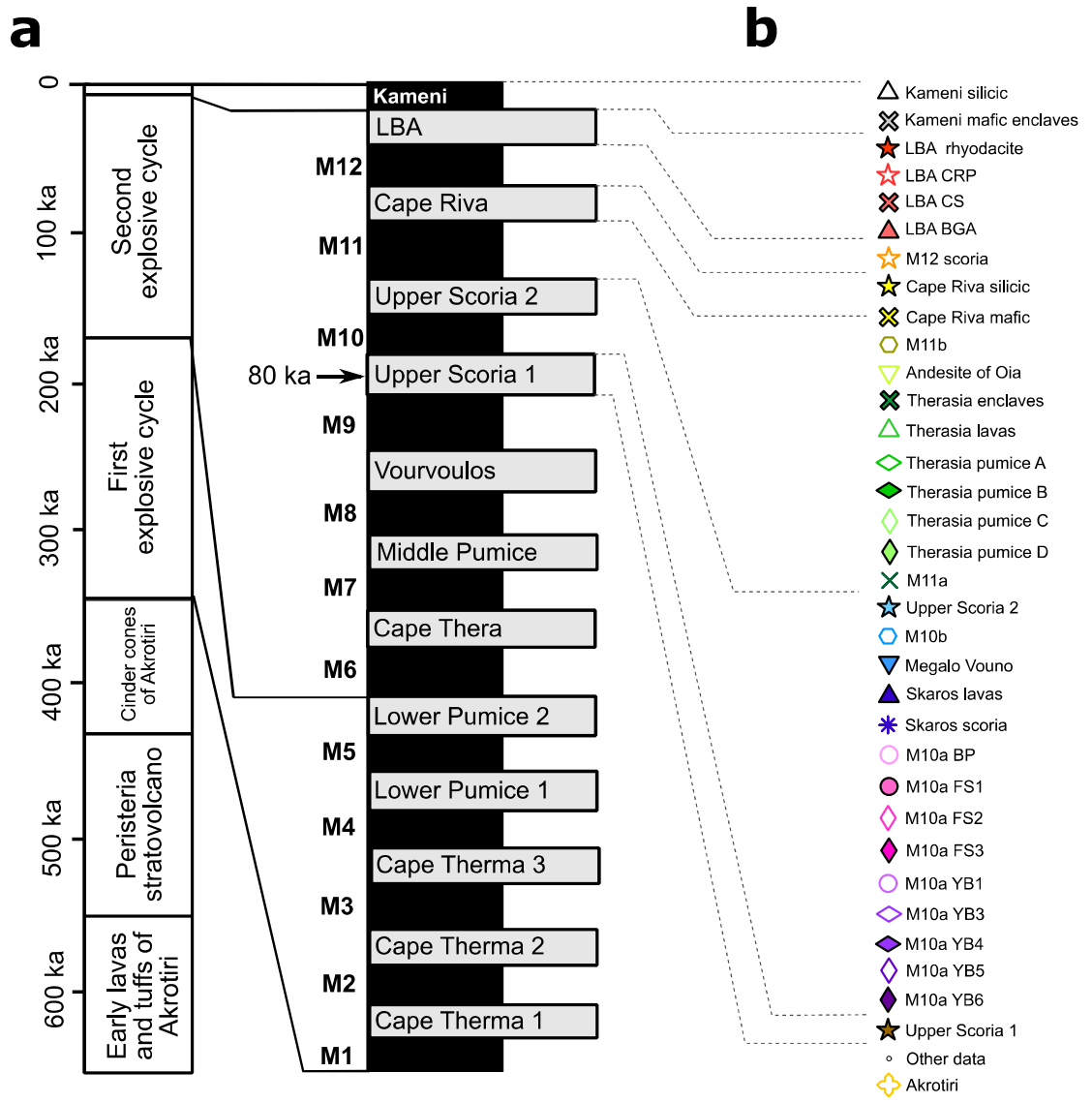

Figure 6.1: Santorini eruptions and symbols used in this chapter. (a) A broad overview of the Santorini eruptive history, with the left approximately to scale, using dates from Druitt et al. (1999) and, on the right, the sequence (not to scale) of twelve identified Plinian eruptions (wide grey rectangles) since 360 ka. Plinian eruptions are separated by interplinian periods (smaller black rectangles) M1 through M12. This chapter focuses on < 80 ka Plinian eruptions (since Upper Scoria 1) and interplinian periods (highlighted as black). Subdivisions follow Druitt et al. (1999) and Vespa et al. (2006). (b) Symbols shown are those used in geochemical diagrams to follow in this chapter. LBA = Late Bronze Age (eruption); CRP = crystal-rich pumice; CS = cauliform andesitic scoria; BGA = black glassy andesite. Other abbreviations are stratigraphic names from Vespa et al. (2006).

The 22 ka **Cape Riva eruption** was a dacitic (with minor andesitic component) caldera-forming eruption that discharged a pumice fall, two welded ignimbrites, and voluminous non-welded ignimbrite (Druitt et al. 1999). The volume of erupted magma and rock debris has been estimated at least 10 km^3 (Fabbro et al. 2013). The Cape Riva caldera occupied much of the northern basin of the present-day caldera (Athanassas et al. 2016).

A single basaltic andesite scoria fall deposit marks the **M12 interplinian period** (Vespa et al. 2006; Vaggelli et al. 2009). It was studied in detail by Vaggelli et al. (2009), who focused on olivine-hosted melt inclusions which represent some of the most primitive compositions found on Santorini. However, abundant lithics of a texturally and chemically distinctive black glassy andesite (hereafter referred to as BGA) in the overlying LBA deposits are interpreted as fragments of an intracaldera lava edifice at least 2 km^3 in volume that was constructed inside of the Cape Riva caldera during the M12 period, then destroyed by the LBA eruption (Druitt 2014; Karátson et al. 2018). One sample of BGA has been dated radiometrically at 20 ka, immediately after the Cape Riva eruption (Karátson et al. 2018).

The **Late Bronze Age eruption** took place 3.6 ka. It occurred in four main stages, preceded by small explosions (Heiken and McCoy 1984): A Plinian phase (phase 1) was followed by eruption of base surges (phase 2), low-temperature pyroclastic flows (phase 3), and hot, fluidized pyroclastic flows that covered the islands in ignimbrite up to 60 m thick (phase 4) (Bond and Sparks 1976; Druitt 2014). The DRE (dense rock equivalent) volume of LBA products has been estimated at between 48 and 86 km^3 (Johnston et al. 2014). Collapse during the LBA eruption deepened and enlarged the pre-existing Cape Riva caldera. The LBA products contain three juvenile components (Druitt et al. 1999; Cottrell et al. 1999; Druitt 2014): (1) ***rhyodacitic*** pumices comprising >99% of the juvenile population, (2) a suite of ***crystal-rich pumices*** co-erupted with the rhyodacite but derived from a small, separate magma reservoir, (3) ***cauliform andesitic scoria*** interpreted as enclaves of andesitic magma quenched in the rhyodacite, then released during magma fragmentation. A prominent lithic component, already mentioned above, is a ***black glassy andesite (BGA)*** interpreted as fragments of a post-Cape Riva intracaldera edifice destroyed during the LBA eruption (Druitt 2014; Karátson et al. 2018). The crystal-rich pumices, cauliform scoria, and BGA form a coherent geochemical series that is notably higher in Ba than

the other <530 ky products of Santorini. Some crystal-rich pumices contain phenocrystic amphibole, and amphibole is present as a groundmass phase in some of the cauliform scoria.

Following the LBA eruption, the volcano returned to typical interplinian activity involving minor effusive activity and small explosive eruptions (Higgins 1996; Druitt et al. 1999). This volcanism has led to the creation of the 470-m-high, largely submarine **Kameni post-caldera Volcano**. Palea Kameni island broke the sea the surface in 197 BCE and was the site of active volcanism until 726 AD. Nea Kameni appeared later and was the site of active volcanism between 1570 and 1950, subdivided into ~10 eruptive episodes (Barton and Huijsmans 1986; Druitt et al. 1999; Martin et al. 2006). The lavas are dacitic, and they contain several different populations of quenched mafic enclaves (Barton and Huijsmans 1986; Holness et al. 2005; Martin et al. 2006). We include data from Kameni in this story, because these eruptions immediately follow the LBA eruption.

6.2 Methodology

The sample set, melt inclusion correction procedures, and analytical procedures were described in Chapter 3. The whole rock database was also described. In the timeframe concerned, we present a dataset of 322 melt inclusions (n_{plag} = 164; n_{oliv} = 132; n_{cpx} = 20, n_{opx} = 6) and 285 groundmass analyses. Not all melt inclusions and groundmass glasses have been analyzed for trace elements, and some were analyzed for major elements for Druitt et al. (2016).

6.3 Results

6.3.1 Melt inclusions and groundmass results

Figures 6.2-6.8 show the melt inclusion (MI) and glass data for the <80 ky individual eruptions described above. Sample symbols are given in Figure 6.1. On each plot we include the field of published whole rock analyses for the given eruption. We also show the low, medium and high Nb series of Chapter 4 as fields on the Nb-Th plots. In all cases the MIs and groundmass glasses lie in the fields of previously published whole rock analyses for the respective eruptions.

Upper Scoria 1. The MIs and groundmass glasses fall on a simple continuous trend corresponding to the low to medium Nb series of Chapter 4 (Figure 6.2).

M10 interplinian period and Skaros Volcano. The M10 period shows a large variation in geochemistry (Figure 6.3). There is a range in primary melts, as seen in Nb and K2O. A clear parallelism between individual trends for different units can be observed, for example on the Nb-Th plot. Melt inclusions and groundmass glasses form linear, continuous trends. The Skaros whole rock data scatters, most likely as it encompasses a large range of compositions from basalts to rhyodacites over a long time period (Huijsmans 1985).

Upper Scoria 2. The MI and groundmass data for Upper Scoria 2 give a relatively simple trend (Figure 6.4). One primitive MI hosted in a Mg-rich cpx crystal may show the chemistry of the basaltic magma giving rise to the more evolved compositions.

M11 (including Therasia) and Cape Riva. The M11 period and Cape Riva eruption are plotted in Figure 6.5. The Therasia lavas (45-25 ka) and Cape Riva (22 ka) data form two parallel vectors, though they are closely spaced in time.

M12 interplinian scoria fall data are plotted in Figure 6.6. Olivine-hosted melt inclusions from the M12 scoria fall are of low Nb melt type; however, there is a lot of scatter, notably in Ba. We have included MI fields of data from Vaggelli et al. (2009) who divided their inclusions into two types. There is generally good agreement between their MI data and ours.

LBA eruption (including the M12 BGA). MIs and glasses of the three different juvenile components of the LBA eruption are plotted in Figure 6.7, along with the BGA lithics. LBA melt inclusions and groundmass glass from the rhyodacite are relatively low in incompatible elements. Like the whole rocks, MIs and glasses from the crystal-rich pumices, cauliform scoria and BGA form a distinct high-Ba lineage compared to the rhyodacite, from the least evolved olivine-hosted MIs of the cauliform scoria to the highest Ba groundmass glasses of the crystal-rich pumices. However, some MIs from the crystal-rich pumices and cauliform scoria form a band that extends down to, and overlaps, the field of the rhyodacite on the Ba-Th plot. Some of the scoria-derived MIs in the rhyodacite field were hosted in crystals with adhering andesitic glass, showing that they truly came from the cauliform scoria. Both the rhyodacite and high-Ba data

mostly lie on a low to medium Nb trend, and are distinguishable from each other only by the different Ba contents for a given silica content.

Kameni Volcano data are plotted in Figure 6.8. Olivine-hosted MIs from the mafic enclaves are Nb-rich but the more evolved MIs from the dacites are relatively Nb-poor. They appear to cut across the trends of the different Nb series modelled in Chapter 5. The reason that we include Kameni in this chapter is for comparison purposes, as it directly follows the LBA eruption and its 80-ka build-up period.

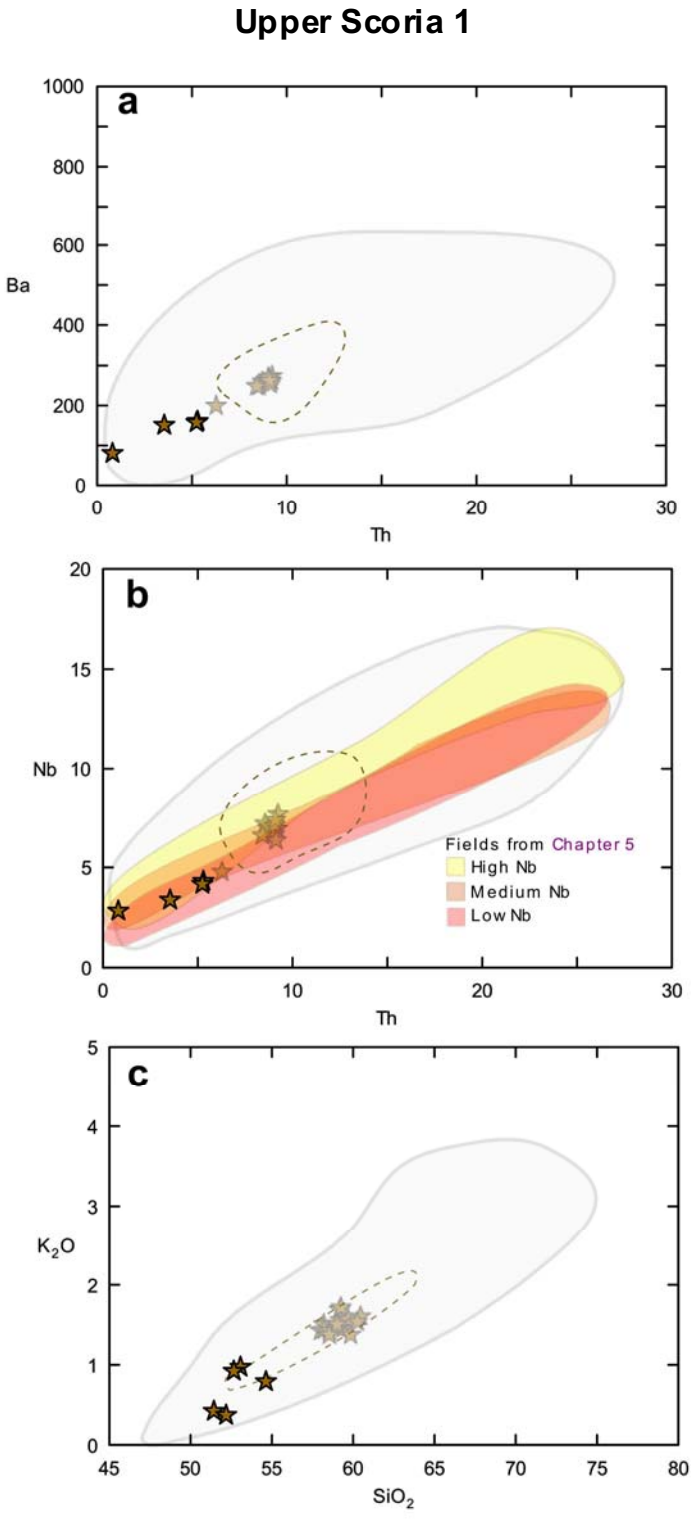

Figure 6.2: Melt inclusion and groundmass glass compositions for the Upper Scoria 1 eruption. Melt inclusions are shown 100% opaque. Groundmass glasses are shown as translucent. The field of published whole rock data for this eruption are shown with a small dashed line. The entire whole rock field for Santorini is shown with a translucent grey line. Trace elements in ppm. Major oxides in wt %.

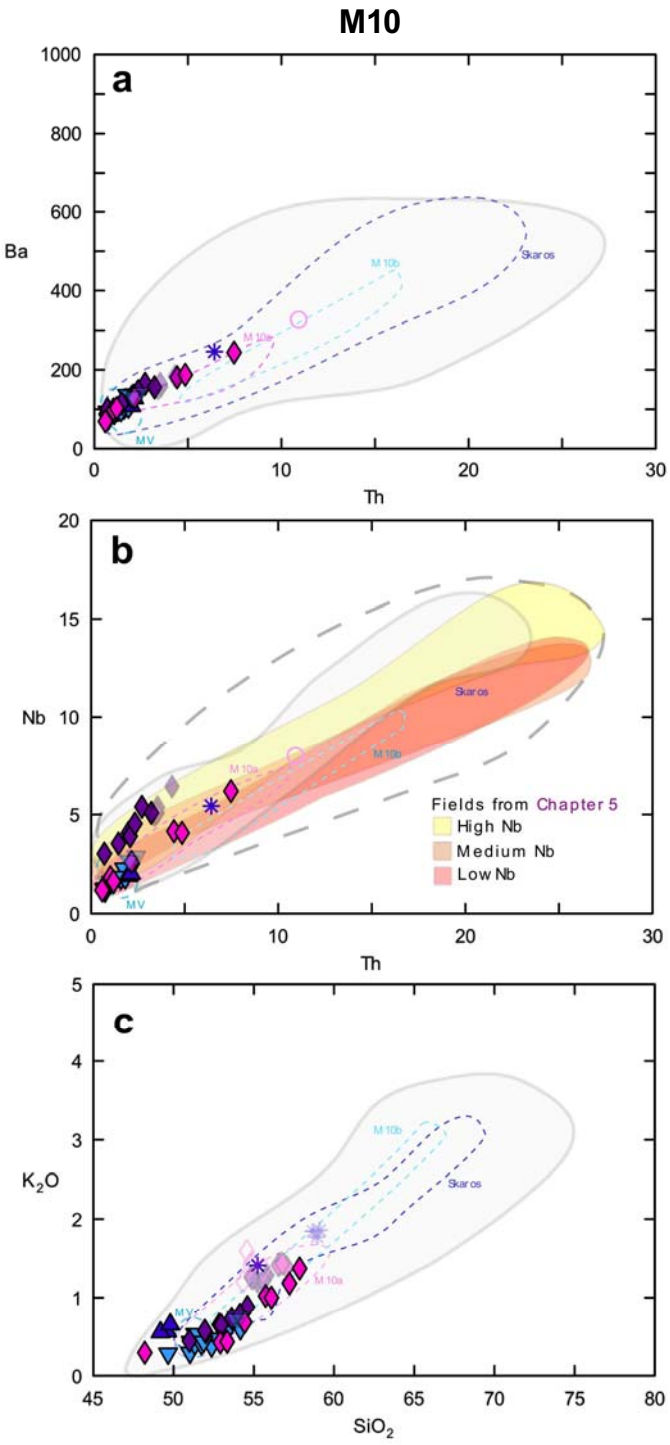

Figure 6.3: Melt inclusion and groundmass glass compositions for the M10 interplinian period including M10a, Skaros, Megalo Vouno and M10b. Melt inclusions are shown 100% opaque. Groundmass glasses are shown as translucent. The fields of published whole rock data for this eruption period are shown with a small dashed line. Nb groups from Chapter 5 are shown as translucent colored fields on the Nb-Th diagram. The entire whole rock field for Santorini is shown with a translucent grey line. Trace elements in ppm. Major oxides in wt %.

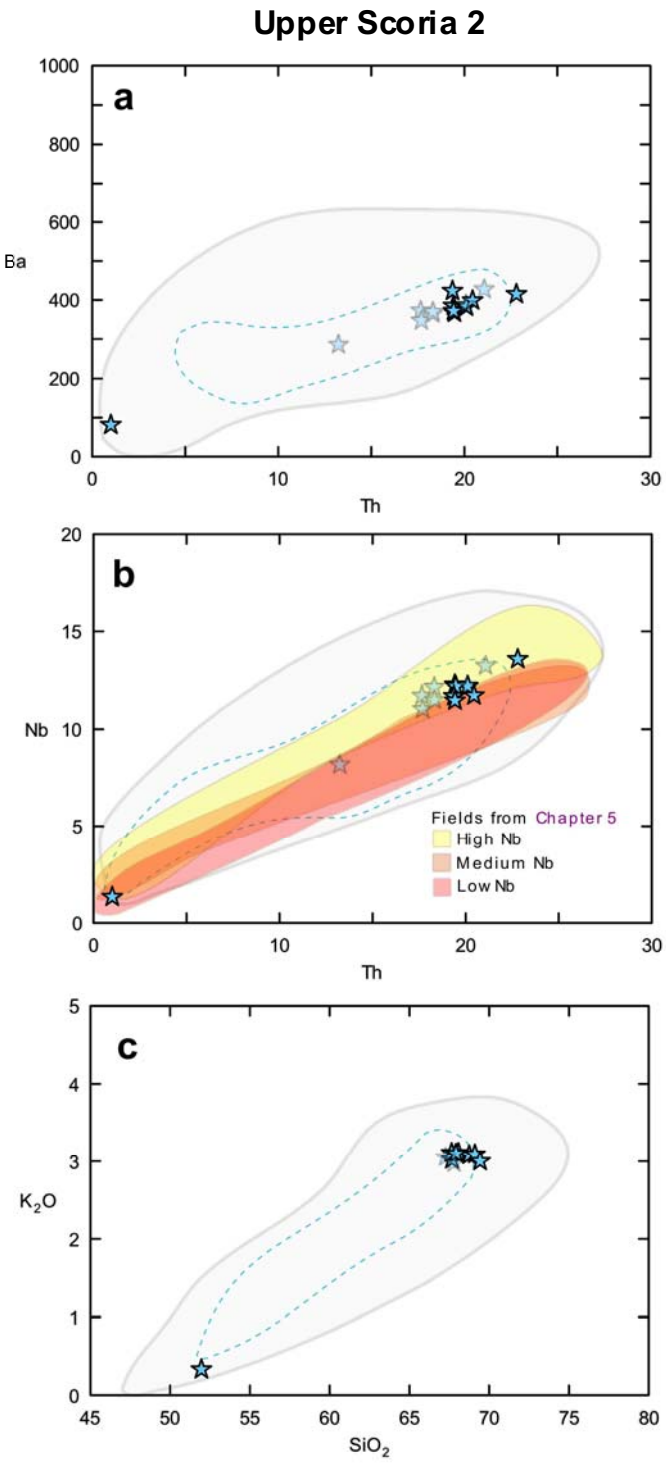

Figure 6.4: Melt inclusion and groundmass glass compositions for the Upper Scoria 2 eruption. Melt inclusions are shown 100% opaque. Groundmass glasses are shown as translucent. The field of published whole rock data for this eruption are shown for with a small dashed line. Nb groups from Chapter 5 are shown as translucent colored fields on the Nb-Th diagram. The entire whole rock field for Santorini is shown with a translucent grey line. Trace elements in ppm. Major oxides in wt %.

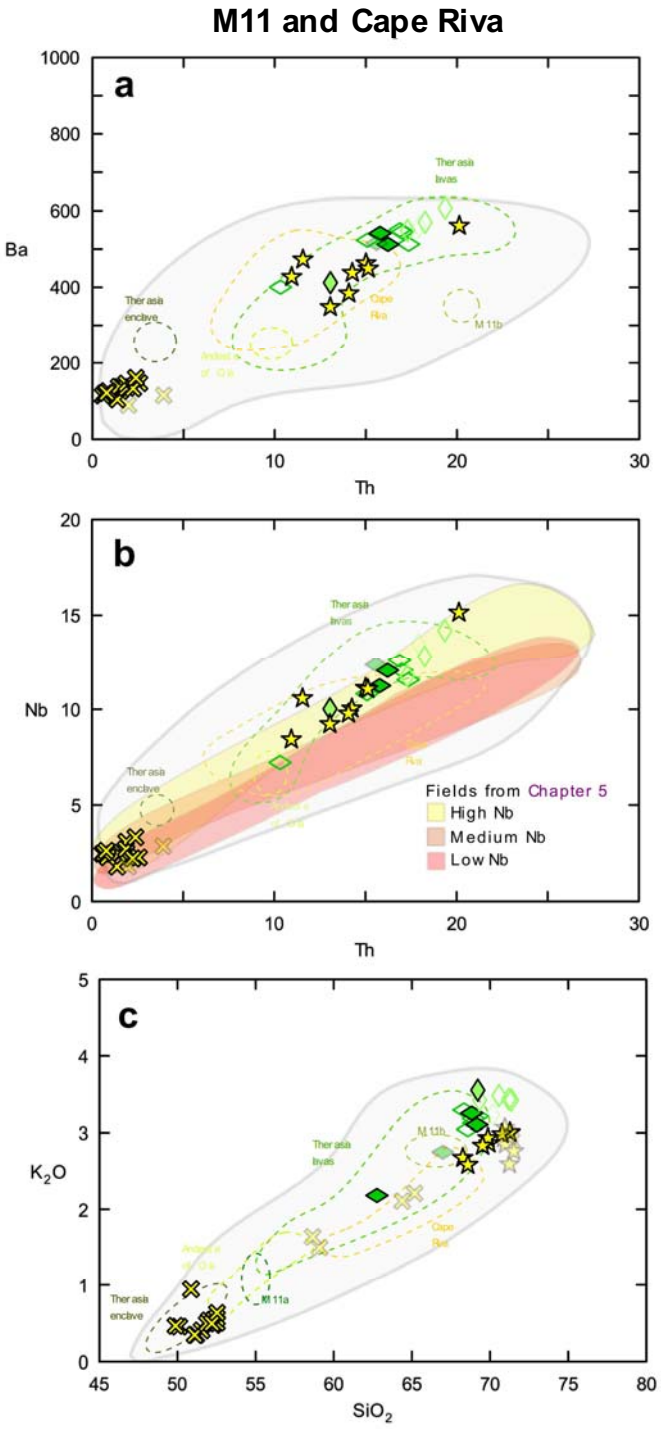

Figure 6.5: Melt inclusion and groundmass glass compositions for the M11 interplinian period including M11a, Therasia lavas, Therasia pumice falls, Therasia enclaves and M11b. Melt inclusions are shown 100% opaque. Groundmass glasses are shown as translucent. The fields of published whole rock data for this series of eruptions are shown for with a small dashed line. Nb groups from Chapter 5 are shown as translucent colored fields on the Nb-Th diagram. The entire whole rock field for Santorini is shown with a translucent grey line. Trace elements in ppm. Major oxides in wt %.

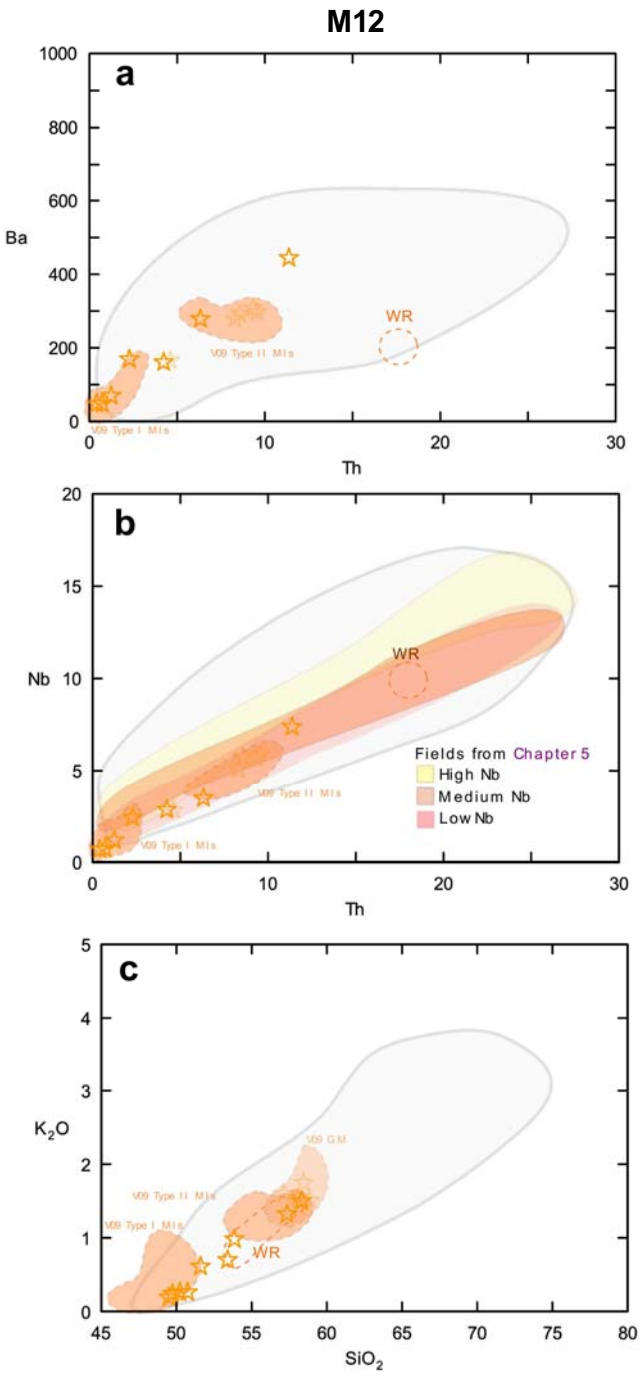

Figure 6.6: Melt inclusion and groundmass glass compositions for the M12 small scoria deposit near Fira. Melt inclusions are shown 100% opaque. Groundmass glasses are shown as translucent. The field of published whole rock data for this eruption are shown with a small dashed line. Nb groups from Chapter 5 are shown as translucent colored fields on the Nb-Th diagram. Melt inclusion data from Vaggelli et al. (2009), abbreviated as V09, is shown as translucent labelled fields. The entire whole rock field for Santorini is shown with a translucent grey line. Trace elements in ppm. Major oxides in wt %.

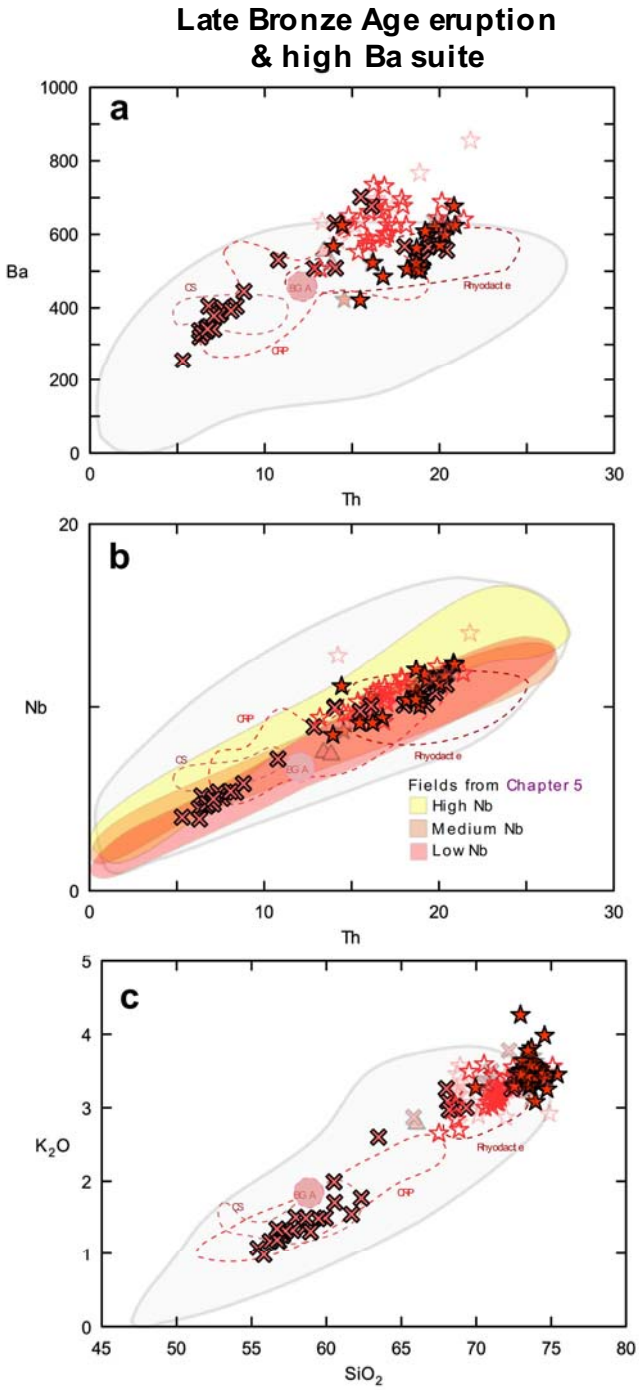

Figure 6.7: Melt inclusion and groundmass glass compositions for the LBA eruption rhyodacite and high-Ba components: cauliform scoria (CS), crystal-rich pumice (CRP) and black glassy andesite (BGA). Melt inclusions are shown 100% opaque. Groundmass glasses are shown as translucent. The fields of published whole rock data for these eruption products are shown with a small dashed line. Nb groups from Chapter 5 are shown as translucent colored fields on the Nb-Th diagram. The entire whole rock field for Santorini is shown with a translucent grey line. Trace elements in ppm. Major oxides in wt %.

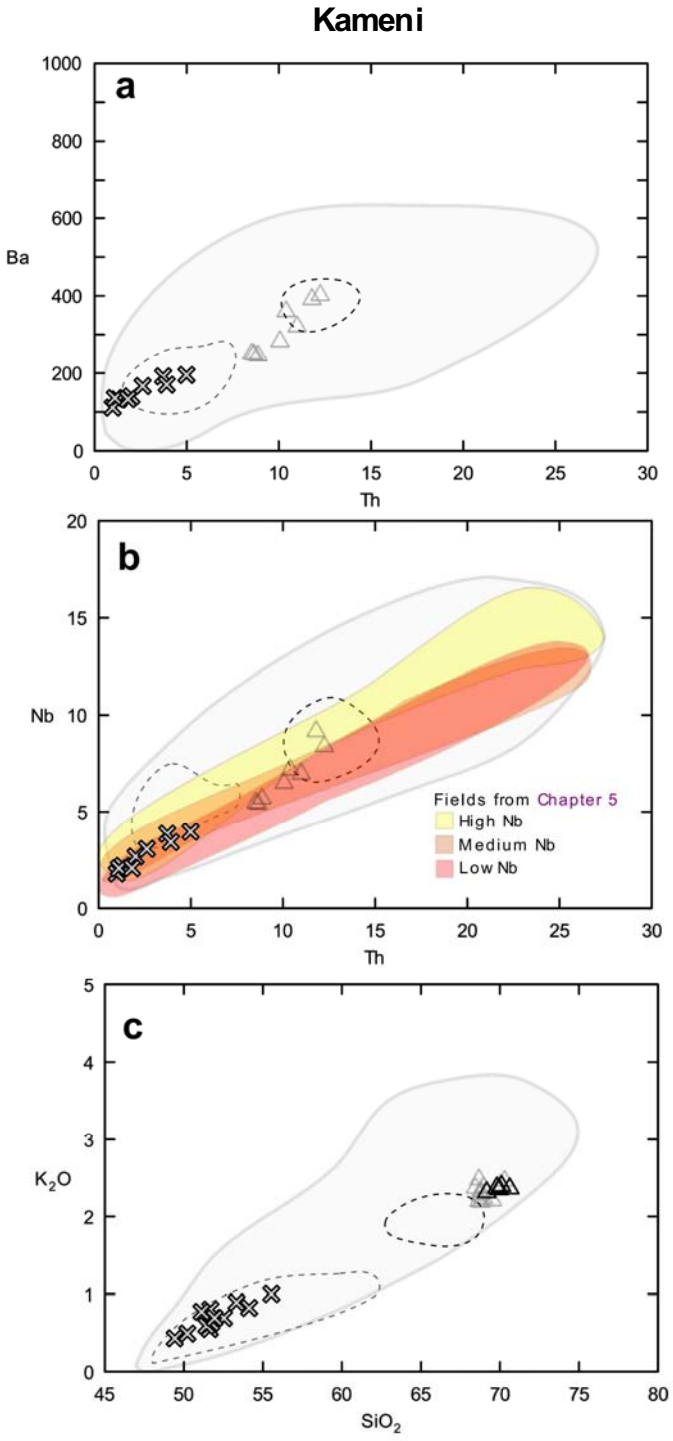

Figure 6.8: Melt inclusion and groundmass glass compositions for Kameni eruptions. Melt inclusions are shown 100% opaque. Groundmass glasses are shown as translucent. The field of published whole rock data for this eruption are shown for with a small dashed line. The entire whole rock field for Santorini is shown with a translucent grey line. Trace elements in ppm. Major oxides in wt %.

6.4 Issue of crystal inheritance

A major issue in drawing conclusions from MI data is the possibility that the crystals containing the MI have been picked up by the host magma and are not inherent to the same magmatic system; i.e., that they are antecrystic. Crystal inheritance is a known to be a common phenomenon in magmas (Davidson et al. 2007a). We certainly cannot rule out some crystal inheritance; for example, the MI-glass trends for some eruptions (Upper Scoria 1; M12, Cape Riva) are somewhat scattered for one or more elements, suggesting that inheritance is possible. On the other hand, the MI-glass data sets for some other eruptions (e.g., M10; LBA high-Ba; Kameni) form well-aligned lineages, suggesting that the MIs are mostly related to the host (groundmass) melt.

6.5 Evidence for amphibole fractionation

Amphibole is absent as a phenocryst phase in almost all of Santorini magmas <530 ky old. Its presence as phenocrysts in some crystal-rich pumices and as a groundmass phase in some cauliform scoria is exceptional (some silicic pumices and enclaves of the 172 ka Lower Pumice 2 eruption also contain amphibole; Gertisser et al. 2009).

There are several geochemical indicators of amphibole involvement in the build-up period to the LBA eruption. Y is strongly compatible in amphibole; thus a decrease in Y could be due to an increasing effect of amphibole in the magmatic system. Figure 6.9 shows a plot of Y versus SiO_2 for the time period. While all units up to and including Upper Scoria 2 (54 ka) lie on a single trend, Y then decreases steadily (at a given SiO_2 content) from 54 ka to 3.6 ka (LBA eruption), with the high-Ba M12 and LBA components having the lowest Y of all. This suggests an increasing role of amphibole in the magmatic system from 54 ka onwards in the build-up period (Figure 6.9). On a plot of Y versus Ba, a clear temporal trend of decreasing Y and increasing Ba is seen (Figure 6.10). As Ba increases, Y decreases. Note that this cannot obviously explained by a compatibility of Ba in amphibole, since amphibole would be expected to lower Y and Ba together, which is not the case.

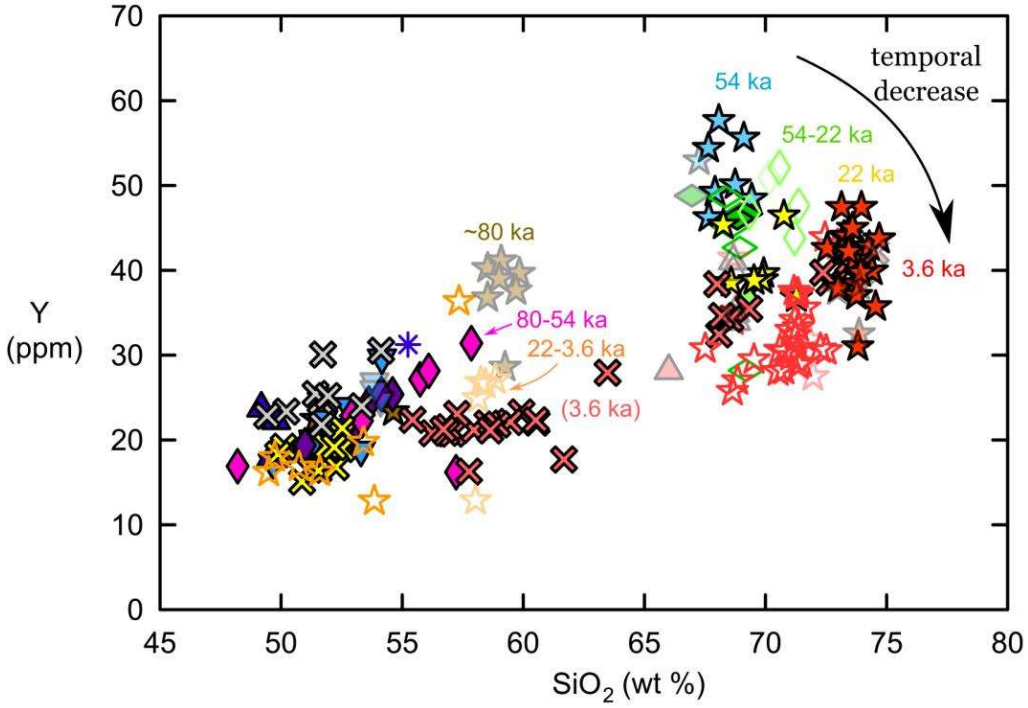

Figure 6.9: Y vs SiO_2 for last 80 ky. A temporal decrease is seen in Y.

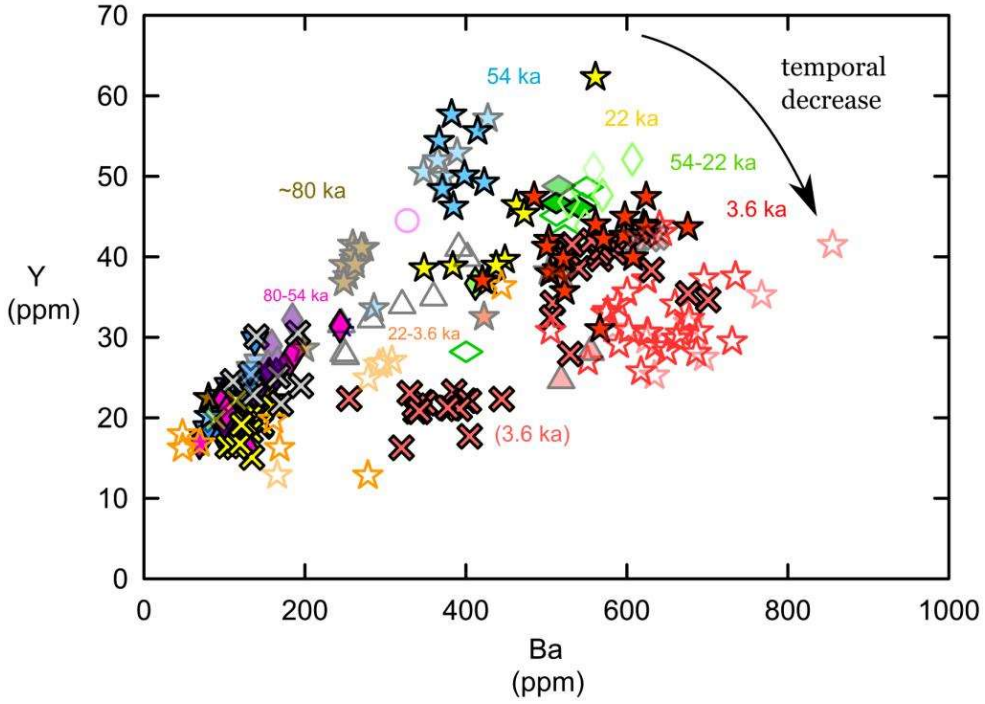

Figure 6.10: Y vs Ba for last 80 ky. An overall temporal decrease in Y/Ba is seen.

Amphibole is found in many continental arc products and is especially common in continental arc cumulates. It is also frequently produced in hydrous, low-pressure crystallization experiments (e.g. Sisson & Grove 1993), but it is not always a part of surface mineralogies of continental arc volcanic products. Erupted arc magmas in general sometimes carry a geochemical signature associated with amphibole involvement (e.g. low Y, low Dy/Yb, etc.) but lack amphibole in surface mineral assemblages. This has led to the ideas of 'cryptic amphibole' (Davidson et al. 2007; Smith 2014; Cooper et al. 2016). The decrease in Y in Santorini products between 54 ka and the LBA eruption, despite the near-absence of amphibole until the LBA eruption, is suggestive that there may be cryptic amphibole in the Santorini magmatic system during this period. Moreover, the correlation between this and the Ba contents of the magmas suggests a further possible link that is now explored.

6.6 Origin of the high-Ba magma suite

The high-Ba melts are represented by MIs and glasses of the LBA crystal-rich pumices, LBA cauliform andesitic scoria and M12-derived BGA lithics. They have higher Ba/Th and La/Th and lower Y/Th, Zr/Th, Hf/Th, Cs/Th, MREE/Th and HREE/Th than other <530 ky Santorini melts (i.e., excluding the 650-550 ka Early Centers of Akrotiri) (Figure 6.12). Otherwise, for other elements, they fall on the general trends (Figure 6.12). They lie on a low to medium Nb trends of Chapter 5 (Figure 6.7). In Figure 6.13 we compare a spider diagram of a high-Ba andesitic (~5 ppm Th) melt with a typical andesitic melt of the low-Nb series, and the only difference is a slight enrichment in Ba, and depletion in Cs, in the high-Ba magma. As well as being enriched in Ba, they are also more radiogenic ($^{87}Sr/^{86}Sr$ between 0.7050 to 0.7058 and are more oxidized (between QFM and NNO fO_2 buffers) than most Santorini magmas (Martin et al. 2010; Druitt 2014). The presence of modal amphibole also suggests a higher H_2O content than other Santorini magmas.

We consider three possible origins for the high Ba melts:

Hypothesis 1: high-Ba primary melt. Unfortunately, the high Ba suite do not include any primitive MIs, the least evolved olivine-hosted MIs being andesitic. It is possible, however, that the high-Ba melts are the products of a low-Nb primary magma that is

slightly enriched in Ba compared to normal low-Nb melts (Figure 6.13). One possibility is that the high-Ba magmas evolved from low-Nb primary melt slightly contaminated by a slab-derived sediment or aqueous fluid particularly rich in Ba, H_2O and ^{87}Sr. High water contents may have suppressed plagioclase crystallization during initial differentiation stages, which may explain why the cauliform enclaves have low-Fo olivines while plagioclase up to An_{95} can be found. Infiltration of particularly hydrous (high-Ba) melts into the plumbing system might have caused reaction with cpx in deep cumulates, generating an amphibole 'sponge' (Davidson et al. 2007a; Smith 2014; Klaver et al. 2018). This amphibole sponge would then generate an amphibole geochemical signature (such as lower Y, lower Dy/YB; spoon-shaped MREE to HREE spectra) that would correlate with higher Ba (higher input of the hydrous melt). This might explain the clear temporal trend on the Ba-Y plot (Figure 6.10). However, amphibole would not necessarily be present as a phenocryst phase in the erupted products. Further data are required to test this idea.

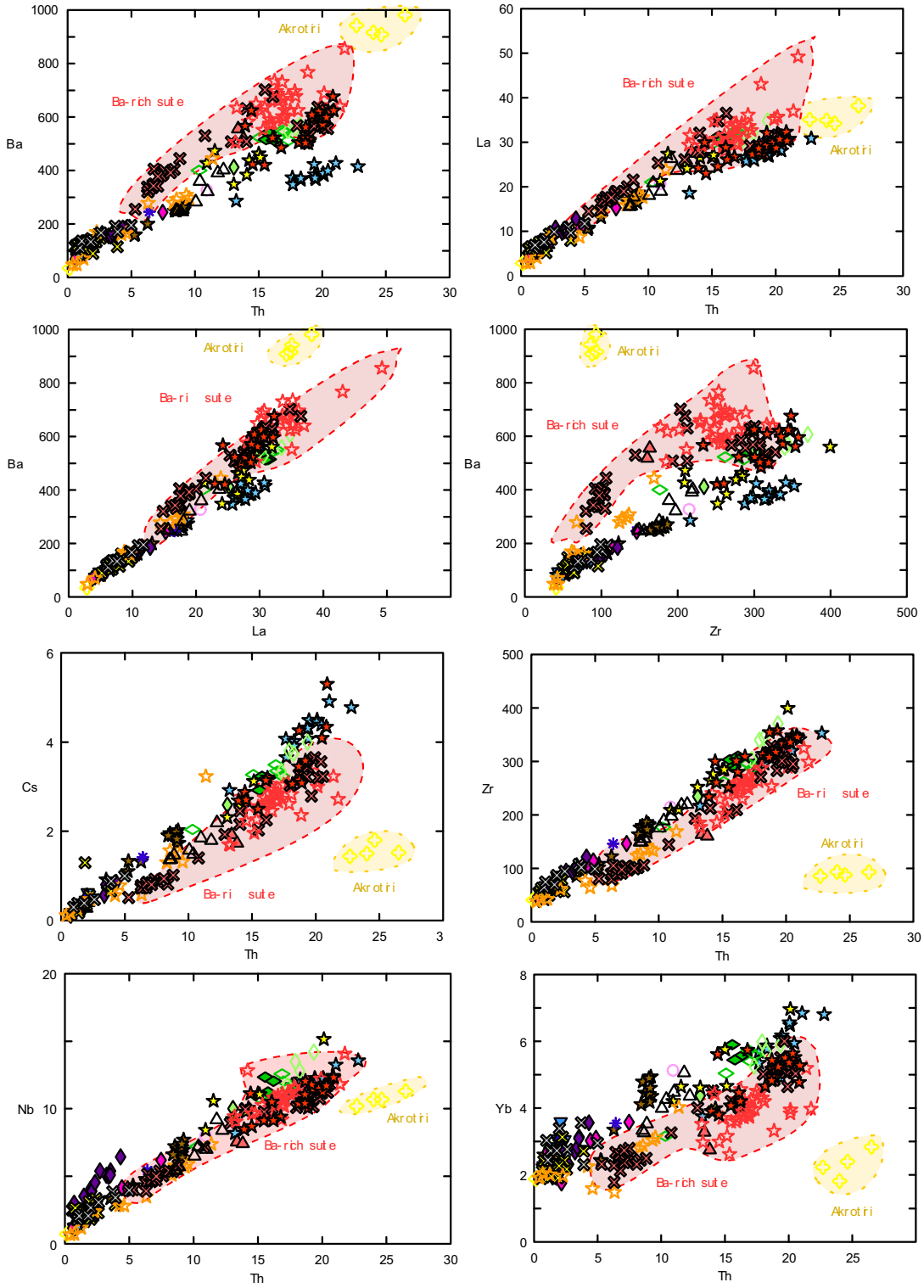

Figure 6.11: Bivariate plots highlighting the high-Ba suite (encircled in red) and Akrotiri groundmass glasses (encircled in yellow). This figure (1) highlights properties of the high-Ba suite and (2) shows that the high-Ba suite and Akrotiri melts do not always fall on the same trend, thus showing they are not genetically related in any simple way and that the high-Ba magmas are not remobilized Akrotiri magmas.

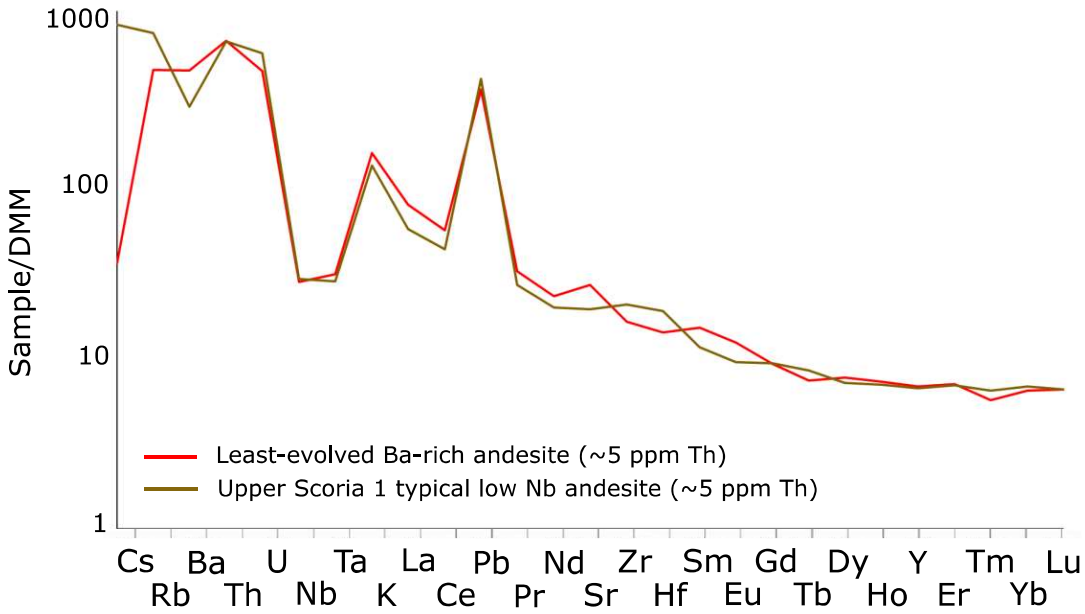

Figure 6.12: Spider diagram showing the least evolved Ba-rich andesitic melt inclusion (~ 5 ppm Th) and a typical low Nb andesitic melt inclusion (also ~ 5 ppm Th). This shows that the high Ba andesites are part of the low Nb series and similar to other andesites, with slight differences (e.g. low Cs, high Ba).

Hypothesis 2: Related to the Early Akrotiri magmas. As already noted by Druitt (2014), the high-Ba magma suite exhibit some geochemical similarities to the early (>650-550 ka) Akrotiri magmas (Figure 6.12). Although the high-Ba and Akrotiri melts clearly lie on different lineages, the high-Ba suite is displaced from 'normal Santorini' magmas in the sense of the Akrotiri magma on all plots in Figure 6.12. So while the high-Ba magmas cannot simply be remobilized Akrotiri magmas, there is a possible common genetic link. This link could be that the high-Ba magmas contain a component of Akrotiri contaminant, or that they share a component of genesis (either mantle or crustal) with the Akrotiri magmas. In both cases, there may be a link with the processes of Hypothesis 1.

Hypothesis 3: Crustal contamination. In Chapter 5 we showed that Santorini magmas are affected by crustal contamination, confirming previous studies (Barton et al. 1983; Druitt et al. 1999; Bailey et al. 2009). The high-Ba magmas may be ordinary low Nb series magmas that have been contaminated by a high-Ba crustal component. Possibilities include upper crustal limestone, or selective melting of, and

contamination by, K-feldspar and/or biotite from upper crustal Miocene granitoids or granitoid mushes related to Quaternary Santorini magmatism.

We are unable to firmly test these hypotheses, in part because the geochemical signatures involved (high Ba, cryptic amphibole) are quite subtle.

6.7 Additional observations serving to constrain processes during the 80 ka build-up to the LBA eruption

We now list some additional observations of the data.

- The magmatic system in the time period concerned was fed by the two primary endmember melts (low Nb and high Nb) described in the previous two chapters. The high-Ba magmas may record a third mantle-derived melt endmember, or low to medium Nb melt (Figure 6.13) contaminated by Ba-rich crustal rocks or minerals.
- Trends of some interplinian MIs and glasses form tight subparallel trends (e.g., M10, Kameni) (Figure 5.16 from Chapter 5; Figures 6.2-6.8), whereas those associated with the large silicic eruptions are more scattered. This may be indicative of larger, more heterogeneous and mushy magmatic systems associated with times of large silicic eruptions, associated with a greater degree of crystal scavenging and inheritance.
- Unlike the M10 data, MIs and glasses for the M12 basaltic interplinian, while belonging to the low Nb series, scatter widely in Ba (Figure 6.6). Given that this basalt was erupted between the two large caldera-forming eruptions (Cape Riva and LBA), this suggests that it passed through crustal rocks and plutonic mushes that were heterogeneous in Ba content.
- The LBA rhyodacitic magma is not a simple differentiate of the high-Ba magmas, since it does not lie on the high Ba liquid line of descent (LLD) given by the MIs and glasses (Figure 6.12). In particular, interstitial glasses in the high-Ba products are significantly richer in Ba than the LBA rhyodacite (Figure 6.12). However, some high Ba MIs form a band between the high Ba LLD and the rhyodacite, suggesting interactions between these two magma batches prior to eruption (Figure 6.12).

- Following the LBA eruption, the high Ba component is no longer evident in the products of Kameni Volcano (Figure 6.8).
- On the plot of Y versus Ba (Figure 6.10), the data overall take the form of a triangle between three components: (1) the range of mantle-derived primary basaltic melts, (2) Upper Scoria 2 type silicic melt, and (3) high-Ba type silicic melt. With time, the magmas from 54 ka to 3.6 ka decrease in component 2 and increase in component 3, reflecting increasing influences in both high Ba magma and cryptic amphibole. MIs and glasses of the M12 basaltic eruption scatter across this triangle, reflecting large heterogeneities in Ba and Y in the magmatic system at that time (Figure 6.10).
- The LBA rhyodacite lies compositionally between components 2 and 3, suggesting that this magma is compositionally an average derivative, and/or mixture, of the different magmas present in the system (Figure 6.10).

6.8 Preliminary model of the build-up to the LBA eruption

The following model is very preliminary and will be refined and extended in the months to come.

During the period from 80 to 54 ka, Santorini erupted both low Nb and high Nb endmember types, which differentiated by AFC to intermediate and minor silicic compositions that were erupted during the Upper Scoria 1, M10, and Upper 2 Scoria 2 eruptions, and constructed the ~12 km^3 Skaros Volcano. At about 54 ka a new basaltic magma, more hydrous, higher in Ba and more Sr-radiogenic, due either to different contamination components from the subducted slab or continental crust, entered the magmatic system. This hydrous magma reacted with cpx-rich cumulates to generate an amphibole 'sponge' beneath the volcano that increasingly imparted its geochemical signature (notably decreasing Y) on magmas in the period leading up to the LBA eruption. As the magmatic system waxed thermally, batches of silicic magmas were successively erupted, first as the ~2 km^3 Therasia lavas and then as the >10 km^3 Cape Riva eruption. Following the Cape Riva eruption and its associated caldera collapse, the high Ba magma finally reached the surface and erupted during the M12 interplinian period. Low to medium Nb basalt (M12) erupted during this period encountered a compositionally heterogeneous, mush column containing evolved melts of a range of Ba contents, from Upper Scoria 2 type melts to high Ba melts. Continued thermal

waxing resulted in generation of 48-86 km^3 of rhyodacite via extraction of silicic melt from this heterogeneous mush column, imparting an 'average' composition on the rhyodacite, which was then erupted during the LBA eruption. Since the LBA eruption, a new batch of low Nb magmas has ascended into the crust and erupted to form the Kameni Volcano.

The question inevitably arises: did the arrival of the hydrous high-Ba magma batch in the crust about 54 ka play a role in causing the LBA eruption? We have no real way to address this question, except to note that no similar magma was associated with the 172 ka Lower Pumice 2 eruption, the caldera-forming eruption that terminated explosive cycle 1. Lower Pumice 2 was similar in composition and style to the LBA eruption, and may even have been of similar or even larger volume (Gertisser et al. 2009; Simmons et al. 2017). No case can therefore be made for a causative relationship between the high-Ba magma batch and the LBA eruption.

Chapter 7: Conclusions and perspectives

Despite previous studies carried out at Santorini Volcano, there are still a number of issues that remain poorly understood about the genesis and differentiation of magmas there. As is the case with other arc volcanoes, these are important aspects to understand in order to have the full picture of the magmatic system's behavior. Some major questions addressed by the thesis were:

- What is the nature of parental magmas and how do they change in space and time?
- What are the origins of more evolved magmas?
- What are the origins of long-term geochemical trends in silicic magmas?
- With new insight, how does the Santorini magmatic system operate physically?
- What happens in the plumbing system of a volcano during the build-up period to a large caldera-forming eruption?

To address these questions, I have presented a new, large high-precision melt inclusion (MI) study on mafic, intermediate and silicic magma compositions throughout the eruptive history of Santorini. In particular, a large number of mafic MIs (less evolved than most existing mafic whole rock data) and the high precision of the trace element data collected on the MIs are some of the biggest factors in being able to answer these questions. The key findings relating to each question will now be summarized before discussing the implications of the findings of this thesis and outlining additional perspectives and future word.

7.1 The nature of parental magmas and how they change in space and time

Our new large dataset of olivine-hosted melt inclusion (MI) data show there is a range in the incompatible trace element chemistry of the least-evolved magmas of Santorini. Primitive MIs, which I defined as melt inclusions with Th < 1 ppm, have typical subduction zone geochemical signatures, with LILE enriched over HFSE, LREE enriched over HREE, prominent negative Nb-Ta anomalies and positive Pb anomalies. The primitive MIs vary between incompatible-poor and incompatible-rich types, which I refer to as low Nb and high Nb primitive melt types, respectively, following Bailey et

al. (2009). The primitive MIs range in La/Yb from 1.5 (flat and tholeiitic-like) in the low Nb type to 3.2 (inclined and calc-alkaline-like) in the high Nb type.

I back-calculate primary melts using several methods. The primary melts parental to the low Nb and high Nb MIs have low Nb and high Nb, respectively (i.e., incompatible-poor and incompatible rich, respectively). The low Nb and high Nb type primitive melts cannot be related by fractional crystallization. Using the petrogenetic modelling software PRIMACALC2 and carrying out mantle melting models, I derive a range of degree of melting (F) of the mantle to produce the different endmember primary melt types. While PRIMACALC2 gives lower melting estimates (6% for high Nb primary melt; 8% for low Nb primary melt) than our mantle melting model (18% for high Nb primary melt; 22% for low Nb primary melt), the two approaches agree that the degree of melting between the two melt types probably differs by a few percent.

The predominant metasomatic signature in the primary melts is from slab-derived sediment melting. There is very little evidence for mantle metasomatism from slab-derived aqueous fluids. The low Nb melts carries a higher sediment melt signature than the high Nb melt. There may be some influence from residual rutile, but this does not dominate the different Nb groupings. The different primary melts are mainly a result of different degrees of partial melting of a mantle wedge metasomatized by slab-derived sediment melts.

There is no consistent temporal change in primary melts with time, suggesting the two different endmember primary melts have been available for ascent into the crust over much of the history of the volcano. This conclusion is in line with the findings of other authors (Vaggelli et al. 2009; Bailey et al. 2009). I conclude that there are at least two mantle source domains below Santorini. The Mantle source of the low Nb basaltic melt is characterized by higher sediment melt signatures and a higher degree of partial melting, leading to more primary melts with an incompatible-poor, more tholeiitic character. The source of the high Nb melt is characterized by a smaller, yet still prominent, sediment melt signature and is associated with a few percent less melting. A slight slab-derived aqueous fluid signature may accompany the high Nb source. The absence of a strong slab-derived aqueous fluid component, coupled with regional extension around the volcanic field and the presence of arc tholeiitic compositions, suggests a possible role of decompression melting at Santorini.

7.2 The origin of more evolved magmas

Santorini melt inclusions and groundmass glasses define trends on geochemical variation plots that can be split into low Nb and high Nb series based on the parental basaltic melts from Chapter 4. Each series exhibits two distinct stages of differentiation on log-log variation plots: Stage 1 from basalt to basaltic andesite, and Stage 2 from basaltic andesite to rhyodacite. These two stages cannot be modelled together by fractional crystallization (FC), as this requires unreasonably high bulk partition coefficients (D) for most incompatible elements. While Stage 2 can be modelled by FC using reasonable Ds (as done by previous authors, such as Mann 1983), Stage 1 cannot.

Stage 1, and to a large extent both stages, can be modelled satisfactorily from the respective parental compositions using Assimilation Fractional Crystallization (AFC) with r (ratio of mass assimilated to mass crystallized) values of 0.15-0.5 and a silicic contaminant with ratios of incompatible elements to Th that are similar to, or lower than those of silicic melts of the magmatic series themselves. Stage 2 can be similarly modelled by AFC, but also by almost pure FC using reasonable D values.

Statistical modelling shows that there are many possible contaminant compositions, but they can be narrowed down based on a mean solution distribution and geological reasoning. One possibility is that the contaminant is a highly evolved, low-fraction silicic melt, which appears from published whole rock Sr isotopic data to be variably radiogenic. I speculate that this melt may be present interstitially, or as veins and dykes, in the variably mushy plutonic products and crustal rocks making up the Santorini crustal magmatic system. Mantle-derived basaltic parent melts may encounter and interact with this contaminant during ascent to the surface.

7.3 The origin of long-term geochemical trends

Melt inclusion and groundmass trends on K_2O versus SiO_2 have the same origin as those on Nb versus Th, which I have explained by AFC differentiation from different primitive parental magmas. It follows that the well-known temporal decrease in K_2O (and other incompatible elements) at Santorini over time since 530 ka is also parent-related, as previously suggested but not proven.

Given that low and high Nb basaltic melts have been generated throughout the history of Santorini in different mantle source domains (Chapter 4), the temporal change in

incompatibles must be due to an increase *in the proportion* of low Nb primary melt relative to high Nb primary melt with time. This could be due to a growing influence of crustal rifting and extension in the region, possibly associated with increasing decompression melting below the volcano relative to subduction-related fluid-flux melting.

7.4 Build-up period to a large caldera-forming eruption

During the 80 ky build-up period to the Late Bronze Age (LBA) eruption, the magmatic system was fed by the two primary endmember melts (low Nb and Nb) described in Chapter 4. Anomalously high Ba magmas erupted between 22 and 3.6 ka, and as minor components in the LBA eruption products, may record a third mantle-derived melt endmember, or low Nb melt contaminated by Ba-rich crustal rocks or minerals.

The LBA rhyodacitic magma is not a simple differentiate of the high-Ba magmas, since it does not lie on the high Ba liquid line of descent (LLD) given by the MIs and glasses. However, some high Ba MIs form a band between the high Ba LLD and the rhyodacite, suggesting interactions between these two magma batches prior to eruption. Following the LBA eruption, the high Ba component is no longer evident in the products of Kameni Volcano. Some geochemical evidence suggests a growing role of cryptic amphibole in the system since 80 ka, but more investigation is needed to show this conclusively. I also observe that trends of some interplinian MIs and glasses from this 80 ky period form tight subparallel trends, whereas those associated with the large silicic eruptions are more scattered. I speculate that this may be indicative of growing, increasingly heterogeneous and mushy magmatic systems associated with times of large silicic eruptions, associated with a greater degree of crystal scavenging and inheritance.

7.5 Perspectives and future work

There are still many questions that remain and directions to take to answer these questions. I now discuss some perspectives and suggestions for future work to follow up on results of this thesis.

Firstly, in the jointly written Chapter 6, we have begun to look in detail at the 80-ka build-up period to the Late Bronze Age (LBA) eruption; however, this is far from a completed work. Further investigation is needed to understand the role of amphibole

involvement during this period. We present some geochemical data to suggest a role of amphibole in the system that perhaps is amplified during the build-up period. Also, in Chapter 6, we present hypotheses for the origins of the high Ba magma suite erupted prior to and during the LBA eruption. Although we are able to essentially rule out some of them, there remain hypotheses we cannot test. For instance, we searched for primitive olivine-hosted melt inclusions in these high Ba magmas without success (the least-evolved composition in olivine-hosted melt inclusion is andesitic, with about ~5 ppm Th); therefore, we cannot rule out the possibility of a high Ba primary magma. We also do not have sufficient data to test the possibility of Ba enrichment by crustal contamination. A detailed further study is needed to understand the role of amphibole and the origins and history of the high Ba magma suite.

Secondly, as mentioned in the Introduction, there was originally a component of isotope geochemistry planned to accompany the melt inclusion aspect of this thesis; however, for numerous reasons but most importantly due to time constraints, it was not able to be completed. There are two main avenues for incorporating isotope geochemistry into the context of this thesis:

1. **Sr isotopes of plagioclase or clinopyroxene zones adjacent to melt inclusions.** Linking trace element geochemistry with isotopic data for the same melt by analyzing the isotopes of the MI-adjacent zone would be a powerful tool for identifying magma batch interactions and crystal recycling.

2. **Sr isotopes (± other isotopes) of primitive olivine-hosted melt inclusions.** This would allow us to know if primitive melts range in their isotopic compositions in addition to their variable trace element chemistry, giving us a better knowledge on the nature of the primary magmas feeding Santorini. It could also help us understand the subduction components that contribute to the generation of primary melts. Additionally, it would allow us to compare isotopic compositions of mafic melts with those of silicic melts belonging to the same unit to better evaluate the degree of assimilation of crustal contaminants through AFC processes.

Lastly, a study on trace element fingerprinting of plagioclase during the build-up period to the LBA eruption would offer important insight about the processes occurring in the plumbing system (e.g. magma batch interactions) and the identification of crystal provenances the degree of crystal recycling.

Appendix 1: Whole Rock Database

A total of 1,158 whole rock analyses (including major elements, trace elements and isotopes) from 39 references were taken from the literature and assembled into an organized tabular database, allowing for data to be sorted (e.g. by eruption, unit, reference, quality of data, etc.). The database was formatted for use with IgPet software. Print sources, electronic tabular supplementary data and online geochemical databases (e.g. GeoRoc, http://georoc.mpch-mainz.gwdg.de; Sarbas et al. 2019) were searched. Some analyses were entered into the spreadsheet by hand, while others were copied in from online repositories and databases such as GEOROC. For all analyses entered in the database, the major elements were recalculated as anhydrous and all Fe was converted to FeO (FeO^T). Analyses of ambiguous samples, extreme outlier values or obvious typos in concentrations given in the literature were rejected and removed from the database. An exception was made for analyses of Santorini dykes, which are ambiguous in terms of stratigraphic placement in the eruptive record. Dykes were kept in a separate category since many dykes are basaltic or basaltic andesite, which are otherwise rare compositions on Santorini, and even though there is no time information the general range of compositions might be helpful later on.

There are a number of inherent issues that were expected to arise when putting together the whole rock database. These problems included a variability in the quality of the data, reliability of sampling methodology (e.g. trusting that the correct unit was sampled, that the samples were free of mixed-in material, not weathered, not taken from a minor component, etc.) and differences between techniques/analytical procedures. Analytical errors were often omitted from the sources as well. Nevertheless, the database could be used to observe general trends. To address these issues, a first-order quality control was put into place, separating older analyses from newer ones, and comparing datasets to find consistent biases. In general, analyses from before 2000 were not used, unless they were the only analyses available, were deemed reliable or constituted a key dataset. We used post-2000 datasets, as well as Druitt, Huijsmans and a few key pre-2000 datasets (termed as “pre-2000 key”) in our quality control measures.

Appendix 2: Constraints for FC and AFC models and additional methodology

A2.1. Modelling constraints

Crystallizing assemblages

Nicholls (1978) proposed that the evolution of Santorini basalts to rhyodacites could be explained by fractionation of plagioclase and cpx, with or without olivine, opx and magnetite. This was primarily based on major element modelling and observed products of Santorini. Mann (1983) used trace elements to model the geochemical evolution of the "Main Series" (i.e. most of the non-anomalous magmas) of Santorini magmas and found that trace element geochemical models were also in agreement with fractional crystallization from basalt to andesite, with a crystallizing assemblage of olivine, An-rich plagioclase and cpx, and then andesite to rhyodacite, with the associated crystallization of plagioclase, cpx, opx, magnetite and apatite.

Experiments by Andújar et al. (2015) showed that differentiation of basalt to andesite be explained by the crystallization of 60-80 wt % olivine, cpx, plagioclase, Ti-magnetite and opx ± pigeonite and ilmenite.

Dacites and rhyodacites contain plagioclase, cpx, opx, magnetite, ilmenite, apatite and pyrrhotite. Fayalitic olivine is present in some dacites of more tholeiitic character (e.g. Vourvoulos).

There is general agreement among previous studies about crystallizing assemblages and a multi-stage differentiation process including at least three steps: (1) early differentiation of mantle-derived basalt (early basalt differentiation), (2) basalt to andesite (mafic to intermediate) and (3) andesite to (rhyo)dacite (intermediate to silicic). We choose to use the crystallizing assemblages in the table below for subsequent modelling. Basaltic to andesitic differentiation is based mostly on Mann (1983), with some modifications. Andesitic to rhyodacitic and rhyolitic differentiation based mostly on Mann (1983) with some modifications.

Table A2.1: Crystallizing assemblages used for modelling, given in weight fraction. anhyd = anhydrous assemblage; hyd = hydrous assemblage.

	Weight fraction of crystallizing minerals (weight fraction)							
	ol	sp	plag	cpx	opx	amph	mag	ilm
Basalt to andesite (anhyd)	0.15	-	0.55	0.30	-	-	-	-
Basalt to andesite (hyd)	0.15	-	0.55	0.15	-	0.15	-	-
Andesite to rhyodacite (anhyd)	-	-	0.60	0.15	0.15	-	0.05	0.05
Andesite to rhyodacite (hyd)	-	-	0.60	0.10	0.10	0.10	0.05	0.05

Bulk distribution coefficients (D)

One of the biggest sources of uncertainty in geochemical modelling is the bulk partition coefficient (D), which can vary widely for each mineral based on many factors, but mostly it is affected by magma composition (Rollinson 1993). A bulk partition coefficient quantifies mineral-melt equilibria with more than one mineral phase present and can be calculated by summing the weight proportion of each mineral in the crystallizing assemblage multiplied by its respective k_D:

$$D = \sum_{i=1}^{n} w_i k_{D_i} \qquad \text{(Eq. A2.1)}$$

where D is the bulk partition coefficient, w is the weight proportion of each mineral.

The bulk partition coefficient (D) can vary widely for each mineral based on many factors, but most of all the D is affected by magma composition (Rollinson 1993). In geochemical modelling, D is one of the biggest sources of uncertainty and can be hard to constrain well due to the variability of k_Ds in the literature for any given mineral and magma composition.

In order to constrain the range of possible Ds for our modelling, a spreadsheet template was created to easily calculate bulk Ds for both mafic and silicic compositions given a

particular crystallizing assemblage. The following minerals are available in the D calculation spreadsheet: olivine, Cr-spinel, cpx, opx, amphibole, plagioclase, magnetite, ilmenite, apatite, zircon, rutile, sulfide (liquid FeS) and garnet. Mineral partition coefficients were taken from our dataset (see Chapter 3) as well as 84 sources from the literature and were entered into a table, organized by mineral and composition, keeping reported ranges and standard deviations attached. Only subalkaline (calc-alkaline to tholeiitic) magma series were considered for k_{DS}; we did not include literature that based k_{DS} on alkaline magma series unless there was little or no other data available. Any modes (volume %) for reasonable crystallizing assemblages were converted to weight fraction using the density of minerals from the online source https://mindat.org (Ralph 2019). These weight fractions were used to calculate bulk Ds for each element used in the study.

In a calculation detailed in Chapter 3, k_{DS} in olivine were calculated using olivine-hosted melt inclusions, knowing the trace element concentration of the melt inclusion and adjacent host as well as the amount of post-entrapment crystallization. These were also included in the D calculation spreadsheet.

An average D (D_{avg}) was calculated using the average k_D for each mineral for the given magma compositional range. Similarly, the minimum D (D_{min}) and maximum D (D_{max}) were calculated from the existing extremes for each mineral and magma composition, including error margins on individual k_{DS}. We report all of these values to know both the average D and the range of possible Ds. We then in turn selected a representative D to use in modelling. If the average D reflected a majority of the studies on the partitioning behavior of a certain element, the average D was used as the selected D. However, if the average D was influenced by a small number of extreme/outlier D values from the literature, we selected a D that either (1) better reflected the consensus of the majority of studies or (2) functioned better in our geochemical modelling. While this approach is subjective, we justify this this because the outlier or extreme values are still conserved in the maximum and/or minimum D values reported; therefore, as long as the range of possible Ds is respected, the D can be modified from its average value.

Table A2.2: Ds selected for a mafic to intermediate crystallizing assemblages and respective potential ranges of Ds possible using literature k_D values. We use the anhydrous crystallizing assemblage ("Anhy") Ds in our modelling and show Ds for a similar but hydrous (amphibole-bearing) assemblage ("Hyd") for comparison.

	Mafic to intermediate			
	Davg Anhy	Range	**Davg** Hyd	Range
Cs	**0.2**	0.02 - 0.8	**0.2**	0.03– 0.8
Rb	**0.07**	0.01 - 0.4	**0.1**	0.02 – 0.6
Ba	**0.2**	0.02 – 0.8	**0.4**	0.03 – 2
Th	**0.06**	0.003 – 0.3	**0.09**	0.005 – 0.3
U	**0.10**	0.0001 – 0.4	**0.1**	0.001 – 0.4
Nb	**0.1**	0.002 – 0.8	**0.2**	0.005 – 0.6
Ta	**0.1**	0.003 – 0.4	**0.2**	0.005 – 0.4
K	**0.09**	0.04 – 0.2	**0.3**	0.1 – 0.5
La	**0.1**	0.02 – 0.3	**0.1**	0.02 – 0.3
Ce	**0.1**	0.03 – 0.5	**0.1**	0.03 – 0.5
Pb	**0.6**	0.2 – 2	**0.6**	0.2 – 2
Pr	**0.1**	0.05 – 0.2	**0.1**	0.04 – 0.2
Nd	**0.2**	0.04 – 0.4	**0.2**	0.05 – 0.5
Sr	**1**	0.5 – 3	**1**	0.5 – 3
Zr	**0.1**	0.002 – 0.6	**0.2**	0.005 – 0.6
Hf	**0.1**	0.03 – 0.7	**0.2**	0.02 – 0.6
Sm	**0.2**	0.06 – 0.8	**0.3**	0.04 – 1
Eu	**0.4**	0.09 – 1	**0.5**	0.1 – 1
Gd	**0.2**	0.09 – 0.3	**0.2**	0.1 – 0.5
Tb	**0.3**	0.3 – 0.9	**0.3**	0.1 – 0.7
Dy	**0.3**	0.1 – 0.9	**0.4**	0.1 - 1
Ho	**0.2**	0.1 – 0.2	**0.3**	0.1 – 0.6
Y	**0.3**	0.08 – 1	**0.5**	0.09 – 1
Er	**0.2**	0.09 – 0.7	**0.3**	0.1 – 0.8
Tm	**0.2**	0.1 – 0.4	**0.2**	0.1 – 0.3
Yb	**0.3**	0.08 – 0.9	**0.3**	0.09 – 1
Lu	**0.2**	0.09 – 0.7	**0.3**	0.08 – 0.7

	Mafic to intermediate			
	Davg Anhy	Range	**Davg** Hyd	Range
Ti	**40**	0.5 - 300	**20**	0.5 – 200
Al	**0.8**	~ 0.8	**0.8**	~ 0.8
Fe	**2.**	2 – 3	**2**	1 – 2
Mn	**1**	0.4 – 2	**1**	0.8 – 2
Mg	**1**	~1	**1**	~1
Ca	**1**	0.6 – 2	**1**	0.6 – 2
Na	**0.5**	0.5 – 0.6	**0.5**	0.5 – 0.6
Li	**0.5**	0.2 – 0.7	**0.4**	0.2 – 0.6
Be	**0.4**	0.1 – 0.5	**0.4**	0.1 – 0.5
Sc	**2**	0.3 – 7	**2**	0.8 – 6
V	**3**	0.8 – 5	**3**	0.8 – 5
Cr	**30**	0.6 – 70	**22**	8 – 60
Mn	**1**	0.4 – 2	**1**	0.8 – 2
Co	**3**	1 - 6	**3**	1 – 5
Ni	**9**	4 – 10	**9**	5 – 14
Cu	**0.3**	0.07 – 0.5	**0.2**	0.07 – 0.4
Zn	**2**	0.4 - 5	**1**	0.4 – 3
Ga	**0.9**	0.5 – 1	**0.8**	0.5 – 1
Ge	**0.5**	~ 0.5	**0.3**	~0.3
As	**0.2**	~ 0.2	**0.2**	~0.1
Mo	**0.0.2**	~0.2	**0.2**	~0.2
Cd	**0.005**	~ 0.0005	**0.005**	~0.005
Sn	**0.002**	~ 0.002	**0.002**	~ 0.002
Sb	**0.002**	~ 0.002	**0.002**	~ 0.002
W	**nd**	nd	**nd**	nd
Tl	**0.06**	~0.06	**0.06**	~0.06
Bi	**nd**	nd	**nd**	nd

A2.2. Additional AFC methodology

A2.2.1 AFC calculations using Method 2

We reduced Equation 5.8 (Chapter 5) by assigning the variables to be imposed in our approach a to a single variable *B*. Thus, the equation reduces to:

$$\frac{C_L}{C_0} = F^{-z} + B(1 - F^{-z}) \qquad \text{(Eq. A3.2)}$$

where $B = \left(\frac{r}{r-1}\right)\frac{C_\alpha}{zC_0}$. The above reduced AFC equation is rearranged and solved for F as a function of the denominator of a given ratio. We used only Th as its highly incompatible nature is a faithful representation of F, though other highly incompatible elements could work as well. The equation for F as a function of Th is given below:

$$F(Th) = \left[\frac{C_{0_{Th}}(1-B_{Th})}{C_{L_{Th}} - C_{0_{Th}}B_{Th}}\right]^{[(z_{Th})^{-1}]} \qquad \text{(Eq. A3.3)}$$

Note that F is the fraction of melt remaining, thus 1–F gives the degree of crystallization.

Finally, using F, corresponding values of the numerator can be calculated using the normal or reduced AFC equation. The sum of squared differences (SSD) was taken between modelled data points and real data points.

We imposed the following restrictions on the models:

1. We only counted the sum of squared differences until approximately andesitic (Th ~ 10 ppm) compositions, because Ds could change a lot during the course of differentiation. Once again, we are most focused on explaining the trends in the basaltic to basaltic andesite compositional range.
2. We imposed a limit on the amount of crystallization (Fc) such that if Fc > 0.95 was required to model the entirety of the data, the model failed. This is because Fc = 0.95 is equivalent to two stages of 80% crystallization, and if this much crystallization is needed, then a huge volume of starting liquid would be needed and this presents a problem when the erupted volume of silicic magma is very high in itself (48-86 km^3 in the case of the LBA eruption; Chapter 6), as is the

case in some Santorini eruptions. Thus Fc of 0.95 is a generous upper limit and incorporating this limit provides a constraint on the parameters needed.

3. We also imposed an upper limit of 50 ppm Th on the contaminant based on the compositions of natural products at Santorini. If the contaminant was a silicic melt, it would likely fall between dacite and high SiO_2 rhyolite. Andesites have ~10 ppm Th, and rhyolitic interstitial glass at Santorini does not exceed ~25 ppm Th. Therefore, imposing a lower and upper limit of 10 ppm and 50 ppm Th, respectively, is realistic and in fact quite generous.

Given a range of input parameters, corresponding solutions were presented in the spreasheet for different combinations of r, contaminant element/Th ratio, and contaminant Th content. The spreadsheet includes a function for automatic spacing. The SSDs for the lowest 2% of values were colored with conditional formatting to highlight the lowest SSDs. An example is shown for part of a spreadsheet in Table A2.3. We investigated the best-fit range for these key contaminant incompatible element ratios: U/Th, Rb/Th, Nb/Th, Zr/Th, Ba/Th and Nd/Th.

A further investigation was undertaken to try to map out all of the possible range of solutions for a given contaminant element/Th ratio. An absolute minimum SSD was identified for some element pairs, otherwise it was imposed. For different contaminant element/Th ratios, different pairs of r and contaminant Th giving this minimum SSD were recorded and plotted (an example is shown in Figure A2.1 for contaminant Rb/Th for the high Nb series). It turns out that for any given contaminant element/Th ratio, there is a strict set of r and contaminant Th values which give best fits and can be described exceptionally well by a power function. Figure A2.1 maps out the range of possible parameters for contaminant Rb/Th ratio. From this further investigation, we see that a wide range of contaminant Rb/Th ratio, r and contaminant Th giving good solutions exist. Therefore, we learn that it is impossible to narrow down the possibilities of what the contaminant can be.

Table A2.3: Example part of a table to explore quality of model fit given different modeling parameters. Possible Th and r values vary considerably, but for different element ratios, the r-Th pairs giving best solutions are correlated, showing a hyperbolic pattern for a given element-Th ratio in the best fit table. Higher Th needed for low r and vice versa. The lower part of the table exemplifies this relationship with a hyperbolic green curve of low sum of squared differences (SSDs).

		r										
Rb/Th	Th	0	0.1	0.2	0.3	0.4	0.5	0.6	0.7	0.8	0.9	1
5.3	10	FAIL	4001.192	1576.887	1568.977	1893.18	2234.935	2537.229	2794.547	3012.297	3197.348	#DIV/0!
5.3	12	FAIL	3083.482	1489.659	1685.566	2047.296	2376.511	2650.977	2876.973	3064.124	3220.75	#DIV/0!
5.3	14	FAIL	2496.294	1491.407	1804.299	2176.07	2487.231	2736.898	2937.891	3101.853	3237.596	#DIV/0!
5.3	16	FAIL	2114.147	1534.306	1914.804	2283.569	2575.755	2803.97	2984.717	3130.541	3250.304	#DIV/0!
5.3	18	FAIL	1863.882	1595.671	2014.464	2373.974	2647.966	2857.732	3021.822	3153.089	3260.23	#DIV/0!
5.3	20	FAIL	1700.911	1664.234	2103.35	2450.745	2707.906	2901.763	3051.941	3171.275	3268.198	#DIV/0!
5.3	22	FAIL	1597.049	1734.263	2182.419	2516.587	2758.411	2938.472	3076.874	3186.254	3274.735	#DIV/0!
5.3	24	FAIL	1533.934	1802.837	2252.842	2573.592	2801.523	2969.54	3097.853	3198.804	3280.195	#DIV/0!
5.3	26	FAIL	1499.296	1868.516	2315.752	2623.374	2838.739	2996.168	3115.748	3209.472	3284.824	#DIV/0!
5.3	28	FAIL	1484.758	1930.657	2372.165	2667.194	2871.182	3019.244	3131.192	3218.651	3288.798	#DIV/0!
5.3	30	FAIL	1484.493	1989.051	2422.958	2706.042	2899.71	3039.431	3144.656	3226.633	3292.247	#DIV/0!
5.3	32	FAIL	1494.387	2043.721	2468.88	2740.706	2924.987	3057.239	3156.497	3233.638	3295.269	#DIV/0!
5.3	34	FAIL	1511.497	2094.814	2510.566	2771.818	2947.537	3073.064	3166.992	3239.834	3297.937	#DIV/0!
5.3	36	FAIL	1533.693	2142.537	2548.552	2799.893	2967.775	3087.22	3176.358	3245.354	3300.312	#DIV/0!
5.3	38	FAIL	1559.42	2187.12	2583.293	2825.349	2986.04	3099.958	3184.768	3250.304	3302.438	#DIV/0!
5.3	40	FAIL	1587.536	2228.798	2615.176	2848.534	3002.606	3111.479	3192.361	3254.766	3304.354	#DIV/0!
5.3	42	FAIL	1617.195	2267.798	2644.531	2869.737	3017.698	3121.95	3199.25	3258.809	3306.088	#DIV/0!
5.3	44	FAIL	1647.771	2304.336	2671.641	2889.199	3031.504	3131.508	3205.529	3262.491	3307.665	#DIV/0!
5.3	46	FAIL	1678.797	2338.612	2696.75	2907.126	3044.182	3140.268	3211.276	3265.857	3309.106	#DIV/0!
5.3	48	FAIL	1709.928	2370.809	2720.066	2923.69	3055.864	3148.325	3216.555	3268.946	3310.427	#DIV/0!
5.3	50	FAIL	1740.906	2401.097	2741.773	2939.042	3066.663	3155.761	3221.421	3271.791	3311.644	#DIV/0!
5.8	10	FAIL	5234.86	2049.489	1522.501	1498.216	1593.684	1713.647	1830.868	1937.735	2032.903	#DIV/0!
5.8	12	FAIL	4170.562	1779.188	1485.97	1533.87	1646.948	1764.074	1870.598	1964.021	2045.185	#DIV/0!
5.8	14	FAIL	3443.918	1631.551	1486.125	1573.408	1692.281	1803.66	1900.542	1983.342	2054.06	#DIV/0!
5.8	16	FAIL	2932.838	1550.822	1502.24	1611.313	1730.456	1835.362	1923.872	1998.133	2060.771	#DIV/0!
5.8	18	FAIL	2564.841	1508.456	1525.049	1645.944	1762.708	1861.24	1942.544	2009.818	2066.024	#DIV/0!
5.8	20	FAIL	2294.889	1488.879	1550.184	1677.027	1790.168	1882.726	1957.815	2019.281	2070.248	#DIV/0!
5.8	22	FAIL	2093.925	1483.166	1575.535	1704.763	1813.755	1900.83	1970.533	2027.098	2073.717	#DIV/0!
5.8	24	FAIL	1942.599	1485.996	1600.087	1729.504	1834.194	1916.281	1981.286	2033.665	2076.617	#DIV/0!
5.8	26	FAIL	1827.671	1494.1	1623.378	1751.619	1852.053	1929.617	1990.495	2039.26	2079.079	#DIV/0!
5.8	28	FAIL	1739.872	1505.419	1645.229	1771.452	1867.777	1941.241	1998.47	2044.082	2081.193	#DIV/0!
5.8	30	FAIL	1672.578	1518.633	1665.613	1789.306	1881.719	1951.46	2005.442	2048.282	2083.029	#DIV/0!
5.8	32	FAIL	1620.971	1532.882	1684.572	1805.442	1894.16	1960.512	2011.589	2051.972	2084.639	#DIV/0!
5.8	34	FAIL	1581.493	1547.605	1702.188	1820.082	1905.326	1968.585	2017.049	2055.241	2086.061	#DIV/0!
5.8	36	FAIL	1551.478	1562.431	1718.557	1833.416	1915.401	1975.83	2021.931	2058.156	2087.327	#DIV/0!
5.8	38	FAIL	1528.904	1577.12	1733.777	1845.605	1924.535	1982.367	2026.322	2060.771	2088.461	#DIV/0!
5.8	40	FAIL	1512.222	1591.513	1747.946	1856.785	1932.854	1988.295	2030.292	2063.132	2089.483	#DIV/0!
5.8	42	FAIL	1500.23	1605.514	1761.153	1867.073	1940.461	1993.695	2033.899	2065.272	2090.409	#DIV/0!
5.8	44	FAIL	1491.992	1619.063	1773.483	1876.569	1947.442	1998.633	2037.191	2067.222	2091.251	#DIV/0!
5.8	46	FAIL	1486.767	1632.128	1785.013	1885.36	1953.871	2003.168	2040.207	2069.006	2092.02	#DIV/0!
5.8	48	FAIL	1483.969	1644.694	1795.811	1893.519	1959.812	2007.345	2042.98	2070.645	2092.726	#DIV/0!
5.8	50	FAIL	1483.131	1656.762	1805.941	1901.112	1965.316	2011.206	2045.539	2072.154	2093.376	#DIV/0!
6.3	10	FAIL	6713.665	2920.584	1959.003	1638.923	1523.965	1487.546	1484.301	1495.651	1513.285	#DIV/0!
6.3	12	FAIL	5537.826	2498.039	1792.82	1573.49	1501.545	1483.554	1487.269	1499.914	1515.971	#DIV/0!
6.3	14	FAIL	4701.573	2225.282	1692.224	1536.725	1490.767	1483.289	1490.529	1503.358	1517.963	#DIV/0!
6.3	16	FAIL	4087.193	2040.5	1627.944	1515.036	1485.696	1484.552	1493.611	1506.161	1519.498	#DIV/0!
6.3	18	FAIL	3623.662	1910.516	1585.177	1501.856	1483.605	1486.423	1496.392	1508.474	1520.716	#DIV/0!
6.3	20	FAIL	3266.113	1816.29	1555.84	1493.74	1483.133	1488.49	1498.862	1510.408	1521.706	#DIV/0!
6.3	22	FAIL	2985.103	1746.292	1535.239	1488.761	1483.56	1490.564	1501.046	1512.046	1522.526	#DIV/0!
6.3	24	FAIL	2760.677	1693.229	1520.516	1485.786	1484.485	1492.559	1502.979	1513.45	1523.217	#DIV/0!
6.3	26	FAIL	2578.936	1652.316	1509.86	1484.123	1485.678	1494.438	1504.696	1514.665	1523.806	#DIV/0!
6.3	28	FAIL	2429.964	1620.316	1502.08	1483.333	1487.005	1496.19	1506.227	1515.726	1524.315	#DIV/0!
6.3	30	FAIL	2306.541	1594.98	1496.376	1483.131	1488.383	1497.814	1507.598	1516.661	1524.758	#DIV/0!
6.3	32	FAIL	2203.311	1574.712	1492.195	1483.328	1489.766	1499.316	1508.832	1517.491	1525.148	#DIV/0!
6.3	34	FAIL	2116.235	1558.353	1489.145	1483.793	1491.124	1500.704	1509.947	1518.232	1525.494	#DIV/0!
6.3	36	FAIL	2042.226	1545.047	1486.947	1484.441	1492.44	1501.989	1510.959	1518.897	1525.803	#DIV/0!
6.3	38	FAIL	1978.889	1534.156	1485.396	1485.208	1493.705	1503.178	1511.882	1519.498	1526.08	#DIV/0!
6.3	40	FAIL	1924.348	1525.192	1484.34	1486.051	1494.916	1504.281	1512.726	1520.044	1526.331	#DIV/0!
6.3	42	FAIL	1877.114	1517.781	1483.665	1486.94	1496.069	1505.305	1513.5	1520.541	1526.558	#DIV/0!
6.3	44	FAIL	1835.997	1511.632	1483.287	1487.853	1497.166	1506.259	1514.213	1520.996	1526.765	#DIV/0!
6.3	46	FAIL	1800.035	1506.515	1483.138	1488.773	1498.208	1507.147	1514.872	1521.414	1526.954	#DIV/0!
6.3	48	FAIL	1768.445	1502.248	1483.169	1489.691	1499.197	1507.978	1515.482	1521.8	1527.128	#DIV/0!
6.3	50	FAIL	1740.583	1498.687	1483.339	1490.599	1500.137	1508.754	1516.049	1522.156	1527.289	#DIV/0!
6.8	10	FAIL	8437.607	4190.173	2878.484	2315.3	2025.78	1858.925	1754.846	1686.043	1638.496	#DIV/0!
6.8	12	FAIL	7185.274	3646.213	2606.116	2166.156	1940.302	1809.42	1726.984	1671.802	1633.106	#DIV/0!
6.8	14	FAIL	6269.261	3272.6	2422.596	2066.021	1882.691	1775.786	1707.852	1661.901	1629.306	#DIV/0!
6.8	16	FAIL	5577.21	3003.338	2291.914	1994.739	1841.477	1751.54	1693.934	1654.625	1626.484	#DIV/0!
6.8	18	FAIL	5040.344	2801.85	2194.848	1941.71	1810.655	1733.279	1683.369	1649.056	1624.306	#DIV/0!
6.8	20	FAIL	4614.583	2646.467	2120.316	1900.884	1786.799	1719.055	1675.082	1644.658	1622.574	#DIV/0!
6.8	22	FAIL	4270.582	2523.642	2061.53	1868.579	1767.825	1707.676	1668.413	1641.097	1621.164	#DIV/0!
6.8	24	FAIL	3988.169	2424.536	2014.13	1842.438	1752.395	1698.373	1662.932	1638.157	1619.993	#DIV/0!
6.8	26	FAIL	3753.09	2343.163	1975.198	1820.887	1739.616	1690.631	1658.35	1635.687	1619.007	#DIV/0!
6.8	28	FAIL	3555.033	2275.346	1942.716	1802.838	1728.866	1684.09	1654.463	1633.583	1618.163	#DIV/0!
6.8	30	FAIL	3386.381	2218.093	1915.248	1787.519	1719.704	1678.493	1651.124	1631.771	1617.434	#DIV/0!
6.8	32	FAIL	3241.405	2169.21	1891.748	1774.364	1711.806	1673.651	1648.226	1630.193	1616.797	#DIV/0!
6.8	34	FAIL	3115.723	2127.057	1871.437	1762.953	1704.931	1669.421	1645.686	1628.806	1616.237	#DIV/0!
6.8	36	FAIL	3005.936	2090.385	1853.722	1752.966	1698.893	1665.696	1643.444	1627.579	1615.739	#DIV/0!
6.8	38	FAIL	2909.374	2058.229	1838.148	1744.157	1693.551	1662.389	1641.448	1626.484	1615.295	#DIV/0!
6.8	40	FAIL	2823.913	2029.834	1824.357	1736.332	1688.79	1659.436	1639.662	1625.502	1614.896	#DIV/0!
6.8	42	FAIL	2747.846	2004.599	1812.068	1729.337	1684.523	1656.782	1638.053	1624.616	1614.535	#DIV/0!
6.8	44	FAIL	2679.787	1982.042	1801.052	1723.048	1680.677	1654.384	1636.596	1623.813	1614.207	#DIV/0!
6.8	46	FAIL	2618.603	1961.773	1791.126	1717.366	1677.192	1652.207	1635.272	1623.081	1613.908	#DIV/0!
6.8	48	FAIL	2563.355	1943.471	1782.139	1712.206	1674.021	1650.222	1634.062	1622.412	1613.635	#DIV/0!
6.8	50	FAIL	2513.264	1926.873	1773.966	1707.502	1671.124	1648.405	1632.953	1621.798	1613.383	#DIV/0!

A2.2.2 r as a function of Th

What have we learned from Method 2 (see main text, Chapter 5) in terms of restrictions on the variables? First, we want to note that one thing we learned from best solution mapping was that the contaminant Th and r have an intricate relationship for any given contaminant element/Th ratio. At a given ratio, there is a trade-off between contaminant Th and r such that a higher Th is needed for small r and lower Th is needed for large r. We can see this clearly as the green hyperbolic pattern in the lower part of Table A2.3. As long as a contaminant has a consistent ratio of element/Th, then r and Th do not necessarily have to remain fixed to give a good solution. Thus, there is a possibility that there may be more evolved and less evolved contaminant with the same element/Th ratio, and that r and Th can vary.

The r-Th dependency may have a physical explanation, where at a given element/Th ratio a higher Th means the contaminant is more evolved, but if it is evolved perhaps it exists at a slightly lower melt fraction and there is less of it available to be assimilated. This would lead to a lower r (mass assimilant/mass crystallized). On the other hand, lower Th would mean it is less evolved, perhaps meaning there is more of it available, and a higher r would therefore accompany assimilation of this lower Th assimilant.

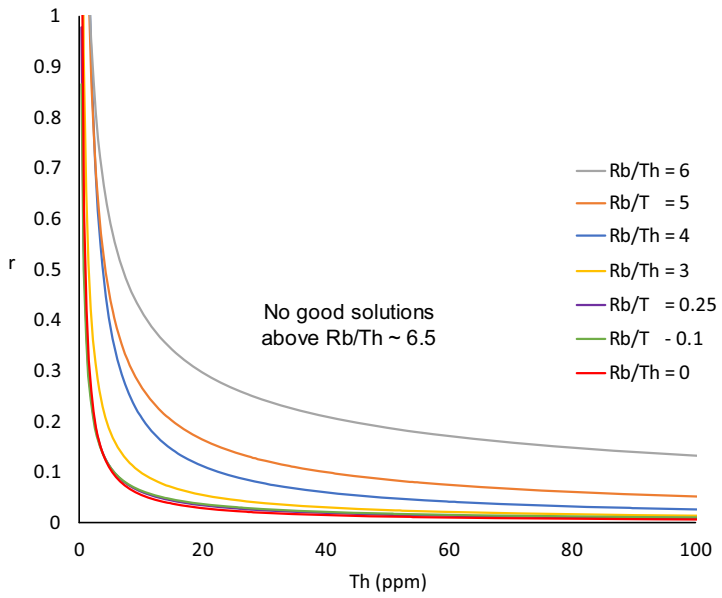

Figure A2.1: Example "map" of parameters giving minimum SSD for different ratios of Rb/Th (for the high Nb series). Each line shows the r-Th pairs that give the minimum sum of squares difference (SSD) for a particular Rb/Th ratio. The lines converge as Rb/Th approaches zero. Above Rb/Th of ~ 6.5, the minimum SSD cannot be attained and SSDs only increase.

Changing the contaminant Th does not affect the trajectory of the AFC trend, because the trajectory will follow the ratio, but there needs to be sufficient contaminant Th to get the model to pass the failure criteria (which is not very much; on the order of ~1 ppm Th). At high contaminant element/Th ratios, the value of r also does not change the trajectory, as in this scenario it basically just represents the amount of mixing, and the data does not need much mixing to occur for it to produce a good model (Figure A2.1).

Solutions also converged at low contaminant element/Th ratios, because at these low ratios, the numerator approaches zero and the contaminant Th is the main contributor to the trajectory of the model (Figure A2.1). The convergence point of the curves defining good solutions shows the range of contaminant Th and r solution pairs that exist when only Th is added from the contaminant and when no contribution from the numerator of the contaminant element/Th ratio is taken into account (i.e. the numerator approaches zero).

References

Aeolus Lee C-T, Leeman WP, Canil D, Li Z-XA (2005) Similar V/Sc systematics in MORB and arc basalts: Implications for the oxygen fugacities of their mantle source regions. Journal of Petrology 46:2313–2336. https://doi.org/10.1093/petrology/egi056

Albarède F (2009) Geochemistry: an introduction. Cambridge University Press

Allègre CJ (1982) Chemical geodynamics. Tectonophysics 81:109–132

Allègre CJ, Treuil M, Minster J-F, et al (1977) Systematic use of trace element in igneous process. Part I: Fractional Crystallization Processes in Volcanic Suites. Contributions to Mineralogy and Petrology 60:57–75

Alvarez W (1982) Geological evidence for the geographical pattern of mantle return flow and the driving mechanism of plate tectonics. Journal of Geophysical Research: Solid Earth 87:6697–6710

Anderson A (1974) Evidence for a picritic, volatile-rich magma beneath Mt. Shasta, California. Journal of Petrology 15:243–267

Anderson A (1976) Magma mixing: petrological process and volcanological tool. Journal of Volcanology and Geothermal Research 1:3–33

Andújar J, Scaillet B, Pichavant M, Druitt TH (2015) Differentiation Conditions of a Basaltic Magma from Santorini, and its Bearing on the Production of Andesite in Arc Settings. Journal of Petrology 56:765–794. https://doi.org/10.1093/petrology/egv016

Andújar J, Scaillet B, Pichavant M, Druitt TH (2016) Generation Conditions of Dacite and Rhyodacite via the Crystallization of an Andesitic Magma. Implications for the Plumbing System at Santorini (Greece) and the Origin of Tholeiitic or Calc-alkaline Differentiation Trends in Arc Magmas. Journal of Petrology 57:1887–1920. https://doi.org/10.1093/petrology/egw061

Annen C (2009) From plutons to magma chambers: Thermal constraints on the accumulation of eruptible silicic magma in the upper crust. Earth and Planetary Science Letters 284:409–416. https://doi.org/10.1016/j.epsl.2009.05.006

Annen C, Blundy JD, Sparks RSJ (2006) The Genesis of Intermediate and Silicic Magmas in Deep Crustal Hot Zones. Journal of Petrology 47:505–539. https://doi.org/10.1093/petrology/egi084

Antonopoulos J (1992) The great Minoan eruption of Thera volcano and the ensuing tsunami in the Greek Archipelago. Natural Hazards 5:153–168

Antoshechkina P, Asimow P (2016) alphaMELTS Software Manual

Arculus RJ (1994) Aspects of magma genesis in arcs. Lithos 33:189–208. https://doi.org/10.1016/0024-4937(94)90060-4

Ariskin AA, Barmina GS (2004) COMAGMAT: Development of a Magma Crystallization Model and Its Petrological Applications. 42:157

Athanassas CD, Bourlès DL, Braucher R, et al (2016) Evidence from cosmic ray exposure (CRE) dating for the existence of a pre-Minoan caldera on Santorini, Greece. Bulletin of Volcanology 78:. https://doi.org/10.1007/s00445-016-1026-3

Athanassas CD, Modis K, Alçiçek MC, Theodorakopoulou K (2018) Contouring the Cataclysm: A Geographical Analysis of the Effects of the Minoan Eruption of the Santorini Volcano. Environmental Archaeology 23:160–176. https://doi.org/10.1080/14614103.2017.1288885

Ayers J (1998) Trace element modeling of aqueous fluid–peridotite interaction in the mantle wedge of subduction zones. Contributions to Mineralogy and Petrology 132:390–404

Bachmann O, Bergantz G (2008) The Magma Reservoirs That Feed Supereruptions. Elements 4:17–21. https://doi.org/10.2113/GSELEMENTS.4.1.17

Bachmann O, Bergantz GW (2004) On the origin of crystal-poor rhyolites: extracted from batholithic crystal mushes. Journal of Petrology 45:1565–1582

Bacon CR, Bruggman PE, Christiansen RL, et al (1997) Primitive magmas at five Cascades volcanic fields: Melts from hot, heterogeneous sub-arc mantle. Canadian Mineralogist 35:397–424

Bacon CR, Newman S, Stolper EM (1992) Water, CO2, Cl, and F in melt inclusions in phenocrysts from three Holocene explosive eruptions, Crater Lake, Oregon. American Mineralogist 77:1021–1030

Bailey JC, Jensen ES, Hansen A, et al (2009) Formation of heterogeneous magmatic series beneath North Santorini, South Aegean island arc. Lithos 110:20–36. https://doi.org/10.1016/j.lithos.2008.12.002

Barka A, Reilinger R (1997) Active tectonics of the Eastern Mediterranean region: deduced from GPS, neotectonic and seismicity data. Annals of Geophysics 40:

Barton M, Huijsmans JPP (1986) Post-caldera dacites from the Santorini volcanic complex, Aegean Sea, Greece: an example of the eruption of lavas of near-constant composition over a 2,200 year period. Contributions to Mineralogy and Petrology 94:472–495. https://doi.org/10.1007/BF00376340

Barton M, Salters V, Huijsmans J (1983) Sr isotope and trace element evidence for the role of continental crust in calc-alkaline volcanism on Santorini and Milos, Aegean Sea, Greece. Earth and Planetary Science Letters 63:273–291

Batanova VG, Savelieva GN (2009) Melt migration in the mantle beneath spreading zones and formation of replacive dunites: a review. Russian Geology and Geophysics 50:763–778. https://doi.org/10.1016/j.rgg.2009.08.008

Baziotis I, Kimura J-I, Pantazidis A, et al (2018) Geophysical source conditions for basaltic lava from Santorini volcano based on geochemical modeling. Lithos 316–317:295–303. https://doi.org/10.1016/j.lithos.2018.07.027

Beattie P (1993) Olivine-melt and orthopyroxene-melt equilibria. Contributions to Mineralogy and Petrology 115:103–111. https://doi.org/10.1007/BF00712982

Ben Othman D, White WM, Patchett J (1989) The geochemistry of marine sediments, island arc magma genesis, and crust-mantle recycling. Earth and Planetary Science Letters 94:1–21. https://doi.org/10.1016/0012-821X(89)90079-4

Bézos A, Escrig S, Langmuir CH, et al (2009) Origins of chemical diversity of back-arc basin basalts: A segment-scale study of the Eastern Lau Spreading Center. Journal of Geophysical Research: Solid Earth 114:

Biju-Duval B, Letouzey J, Montadert L, et al (1974) Geology of the Mediterranean Sea basins. In: The geology of continental margins. Springer, pp 695–721

Bindeman IN, Bailey JC (1999) Trace elements in anorthite megacrysts from the Kurile Island Arc: a window to across-arc geochemical variations in magma compositions. Earth and Planetary Science Letters 169:209–226

Biryol CB, Beck SL, Zandt G, Özacar AA (2011) Segmented African lithosphere beneath the Anatolian region inferred from teleseismic P-wave tomography: Segmented lithosphere beneath Anatolia. Geophysical Journal International 184:1037–1057. https://doi.org/10.1111/j.1365-246X.2010.04910.x

Blum JD, Blum AE, Davis TE, Dillon JT (1987) Petrology of cogenetic silica-saturated and-oversaturated plutonic rocks in the Ruby geanticline of north-central Alaska. Canadian Journal of Earth Sciences 24:159–169

Blundy JD, Shimizu N (1991) Trace element evidence for plagioclase recycling in calc-alkaline magmas. Earth and Planetary Science Letters 102:178–197. https://doi.org/10.1016/0012-821X(91)90007-5

Bond A, Sparks RSJ (1976) The Minoan eruption of Santorini, Greece. Journal of the Geological Society 132:1–16. https://doi.org/10.1144/gsjgs.132.1.0001

Boström K, Joensuu O, Moore C, et al (1973) Geochemistry of barium in pelagic sediments. Lithos 6:159–174

Bowen N (1919) Crystallization-differentiation in igneous magmas. The Journal of Geology 27:393–430

Boyle, C. Julie (1994) Formation des enclaves comagmatiques de Santorin (Grèce): Implications au niveau de l'éruption Minoënne. Master's Thesis, Université Blaise Pascal

Brenan J, Shaw H, Phinney D, Ryerson F (1994) Rutile-aqueous fluid partitioning of Nb, Ta, Hf, Zr, U and Th: implications for high field strength element depletions in island-arc basalts. Earth and Planetary Science Letters 128:327–339

Brenan JM, Shaw HF, Ryerson FJ, Phinney DL (1995) Experimental determination of trace-element partitioning between pargasite and a synthetic hydrous andesitic melt. Earth and Planetary Science Letters 135:1–11. https://doi.org/10.1016/0012-821X(95)00139-4

Briqueu L, Javoy M, Lancelot J, Tatsumoto M (1986) Isotope geochemistry of recent magmatism in the Aegean arc: Sr, Nd, Hf, and O isotopic ratios in the lavas of Milos and Santorini—geodynamic implications. Earth and Planetary Science Letters 80:41–54

Bucholz CE, Gaetani GA, Behn MD, Shimizu N (2013) Post-entrapment modification of volatiles and oxygen fugacity in olivine-hosted melt inclusions. Earth and Planetary Science Letters 374:145–155

Bureau H, Keppler H (1999) Complete miscibility between silicate melts and hydrous fluids in the upper mantle: experimental evidence and geochemical implications. Earth and Planetary Science Letters 165:187–196

Cadoux A, Scaillet B, Bekki S, et al (2015) Stratospheric Ozone destruction by the Bronze-Age Minoan eruption (Santorini Volcano, Greece). Sci Rep 5:12243. https://doi.org/10.1038/srep12243

Cadoux A, Scaillet B, Druitt TH, Deloule E (2014) Magma storage conditions of large Plinian eruptions of Santorini Volcano (Greece). Journal of Petrology 55:1129–1171. https://doi.org/10.1093/petrology/egu021

Canil D (1997) Vanadium partitioning and the oxidation state of Archaean komatiite magmas. Nature 389:842

Canil D (2002) Vanadium in peridotites, mantle redox and tectonic environments: Archean to present. Earth and Planetary Science Letters 195:75–90

Cashman KV, Giordano G (2014) Calderas and magma reservoirs. Journal of Volcanology and Geothermal Research 288:28–45. https://doi.org/10.1016/j.jvolgeores.2014.09.007

Castillo PR (2012) Adakite petrogenesis. Lithos 134–135:304–316. https://doi.org/10.1016/j.lithos.2011.09.013

Chen W, Xiong X, Wang J, et al (2018) TiO2 Solubility and Nb and Ta Partitioning in Rutile-Silica-Rich Supercritical Fluid Systems: Implications for Subduction Zone Processes. J Geophys Res Solid Earth 123:4765–4782. https://doi.org/10.1029/2018JB015808

Chen Y, Provost A, Schiano P, Cluzel N (2011) The rate of water loss from olivine-hosted melt inclusions. Contributions to Mineralogy and Petrology 162:625–636

Chin EJ, Shimizu K, Bybee GM, Erdman ME (2018) On the development of the calc-alkaline and tholeiitic magma series: A deep crustal cumulate perspective. Earth and Planetary Science Letters 482:277–287

Clift P, Vannucchi P (2004) Controls on tectonic accretion versus erosion in subduction zones: Implications for the origin and recycling of the continental crust. Reviews of Geophysics 42:

Clift PD, Vannucchi P, Morgan JP (2009) Crustal redistribution, crust–mantle recycling and Phanerozoic evolution of the continental crust. Earth-Science Reviews 97:80–104

Codillo EA, Le Roux V, Marschall HR (2018) Arc-like magmas generated by mélange-peridotite interaction in the mantle wedge. Nature Communications 9:. https://doi.org/10.1038/s41467-018-05313-2

Cohen R, O'Nions R (1982) The Lead, Neodymium and Strontium Isotopic Structure of Ocean Ridge Basalts. Journal of Petrology 23:299–324

Cooper KM, Kent AJ (2014) Rapid remobilization of magmatic crystals kept in cold storage. Nature 506:480

Cottrell E, Gardner JE, Rutherford MJ (1999) Petrologic and experimental evidence for the movement and heating of the pre-eruptive Minoan rhyodacite (Santorini, Greece). Contributions to Mineralogy and Petrology 135:315–331. https://doi.org/10.1007/s004100050514

Cottrell E, Spiegelman M, Langmuir C (2002) Consequences of diffusive reequilibration for the interpretation of melt inclusions. Geochemistry, Geophysics, Geosystems 3:1–26

Cousens BL, Allan JF, Leybourne MI, et al (1995) Mixing of magmas from enriched and depleted mantle sources in the northeast Pacific: West Valley segment, Juan de Fuca Ridge. Contributions to Mineralogy and Petrology 120:337–357

Crawford AJ, Falloon TJ, Eggins S (1987) The origin of island arc high-alumina basalts. Contributions to Mineralogy and Petrology 97:417–430

Daly RA (1933) The depths of the Earth. Bulletin of the Geological Society of America 44:243–264

Danyushevsky L, Della-Pasqua F, Sokolov S (2000) Re-equilibration of melt inclusions trapped by magnesian olivine phenocrysts from subduction-related magmas: petrological implications. Contributions to Mineralogy and Petrology 138:68–83

Danyushevsky L, Plechov P (2011) Petrolog v. 3 Manual.pdf

Danyushevsky LV, Sokolov S, Falloon TJ (2002) Melt inclusions in olivine phenocrysts: using diffusive re-equilibration to determine the cooling history of a crystal, with implications for the origin of olivine-phyric volcanic rocks. Journal of Petrology 43:1651–1671

Davidson J, Turner S, Handley H, et al (2007a) Amphibole "sponge" in arc crust? Geology 35:787. https://doi.org/10.1130/G23637A.1

Davidson JP, Morgan DJ, Charlier BLA, et al (2007b) Microsampling and Isotopic Analysis of Igneous Rocks: Implications for the Study of Magmatic Systems. Annu Rev Earth Planet Sci 35:273–311. https://doi.org/10.1146/annurev.earth.35.031306.140211

Davies GF (1999) Geophysically constrained mantle mass flows and the 40Ar budget: a degassed lower mantle? Earth and Planetary Science Letters 166:149–162

Davis E, Gartzos E, Dietrich V (1998) Magmatic evolution of the Pleistocene Akrotiri volcanoes. pp 2–4

Debari SM, Sleep NH (1991) High-Mg, low-Al bulk composition of the Talkeetna island arc, Alaska: Implications for primary magmas and the nature of arc crust. Geological Society of America Bulletin 103:37–47

Defant MJ, Drummond MS (1990) Derivation of some modern arc magmas by melting of young subducted lithosphere. Nature 347:662

Defant MJ, Drummond MS (1993) Mount St. Helens: potential example of the partial melting of the subducted lithosphere in a volcanic arc. Geology 21:547–550

Delibasis N, Chailas S, Lagios E, Drakopoulos J (1990) Surveillance of Thera volcano, Greece: microseismicity monitoring. Thera and the Aegean World III 2:199–206

DePaolo DJ (1981) Trace element and isotopic effects of combined wallrock assimilation and fractional crystallization. Earth and Planetary Science Letters 53:189–202. https://doi.org/10.1016/0012-821X(81)90153-9

DePaolo DJ, Wasserburg GJ (1976) Nd isotopic variations and petrogenetic models. Geophysical Research Letters 3:249–252. https://doi.org/10.1029/GL003i005p00249

Dilek Y, Altunkaynak Ş (2009) Geochemical and temporal evolution of Cenozoic magmatism in western Turkey: mantle response to collision, slab break-off, and lithospheric tearing in an orogenic belt. Geological Society, London, Special Publications 311:213–233. https://doi.org/10.1144/SP311.8

Dohmen R, Becker H-W, Chakraborty S (2007) Fe–Mg diffusion in olivine I: experimental determination between 700 and 1,200 C as a function of composition, crystal orientation and oxygen fugacity. Physics and Chemistry of Minerals 34:389–407

Druitt T, Francaviglia V (1992) Caldera formation on Santorini and the physiography of the islands in the late Bronze Age. Bulletin of Volcanology 54:484–493. https://doi.org/10.1007/BF00301394

Druitt T, Mercier M, Florentin L, et al (2016) Magma storage and extraction associated with Plinian and Interplinian activity at Santorini caldera (Greece). Journal of Petrology 57:461–494

Druitt TH (2014) New insights into the initiation and venting of the Bronze-Age eruption of Santorini (Greece), from component analysis. Bulletin of Volcanology 76:. https://doi.org/10.1007/s00445-014-0794-x

Druitt TH (ed) (1999) Santorini Volcano. Geological Society, London

Druitt TH, Costa F, Deloule E, et al (2012) Decadal to monthly timescales of magma transfer and reservoir growth at a caldera volcano. Nature 482:77–80. https://doi.org/10.1038/nature10706

Druitt TH, Edwards L, Mellors R, et al (1999) Santorini volcano. Geological Society Memoir 19:

Druitt TH, Francalanci L, Fabbro, G (2015) Field guide to Santorini Volcano. p 57

Druitt TH, McCoy FW (2019) The Late Bronze Age Eruption of Santorini Volcano and Its Impact on the Ancient Mediterranean World. 6

Druitt TH, Pyle DM, Mather TA (2019) Santorini Volcano and its Plumbing System. 8

Drummond M, Defant M, Kepezhinskas P (1996) Petrogenesis of slab-derived trondhjemite–tonalite–dacite/adakite magmas. Earth and Environmental Science Transactions of the Royal Society of Edinburgh 87:205–215

Ducea MN, Saleeby JB, Bergantz G (2015) The architecture, chemistry, and evolution of continental magmatic arcs. Annual Review of Earth and Planetary Sciences 43:299–331

Dufek J, Bachmann O (2010) Quantum magmatism: Magmatic compositional gaps generated by melt-crystal dynamics. Geology 38:687–690. https://doi.org/10.1130/G30831.1

Dufek J, Bergantz G (2005) Lower crustal magma genesis and preservation: a stochastic framework for the evaluation of basalt–crust interaction. Journal of Petrology 46:2167–2195

Dunbar NW, Hervig RL (1992) Volatile and trace element composition of melt inclusions from the Lower Bandelier Tuff: implications for magma chamber processes and eruptive style. Journal of Geophysical Research: Solid Earth 97:15151–15170

Eastwood W, Tibby J, Roberts N, et al (2002) The environmental impact of the Minoan eruption of Santorini (Thera): statistical analysis of palaeoecological data from Golbisar, southwest Turkey. The Holocene 12:431–444

Eichelberger J (1978) Andesitic volcanism and crustal evolution. Nature 275:21

Elburg MA, Smet I, De Pelsmaeker E (2014) Influence of source materials and fractionating assemblage on magmatism along the Aegean Arc, and implications for crustal growth. Geological Society, London, Special Publications 385:137–160. https://doi.org/10.1144/SP385.1

Ellam RM, Hawkesworth CJ (1988) Elemental and isotopic variations in subduction related basalts: evidence for a three component model. Contributions to Mineralogy and Petrology 98:72–80. https://doi.org/10.1007/BF00371911

Elliott T (2003) Tracers of the slab. Geophysical Monograph-American Geophysical Union 138:23–46

Elliott T, Plank T, Zindler A, et al (1997) Element transport from slab to volcanic front at the Mariana arc. Journal of Geophysical Research: Solid Earth 102:14991–15019

Elsasser WM (1971) Two-layer model of upper-mantle circulation. Journal of Geophysical Research 76:4744–4753

Fabbro, Gareth (2014) The timescales of magmatic processes prior to a caldera-forming eruption. Doctoral Thesis, Université Blaise Pascal

Fabbro GN, Druitt TH, Costa F (2017) Storage and Eruption of Silicic Magma across the Transition from Dominantly Effusive to Caldera-forming States at an Arc Volcano (Santorini, Greece). Journal of Petrology 58:2429–2464. https://doi.org/10.1093/petrology/egy013

Fabbro GN, Druitt TH, Scaillet S (2013) Evolution of the crustal magma plumbing system during the build-up to the 22-ka caldera-forming eruption of Santorini (Greece). Bulletin of Volcanology 75:. https://doi.org/10.1007/s00445-013-0767-5

Falloon TJ, Danyushevsky LV, Ariskin A, et al (2007) The application of olivine geothermometry to infer crystallization temperatures of parental liquids: Implications for the temperature of MORB magmas. Chemical Geology 241:207–233

Ferrando S, Frezzotti M, Dallai L, Compagnoni R (2005) Multiphase solid inclusions in UHP rocks (Su-Lu, China): Remnants of supercritical silicate-rich aqueous fluids released during continental subduction. Chemical Geology 223:68–81

Ferrara G, Fytikas M, Giuliani O, Marinelli G (1980) Age of the formation of the Aegean active volcanic arc. Thera and the Aegean world II 37:41

Flaherty T, Druitt TH, Tuffen H, et al (2018) Multiple timescale constraints for high-flux magma chamber assembly prior to the Late Bronze Age eruption of Santorini (Greece). Contributions to Mineralogy and Petrology 173:. https://doi.org/10.1007/s00410-018-1490-1

Foley SF, Barth MG, Jenner GA (2000) Rutile/melt partition coefficients for trace elements and an assessment of the influence of rutile on the trace element characteristics of subduction zone magmas. Geochimica et Cosmochimica Acta 64:933–938

Ford CE, Russell DG, Craven JA, Fisk MR (1983) Olivine-liquid equilibria: Temperature, pressure and composition dependence of the crystal/liquid cation

partition coefficients for Mg, Fe2+, Ca and Mn. Journal of Petrology 24:256–266. https://doi.org/10.1093/petrology/24.3.256

Francalanci L, Davies GR, Lustenhouwer W, et al (2005a) Intra-Grain Sr Isotope Evidence for Crystal Recycling and Multiple Magma Reservoirs in the Recent Activity of Stromboli Volcano, Southern Italy. Journal of Petrology 46:1997–2021. https://doi.org/10.1093/petrology/egi045

Francalanci L, Vougioukalakis G, Eleftheriadis G, et al (1998) Petrographic, chemical and isotope variations in the intracaldera post-Minoan rocks of the Santorini volcanic field, Greece. pp 175–186

Francalanci L, Vougioukalakis G, Perini G, Manetti P (2005b) A West-East Traverse along the magmatism of the south Aegean volcanic arc in the light of volcanological, chemical and isotope data. In: Developments in Volcanology. Elsevier, pp 65–111

Francalanci L, Zellmer GF (2019) Magma Genesis at the South Aegean Volcanic Arc. 6

Friedrich W, Wagner P, Tauber H (1990) Radiocarbon dated plant remains from the Akrotiri excavation on Santorini, Greece. Thera and the Aegean world III 3:188–196

Friedrich WL, Kromer B, Friedrich M, et al (2006) Santorini eruption radiocarbon dated to 1627-1600 BC. Science 312:548–548

Friedrich WL, Sigalas N (2009) The effects of the Minoan eruption. In: Time's Up! Dating the Minoan Eruption of Santorini. Aarhus Universitetsforlag, pp 91–100

Fytikas M, Innocenti F, Kolios N, et al (1986) Volcanology and petrology of volcanic products from the island of Milos and neighbouring islets. Journal of Volcanology and Geothermal Research 28:297–317. https://doi.org/10.1016/0377-0273(86)90028-4

Fytikas M, Vougioukalakis G (2005) The South Aegean Active Volcanic Arc: Present Knowledge and Future Perspectives. Elsevier

Gaetani GA, Grove TL (1998) The influence of water on melting of mantle peridotite. Contributions to Mineralogy and Petrology 131:323–346

Gaetani GA, Watson EB (2000) Open system behavior of olivine-hosted melt inclusions. Earth and Planetary Science Letters 183:27–41. https://doi.org/10.1016/S0012-821X(00)00260-0

Gale A, Dalton CA, Langmuir CH, et al (2013) The mean composition of ocean ridge basalts. Geochemistry, Geophysics, Geosystems 14:489–518

Ganne J, Bachmann O, Feng X (2018) Deep into magma plumbing systems: Interrogating the crystal cargo of volcanic deposits. Geology 46:415–418. https://doi.org/10.1130/G39857.1

Garfunkel Z, Anderson C, Schubert G (1986) Mantle circulation and the lateral migration of subducted slabs. Journal of Geophysical Research: Solid Earth 91:7205–7223

Gartzos E, Dietrich VJ, Davis E (1998) Magma mixing in basaltic andesites of Cape Mavrorachidi (Akrotiri Volcanoes). pp 81–88

Georgalas G (1953) L'éruption du volcan de Santorin en 1950. Bulletin of Volcanology 13:39–55

George R, Turner S, Hawkesworth C, et al (2003) Melting processes and fluid and sediment transport rates along the Alaska-Aleutian arc from an integrated U-Th-Ra-Be isotope study. Journal of Geophysical Research: Solid Earth 108:

George R, Turner S, Morris J, et al (2005) Pressure–temperature–time paths of sediment recycling beneath the Tonga–Kermadec arc. Earth and Planetary Science Letters 233:195–211

Gertisser R, Preece K, Keller J (2009) The Plinian Lower Pumice 2 eruption, Santorini, Greece: Magma evolution and volatile behaviour. Journal of Volcanology and Geothermal Research 186:387–406. https://doi.org/10.1016/j.jvolgeores.2009.07.015

Ghikas C, Dilek Y, Rassios AE (2010) Structure and tectonics of subophiolitic mélanges in the western Hellenides (Greece): implications for ophiolite emplacement tectonics. International Geology Review 52:423–453. https://doi.org/10.1080/00206810902951106

Gill JB (1981) Orogenic andesites and plate tectonics. Springer Science & Business Media

Glazner AF, Coleman DS, Bartley JM (2008) The tenuous connection between high-silica rhyolites and granodiorite plutons. Geol 36:183. https://doi.org/10.1130/G24496A.1

Gordeychik B, Churikova T, Kronz A, et al (2018) Growth of, and diffusion in, olivine in ultra-fast ascending basalt magmas from Shiveluch volcano. Scientific reports 8:11775

Govers R, Wortel M (2005) Lithosphere tearing at STEP faults: Response to edges of subduction zones. Earth and Planetary Science Letters 236:505–523

Greene AR, DeBari SM, Kelemen PB, et al (2006) A detailed geochemical study of island arc crust: the Talkeetna arc section, south–central Alaska. Journal of Petrology 47:1051–1093

Griffin W, Doyle B, Ryan C, et al (1999) Layered mantle lithosphere in the Lac de Gras area, Slave craton: composition, structure and origin. Journal of Petrology 40:705–727

Grove TL, Baker MB (1984) Phase equilibrium controls on the tholeiitic versus calc-alkaline differentiation trends. Journal of Geophysical Research: Solid Earth 89:3253–3274. https://doi.org/10.1029/JB089iB05p03253

Grove TL, Elkins-Tanton LT, Parman SW, et al (2003) Fractional crystallization and mantle-melting controls on calc-alkaline differentiation trends. Contributions to Mineralogy and Petrology 145:515–533. https://doi.org/10.1007/s00410-003-0448-z

Grove TL, Till CB, Krawczynski MJ (2012) The role of H2O in subduction zone magmatism. Annual Review of Earth and Planetary Sciences 40:413–439

Gualda GAR, Sutton SR (2016) The Year Leading to a Supereruption. PLOS ONE 11:e0159200. https://doi.org/10.1371/journal.pone.0159200

Hawkesworth CJ, Gallagher K, Hergt JM, McDermott F (1993) Mantle and Slab Contributions in Arc Magmas. Annual Review of Earth and Planetary Sciences 21:175–204. https://doi.org/10.1146/annurev.ea.21.050193.001135

Hawkesworth CJ, Hergt J, Ellam R, McDermott F (1991) Element fluxes associated with subduction related magmatism. Philosophical Transactions of the Royal Society of London Series A: Physical and Engineering Sciences 335:393–405

Hawkesworth CJ, Vollmer R (1979) Crustal contamination versus enriched mantle: 143Nd/144Nd and 87Sr/86Sr evidence from the Italian volcanics. Contr Mineral and Petrol 69:151–165. https://doi.org/10.1007/BF00371858

Heiken G, McCoy F (1984) Caldera development during the Minoan eruption, Thira, Cyclades, Greece. Journal of Geophysical Research: Solid Earth 89:8441–8462

Hermann J, Rubatto D (2009) Accessory phase control on the trace element signature of sediment melts in subduction zones. Chemical Geology 265:512–526. https://doi.org/10.1016/j.chemgeo.2009.05.018

Hermann J, Spandler C, Hack A, Korsakov A (2006) Aqueous fluids and hydrous melts in high-pressure and ultra-high pressure rocks: Implications for element transfer in subduction zones. Lithos 92:399–417. https://doi.org/10.1016/j.lithos.2006.03.055

Herzberg C, Asimow PD (2008) Petrology of some oceanic island basalts: PRIMELT2.XLS software for primary magma calculation: PRIMELT2.XLS SOFTWARE FOR PRIMARY MAGMA CALCULATION. Geochemistry, Geophysics, Geosystems 9:n/a-n/a. https://doi.org/10.1029/2008GC002057

Herzberg C, Asimow PD, Arndt N, et al (2007) Temperatures in ambient mantle and plumes: Constraints from basalts, picrites, and komatiites: Mantle temperatures inferred from volcanoes. Geochem Geophys Geosyst 8:n/a-n/a. https://doi.org/10.1029/2006GC001390

Higgins MD (1996) Magma dynamics beneath Kameni volcano, Thera, Greece, as revealed by crystal size and shape measurements. Journal of Volcanology and

Geothermal Research 70:37–48. https://doi.org/10.1016/0377-0273(95)00045-3

Hildreth W (1979) The Bishop Tuff: Evidence for the origin of compositional zonation in silicic magma chambers. In: Geological Society of America Special Papers. Geological Society of America, pp 43–76

Hildreth W, Moorbath S (1988) Crustal contributions to arc magmatism in the Andes of Central Chile. Contributions to Mineralogy and Petrology 98:455–489. https://doi.org/10.1007/BF00372365

Hole MJ, Saunders AD, Marriner GF, Tarney J (1984) Subduction of pelagic sediments: implications for the origin of Ce-anomalous basalts from the Mariana Islands. Journal of the Geological Society 141:453–472. https://doi.org/10.1144/gsjgs.141.3.0453

Holness MB, Martin VM, Pyle DM (2005) Information about open-system magma chambers derived from textures in magmatic enclaves: the Kameni Islands, Santorini, Greece. Geological Magazine 142:637. https://doi.org/10.1017/S0016756805001172

Hooft EEE, Heath BA, Toomey DR, et al (2019) Seismic imaging of Santorini: Subsurface constraints on caldera collapse and present-day magma recharge. Earth and Planetary Science Letters 514:48–61. https://doi.org/10.1016/j.epsl.2019.02.033

Hooft EEE, Nomikou P, Toomey DR, et al (2017) Backarc tectonism, volcanism, and mass wasting shape seafloor morphology in the Santorini-Christiana-Amorgos region of the Hellenic Volcanic Arc. Tectonophysics 712–713:396–414. https://doi.org/10.1016/j.tecto.2017.06.005

Hora JM, Singer BS, Wörner G, et al (2009) Shallow and deep crustal control on differentiation of calc-alkaline and tholeiitic magma. Earth and Planetary Science Letters 285:75–86. https://doi.org/10.1016/j.epsl.2009.05.042

Huber C, Bachmann O, Dufek J (2010) The limitations of melting on the reactivation of silicic mushes. Journal of Volcanology and Geothermal Research 195:97–105. https://doi.org/10.1016/j.jvolgeores.2010.06.006

Hughes SS (1990) Mafic magmatism and associated tectonism of the central High Cascade Range, Oregon. Journal of Geophysical Research: Solid Earth 95:19623–19638

Huijsmans JPP (1985) Calc-alkaline lavas from the volcanic complex of Santorini, Aegean Sea, Greece: a petrological, geochemical and stratigraphic study. Doctoral Thesis, Instituut voor Aardwetenschappen Rijksuniversiteit Utrecht

Huijsmans JPP, Barton M (1989) Polybaric geochemical evolution of two shield volcanoes from Santorini, Aegean Sea, Greece: Evidence for zoned magma chambers from cyclic compositional variations. Journal of Petrology 30:583–625. https://doi.org/10.1093/petrology/30.3.583

Huijsmans JPP, Barton M, Salters VJM (1988) Geochemistry and evolution of the calc-alkaline volcanic complex of santorini, Aegean Sea, Greece. Journal of Volcanology and Geothermal Research 34:283–306. https://doi.org/10.1016/0377-0273(88)90039-X

Iacono Marziano G, Gaillard F, Pichavant M (2008) Limestone assimilation by basaltic magmas: an experimental re-assessment and application to Italian volcanoes. Contributions to Mineralogy and Petrology 155:719–738. https://doi.org/10.1007/s00410-007-0267-8

Ildefonse B, Blackman D, John B, et al (2007) Oceanic core complexes and crustal accretion at slow-spreading ridges. Geology 35:623–626

Irifune T (1993) Phase transformations in the earth's mantle and subducting slabs: Implications for their compositions, seismic velocity and density structures and dynamics. Island Arc 2:55–71

Irvine TN, Baragar WRA (1971) A Guide to the Chemical Classification of the Common Volcanic Rocks. Canadian Journal of Earth Sciences 8:523–548. https://doi.org/10.1139/e71-055

Jackson J (1994) Active tectonics of the Aegean region. Annual Review of Earth and Planetary Sciences 22:239–271

Jackson M, Blundy JD, Sparks RSJ (2019) Thermal histories of crystals formed in crustal magma reservoirs. AGU

Jagoutz OE (2010) Construction of the granitoid crust of an island arc. Part II: a quantitative petrogenetic model. Contributions to Mineralogy and Petrology 160:359–381

Janoušek V, Moyen J-F, Martin H, et al (2016) Geochemical Modelling of Igneous Processes – Principles And Recipes in R Language. Springer Berlin Heidelberg, Berlin, Heidelberg

Jarosewich E, Nelen JA, Norberg JA (1979) Electron microprobe reference samples for mineral analyses. Smithsonian contributions to the earth sciences 22:68–72

Jerram DA, Martin VM (2008) Understanding crystal populations and their significance through the magma plumbing system. Geological Society, London, Special Publications 304:133–148. https://doi.org/10.1144/SP304.7

Johnson MC, Plank T (2000) Dehydration and melting experiments constrain the fate of subducted sediments. Geochemistry, Geophysics, Geosystems 1:n/a-n/a. https://doi.org/10.1029/1999GC000014

Johnston EN, Sparks RSJ, Phillips JC, Carey S (2014) Revised estimates for the volume of the Late Bronze Age Minoan eruption, Santorini, Greece. Journal of the Geological Society 171:583–590. https://doi.org/10.1144/jgs2013-113

Jolivet L, Faccenna C, Huet B, et al (2013) Aegean tectonics: Strain localisation, slab tearing and trench retreat. Tectonophysics 597–598:1–33. https://doi.org/10.1016/j.tecto.2012.06.011

Kahle H-G, Straub C, Reilinger R, et al (1998) The strain rate field in the eastern Mediterranean region, estimated by repeated GPS measurements. Tectonophysics 294:237–252. https://doi.org/10.1016/S0040-1951(98)00102-4

Kalogeropoulos S, Paritsis S (1990) Geological and geochemical evolution of the Santorini Volcano: a review. pp 164–71

Kamenetsky VS (2001) Factors controlling chemistry of magmatic spinel: an empirical study of associated olivine, Cr-spinel and melt inclusions from primitive rocks. Journal of Petrology 42:655–671. https://doi.org/10.1093/petrology/42.4.655

Karagianni E, Papazachos C, Panagiotopoulos D, et al (2005) Shear velocity structure in the Aegean area obtained by inversion of Rayleigh waves. Geophysical Journal International 160:127–143

Karátson D, Gertisser R, Telbisz T, et al (2018) Towards reconstruction of the lost Late Bronze Age intra-caldera island of Santorini, Greece. Scientific Reports 8:. https://doi.org/10.1038/s41598-018-25301-2

Katz RF, Spiegelman M, Langmuir CH (2003) A new parameterization of hydrous mantle melting. Geochemistry, Geophysics, Geosystems 4:

Kawamoto T, Kanzaki M, Mibe K, et al (2012) Separation of supercritical slab-fluids to form aqueous fluid and melt components in subduction zone magmatism. Proceedings of the National Academy of Sciences 109:18695–18700. https://doi.org/10.1073/pnas.1207687109

Kay SM, Kay RW (1994) Aleutian magmas in space and time. The Geology of North America 1:687–722

Keller J (1982) Mediterranean island arcs. Andesites Wiley, New York 307–325

Kent AJR (2008) Melt Inclusions in Basaltic and Related Volcanic Rocks. 60

Keppler H (2017) Fluids and trace element transport in subduction zones. American Mineralogist 102:5–20

Keppler H (1996) Constraints from partitioning experiments on the composition of subduction-zone fluids. Nature 380:237–240. https://doi.org/10.1038/380237a0

Kessel R, Schmidt MW, Ulmer P, Pettke T (2005) Trace element signature of subduction-zone fluids, melts and supercritical liquids at 120–180 km depth. Nature 437:724–727. https://doi.org/10.1038/nature03971

Kilias A, Mountrakis D, Tranos M, Pavlides S (1998) The prevolcanic metamorphic rocks of Santorini island: structural evolution and kinematics during the Tertiary (South Aegean, Greece). pp 23–36

Kilias SP, Nomikou P, Papanikolaou D, et al (2013) New insights into hydrothermal vent processes in the unique shallow-submarine arc-volcano, Kolumbo (Santorini), Greece. Scientific Reports 3:. https://doi.org/10.1038/srep02421

Kimura J, Kawabata H, Hacker B, et al (2010) Arc Basalt Simulator version 3: Spreadsheet mass balance for exploring on element behavior between subducted slab, mantle wedge, and magma

Kimura J-I, Ariskin AA (2014) Calculation of water-bearing primary basalt and estimation of source mantle conditions beneath arcs: PRIMACALC2 model for WINDOWS. Geochemistry, Geophysics, Geosystems 15:1494–1514. https://doi.org/10.1002/2014GC005329

Kitsopoulos K (2007) Mg-Fe-Rich amphiboles associated to pyroclastics from Santorini island, south Aegean sea volcanic arc, Greece. Bull Geol Soc Greece 40:851–858

Klaver M, Blundy JD, Vroon PZ (2018) Generation of arc rhyodacites through cumulate-melt reactions in a deep crustal hot zone: Evidence from Nisyros volcano. Earth and Planetary Science Letters 497:169–180

Klaver M, Carey S, Nomikou P, et al (2016) A distinct source and differentiation history for Kolumbo submarine volcano, Santorini volcanic field, Aegean arc: KOLUMBO SUBMARINE VOLCANO. Geochemistry, Geophysics, Geosystems 17:3254–3273. https://doi.org/10.1002/2016GC006398

Klaver M, Djuly T, de Graaf S, et al (2015) Temporal and spatial variations in provenance of Eastern Mediterranean Sea sediments: Implications for Aegean and Aeolian arc volcanism. Geochimica et Cosmochimica Acta 153:149–168. https://doi.org/10.1016/j.gca.2015.01.007

Klemme S, O'Neill HS (2000) The near-solidus transition from garnet lherzolite to spinel lherzolite. Contributions to Mineralogy and Petrology 138:237–248

Klemme S, Prowatke S, Hametner K, Günther D (2005) Partitioning of trace elements between rutile and silicate melts: Implications for subduction zones. Geochimica et Cosmochimica Acta 69:2361–2371. https://doi.org/10.1016/j.gca.2004.11.015

Kohut EJ, Stern RJ, Kent AJR, et al (2006) Evidence for adiabatic decompression melting in the Southern Mariana Arc from high-Mg lavas and melt inclusions. Contrib Mineral Petrol 152:201–221. https://doi.org/10.1007/s00410-006-0102-7

Konstantinou KI (2010) Crustal rheology of the Santorini–Amorgos zone: Implications for the nucleation depth and rupture extent of the 9 July 1956 Amorgos earthquake, southern Aegean. Journal of Geodynamics 50:400–409. https://doi.org/10.1016/j.jog.2010.05.002

Korenaga J, Kelemen PB (2000) Major element heterogeneity in the mantle source of the North Atlantic igneous province. Earth and Planetary Science Letters 184:251–268. https://doi.org/10.1016/S0012-821X(00)00308-3

Kress VC, Carmichael IS (1991) The compressibility of silicate liquids containing Fe2O3 and the effect of composition, temperature, oxygen fugacity and pressure on their redox states. Contributions to Mineralogy and Petrology 108:82–92

Kress VC, Ghiorso MS (2004) Thermodynamic modeling of post-entrapment crystallization in igneous phases. Journal of Volcanology and Geothermal Research 137:247–260. https://doi.org/10.1016/j.jvolgeores.2004.05.012

Laubier M, Grove TL, Langmuir CH (2014) Trace element mineral/melt partitioning for basaltic and basaltic andesitic melts: An experimental and laser ICP-MS study with application to the oxidation state of mantle source regions. Earth and Planetary Science Letters 392:265–278. https://doi.org/10.1016/j.epsl.2014.01.053

Le Pichon X, Angelier J (1981) The Aegean Sea. Philosophical Transactions of the Royal Society of London Series A, Mathematical and Physical Sciences 300:357–372

Le Pichon X, Angelier J (1979) The Hellenic arc and trench system: a key to the neotectonic evolution of the eastern Mediterranean area. Tectonophysics 60:1–42

Le Pichon X, Lallemant SJ, Chamot-Rooke N, et al (2002) The Mediterranean Ridge backstop and the Hellenic nappes. Marine Geology 186:111–125. https://doi.org/10.1016/S0025-3227(02)00175-5

Leeman WP, Smith DR, Hildreth W, et al (1990) Compositional diversity of late Cenozoic basalts in a transect across the southern Washington Cascades: implications for subduction zone magmatism. Journal of Geophysical Research: Solid Earth 95:19561–19582

Li Z-XA, Lee C-TA (2004) The constancy of upper mantle fO2 through time inferred from V/Sc ratios in basalts. Earth and Planetary Science Letters 228:483–493

Long MD, Silver PG (2008) The subduction zone flow field from seismic anisotropy: A global view. science 319:315–318

Lowenstern JB (1995) Applications of silicate-melt inclusions to the study of magmatic volatiles. Magmas, fluids, and ore deposits 23:71–99

Lowenstern JB, Mahood GA (1991) Petrogenesis of high-silica rhyolite on the Alaska Peninsula. Geophysical Research Letters 18:1565–1568

Makris J (1977) Crustal structure of the central Aegean Sea and the islands of Evia and Crete, Greece, obtained by refraction seismic experiments. Journal of Geophysics 42:

Mallmann G, O'Neill HStC (2009) The Crystal/Melt partitioning of V during mantle melting as a function of oxygen fugacity compared with some other elements (Al, P, Ca, Sc, Ti, Cr, Fe, Ga, Y, Zr and Nb). Journal of Petrology 50:1765–1794. https://doi.org/10.1093/petrology/egp053

Mann AC (1983) Trace element geochemistry of high alumina basalt - Andesite - Dacite - Rhyodacite lavas of the Main Volcanic Series of Santorini Volcano, Greece. Contributions to Mineralogy and Petrology 84:43–57. https://doi.org/10.1007/BF01132329

Manning C (2004) The chemistry of subduction-zone fluids. Earth and Planetary Science Letters 223:1–16. https://doi.org/10.1016/j.epsl.2004.04.030

Marsellos AE, Foster DA, Min K, et al (2016) An application of GIS analysis on structural data from metamorphic rocks in Santorini Island. Bulletin of the Geological Society of Greece 47:1479. https://doi.org/10.12681/bgsg.10986

Marsh JS (1989) Geochemical constraints on coupled assimilation and fractional crystallization involving upper crustal compositions and continental tholeiitic magma. Earth and Planetary Science Letters 92:70–80. https://doi.org/10.1016/0012-821X(89)90021-6

Martin H, Smithies R, Rapp R, et al (2005) An overview of adakite, tonalite–trondhjemite–granodiorite (TTG), and sanukitoid: relationships and some implications for crustal evolution. Lithos 79:1–24

Martin VM, Davidson J, Morgan D, Jerram DA (2010) Using the Sr isotope compositions of feldspars and glass to distinguish magma system components and dynamics. Geology 38:539–542. https://doi.org/10.1130/G30758.1

Martin VM, Holness MB, Pyle DM (2006) Textural analysis of magmatic enclaves from the Kameni Islands, Santorini, Greece. Journal of Volcanology and Geothermal Research 154:89–102. https://doi.org/10.1016/j.jvolgeores.2005.09.021

Mason BG, Pyle DM, Oppenheimer C (2004) The size and frequency of the largest explosive eruptions on Earth. Bulletin of Volcanology 66:735–748

McClusky S, Balassanian S, Barka A, et al (2000) Global Positioning System constraints on plate kinematics and dynamics in the eastern Mediterranean and Caucasus. Journal of Geophysical Research: Solid Earth 105:5695–5719

McCulloch MT, Gamble J (1991) Geochemical and geodynamical constraints on subduction zone magmatism. Earth and Planetary Science Letters 102:358–374

McKenzie D, O'Nions RK (1991) Partial melt distributions from inversion of rare earth element concentrations. Journal of Petrology 32:1021–1091

McKenzie DP (1969) Speculations on the consequences and causes of plate motions. Geophysical Journal International 18:1–32

Menand T, Annen C, de Saint Blanquat M (2015) Rates of magma transfer in the crust: Insights into magma reservoir recharge and pluton growth. Geology 43:199–202. https://doi.org/10.1130/G36224.1

Mercier J (1981) Extensional-compressional tectonics associated with the Aegean Arc: comparison with the Andean Cordillera of south Peru-north Bolivia.

Philosophical Transactions of the Royal Society of London Series A, Mathematical and Physical Sciences 300:337–355

Metrich N, Clocchiatti R (1996) Sulfur abundance and its speciation in oxidized alkaline melts. Geochimica et Cosmochimica Acta 60:4151–4160. https://doi.org/10.1016/S0016-7037(96)00229-3

Michaud V, Clocchiatti R, Sbrana S (2000) The Minoan and post-Minoan eruptions, Santorini (Greece), in the light of melt inclusions: chlorine and sulphur behaviour. Journal of Volcanology and Geothermal Research 99:195–214. https://doi.org/10.1016/S0377-0273(00)00173-6

Miller MS, Gorbatov A, Kennett BL (2006) Three-dimensional visualization of a near-vertical slab tear beneath the southern Mariana arc. Geochemistry, Geophysics, Geosystems 7:

Minster J, Minster J, Treuil M, Allègre CJ (1977) Systematic use of trace elements in igneous processes. Part II. Inverse problem of the fractional crystallization process in volcanic suites. Contributions to mineralogy and petrology 61:49–78

Mitropolous P, Tarney J, Saunders A, Marsh N (1987) Petrogenesis of Cenezoic volcanic rocks from the Aegean island arc. Journal of Volcanology and Geothermal Research 32:177–193

Miyashiro A (1974) Volcanic rock series in island arcs and active continental margins. Amer Jour Sci 274:321–355

Moore JG, Clague DA (1992) Volcano growth and evolution of the island of Hawaii. Geological Society of America Bulletin 104:1471–1484

Morris J, Leeman WP, Tera F (1990) The subducted component in island arc lavas: constraints from Be isotopes and B–Be systematics. Nature 344:31

Morris J, Tera F (1989) 10Be and 9Be in mineral separates and whole rocks from volcanic arcs: Implications for sediment subduction. Geochimica et Cosmochimica Acta 53:3197–3206

Mortazavi M, Sparks RSJ (2004) Origin of rhyolite and rhyodacite lavas and associated mafic inclusions of Cape Akrotiri, Santorini: the role of wet basalt in generating calcalkaline silicic magmas. Contributions to Mineralogy and Petrology 146:397–413. https://doi.org/10.1007/s00410-003-0508-4

Mullen EK, Weis D, Marsh NB, Martindale M (2017) Primitive arc magma diversity: New geochemical insights in the Cascade Arc. Chemical Geology 448:43–70. https://doi.org/10.1016/j.chemgeo.2016.11.006

Münker C, Wörner G, Yogodzinski G, Churikova T (2004) Behaviour of high field strength elements in subduction zones: constraints from Kamchatka–Aleutian arc lavas. Earth and Planetary Science Letters 224:275–293

Müntener O, Ulmer P (2006) Experimentally derived high-pressure cumulates from hydrous arc magmas and consequences for the seismic velocity structure of lower arc crust. Geophysical Research Letters 33:

Myers JD, Marsh BD, Sinha AK (1985) Strontium isotopic and selected trace element variations between two Aleutian volcanic centers (Adak and Atka): implications for the development of arc volcanic plumbing systems. Contributions to Mineralogy and Petrology 91:221–234

Myers M, Druitt TH, Gurioli L, et al (2018) Evolution of mass discharge and decompression rates during the Plinian phase of the Bronze-Age eruption of Santorini

Nandedkar RH, Ulmer P, Müntener O (2014) Fractional crystallization of primitive, hydrous arc magmas: an experimental study at 0.7 GPa. Contrib Mineral Petrol 167:1015. https://doi.org/10.1007/s00410-014-1015-5

Ni H, Zhang L, Xiong X, et al (2017) Supercritical fluids at subduction zones: Evidence, formation condition, and physicochemical properties. Earth-Science Reviews 167:62–71. https://doi.org/10.1016/j.earscirev.2017.02.006

Nicholls I (1978) Primary basaltic magmas for the pre-caldera volcanic rocks of Santorini. Thera and the Aegean World 1:109–120

Nicholls IA (1971) Petrology of Santorini Volcano, Cyclades, Greece. Journal of Petrology 12:67–119. https://doi.org/10.1093/petrology/12.1.67

Nielsen CH, Sigurdsson H (1981) Quantitative methods for electron microprobe analysis of sodium in natural and synthetic glasses. American Mineralogist 66:547–552

Nielsen SG, Marschall HR (2017) Geochemical evidence for mélange melting in global arcs. Science Advances 3:e1602402. https://doi.org/10.1126/sciadv.1602402

Nitsan U (1974) Stability field of olivine with respect to oxidation and reduction. Journal of Geophysical Research 79:706–711. https://doi.org/10.1029/JB079i005p00706

Nomikou P, Druitt TH, Hübscher C, et al (2016) Post-eruptive flooding of Santorini caldera and implications for tsunami generation. Nature Communications 7:13332. https://doi.org/10.1038/ncomms13332

Nomikou P, Hübscher C, Carey S (2019) The Christiana–Santorini– Kolumbo Volcanic Field. 6

Nomikou P, Hübscher C, Papanikolaou D, et al (2018) Expanding extension, subsidence and lateral segmentation within the Santorini - Amorgos basins during Quaternary: Implications for the 1956 Amorgos events, central - south Aegean Sea, Greece. Tectonophysics 722:138–153. https://doi.org/10.1016/j.tecto.2017.10.016

Nomikou P, Parks MM, Papanikolaou D, et al (2014) The emergence and growth of a submarine volcano: The Kameni islands, Santorini (Greece). GeoResJ 1–2:8–18. https://doi.org/10.1016/j.grj.2014.02.002

Oikonomidis D, Pavlides S (2017) Geological mapping of Santorini Volcanic island (Greece), with the combined use of Pleiades 1A and ENVISAT satellite images. Arabian Journal of Geosciences 10:. https://doi.org/10.1007/s12517-017-2972-6

O'Neill HSC (1981) The transition between spinel lherzolite and garnet lherzolite, and its use as a geobarometer. Contributions to Mineralogy and Petrology 77:185–194

Özbakır AD, Şengör AMC, Wortel MJR, Govers R (2013) The Pliny–Strabo trench region: A large shear zone resulting from slab tearing. Earth and Planetary Science Letters 375:188–195. https://doi.org/10.1016/j.epsl.2013.05.025

Pantazidis A, Baziotis I, Solomonidou A, et al (2019) Santorini volcano as a potential Martian analogue: The Balos Cove Basalts. Icarus 325:128–140. https://doi.org/10.1016/j.icarus.2019.02.026

Papadopoulos G (1982) Active deep tectonics of the Aegean and surrounding area

Papadopoulos G, Kondopoulou D, Leventakis G-A, Pavlides S (1986) Seismotectonics of the Aegean region. Tectonophysics 124:67–84

Papadopoulos G, Orfanogiannaki K (2005) Long-term prediction of the next eruption in Thera volcano from conditional probability estimates. In: Developments in Volcanology. Elsevier, pp 211–216

Papageorgiou E, Foumelis M, Trasatti E, et al (2019) Multi-Sensor SAR Geodetic Imaging and Modelling of Santorini Volcano Post-Unrest Response. Remote Sensing 11:259. https://doi.org/10.3390/rs11030259

Papazachos BC, Karakostas VG, Papazachos CB, Scordilis EM (2000) The geometry of the Wadati–Benioff zone and lithospheric kinematics in the Hellenic arc. Tectonophysics 319:275–300. https://doi.org/10.1016/S0040-1951(99)00299-1

Papazachos CB (2019) Deep Structure and Active Tectonics of the South Aegean Volcanic Arc. 6

Parks MM, Biggs J, England P, et al (2012) Evolution of Santorini Volcano dominated by episodic and rapid fluxes of melt from depth. Nature Geoscience 5:749–754. https://doi.org/10.1038/ngeo1562

Parks MM, Moore JDP, Papanikolaou X, et al (2015) From quiescence to unrest: 20 years of satellite geodetic measurements at Santorini volcano, Greece. Journal of Geophysical Research: Solid Earth 120:1309–1328. https://doi.org/10.1002/2014JB011540

Pasqualon NG, Santos KNS, Marsellos AE, Kyriakopoulos K (2017) Implications of petrography and geochemistry of Athinios metamorphic units using PXRF and GIS analyses in Thera (Santorini, Greece). Bulletin of the Geological Society of Greece 50:1980. https://doi.org/10.12681/bgsg.11944

Pearce JA (1982) Trace element characteristics of lavas from destructive plate boundaries. Andesites 8:525–548

Pearce JA (1983) Role of the sub-continental lithosphere in magma genesis at active continental margins

Pearce JA, Parkinson IJ (1993) Trace element models for mantle melting: application to volcanic arc petrogenesis. Geological Society, London, Special Publications 76:373–403. https://doi.org/10.1144/GSL.SP.1993.076.01.19

Pearce JA, Peate DW (1995) Tectonic implications of the composition of volcanic arc magmas. Annual review of Earth and planetary sciences 23:251–285

Pearce JA, Stern RJ (2006) Origin of back-arc basin magmas: Trace element and isotope perspectives. In: Christie DM, Fisher CR, Lee S-M, Givens S (eds) Geophysical Monograph Series. American Geophysical Union, Washington, D. C., pp 63–86

Pe-Piper G, Piper DJW (2005) The South Aegean active volcanic arc: relationships between magmatism and tectonics. In: Developments in Volcanology. Elsevier, pp 113–133

Petford N, Atherton M (1996) Na-rich partial melts from newly underplated basaltic crust: the Cordillera Blanca Batholith, Peru. Journal of petrology 37:1491–1521

Petford N, Gallagher K (2001) Partial melting of mafic (amphibolitic) lower crust by periodic influx of basaltic magma. Earth and Planetary Science Letters 193:483–499

Peyton V, Levin V, Park J, et al (2001) Mantle flow at a slab edge: Seismic anisotropy in the Kamchatka region. Geophysical Research Letters 28:379–382

Pitcher BW, Kent AJ (2019) Statistics and segmentation: Using Big Data to assess Cascades Arc compositional variability. Geochimica et Cosmochimica Acta 265:443–467

Plank T (2005) Constraints from Thorium/Lanthanum on Sediment Recycling at Subduction Zones and the Evolution of the Continents. Journal of Petrology 46:921–944. https://doi.org/10.1093/petrology/egi005

Plank T, Kelley KA, Zimmer MM, et al (2013) Why do mafic arc magmas contain~ 4 wt% water on average? Earth and Planetary Science Letters 364:168–179

Plank T, Langmuir CH (1998) The chemical composition of subducting sediment and its consequences for the crust and mantle. Chemical Geology 145:325–394. https://doi.org/10.1016/S0009-2541(97)00150-2

Poli S, Schmidt MW (2002) Petrology of Subducted Slabs. Annual Review of Earth and Planetary Sciences 30:207–235. https://doi.org/10.1146/annurev.earth.30.091201.140550

Presnall DC, Dixon JR, O'Donnell TH, Dixons SA (1979) Generation of Mid-ocean Ridge Tholeiites. Journal of Petrology 20:3–35. https://doi.org/10.1093/petrology/20.1.3

Puchelt H (1978) Evolution of the volcanic rocks of Santorini. Thera and Aegean World 1:131–146

Putirka KD (2008) Minerals, inclusions and volcanic processes. Mineralogical Society of America

Pyle D, Ivanovich M, Sparks R (1988) Magma–cumulate mixing identified by U–Th disequilibrium dating. Nature 331:157

Pyle DM (1997) The global impact of the Minoan eruption of Santorini, Greece. Environmental Geology 30:59–61. https://doi.org/10.1007/s002540050132

Pyle DM, Elliott JR (2006) Quantitative morphology, recent evolution, and future activity of the Kameni Islands volcano, Santorini, Greece. Geosphere 2:253. https://doi.org/10.1130/GES00028.1

Qin Z, Lu F, Anderson AT (1992) Diffusive reequilibration of melt and fluid inclusions. American Mineralogist 77:565–576

Ralph J (2019) Mindat.org - Mines, Minerals and More. In: Mindat.org - Mines, Minerals and More. https://www.mindat.org/. Accessed 29 Nov 2019

Ramsey CB, Albert PG, Blockley SP, et al (2015) Improved age estimates for key Late Quaternary European tephra horizons in the RESET lattice. Quaternary Science Reviews 118:18–32

Reubi O, Blundy J (2009) A dearth of intermediate melts at subduction zone volcanoes and the petrogenesis of arc andesites. Nature 461:1269–1273. https://doi.org/10.1038/nature08510

Ring U, Glodny J, Will T, Thomson S (2010) The Hellenic subduction system: high-pressure metamorphism, exhumation, normal faulting, and large-scale extension. Annual Review of Earth and Planetary Sciences 38:45–76

Rizzo AL, Barberi F, Carapezza ML, et al (2015) New mafic magma refilling a quiescent volcano: Evidence from He-Ne-Ar isotopes during the 2011-2012 unrest at Santorini, Greece: RESEARCH ARTICLE. Geochemistry, Geophysics, Geosystems 16:798–814. https://doi.org/10.1002/2014GC005653

Robertson A, Grasso M (1995) Overview of the Late Tertiary–Recent tectonic and palaeo-environmental development of the Mediterranean region. Terra Nova 7:114–127

Roedder E (1984) Volume 12: Fluid inclusions. Reviews in mineralogy 12:

Roeder PL, Emslie RF (1970) Olivine-liquid equilibrium. Contributions to Mineralogy and Petrology 29:275–289. https://doi.org/10.1007/BF00371276

Rollinson HR (1993) Using geochemical data: evaluation, presentation, interpretation. Routledge

Rosenbaum G, Gasparon M, Lucente FP, et al (2008) Kinematics of slab tear faults during subduction segmentation and implications for Italian magmatism. Tectonics 27:

Rudnick RL, Barth M, Horn I, McDonough WF (2000) Rutile-bearing refractory eclogites: missing link between continents and depleted mantle. Science 287:278–281

Rudnick RL, Fountain DM (1995) Nature and composition of the continental crust: a lower crustal perspective. Reviews of geophysics 33:267–309

Rudnick RL, Gao S (2003) Composition of the continental crust. Treatise on geochemistry 3:659

Russell AE (1999) Normally Zoned Olivines from Santorini, Greece: Evidence for Magma Mixing. Bachelor's thesis, The Ohio State University

Russo R, Silver P (1994) Trench-parallel flow beneath the Nazca plate from seismic anisotropy. Science 263:1105–1111

Saleeby J (2003) Segmentation of the Laramide slab—Evidence from the southern Sierra Nevada region. Geological Society of America Bulletin 115:655–668

Salters VJM, Stracke A (2004) Composition of the depleted mantle. Geochemistry, Geophysics, Geosystems 5:n/a-n/a. https://doi.org/10.1029/2003GC000597

Sarbas B, Kalbskopf B, Nohl U, Busch U (2019) Geochemical Rock Database-Query. In: GEOROC: Geochemistry of Rocks of the Oceans and Continents. http://georoc.mpch-mainz.gwdg.de/georoc/. Accessed 29 Nov 2019

Satow C, Tomlinson EL, Grant KM, et al (2015) A new contribution to the Late Quaternary tephrostratigraphy of the Mediterranean: Aegean Sea core LC21. Quaternary Science Reviews 117:96–112. https://doi.org/10.1016/j.quascirev.2015.04.005

Satow CG (2012) The Tephrostratigraphy of three, late Quaternary, Mediterranean marine cores. Doctoral Thesis, Royal Holloway College, University of London

Saunders AD, Tarney J (1984) Geochemical characteristics of basaltic volcanism within back-arc basins. Geological Society, London, Special Publications 16:59–76. https://doi.org/10.1144/GSL.SP.1984.016.01.05

Schiano P (2003) Primitive mantle magmas recorded as silicate melt inclusions in igneous minerals. Earth-Science Reviews 63:121–144. https://doi.org/10.1016/S0012-8252(03)00034-5

Schmidt A, Weyer S, John T, Brey GP (2009) HFSE systematics of rutile-bearing eclogites: new insights into subduction zone processes and implications for the earth's HFSE budget. Geochimica et Cosmochimica Acta 73:455–468

Schmidt MW, Dardon A, Chazot G, Vannucci R (2004) The dependence of Nb and Ta rutile–melt partitioning on melt composition and Nb/Ta fractionation during subduction processes. Earth and Planetary Science Letters 226:415–432. https://doi.org/10.1016/j.epsl.2004.08.010

Schmidt MW, Jagoutz O (2017) The global systematics of primitive arc melts. Geochem Geophys Geosyst 18:2817–2854. https://doi.org/10.1002/2016GC006699

Schmitt AK, Stockli DF, Song EJ, Storm S (2016) Equilibrium and Disequilibrium of 230Th-238U in Zircon from the Minoan Eruption, Santorini, Aegean Sea, Greece

Seidenkrantz M, Friedrich W (1993) Santorini, part of the Hellinic arc: age of the earliest volcanism documented by foraminifera. Δελτίον της Ελληνικής Γεωλογικής Εταιρίας 28:99

Self S (2006) The effects and consequences of very large explosive volcanic eruptions. Philosophical Transactions of the Royal Society A: Mathematical, Physical and Engineering Sciences 364:2073–2097. https://doi.org/10.1098/rsta.2006.1814

Sigurdsson H, Carey S, Devine J (1990) Assessment of mass, dynamics and environmental effects of the Minoan eruption of Santorini volcano. Thera and the Aegean world III 2:100–112

Simmons JM, Carey RJ, Cas RAF, Druitt TH (2017) High magma decompression rates at the peak of a violent caldera-forming eruption (Lower Pumice 1 eruption, Santorini, Greece). Bulletin of Volcanology 79:. https://doi.org/10.1007/s00445-017-1120-1

Simmons JM, Cas RAF, Druitt TH, Folkes CB (2016) Complex variations during a caldera-forming Plinian eruption, including precursor deposits, thick pumice fallout, co-ignimbrite breccias and climactic lag breccias: The 184 ka Lower Pumice 1 eruption sequence, Santorini, Greece. Journal of Volcanology and Geothermal Research 324:200–219. https://doi.org/10.1016/j.jvolgeores.2016.05.013

Sinton JM, FORD LL, Chappell B, McCULLOCH MT (2003) Magma genesis and mantle heterogeneity in the Manus back-arc basin, Papua New Guinea. Journal of Petrology 44:159–195

Sisson T, Grove T (1993a) Experimental investigations of the role of H 2 O in calc-alkaline differentiation and subduction zone magmatism. Contributions to mineralogy and petrology 113:143–166

Sisson TW, Grove TL (1993b) Experimental investigations of the role of H20 in calc-alkaline differentiation and subduction zone magmatism. 24

Skarpelis N, Kyriakopoulos K, Villa I (1992) Occurrence and 40 Ar/39 Ar dating of a granite in Thera (Santorini, Greece). Geologische Rundschau 81:729–735

Skarpelis N, Liati A (1990) The prevolcanic basement of Thera at Athinios: metamorphism, plutonism and mineralization. Thera and the Aegean World III 2:172–82

Skora S, Blundy J (2010) High-pressure hydrous phase relations of radiolarian clay and implications for the involvement of subducted sediment in arc magmatism. Journal of Petrology 51:2211–2243

Smith DJ (2014) Clinopyroxene precursors to amphibole sponge in arc crust. Nat Commun 5:4329. https://doi.org/10.1038/ncomms5329

Sobolev A, Dmitriev L, Barsukov V, et al (1980) The formation conditions of the high-magnesium olivines from the monomineralic fraction of Luna 24 regolith. pp 105–116

Sobolev AV (1994) The origin of typical NMORB: The evidence from a melt inclusions study. Mineralogical Magazine 58A:862–863. https://doi.org/10.1180/minmag.1994.58A.2.184

Sobolev AV, Chaussidon M (1996) H2O concentrations in primary melts from supra-subduction zones and mid-ocean ridges: Implications for H2O storage and recycling in the mantle. Earth and Planetary Science Letters 137:45–55. https://doi.org/10.1016/0012-821X(95)00203-O

Solano JMS, Jackson MD, Sparks RSJ, et al (2012) Melt Segregation in Deep Crustal Hot Zones: a Mechanism for Chemical Differentiation, Crustal Assimilation and the Formation of Evolved Magmas. Journal of Petrology 53:1999–2026. https://doi.org/10.1093/petrology/egs041

Spandler C, Hermann J, Arculus R, Mavrogenes J (2003) Redistribution of trace elements during prograde metamorphism from lawsonite blueschist to eclogite facies; implications for deep subduction-zone processes. Contributions to Mineralogy and Petrology 146:205–222

Spandler C, Hermann J, Faure K, et al (2008) The importance of talc and chlorite "hybrid" rocks for volatile recycling through subduction zones; evidence from the high-pressure subduction mélange of New Caledonia. Contributions to Mineralogy and Petrology 155:181–198

Spandler C, Pirard C (2013) Element recycling from subducting slabs to arc crust: A review. Lithos 170:208–223

Sparks R, Wilson C (1990) The Minoan deposits: a review of their characteristics and interpretation

Spera FJ (2001) Energy-Constrained Open-System Magmatic Processes I: General Model and Energy-Constrained Assimilation and Fractional Crystallization (EC-AFC) Formulation. Journal of Petrology 42:999–1018. https://doi.org/10.1093/petrology/42.5.999

Stalder R, Foley SF, Brey GP, Horn I (1998) Mineral-aqueous fluid partitioning of trace elements at 900–1200°C and 3.0–5.7 GPa: new experimental data for garnet, clinopyroxene, and rutile, and implications for mantle metasomatism. Geochimica et Cosmochimica Acta 62:1781–1801. https://doi.org/10.1016/S0016-7037(98)00101-X

Stegman DR, Freeman J, Schellart WP, et al (2006) Influence of trench width on subduction hinge retreat rates in 3-D models of slab rollback. Geochemistry, Geophysics, Geosystems 7:

Stern RJ (2002) Subduction zones. Rev Geophys 40:1012. https://doi.org/10.1029/2001RG000108

Stolper E, Newman S (1994) The role of water in the petrogenesis of Mariana trough magmas. Earth and Planetary Science Letters 121:293–325

Sun S-S, McDonough W (1989) Chemical and isotopic systematics of oceanic basalts: implications for mantle composition and processes. Geological Society, London, Special Publications 42:313–345

Sun S-S, Nesbitt RW, Sharaskin AY (1979) Geochemical characteristics of mid-ocean ridge basalts. Earth and Planetary Science Letters 44:119–138

Syracuse EM, van Keken PE, Abers GA (2010) The global range of subduction zone thermal models. Physics of the Earth and Planetary Interiors 183:73–90. https://doi.org/10.1016/j.pepi.2010.02.004

Tait S (1992) Selective preservation of melt inclusions in igneous phenocrysts. American Mineralogist 77:146–155

Tarney J, Barr S, Mitropoulos P, et al (1998) Santorini: geochemical constraints on magma sources and eruption mechanisms. The European Laboratory Volcanoes, EUR 18161:89–111

Tarney J, Wood D, Saunders A, et al (1980) Nature of mantle heterogeneity in the North Atlantic: evidence from deep sea drilling. Phil Trans R Soc Lond A 297:179–202

Tatsumi Y (2005) The subduction factory: how it operates in the evolving Earth. GSA today 15:4

Tatsumi Y, Eggins S (1995) Subduction zone magmatism. Wiley

Tatsumi Y, Hamilton DL, Nesbitt RW (1986) Chemical characteristics of fluid phase released from a subducted lithosphere and origin of arc magmas: Evidence from high-pressure experiments and natural rocks. Journal of Volcanology and Geothermal Research 29:293–309. https://doi.org/10.1016/0377-0273(86)90049-1

Tatsumi Y, Ishizaka K (1982) Magnesian andesite and basalt from Shodo-Shima sland, southwest Japan, -and their bearing on the genesis of calc- alkaline andesites. Lithos 15:161–172

Tatsumi Y, Suzuki T (2009) Tholeiitic vs calc-alkalic differentiation and evolution of arc crust: Constraints from melting experiments on a basalt from the Izu-Bonin-Mariana Arc. Journal of Petrology 50:1575–1603. https://doi.org/10.1093/petrology/egp044

Tatsumi Y, Tsunakawa H (1992) Cenozoic volcanism, stress gradient and back-arc opening in the North Island, New Zealand: Origin of Taupo-Rotorua Depression. Island Arc 1:40–50

Taylor B, Martinez F (2003) Back-arc basin basalt systematics. Earth and Planetary Science Letters 210:481–497

Taylor Jr HP (1980) The effects of assimilation of country rocks by magmas on 18O/16O and 87Sr/86Sr systematics in igneous rocks. Earth and Planetary Science Letters 47:243–254

Taylor SR, McLennan SM (1985) The continental crust: Its composition and evolution. Blackwell Scientific Pub.,Palo Alto, CA, United States

ten Veen JH, Kleinspehn KL (2002) Geodynamics along an increasingly curved convergent plate margin: Late Miocene-Pleistocene Rhodes, Greece. Tectonics 21:8–1

Tera F, Brown L, Morris J, et al (1986) Sediment incorporation in island-arc magmas: Inferences from 10Be. Geochimica et Cosmochimica Acta 50:535–550

Thomson SN, Ring U, Brichau S, et al (2009) Timing and nature of formation of the Ios metamorphic core complex, southern Cyclades, Greece. Geological Society, London, Special Publications 321:139–167

Tibaldi A (2015) Structure of volcano plumbing systems: A review of multi-parametric effects. Journal of Volcanology and Geothermal Research 298:85–135. https://doi.org/10.1016/j.jvolgeores.2015.03.023

Tirel C, Gueydan F, Tiberi C, Brun J-P (2004) Aegean crustal thickness inferred from gravity inversion. Geodynamical implications. Earth and Planetary Science Letters 228:267–280

Toksöz MN, Bird P (1977) Formation and evolution of marginal basins and continental plateaus. Island Arcs, Deep Sea Trenches and Back-Arc Basins 1:379–393

Toplis MJ (2005) The thermodynamics of iron and magnesium partitioning between olivine and liquid: criteria for assessing and predicting equilibrium in natural and experimental systems. Contributions to Mineralogy and Petrology 149:22–39. https://doi.org/10.1007/s00410-004-0629-4

Tsunakawa H (1986) Stress field during the rotation of Southwest Japan. Journal of geomagnetism and geoelectricity 38:537–543

Turner SJ, Langmuir CH (2015) The global chemical systematics of arc front stratovolcanoes: Evaluating the role of crustal processes. Earth and Planetary Science Letters 422:182–193

Ulmer P, Trommsdorff V (1995) Serpentine stability to mantle depths and subduction-related magmatism. Science 268:858–861

Vaggelli G, Francalanci L (1998) The composition of post-Minoan parental magmas of Santorini inferred from the study of the silicate-melt inclusions in mafic enclaves of dacitic lavas. pp 187–192

Vaggelli G, Pellegrini M, Vougioukalakis G, et al (2009) Highly Sr radiogenic tholeiitic magmas in the latest inter-Plinian activity of Santorini volcano, Greece. Journal of Geophysical Research: Solid Earth 114:

van Hinsbergen DJJ, Hafkenscheid E, Spakman W, et al (2005) Nappe stacking resulting from subduction of oceanic and continental lithosphere below Greece. Geology 33:325–328

van Keken PE (2003) The structure and dynamics of the mantle wedge. Earth and planetary science letters 215:323–338

Vespa M, Keller J, Gertisser R (2006) Interplinian explosive activity of Santorini volcano (Greece) during the past 150,000 years. Journal of Volcanology and Geothermal Research 153:262–286. https://doi.org/10.1016/j.jvolgeores.2005.12.009

Vougioukalakis GE, Satow CG, Druitt TH (2019) Volcanism of the South Aegean Volcanic Arc. 6

Wallace PJ, Carmichael IS (1999) Quaternary volcanism near the Valley of Mexico: implications for subduction zone magmatism and the effects of crustal thickness variations on primitive magma compositions. Contributions to Mineralogy and Petrology 135:291–314

Wanke M, Clynne MA, von Quadt A, et al (2019) Geochemical and petrological diversity of mafic magmas from Mount St. Helens. Contributions to Mineralogy and Petrology 174:. https://doi.org/10.1007/s00410-018-1544-4

Watson EB, Sneeringer MA, Ross A (1982) Diffusion of dissolved carbonate in magmas: experimental results and applications. Earth and Planetary Science Letters 61:346–358

Watt SF, Pyle DM, Mather TA, Naranjo JA (2013) Arc magma compositions controlled by linked thermal and chemical gradients above the subducting slab. Geophysical Research Letters 40:2550–2556

Wedepohl KH (1995) The composition of the continental crust. Geochimica et cosmochimica Acta 59:1217–1232

Wehrmann H, Hoernle K, Garbe-Schönberg D, et al (2014) Insights from trace element geochemistry as to the roles of subduction zone geometry and subduction input on the chemistry of arc magmas. International Journal of Earth Sciences 103:1929–1944

Weller DJ, Stern CR (2018) Along-strike variability of primitive magmas (major and volatile elements) inferred from olivine-hosted melt inclusions, southernmost Andean Southern Volcanic Zone, Chile. Lithos 296–299:233–244. https://doi.org/10.1016/j.lithos.2017.11.009

White WM, Dupré B (1986) Sediment subduction and magma genesis in the Lesser Antilles: Isotopic and trace element constraints. Journal of Geophysical Research 91:5927. https://doi.org/10.1029/JB091iB06p05927

Whitley S, Halama R, Gertisser R, et al (2018) Plutonic Xenoliths from Santorini Volcano, Aegean Arc, Greece. p 1269

Wiens DA, Conder JA, Faul UH (2008) The seismic structure and dynamics of the mantle wedge. Annu Rev Earth Planet Sci 36:421–455

Wilson BM (1989) Igneous petrogenesis a global tectonic approach. Springer Science & Business Media

Winter JD (2013) Principles of igneous and metamorphic petrology. Pearson education

Woelki D, Haase KM, Schoenhofen MV, et al (2018) Evidence for melting of subducting carbonate-rich sediments in the western Aegean Arc. Chemical Geology 483:463–473. https://doi.org/10.1016/j.chemgeo.2018.03.014

Workman RK, Hart SR (2005) Major and trace element composition of the depleted MORB mantle (DMM). Earth and Planetary Science Letters 231:53–72. https://doi.org/10.1016/j.epsl.2004.12.005

Wortel M, Spakman W (2000) Subduction and slab detachment in the Mediterranean-Carpathian region. Science 290:1910–1917

Wulf S, Keller J, Satow C, et al (2020) Advancing Santorini's tephrostratigraphy: New glass geochemical data and improved marine-terrestrial tephra correlations for the past ~360 kyrs. Earth-Science Reviews 200:102964. https://doi.org/10.1016/j.earscirev.2019.102964

Wyers, Gerard Paul (1987) Petrogenesis of calc-alkaline and alkaline magmas from the southern and eastern Aegean Sea, Greece. Doctoral Thesis, The Ohio State University

Zellmer G (1998) U-Th-Ra Isotope Evidence for Rates of Fluid Transport and Magmatic Processes Beneath Santorini, Aegean Volcanic Arc, Greece. Mineralogical Magazine 62A:1685–1686. https://doi.org/10.1180/minmag.1998.62A.3.216

Zellmer G, Turner S, Hawkesworth C (2000) Timescales of destructive plate margin magmatism: new insights from Santorini, Aegean volcanic arc. Earth and Planetary Science Letters 174:265–281. https://doi.org/10.1016/S0012-821X(99)00266-6

Zellmer GF, Annen C, Charlier BLA, et al (2005) Magma evolution and ascent at volcanic arcs: constraining petrogenetic processes through rates and

chronologies. Journal of Volcanology and Geothermal Research 140:171–191. https://doi.org/10.1016/j.jvolgeores.2004.07.020

Zellmer GF, Edmonds M, Straub SM (2015) Volatiles in subduction zone magmatism. Geological Society, London, Special Publications 410:1–17

Zellmer GF, Turner SP (2007) Arc dacite genesis pathways: Evidence from mafic enclaves and their hosts in Aegean lavas. Lithos 95:346–362. https://doi.org/10.1016/j.lithos.2006.08.002

Zheng Y-F (2019) Subduction zone geochemistry. Geoscience Frontiers 10:1223–1254. https://doi.org/10.1016/j.gsf.2019.02.003

Zheng Y-F, Xia Q-X, Chen R-X, Gao X-Y (2011) Partial melting, fluid supercriticality and element mobility in ultrahigh-pressure metamorphic rocks during continental collision. Earth-Science Reviews 107:342–374. https://doi.org/10.1016/j.earscirev.2011.04.004

Appended papers

The following two publications, which I have either authored or co-authored, were published during the course of my thesis. The work was not part of my doctoral research project and thus are not included in this thesis as results chapters. The first paper (Flaherty et al. 2018) combines results of my Master's research on the timescales of magma chamber assembly prior to the Late Bronze Age (LBA) eruption of Santorini with other previously acquired timescale data to give a comprehensive view of the sequence and timescales of pre-eruptive events in the magmatic system. It has implications for the plumbing system of Santorini, and consequently for this thesis, in particular Chapter 6 on the build-up period to the LBA eruption. Ideally, the final publication resulting from Chapter 6 will complement this timescale study, providing further refinement of the pre-eruptive processes from a geochemical and petrological point of view.

The second paper (Schiavi et al. 2018) is a technique development study for improving dissolved H_2O quantification in glasses using Raman spectroscopy, led by Federica Schiavi at the Laboratoire Magmas et Volcans (LMV). We used Raman spectroscopy H_2O data gathered for some melt inclusions in this thesis, which had previously been analyzed by secondary ion mass spectrometry (SIMS) in Druitt et al. (2016), to show that the calibration gives comparable H_2O results to the SIMS-analyzed melt inclusions therefore confirming that the calibration works on natural glasses. We did not analyze many melt inclusions from our melt inclusion dataset; thus, we do not report or use the Raman microscopy data in the thesis.

Contributions to Mineralogy and Petrology (2018) 173:75
https://doi.org/10.1007/s00410-018-1490-1

ORIGINAL PAPER

Multiple timescale constraints for high-flux magma chamber assembly prior to the Late Bronze Age eruption of Santorini (Greece)

T. Flaherty[1] · T. H. Druitt[1] · H. Tuffen[2] · M. D. Higgins[3] · F. Costa[4] · A. Cadoux[5]

Received: 16 June 2017 / Accepted: 16 July 2018

Abstract

The rhyodacitic magma discharged during the 30–80 km^3 DRE (dense rock equivalent) Late Bronze Age (LBA; also called 'Minoan') eruption of Santorini caldera is known from previous studies to have had a complex history of polybaric ascent and storage prior to eruption. We refine the timescales of these processes by modelling Mg–Fe diffusion profiles in orthopyroxene and clinopyroxene crystals. The data are integrated with previously published information on the LBA eruption (phase equilibria studies, melt inclusion volatile barometry, Mg-in-plagioclase diffusion chronometry), as well as new plagioclase crystal size distributions and the established pre-LBA history of the volcano, to reconstruct the events that led up to the assembly and discharge of the LBA magma chamber. Orthopyroxene, clinopyroxene and plagioclase crystals in the rhyodacite have compositionally distinct rims, overgrowing relict, probably source-derived, more magnesian (or calcic) cores, and record one or more crystallization (plag $\gg$ opx $>$ cpx) events during the few centuries to years prior to eruption. The crystallization event(s) can be explained by the rapid transfer of rhyodacitic melt from a dioritic/gabbroic region of the subcaldera pluton (mostly in the 8–12 km depth range), followed by injection, cooling and mixing in a large melt lens at 4–6 km depth (the pre-eruptive magma chamber). Since crystals from all eruptive phases yield similar timescales, the melt transfer event(s), the last of which took place less than 2 years before the eruption, must have involved most of the magma that subsequently erupted. The data are consistent with a model in which prolonged generation, storage and segregation of silicic melts were followed by gravitational instability in the subcaldera pluton, causing the rapid interconnection and amalgamation of melt-rich domains. The melts then drained to the top of the pluton, at fluxes of up to 0.1–1 km^3 year^{-1}, where steep vertical gradients of density and rheology probably caused them to inject laterally, forming a short-lived holding chamber prior to eruption. This interpretation is consistent with growing evidence that some large silicic magma chambers are transient features on geological timescales. A similar process preceded at least one earlier caldera-forming eruption on Santorini, suggesting that it may be a general feature of this rift-hosted magmatic system.

Keywords Diffusion chronometry · Crystal size distribution · Santorini · Minoan eruption · Magma chamber · Magma ascent

Introduction

Caldera-forming eruptions of silicic magma, such as the magnitude 7, Late Bronze Age (LBA; also called 'Minoan') eruption of Santorini, are low-frequency,

Communicated by Timothy L. Grove.

Electronic supplementary material The online version of this article (https://doi.org/10.1007/s00410-018-1490-1) contains supplementary material, which is available to authorized users.

✉ T. H. Druitt
tim.druitt@uca.fr

[1] Laboratoire Magmas et Volcans, Université Clermont Auvergne-CNRS-IRD, OPGC, 63100 Clermont-Ferrand, France

[2] Lancaster Environment Centre, Lancaster University, Lancaster LA1 4YQ, UK

[3] Sciences de la Terre, Université du Québec à Chicoutimi, 555 Boulevard de l'Université, Chicoutimi, QC G7H 2B1, Canada

[4] Earth Observatory of Singapore, Nanyang Technological University, Singapore 639798, Singapore

[5] GEOPS, Université Paris-Sud, CNRS, Université Paris-Saclay, 91405 Orsay, France

Published online: 20 August 2018

high-impact events with effects at global scales (Mason et al. 2004; Self 2006; Oppenheimer 2013). The processes leading to reactivation of long-dormant caldera volcanoes are of societal interest, in particular for interpreting geophysical signals in times of unrest. Recent studies have shown that such systems can build up to eruption on geologically short timescales, raising the question of how this occurs (Morgan et al. 2006; Wark et al. 2007; Wilson and Charlier 2009; Gualda et al. 2012; Druitt et al. 2012; Matthews et al. 2012; Allan et al. 2013, 2017; Fabbro et al. 2013, 2017; Chamberlain et al. 2014; Pamukcu et al. 2015; Barker et al. 2016).

Silicic magmas are believed to be generated in bodies of crystal mush, where they can be stored in the crust for long periods of time (Bacon and Druitt 1988; Brophy 1991; Hildreth and Wilson 2007; Bachmann and Bergantz 2004, 2008; Deering et al. 2010; Bégué et al. 2014; Bergantz et al. 2015; Bachmann and Huber 2016; Cooper 2017; Rubin et al. 2017). Whereas large volumes of melt lose heat rapidly by convection, locked-in mushes cool slowly by conduction (Koyaguchi and Kaneko 1999), providing a long-lived source of melt that can be periodically tapped. Creation of large chambers of melt-dominated silicic magma requires: (1) production and incubation of the melt within mush bodies, (2) extraction of that melt, and (3) its accumulation in magma chambers (Annen et al. 2006; Brown 2013, and references therein). Low rates of melt accumulation lead to pluton construction through freezing of successive batches, whereas the runaway addition of mass and heat associated with high accumulation rates generates magma chambers (Annen 2009). The critical accumulation rate for magma chamber formation probably lies between 10^{-3} and 10^{-1} km^3 year^{-1} for a Santorini-sized system (Schopa and Annen 2013; Gelman et al. 2013; Karakas et al. 2017). The flow rate necessary to transport the melt through a dyke up to the magma chamber without freezing provides an additional constraint ($\sim 10^{-2}$ km^3 year^{-1}; Menand et al. 2015). Theoretical models of silicic melt extraction from crystal mushes by intergranular porous flow can explain magma chamber formation on timescales of 10^4–10^6 years (Bachmann and Bergantz 2004; Solano et al. 2012). However, silicic magma chambers in some cases are assembled much faster than predicted theoretically, at rates as high as 0.05–1 km^3 year^{-1} and on timescales as low as 10–10^3 years (Druitt et al. 2012; Allan et al. 2013, 2017; Barker et al. 2016; Cooper et al. 2017; Fabbro et al. 2017). A possible explanation is that melt-rich domains present in the mush body interconnect and amalgamate very rapidly to form a magma chamber (Christopher et al. 2015; Cashman et al. 2017; Sparks and Cashman 2017). Some questions arise from these concepts. How common is rapid magma chamber assembly in silicic systems? What is the mechanism driving high-flux melt transfer? How does the timescale of magma chamber development scale with the size of the system? Following chamber assembly, what finally triggers the eruption?

The LBA eruption of Santorini has played a role in the development of these ideas. Cottrell et al. (1999) proposed, based on a combination of phase equilibria experiments and melt inclusion H_2O barometry, that the LBA silicic magma underwent polybaric ascent from a deep storage zone to a shallow magma chamber about 300 years prior to eruption. Their model was extended by Druitt et al. (2012), who used Mg-in-plagioclase diffusion modelling to reduce the timescale from 300 years to a few decades. While Cottrell et al. (1999) proposed that the entire erupted magma volume was transferred in this time, Druitt et al. (2012) envisaged the late-stage replenishment of a pre-existing chamber by several km^3 of silicic magma. In both interpretations, however, magma chamber assembly took place on timescales that were geologically very short. Other data have subsequently been published on the LBA magma: micro-Sr isotopic analyses of plagioclase (Martin et al. 2010), phase equilibria experiments on Santorini silicic magmas (Cadoux et al. 2014) and the basaltic/andesitic magmas parental to them (Andújar et al. 2015, 2016), $H_2O + CO_2$ melt inclusion barometry (Druitt et al. 2016), and the chemistry and petrology of minor juvenile and cognate components in the LBA eruption products (Druitt 2014).

In the present paper, we present new data on the compositions and zoning patterns of orthopyroxene and clinopyroxene crystals and, in particular, on timescales of pre-eruptive crystal residence estimated by modelling of Mg–Fe diffusion gradients in these minerals (Morgan et al. 2004; Saunders et al. 2012; Allan et al. 2013; Costa et al. 2013; Chamberlain et al. 2014; Kilgour et al. 2014; Petrone et al. 2016; Singer et al. 2016; Krimer and Costa 2017; Fabbro et al. 2017). We also derive updated timescale information from plagioclase crystals. We then integrate the new, and previously published, information into a model for the architecture and dynamics of the Santorini plumbing system in the period leading up to the LBA eruption, and place constraints on the physical mechanisms at play.

The Late Bronze Age eruption: context and products

Santorini is the southernmost volcanic centre of the South Aegean Volcanic Arc in Greece. It lies in a 100-km-long, 45-km-wide SW–NE rift zone (Nomikou et al. 2016; Hooft et al. 2017; Fig. 1a) on 25-km-thick continental crust with seismically distinct upper (0–15 km) and lower (15–25 km) layers (Konstaninou 2010).

The earliest preserved volcanic products on Santorini date from 650 ka. Since 350 ka the volcano has produced twelve Plinian eruptions (Druitt et al. 1999), at least four

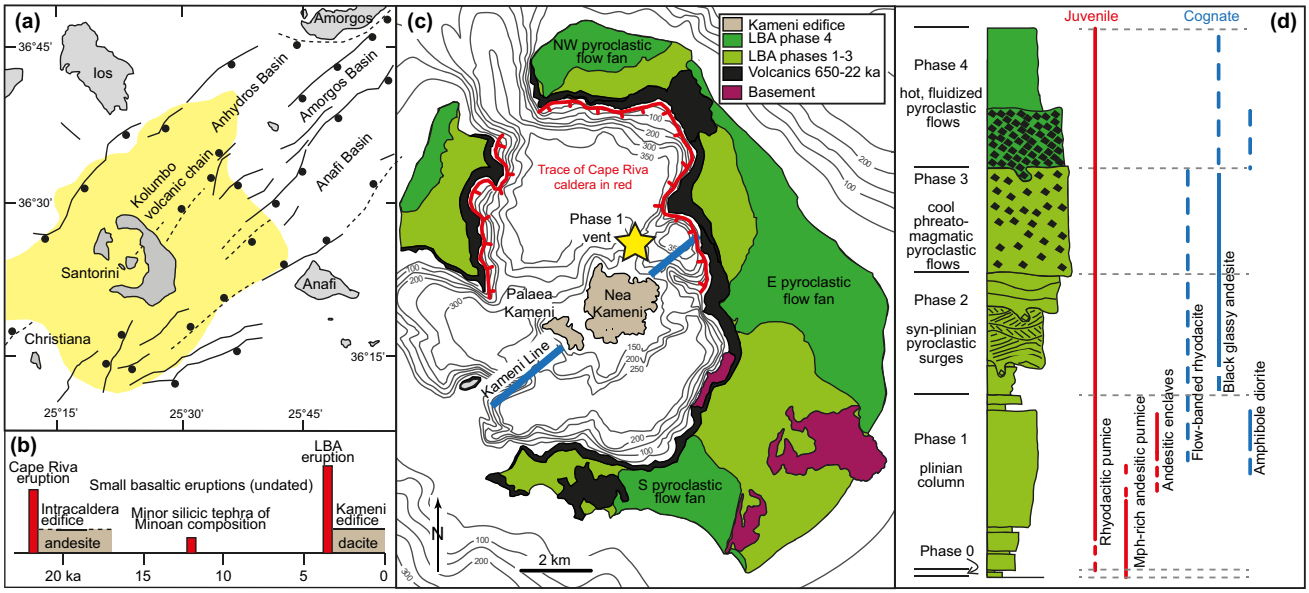

Fig. 1 Summary of geological features of Santorini and the Late Bronze Age (LBA) eruption. **a** Map of the Santorini–Amorgos rift zone showing major normal faults (circle on the hanging wall), and the three main subsidence basins. The extent of submarine ignimbrite from the LBA eruption mapped from seismic profiles is shown in yellow (after Sigurdsson et al. 2006). **b** Summary of the activity of Santorini since the 22-ka Cape Riva caldera-forming eruption. **c** Map of Santorini caldera, showing the products of the LBA eruption (including the three main ignimbrite fans from eruptive phase 4), the outline of the shallow Cape Riva caldera that existed prior to the LBA eruption (after Athanassas et al. 2016), the Kameni Line, and the site of the phase 1 vent (after Bond and Sparks 1976). **d** Schematic log of the products of the LBA eruption, with the distributions of the juvenile components and some key cognate components (after Druitt 2014)

of which caused edifice collapse resulting in the present-day 10 × 7 km, multi-cyclic caldera. The Plinian eruptions were separated by inter-Plinian periods of 10–30 ky durations and characterized by intracaldera effusive volcanism and lower intensity (sub-Plinian or less) explosive activity. Following over half a million years of activity, Santorini must be underlain by a large pluton, probably zoned from granodiorite through diorite to gabbro with increasing depth (Druitt et al. 2016). Mantle-derived basalt fractionates to andesite beneath Santorini near the upper-lower crustal boundary (~ 400 MPa), and andesite fractionates to silicic magma in the upper crust (200–400 MPa) (Andújar et al. 2015, 2016). Santorini magmas are calcalkaline to mildly tholeiitic in nature (Huijsmans 1985; Huijsmans and Barton 1989; Druitt et al. 1999).

The Plinian eruption prior to the LBA eruption (the > 10 km^3 DRE Cape Riva eruption) has been dated at 21.8 ± 0.4 ka and formed a caldera located in the northern basin of the present-day caldera (Athanassas et al. 2016, and references therein; Fig. 1c). A sequence of events then occurred within the crust during the subsequent 17.2-ky inter-Plinian period that culminated in the LBA eruption (Fig. 1b). There is evidence for three eruptive events during this period: (1) immediately following the Cape Riva eruption, an andesitic edifice at least 2.5 km^3 in volume was built within the Cape Riva caldera. Blocks of this former edifice occur as black glassy lithic blocks in the LBA ejecta (Druitt 2014); one block has been dated at 20.2 ± 1.0 ka (Karátson et al. 2018). The andesite was a distinctive high-Ba magma unrelated to either the Cape Riva or LBA silicic magmas (Druitt 2014). (2) At 12–13 ka, a small eruption of LBA-like silicic magma took place, forming a crypto-ash layer in marine and terrestrial sediments (St. Seymour et al. 2004; Satow et al. 2015). (3) A number of small basaltic eruptions of unknown age also took place (Vespa et al. 2006; Vaggelli et al. 2009).

The LBA eruption occurred in the late seventeenth century BCE, and discharged 30–80 km^3 DRE of magmatic and accidental materials (Pyle 1990; Sigurdsson et al. 2006; Johnston et al. 2014). The eruption has been reconstructed in detail (Bond and Sparks 1976; Heiken and McCoy 1984; Sigurdsson et al. 1990; Pyle 1990; Sparks and Wilson 1990; Cioni et al. 2000; Druitt 2014). It comprised five phases, here numbered 0 to 4: (0) a precursory Vulcanian phase, (1) a Plinian phase, (2) a phase of syn-Plinian base surges, (3) a phase of phreatomagmatic activity with low-temperature pyroclastic flows, and (4) a phase of hot, fluidized pyroclastic flows, which accounted for most of the magma discharged (Fig. 1d). Phases 0 and 1 took place from a subaerial vent (star, Fig. 1c). The vent then migrated during phase 2 into the flooded Cape Riva caldera, such that phase 3 was strongly phreatomagmatic. Phase 4 appears to have been fed

from multiple subaerial vents of poorly constrained locations. Caldera collapse probably took place during phase 4, deepening and enlarging the extant Cape Riva caldera.

Since the LBA eruption, repeated effusion of dacitic magma (4.85 ± 0.7 km^3 in total) has built up the largely submerged Kameni intracaldera edifice on the floor of the present-day caldera, with its subaerial summits forming the islands of Palaea and Nea Kameni (Pyle and Elliot 2006; Nomikou et al. 2014). The first recorded eruption of Kameni took place in 197 BCE, and the most recent in 1950. The mean eruption rate over this time has been 1.3×10^{-3} km^3 year^{-1} (Nomikou et al. 2014), similar to that estimated for a previous inter-Plinian period between 70 and 55 ka ($\sim 1 \times 10^{-3}$ km^3 year^{-1}; Druitt et al. 1999). The Kameni vents lie along a NE–SW lineament called the Kameni Line, which lies parallel to the regional fault trend and which has played a central role in Santorini volcanism (Fig. 1c). Several Plinian eruptions, including the LBA, began at a vent on or near the Kameni Line. Seismicity was strongly concentrated along the Kameni Line during a period of bradyseismic unrest in 2011–2012 (Newman et al. 2012).

Summary of previously published data on the LBA rhyodacite

Petrology and geochemistry

Analyses of 23 visually homogeneous pumice clasts of the rhyodacite presented by Druitt (2014) reveal a restricted range of whole-rock compositions (70–71 wt% SiO_2, recalculated volatile-free; FeO/MgO of 3–5), irrespective of eruptive phase. The crystalline phases are plagioclase, orthopyroxene, clinopyroxene (weight proportions plag:opx:cpx of 0.84:0.10:0.06; Cadoux et al. 2014), magnetite and ilmenite set in 73–74 wt% SiO_2 rhyolitic glass. Apatite and pyrrhotite occur mostly as inclusions in pyroxenes and magnetite. Trace quantities of zircon are present (Schmitt et al. 2016). Crystal contents based on *K* mass balance in nine pumice–glass pairs range from < 5 to 20 wt%, the lowest values occurring in phase 1 (< 5–12 wt%), and the highest in phase 4 (12–20 wt%) (Online Resource 1). New measurements of plagioclase contents in 15 thin sections by image analysis (3–16 vol%; Online Resource 2) are consistent with this range.

Plagioclases (≤ 3 mm in length) were described by Druitt et al. (2012) based on BSE images of 300 crystals (Fig. 2a). Most have compositions of $An_{40 \pm 3}$ (with rare thin zones as sodic as An_{30}) and are weakly normally

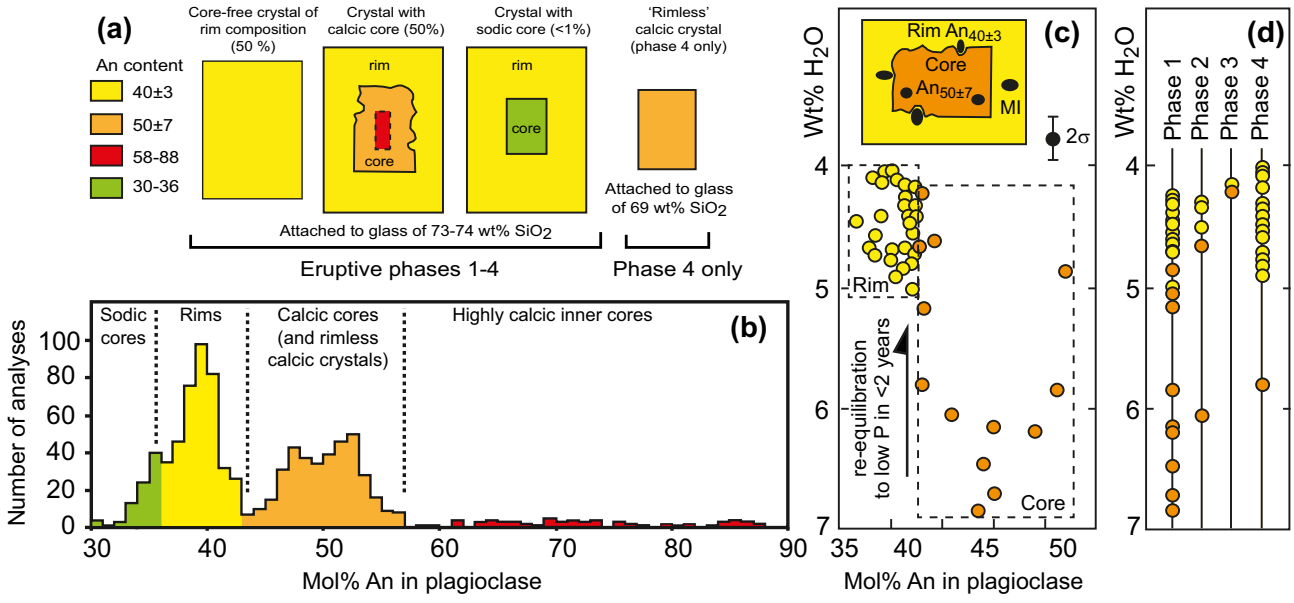

Fig. 2 Summary of some previously published petrological features of the Late Bronze Age rhyodacite. **a** Schematic of the different plagioclase types (after Druitt et al. 2012). **b** Histogram of anorthite (An) contents of microprobe analyses, showing that the $An_{40 \pm 3}$ rims and $An_{50 \pm 7}$ calcic cores of the crystals form two distinct populations (after Druitt et al. 2012). **c** Water contents of plagioclase-hosted melt inclusions as functions of An content, with relationship to the core/rim stratigraphy of a typical core-bearing plagioclase crystal (from Druitt et al. 2016). **d** Water contents of plagioclase-hosted melt inclusions in the rhyodacite as functions of eruptive phase, showing that most H_2O-rich melt inclusions occur in the cores of phenocrysts of phase 1

zoned to euhedral edges of $An_{37–40}$. Superimposed on the overall normal zoning are multiple (typically 3–6), 50–100-µm-wide, sawtooth-zoned packets, each consisting of normally zoned plagioclase terminated by a subtle resorption surface and a small (< few molar %) increase in An content. About half of the crystals have $An_{30–88}$ composition cores that are variably euhedral to corroded (Fig. 2a), and exhibit complex combinations of normal, reverse, sawtooth, oscillatory or patchy zoning, with multiple resorption surfaces, indicative of long and complex histories prior to overgrowth by the $An_{40\pm3}$ rims. The majority of the cores have compositions of $An_{50\pm7}$, sometimes with inner cores of $An_{58–88}$ (Fig. 2b). Very rarely (≪ 1%) the cores are more sodic ($An_{30–36}$) than the rims. An additional group of plagioclase crystals occurs in small quantities, and uniquely in pumices from eruptive phase 4. Their distribution is very heterogeneous; they are present in some phase-4 pumices but not in others. They have the same compositions as the calcic cores ($An_{50\pm7}$), but lack the $An_{40\pm3}$ rims (Fig. 2a). Druitt et al. (2012) referred to them as 'rimless $An_{50\pm7}$ crystals'. These rimless crystals have thin selvages of a glass that is slightly less evolved than the normal interstitial glass (Online Resource 1).

Martin et al. (2010) measured the $^{87}Sr/^{86}Sr$ ratios of plagioclase crystals in phase-1 pumices to be 0.7049–0.7051, slightly less Sr-radiogenic than the interstitial glass (0.7051–0.7054). Seven of their eight isotopic analyses were from the $An_{40\pm3}$ plagioclase, and one was from a $An_{50\pm7}$ core; there was no difference in $^{87}Sr/^{86}Sr$ between the two compositions. Di Salvo et al. (2013) also isotopically analyzed some rims, calcic cores and highly calcic inner cores, and found that they all had similar range of $^{87}Sr/^{86}Sr$. Martin et al. (2010) attributed the relatively high $^{87}Sr/^{86}Sr$ of the interstitial glass to post-crystallization contamination of the rhyodacitic magma by a more Sr-radiogenic melt.

Melt inclusions (MIs) in $An_{40\pm3}$ plagioclase contain 69–75 wt% SiO_2 (Online Resource 1). Secondary ion mass spectrometry (SIMS) analysis of > 60 isolated, crack-free MIs hosted in plagioclase, opx and cpx revealed volatile concentrations of 4.0–6.9 wt% H_2O, 20–200 ppm CO_2, 40–100 ppm S, and 3000–4500 ppm Cl (Cadoux et al. 2014; Druitt et al. 2016). MIs within plagioclase $An_{50\pm7}$ cores are more H_2O-rich (4.2–6.9 wt%) than those within $An_{40\pm3}$ rims (4.0–5.0 wt%) (Fig. 2c). Cottrell et al. (1999) also measured ≤ 6.5 wt% H_2O in seven MIs within $An_{50\pm7}$ cores. If corrected for ~ 10 wt% post-entrapment crystallization (in the cooler environment of rim overgrowth; Online Resource 1), then the highest H_2O content of the core-hosted MIs at the moment of entrapment falls to 6.1 wt%. CO_2, S and Cl concentrations of MIs in the cores and rims are similar. Although $An_{50\pm7}$ cores with H_2O-rich MIs occur in pumices from eruptive phase 1, 2 and 4, they are particularly abundant in phase 1 (Fig. 2d).

Druitt et al. (2016) used MI $H_2O + CO_2$ contents and the solubility models of Newman and Lowenstern (2002) and Papale et al. (2006) to estimate entrapment pressures, which were converted to entrapment depths using a mean upper crust density of 2640 kg m^{-3} (Konstantinou 2010) assuming volatile saturation (Cadoux et al. 2014; Druitt et al. 2016). MI entrapment in the $An_{40\pm3}$ plagioclase occurred at 100–160 MPa (4–6 km depth). However, MI entrapment within $An_{50\pm7}$ plagioclase cores extended to higher inferred pressures (240 MPa for 6.1 wt% H_2O and 100 ppm CO_2, corresponding to a depth of 9 km). The proposed explanation is that the cores were derived from depth and transferred to shallower levels where rim overgrowth occurred, in accordance with the earlier model of Cottrell et al. (1999).

Pre-eruptive temperatures and oxygen fugacities (fO_2) based on touching Fe–Ti oxide pairs in contact with the glass were estimated to be 885 ± 7 °C and $10^{-6.7\pm0.2}$ Pa by Cottrell et al. (1999) using the algorithm of Andersen and Lindsley (1988). Cadoux et al. (2014) and Druitt (2014) estimated 853 ± 7 °C and $10^{-7.8\pm0.2}$ Pa using the same algorithm, and 866 ± 9 °C and $10^{-7.86\pm0.07}$ Pa using that of Ghiorso and Evans (2008). There is no systematic variation of temperature with eruptive phase.

Pre-eruptive magma chamber

The LBA rhyodacite is inferred to have been erupted from a single interconnected magma reservoir (henceforth termed the magma chamber), because similar whole rock and glass compositions, phenocryst edge compositions, phenocryst MI compositions, and Fe–Ti oxide temperatures are found for pumices from all eruptive phases (Cottrell et al. 1999; Cadoux et al. 2014; Druitt 2014). Cottrell et al. (1999) used phase equilibria, MI H_2O contents, and the absence of stable phenocrystic amphibole to infer pre-eruptive storage of the magma at 50 MPa, 885 °C, and H_2O-saturated conditions. These values were revised by Cadoux et al. (2014), who experimentally reproduced the phenocryst–glass assemblage at higher pressure (≥ 200 MPa) and lower temperature (860 °C), with melt saturated with respect to $H_2O + Cl + CO_2$, but slightly undersaturated with respect to pure H_2O ($X_{H_2O} = H_2O/[H_2O + CO_2]$ of 0.8–0.9). Cadoux et al. (2014) also proposed that the melt co-existed with a H_2O + Cl-rich hydrosaline liquid. The MI $H_2O + CO_2$ data of Druitt et al. (2016) yielded pre-eruptive storage pressures (100–160 MPa; 4–6 km) intermediate between the estimates of the previous authors. Combining the different constraints, the best-fit pre-eruptive conditions for the LBA rhyodacite are 850–880 °C, fO_2 ~ NNO, 100–160 MPa (4–6 km depth), melt saturated with 4.0–5.0 wt% H_2O, < 200 ppm CO_2, < 150 ppm S and 3000–5000 ppm Cl, a free H_2O-rich vapour phase, and possibly a H_2O + Cl-rich hydrosaline liquid. The magma chamber was less than 2 km thick (4–6 km depth).

Source region of the rhyodacite

Cottrell et al. (1999) proposed a rhyodacite source reservoir at 210–240 MPa and 825 ± 25 °C. However, phase equilibrium experiments on a typical 59 wt% SiO_2 Santorini andesite (Andújar et al. 2016) generated 68–70 wt% SiO_2 melt, similar to LBA rhyodacite, at 900–950 °C and under relatively oxidizing conditions (NNO + 1.5). Andújar et al. noted that, while most LBA pumices are calcalkaline rhyodacite with Fe/Mg ratios of about 3, some are more tholeiitic with Fe/Mg ratios of up to 5. The main, calcalkaline rhyodacite was produced experimentally at 200 MPa and 6 wt% H_2O in an assemblage containing plagioclase ($An_{50\pm5}$), cpx (Mg# 70–75) and opx (Mg# 70–75). More tholeiitic rhyodacitic melts were produced at higher pressure (400 MPa). The LBA rhyodacite was thus generated at 900–950 °C over the pressure range 200–400 MPa, but mostly at ~200 MPa (Andújar et al. 2016). The high H_2O contents and entrapment pressures recorded by plagioclase core-hosted MIs (up to 240 MPa, or 9 km) agree with the experimental constraints. Our best estimate is that the LBA rhyodacitic melts were extracted mostly from a 900–950 °C, dioritic/gabbroic region of the subcaldera pluton at 8–12 km depth (200–300 MPa), possibly with lesser quantities of more tholeiitic silicic melts extracted from deeper levels (~400 MPa).

Amphibole may have been present at 200 MPa in the source region, but only at temperatures of < 940 °C (Fig. 3a, c of Andújar et al. 2016). Any source-derived amphiboles must have been resorbed prior to eruption because amphibole was not stable in the magma chamber (Cottrell et al. 1999; Cadoux et al. 2014). The presence of amphibole in the source region is consistent with the low *Y* and Dy/Yb of the LBA rhyodacite (Klaver et al. 2016).

Minor andesitic components

Two minor (< 1%) andesitic components were co-erupted with the rhyodacite (Sparks et al. 1977; Druitt et al. 1999; Cottrell et al. 1999; Druitt 2014) (Fig. 1d):

- A suite of microphenocryst-rich andesitic pumices and dioritic plutonic nodules (55–100 vol% crystals) that were erupted at the start of phase 0, and throughout phase 1, but as only trace amounts in phases 2–4 (Fig. 1d). These have the same high-Ba composition as the post-Cape Riva intracaldera edifice, and are interpreted as samples of a variably crystalline residual pocket of the

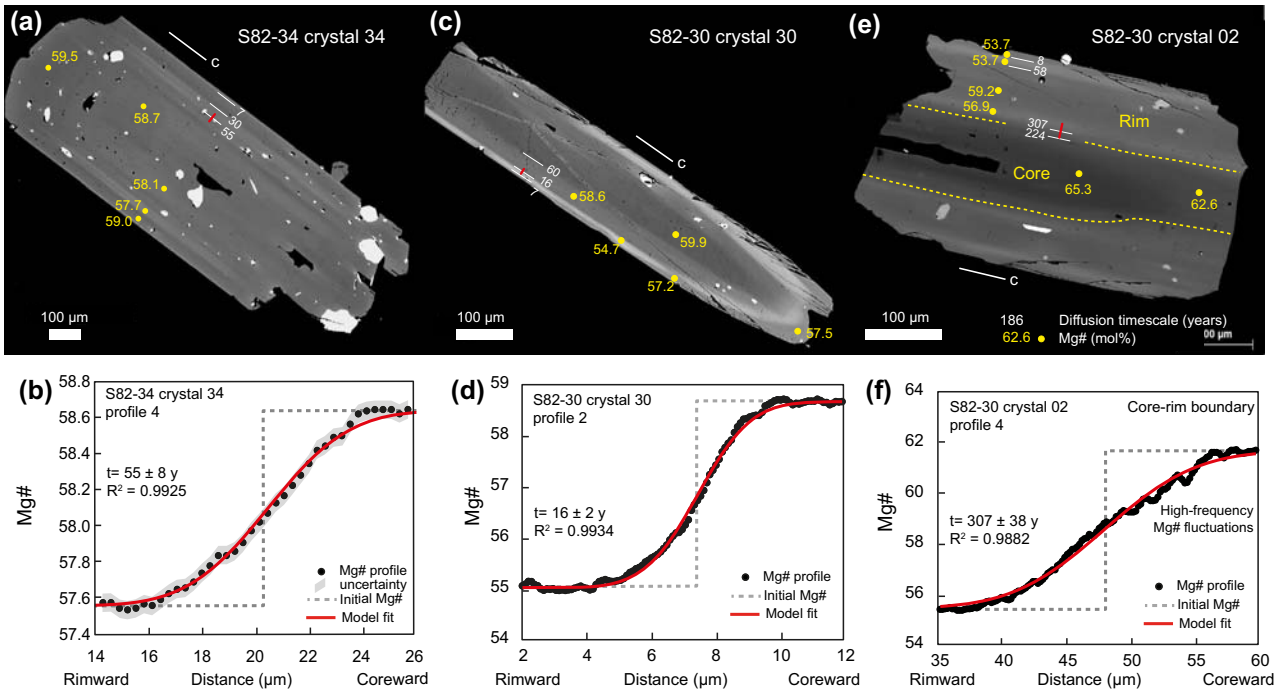

Fig. 3 **a, c, e** Back-scattered electron (BSE) images of three representative opx crystals. Crystal S82-30 02 has a magnesian core, whereas crystals S82-34 34 and S82-30 30 each lack one. Numbers in yellow are spot analyses of Mg# (mol%). Numbers in white are diffusion timescales (in years) across the boundaries shown by white lines. **b, d, f** Diffusion profiles for representative zone boundaries (profiles shown by red lines on the BSE images). For reasons of clarity, only the central parts of the profiles appear on the figure. The grey zone around the profile data points shows the analytical uncertainty on the measurements

same magma that was pushed out by the ascending LBA rhyodacite (Druitt 2014).

- Enclaves of andesitic magma that were mingled into the rhyodacite within a few months of the eruption, quenched, then released during eruptive fragmentation (Cottrell et al. 1999). They were erupted mainly during phase 1. These enclaves are also enriched in Ba (Druitt 2014).

Methods and assumptions

Orthopyroxene (opx) and clinopyroxene (cpx) crystals were extracted from the 250–400 and 400–700-µm size fractions of ten gently crushed pumice lumps (2–4 per eruptive phase) and mounted in epoxy resin. Crystals with adhering grey, microlite-rich groundmass derived from disaggregated andesitic enclaves were excluded. Pyroxene zoning textures were studied using greyscale back-scattered electron (BSE) images calibrated for Mg number (Mg# = $100 \times Mg/[Mg + Fe^{Total}]$ atomic). Only crystals judged by visual inspection to be symmetrically mounted and polished through their centres were imaged. A total of 65–120 opx crystals (eruptive phases 1–4) and 12 cpx crystals (eruptive phases 1, 2 and 4) were examined. All the opx and cpx crystals had their long (*c*) axes parallel to the surface of the grain mount. Compositional images were made of selected opx crystals. Full details of sample preparation and analysis are given in Online Resource 3.

Diffusive re-equilibration timescales were determined for opx and cpx using binary element diffusion modelling of Mg–Fe profiles across inter-zonal boundaries (Morgan et al. 2004, 2006; Allan et al. 2013, 2017; Chamberlain et al. 2014; Barker et al. 2016) (Online Resource 4). We implemented an analytical solution to the one-dimensional diffusion equation, assuming an initial step function in Mg#, then fitted the measured profiles by a least squares method, with maximum and minimum uncertainties and a correlation index, R^2 (Online Resource 3). Diffusion modelling was carried out perpendicular to crystal length (*c* axis) in both pyroxene species. In opx, it was carried out parallel to the *a* axis, sections through the *c*–*a* plane being recognized by the presence of {201} crystal terminations. Orientations of the cpx crystals were determined using the SHAPE software (Dowty 1987) by matching measured interfacial angles with those of modelled cpx sections. The diffusion coefficients of Ganguly and Tazzoli (1994) and Dohmen et al. (2016) were used for opx, and that of Müller et al. (2013) was used for cpx, with corrections for diffusion anisotropy of opx and cpx explained in Online Resource 3. Uncertainties on the diffusion timescales were calculated using standard error propagation (Online Resource 3).

The timescale derived by modelling of Mg–Fe diffusion across a particular zone boundary is the time elapsed between zone boundary formation and eruption quench, at the assumed temperature of residence. The modelling was carried out at 855 ± 15 °C and $fO_2 = 10^{-7.8 \pm 0.2}$ Pa (~NNO), representative of the pre-eruptive conditions (Cadoux et al. 2014; Druitt 2014).

Crystal residence timescales obtained by 1D diffusion modelling are maximum estimates (Costa et al. 2008; Shea et al. 2015; Krimer and Costa 2017). However, modelling along short profiles perpendicular to the long (*c*) axis in prismatic crystals of high aspect ratio (up to 4 in cpx, up to 8 in opx) is pseudo-1D, reducing any overestimation due to this effect. By assuming an initial step function, the approach also ignores the presence of any growth zoning, also resulting in an overestimation of residence time (Costa et al. 2008; Costa and Morgan 2010; Chamberlain et al. 2014; Till et al. 2015). However, any growth-generated zoning is less important perpendicular to the *c* axis than parallel to it.

New insights from pyroxenes

Pyroxene zoning patterns

In the following descriptions, compositionally distinct inner and outer zones of a crystal are referred to as the core and rim. The outer limit of the crystal in contact with glass is referred to as the crystal (or rim) edge.

Orthopyroxene crystals (≤ 3 mm in length) occur with length/width ratios of up to 8 (Fig. 3). Compositions span the range $Wo_{2-3}En_{52-70}Fs_{28-45}$ (Mg# 53–71), with Al_2O_3 contents of 0.4–0.7 wt% (rarely up to 1.4 wt%). Most crystals have restricted compositions (Mg# 57–61), and diffuse, short-wavelength (5–15 µm) oscillatory zoning, particularly evident parallel to the *c* axis. Some contain sharply defined, 2–30 µm-thick growth zones of slightly more Fe-rich compositions (Mg# 53–55; e.g., bright zone in Fig. 3c), although the euhedral edge composition is always in the range Mg# 57–61. Many crystals that appear homogeneous at low BSE resolutions contain complex, low-magnitude oscillatory zoning visible at high BSE resolutions. Of five opx crystals imaged compositionally, four exhibit sector zoning of Al. (Fig. 4a). Al, being trivalent, diffuses two orders of magnitude slower than Mg and Fe in opx (Nakagawa et al. 2005), and so may preserve the original small-scale growth zoning that is partially re-equilibrated in more rapidly diffusing Mg and Fe. While Al and Mg# are correlated at large scales, they are de-correlated at shorter scales, Al exhibiting sharper fluctuations than Mg# (Fig. 4b). This suggests that growth-generated compositional gradients are narrow, justifying a step-function initial condition for Mg–Fe in the diffusion modelling.

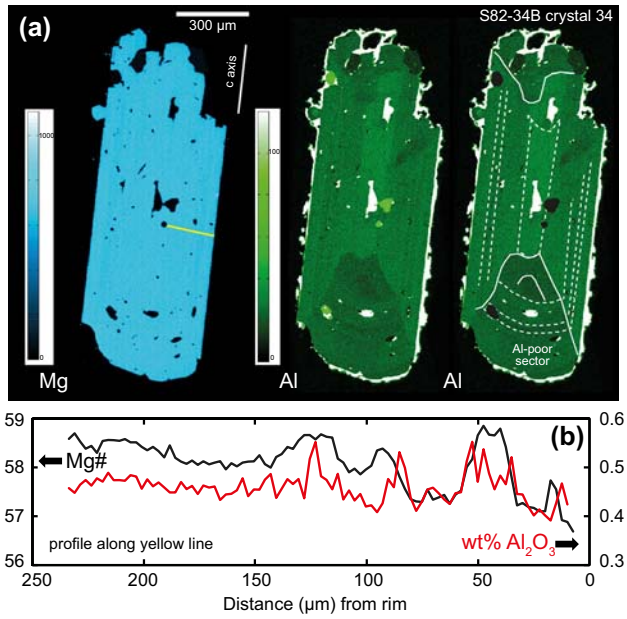

Fig. 4 **a** Compositional maps for Mg and Al for a typical weakly zoned opx crystal. The Al map shows clear evidence for sector zoning. **b** Profiles of Mg# (mol%) and Al_2O_3 content (wt%) showing decoupling of the two and higher frequency variations in Al than in Mg#, suggesting that most of the gradients in Mg# are due to diffusion, not growth. The location of the profile is shown by a yellow line on the Mg map

One-fifth of the opx crystals have magnesian cores with Mg# 63–71 (Fig. 3e), commonly containing multiple resorption surfaces, melt inclusions, and patchy zoning. The melt inclusions are surrounded by streaky compositional zoning elongated parallel to the *c* axis, formed by diffusional Mg–Fe exchange between the melt inclusions and host opx (e.g., Tomiya and Takahashi 2005; Allan et al. 2013; Barker et al. 2016).

Clinopyroxene crystals (≤ 2 mm in length) have aspect ratios of up to 4 (Fig. 5). Compositions span the range $Wo_{39–44}En_{36–44}Fs_{14–22}$ (Mg# 62–78), but most crystals have Mg# of 62–70, with edges of 66–70 (Fig. 5a). Both normal and reverse zoning are observed in these crystals, but 2–30 µm-scale oscillatory zoning is most common. Al_2O_3 contents are typically 0.7–1.0 wt%, but can reach 2.0–2.5 wt% in more Fe-rich zones. Four of the twelve crystals examined in detail contain magnesian cores with Mg# 72–78 and Al_2O_3 contents of 1.4–1.7 wt% (Fig. 5c, e). Some cores are riddled with melt inclusions, and have a wispy zoning due to partial diffusive Mg–Fe overprinting by the Mg# ~ 67 composition around melt inclusions and along fractures and cleavage planes (Fig. 5c).

Diffusion timescales of pyroxene residence

Diffusion timescales were measured across (1) the inner limit (core-rim boundary) of the crystal rim, and (2) zone boundaries within the rims. The aim was to estimate the residence time of the crystal rim of each pyroxene species since its formation. The results are given in full in Online Resource 4, and summarized in Table 1.

A total of 85 zone boundaries in 16 opx crystals were modelled, but application of quality-control criteria (Online Resource 3) retained only 32 of the profiles for timescale calculation, all models fitting the actual profiles with $R^2 > 0.95$. The Mg–Fe gradients ranged in width from 0.4 to 48 µm. Three examples are shown in Fig. 3. Diffusion profiles with $R^2 > 0.99$ give visually good fits (Fig. 3b, d). Those with R^2 of 0.98–0.99 give less good fits, commonly due to the presence of micron-scale fluctuations of Mg# in the crystal (e.g., Fig. 3f). These fluctuations may show that the entire profile was generated by growth, not diffusion. However, such fluctuations are also observed in experimental studies of diffusion due to the presence of crystal microfractures not visible on BSE images (J. Ganguly, written communication). Profiles with $R^2 < 0.98$, on the other hand, probably have significant components of growth zoning. We place emphasis on those profiles with $R^2 > 0.99$.

Diffusion timescales across the core-rim boundaries in two opx crystals give 138–459 years using the Dohmen et al. (2016) diffusion coefficient (Fig. 6a). Timescales from zone boundaries within the crystal rims range from < 1 to 420 years, largely consistent with the core-rim boundaries, with a single outlier at 852 years (Fig. 6a). However, all except one of the timescales with the highest quality fit ($R^2 > 0.99$) are < 55 years (Fig. 3b, d). The timescales from within the rims themselves suggests that rim growth continued until eruption-driven quench took place. The single longer timescale (852 years) comes from near the centre of a core-free crystal (Fig. 6), and may record an earlier phase of rim growth. There are no systematic differences in the timescale ranges in opx crystals from the different eruptive phases.

Orthopyroxene diffusion timescales calculated using the Ganguly and Tazzoli (1994) diffusion coefficient are five times shorter than those using Dohmen et al. (2016). The core-rim boundaries give timescales of 42–110 years, and zone boundaries within the rims give < 1–36 years (with the best fits being < 10 years), with the single outlier at 157 years.

We have no firm basis for favouring one opx diffusion coefficient over the other (as discussed in Online Resource 3); however, by placing emphasis on the Dohmen et al. (2016) results, we are inferring maximum timescales. Moreover, the opx timescales derived using Dohmen et al. (2016) are similar to those obtained from cpx (see below). We, therefore, conclude that the main phase of opx

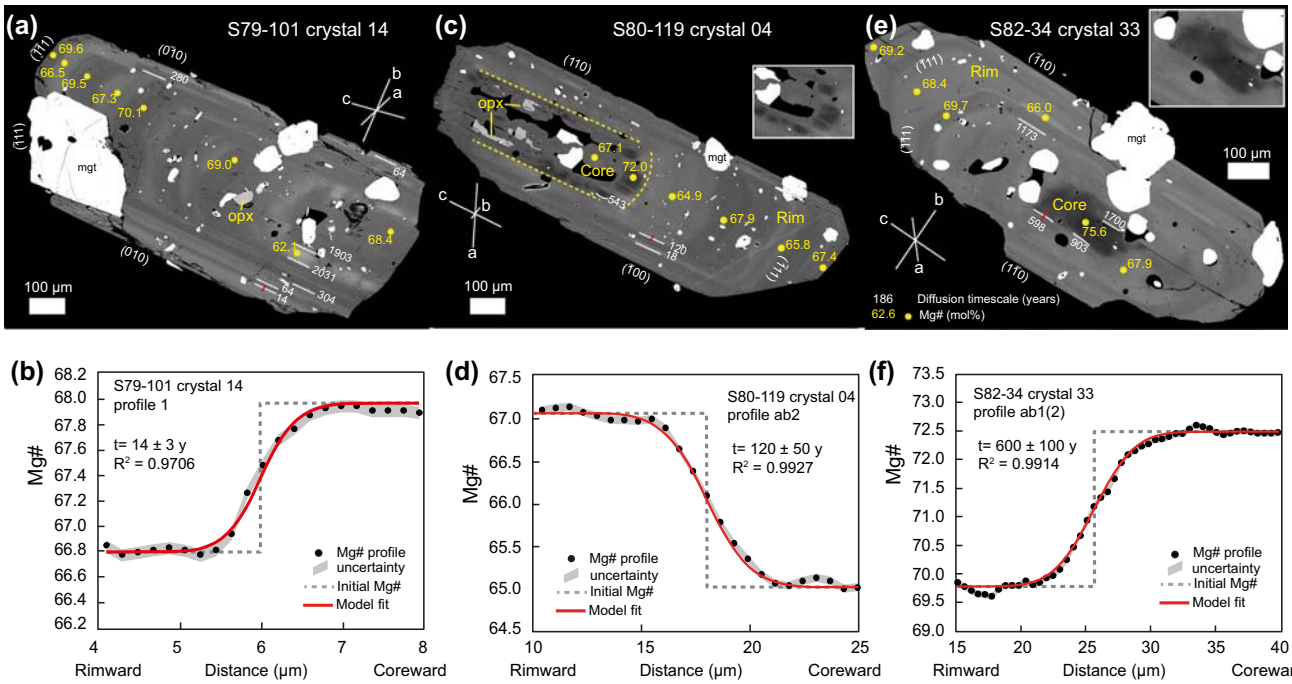

Fig. 5 **a, c, e** Back-scattered electron (BSE) images of three representative cpx crystals. Crystals S80-119 04 and S82-34 33 have magnesian cores eaten into by wispy diffusion fronts of more Fe-rich compositions (see insets), whereas crystal S79-101 14 has no core. Numbers in yellow are spot analyses of Mg# (mol%). Numbers in white are diffusion timescales (in years) across the boundaries shown. **b, d, f** Diffusion profiles for representative zone boundaries (profiles shown by red lines on the BSE images). The grey zone around the data points shows the analytical uncertainty on the measurements. Orientations of the cpx crystals were determined using the SHAPE software (Dowty 1987), using cpx unit cell parameters *a:b:c* = 1.097:1:0.596 and β = 106.97°, by matching measured interfacial angles with those of modelled cpx sections

Table 1 Summary of timescales of crystal growth and residence in the Late Bronze Age rhyodacite

Mineral	Method	Time prior to eruption (years)	Geological interpretation of timescale
Orthopyroxene	Mg–Fe diffusion (Dohmen et al. 2016)	1–459; outlier at 852	High-T opx phenocryst residence
	Mg–Fe diffusion (Ganguly & Tazzoli 1994)	1–110; outlier at 157	High-T opx phenocryst residence
Clinopyroxene	Mg–Fe diffusion	2–500; outliers at 1173–2031	High-T cpx phenocryst residence
Plagioclase	Mg diffusion	1.5–60	High-T plag phenocryst residence
Plagioclase	Mg diffusion	< 1.5	High-T residence of rimless calcic plag crystals
Plagioclase	Crystal size distribution	40–800	Growth time of plag phenocrysts
Plagioclase	H_2O diffusion	< 2	Arrival of last silicic input into the magma chamber

Opx orthopyroxene, *cpx* clinopyroxene, *plag* plagioclase, *High-T* high temperature

crystallization began no more than 450 years prior to eruption (possibly with an earlier phase at ~ 850 years; Fig. 6a) and was still ongoing within the last few years prior to the eruption.

A total of 26 profiles in seven cpx crystals were modelled perpendicular to the *c* axis assuming initial step functions in Mg# and distinguishing between profiles across the wispy diffusion fronts defining the core-rim boundary (Fig. 5c, e), and profiles across zone boundaries within the rims (Figs. 5a, c, e, 6b). The wispy core-rim boundaries of three cpx crystals give 543–1700 years, but are probably significantly overestimated because the boundaries are not planar and hence not well represented by 1D modelling (Fig. 5c, e). This is unlike the core-rim boundaries in the opx crystals, which are approximately planar (Fig. 3e). Zone boundaries within the cpx rims, all of which are planar, give timescales of 2–500 years, with the best-quality fits ($R^2 > 0.99$) giving 2–120 years (Fig. 6b). Fuzzier planar boundaries deeper in the rims give 1173–2031 years.

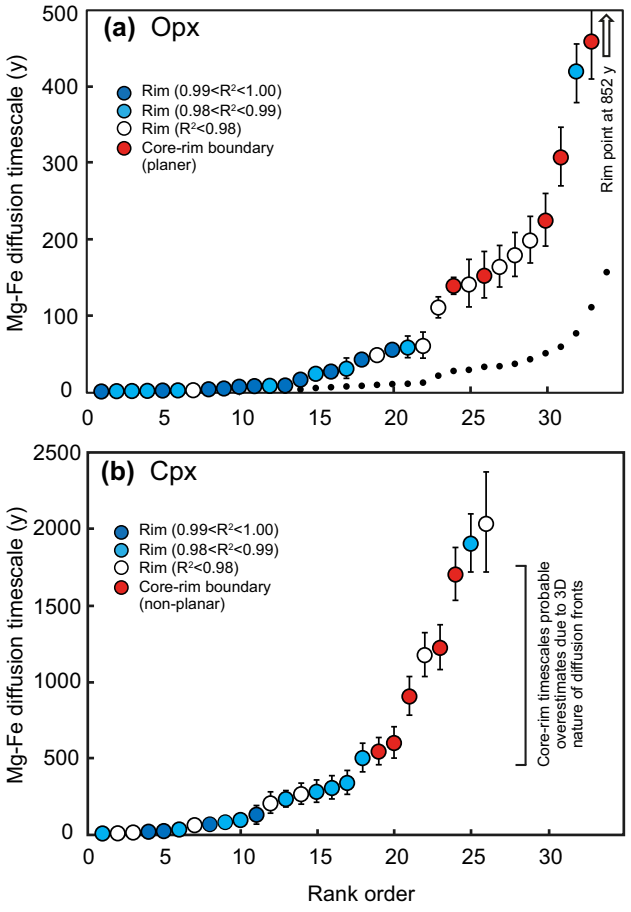

Fig. 6 Mg–Fe diffusion timescale spectra for **a** opx and **b** cpx, determined in both cases perpendicular to the *c* axes of the crystals, as described in the text. Timescales determined on zone boundaries within the crystal rims are colour coded according to fit quality of the diffusion model to the measured Mg# profile. The error bars are calculated from the uncertainty on the $\sqrt{4Dt}$ fit parameter, which takes into account the small analytical error (the error propagation calculation is explained in Online Resource 3). The insets on both figures show diffusion timescale as a function of distance from the crystal edge to the core-rim boundary (or centre of crystal in crystals lacking cores), normalized to one. The opx timescales are calculated using the diffusion coefficient of Dohmen et al. (2016); the small dots show the timescales obtained using Ganguly and Tazzoli (1994) for comparison. The cpx timescales are calculated using the diffusion coefficient of Müller et al. (2013) corrected for diffusion anisotropy, as explained in Online Resource 3

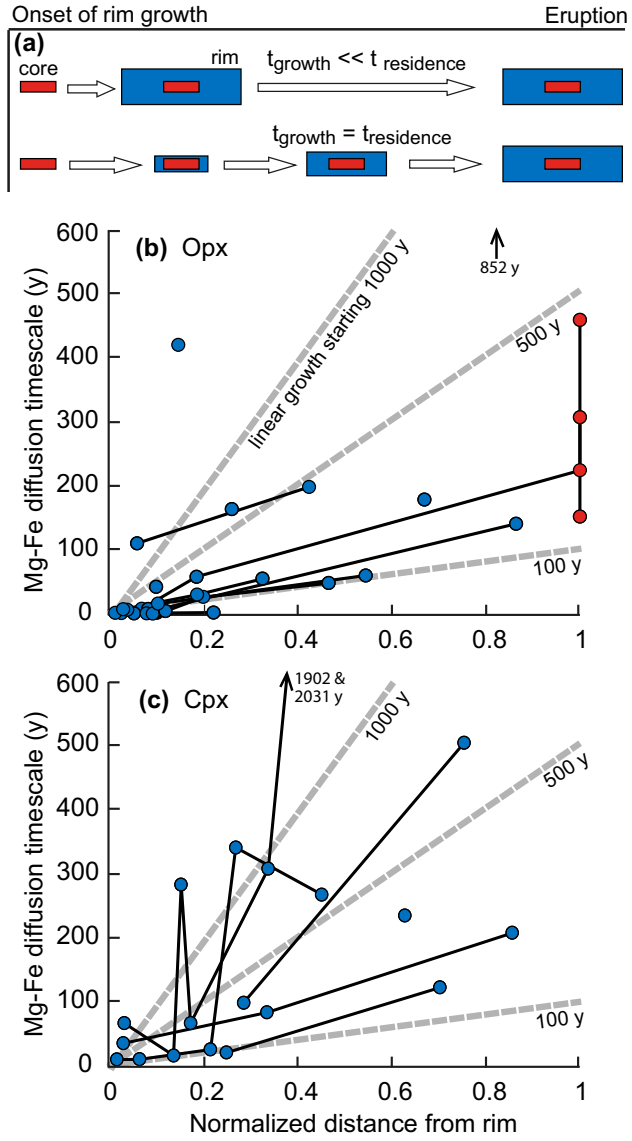

Fig. 7 **a** Sketches of two endmember scenarios for the growth of pyroxene phenocrysts in the Late Bronze Age magma. In the upper scenario, the crystal grows to its final size, then sits at high temperature until eruption; in the lower scenario the crystal grows progressively. **b, c** Variation of diffusion–derived residence timescales for intra-rim zone boundaries as a function of depth in the crystal. The grey lines depict linear growth from different onset times. Blue dots are timescales from within the crystal rim, and red dots are timescales from the core-rim boundary. Data for the wispy core-rim boundaries in cpc crystals have been omitted, for reasons discussed in the text. Most crystals appear to have grown progressively until the moment of eruption quench, corresponding to the lower case in **a**

The diffusion timescales for cpx are longer than those of opx. However, if the wispy core-rim boundary timescales are excluded, then the timescales for cpx range from < 1 to 500 years prior to eruption (possibly extending to 1000–2000 years; Fig. 6b), which is consistent with the opx timescales using the diffusion coefficient of Dohmen et al. (2016). We accept this interpretation, while recognizing that some inner zones of the cpx rims may pre-date the rims on the opx crystals.

Two endmember situations can be envisaged for crystal rim growth. In one, growth occurred very rapidly and the crystal then resided at high temperature until eruption (case $t_{growth} \ll t_{residence}$; Fig. 7a). Alternatively, the rims grew continuously from initiation until eruption (case $t_{growth} = t_{residence}$; Fig. 7a). The diffusion timescales for both opx and

cpx generally increase from small values near crystal edges to much larger values in the interior (Fig. 7b, c). Although this may in part be an artefact due to the higher probability of more oblique intersection of zone boundaries at depth than near the crystal surface, it suggests that the scenario $t_{growth} = t_{residence}$ is more realistic for LBA magma. Visual extrapolation of the timescales back to the core-rim boundary (or to the centre of the phenocryst, if core-free) suggests the onset of rim growth as early as > 1000–2000 years to as late as < 100 years, with most lying in the range 600–100 years. Converting this to growth rate gives 10^{-11}–10^{-10} mm s^{-1} for both pyroxene species.

Additional timescale information from plagioclase

Three additional timescale constraints are provided by studies involving plagioclase. First, Druitt et al. (2012) placed constraints on the pre-eruptive residence timescale of $An_{40\pm3}$ plagioclase by characterizing Mg contents across core-rim boundaries using SIMS, reconstructing the initial growth profiles, and then modelling subsequent Mg diffusion. The $An_{40\pm3}$ rims were proposed to have overgrown the $An_{50\pm7}$ cores 0.3–12 years prior to eruption, with the rimless $An_{50\pm7}$ crystals residing in the rhyodacite for ≤ 0.3 years prior to eruption. However, application of a new, better-constrained plagioclase Mg diffusion coefficient (Van Orman et al. 2014) raises the timescale of $An_{40\pm3}$ plagioclase residence from 0.3–12 years to 1.5–60 years, and that of the rimless $An_{50\pm7}$ crystals from < 0.3 to < 1.5 years (Online Resource 2).

Second, crystal size distributions (CSD) can provide time information if assumptions are made concerning crystal growth rate (see reviews by Higgins 2006 and; Armienti 2008). New plagioclase CSDs (Online Resource 2), when combined with a crystal growth rate derived from the Mg diffusion data, give a characteristic plagioclase growth timescale of < 40–800 years, which is similar to the residence timescales derived from the pyroxenes. This approach is circular in that we require a growth rate based on diffusion modelling to obtain a timescale from the CSD data. However, it shows that the CSDs and diffusion profiling return mutually consistent timescales.

Third, some MIs in plagioclase $An_{50\pm7}$ cores contain higher H_2O (≤ 6.9 wt%) than those in the $An_{40\pm3}$ rims (4.0–5.0 wt%) (Druitt et al. 2016). We have used the H_2O diffusion model of Qin et al. (1992) to estimate that a core-hosted MI with 6.9 wt% H_2O requires < 2 years to diffusively re-equilibrate through its host plagioclase with ambient melt containing 4.5 wt% H_2O (Online Resource 2). This shows that cores containing H_2O-rich MIs must have arrived in the magma chamber < 2 years preceding the eruption to have avoided diffusive re-equilibration.

Discussion

We now bring together previously published data on the LBA rhyodacite with the new timescale constraints to interpret the processes that took place during build-up to the LBA eruption. The term 'phenocryst' is used for a crystal that grew from its co-erupted host melt (allowing for small compositional variations), 'antecryst' is used for a crystal grown from a melt different from the host, but related to the same magmatic system (e.g., Hildreth and Wilson 2007), and 'xenocryst' is used for a crystal derived from an earlier magmatic system.

Origins of the crystal populations

Phenocryst crystallization

The main plagioclase ($An_{40\pm3}$), opx (Mg# 57–61) and cpx (Mg# 63–68) components (constituting the rims on core-bearing crystals, and core-free crystals of rim composition) are interpreted as phenocrystic, for the following reasons: (1) values of K_D (=$[Fe^{tot}/Mg]_{mineral}/[Fe^{tot}/Mg]_{melt}$; where Fe^{tot} is total iron) for opx and cpx derived from the phase equilibria data of Cadoux et al. (2014) on LBA pumice are 0.29 ± 0.07 and 0.22 ± 0.05, respectively. The opx, therefore, crystallized from melt with Mg# of 24–31, and the cpx from melt with Mg# of 26–32, which span the compositional range between bulk rhyodacite pumice (Mg# 26–32) and its interstitial glass (Mg# of 18–24). Assuming equilibrium between the rims of opx and cpx crystals, the two-pyroxene thermometer of Putirka (2008; Eq. 36) yields a temperature of ~ 850 °C, which is consistent with the Fe–Ti oxide estimates. (2) Plagioclase $An_{40\pm3}$ compositions are also consistent with crystallization from this range of melts, based on their Sr contents (Druitt et al. 2012) and on phase equilibria (Cadoux et al. 2014). (3) Melt inclusions in all three minerals have compositions ranging from bulk pumice to interstitial glass (Online Resource 1). Although the plagioclase crystals have slightly different Sr isotopic ratios than the host glass, this is attributed to post-crystallization contamination of the melt by a more radiogenic component (Martin et al. 2010; see below).

The phenocrysts are interpreted as recording one or more events of crystallization of the rhyodacitic magma in the proportions plag ≫ opx > cpx. All three phenocryst phases exhibit oscillatory zoning indicative either of varying P–T–X conditions, or of kinetic effects, during growth (Streck 2008). Multiple sawtooth zoning in $An_{40\pm3}$ plagioclase phenocrysts may record repeated cycles of

dissolution–precipitation due to fluctuations of temperature, P_{H_2O}, and/or melt composition, probably during slow growth (Streck 2008). On the other hand, the presence of Al sector zoning in a small proportion of opx phenocrysts is indicative of fast growth, at least initially. Sector zoning of Al has been generated experimentally in opx by Schwandt and McKay (2006), who showed that it is characteristic of rapid crystal growth with differential entrapment of highly charged cations such as Al^{3+}.

Antecrystic cores of plagioclase, opx and cpx

The compositional and textural diversities of the plagioclase, opx and cpx cores—patchy zoning, multiple dissolution–reaction–precipitation textures, and (in cpx) wispy diffusional overprinting (Fig. 5)—are suggestive of protracted open-system histories prior to incorporation into the rhyodacite. The corroded forms of many cores record a perturbation of P–T–X conditions prior to rim overgrowth.

Possible origins for the cores include (1) xenocrysts derived from older volcanic formations, (2) in-mingled antecrysts from the co-erupted andesitic components (which indeed contain crystals that overlap compositionally with the cores; see Table 4 in Druitt 2014), or (3) antecrysts derived from the source region of the rhyodacite. In some of the plagioclase crystals, the $An_{50\pm7}$ cores and $An_{58–88}$ inner cores have the same ranges of Sr isotopic compositions as the $An_{40\pm3}$ rims (Martin et al. 2010; Di Salvo et al. 2013), which would tend to rule out origin 1. It would also rule out origin 2, since plagioclase in the co-erupted high-Ba andesitic components is more radiogenic ($^{87}Sr/^{86}Sr$ of 0.7051–0.7055) than that in the rhyodacite (0.7049–0.7051) (Martin et al. 2010). The plagioclase cores would thus have had to have resided long enough in the rhyodacite to come to isotopic equilibrium, which for a 100-µm-diameter An_{50} crystal would take 10^3 years at 860 °C (Davidson et al. 2001).

We tentatively interpret many of the plagioclase, opx and cpx cores as antecrysts derived from the source region of the rhyodacite. Several lines of evidence are consistent with this: (1) the compositions of the cores (plag $An_{50\pm7}$; cpx Mg# 70–74; opx Mg# 65–71) are very similar to those of the crystal assemblage in equilibrium with LBA-like, 69 wt% SiO_2 melt (plag $An_{50\pm5}$; cpx Mg# 70–75; opx Mg# 70–75) at the postulated source conditions in the experiments of Andújar et al. (2016). (2) Compositions of MIs within the plagioclase $An_{50\pm7}$ cores are consistent with equilibrium with 69 wt% SiO_2 melt (Online Resource 1). (3) Rimless $An_{50\pm7}$ plagioclases have glass selvages of this same composition (Online Resource 1). (4) Sr contents of $An_{50\pm7}$ plagioclase cores and rimless $An_{50\pm7}$ plagioclase imply equilibrium with melts of 63–69 wt% SiO_2 (see Fig. 3d of Druitt et al. 2012).

The rimless $An_{50\pm7}$ plagioclase

The rimless $An_{50\pm7}$ plagioclase crystals were introduced (immersed in 69 wt% SiO_2 melt) into the magma within 1.5 years of the eruption, probably immediately prior to, or during, eruptive phase 4. Their heterogeneous distribution implies that intermingling was still ongoing at the time of eruption. We do not have H_2O analyses of MIs in these crystals, so their depth of origin is unconstrained. These crystals lack $An_{40\pm3}$ rims, implying insufficient time for rim growth prior to eruption quench. They may have been entrained into the magma chamber from underlying crystal mushes during phase 4 caldera collapse.

Rapid magma transfer and chamber assembly

The collective dataset shows that: (1) the LBA rhyodacite was derived mostly from a source region of gabbroic/dioritic composition at 8–12 km depth in the subcaldera pluton, and was transferred to a well-mixed magma chamber at 4–6 km, from where it was erupted; (2) almost all discharged plagioclase, opx and cpx phenocrysts had crystallized within 1000–2000 years of the eruption, mostly within 600–100 years, and that they had grown continuously from initiation until eruption quench; (3) growth of phenocrysts with antecrystic cores containing H_2O-rich melt inclusions must have occurred ≤ 2 years prior to eruption.

Why did most of the crystals form so late relative to the 17,000-year-preceding inter-Plinian period? One possibility is that the LBA magma chamber grew incrementally in the upper crust over many thousands of years, and that crystals were progressively removed by sedimentation. In this case, only the most recently formed phenocrysts would have been retained by the magma and erupted. To test this, we have modelled in Online Resource 5 the sedimentation rate of plagioclase and pyroxene crystals in the rhyodacite, taking reasonable values for the magma properties (viscosity of 3×10^4 Pa.s and density of 2300 kg m^{-3}) and chamber thickness (~ 1 km), and accounting for convection. The results show that the characteristic timescale of crystal extraction by sedimentation, even for the largest crystals, is at least an order of magnitude longer than the residence timescales recorded by most of the crystals themselves. We, therefore, conclude that the data are not consistent with phenocryst growth in a slowly cooling and progressively crystallizing magma chamber over many thousands of years, but instead imply the existence of a crystallization event (or several events) within a few centuries to years of the eruption.

We consider three processes that could have caused such a crystallization event: (1) CO_2 flushing from underplated mafic magma (Caricchi et al. 2018), (2) polybaric ascent and cooling (Cottrell et al. 1999), and (3) injection of a hotter, antecryst-bearing melt into a cooler magma chamber (Druitt

et al. 2012). A fourth possibility, overpressure release during eruption, is not viable because the timescales are much longer than those of the eruption (probably months to weeks for phase P0, days to hours for phases 1–4; Druitt 2014).

Inspection of Fig. 3 of Cadoux et al. (2014) shows that (at 200 MPa) 13% crystallization could be produced by a drop of H_2O content from 6.3 to 5.2 wt%, which could be achieved by adding about 400 ppm CO_2 (process 1; estimated using the algorithm VolatileCalc of Newman and Lowenstern 2002). However, MIs in the rhyodacite phenocrysts contain much lower CO_2 (all < 200 ppm and most < 100 ppm; Druitt et al. 2016), so while we cannot firmly exclude some CO_2 flushing from underplated basalt, it was probably not the main process driving crystallization. Some combination of processes 2 and 3 must have been mainly responsible.

To test this, we have plotted on a pressure–temperature diagram (Fig. 8) the conditions of the source region (green box) and pre-eruptive magma chamber (orange box). We have also superimposed the liquidus of the LBA rhyodacite and contours of crystallinity from the experiments of Cadoux et al. (2014) at the slightly H_2O-undersaturated conditions appropriate for the LBA magma chamber. Ascent of the rhyodacitic melt from the source region to the magma chamber

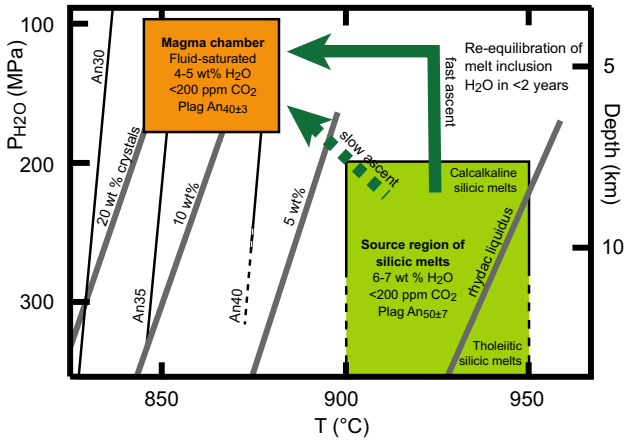

Fig. 8 Pressure–temperature diagram showing the pre-eruptive magma chamber (orange) and the main source region for the rhyodacite (green). Crystallinity contours (in wt%, grey lines) and plagioclase anorthite content (An%, black lines) for the LBA rhyodacite are extrapolated from the phase equilibria experiments of Cadoux et al. (2014) under volatile-saturated conditions at X_{H_2O} =0.85, where X_{H_2O} = molar $H_2O/[H_2O+CO_2]$. Green arrows show possible P–T trajectories from the deep source region to the magma chamber. The dashed green arrow depicts ascent slow enough that the magma remains in thermal equilibrium with its surroundings, and involves crystal growth by both decompression and cooling. The solid green arrow depicts very fast, isothermal ascent, and involves crystal growth mostly at shallow depths by cooling and much less by decompression. Note that the paths are schematic and do not take into account adiabatic cooling or release of latent heat of crystallization. The data presented in this paper are more consistent with fast ascent (solid green arrow), as discussed in the text

would have involved 40–140 MPa of decompression and 40–100 °C of cooling, resulting in growth of 5–15 wt% of phenocrysts of An_{35-40} plag ≫ opx > cpx (Cadoux et al. 2014), in agreement with observations. Plagioclase-melt temperatures given by MIs in the $An_{40±3}$ phenocrysts and phenocrystic rims span a range of 30–60 °C (Table 3 in Druitt et al. 2016), broadly consistent with this amount of cooling. Had melt ascent been slow (dashed green arrow, Fig. 8), crystal growth would have occurred through a combination of cooling and decompression prior to injection into the magma chamber, whereas had it been rapid (solid green arrow, Fig. 8), most crystal growth would have occurred subsequently by cooling in the chamber.

Our observations favour mainly rapid melt transfer. First, the antecrystic plagioclase $An_{50±7}$ cores containing H_2O-rich melt inclusions were transferred from depth into the magma chamber (and overgrown by the $An_{40±3}$ rims) less than 2 years before the eruption onset. Hence at least that late magma batch must have ascended rapidly. Second, many pyroxene phenocrysts appear to have grown continuously from their initiation until the eruption (Fig. 7b, c). Had growth been driven partly by decompression (dashed green arrow), then ascent of the magma from depth to the magma chamber would have had to have taken many centuries to decades, which is inconsistent with the first line of evidence and also seems unlikely given current models of silicic magma transfer through the crust (Petford et al. 1993; Menand et al. 2015). Third, some opx crystals exhibit Al sector zoning, possibly consistent with rapid initial crystallization followed by prolonged residence in the magma chamber accompanied by further growth. The data, therefore, favour an interpretation involving rapid magma ascent followed by prolonged phenocryst growth in the cooler environment of the upper crust. Sawtooth zoning in plagioclase phenocrysts may record repeated precipitation–dissolution cycles in the magma chamber due to convective turnover and heating by the arrival of successive batches of hotter silicic melt.

We note that if phenocryst growth took place mainly by cooling over a 30–60 °C window, then the residence timescales calculated at the final, pre-eruptive temperature of 855 °C may be overestimated. For example, a 30 °C higher mean residence temperature (i.e. 885 °C), would half the modelled diffusion timescales.

The magma chamber was assembled over ~ 10^3 years, and mostly over a few centuries to decades prior to the eruption. While Cottrell et al. (1999) assumed that this involved most of the erupted magma, Druitt et al. (2012) suggested more conservatively that it involved just the last silicic melt batch to enter the chamber. However, our pyroxene timescale data now lead us to prefer the interpretation of Cottrell et al. (1999), since most of the opx and cpx phenocrysts form a single timescale population (Fig. 6).

Reconstruction of the events

Figure 9 summarizes the different events inferred to have occurred over the 17-ky-long inter-Plinian period prior to the LBA eruption. Following the 22-ka Cape Riva eruption, repeated crustal intrusion of hydrous basaltic to andesitic melts generated LBA-like silicic melts, probably through a combination of fractional crystallization, crustal melting and pluton defrosting. Explosive eruption of small volumes of this silicic magma at 12–13 ka shows that these LBA-like melts were already present at depth by this time (Satow et al. 2015). By several hundred years prior to the LBA eruption, a region of variably mushy gabbro/diorite extended from an unknown upper limit to at least 12 km beneath the volcano. The region consisted of plagioclase, cpx, opx and calcalkaline silicic melts with 6–7 wt% H_2O. Amphibole was probably present in cooler (< 940 °C) parts of the body. Smaller quantities of more tholeiitic silicic melts may have been present at greater depths. Thermal waxing and waning during prolonged incubation of crystals and melt may have imparted disequilibrium textures on the crystals that were subsequently erupted as phenocryst cores.

Following possible initial upwellings of LBA-like silicic melt, runaway magma chamber assembly began a few centuries prior to the eruption. Rupturing of the mush structure by ascending melts caused entrainment of plagioclase ($An_{50\pm7}$), cpx (Mg# 70–74) and opx (Mg# 65–71) crystals (antecrystic cores). Decompression of volatile-saturated melts with 6–7 wt% dissolved H_2O from 240 MPa to 100–160 MPa caused exsolution of 10–15 vol% of vapour during ascent (Druitt et al. 2016). Upon reaching 4–6 km depth, bubbly melts spread out and accumulated in a single large lens (the magma chamber).

Growth of plagioclase, opx and cpx in the ascending melts was driven partly by volatile-saturated decompression during ascent, but mostly by several tens of °C cooling in the new upper crustal environment. Any amphibole inherited from the source was resorbed. Silicic melts arriving in the magma chamber were progressively homogenized by convection (Druitt et al. 2012, supplementary discussion). Arrival of silicic melts (carrying source-derived plagioclase

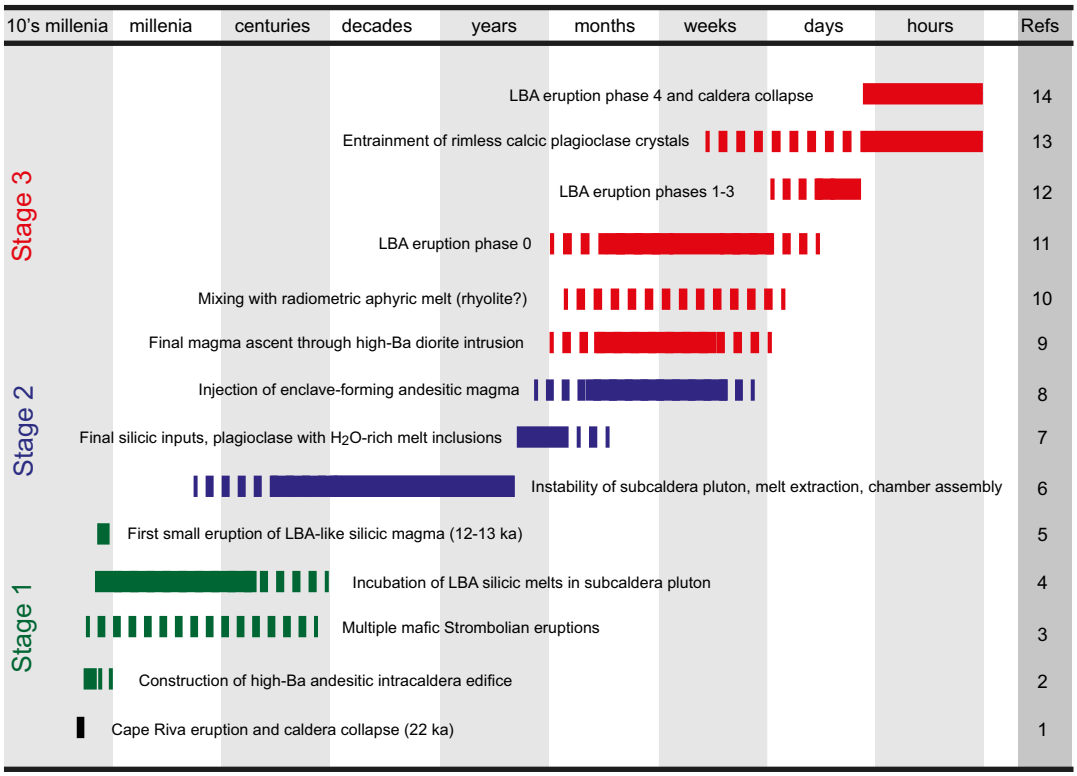

Fig. 9 Timeline of events leading up to, and during, the Late Bronze Age (LBA) eruption, following the 22-ka Cape Riva eruption. Timescales are schematic, with solid lines showing best constraints, and dashed lines showing possible extensions. The timelines are coloured according to the three stages, discussed in the main text. Source references for the events are as follows: 1. Druitt et al. (1999), Fabbro et al. (2013). 2 and 9. Druitt (2014), Karátson et al. (2018). 3. Vespa et al. (2006), Vaggelli et al. (2009). 4 and 6. Cottrell et al. (1999), Druitt et al. (2012, 2016), Cadoux et al. (2014), Andújar et al. (2016), present paper. 5. Satow et al. (2015). 7. Druitt et al. (2016), present paper. 8. Cottrell et al. (1999). 10. Martin et al. (2010). 11. Cioni et al. (2000). 12 and 14. Sparks and Wilson (1990), Druitt (2014). 13. Druitt et al. (2012), present paper

antecrysts with H_2O-rich MIs) were still ongoing within 2 years of the eruption, and a small volume of andesite was introduced in the final months to days before eruption (Cottrell et al. 1999). At some late stage, after the growth of most crystals, the rhyodacite mixed with a radiogenic, aphyric melt (Martin et al. 2010).

Finally, conditions were attained within the magma chamber for the propagation of a dyke to the surface, and the eruption began. During ascent, the dyke intersected a variably crystallized shallow intrusion of high-Ba, amphibole-bearing diorite, pushing out some of its contents (see Fig. 12 in Druitt 2014). It is possible that the radiogenic, aphyric melt recognized by Martin et al. (2010) resided within this intrusion, which was indeed more radiogenic than the rhyodacite. Entrainment of rimless $An_{50\pm7}$ plagioclase and 69 wt% SiO_2 melt may have taken place from crystal mushes of the magma chamber floor as the caldera collapsed during phase 4. Assuming a 45-km^2 area comparable to that of the caldera, a large proportion of the < 2-km-thick magma chamber must have been emptied during the eruption to account for the 30–80 km^3 DRE volume discharged.

Dynamics of melt extraction and ponding

Our evidence for the LBA eruption agrees with an emerging consensus that large silicic magma chambers can be assembled on geologically short timescales through high-flux melt transfer events (Allan et al. 2013, 2017; Wotzlaw et al. 2014; Barker et al. 2016; Cooper et al. 2017; Fabbro et al. 2017). It is also consistent with the mush instability model, in which dispersed melt-rich domains rapidly amalgamate to form one or more large lenses of eruptible magma (Christopher et al. 2015; Cashman et al. 2017; Sparks and Cashman 2017). The time-averaged flux of melts into the LBA magma chamber during assembly is estimated at 0.1–1 $km^3\ year^{-1}$ (50 km^3 in 500–50 years). These estimates are higher than that of Druitt et al. (2012) (> 0.05 $km^3\ year^{-1}$), who envisaged that only a few km^3 of the magma ascended on these timescales, not all of it. Rapid transfer of such large volumes of viscous, silicic magma would require three conditions.

1. The melt was already segregated into macroscopic melt-rich pockets and lenses in the source region, perhaps due to porous flow instabilities (Solano et al. 2012) or tectonic stresses (Katz et al. 2006; Weinberg et al. 2015), as observed in some fossilized intrusions (Brown 2013; Holness 2018 and references therein); another possibility is that the melt was stored as a sill complex deep within the subcaldera pluton (Jaxybulatov et al. 2014).
2. Compaction-driven melt flow took place through a network of high-permeability conduits or dykes (Petford et al. 1993; Menand et al. 2015), since intergranular flow of silicic melt would be far too slow (e.g., Solano et al. 2012).
3. Unless compensated by basaltic intrusion at depth, rapid extraction of large volumes of silicic melt from the source region was accompanied by (or driven by) subsidence, creating space for the inflating magma chamber higher up (Weibe and Collins 1998; Cruden 1998; Grocott et al. 2009).

Instability of the source region would have initiated a complex chain of magmatic processes consistent with our observations: mixing of compositionally and thermally diverse melt batches, thermal cycling of entrained crystals, polybaric melt ascent, and decompression- and/or cooling-driven crystal growth as the heterogeneous melt mixture drained upwards. The appeal of this mechanism is that it might have occurred on timescales governed by the rheology of the crystal mush, possibly as short as a few years (Sparks and Cashman 2017). More research is required to understand what caused the LBA source region to unlock and compact. It may have occurred spontaneously once (following melt production over many thousands of years) the melt fraction exceeded some threshold. Alternatively, some combination of basaltic intrusion (Cottrell et al. 1999), seismic shaking (Davis et al. 2007; Gottsman et al. 2009) and faulting (Allan et al. 2017) due to a regional rifting event may have been responsible.

It is also unclear why the ascending melts injected to form a short-lived holding chamber at 4–6 km depth, rather than vent directly at the surface. One possibility is that the top of the subcaldera pluton was a level of steep vertical gradients in density and rheology between underlying ductile mushes and overlying brittle subsolidus rock. Sill formation occurs where dykes encounter layers of low density or high rigidity, causing magma to inject laterally (Menand 2011). Epicentres of earthquakes beneath the caldera during unrest in 2011–2012 were limited to the upper few km of the crust (Newman et al. 2012), suggesting that the brittle–ductile transition indeed lies a few km beneath the caldera. The LBA magma chamber might be visualized as a 'tear' near the top of the foundering subcaldera pluton, into which the ascending melts injected. Other possibilities are that the ascending melts intruded by hydrofracturing along a level of crustal weakness (Castro et al. 2016), or that they injected along a low-angle shear zone, as observed in some exhumed intrusive complexes in the Aegean region (Rabillard et al. 2015). We envisage that the bubbly magma remained in this transient holding chamber until sufficient overpressure had developed to drive a dyke to the surface through the cool, brittle uppermost crust and initiate eruption (Degruyter et al. 2016). Uplift and rifting of the surface above the magma chamber may have caused reactivation of caldera faults like the Kameni line, along which the eruption began (Fig. 1c).

The eruption `trigger'

The evidence for high-flux transfer of large volumes of bubbly silicic melt into the upper crust over the centuries and decades prior to the LBA eruption implies that the eruption itself was almost certainly a consequence of that process. The final input of silicic magma occurred less than 2 years before the eruption onset; the bubbly magma may have risen to the top of the chamber and been discharged first, explaining the presence of H_2O-rich plagioclase-hosted MIs early in the eruption. It was conceivably this final melt batch that tipped the magma overpressure over the threshold for dyke propagation, triggering the eruption. However, in another sense the eruption had been 'triggered' as much as several centuries previously by the onset of instability deep within the subcaldera pluton. The LBA eruption was probably not the result of a single trigger process, but a complex chain of events.

The presence of quenched andesitic enclaves in the LBA magma led Sparks et al. (1977) to propose that replenishment by andesitic magma played a fundamental role in causing the eruption by pressurizing the chamber. Indeed, the concept of 'mafic' triggering of silicic eruptions is widespread (Pallister et al. 1992; Murphy et al. 1998; Snyder 2000; Leonard et al. 2002; Ruprecht and Bachmann 2010). Cottrell et al. (1999) argued that the andesite was introduced into the magma chamber within a few months to days of the eruption. However, our evidence suggests that the volume of silicic melt flooding into the magma chamber was probably much larger than that of the associated andesitic magma. While deep injection of andesite (along with other factors) may have initially played a role in driving the pluton into a state of instability, once silicic melt transfer was underway the andesite may have simply been carried passively from depth by its silicic host, or entrained from nearby intrusions, and have contributed little to pressurizing the chamber.

High-flux melt transfer events at Santorini

Study of the dacitic products of the Cape Riva eruption has revealed a similar story to that proposed for the LBA eruption (Fabbro et al. 2013, 2017). The Cape Riva eruption was preceded by prolonged leakage of a chemically different dacite, showing that the Cape Riva magma chamber did not exist for more than 2800 ± 1400 years, making it a short-lived feature on geological timescales. Furthermore, phenocryst rim timescales for Cape Riva dacite (1–25 years for plagioclase using the Van Ormen et al. 2014 diffusion coefficient; from 4 to ~ 1000 years for opx using the Dohmen et al. 2016 diffusion coefficient) are broadly similar to those for the LBA magma, and record phenocryst residence over the centuries to years prior to eruption. Drawing on MI $H_2O + CO_2$ barometry and phase equilibria data, Fabbro et al. (2017) postulated that the Cape Riva dacitic magma ascended in a runaway process from a deep source reservoir to a short-lived, shallow-holding chamber, from which it subsequently erupted.

It, therefore, seems likely that rapid magma chamber assembly prior to Plinian eruptions is a general process at Santorini volcano. This behaviour resembles that of Taupo caldera, where studies also imply rapid magma chamber assembly prior to large eruptions (Allan et al. 2013, 2017; Barker et al. 2016; Cooper et al. 2017). Both Santorini and Taupo lie in active continental rift environments (Nomikou et al. 2016; Beaven et al. 2016), suggesting possible roles of seismicity and crustal extension in triggering high-flux melt transfer events at the two systems.

While the normal ascent rate of silicic magma into the upper crust below Santorini through slow compaction of crystal mushes may be sufficient to form small, shallow magma pockets, major destabilization events may be required to build the large magma chambers that feed Plinian eruptions and form calderas. Indeed, if magma chamber formation is driven and accommodated by deep instabilities, then Santorini caldera might be the surface expression of foundering extending down to the middle crust, both above and below the upper crustal chamber (Fig. 10). The estimated flux of melt to the inflating magma chamber prior to the LBA eruption (0.1–1 km^3 $year^{-1}$) is two to three orders of magnitude higher than eruption rates during inter-Plinian periods (0.001 km^3 $year^{-1}$). Repeated destabilization events in the pluton beneath Santorini may provide a way of reconciling a continuous supply of basaltic magma and heat to the base of the crust with the intermittency of large silicic eruptions.

Conclusions

Integration of mineral zoning patterns, modelling of multi-mineral diffusion profiles, analysis of crystal size distributions, mineral thermometry, laboratory phase equilibria experiments, and mixed-volatile melt inclusion barometry have enabled us to unravel the history of the rhyodacitic magma of the 30–80-km^3 DRE Late Bronze Age (LBA) caldera-forming eruption, and to refine and reconcile the different models that have been proposed previously for this system (Cottrell et al. 1999; Martin et al. 2010; Druitt et al. 2012). Diffusion profile modelling provides timescales for high-temperature residence of three main phenocryst phases (plagioclase, opx, and cpx) that are consistent to within an order of magnitude, and records one or more events of phenocryst crystallization that took place over the several centuries to years prior to the eruption.

The LBA magma had a two-step history, in accordance with recent conceptual models (Fig. 10; Annen et al. 2006;

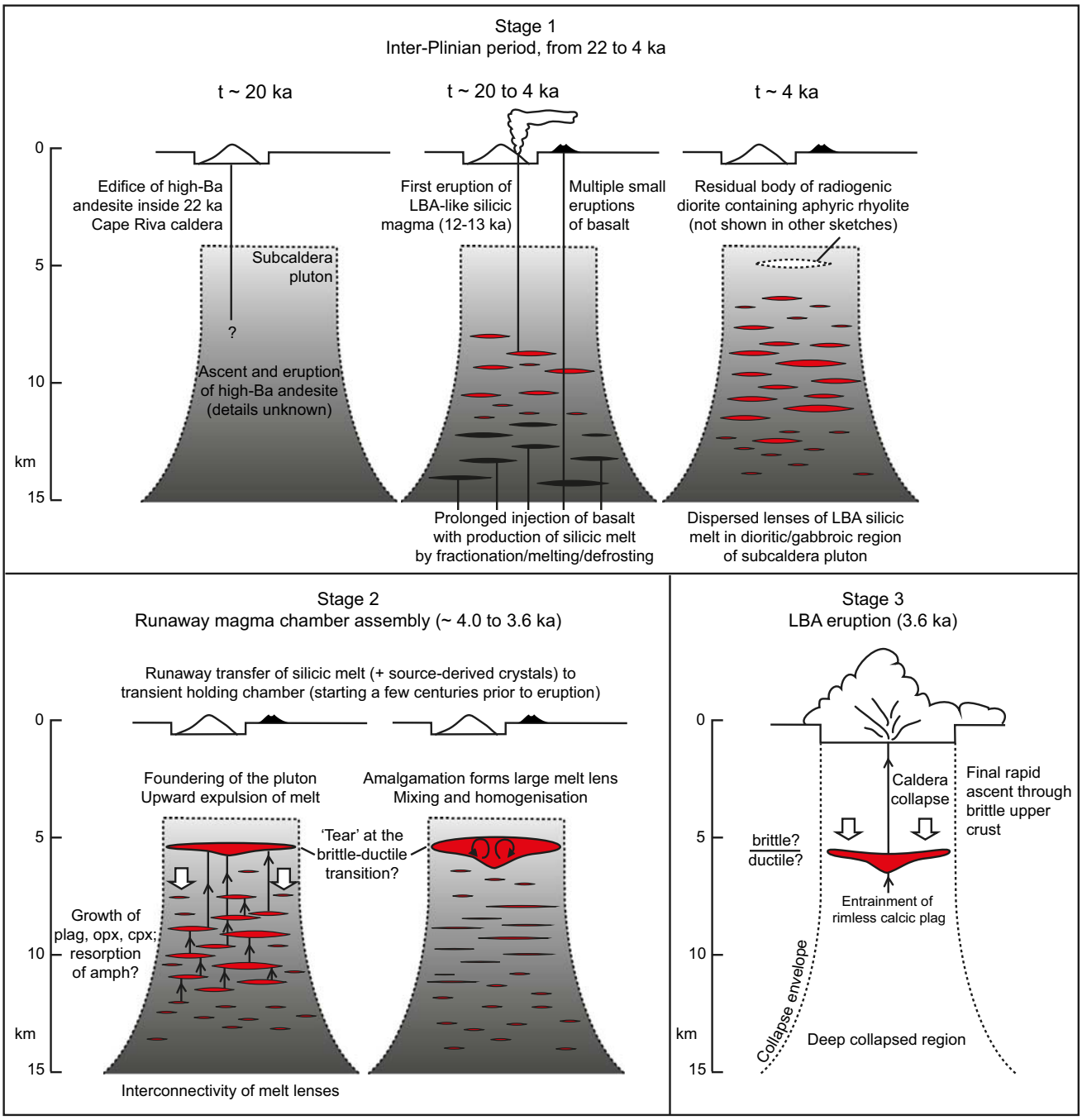

Fig. 10 Model for the events leading up to the Late Bronze Age (LBA) eruption, showing the three main stages discussed in the text: Stage 1—prolonged generation of silicic melts in a dioritic/gabbroic region of the subcaldera pluton; stage 2—instability and compaction-driven transfer of melts to near the top of the pluton, where they accumulate to form a magma chamber; stage 3—final dyke ascent and the LBA eruption

Brown 2013, and references therein): (1) prolonged production over at least 8–9 ky (from 12 to 13 ka to eruption) of silicic melt, mostly in a dioritic/gabbroic region at 8–12 km depth in the subcaldera pluton. (2) Rapid transfer of large volumes of silicic melt to the top of the pluton, where it accumulated to form a magma chamber (4–6 km depth). The crystallization event records the ascent of the vapour-saturated silicic melt and its subsequent cooling in the magma chamber. Magma chamber assembly may have been driven by sudden instability and compaction of the source region (Christopher et al. 2015; Sparks and Cashman 2017), with extraction of melt and associated fluids over a geologically

short period of time. The magma chamber may have been a transient holding level near the top of the subcaldera pluton, at the boundary between underlying ductile mushes and overlying brittle, subsolidus crust.

The location of Santorini in a seismically active continental rift zone raises the possibility that magma chamber assembly was triggered by an episode of tectonic rifting and seismicity, possibly accompanied by basaltic injection into the deep crust. The high rates of upper crustal melt accumulation inferred prior to the LBA eruption (0.1–1 km^3 $year^{-1}$) are two to three orders of magnitude higher than the time-averaged eruptive rates during inter-Plinian periods (0.001 km^3 $year^{-1}$), and are consistent with accumulation rates necessary to build shallow magma chambers in thermal models (Annen 2009; Gelman et al. 2013; Menand et al. 2015).

Rapid magma chamber assembly also took place prior to the 22-ka Cape Riva eruption (Fabbro et al. 2013, 2017), and may be a general process for caldera-forming eruptions at Santorini. Repeated deep destabilization events provide a way of reconciling a continuous supply of basaltic magma and heat to the base of the crust with the intermittency of caldera-forming eruptions. It is consistent with the emerging view that large melt-dominated magma chambers are transient features on geologic timescales (Glazner et al. 2004; Druitt et al. 2012; Cooper and Kent 2014; Barboni and Schoene 2014). Had modern geophysical techniques been available a few centuries or decades prior to the LBA eruption, they might have detected a thick column of crystal mush (e.g., Chu et al. 2010; Huang et al. 2015) or mid-crustal sill complex (Jaxybulatov et al. 2014) beneath Santorini, but probably not a large shallow chamber of melt.

Acknowledgements We thank Jean-Luc Devidal and Jean-Marc Hénot for their expertise in electron microprobe analysis and electron microscopy, respectively, Gareth Fabbro for allowing us to modify his pyroxene diffusion program, Julia Hammer for her introduction to the SHAPE software, Chad Deering for discussions, and Madison Myers for comments on the manuscript. Reviews by J. Ganguly and C.J.N. Wilson were very helpful. TF acknowledges support from the Atlantis-INVOGE program and a National Science Foundation (NSF) EAPSI fellowship grant. HT is supported by a Royal Society University Research Fellowship. MDH acknowledges support from NSERC (Canada) Discovery grants. This is Laboratory of Excellence ClerVolc contribution number 305.

References

Allan ASR, Morgan DJ, Wilson CJN, Millet MA (2013) From mush to eruption in centuries: assembly of the super-sized Oruanui magma body. Contrib Mineral Petrol 166:143–164

Allan ASR, Barker SJ, Millet M-A, Morgan DJ, Rooyakkers SJ, Schipper CI, Wilson CJN (2017) A cascade of magmatic events during the assembly and eruption of a super-sized magma body. Contrib Mineral Petrol 172:49

Andersen DJ, Lindsley DH (1988) Internally consistent solution models for Fe-Mg-Mn-Ti oxides: Fe–Ti oxides. Am Mineral 73:714–726

Andújar J, Scaillet B, Pichavant M, Druitt TH (2015) Differentiation conditions of a basaltic magma from Santorini, and its bearing on the production of andesite in arc settings. J Petrol 56:765–794

Andújar J, Scaillet B, Pichavant M, Druitt TH (2016) Generation conditions of dacite and rhyodacite via the crystallization of an andesitic magma. Implications for the plumbing system at Santorini (Greece) and the origin of tholeiitic or calc-alkaline differentiation trends in arc magmas. J Petrol 57:1887–1920

Annen C (2009) From plutons to magma chambers: thermal constraints on the accumulation of eruptible silicic magma in the upper crust. Earth Planet Sci Lett 284:409–416

Annen C, Blundy JD, Sparks RSJ (2006) The genesis of intermediate and silicic magmas in deep crustal hot zones. J Petrol 47:505–539

Armienti P (2008) Decryption of igneous rock textures: crystal size distribution tools. Rev Mineral Geochem 69:623–649

Athanassas CD, Bourlès DL, Braucher R, Druitt TH, Nomikou P, Léanni L (2016) Evidence from cosmic ray exposure (CRE) dating for the existence of a pre-Minoan caldera on Santorini, Greece. Bull Volcanol 78:35

Bachmann O, Bergantz GW (2004) On the origin of crystal-poor rhyolites: extracted from batholithic crystal mushes. J Petrol 45:1565–1582

Bachmann O, Bergantz G (2008) The magma reservoirs that feed supereruptions. Elements 4:17–21

Bachmann O, Huber C (2016) Silicic magma reservoirs in the Earth's crust. Am Mineral 101:2377–2404

Bacon CR, Druitt TH (1988) Compositional evolution of the zoned calcalkaline magma chamber of Mount Mazama, Crater Lake, Oregon. Contrib Mineral Petrol 98:224–256

Barboni M, Schoene B (2014) Short eruption window revealed by absolute crystal growth rates in a granitic magma. Nat Geosci 7:524–528

Barker SJ, Wilson CJN, Morgan DJ, Rowland JV (2016) Rapid priming, accumulation, and recharge of magma driving recent eruptions at a hyperactive caldera volcano. Geology 44:323–326

Beavan J, Wallace LM, Palmer N, Denys P, Ellis S, Fournier N, Hreinsdottir S, Pearson C, Denham M (2016) New Zealand GPS velocity field: 1995–2013. N Z J Geol Geophys 59:5–14

Bégué F, Deering CD, Gravley DM, Kennedy BM, Chambefort I, Gualda GAR, Bachmann O (2014) Extraction, storage and eruption of multiple isolated magma batches in the paired Mamaku and Ohakuri eruption, Taupo Volcanic Zone, New Zealand. J Petrol 55:1653–1684

Bergantz GW, Schleicher JM, Burgisser A (2015) Open-system dynamics and mixing in magma mushes. Nat Geosci 8:793–796

Bond A, Sparks RSJ (1976) The Minoan eruption of Santorini, Greece. J Geol Soc Lond 132:1–16

Brophy JG (1991) Composition gaps, critical crystallinity, and fractional crystallization in orogenic (calc-alkaline) magmatic systems. Contrib Mineral Petrol 109:173–182

Brown M (2013) Granite: from genesis to emplacement. Geol Soc Am Bull 125:1079–1113

Cadoux A, Scaillet B, Druitt TH, Deloule E (2014) Magma storage conditions of large Plinian eruptions of Santorini Volcano (Greece). J Petrol 55:1129–1171

Caricchi L, Sheldrake TE, Blundy J (2018) Modulation of magmatic processes by CO_2 flushing. Earth Planet Sci Lett 491:160–171

Cashman KV, Sparks RSJ, Blundy JD (2017) Vertically extensive and unstable magmatic systems: a unified view of igneous processes. Science 355:1280

Castro JM, Cordonnier B, Schipper CI, Tuffen H, Baumann TS, Feisel Y (2016) Rapid laccolith intrusion driven by explosive volcanic eruption. Nat Comm 7:13585

Chamberlain KJ, Morgan DJ, Wilson CJN (2014) Timescales of mixing and mobilisation in the Bishop Tuff magma body: perspectives from diffusion chronometry. Contrib Mineral Petrol 168:1034

Christopher TE, Blundy J, Cashman K, Cole P, Edmonds M, Smith PJ, Sparks RSJ, Stinton A (2015) Crustal-scale degassing due to magma system destabilization and magma-gas decoupling at Soufriere Hills Volcano, Montserrat. Geochem Geophys 16:2797–2811

Chu R, Helmberger DV, Sun D, Jackson JM, Zhu L (2010) Mushy magma beneath Yellowstone. Geophys Res Lett 37:L01306

Cioni R, Gurioli L, Sbrana A, Vougioukalakis G (2000) Precursors to the Plinian eruptions of Thera (Late Bronze Age) and Vesuvius (AD 79): Data from archaeological areas. Phys Chem Earth (A) 25:9–11

Cooper KM (2017) What Does a Magma Reservoir Look Like? The "Crystal's-Eye" View. Elements 13:23–28. https://doi.org/10.2113/gselements.13.1.23

Cooper KM, Kent AJR (2014) Rapid remobilization of magmatic crystals kept in cold storage. Nature 506:480–483. https://doi.org/10.1038/nature12991

Cooper GF, Morgan DJ, Wilson CJN (2017) Rapid assembly and rejuvenation of a large silicic magmatic system: insights from mineral diffusive profiles in the Kidnappers and Rocky Hill deposits, New Zealand. Earth Planet Sci Lett 473:1–13

Costa F, Morgan D (2010) Time constraints from chemical equilibration in magmatic crystals. In: Dosseto A, Turner SP, Van Orman JA (eds) Timescales of magmatic processes: from core to atmosphere. Wiley, Chichester, pp 125–159

Costa F, Dohmen R, Chakraborty S (2008) Time scales of magmatic processes from modelling the zoning patterns of crystals. Rev Mineral Geochem 69:545–594

Costa F, Andreastuti S, Bouvet de Maisonneuve C, Pallister JS (2013) Petrological insights into the storage conditions, and magmatic processes that yielded the centennial 2010 Merapi explosive eruption. J Volcanol Geotherm Res 261:209–235

Cottrell E, Gardner JE, Rutherford MJ (1999) Petrologic and experimental evidence for the movement and heating of the pre-eruptive Minoan rhyodacite (Santorini, Greece). Contrib Mineral Petrol 135:315–331

Cruden AR (1998) On the emplacement of tabular granites. J Geol Soc Lond 155:853–862

Davidson J, Tepley F III, Palacz Z, Meffan-Main S (2001) Magma recharge, contamination and residence times revealed by in situ laser ablation isotopic analysis of feldspar in volcanic rocks. Earth Planet Sci Lett 184:427–442

Davis M, Koenders MA, Petford N (2007) Vibro-agitation of chambered magma. J Volcanol Geotherm Res 167:24–36

Deering CD, Cole JW, Vogel TA (2010) Extraction of crystal-poor rhyolite from a hornblende-bearing intermediate mush: a case study of the caldera-forming Matahina eruption, Okataina volcanic complex. Contrib Mineral Petrol 161:129–151

Degruyter W, Huber C, Bachmann O, Cooper KM, Kent AJR (2016) Magma reservoir response to transient recharge events: the case of Santorini Volcano (Greece). Geology 44:23–26

Di Salvo S, Francalanci L, Druitt TH, Braschi E (2013) Short crystal history in the recent magmatic system of Santorini volcano, Greece: inferences from micro-Sr isotope data. Min Mag 77:993 (abstract)

Dohmen R, Ter Heege JH, Becker HW, Chakraborty S (2016) Fe-Mg interdiffusion in orthopyroxene. Am Mineral 101:2210–2221

Dowty E (1987) SHAPE Copyright 1994, Shape Software 521 Hidden Valley Road, Kingsport, TN 37663 USA. http://www.shapesoftware.com

Druitt TH (2014) New insights into the initiation and venting of the Bronze-Age eruption of Santorini (Greece), from component analysis. Bull Volcanol 76:794

Druitt TH, Edwards L, Mellors RM, Pyle DM, Sparks RSJ, Lanphere M, Davies M, Barriero B (1999) Santorini volcano. Geol Soc Lond Memoir 19

Druitt TH, Costa F, Deloule E, Dungan M, Scaillet B (2012) Decadal to monthly timescales of magma transfer and reservoir growth at a caldera volcano. Nature 482:77–80

Druitt TH, Mercier M, Florentin L, Deloule E, Cluzel N, Flaherty T, Médard E, Cadoux A (2016) Magma storage and extraction associated with Plinian and interplinian activity at Santorini caldera (Greece). J Petrol 57:461–494

Fabbro GN, Druitt TH, Scaillet S (2013) Evolution of the crustal plumbing system during the build-up to the 22 ka caldera-forming eruption of Santorini (Greece). Bull Volcanol 75:767

Fabbro GN, Druitt TH, Costa F (2017) Storage and eruption of silicic magma across the transition from dominantly effusive to caldera-forming states at an arc caldera (Santorini, Greece). J Petrol 58:2429–2464

Ganguly J, Tazzoli V (1994) Fe2+–Mg interdiffusion in orthopyroxene: retrieval from the data on intracrystalline exchange reaction. Am Mineral 79:930–937

Gelman SE, Gutiérrez FJ, Bachmann O (2013) On the longevity of large upper crustal silicic magma reservoirs. Geology 41:759–762

Ghiorso MS, Evans BW (2008) Thermodynamics of rhombohedral oxide solid solutions and a revision of the Fe–Ti two-oxide geothermometer and oxygen-barometer. Amer J Sci 308:957–1039

Glazner AF, Bartley JM, Coleman DS, Taylor RZ (2004) Are plutons assembled over millions of years by amalgamation from small magma chambers? GSA Today 14:4–12

Gottsmann J, Lavallée Y, Martí J, Aguirre-Díaz G (2009) Magma-tectonic interaction and the eruption of silicic batholiths. Earth Planet Sci Lett 284:426–434

Grocott J, Arévalo C, Welkner D, Cruden A (2009) Fault-assisted vertical pluton growth: Coastal Cordillera, north Chilean Andes. J Geol Soc Lond 166:295–301

Gualda GAR, Pamukcu AS, Ghiorso MS, Anderson AT, Sutton SR, Rivers ML (2012) Timescales of quartz crystallization and the longevity of the Bishop giant magma body. PloS One 7:e37492

Heiken G, McCoy F Jr (1984) Caldera development during the Minoan eruption, Thira, Cyclades, Greece. J Geophys Res 89:8441–8462

Higgins MD (2006) Quantitative textural measurements in igneous and metamorphic petrology. Cambridge University Press, Cambridge

Hildreth W, Wilson CJN (2007) Compositional zoning of the Bishop Tuff. J Petrol 48:951–999

Holness MB (2018) Melt segregation from silicic crystal mushes: a critical appraisal of possible mechanisms and their microstructural record. Contrib Mineral Petrol 173:48

Hooft EEE, Nomikou P, Toomey DR, Lampridou D, Getz C, Christopoulou M-E, O'Hara D, Arnoux GM, Bodmer M, Gray M, Heath BA, VanderBeek BP (2017) Backarc tectonism, volcanism, and mass wasting shape seafloor morphology in the Santorini-Christiana-Amorgos region of the Hellenic Volcanic Arc. Tectonophys 712–713:396–414

Huang H-H, Lin F-C, Schmandt B, Farrell J, Smith RB, Tsai VC (2015) The Yellowstone magmatic system from the mantle plume to the upper crust. Science 15:773–776

Huijsmans J (1985) Calc-alkaline lavas from the volcanic complex of Santorini, Aegean Sea, Greece. Geol Ultraiect 41:316 pp

Huijsmans JPP, Barton M (1989) Polybaric geochemical evolution of two shield volcanoes from Santorini, Aegean Sea, Greece: evidence for zoned magma chambers from cyclic compositional variations. J Petrol 30:583–625

Jaxybulatov K, Shapiro NM, Koulakov I, Mordret I, Landès M, Sens-Schönfelder C (2014) A large magmatic sill complex beneath the Toba caldera. Science 31:617–619

Johnston EN, Sparks RSJ, Phillips JC, Carey S (2014) Revised estimates for the volume of the Late Bronze Age Minoan eruption, Santorini, Greece. J Geol Soc Lond 171:583–590

Karakas O, Degruyter W, Bachmann O, Dufek J (2017) Lifetime and size of shallow magma bodies controlled by crustal-scale magmatism. Nat Geosci 10:446–450

Karátson D, Gertisser R, Telbisz T, Vereb V, Quidelleur X, Druitt TH, Nomikou P, Kósik S (2018) Towards reconstruction of the lost Late Bronze Age intra-caldera island of Santorini, Greece. Sci Rep 8:7026. https://doi.org/10.1038/s41598-018-25301-2

Katz RF, Spiegelman M, Holtzman B (2006) The dynamics of melt and shear localization in partially molten aggregates. Nature 442:676–679

Kilgour GN, Saunders KE, Blundy JD, Cashman KV, Scott BJ, Miller CA (2014) Timescales of magmatic processes at Ruapehu Volcano from diffusion chronometry and their comparison to monitoring data. J Volcanol Geotherm Res 288:62–75

Klaver M, Carey S, Nomikou P, Smet I, Godelitsas A, Vroon P (2016) A distinct source and differentiation history for Kolumbo submarine volcano, Santorini volcanic field, Aegean arc. Geochem Geophys Geosyst 17:3254–3273

Konstantinou KI (2010) Crustal rheology of the Santorini–Amorgos zone: implications for the nucleation depth and rupture extent of the 9 July 1956 Amorgos earthquake, southern Aegean. J Geodynam 50:400–409

Koyaguchi T, Kaneko K (1999) A two-stage thermal evolution model of magmas in continental crust. J Petrol 40:241–254

Krimer D, Costa F (2017) Evaluation of the effects of 3D diffusion, crystal geometry, and initial conditions on retrieved time-scales from Fe-Mg zoning in natural oriented orthopyroxene crystals. Geochim Cosmochim Acta 196:271–288

Leonard GS, Cole JW, Nairn IA, Self S (2002) Basalt triggering of the c. AD 1305 Kaharoa rhyolite eruption, Tarawera Volcanic Complex, New Zealand. J Volcanol Geotherm Res 115:461–486

Martin VM, Davidson J, Morgan D, Jerram DA (2010) Using the Sr isotope compositions of feldspars and glass to distinguish magma system components and dynamics. Geology 38:539–542

Mason BG, Pyle DM, Oppenheimer C (2004) The size and frequency of the largest explosive eruptions on Earth. Bull Volcanol 66:735–748

Matthews NE, Huber C, Pyle DM, Smith VC (2012) Timescales of magma recharge and reactivation of large silicic systems from Ti diffusion in quartz. J Petrol 53:1385–1416

Menand T (2011) Physical controls and depth of emplacement of igneous bodies: a review. Tectonophys 500:11–19

Menand T, Annen C, de Saint Blanquat M (2015) Rates of magma transfer in the crust: Insights into magma reservoir recharge and pluton growth. Geology 43:199–202

Morgan DJ, Blake S, Rogers NW, DeVivo B, Rolandi G, Macdonald R, Hawkesworth CJ (2004) Time scales of crystal residence and magma chamber volume from modelling of diffusion profiles in phenocrysts: Vesuvius 1944. Earth Planet Sci Lett 222:933–946

Morgan DJ, Blake S, Rogers NW, De Vivo B, Rolandi G, Davidson JP (2006) Magma chamber recharge at Vesuvius in the century prior to the eruption of AD 79. Geology 38:845–848

Müller T, Dohmen R, Becker HW, ter Heege JH, Chakraborty S (2013) Fe–Mg interdiffusion rates in clinopyroxene: experimental data and implications for Fe–Mg exchange geothermometers. Contrib Mineral Petrol 166:1563–1576

Murphy MD, Sparks RSJ, Barclay J, Carroll MR, Lejeune A-M, Brewer TS, Macdonald R, Black S, Young S (1998) The role of magma mixing in triggering the current eruption at the Soufriere Hills Volcano, Montserrat, West Indies. Geophys Res Lett 25:3433–3436. https://doi.org/10.1029/98GL00713

Nakagawa K, Nagahara H, Ozawa K, Tachibana S, Yasuda A (2005) Experimental determination of AlAl–SiMg interdiffusion coefficient in orthopyroxene. Japan Geoscience Union Meeting, Tokyo, pp K038–K013 (abstract)

Newman S, Lowenstern J (2002) VolatileCalc: a silicate melt–H_2O–CO_2 solution model written in Visual Basic for excel. Comput Geosci 28:597–604

Newman AV, Stiros S, Feng L, Psimoulis P, Moschas F, Saltogianni V, Jiang Y, Papazachos C, Panagiotopoulos D, Karagianni E, Vamvakaris D (2012) Recent geodetic unrest at Santorini Caldera, Greece. Geophys Res Lett 39:L06309

Nomikou P, Parks MM, Papanikolaou D, Pyle DM, Mather TA, Carey S, Watts AB, Paulatto M, Kalnins ML, Livanos I, Bejelou K, Simou E, Perros I (2014) The emergence and growth of a submarine volcano: the Kameni islands, Santorini (Greece). GeoResJ 1–2:8–18

Nomikou P, Hübscher C, Ruhnau M, Bejelou K (2016) Tectonostratigraphic evolution through successive extensional events of the Anydros Basin, hosting Kolumbo volcanic field at the Aegean Sea. Greece Tectonophys 671:202–217

Oppenheimer C (2013) Nature and impacts of the Minoan eruption of Santorini in 1600. In: Meller H, Bertemes F, Bork HR (eds) Cultural change in the shadow of the Thera eruption? Tagungen des Landesmuseums für Vorgeschichte Halle, Band 9, pp 49–58

Pallister JS, Hoblitt RP, Reyes AG (1992) A basalt trigger for the 1991 eruptions of Pinatubo volcano? Nature 356:426–428. https://doi.org/10.1038/356426a0

Pamukcu AS, Gualda GAR, Bégué F, Gravley DM (2015) Melt inclusion shapes: timekeepers of short-lived giant magma bodies. Geology 43:947–950

Papale P, Moretti R, Barbato D (2006) The compositional dependence of the saturation surface of $H_2O + CO_2$ fluids in silicate melts. Chem Geol 229:78–95. https://doi.org/10.1016/j.chemgeo.2006.01.013

Petford N, Kerr RC, Lister JR (1993) Dike transport of granitoid magmas. Geology 21:845–848

Petrone CM, Bugatti G, Braschi E, Tommasini S (2016) Pre-eruptive magmatic processes re-timed using a non-isothermal approach to magma chamber dynamics. Nat Comm 7:12946

Putirka KD (2008) Thermometers and barometers for volcanic systems. Rev Mineral Geochem 69:61–120

Pyle DM (1990) New estimates for the volume of the Minoan eruption. In: Hardy DA, Keller J, Galanopoulos VP, Flemming NC, Druitt TH (eds) Thera and the Aegean World III, vol 2. Thera Foundation, London, pp 113–121

Pyle DM, Elliott JR (2006) Quantitative morphology, recent evolution, and future activity of the Kameni Islands volcano, Santorini, Greece. Geosphere 2:253–268

Qin Z, Fangqiong L, Anderson A (1992) Diffusive reequilibration of melt and fluid inclusions. Am Miner 77:565–576

Rabillard A, Arbaret L, Jolivet L, Le Breton N, Gumiaux C, Augier R, Grasemann B (2015) Interactions between plutonism and detachments during metamorphic core complex formation, Serifos Island (Cyclades, Greece). Tectonics. https://doi.org/10.1002/2014TC003650

Rubin AE, Cooper KM, Till CB, Kent AJR, Costa F, Bose M, Gravley D, Deering C, Cole J (2017) Rapid cooling and cold storage in a silicic magma reservoir recorded in individual crystals. Science 356:1154–1156. https://doi.org/10.1126/science.aam8720

Ruprecht P, Bachmann O (2010) Pre-eruptive reheating during magma mixing at Quizapu volcano and the implications for the explosiveness of silicic arc volcanoes. Geology 38:919–922

Satow C, Tomlinson EL, Grant KM, Albert PG, Smith VC, Manning CJ, Ottolini L, Wulf S, Rohling EJ, Lowe JJ, Blockley SPE, Menzies MA (2015) A new contribution to the Late Quaternary tephrostratigraphy of the Mediterranean: Aegean Sea core LC21. Quat Sci Rev 117:96–112

Saunders K, Blundy J, Dohmen R, Cashman K (2012) Linking petrology and seismology at an active volcano. Science 336:1023–1027

Schmitt AK, Stockli DF, Song EJ, Storm S (2016) Equilibrium and Disequilibrium of 230Th-238U in Zircon from the Minoan Eruption, Santorini, Aegean Sea, Greece. In: American Geophysical Uniion General Assembly (**abstract**)

Schöpa A, Annen C (2013) The effects of magma flux variations on the formation and lifetime of large silicic magma chambers. J Geophys Res 118:926–942

Schwandt CS, McKay GA (2006) Minor- and trace-element sector zoning in synthetic enstatite. Am Mineral 91:1607–1615. https://doi.org/10.2138/am.2006.2093

Self S (2006) The effects and consequences of very large explosive volcanic eruptions. Philos Trans R Soc 364:2073–2097

Shea T, Costa F, Krimer D, Hammer JE (2015) Accuracy of timescales retrieved from diffusion modeling in olivine: a 3D perspective. Am Mineral 100:2026–2042

Sigurdsson H, Carey S, Devine JD (1990) Assessment of the mass, dynamics, and environmental effects of the Minoan eruption of Santorini Volcano. In: Hardy DA, Keller J, Galanopoulos VP, Flemming NC, Druitt TH (eds) Thera and the Aegean World III, vol 2. Thera Foundation, London, pp 100–112

Sigurdsson H, Carey S, Alexandri M, Vougioukalakis G, Croff K, Roman C, Sakellariou D, Anagnostou C, Rousakis G, Ioakim C, Goguo A, Ballas D, Misaridis T, Nomikou P (2006) Marine investigations of Greece's Santorini volcanic field. EOS Trans Am Geophys Union 87:337–342

Singer BS, Costa F, Herrin JS, Hildreth W, Fierstein J (2016) The timing of compositionally-zoned magma reservoirs and mafic "priming" weeks before the 1912 Novarupta-Katmai rhyolite eruption. Earth Planet Sci Lett 451:125–137

Snyder D (2000) Thermal effects of the intrusion of basaltic magma into a more silicic magma chamber and implications for eruption triggering. Earth Planet Sci Lett 175:257–273

Solano JMS, Jackson MD, Sparks RSJ, Blundy JD, Annen C (2012) Melt segregation in deep crustal hot zones: a mechanism for chemical differentiation, crustal assimilation and the formation of evolved magmas. J Petrol 53:1999–2026

Sparks RSJ, Cashman KV (2017) Dynamic magma systems: implications for forecasting volcanic activity. Elements 13:35–40

Sparks RSJ, Wilson CJN (1990) The Minoan deposits: a review of their characteristics and interpretation. In: Hardy DA, Keller J, Galanopoulos VP, Flemming NC, Druitt TH (eds) Thera and the Aegean World III, vol 2. Thera Foundation, London, pp 89–99

Sparks SRJ, Sigurdsson H, Wilson L (1977) Magma mixing: a mechanism for triggering acid explosive eruptions. Nature 267:315–318

St. Seymour K, Christanis K, Bouzinos A, Papazisimou S, Papatheodorou G, Moran E, Dénès G (2004) Tephrostratigraphy and tephrochronology in the Philippi peat basin, Macedonia, Northern Hellas (Greece). Quat Int 121:53–65

Streck MJ (2008) Mineral textures and zoning as evidence for open system processes. Rev Mineral Geochem 69:595–622

Till CB, Vazquez JA, Boyce JW (2015) Months between rejuvenation and volcanic eruption at Yellowstone caldera, Wyoming. Geology 43:695–698

Tomiya A, Takahashi E (2005) Evolution of the magma chamber beneath Usu Volcano since 1663: a natural laboratory for observing changing phenocryst compositions and textures. J Petrol 46:2395–2426

Vaggelli G, Pellegrini M, Vougioukalakis G, Innocenti S, Francalanci L (2009) Highly Sr radiogenic tholeiitic magmas in the latest inter-Plinian activity of Santorini volcano, Greece. J Geophy Res 114:B06201

Van Orman JA, Cherniak DJ, Kita NT (2014) Magnesium diffusion in plagioclase: dependence on composition, and implications for thermal resetting of the 26Al–26 Mg early solar system chronometer. Earth Planet Sci Lett 385:79–88

Vespa M, Keller J, Gertisser R (2006) Interplinian explosive activity of Santorini volcano (Greece) during the past 150,000 years. J Volcanol Geotherm Res 153:262–286

Wark DA, Hildreth W, Spear FS, Cherniak DJ, Watson EB (2007) Pre-eruption recharge of the Bishop magma system. Geology 35:235–238

Weinberg RF, Veveakis E, Regenauer-Lieb K (2015) Compaction-driven melt segregation in migmatites. Geology 43:471–474

Wiebe RA, Collins WJ (1998) Depositional features and stratigraphic sections in granitic plutons: implications for the emplacement and crystallization of granitic magma. J Struc Geol 20:1273–1289

Wilson CJN, Charlier BLA (2009) Rapid rates of magma generation at contemporaneous magma systems, Taupo Volcano, New Zealand: insights from U–Th model-age spectra in zircons. J Petrol 50:875–907

Wotzlaw J-F, Bindeman IN, Watts KE, Schmitt AK, Caricchi L, Schaltegger U (2014) Linking rapid magma reservoir assembly and eruption trigger mechanisms at evolved Yellowstone-type supervolcanoes. Geology 42:807–810

Chemical Geology 483 (2018) 312–331

Contents lists available at ScienceDirect

Chemical Geology

journal homepage: www.elsevier.com/locate/chemgeo

Invited research article

Water quantification in silicate glasses by Raman spectroscopy: Correcting for the effects of confocality, density and ferric iron

Federica Schiavi[a,*], Nathalie Bolfan-Casanova[a], Anthony C. Withers[b], Etienne Médard[a,c], Mickaël Laumonier[a], Didier Laporte[a], Taya Flaherty[a], Alejandra Gómez-Ulla[a]

[a] Université Clermont Auvergne, CNRS, IRD, OPGC, Laboratoire Magmas et Volcans, F-63000 Clermont-Ferrand, France
[b] Department of Earth Sciences and Centre for Planetary Science and Exploration, University of Western Ontario, 1151 Richmond Street, London, Ontario, Canada
[c] Universities Space Research Association, Lunar and Planetary Institute, Houston, TX, United States

ARTICLE INFO

Editor: D.B. Dingwell

Keywords:
Confocal Raman spectroscopy
Water quantification
Alumino-silicate glasses
Glass density
Peak fitting
Glass inclusions

ABSTRACT

New series of alumino-silicate glasses spanning a wide range of chemical compositions (basanites, tholeiitic basalts, calcalkaline andesites, peraluminous and peralkaline rhyolites) and with water contents from 0.02 to 6.70 wt% were used for improving the method of quantification of dissolved water with a highly confocal Raman micro-spectrometer. After reconsideration of previously proposed methods for spectra acquisition and post-analysis data treatment, we define the main critical steps that allow minimizing glass matrix effects. First, we carefully assess the variation of Raman band intensities, in both water (~3000–3800 cm^{-1}) and alumino-silicate vibration (~200–1250 cm^{-1}) regions with focus depth of the laser beam inside the sample. Our results indicate that in the first 2–10 μm depth, the intensity increase in the alumino-silicate region is twice as high as that in the water region. Optimal focus depths, where the signal of the water band is maximum and the intensity ratio of the water band to alumino-silicate band is minimum, vary with glass composition and confocal performance of the Raman spectrometer. This influences both external and internal calibration slopes. Second, this study recognizes critical parameters related with glass density, presence of ferric iron and dissolved carbonates as mainly responsible for matrix effects on the internal calibration method. (a) We provide a procedure for correcting the effect of glass density on water internal calibration based on the observation that the integrated intensity (i.e. the area) of the alumino-silicate envelope generally drops with the increase of water content and decrease of glass density. (b) In CO_2-bearing glasses, the intensity of the ν_1 Raman vibration of dissolved carbonate at ~1087 cm^{-1} has to be subtracted from the intensity of the alumino-silicate envelope before applying the density correction. (c) Using peak-fitting, the intensity of the 850–1250 cm^{-1} envelope of peralkaline rhyolitic glasses is corrected for the effect of the presence of four-fold coordinated Fe^{3+}, as revealed by the strong Raman scattering of the vibrational mode at ~980 cm^{-1}. Following this procedure, all the studied glasses define a single calibration line in spite of their compositional variability, when using either of the two classical approaches referred to as *external* and *internal* calibration methods. The linear fits of the external and internal calibrations reproduce the whole dataset within 0.13–0.11 wt% (high and standard confocality) and 0.17 wt%, respectively. The accuracy of the external calibration is evaluated based upon comparison with ion-probe measurements of water dissolved in natural glass inclusions: the relative standard deviation is ~4% (1σ) on average, and reaches ~12% (1σ) for water contents of ~0.1 wt%.

1. Introduction

Concentration, speciation and distribution of volatile species dissolved in silicate melts are key factors that control the physico-chemical evolution of magmas from their genesis to their final emplacement and affect the dynamics, style, and intensity of volcanic eruptions (e.g., Carroll and Holloway, 1994; Cashman, 2004; Sanchez-Valle et al., 2015). Volatiles are also important in mantle processes as they control melting and mantle rheology. Crucial information about volatile contents of magmas and behavior of volatiles at depth is usually recorded in small objects, such as phenocryst-hosted melt and fluid inclusions and tiny pockets of glassy matrix (e.g., Andersen and Neumann, 2001; Métrich and Wallace, 2008).

Raman spectroscopy is a useful micro-analytical technique for

* Corresponding author.
E-mail address: federica.schiavi@uca.fr (F. Schiavi).

https://doi.org/10.1016/j.chemgeo.2018.02.036
Received 11 September 2017; Received in revised form 2 February 2018; Accepted 27 February 2018
Available online 01 March 2018

identification and quantification of volatiles contained in a variety of materials, which are of interest in volcanological and petrological studies, in particular water (regardless of speciation) dissolved in natural glasses. With respect to the other micro-analytical techniques used for quantification of water in rock samples, such as Fourier transform infrared spectroscopy (FTIR), secondary ion mass spectrometry (SIMS), and elastic recoil detection analysis (ERDA), Raman spectroscopy has several advantages: (i) it requires minimal sample preparation, (ii) it is non-destructive, (iii) it allows rapid analysis with high spatial resolution, which is of utmost importance for characterization of small samples and samples with small-scale heterogeneity, and (iv) it allows analysis of unexposed glass, fluid and solid inclusions contained in transparent minerals and interstitial glass pockets (e.g., Thomas, 2000; Thomas et al., 2006; Chabiron et al., 2004; Zajacz et al., 2005; Di Muro et al., 2006a; Severs et al., 2007; Frezzotti et al., 2012; Morizet et al., 2013; Freitas et al., 2017).

Since the work by Thomas (2000), several studies have shown that accurate quantification of water dissolved in natural glasses can be achieved after proper calibration of Raman spectrometers (Chabiron et al., 2004; Zajacz et al., 2005; Behrens et al., 2006; Di Muro et al., 2006a, 2006b; Thomas et al., 2006; Mercier et al., 2009, 2010; Le Losq et al., 2012; Di Genova et al., 2017). These studies investigated the advantages and limitations of distinct calibration methods. The first method is called “external calibration”, as quantification of water in the unknown sample is obtained by comparing the intensity (i.e. the height, hereafter I_{OH}) or the integrated intensity (i.e. the area, hereafter A_{OH}) of the water band located around 3570 cm^{-1} (Fig. 1b) with water band intensities or integrated intensities of well-characterized standard glasses. The relationship between intensity of the water Raman band and water concentration (hereafter referred to as “calibration curve”) determined in previous studies displays a slope that varies as a function of glass type. Dependence of the slope on glass composition is especially apparent when glasses belonging to alkaline and sub-alkaline series are compared (Behrens et al., 2006; Di Muro et al., 2006b; Mercier et al., 2010). According to Mercier et al. (2010), glass reflectance and density, as well as water environment, are the main parameters causing matrix effects on the external calibration. Thus, a set of glass standards spanning a wide range of compositions seems required for accurate quantification of water in natural glass samples.

The second calibration method is known as “internal calibration” because the intensity of the Raman water band is normalized to the intensity of bands located in the silicate region: either in the entire alumino-silicate region between 200 and 1250 cm^{-1} (Behrens et al., 2006; Le Losq et al., 2012; Di Genova et al., 2017), the band located at high wavenumbers between 850 and 1250 cm^{-1} (Zajacz et al., 2005; Behrens et al., 2006; Severs et al., 2007; Mercier et al., 2009), or the band at low wavenumbers ranging from 200 to 650 cm^{-1} (Thomas, 2000; Chabiron et al., 2004; Behrens et al., 2006; Mercier et al., 2009) (Fig. 1a,c). Intensity versus content relationships obtained with an internal calibration procedure are expected to be less affected by instrumental and analytical conditions, such as laser power fluctuations, focusing errors, and differences in confocal volume size, light absorption and reflectance that depend on glass structure and composition. In reality, internal calibrations also depend on glass chemical composition, because both bands in the alumino-silicate region and the average Raman scattering cross section of all the different alumino-silicate structural units (Q^n) depend on glass composition (Frantz and Mysen, 1995).

In order to correct the calibration of water concentration for compositional dependence, some authors have proposed additional normalization procedures taking into account the degree of glass polymerization (Zajacz et al., 2005; Mercier et al., 2010). Le Losq et al. (2012) defined a new protocol for spectra background subtraction that partly eliminates the effects of matrix composition. However, this method tends to overestimate and underestimate the water content of iron-poor and iron-rich samples, respectively (Di Genova et al., 2017). According to Di Genova et al. (2017), the use of different baseline procedures is not sufficient to remove the dependence of the internal calibration procedure on the iron content and oxidation state.

So far, there is no satisfactory methodology that allows quantifying the water content in glasses of variable composition using Raman spectroscopy. In this study, we reconsider previously proposed strategies for spectra acquisition and post-analysis data treatment, with the aim to establish the procedures under which a composition-independent calibration can be obtained when applying both external and internal calibration methods. For this purpose, we have studied glasses spanning a wide range of compositions belonging to both sub-alkaline and alkaline magma series. First, we investigate in detail how confocal performance and focus depth of the laser beam affect the calibration and highlight the importance of considering these parameters. Then, the effects of physico-chemical characteristics of alumino-silicate glasses, in particular those in relation to density and presence of ferric iron, are quantified, and we propose correction strategies to minimize matrix effects on the internal calibration. Finally, we test our method by analyzing natural glass inclusions of variable composition, whose water content was measured using SIMS or FTIR techniques.

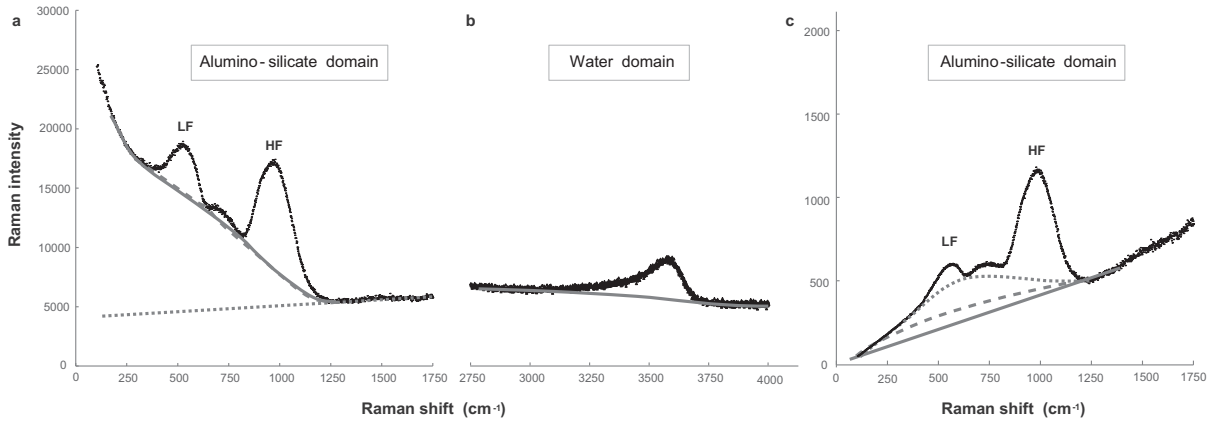

Fig. 1. Procedures for background subtraction used in previous studies. (a–b) Baseline fitting on raw Raman spectra. (a) In the alumino-silicate domain: cubic baseline (Mercier et al., 2009; dashed curve), cubic spline baseline (Behrens et al., 2006; continuous curve), and linear extrapolation method by Zajacz et al. (2005, dotted line); (b) cubic baseline in the water domain. (c) Baseline fitting on Long-corrected spectra in the alumino-silicate domain: cubic baseline (Di Muro et al., 2009; dashed curve) and cubic spline baseline (Behrens et al., 2006; continuous line) anchored at the extremities of the domain, or to a limited number of intermediate minima (Le Losq et al., 2012; dotted curve). LF and HF indicate low-frequency and high-frequency bands.

Table 1
Synthesis conditions and volatile composition of reference glasses.

GLASSES	Series	Starting material	Synthesis method		Capsule material	P (GPa)	T (K)	Time (h)	Loaded H_2O wt%	Analytical technique	Thickness (cm)	Density[a]	Water content			CO_2	References
												(kg m^{-3})	wt%	1σ[c]	mol	wt%	
Basanitic																	
BSN050417	Alkaline	Thueyts tephra	GMF		$Au_{80}Pd_{20}$	0	1573	4		FTIR	0.0410(5)	2841(37)	0.023	0.001	0.001		This study
BSN081117–1	Alkaline	Thueyts tephra	PC	1/2″	$Au_{80}Pd_{20}$	1.5	1598	3		FTIR	0.0054(7)	2811(21)	2.21	0.13	0.072	0.48 ± 0.07	This study
BSN081117–2	Alkaline	Thueyts tephra	PC	1/2″	$Au_{80}Pd_{20}$	1.5	1598	3		FTIR/CHNS	0.0055(7)	2794(11)	2.48	0.10	0.080	1.76 ± 0.03	This study
BSN101117–1	Alkaline	Thueyts tephra	PC	1/2″	$Au_{80}Pd_{20}$	1.5	1598	3		FTIR/CHNS	0.0095(1)	2793(43)	1.92	0.07	0.063	0.82 ± 0.03	This study
BSN101117–2	Alkaline	Thueyts tephra	PC	1/2″	$Au_{80}Pd_{20}$	2.2	1598	3		FTIR/CHNS	0.0022(3)	2790(48)	2.86	0.17	0.092	2.35 ± 0.15	This study
Basaltic																	
82-72f#22	Tholeiitic	Giant Crater Lava Field	GMF			0	1564	5.0				2806	< 0.05				[1],[2]
82-72f#19	Tholeiitic	Giant Crater Lava Field	MHC		$Au_{80}Pd_{20}$	0.01	1503	2.1		SIMS/FTIR		2795[b]	0.58	0.05	0.020		[1]
82-72f#10	Tholeiitic	Giant Crater Lava Field	MHC		$Au_{80}Pd_{20}$	0.025	1486	2.0		SIMS		2797	1.39	0.08	0.046		[1],[2]
82-72f#9	Tholeiitic	Giant Crater Lava Field	MHC		$Au_{90}Pd_{10}$	0.05	1472	2.0		SIMS		2756	2.28	0.13	0.074		[1],[2]
82-72f#7	Tholeiitic	Giant Crater Lava Field	MHC		$Au_{90}Pd_{10}$	0.10	1446	2.0		SIMS		2739	3.03	0.25	0.097		[1],[2]
82-72f#12	Tholeiitic	Giant Crater Lava Field	MHC		$Au_{90}Pd_{10}$	0.20	1443	3.1		SIMS		2701	4.40	0.16	0.137		[1],[2]
B250317	Tholeiitic	Holuhraun tephra	GMF		$Au_{80}Pd_{20}$	0	1573	3.0		FTIR	0.0250(4)	2850(33)	0.017	0.001	0.001		This study
WM23/3	Tholeiitic	Holuhraun tephra	PC	1/2″	$Au_{80}Pd_{20}$	1.0	1573	68	3.7	FTIR	0.0324(4)	2815[b]	1.53	0.19	0.051		This study
B6b	Tholeiitic	Holuhraun tephra	PC	1/2″	$Au_{80}Pd_{20}$	1.0	1473	2.0	5	FTIR	0.0016(1)	2749(11)	4.33	0.41	0.136		This study
Andesitic																	
A040417	Calcalkaline	Synthetic	GMF		$Au_{80}Pd_{20}$	0	1573	20		FTIR	0.0181(6)	2580(1)	0.024	0.003	0.001		This study
A030417	Calcalkaline	Synthetic	PC	1/2″	$Au_{80}Pd_{20}$	0.75	1573	24	1.0	FTIR	0.0120(2)	2565(4)	0.95	0.05	0.033	0.28 ± 0.02	This study
A310317	Calcalkaline	Synthetic	PC	1/2″	$Au_{80}Pd_{20}$	1.1	1573	24	2.7	FTIR/CHNS	0.0451(2)	2542(22)	3.17	0.22	0.104	0.59 ± 0.01	This study
A031215	Calcalkaline	Synthetic	PC	3/4″	$Au_{80}Pd_{20}$	1.0	1573	17	2.5	FTIR	0.0357(2)	2551(5)	2.24	0.11	0.075		This study
A131115	Calcalkaline	Synthetic	PC	3/4″	$Au_{80}Pd_{20}$	1.0	1573	18	3.5	FTIR/CHNS	0.0298(5)	2520(5)	3.23	0.15	0.106		This study
A071215	Calcalkaline	Synthetic	PC	3/4″	$Au_{80}Pd_{20}$	1.0	1573	24	4.0	FTIR	0.0521(2)	2516(9)	3.71	0.18	0.120		This study
Rhyolitic																	
NSL-N1	Peralkaline	obsidian from New Zealand	IHPV		Au		1273			FTIR		2403	1.16	0.06	0.040		[3]
NSL-N3	Peralkaline	obsidian from New Zealand	IHPV		Au		1273			FTIR		2378	3.30	0.16	0.109		[3]
NSL-N3.3	Peralkaline	obsidian from New Zealand	IHPV		Au		1273			FTIR		2375	3.51	0.18	0.115		[3]
NSL-N4b	Peralkaline	obsidian from New Zealand	IHPV		Au		1273			FTIR		2366	4.11	0.20	0.133		[3]
NSL-N5	Peralkaline	obsidian from New Zealand	IHPV		Au		1273			FTIR		2354	5.06	0.25	0.160		[3]
NSL-N6	Peralkaline	obsidian from New Zealand	IHPV		Au		1273			FTIR		2330	6.09	0.30	0.188		[3]

(*continued on next page*)

Table 1 (*continued*)

GLASSES	Series	Starting material	Synthesis method	Capsule material	P (GPa)	T (K)	Time (h)	Loaded H_2O wt%	Analytical technique	Thickness (cm)	Density[a]	Water content			CO_2		References
											(kg m^{-3})	wt%	1σ[c]	mol	wt%		
R041215	Peraluminous	Güney Dag obsidian	PC	3/4″	$Au_{80}Pd_{20}$	1.0	1373	64	2[d]	FTIR	0.0371(2)	2326(7)	3.15	0.10	0.105		This study
R261115	Peraluminous	Güney Dag obsidian	PC	3/4″	$Au_{80}Pd_{20}$	1.0	1373	70	4[d]	FTIR	0.0434(3)	2297(2)	5.21	0.18	0.165		This study
R201115	Peraluminous	Güney Dag obsidian	PC	3/4″	$Au_{80}Pd_{20}$	1.0	1323	63	6[d]	FTIR	0.0228(3)	2265(20)	6.70	0.35	0.205		This study
Microlites-bearing																	
A011215	Calcalkaline	Synthetic	PC	3/4″	$Au_{80}Pd_{20}$	1.0	1573	18	6	FTIR	0.0135(3)	2486(27)	5.65	0.30	0.175		This study

Notes
GMF is gas-mixing furnace; MHC is Molybdenum-Hafnium-Carbide cold-seal pressure vessel; PC is non-endloaded piston cylinder; IHPV internally heated pressure vessel.
The numbers in parentheses are 1σ standard deviations, given in terms of the last unit cited.
References: [1] Médard and Groove (2008); [2] Malfait et al. (2011); [3] Withers and Behrens (1999).
[a] The sink/float method was used to measure the density of the 82-72f series of basaltic glasses; Archimedes' method for the other glasses.
[b] Density calculated using the regression line of Fig. 2.
[c] Uncertainty resulting from error propagation in Beer-Lambert equation.
[d] In addition to ~1.39 wt% H_2O of Güney Dag obsidian starting material.

2. Methodology

2.1. Starting materials

Thirty alumino-silicate glasses including basanites, tholeiitic basalts, calcalkaline andesites, peraluminous and peralkaline rhyolites were used for calibration of water contents by Raman spectroscopy (Table 1, Fig. 1S in Supplementary data). Their polymerization degree (expressed as the ratio of nonbridging oxygens per tetrahedrally coordinated cations, NBO/T) calculated on an iron-free and H_2O-free basis varies from 0.0 to 0.78 (Table 2).

Two distinct sets of rhyolitic glasses were synthesized from the Güney Dag obsidian (Turkey; Druitt et al., 1995) and from a peralkaline rhyolite (labeled as NSL) from New Zealand, whose exact provenance is unknown (Behrens and Jantos, 2001) (Table 1). Both rhyolites are very poor in microlites. The Güney Dag rhyolite is mildly peraluminous, SiO_2- and Al_2O_3-rich (~77 and 12.5 wt%, respectively), FeO- and CaO-poor (0.8 and 0.25 wt%, respectively) and contains 1.39 wt% H_2O (Mourtada-Bonnefoi and Laporte, 2002). This relatively large H_2O content is due to the water contained in the glass phase of the obsidian (1.05 ± 0.05 wt%; Mourtada-Bonnefoi and Laporte, 2002) and to the presence of biotite and amphibole microlites (Cluzel et al., 2008). The rhyolite from New Zealand has lower SiO_2 (~75 wt%) and Al_2O_3 (~10 wt%), higher Fe (as total FeO ~4 wt%) and Na_2O (~5.5 wt%) contents, and contains 0.1–0.4 wt% H_2O.

Two sets of basaltic glasses were synthesized starting from a primitive high-alumina basalt erupted from the Giant Crater Lava Field (Medicine Lake volcano, California; Médard and Groove, 2008; Malfait et al., 2011) and from tephra erupted from Holuhraun volcano (Iceland) in 2014 (Haddadi, 2016). The composition of the Medicine Lake volcano basalt (labeled as 82-72f) is very close to that of primitive mid-ocean ridge basalts, with a higher Al_2O_3 content (~18.5 wt%). The composition of the basalt from Holuhraun is richer in FeO (~12.5 wt%) and poorer in Al_2O_3 (~14 wt%) and is typical of lavas erupted from the Bárðarbunga magmatic system (Sigmarsson and Halldorsson, 2015).

A set of reference glasses with basanitic composition and bearing different amounts of H_2O and CO_2 were synthesized from a natural basanitic tephra sampled at Thueyts volcano (Ardèche, France). The tephra composition is characterized by low SiO_2 (~45 wt%) and high total alkali (~6 wt%).

We also synthesized an intermediate (andesitic) composition closely reproducing the andesites erupted at Mt. Shasta (California, Grove et al., 2002) with a slight difference in Na_2O concentration. The details of the syntheses are presented below.

2.2. Experimental procedures

The experimental work was carried out at the Laboratoire Magmas et Volcans (Clermont-Ferrand), except for the synthesis of glasses derived from the NSL and 82-72f starting materials. The synthesis of the 82-72f basaltic set is reported in Médard and Groove (2008) and is summarized in Table 1. Hydrous glasses were synthesized from the NSL rhyolitic obsidian using an internally heated pressure vessel at the Institut für Mineralogie of Hannover (Germany). The natural rhyolitic composition and double-distilled water were sealed in gold capsules and held at 1000 °C and 300–500 MPa for 72–120 h before quenching (for further details see Withers and Behrens, 1999).

For the synthesis of the andesitic glasses, we used a decarbonated mixture of oxide (SiO_2, TiO_2, Al_2O_3, FeO, MnO and MgO), silicate ($CaSiO_3$) and carbonate (Na_2CO_3, K_2CO_3) reagent powders. SiO_2, Al_2O_3, and MgO powders were dried in platinum crucibles in air at 1000–1100 °C overnight. $CaSiO_3$ and carbonate powders were dried in air at 250–400 °C overnight. These dried powders were weighed and ground altogether in an agate mortar to ensure a homogeneous starting mixture. For decarbonation and fusion, the mixture was held in a platinum crucible and heated by a gas-mixing furnace at one bar; as

Table 2
Major element composition of reference glasses.

GLASSES	*n*	SiO_2	TiO_2	Al_2O_3	FeO	MnO	MgO	CaO	Na_2O	K_2O	P_2O_5[a]	Total	NBO/T[b]
		wt%	wt%	wt%	wt%	wt%	wt%	wt%	wt%	wt%	wt%		
BASANITIC[a]													
BSN050417	12	45.1(2)	2.47(7)	13.64(8)	10.05(11)	0.19(4)	11.16(14)	10.09(10)	3.99(12)	1.77(8)	–	98.45	0.780
BSN081117–1	12	43.8(2)	2.40(9)	13.29(9)	9.36(9)	0.19(5)	10.65(9)	9.82(17)	3.83(9)	1.76(7)	–	95.11	0.769
BSN081117–2	12	43.5(2)	2.40(11)	13.42(8)	9.07(14)	0.18(4)	10.09(7)	9.81(11)	3.78(14)	1.75(8)	–	93.97	0.739
BSN101117–1	12	43.7(3)	2.46(7)	13.57(13)	9.19(17)	0.18(4)	10.09(13)	10.15(10)	3.94(14)	1.80(9)	–	95.05	0.749
BSN101117–2	12	42.7(3)	2.48(11)	13.58(13)	9.19(17)	0.20(6)	9.69(7)	8.77(8)	3.90(14)	1.87(5)	–	92.37	0.693
BASALTIC													
82-72f#22	15	47.6(4)	0.60(6)	18.43(14)	8.13(11)	0.16(3)	10.58(10)	11.57(9)	2.33(16)	0.08(3)	0.07(3)	99.57	0.572
82-72f#19	20	46.4(5)	0.56(6)	18.26(2)	8.41(3)	0.15(2)	10.40(2)	11.51(13)	2.20(11)	0.07(3)	0.06(2)	98.05	0.571
82-72f#10	20	46.7(3)	0.52(6)	18.14(13)	8.39(23)	0.16(3)	10.44(10)	11.41(15)	2.17(11)	0.08(3)	0.06(2)	98.08	0.570
82-72f#9	20	46.9(1)	0.54(9)	18.17(12)	7.20(13)	0.15(3)	10.43(10)	11.40(15)	2.23(14)	0.07(3)	0.06(2)	97.18	0.567
82-72f#7	20	45.8(2)	0.55(7)	17.82(10)	7.41(14)	0.15(3)	10.24(14)	11.16(12)	2.18(12)	0.08(3)	0.05(2)	95.43	0.569
82-72f#12	10	45.0(2)	0.54(7)	18.25(17)	7.10(10)	0.10(2)	10.02(9)	11.28 (9)	2.09 (9)	0.07(3)	0.05(2)	94.52	0.554
B250317	15	49.7(3)	1.87(6)	13.67(14)	11.88(25)	0.21(3)	6.72(17)	11.55(21)	2.26(24)	0.21(3)	0.21(7)	98.24	0.515
WM23/3	15	48.8(2)	1.80(9)	13.31(10)	12.00(22)	0.21(4)	6.87 (9)	11.46(22)	1.98(42)	0.20(3)	0.17(5)	96.80	0.524
B6b	12	47.3(3)	1.71(11)	12.89(10)	11.54(18)	0.19(5)	6.45(10)	11.03(17)	2.08(11)	0.20(3)	0.19(5)	93.55	0.519
ANDESITIC													
A040417	10	60.0(4)	0.75 (7)	17.00(13)	4.77(11)	0.17(3)	4.32(7)	6.82(9)	4.05(45)	1.38(5)	–	99.29	0.215
A030417	10	60.5(3)	0.67 (7)	15.53(18)	5.19(10)	0.15(3)	3.69(6)	6.79(17)	3.43(34)	1.32(5)	–	97.27	0.200
A310317	10	60.0(4)	0.69 (5)	15.57(11)	4.08(13)	0.17(3)	3.44(8)	6.50(5)	3.28(38)	1.33(7)	–	95.10	0.180
A031215	9	59.9(6)	0.72(11)	16.23(20)	4.51(22)	0.18(5)	4.03(15)	6.36(23)	3.71(15)	1.42(11)	–	97.05	0.199
A131115	8	58.5(3)	0.79(10)	16.18(15)	4.41(15)	0.15(4)	4.08(9)	6.42(9)	3.73(9)	1.46(9)	–	95.71	0.207
A071215	8	57.8(3)	0.67 (6)	15.81(13)	4.79(10)	0.16(3)	3.86(16)	6.71(13)	3.70(7)	1.39(7)	–	94.87	0.214
RHYOLITIC													
NSL-N1	12	72.3(2)	0.26(5)	10.45(4)	4.15(4)	0.07(3)	0.008(3)	0.20(1)	5.28(28)	4.45(16)	–	97.15	0.049
NSL-N3	12	72.1(2)	0.21(5)	10.25(3)	4.05(5)	0.08(4)	0.011(4)	0.19(2)	5.45(31)	4.28(16)	–	96.63	0.054
NSL-N3.3	12	70.4(3)	0.22(7)	10.25(6)	4.22(5)	0.10(3)	0.006(5)	0.19(2)	5.09(37)	4.30(21)	–	94.79	0.047
NSL-N4b	12	71.3(3)	0.22(6)	10.24(5)	3.93(8)	0.09(2)	0.010(3)	0.20(2)	5.16(39)	4.22(13)	–	95.40	0.047
NSL-N5	12	70.6(3)	0.20(3)	10.17(7)	4.05(4)	0.08(2)	0.008(7)	0.19(2)	4.55(37)	4.21(9)	–	94.02	0.034
NSL-N6[c]		70.4	0.20	9.86	3.87	0.07	0.004	0.17	5.17	4.18	–	93.91	0.051
R041215[a]	10	75.1(4)	0.04(5)	12.22(8)	0.74(10)	0.07(4)	0.03(2)	0.42(5)	4.09(14)	4.46(26)	–	97.20	0.004
R261115[a]	10	73.4(3)	0.05(5)	11.89(12)	0.74 (4)	0.08(6)	0.02(2)	0.41(6)	3.92(17)	4.24(19)	–	94.76	0.001
R201115[a]	10	72.3(4)	0.04(4)	11.69(13)	0.72 (8)	0.07(4)	0.02(2)	0.32(4)	3.82(15)	4.16(24)	–	93.12	0.000
Microlites-bearing													
A011215	11	57.7(3)	0.71(5)	15.60(14)	4.49(10)	0.14(2)	3.74(10)	6.08(13)	3.59(11)	1.38(7)	–	93.39	0.192

Notes
n is the number of measurements; the numbers in parentheses are 1σ standard deviations, given in terms of the last unit cited. All Fe is reported as FeO.
[a] The P_2O_5 content of reference glasses was only measured for basaltic compositions. The P_2O_5 content of the basanitic starting material is equal to 0.7 wt%.
[b] NBO/T (i.e., non-bridging oxygen per tetrahedrally coordinated cation) is calculated on an Fe- and H_2O-free basis, following Behrens et al. (2006).
[c] calculated based on the starting composition of the dry natural obsidian.

temperature changed, the gas mixture was adjusted to maintain fO_2 near FMQ buffering conditions. Temperature was increased to 1000 °C in 6 h, kept constant overnight, then increased and held for 30 min at 1400 °C before quenching the glass in water. In order to obtain a homogeneous glass, grinding and fusion were repeated a second time. Finally, the glass was ground for two more hours in an agate mortar to produce a very fine powder used in hydration experiments.

Cylinders of natural Güney Dag obsidian were drilled (4.5 mm in diameter, 4–5 mm in length) and cleaned with acetone in an ultrasonic bath. The Holuhraun basaltic tephra were crushed into small chips, carefully examined in order to remove possible crustal contaminants, and then ground in an agate mortar for ~2 h. An analogous procedure was used for preparation of the starting powder with basanitic composition.

Anhydrous glasses were synthesized by re-melting the starting materials in a gas-mixing furnace at one bar, 1300 °C and fO_2 ~FMQ (Table 1). The starting materials were loaded into Au_{80}-Pd_{20} capsules whose upper side was left open to allow degassing, held at high temperature for several hours, and finally drop-quenched in water.

The hydrous glasses were synthesized in a piston-cylinder apparatus using a Pyrex-MgO assembly, a graphite heater, an outer NaCl cell, and Au_{80}-Pd_{20} capsules (5 and 4 mm outer diameter for 3/4″ and 1/2″ assemblies, 0.2 mm wall thickness, 4–5 mm length). First, deionized water was added at the bottom of the capsule using a micro-syringe; after loading and compacting ~100 mg of glass powders (or cylinders), the capsule was welded shut. We checked for leaks during capsule preparation by weighing the welded capsules before and after 1-h heating at 120 °C in an oven. For the synthesis of H_2O and CO_2-bearing glasses of andesitic and basanitic compositions (Table 1), we added a mixture of water and oxalic acid dehydrate ($C_2H_2O_4{\cdot}2H_2O$) to glass powders. After welding, the capsules were placed in an oven first at 350 °C for 1 h to decompose the oxalic acid, and then at 120 °C overnight to ensure homogenous distribution of the volatiles. In all experiments, the *P-T* conditions were chosen to be well above the volatile saturation curve (Duan, 2014). The temperature was measured very close to the capsule by a $W_{95}Re_5$-$W_{74}Re_{26}$ thermocouple. Hydration experiments were ended by switching off the heating power, quenching the samples at cooling rate > 80 °C/s. Experimental conditions are reported in Table 1.

The glasses recovered from the experiments were cut and polished on one or both sides for major element characterization by electron microprobe and water and CO_2 concentration measurements by infrared and Raman spectroscopies. Homogeneity of the glasses was first checked under the microscope. All analyzed glasses were bubble- and crystal-free, except for one andesitic water-rich glass (A011215) that contains microlites crystallized upon quenching. The microlite-bearing

glass is not suitable as standard; however, since the percentage of microlites is small and glass composition is homogeneous, it was used for comparison in Raman measurements.

2.3. Electron microprobe

Major element composition of glass samples was determined with a CAMECA SX100 electron microprobe (EMP) at the LMV. Glass analyses were performed with 15 kV accelerating voltage, 4–8 nA beam current, and a 20 μm (10 μm for basanitic glasses) defocused beam in order to reduce Na loss. The acquisition time was 20 s for Al (and for Mg and Ca in basanitic glasses) and 10 s for the other elements. Average major element compositions of the glasses are reported in Table 2. EMP measurements confirm compositional homogeneity of the studied glass samples.

2.4. Infrared spectroscopy

Total water content of reference glasses was determined by Fourier Transform Infrared Spectroscopy, using a Bruker Vertex 70 spectrometer coupled with a Hyperion microscope system, housed at LMV. Spectra were recorded using a Globar light source, a KBr beamsplitter and a MCT (Mercury-Cadmium-Tellurium alloy) detector. Plane parallel, double polished glass samples were placed on a CaF_2 window. Absorbance and background spectra of the glasses were obtained by acquisition of 300 and 100 scans, respectively. Beam size was 70 × 70 μm and spectral resolution was 4 cm^{-1}. Concentrations of OH groups and molecular H_2O were determined from the height of the absorbance bands at 4500 and 5240 cm^{-1}, respectively, using the Beer-Lambert law (e.g. Stolper, 1982). The 4500 and 5240 cm^{-1} bands are commonly assigned to a combination of the stretching vibrations of OH groups attached to Si and the combination of the stretching and bending vibrations of the H_2O molecule, respectively. Total water contents of the basaltic glasses belonging to the Holuhraun set, the basanitic glasses and two water-poor andesitic glasses (A030417 and A040417) were derived from the height of the broad asymmetric band at 3570 cm^{-1}, which contains the fundamental OH stretching vibrations of both molecular H_2O and Si-OH (and Al-OH) structural groups (e.g. Stolper, 1982). Baseline correction (see below) and peak integration were performed using OPUS software. On each sample, we carried out several measurements in order to verify compositional homogeneity. Homogeneity was confirmed by small relative standard deviations (RSD < 5%) associated with water measurements on each sample.

Sample thickness was typically measured with a Mitutoyo digital gauge, except for very thin or small samples. In the latter case, we measured the sample thickness by reading the vertical displacement of the microscope stage between the top surface of the polished sample and the sample holder accurately determined when the Raman laser beam is focused. The accuracies of the two methods are ± 1 μm and < 1 μm, respectively. Thicknesses (and associated standard deviations) reported in Table 1 are average values of 4–8 measurements.

Glass density (ρ) was accurately measured with a microbalance using Archimedes' method and deionized water as the immersion liquid. Two to six repeated measurements on each glass sample gave reproducibility better than 2% relative. Densities of the studied reference glasses are reported in Table 1 and Fig. 2.

The largest uncertainty in water contents determined by FTIR analysis is due to the uncertainty on the molar absorptivity (i.e. extinction coefficient) for the absorbance bands at 4500 and 5240 cm^{-1}. As estimated absorptivity coefficients depend on the baseline subtraction method (e.g. Ohlhorst et al., 2001), we followed guidelines provided by Ohlhorst et al. (2001) and Mandeville et al. (2002) for proper choice of baseline fitting procedure and molar absorptivity values.

In rhyolitic glass spectra, a linear baseline was fitted as tangent through the minima on both sides of the 5240 cm^{-1} band and then extrapolated below the 4500 cm^{-1} band (GG baseline of Withers and Behrens, 1999). For peraluminous rhyolites, we used the absorption coefficients provided by Withers and Behrens (1999): 1.52 ± 0.08 L mol^{-1} cm^{-1} for ε_{4500} (OH) and 1.72 ± 0.06 L mol^{-1} cm^{-1} for ε_{5240} (H_2O). Measured water concentrations in rhyolitic glasses match with target compositions (i.e. the amount of water loaded into the capsule) and are close to the difference of EMP analyses total from 100 wt%.

For andesitic glasses, we used the average values of the extinction coefficients determined by King et al. (2002) and Mandeville et al. (2002): 0.97 L mol^{-1} cm^{-1} for ε_{4500} (OH), 1.08 L mol^{-1} cm^{-1} for ε_{5240} (H_2O), and 66.32 L mol^{-1} cm^{-1} for ε_{3570} (total water). Mandeville et al. (2002) showed that ε_{4500} and ε_{5240} molar absorptivities have significant compositional dependency and can be predicted if the tetrahedral (Si^{4+}, Al^{3+}) cation/total cation fraction of the glass is known. Molar absorptivity values calculated for the andesitic glasses using the regression line equations provided by Mandeville et al. (2002) are ~1.00 and 1.19 (L mol^{-1} cm^{-1}) for ε_{4500} and ε_{5240}, respectively, which are very close to the adopted values. The baseline of andesitic glass spectra was fitted as tangent through three points: the minima on both sides of the 4500 cm^{-1} band and the minimum on the low wavenumber side of the 5240 cm^{-1} band. On its high wavenumber side (at ~5400 cm^{-1}), the linear baseline intersects the absorbance curve. This baseline fitting procedure is analogous to the one performed by Mandeville et al. (2002). Measured water concentrations in andesitic glasses are slightly lower than target amounts loaded into the capsule due to minor loss either during capsule preparation or upon the synthesis experiments.

We determined water contents in the basanitic and Holuhraun basaltic glasses based on the height of the absorbance band at ~3570 cm^{-1}. This choice was driven by the observation that the spectrum background around the 4500 and 5240 cm^{-1} bands is strongly affected by the absorption of near infrared and visible electronic transitions or crystal field bands of iron (Ohlhorst et al., 2001). Consequently, baseline fitting around these bands becomes more laborious and the choice of ε_{4500} and ε_{5240} for basanites and iron-rich basalts may be less accurate. In contrast, the linear baseline under the large band at 3570 cm^{-1} is unambiguously defined. For basanites, we used the molar absorption coefficient provided by Shishkina et al. (2014), 57.3 ± 1.8 L mol^{-1} cm^{-1}. For basalts, we adopted the molar absorption coefficient provided by Mercier et al. (2010), 62.8 ± 0.8 L mol^{-1} cm^{-1}, which is very close to the coefficient measured by Dixon et al. (1995).

Carbon dioxide concentrations in four basanitic and two andesitic glasses were determined from the heights of the absorbance bands at 1430 and 1520 cm^{-1}, which correspond to antisymmetric stretching of distorted carbonate groups (Dixon et al., 1995). For basanitic and andesitic glasses, we adopted respectively the molar absorption coefficients provided by Shishkina et al. (2014) (306 ± 32 L mol^{-1} cm^{-1} for 1430 and 349 ± 25 L mol^{-1} cm^{-1} for 1520) and those given by King et al. (2002) (269 and 271 L mol^{-1} cm^{-1} for the 1430 and 1520 bands, respectively).

Water and CO_2 contents of a few andesitic and basanitic samples measured both by FTIR and elemental analyzer (Flash 2000 CHNS Thermo Electron housed at LMV) match within 5%.

2.5. Raman spectroscopy

Raman spectra were collected at LMV using an InVia confocal Raman micro-spectrometer manufactured by Renishaw and equipped with a 532 nm diode laser (200 mW output power), a Peltier-cooled CCD detector of 1024 × 256 pixels, a motorized XY stage and a Leica DM 2500 M optical microscope. Scattered light was collected by a backscattered geometry. An edge filter effectively reduced both Rayleigh scattered photons and photons from the exciting laser source at 0 cm^{-1} that had been reflected by the sample surface.

Laser power on the sample was reduced by filters in order to operate at three different powers of ~1, 8 and 16 mW. Laser power on the

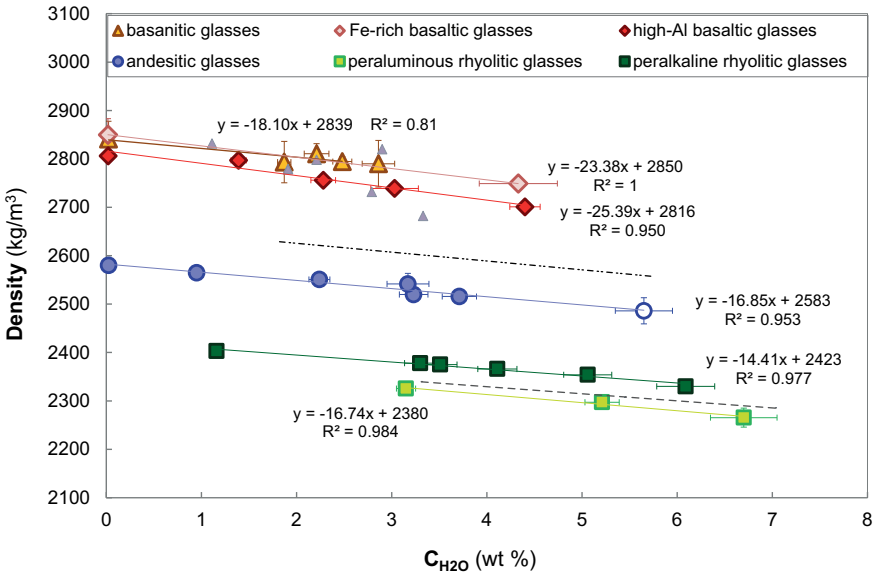

Fig. 2. Glass density versus glass water content determined by FTIR or SIMS measurements (see Table 1). A decrease of slope value from basaltic to rhyolitic glasses is observed. The dashed line represents the density of rhyolitic glasses calculated from Behrens et al. (2006). The dashed-dotted line shows the density of andesitic glasses determined by Ohlhorst et al. (2001). Small grey triangles are calculated basanitic glass densities by Iacovino et al. (2016). Microlite-bearing A011215 glass is the andesitic glass with the highest water content (empty circle). WM23-3 and 82-72f#19 glasses are not plotted because their densities were calculated, not measured.

sample was periodically checked. A 2400 grooves/mm grating was used for the analyses, which resulted in a spectral resolution better than 1 cm^{-1}. A 100× microscope objective (numerical aperture 0.9) was used and the slit aperture was set to 65 µm (standard confocality setting) or 20 µm (high confocality setting). These analytical conditions result in lateral and axial spatial resolutions of ~1 and 2–3 µm, respectively, near the sample surface. Daily calibration of the spectrometer was performed based on a Si 520.5 cm^{-1} peak. The 82-72f#9 basaltic glass was used as internal standard and analyzed several times during each analytical session in order to correct for the dependence of band intensities on delivered energy. The spectra were recorded from ~100 to 1350 cm^{-1} (alumino-silicate network domain) and from ~2900 to 3800 cm^{-1} (water domain) Raman shifts using Wire 4.2 software. Acquisition times were set to 120–180 s and 120–600 s for the alumino-silicate and water domains, respectively. The longest acquisition was adopted for analysis of water-poor glasses at 1 mW laser power, in order to obtain high signal-to-noise ratios. Under these operating conditions, no melting or water loss was detected. However, we observed that the Raman signal intensity of the dark H_2O– and Fe-rich basalt from the Holuhraun set was unstable at the highest laser power we used, possibly due to glass heating by the laser beam.

The lower limit of water detection using the analytical conditions detailed above was measured in olivine-hosted glass inclusions from FAMOUS Zone (Mid-Atlantic Ridge; Schiavi et al., 2016) and was slightly lower than 0.1 wt%.

Analytical precision calculated based on repeated daily measurements of reference glasses is generally better than 6% and 2% relative, respectively, in water-poor and water-rich glasses in highly confocal setting. This difference is mainly related to degradation of the signal-to-noise ratio in spectra of water-poor glasses. Performing measurements under standard confocality conditions yields better analytical precision because the analyzed volume is larger, so Raman signal is more intense and small differences in focusing depth are less critical. We observed that reproducibility decreases for measurements performed on the sample surface, especially for laser powers < 10 mW. When the laser beam is focused on the sample surface, in fact, small variations of the excited sample volume are more likely to occur because the beam is not entirely inside the sample and reflectance at the sample surface has a more important effect.

In this study, reference glasses for Raman spectroscopy analysis were prepared as large free chips (i.e. not embedded in epoxy resin or other embedding medium). We verified the homogeneity of the reference glasses by acquiring several spectra on each glass during the same analytical session. In addition, repeated measurements confirmed that no water loss occurred over several months. In A011215, presence of microlites was not detected most likely due to wide spacing between microlites relative to the diameter of the analysis spot.

3. Glass density

Fig. 2 shows the relationship between glass densities, ρ (kg/m^3), and water contents, C_{H2O} (wt%), determined by FTIR spectroscopy or SIMS (Table 1). A linear relationship $\rho = \rho_0 + b\, C_{H2O}$, where ρ_0 is the density of the anhydrous glass and b the slope of the line, is observed. Density diminishes with increasing water content. The slope for mafic glasses is more important than the ones for intermediate and felsic glasses. The slopes defined by the rhyolitic and andesitic sample sets are in agreement with those found by Ohlhorst et al. (2001) and Behrens et al. (2006) for similar glass compositions. Moreover, the measured rhyolitic and andesitic glass densities are very close to densities measured by Withers and Behrens (1999) and Mandeville et al. (2002). The slope obtained for the 82-72f basaltic set is slightly more pronounced than the slope reported by Ohlhorst et al. (2001) for basaltic composition. As expected, the Fe-richer sets of basaltic and rhyolitic glasses are characterized by higher densities than the Fe-poorer sets. The measured basanitic glass densities fall within the range of values calculated by Iacovino et al. (2016). Density of the A011215 sample is aligned with that of the other andesitic glasses, even though it contains microlites.

4. Raman spectral treatment

4.1. Baseline fitting

Raman spectra of glass samples required baseline correction before being used for quantification of volatile species. In fact, a high signal intensity characterizes glass spectra at low wavenumbers (i.e. small Raman shifts, Fig. 3) due to the influence of the intense Rayleigh diffusion tail superimposed by the boson peak (e.g. Le Losq et al., 2012). Long (1977) was the first to highlight the need for correcting the raw spectra for the dependence of Raman scattering on frequency and temperature. Glasses, in particular rhyolitic ones, can be affected by fluorescence, which modifies the shape and intensity of the spectrum background. Moreover, the slope of the background is influenced by the total glass iron and oxidation degree (Di Muro et al., 2009). As spectrum topology strongly depends on glass composition and degree of polymerization, baseline correction is a critical step in the treatment of

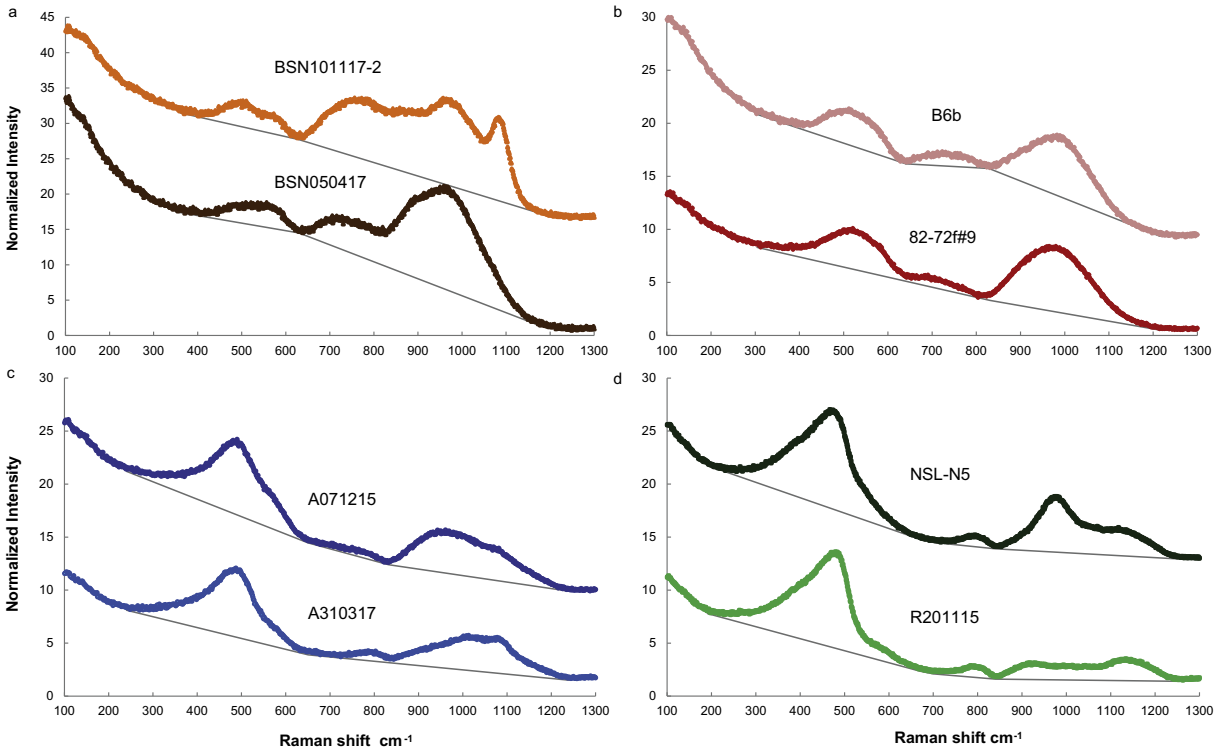

Fig. 3. Raw Raman spectra of the alumino-silicate vibration bands of the glasses with basanitic (a), basaltic (b), andesitic (c) and rhyolitic (d) compositions. Linear baselines adopted for background subtraction are shown with anchor points. Spectra are displaced vertically for clarity. Intensities were normalized to laser power and acquisition time.

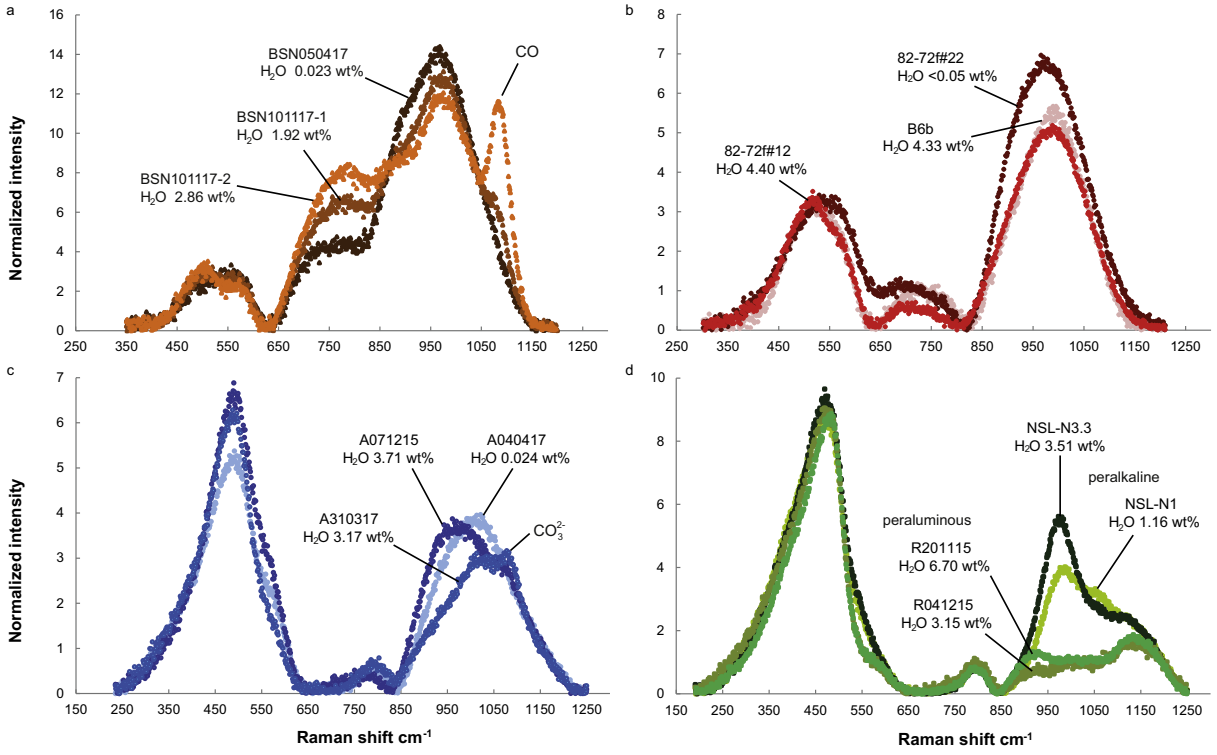

Fig. 4. Alumino-silicate region of raw Raman spectra of basanitic (a), basaltic (b), andesitic (c) and rhyolitic (d) glasses after subtraction of linear baselines. Spectra were measured under the same conditions of laser power and confocality. Intensities were normalized to acquisition time. Laser beam was focused at the optimal depth as defined in the text. Note differences in band topology associated with different major element compositions, water contents, degree of polymerization, and oxidation state (see text).

Raman spectra, especially in the alumino-silicate vibration region (Figs. 3 and 4). On the other hand, the baseline subtraction procedure does not affect significantly the treatment of the total water band around 3570 cm^{-1}.

In previous studies, different approaches were adopted for defining the baseline shape and the choice of anchor points (e.g., Zajacz et al.,

2005; Behrens et al., 2006; Severs et al., 2007; Di Muro et al., 2009; Mercier et al., 2009, 2010; Le Losq et al., 2012). A first approach consisted in fitting the baseline of raw spectra using either a combination of linear baselines (Severs et al., 2007), a cubic baseline (Mercier et al., 2009) or a cubic spline baseline (Behrens et al., 2006) with three/four anchor points in the alumino-silicate vibration region and two anchor points in the water domain (Fig. 1a,b). Zajacz et al. (2005) used a linear extrapolation of the flat signal from the 1250 to 1850 cm^{-1} spectral region towards low wavenumbers (Fig. 1). Such an extrapolation is possible only if the spectral background between 1250 and 1850 cm^{-1} is not too steep. In a second approach, the baseline was subtracted from spectra that had been previously corrected for Long's correction (Long, 1977). Behrens et al. (2006) and Di Muro et al. (2009) adopted, respectively, a cubic spline and a cubic baseline anchored only at the extremities of the alumino-silicate and water domains, whereas Le Losq et al. (2012) anchored the spline to a limited number of intermediate minima (Fig. 1c). In general, we observe that discrepancies between different spectral corrections arise from unconstrained concavity of the spline baseline.

Difficulties are encountered in fitting the baseline in the alumino-silicate vibration region, because there is no simple a priori way to relate the shape of broad Raman bands to specific network vibrations and structures, although statistical analysis and peak fitting algorithms provided interesting results in this direction (e.g., Herzog and Zakaznova-Herzog, 2011; Woelffel et al., 2015). Moreover, overlapping of bending and stretching bands occurs in the alumino-silicate region (e.g. Mysen et al., 1980), resulting in substantial uncertainty in selecting physically meaningful anchor points. The observed minima between the bands, in fact, may include contributions of the vibration bands (e.g. Le Losq et al., 2012).

For baseline correction and subsequent peak integration, we used PeakFit package software (Jandel Scientific). We used several procedures based on subtraction of linear (more often a sequence of linear segments) and cubic baselines from raw spectra or Long-corrected data (Fig. 3). Choice of anchor points for definition of linear and cubic baselines was dictated by two requirements (Le Losq et al., 2012): 1) making our procedure simple and reproducible, 2) minimizing the arbitrariness due to operators' choices. In the alumino-silicate network domain, we first fixed the anchor points at the two extremities of the spectrum where no Raman signal occurs. In the case of linear baselines, these are tangent points to the curve (Fig. 3), whereas a wider range of points on the background was selected for cubic baselines. So, anchor points at the two extremities were fixed at 340–360 and 1190–1200 cm^{-1} in basanitic glass spectra, at 300–340 and 1200–1220 cm^{-1} in basaltic glass spectra, at 230–250 and 1230–1250 cm^{-1} in andesitic glass spectra, and 190–210 and 1250–1260 cm^{-1} in rhyolitic glass spectra. For cubic baselines, the background at the high frequencies was extended up to 1350 cm^{-1}. Then, a minimal number of intermediate anchor points were set in order to: a) prevent linear baselines from crossing the spectrum, especially in rhyolites, andesites and basalts spectra, and b) minimize the influence of the background characterized by different slopes at the low frequencies, especially in basanites spectra (Fig. 3). For these reasons, an intermediate anchor point was placed near 630 and 640 cm^{-1} in basanitic and basaltic glasses, and in the 645–700 and 670–710 cm^{-1} ranges in andesitic and rhyolitic glasses, respectively. Around the minimum at 670–710 cm^{-1} of rhyolitic spectra, linear baselines resemble cubic baselines, as several short linear segments are necessary to fit the curve. A second intermediate anchor point was set around 800–830 cm^{-1} in basalts, 825–840 cm^{-1} in andesites, and ~840 cm^{-1} in rhyolites. We did not fix an anchor near 820 cm^{-1} in basanites because the corresponding minimum tends to disappear in H_2O and CO_2-bearing basanites. The defined anchors correspond to minima regions, and in some cases are defined by tangent lines to the spectra. We note that the positions of the intermediate anchor points and that of the anchor at the high wavenumber end of the spectrum shift to higher frequency as the polymerization increases, in agreement with previous observations (Le Losq et al., 2012).

In the water domain of the spectra, linear baselines were anchored (~2980 and 3780 cm^{-1}) and cubic baselines were fit (from 2980 to 3000–3008 and from 3725 to 3780 cm^{-1}) at both band extremities without any distinction between glasses of different composition. As the shape of cubic baseline is more sensitive to the topology and length of the fitted background, the more adequate cubic fitting was considered the one with the closest match of the baseline on the background on both sides of the band.

4.2. Alumino-silicate band topology and assignment

4.2.1. Topology of Raman spectra

In the alumino-silicate region of the Raman spectrum (200 to 1250 cm^{-1}), glass samples typically show two main broad bands. The position of the bands and their topology, i.e. relative band intensities, band shape and FWHM (full width at half maximum), vary from one sample to another (Fig. 4), as they depend on glass structure, chemical composition and oxidation state. Note that the spectral features detailed in the following section are scarcely affected by the chosen method for baseline correction.

In basanitic and basaltic glasses, the most intense band occurs at higher frequency than the less intense one (Fig. 4). Following previous studies (Mercier et al., 2009), we label these bands as High-Frequency (HF) and Low-Frequency (LF) bands. Increasing water content in basanitic and basaltic glasses has several effects: a) the maximum peak position of the LF bands shifts from 556 to 510 cm^{-1} and from 532 to 512 cm^{-1} in basanites and basalts, respectively; b) the maximum peak position of the HF bands shifts from 968 to 975 cm^{-1} in basanites, and from 966 to 990 cm^{-1} in basalts. c) The FWHM of the HF band slightly decreases from 181 to 164 cm^{-1} and from 184 to 177 cm^{-1} in the Fe-rich (Holuhruan) and high-Al (82-72f) basaltic sets, respectively (Fig. 2Sb). d) In basalts, the ratio of LF band (integrated) intensity to HF band (integrated) intensity increases due to apparent decrease of the HF band height (Fig. 2Sd). The latter observation is in agreement with previous observations on different basaltic glasses (Mercier et al., 2009). A shoulder at ~580 cm^{-1} characterizes the LF bands. A broad weak band centered at ~710 cm^{-1} defines the spectrum topology in the intermediate wavenumber range (650–800 cm^{-1}). In basanites, the relative intensity of this middle-region band with respect to LF and HF bands is higher than in the other glasses, and increases with the volatile content. Dissolved CO_3^{2-} molecules in basanites produce a peak near 1083 cm^{-1}, whose intensity increases with the CO_2 content, in agreement with Morizet et al. (2013).

With increasing polymerization, the relative intensity of the two main silicate bands inverts and the LF and HF maximum peaks shift, respectively, to lower and higher frequencies, in agreement with previous studies (e.g., Matson et al., 1983; Mercier et al., 2009). Moreover, the FWHM of the LF band diminishes with increasing degree of polymerization (Fig. 2Se,i).

In andesitic glasses, the maximum peak of the LF band occurs at 488 ± 3 cm^{-1}. The broader HF band is centered at ~1013–1022 cm^{-1} (with the only exception of the A071215 glass whose maximum peak is at 970 cm^{-1}). The ratio of LF band (integrated) intensity to HF band (integrated) intensity increases with increasing degree of polymerization (Fig. 2Sg). With increasing water content, the FWHM of the LF band decreases from 137 to 114 cm^{-1} (Fig. 2Sf). As in basalts, the LF band exhibits a shoulder at ~580 cm^{-1}. A small asymmetric band centered at 795 cm^{-1} is present in all andesitic glasses (Fig. 4). Dissolved CO_3^{2-} molecules in A310317 and A030417 glass samples produce a peak near 1078 cm^{-1}, which is more pronounced in A310317.

Rhyolitic glasses are characterized by a main asymmetric band centered at 467–484 cm^{-1}. Maximum LF peak position shifts to higher frequency with increase of water content dissolved in the glass, contrary to what is observed in basalts. Its FWHM varies from 122 to

130 cm^{-1} and from 134 to 145 cm^{-1} in the peraluminous (Güney Dag obsidian) and peralkaline (NSL obsidian) glass sets, respectively; there is a negative correlation between FWHM and water content (Fig. 2Sj), as pointed in andesitic glasses. In the peraluminous rhyolites, the LF band has a shoulder at ~580 cm^{-1}. A small band centered at 795 cm^{-1} is present in all rhyolitic spectra; its intensity slightly decreases with increased water content of peraluminous glasses. Major differences between the two glass sets and within each set are principally observed in the high wavenumber range (850 to 1200 cm^{-1}). In this range, the spectra are defined by several sub-bands, whose position, shape and relative intensities are strongly affected by glass composition and degree of polymerization (Fig. 4). Peraluminous rhyolites spectra show a less intense band centered at ~930 cm^{-1} and a more intense band centered at ~1135 cm^{-1}. The intensity of the band near 930 cm^{-1} slightly increases with water content. In the peralkaline rhyolites, instead, the band occurring at 1135 cm^{-1} is much smaller than the band located around 980 cm^{-1}. Compared to the glasses of the same set, the water-poor NSL-N1 glass differs in that its spectrum has a more pronounced band near 1050 cm^{-1}.

4.2.2. Review of the interpretation of bands

In the 200–1300 cm^{-1} region of the Raman spectrum, bands correspond to different bridging and non-bridging T—O vibrations in the glass structure (e.g., Brawer and White, 1977; Matson et al., 1983; McMillan, 1984; McMillan et al., 1992). The LF band near 400–500 cm^{-1}, which is dominant in polymerized glasses, is traditionally assigned to: a) rocking motion in fully polymerized Q^4 units (where Q^4 denotes a tetrahedron linked by bridging O atoms to 4 adjacent tetrahedra), b) breathing modes of four- and six-membered rings of TO_4 tetrahedra in polymerized glasses (Sharma et al., 1981; Matson et al., 1983; Rossano and Mysen, 2012), but also c) T—O—T symmetric stretching vibrations involving bridging oxygens and four-fold coordinated cations (Zotov et al., 1992) and d) T-O-T bending vibrations in glasses containing non-bridging oxygens (McMillan, 1984; Rossano and Mysen, 2012 and references therein). In rhyolitic glasses, decreasing FWHM of the LF band (Fig. 2Sj) and its shift to higher frequency with increasing water content have been explained by a possible decrease in the average T-O-T angle (McMillan and Remmele, 1986).

The vibrational mode at 570–580 cm^{-1} has been attributed to either structural defects (i.e. broken oxygen bridges, Stolen and Walrafen, 1976; Seifert et al., 1981; McMillan and Remmele, 1986) or a mixed stretch-bend vibration in Q^2 structural units (Furukawa et al., 1981). The bands near 700 and 800 cm^{-1} have been respectively ascribed to T—O—T bending motions (Mysen et al., 1980; Furukawa et al., 1981; McMillan, 1984; Rossano and Mysen, 2012) and to cage-like vibrations of Si atoms mainly in Q^4 tetrahedra (Zotov and Keppler, 1998).

The main HF envelope at 900–1200 cm^{-1} can be decomposed into several bands associated with localized symmetric and asymmetric T—O and T—O—T stretching modes of distinct structural species, i.e. Q^2, Q^3, Q^4 (2, 3, 4 being the number of bridging oxygens; Mysen et al., 1980; Matson et al., 1983; McMillan, 1984; Zotov and Keppler, 1998; Rossano and Mysen, 2012). Substitution of Al^{3+} and Fe^{3+} for Si^{4+} as network-forming cations strongly influences the spectral composition of this band; in particular, increasing the Al content of the glass results in the shifting of Raman bands to lower frequencies (Brawer and White, 1977; Mysen et al., 1980; Neuville et al., 2004). The intensity ratio between the bands near 950 and 1135 cm^{-1} in rhyolitic glasses is indicative of relative proportions of structural units, which are likely Q^2 and a combination of Q^3 and Q^4 units, respectively (Mysen et al., 1980; Zotov and Keppler, 1998). The band near 1050 cm^{-1} that characterizes the water-poor NSL-N1 glass is tentatively assigned to T—O stretching vibrations in distinct Q^3 or Q^4 units (Mysen et al., 1980; Zotov and Keppler, 1998). In the peraluminous rhyolites, the increased intensity of the band at ~930 cm^{-1} with increasing water content can be attributed to the formation of T-OH units (Zotov and Keppler, 1998). In peralkaline glasses, the sharp increase of the band at 970–980 cm^{-1} is attributed to progressive entry of four-fold Fe^{3+} in alkali-bonded Q^3 units (Wang et al., 1995; Di Muro et al., 2009; Di Genova et al., 2016).

The cause of the HF band shift of the andesitic glass A071215 to lower wavenumber compared to the other andesitic glasses is uncertain: it is probably related to differences in their Fe^{3+}/Fe_{tot} ratios.

In basaltic glasses, the increased intensity of the HF envelope and its shift to lower wavenumbers compared to polymerized glasses are consistent with the increase of Q^2 and Q^3 units. In the high-Al basaltic set, both water content and polymerization degree correlate negatively with the FWHM of the HF band (Fig. 2Sa, b) and positively with the intensity ratio of LF band to HF band (Fig. 2Sc, d). This seems to be contradictory as water dissolution is expected to enhance depolymerization. Although investigation of dissolution mechanisms of water in basaltic melts is beyond the scope of this study, it is worth noting that the described spectral features likely suggest dissolution mechanisms other than those occurring in more polymerized glasses. In depolymerized CaO-MgO-SiO_2 glasses, Xue and Kanzaki (2004) highlighted formation of (Ca, Mg)-OH groups, in which OH groups are only linked to network-modifying metal cations, not to the silicate network. This is expected to cause an increase in the melt polymerization, contrary to the effect of Si-OH formation (Mysen and Virgo, 1986; Xue and Kanzaki, 2004). These water dissolution mechanisms, associated with major changes in the local environment of metal cations, are probably responsible for the trends defined by the high-Al basaltic set.

4.3. Water band topology

The topology of the water stretching vibration band depends on glass matrix composition and water concentration (Fig. 5), but also on water speciation (e.g., Mysen and Virgo, 1986) and strength of H-bonding (e.g., Zajacz et al., 2005; Behrens et al., 2006; Di Muro et al., 2006a, 2006b). Different water species (metal-hydroxyl and molecular H_2O) contribute to the intensity of the broad water band (e.g., Mysen and Virgo, 1986). The latter is asymmetric in shape with a long tail on the lower wavenumber side, and is characterized by two shoulders near 3250 cm^{-1} and 3640 cm^{-1} that are readily observed in rhyolitic glasses (Fig. 5). The exact position of the maximum peak of the water band shifts to lower frequency with increase of polymerization degree and water content (Fig. 5), in agreement with previous studies. The maximum is located within the 3565–3582 cm^{-1} range in basaltic glasses and at 3552–3570 cm^{-1} in basanitic, andesitic and rhyolitic glasses. In the basanitic, basaltic and andesitic glass sets, the FWHM of the band increases by 15–25% relative with increasing water content.

The H_2O bending vibration at ca. 1630 cm^{-1} (not shown) can be clearly distinguished from the background in spectra of water-rich glasses.

4.4. Peak fitting of the HF and water bands

We performed spectral deconvolution using OriginPro software in order to quantify differences in spectral components of the water band and the HF alumino-silicate envelope of basanitic and rhyolitic glasses (Tables 1S, 2S and 3S). Spectra were fitted with a finite number of Gaussian components using the Multiple Peak Fit tool and following a procedure analogous to the one described by Morizet et al. (2013). This procedure consists of: i) locating a certain number of peaks based on results of previous studies (e.g., Di Muro et al., 2009; Rossano and Mysen, 2012; Morizet et al., 2013); ii) performing a first set of iterations with peak position and/or FWHM fixed until the quality of fit (expressed as χ^2) does not change; and iii) performing a second set of iterations in which peak position and areas are left free to evolve, until the best fit possible (i.e., the lowest χ^2) is obtained. Fitting parameters were iterated until the fit converged using both Simplex method and Levenberg-Marquardt algorithm available in OriginPro, and the two algorithms provided comparable results. In our simulations, the χ^2 tolerance value of 10^{-9} was always reached. The errors associated with

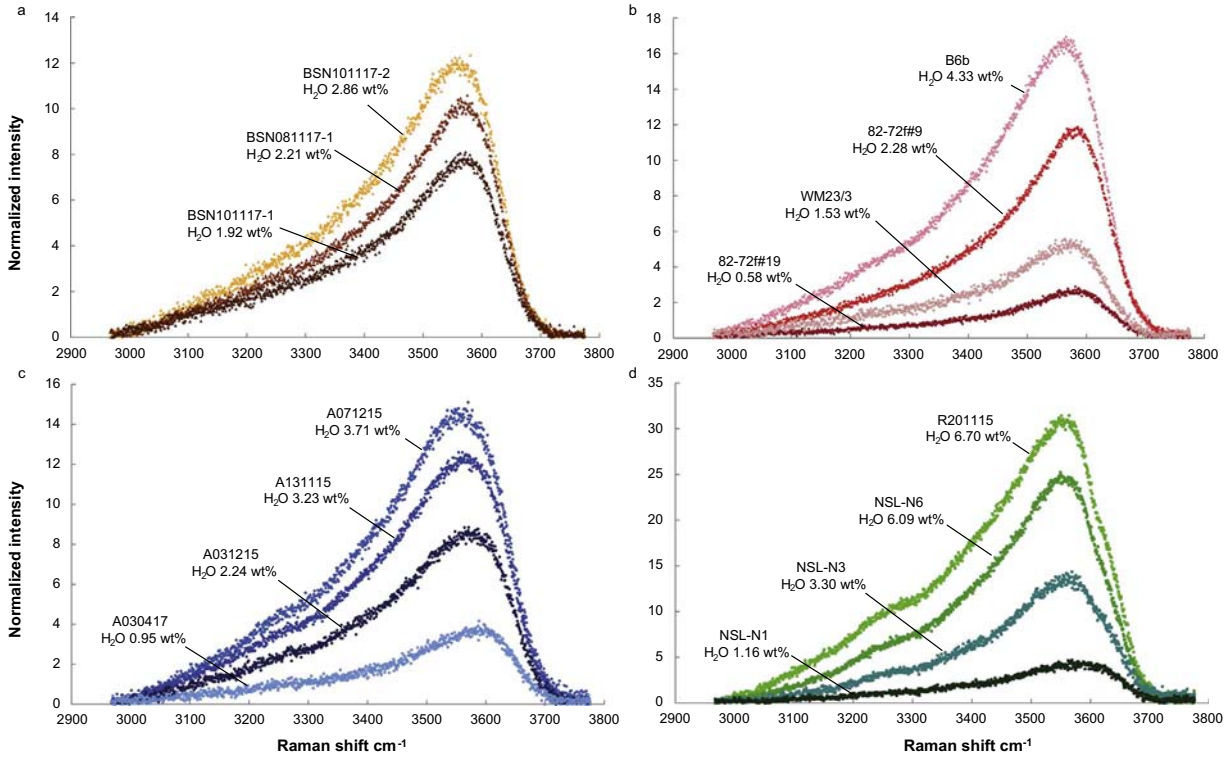

Fig. 5. Baseline-corrected Raman spectra in the water region of reference glasses: basanites (a), basalts (b), andesites (c) and rhyolites (d) with different water contents. Spectra were measured under the same conditions of laser power and confocality. Intensities were normalized to acquisition time. Laser beam was focused at optimal depths as defined in the text.

the simulations are reported in Tables 1S, 2S and 3S. The proposed simulations may represent one of several possible fits; however, consistency in fitting parameters within each glass series and general agreement with deconvolutions reported in the literature (e.g., Di Muro et al., 2009; Rossano and Mysen, 2012; Morizet et al., 2013) ensure the reproducibility of the calibrations established in the next sections. In fact, we verified that the small changes in the constrained parameters had a negligible effect on the ratios between the areas of different spectral components.

Five components are required to fit the spectra of rhyolitic glasses (Fig. 6). Peak fitting of peraluminous and peralkaline glass spectra differs in the position of component II and in the relative intensities of the five components (Table 1S). Band positions are: I) 901–917 cm^{-1}, II) 975–1000 cm^{-1} (with the highest frequencies in peraluminous rhyolites), III) 1047–1060 cm^{-1}, IV) 1113–1126 cm^{-1}, and V) 1174–1182 cm^{-1}. The good quality of the fit is indicated by the randomness of the residuals. Fitting six components instead of five reduces the quality of the fit.

Concerning CO_2-bearing basanitic glasses, best fitting in the 630–1200 cm^{-1} spectral range was achieved with six to seven components, whose positions are: I) 707–715 cm^{-1}, II) 779–789 cm^{-1}, III) 864–891 cm^{-1}, IV) 930–963 cm^{-1}, V) 990–1021 cm^{-1}, VI) 1061–1077 cm^{-1} and VII) 1084–1088 cm^{-1} (Fig. 3S, Table 2S). The last component refers to the ν_1 Raman vibration of dissolved carbonate (Morizet et al., 2013).

Peak fitting of the total water band requires a minimum of four Gaussian components (Table 3S, Fig. 4S), in agreement with previous studies (e.g., Chabiron et al., 2004; Behrens et al., 2006; Di Muro et al., 2006a, 2006b). The positions of these components are: I) 3080–3098 cm^{-1}, II) 3250–3298 cm^{-1}, III) 3420–3487 cm^{-1} (with the highest frequencies in rhyolites), IV) 3540–3575 cm^{-1}, and V) 3600–3645 cm^{-1} (with the lowest frequencies in basanites and basalts); these positions match those determined by Di Muro et al. (2006a, 2006b). The small component I is only present in water-rich glasses (Fig. 5), as observed by Behrens et al. (2006). In general, the intensity of the low frequency components increases with total dissolved water, in agreement with the expected increase of molecular water (e.g. Mysen and Virgo, 1986).

5. Depth profiles

Intensities (i.e. height of the dominant band) and integrated intensities (i.e. total area) of the Raman bands vary with focusing depth of the laser beam (e.g., Behrens et al., 2006; Mercier et al., 2009). Depth profiles measured in the alumino-silicate vibration region and water region, under both high and standard confocality conditions, are shown in Fig. 7 for basanitic, basaltic, andesitic and rhyolitic compositions. Differences appear between glasses with different compositions and absorptivities.

In the alumino-silicate domain of basanitic and basaltic glass spectra, signal intensity increases from the surface to a depth of 2–3 μm and 3–4 μm in high and standard confocality, respectively. The maximum intensity is 22% (basanitic) and 35% (basalt) higher than the signal intensity at the surface in high confocality, whereas it increases by ~45% in standard confocality (Fig. 7). In andesitic glasses, maximum intensity, which is attained at 3–4 μm depth, is 50% higher than the signal at the surface. Below the maximum normalized intensity, the intensity decreases with depth by 3%/μm in the first 30 μm in basanitic glasses and by 2%/μm in both basaltic and andesitic glasses (Fig. 7). Maximum alumino-silicate signal intensity in rhyolitic glasses is attained at ~5 μm depth in a highly confocal setting, but at 7–10 μm depth under standard confocality conditions. At these depths the intensity is 55 and 65% higher (in high and standard confocality, respectively) compared to the one measured at the surface; then it diminishes by 1%/μm (high confocality) and 0.5%/μm (standard confocality) for the remainder of the first 30 μm.

Maximum signal intensity of the water band is attained at the same depths as for the alumino-silicate bands (Fig. 7). However, the percentages of increase with respect to signal at the surface are lower for water bands than observed for alumino-silicate bands. In the high

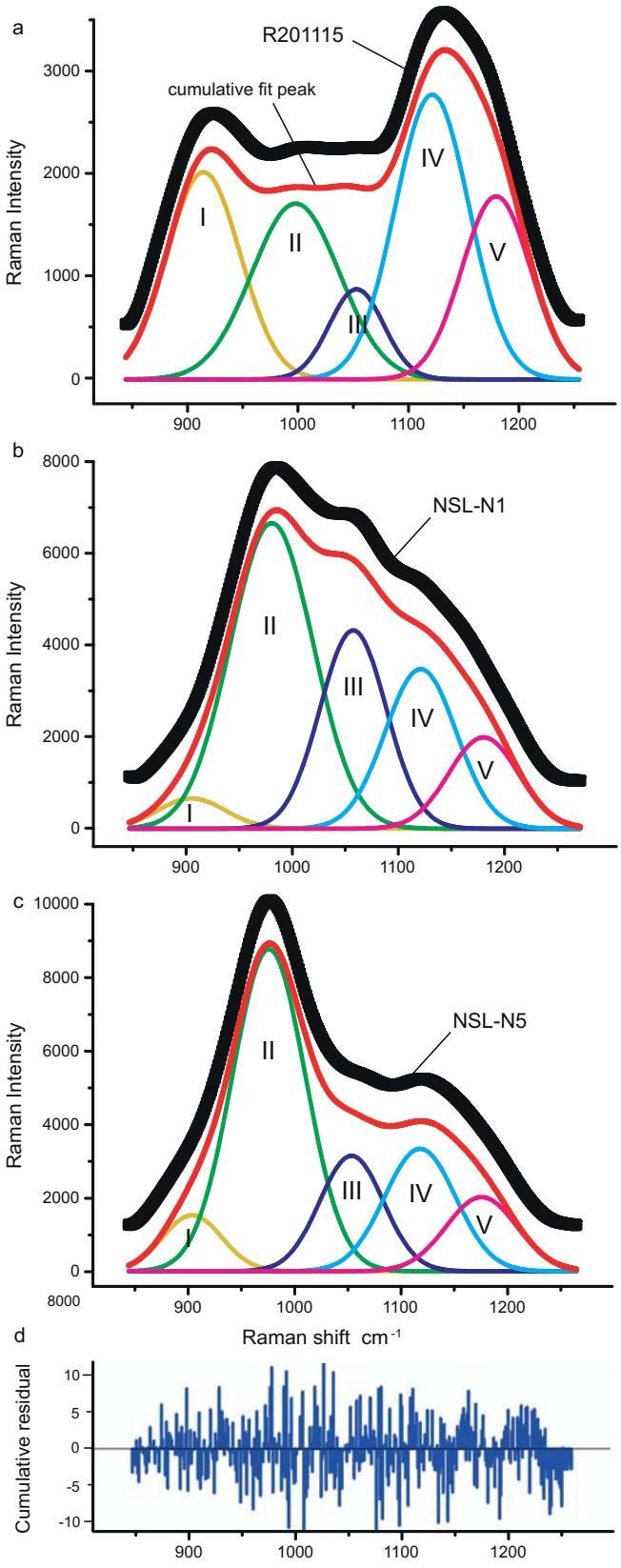

Fig. 6. Peak fitting of the HF alumino-silicate envelope of peraluminous (a), water-poor (b) and water-rich peralkaline (c) rhyolitic glasses with a finite number of Gaussian components performed with OriginPro software. The good quality of the fit is indicated by the randomness of the residuals (d).

confocality setting, the increase ranges from 15 to 18% in basaltic and basanitic glasses to 20–25% in andesitic and rhyolitic glasses, whereas in the standard confocality setting, it varies from 20 to 25% in basaltic and andesitic glasses to 29–35% in basanitic and rhyolitic glasses. That is, the intensity increase in the alumino-silicate region is twice as high as that in the water region. This causes the observed variability of the ratio between the intensity of the water band and the intensity of the silicate band ("OH/Si"). Below the depth of maximum signal intensity, Raman intensity of the water band decreases more slowly with depth compared to the alumino-silicate bands. Specifically, it drops by 2.6%/μm in basanites, by 1.5%/μm in basaltic and andesitic compositions, whereas it remains almost constant over 12 μm in rhyolitic glasses before dropping by 0.7%/μm. The evolution with depth of the OH/Si band intensity ratio is significantly different in high and standard confocality settings. Indeed, under less confocal conditions this ratio remains almost constant at minimum values within the first 5–20 μm, irrespective of glass composition. In contrast, the OH/Si band intensity ratio is much more sensitive to depth when using the high confocality setting. Thus, under confocal conditions depth precision is required to get reproducible OH/Si values.

Measurements of peak height and area provided consistent results. Moreover, similar depth profiles were obtained at laser power conditions ranging from 1 to 16 mW. In contrast, the signal intensities of both alumino-silicate and water bands drop faster with depth when the laser power on the sample is about 75 mW. This is especially relevant for basaltic glasses, in which maximum signal intensity occurs at the glass surface at these high laser-power conditions. These observations are consistent with more intense self-absorption expected in basaltic glasses compared to more silica-rich glasses (e.g., Behrens et al., 2006; Mercier et al., 2009). Excitation of (iron-bearing) basaltic samples, in fact, results in attenuation of both the exciting light and the Raman scattered light.

Depths where both signals of the alumino-silicate and water bands are the highest were considered as optimal focusing depths. For measurements performed in high confocality setting, the adopted focusing depths correspond to the depth of minimum OH/Si band intensity ratio. As shown in the following sections, this is a critical step to ensure a good calibration. We highlight that a focusing error of about 1 μm near the depth of maximum signal intensity causes a relatively small error (< 3% relative) in measured band intensity. Larger focusing errors, however, result in non-negligible drop of the measured intensity.

6. Calibration

6.1. External calibration method

In the external calibration method, water concentration in an unknown glass sample is derived from the absolute (integrated) intensity of the band at ~3570 cm^{-1} compared to band (integrated) intensities of reference glasses with known water contents defining a calibration line (e.g., Behrens et al., 2006; Di Muro et al., 2006a, 2006b; Mercier et al., 2010).

When spectra are treated using the described procedure for focus depth selection and baseline correction, both I_{OH} and A_{OH} show positive linear correlation with glass water contents determined by FTIR spectroscopy or SIMS. Correlations based on peak height measurements, however, are affected by a larger scatter than correlations based on peak area (Fig. 5S), therefore, only calibrations based on area measurements are considered hereafter. Such a difference is explained by the observation that varying amounts of water dissolved in glasses with different compositions produce not only variations in peak height, but also in total band width and distribution of spectral components (as summarized in the previous section).

Fig. 8(a–c) shows calibration lines obtained in high or standard confocality setting after subtracting a cubic or a linear baseline from raw data. In these plots, reference glasses define a single composition-

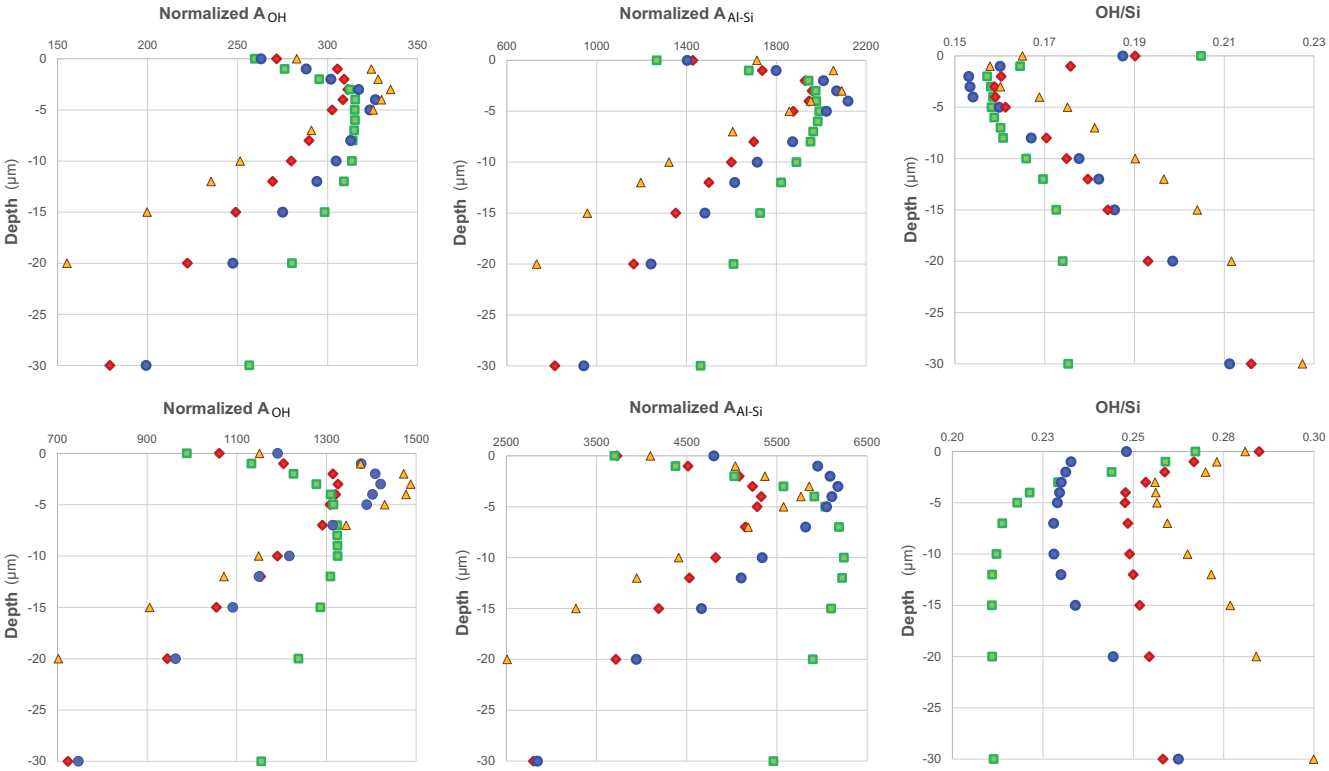

Fig. 7. Depth profiles measured in the water and alumino-silicate vibration regions of basanitic (yellow triangles), basaltic (red diamonds), andesitic (blue circles) and rhyolitic (green squares) glasses under high (upper row) and standard (lower row) confocality conditions. Integrated intensities of the water band (A_{OH}) and the alumino-silicate envelope ($A_{Al\text{-}Si}$) were normalized to laser power and acquisition time; water band intensities were also normalized to water content. (For interpretation of the references to colour in this figure legend, the reader is referred to the web version of this article.)

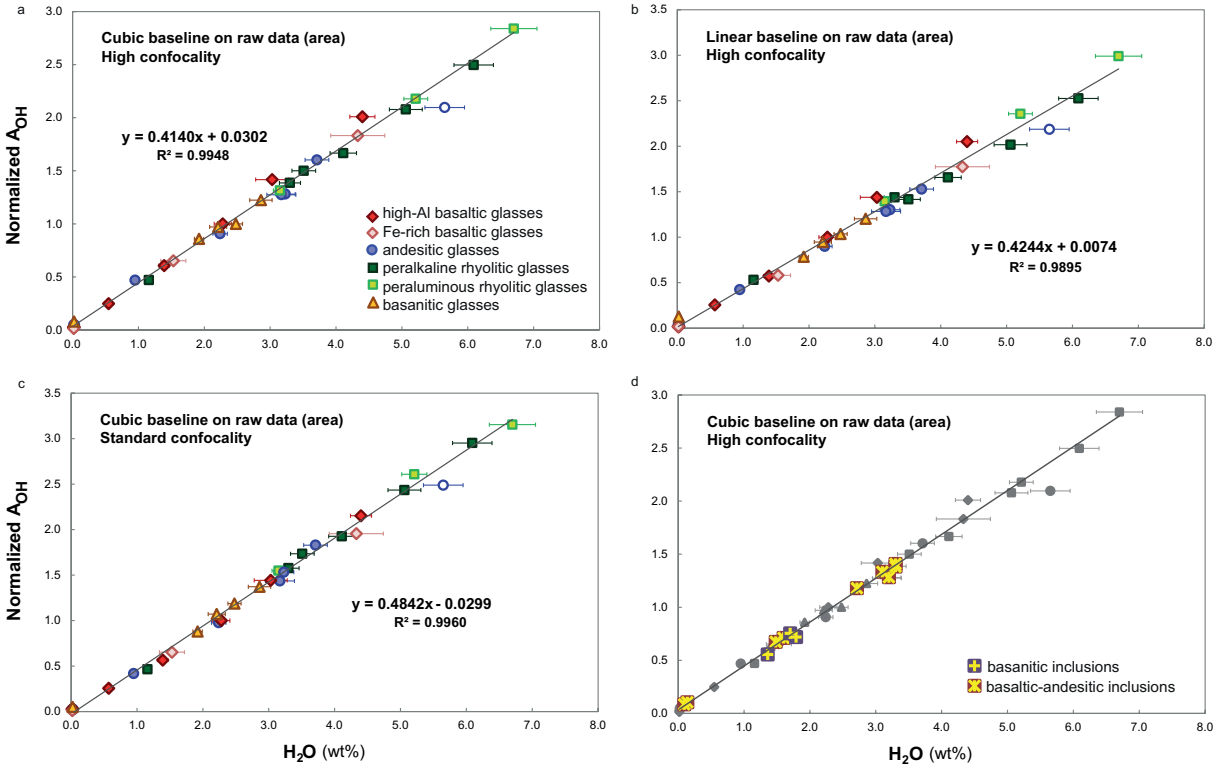

Fig. 8. External calibration lines for quantification of water contents in glasses, obtained after subtracting a cubic or a linear baseline from raw data: areas in high confocality setting (a–b, d), and in standard confocality setting (c). Reference glasses define a composition-independent linear relationship. In (d) glass inclusions are plotted over the reference glasses. Microlite-bearing A011215 glass (empty circle) is shown but is not considered for calibration line definition. Water band areas were normalized to the water band area of the 82-72f#9 basaltic glass, which was used as internal standard to eliminate small variations in measurement conditions. For glass inclusions, errors associated with SIMS measurements are smaller than symbols.

independent linear relationship between water band intensity and water concentration. The calibration based on cubic background subtraction provides the best fit in both high confocality:

$$C_{H2O}\ (wt\%) = 2.403\ (\pm 0.033)\cdot A_{OH} - 0.058\ (\pm 0.046)\ (R^2 = 0.995) \quad (1)$$

and standard confocality setting:

$$C_{H2O}\ (wt\%) = 2.057(\pm 0.025)\cdot A_{OH} + 0.072\ (\pm 0.039)\ (R^2 = 0.996) \quad (2)$$

The data are reproduced with a root-mean-square error of ~0.13 and ~0.11 wt% in high and standard confocality, respectively (Fig. 8, Table 4S). The linear regressions do not take into account the uncertainties on H_2O content of the reference glasses. Their intercepts pass very close to the origin. Linear calibrations with similar slopes (within 15% difference) were reproduced using a range (1–16 mW) of laser powers in different sessions over several months.

It is worth noting that measurements performed by focusing the laser beam on the surface of the alumino-silicate glasses yielded slightly divergent calibration lines whose slopes depend on glass composition: the slope decreases from basaltic to rhyolitic compositions, as previously observed by Mercier et al. (2010).

6.2. Internal calibration method

The internal calibration procedure is based on the correlation between the glass water concentration and the relative (integrated) intensities of the water and alumino-silicate Raman bands. To compare spectra of alumino-silicate glasses with different compositions, and because Mercier et al. (2009) reported a significant effect of bulk chemical composition on internal calibrations based on normalization to either LF or HF band heights, we built our internal calibration procedure on the measurement of band total area, instead of band height (Fig. 9).

OH/Si increases with water content and the increase is generally higher for mafic than for felsic glasses (Fig. 9a). Between the two felsic compositions, the increase of the OH/Si ratio with water of the peraluminous rhyolite is noticeably more important than the peralkaline one. More precisely, calcalkaline and tholeiitic glasses containing < 3 wt% H_2O and the peraluminous rhyolite with various water contents fit on a single trend, whereas the other glasses diverge from the general trend to higher OH/Si ratios (the water-rich basalts) or lower OH/Si ratios (the basanites and peralkaline rhyolites) (Fig. 9a). Similar trends are obtained when subtracting a linear/cubic baseline from raw or Long-corrected data. Measurements performed in a standard confocality setting (not shown) yield a ~50% steeper calibration line than measurements done under high confocality conditions.

The divergence of water-rich basalts and peralkaline rhyolites from the main trend in Fig. 9a is due to the effect of water content on the integrated intensity of the alumino-silicate region and to the behavior of the band at 980 cm^{-1}, respectively. Careful inspection of spectra in the alumino-silicate vibration region reveals that the integrated intensity (hereafter $A_{Al\text{-}Si}$) of this region generally decreases with increasing water content and decreasing density (Fig. 10), regardless of analytical conditions (i.e. laser power on sample and confocality) and baseline treatment, except for the peralkaline and basanitic glasses. The effect of water in lowering $A_{Al\text{-}Si}$ is maximum in basaltic glasses, in particular in the 82-72f set with 30% intensity reduction for 15 mol% H_2O (Fig. 10c), and becomes smaller in andesitic and rhyolitic glasses characterized by < 12% and 10% reduction for 18 mol% H_2O and 25 mol% H_2O, respectively (Fig. 10e, g). In CO_2-bearing basanitic glasses, the observed increase of $A_{Al\text{-}Si}$ with decreasing density (Fig. 10b) is due to the presence of CO_3^{2-} dissolved in these glasses; the intensity of the ν_1 Raman vibration of dissolved carbonate at ~1087 cm^{-1} (Fig. 3S) has to be subtracted from the intensity of the alumino-silicate envelope (Table 2S). Adjustments of the internal calibration method to take into account the effect of water content on $A_{Al\text{-}Si}$, the behavior of the band at 980 cm^{-1} in peralkaline rhyolites and the presence of CO_3^{2-} in basanites are presented in the Discussion section.

Small deviations from the general trends of Fig. 10 in a given set of glasses reflect differences in glass structure. For instance, the higher $A_{Al\text{-}Si}$ measured in the A071215 sample is probably due to a different iron oxidation state compared to the other andesitic glasses (see spectra of Fig. 4c). The HF band in A310317 and A030417 glass spectra contains an additional contribution from the vibration of CO_3^{2-} molecules (Fig. 10e). The basaltic sample 82-72f#10 is characterized by a larger $A_{Al\text{-}Si}$ than expected from the general trend of the 82-72f basaltic set (Fig. 10c). This may be due to the slightly higher density of this sample compared to the other glasses of the same basaltic set (Fig. 2). Analogously, the higher synthesis pressure (and thus the relatively higher density) of the basanite BSN101117-2 compared to the other basanitic glasses (Table 1) may be partly responsible for its significantly larger $A_{Al\text{-}Si}$ (Fig. 10a, b).

7. Discussion

7.1. Parameters controlling the Raman signal

Raman vibration intensity of a molecule is proportional to the quantity of the analyzed molecule and to its Raman scattering cross-section (which expresses the Raman scattering efficiency of a molecule) (e.g. Dubessy et al., 2012), but it depends also on analytical conditions and instrumental features that influence the excited volume (e.g., laser wavelength and power, confocal aperture of slits or pinholes, microscope magnification, numerical aperture of the objective, grating). These relationships are expressed in the following equation:

$$N = N_{V0}/A\cdot d\sigma/d\Omega\cdot\Delta\Omega\cdot N_m \quad (3)$$

where N is the total number of Raman photons for a specific vibrational mode, N_m is the number of molecules contained in the scattering volume V that are responsible for that vibrational mode (i.e. $N_m = \rho V$ if ρ is the number of molecules per unit volume), $d\sigma/d\Omega$ is the differential Raman scattering cross-section of a specific Raman mode, N_{V0}/A is the flux of photons of the laser focused onto the sample area A, and $\Delta\Omega$ is the solid angle of light collection.

Previous studies showed that the Raman scattering cross-section of different Q^n species and dissolved hydrous species depends on glass composition and structure (Fukumi et al., 1990; Zotov, 2001; Zajacz et al., 2005; Behrens et al., 2006; Mercier et al., 2010). Mercier et al. (2010) highlighted that the matrix effect on the total water band is related to differences in glass reflectance and water bonding environment. Moreover, they reported positive correlations between the slope of the calibration line and both reflectance and density of the glass.

The size of the scattering volume of the glass is affected by its physico-chemical characteristics such as chemical composition, structure, density, reflectance, refractivity and absorptivity. The confocal scattering volume can be expressed by the product of the illumination volume (i.e. the volume of the laser focus) and the detection volume (which is defined by Raman photons generated within the illumination volume that are relayed back into the spectrometer via the confocal aperture, Everall, 2004; Maruyama and Kanematsu, 2011). In particular, these two volume components determine the depth resolution of Raman measurements. Therefore, in order to interpret correctly confocal Raman measurements, one should take the spread in focal position due to light refraction into account (Everall, 2004; Maruyama and Kanematsu, 2011). When focusing beneath the surface of a sample with a refraction index above 1, the light rays are slowed down and refracted according to Snell's law. In general, upon moving deeper into the sample the axial laser focus broadens and focus position shifts to lower depth than indicated by microscope vertical displacement, because depth resolution degrades with depth below the surface (Everall, 2004; Maruyama and Kanematsu, 2011). These processes can explain the different depth profiles and distinct slopes of the calibration lines we obtained when changing from high confocality to standard confocality

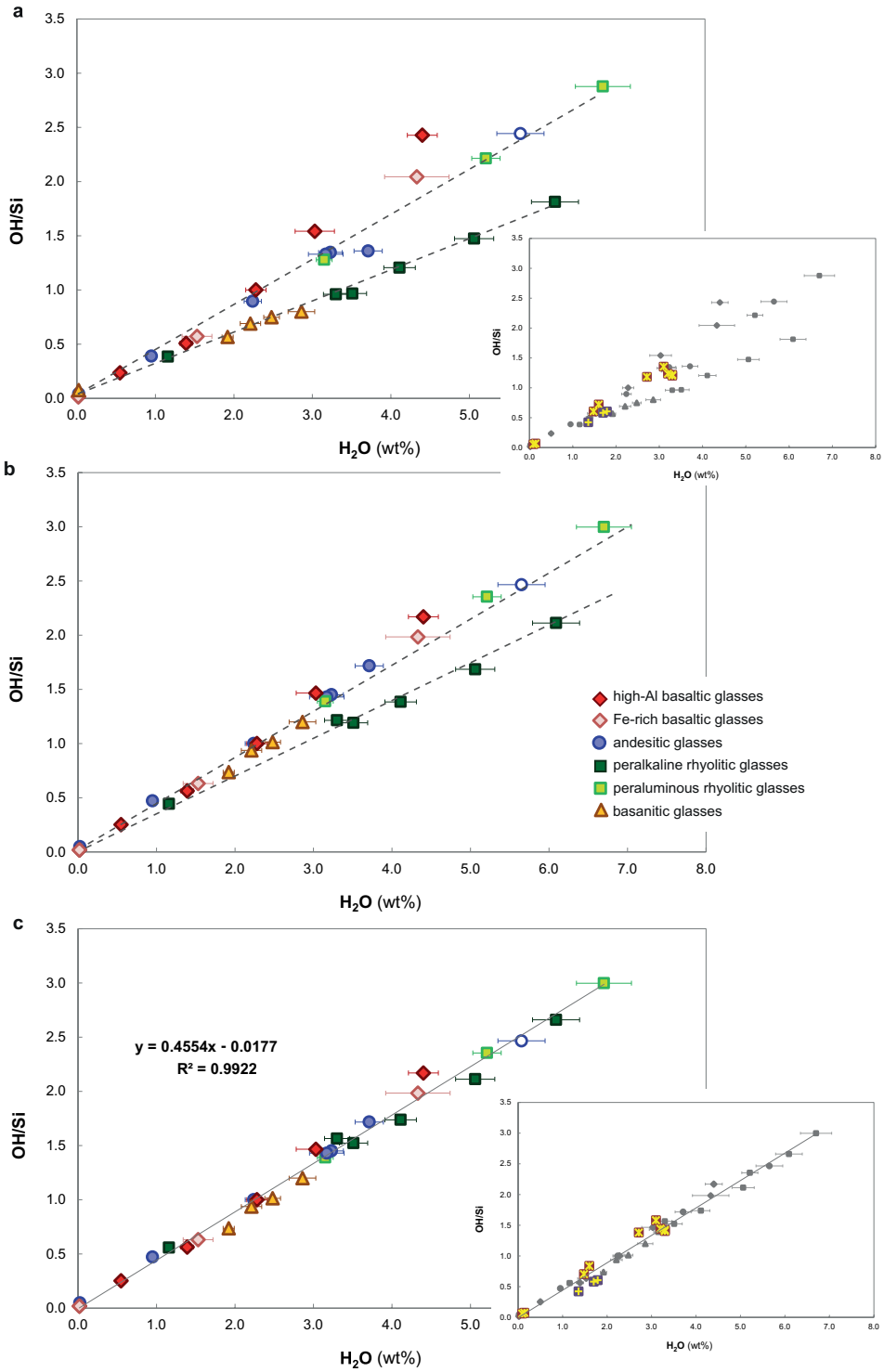

Fig. 9. a) Internal calibration diagram showing variation of the "OH/Si" ratio (i.e. the area ratio between the total water band, A_{OH}, and the total alumino-silicate band region, $A_{Al\text{-}Si}$) versus water content. b) Internal calibration lines after applying the density-related correction. c) Internal calibration line after correcting for the high Raman scattering of the 980 cm^{-1} band in peralkaline rhyolites. All samples define a single calibration line passing through the origin. The insets show the non-corrected glass inclusion compositions (symbols as in Fig. 8). Signal intensities were normalized to laser power and acquisition time, and to the areas of the 82-72f#9 internal standard.

settings (Figs. 7 and 8). Because the observed shapes of OH/Si depth profiles vary with confocality (Fig. 7), we expect these differences to be reflected in calibration lines. Different slopes of the internal calibration lines obtained for high and standard confocality conditions suggest that the internal calibration does not correct for the effect due to changes in confocal volume size.

7.2. External versus internal calibration

Concerning the external calibration, the linear relationship between water contents (as determined by FTIR or SIMS) and A_{OH} (Fig. 8) can be explained in two ways: either the scattering cross-section of the water stretching vibration mode is independent of the glass matrix composition, or the procedure established for spectra acquisition and baseline

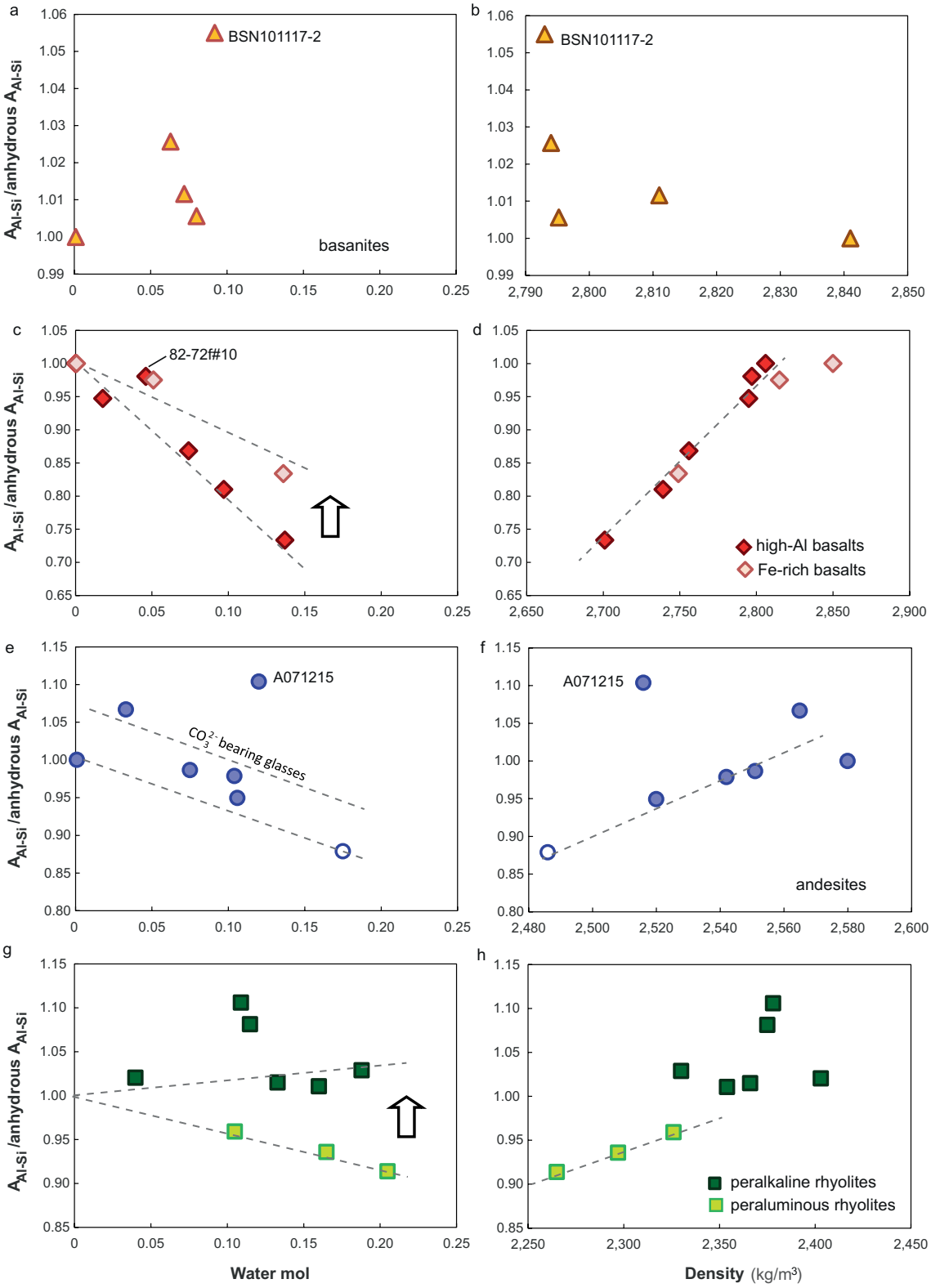

Fig. 10. Evolution of the area of the alumino-silicate band (expressed as ratio between the alumino-silicate band area of hydrous glasses and that of the anhydrous glass) with water content (left column) and density (right column) of basanitic (a–b), basaltic (c–d), andesitic (e–f) and rhyolitic (g–h) glasses. Grey dashed curves show the main trends. The arrows highlight the different behavior of Fe-rich and Fe-poor glasses with similar compositions. Microlite-bearing andesitic glass A011215 is represented by an empty blue circle. (For interpretation of the references to colour in this figure legend, the reader is referred to the web version of this article.)

treatment minimizes the differences in Raman cross-section and the effects related with size of the confocal volume, self-absorption and reflectance at the sample surface. Taking into account the findings of previous studies (e.g. Mercier et al., 2010), we believe this second hypothesis is more likely. Small differences in shape and componentry between the water bands of the studied glasses (Fig. 5 and Fig. 4S) are consistent with differences in water bonding environments and speciation, as previously discussed by Behrens et al. (2006), Di Muro et al.

(2006b) and Mercier et al. (2010). The external calibration method proposed here yields a single calibration line allowing analysis of all alumino-silicate glasses with the same level of accuracy as previous studies (e.g., Behrens et al., 2006). This suggests that measurements performed following the procedure established in this study (i.e., measurements performed at optimal focus depths rather than on sample surface, and based on quantification of the water band area instead of band height) provide the best conditions for correction of differences in Raman scattering efficiency between glasses of variable subalkaline and alkaline compositions.

In the case of internal calibration, the intensity of the water band is scaled to the alumino-silicate band intensity, resulting in a stronger dependence on glass composition (Fig. 9a), in agreement with previous works (e.g., Zajacz et al., 2005; Mercier et al., 2009). To better compare all the glass sets, the CO_2-bearing glasses need to be corrected for the contribution of the CO_3^{2-}-related spectral component (Fig. 3S). This is simply achieved by multiplying the $A_{Al\text{-}Si}$ by a factor that takes into account the contribution of the component VII relative to the sum of the areas of all spectral components (Table 2S). In line with the results of Morizet et al. (2013), we found that the relative contribution of the CO_3^{2-} is proportional to the total CO_2 content.

The observed relationships between $A_{Al\text{-}Si}$, glass density and water content (Fig. 10) indicate that glass density strongly affects Raman scattering of the alumino-silicate vibration region. When we consider the glass density dependence, by normalizing the intensity of the alumino-silicate envelopes to the intensity measured in anhydrous glasses, the studied glasses define a single positive linear correlation, except for the peralkaline ones (Fig. 9b). This linear relationship is expressed by the following equation:

$$OH/Si = [A_{OH}/(p \cdot t_1)]/[A_{Al-Si}/(p \cdot t_2) \cdot (1 + \alpha_1)] \quad (4)$$

where $\alpha_1 = 1 - (A_{Al\text{-}Si\ hydrous}/A_{Al\text{-}Si\ anhydrous})$, p is the laser power, and t_1 and t_2 are the acquisition times in the water and alumino-silicate regions, respectively. In other words, the correction factor (α_1, Table 4S) is proportional to the difference between the $A_{Al\text{-}Si}$ of the anhydrous glass and that of the hydrous glasses of each set (Fig. 10). The correction factor depends on both glass composition and water content (see Fig. 2); either density or mol% H_2O estimated with the external calibration method can be used to estimate α_1 (Fig. 10). Up to ~7 wt% H_2O contents, rhyolitic, andesitic and basanitic glasses require a minor correction (< 10–12% in the studied range of water contents). In contrast, water-rich (> 3 wt% H_2O) basaltic glasses need more important corrections.

Peralkaline glasses are well aligned below the calibration line defined by peraluminous rhyolites (Fig. 9a). In order to understand their distinct behavior, we performed peak fitting of the alumino-silicate HF envelope of both peralkaline and peraluminous glasses (Fig. 6). The spectral components I, IV and V are more important in peraluminous rhyolites than in peralkaline ones, whereas the opposite behavior is observed for the components II and III. The sum of the components III, IV and V represents approximately 50% of the total area in both glass sets (51 ± 6, 1σ). In contrast, the sum of the areas of the components I, II and III varies significantly from peraluminous (~50% of the total area) to peralkaline (70–75% of the total area) glasses, with a 20–25% difference. This difference can be explained by the higher Fe content and oxidation state of peralkaline glasses, as revealed by the sharp increase of the component (II) at ~980 cm^{-1}, which is attributed to the presence of four-fold coordinated Fe^{3+} in alkali-bonded Q^3 units (e.g., Wang et al., 1995; Di Muro et al., 2009; Di Genova et al., 2016). The internal calibration procedure can be improved by taking into account the high Raman scattering of the 980 cm^{-1} band in peralkaline rhyolites, and this can be performed by calculating a correction factor:

$$\alpha_2 = [100 - ((I - II - III)_{peralkaline} - (I - II - III)_{peraluminous})]/100 \quad (5)$$

where (I-II-III) represents the sum of the areas of the components I, II and III (Table 1S). Once the $A_{Al\text{-}Si}$ of peralkaline glasses is corrected for the difference in componentry compared to peraluminous glasses, all rhyolitic glasses follow the same calibration line defined by all other compositions (Fig. 9c). This observation suggests that Fe^{3+} has an important effect on the Raman scattering efficiency of alumino-silicate glasses; in rhyolitic glasses the vibrational mode at 970–980 cm^{-1} has an important Raman scattering cross-section.

The linear fit of the internal calibration is expressed by the following equation (Fig. 9c):

$$C_{H2O}\ (wt\%) = 2.179\ (\pm 0.037) \cdot A_{OH}/A_{Al-Si\ corr} + 0.060\ (\pm 0.055)\ (R^2 = 0.992) \quad (6)$$

where $A_{Al\text{-}Si\ corr}$ is the corrected area of the alumino-silicate envelope and $A_{OH}/A_{Al\text{-}Si\ corr}$ (i.e., OH/Si in Fig. 9c) = $A_{OH}/(\alpha_1 \cdot A_{Al\text{-}Si} + \alpha_2 \cdot A_{Al\text{-}Si})$. The linear fit reproduces the whole dataset within 0.17 wt% (root-mean-square error).

7.3. Application to natural glass inclusions

As a final step, we examine if the calibration procedures described in the previous sections can be applied to the study of natural hydrous glasses. We tested them on natural olivine-hosted glass inclusions from Santorini volcano, Lanzarote Island and FAMOUS Zone (Mid Atlantic Ridge) (Table 3). For the geochemical characterization of Santorini inclusions, including their volatile contents and details on secondary ion mass spectrometry (SIMS) measurements, we refer the reader to Druitt et al. (2016). Inclusions from Lanzarote have been studied by Gómez-Ulla et al. (under review) and analyzed using a CAMECA ims-4f ion probe at the NERC Ion Microprobe Facility at the University of Edinburgh. The reader is referred to Schiavi et al. (2016) for details on the inclusions from FAMOUS Zone and FTIR measurements.

The studied inclusions have variable composition spanning from basanitic to basaltic and andesitic, and contain different amounts of water ranging from 0.1 to 3.3 wt% (Table 3). They contain < 0.13 wt% CO_2, except for two basanitic inclusions, TAO-ol1 and TGN-ol18 bearing, respectively, 0.43 ± 0.09 and 0.21 ± 0.09 wt% CO_2. As CO_2 contents < 0.2 wt% are not detected using Raman spectroscopy (Morizet et al., 2013), only the two basanitic inclusions were corrected for the presence of dissolved carbonate. The relatively large size of the analyzed glass inclusions and the very weak or absent scattering from the embedding olivine crystals allowed focusing the laser beam at depths where the intensity of the water signal was maximum (−2 or −3 μm). These correspond to the optimal depths reported in Fig. 7 for the reference glasses.

We were unable to test our calibration procedure on silica-rich glasses with dacitic or rhyolitic compositions because all the tested inclusions contained magnetite nanocrystals, as revealed by the intense scattering of a Raman band near 670 cm^{-1} (Frezzotti et al., 2012). In line with the findings by Di Genova et al. (2017), we observed that presence of Fe-oxides dispersed in the glass causes underestimation of the water content of the inclusion, most likely due to light absorbance and possible heating and oxidation of the oxide phases.

Fig. 8d shows the results of the external calibration procedure applied to glass inclusions. The estimated water contents are in very good agreement with SIMS measurements and provide information about the accuracy of the method. The average relative standard deviations (RSD) between Raman and SIMS analyses are ~3% and 5% (1σ) when using a cubic or a linear baseline correction, respectively. It is worth noting that SIMS measurements were carried out first, so we cannot exclude that some water loss occurred from the inclusion before Raman analyses. For glass inclusions bearing H_2O contents close to the detection limit of the method (i.e. ~0.1 wt%), the RSD between FTIR and Raman measurements increases (4–22%, with maximum values for cubic background subtraction), partly due to decreasing signal/noise intensity ratio.

When using the internal calibration approach without applying the

Table 3
Water quantification in glass inclusions.

Sample	Provenance	Host phase	Glass composition	2D size	H_2O wt%							% host phase correct.[d]
				(μm)	SIMS/ FTIR[a]	± 1 σ	External cal. (cubic bas.)[b]	± 1 σ[c]	External cal. (linear bas.)[b]	± 1 σ[c]	
Vaggelli-3-1[e]	Santorini	Olivine	Basalt	110 × 50	3.10	0.06	3.15	0.12	3.25	0.17	0.0
Vaggelli-4-1[e]	Santorini	Olivine	Basalt	140 × 120	3.20	0.05	3.02	0.12	3.15	0.17	0.0
Vaggelli-6-1[e]	Santorini	Olivine	Basaltic andesite	210 × 110	3.30	0.04	3.27	0.13	2.98	0.19	0.0
Vaggelli-2-1[e]	Santorini	Olivine	Andesite	130 × 80	3.30	0.10	3.33	0.13	3.10	0.19	0.5
S12-371-3[e]	Santorini	Olivine	Basalt	190 × 115	2.71	0.03	2.77	0.11	2.71	0.15	0.0
S12-43-7-1[e]	Santorini	Olivine	Basalt	255 × 135	1.48	0.01	1.55	0.06	1.29	0.08	0.0
S12-43-1-1[e]	Santorini	Olivine	Basaltic andesite	65 × 50	1.60		1.64	0.06	1.62	0.09	1.0
TAO-ol1	Lanzarote	Olivine	Basanite	62 × 52	1.70	0.05	1.74	0.07	1.53	0.10	4.0
TAO-ol20	Lanzarote	Olivine	Basanite	101 × 25	1.36	0.05	1.26	0.06	1.14	0.08	1.5
TGN-ol18	Lanzarote	Olivine	Basanite	244 × 154	1.79	0.05	1.66	0.07	1.73	0.11	0.0
FZ OL37b	FAMOUS Zone	Olivine	Basalt	75 × 70	0.093	0.003	0.127	0.007	0.105	0.007	not embedded
FZ OL39	FAMOUS Zone	Olivine	Basalt	150 × 125	0.140	0.006	0.173	0.008	0.132	0.009	not embedded

Notes
[a] Water contents measured by SIMS, except for FZ OL37b and OL39 analyzed with FTIR (Schiavi et al., 2016).
[b] Water contents estimated from the regression lines of Fig. 8 (high confocality setting).
[c] Uncertainties calculated from the errors related to the linear regression (see Eq. 1 in the text) for 95% confidence interval.
[d] Arithmetic subtraction of host phase spectrum from glass spectrum.
[e] Reference: Druitt et al., 2016

corrections (for density and componentry) defined above, a first approximate estimate of the water dissolved in the glasses is obtained (inset in Fig. 9a). Basaltic and andesitic inclusions fall close to the main trend defined by the reference glasses, although some scatter is observed in inclusions containing ~3 wt% H_2O. The basanitic inclusions, instead, are aligned with the basanitic reference glasses below the main trend.

On quantifying water in glass inclusions, we are faced with the difficulty of measuring density of natural glass inclusions. Ardia et al. (2014) studied the evolution of haplogranite glass structure with pressure and water content, and observed that at a fixed water content and glass composition, density is a function of quench pressure. Thus, Raman spectra of melt inclusions trapped over a large pressure range are potentially influenced by the trapping pressure as well. In principle, the relationship observed between density, water content and $A_{Al\text{-}Si}$ will hold when a set of natural glass inclusions with similar composition that were quenched from similar pressure are analyzed, regardless of the absolute value of their density and quench pressure. In this case, corrections can be attempted within each set of glass inclusions based on the relationship between water contents estimated using the external calibration method and $A_{Al\text{-}Si}$. In some cases, calculating the density of glass inclusions could help decreasing the uncertainties of the method. Where these methods cannot be applied, water quantification should be performed based on reference glasses with similar composition, which do not require density-related correction.

Attempts to estimate the density-related factor α_1 for the studied inclusions resulted in non-negligible uncertainties on the OH/Si ratio. This is mainly due to the small number of analyzed inclusions with similar composition that did not allow defining trends as in Fig. 10 without uncertainty. For a qualitative analysis, the compositions of the inclusions, not corrected for density, are plotted on the main density-corrected trend defined by the reference glasses (inset in Fig. 9c). The observed distribution of the glass inclusions is in line with our expectations based on the behavior of the reference compositions (Fig. 10): the andesitic glass falls on the main trend as it is not expected to be strongly influenced by the density correction, several basaltic inclusions fall slightly above the main trend as observed for non-corrected reference basalts, while basanitic inclusions behave analogously to the reference basanites. Although this may be speculative, the strong similarities observed between reference samples and uncorrected glass inclusions probably suggest that differences of quench pressure in the studied inclusions has a minor influence on the established water quantification procedures.

8. Concluding remarks

This study contributes to the ongoing research dedicated to the development of precise micro-Raman routines for water quantification in alumino-silicate hydrous glasses. Here we summarize the main new findings of our study.

We examined in detail how the Raman intensities of the water band and the alumino-silicate envelope change with confocality performance and focus depth of the laser beam, as previously investigated (e.g., Behrens et al., 2006; Mercier et al., 2009). We found that the extent of increase of water band intensity with focus depth is lower than that measured in the alumino-silicate envelope. This results in a variable OH/Si band intensity ratio, and highlights the importance of measuring glasses at their optimal focus depth, which corresponds to the depth of maximum intensity of the water band and minimum OH/Si ratio. The optimal focus depth depends on glass composition and confocal performance of the Raman instrument, and is expected to change with laser wavelength as well. Maximum intensity in both water and alumino-silicate regions is attained at 2–3 μm, 3–4 μm and 5–10 μm depth, respectively in basanitic-basaltic, andesitic and rhyolitic glasses under the instrumental and analytical conditions used in this study.

Thirty reference glasses belonging to both alkaline and subalkaline magmatic series and containing up to ~7 wt% H_2O define a single external calibration line when they are analyzed at their optimal focus depth. In contrast, measurements performed on the sample surface did not yield a single calibration curve for glasses of different compositions. Our study suggests that water content of unknown samples can be determined based on a minimum of two reference glasses whose compositions do not need to match that of the unknown samples. However, using three or more reference glasses is recommended to improve the accuracy of water content quantification. In general, accurate water quantification using the external calibration method requires careful, repeated measurement of reference glasses because small variations in laser power can occur during long analytical runs, lowering the analytical precision.

For the reasons illustrated above, depth profile measurements are important even when using the internal calibration method for water quantification, because the normalization to the intensity of the alumino-silicate envelope does not cancel completely the differences in confocal volume size, as previously expected. A universal calibration

curve for quantification of water content in glasses cannot be established, unless the dependence of the confocal volume on different instrumental parameters is accurately known. Sharing common reference glasses between different laboratories may help future work for establishing a universal calibration.

This study recognizes critical parameters related with glass density, presence of ferric iron and dissolved carbonates as mainly responsible for matrix effects on the internal calibration method. We provide simple procedures for correcting and/or minimizing the effects of these parameters. Increasing water content lowers glass density and results in reduction of the area of the alumino-silicate envelope ($A_{Al\text{-}Si}$); we measured up to 30% intensity reduction in a high-Al basaltic glass bearing 15 mol% water. The correction method that we propose is based on the relative difference between $A_{Al\text{-}Si}$ of anhydrous and hydrous glasses with similar composition.

Peak fitting of the alumino-silicate high frequency envelope (approximately located between 800 and 1250 cm^{-1}) is required to quantify the intense scatterings around 980 cm^{-1} and 1080 cm^{-1} caused, respectively, by Fe^{3+} in four-fold coordination and CO_3^{2-} dissolved in glasses. Concerning the Fe^{3+}-related matrix effect, we must point out that, in principle, all Fe^{3+}-bearing glasses should be corrected for it. Nevertheless, only peralkaline rhyolites were corrected in this study because the area of the high frequency envelope in peralkaline rhyolites is far more sensitive to changes in Fe^{3+}/Fe_{tot} than in mafic compositions (Di Muro et al., 2009; Di Genova et al., 2016). Once the proposed corrections are performed, all the studied glasses define a single internal calibration line in spite of their compositional variability. Alkaline glasses, specifically basanites, behave coherently with the other glass compositions when the analytical strategies and data treatment procedures (i.e., for baseline subtraction, peak fitting and density correction) established in the present study are used.

Accuracy of the external calibration in the high confocality setting was determined by testing our method on olivine-hosted glass inclusions whose water content was measured using SIMS or FTIR. The calculated average RSD is ~4% (1σ) for most samples, and increases to ~12% (1σ) for glass inclusions with H_2O contents close to the detection limits (~0.1 wt%).

Because of their specific textural complexities, natural glass inclusions provide a unique laboratory for testing further the proposed calibration method.

Acknowledgements

We acknowledge Claire Fonquernie for CHNS analyses. Nicolas Cluzel, Jean-Luc Devidal, Franck Pointud, Mhammed Benbakkar, and Geeth Manthilake are warmly thanked for laboratory assistance. FS is grateful to Sébastien Maussang (Renishaw) for helpful discussion and to the scientific coordinator of Cler*V*olc, Tim Druitt, for supporting the Raman project. We thank Andrea Di Muro and an anonymous reviewer for their constructive comments. ACW acknowledges support from the NSERC discovery program and an Invited professor position from the Université Clermont-Auvergne of Clermont-Ferrand. SIMS analysis on basanitic glass inclusions at Cambridge was supported by NERC grant number IMF535/1114 to Dr. M. Edmonds. This research was financed by the French Government Laboratory of Excellence initiative (ClerVolc LabEx), the Région Auvergne and the European Regional Development Fund. This is Cler*V*olc contribution number 264.

Appendix A. Supplementary data

Supplementary data to this article can be found online at https://doi.org/10.1016/j.chemgeo.2018.02.036.

References

Andersen, T., Neumann, E.-R., 2001. Fluid inclusions in mantle xenoliths. Lithos 55, 301–320.

Ardia, P., Di Muro, A., Giordano, D., Massare, D., Sanchez-Valle, C., Schmidt, M.W., 2014. Densification mechanisms of haplogranite glasses as a function of water content and pressure based on density and Raman data. Geochim. Cosmochim. Acta 138, 158–180.

Behrens, H., Jantos, N., 2001. The effect of anhydrous composition on water solubility in granitic melts. Am. Mineral. 86, 14–20.

Behrens, H., Roux, J., Neuville, D.R., Siemann, M., 2006. Quantification of dissolved H_2O in silicate glasses using confocal microRaman spectroscopy. Chem. Geol. 229 (1), 96–112.

Brawer, S.A., White, W.B., 1977. Raman spectroscopic investigation of the structure of silicate glasses (II). Soda-alkaline earth-alumina ternary and quaternary glasses. J. Non-Cryst. Solids 23, 261–278.

Carroll, M.R., Holloway, J.R., 1994. Volatiles in Magmas, Reviews in Mineralogy. vol. 30 Mineralogical Society of America.

Cashman, K.V., 2004. Volatile Controls on Magma Ascent and Eruption. In: Sparks, R.S.J., Hawkesworth, C.J. (Eds.), The State of the Planet: Frontiers and Challenges in Geophysics. American Geophysical Union, Washington, D. C..

Chabiron, A., Pironon, J., Massare, D., 2004. Characterization of water in synthetic rhyolitic glasses and natural melt inclusions by Raman spectroscopy. Contrib. Mineral. Petrol. 146, 485–492.

Cluzel, N., Laporte, D., Provost, A., Kannewischer, I., 2008. Kinetics of heterogeneous nucleation in rhyolitic melts: implications for the number density of bubbles in volcanic conduits and for pumice textures. Contrib. Mineral. Petrol. 156 (6), 745–763.

Di Genova, D., Hess, K.-U., Chevrel, M.O., Dingwell, D., 2016. Models for the estimation of Fe^{3+}/Fe_{tot} ratio in terrestrial and extraterrestrial alkali- and iron-rich silicate glasses using Raman spectroscopy. Am. Mineral. 101, 943–952.

Di Genova, D., Sicola, S., Romano, C., Vona, A., Fanara, S., Spina, L., 2017. Effect of iron and nanolites on Raman spectra of volcanic glasses: a reassessment of existing strategies to estimate the water content. Chem. Geol. 475, 76–86.

Di Muro, A., Giordano, D., Villemant, B., Montagnac, G., Scaillet, B., Romano, C., 2006a. Influence of composition and thermal history of volcanic glasses on water content as determined by micro-Raman spectrometry. Appl. Geochem. 21, 802–812.

Di Muro, A., Villemant, B., Montagnac, G., Scaillet, B., Reynard, B., 2006b. Quantification of water content and speciation in natural silicic glasses (phonolite, dacite, rhyolite) by confocal microRaman spectrometry. Geochim. Cosmochim. Acta 70, 2868–2884.

Di Muro, A., Métrich, N., Mercier, M., Giordano, D., Massare, D., Montagnac, G., 2009. Micro-Raman determination of iron redox state in dry natural glasses: application to peralkaline rhyolites and basalts. Chem. Geol. 259, 78–88.

Dixon, E.J., Stolper, E.M., Holloway, J.R., 1995. An experimental study of water and carbon dioxide solubilities in mid-ocean ridge basaltic liquids: part I. Calibration and solubility models. J. Petrol. 36, 1607–1631.

Druitt, T.H., Brenchley, P.J., Gökten, Y.E., Francaviglia, V., 1995. Late quaternary rhyolitic eruptions from Acigöl complex, Central Turkey. J. Geol. Soc. Lond. 152, 655–667.

Druitt, T.H., Mercier, M., Florentin, L., Deloule, E., Cluzel, N., Flaherty, T., Médard, E., Cadoux, A., 2016. Magma storage and extraction associated with plinian and interplinian activity at Santorini caldera (Greece). J. Petrol. 57, 461–494.

Duan, X., 2014. A general model for predicting the solubility behaviour of H_2O–CO_2 fluids in silicate melts over a wide range of pressure, temperature and compositions. Geochim. Cosmochim. Acta 125, 582–609.

Dubessy, J., Caumon, M.-C., Rull, F., Sharma, S., 2012. Instrumentation in Raman spectroscopy: elementary theory and practice. In: Dubessy, J., Caumon, M.-C., Rull, F. (Eds.), Raman Spectroscopy Applied to Earth Sciences and Cultural Heritage, EMU Notes in Mineralogy. vol. 12. European Mineralogical Union, London, pp. 83–172.

Everall, N., 2004. Depth profiling with confocal Raman microscopy, part 1. Spectroscopy 19 (10), 22–27.

Frantz, J.D., Mysen, B.O., 1995. Raman spectra and structure of $BaO\text{-}SiO_2$, $SrO\text{-}SiO_2$, and $CaO\text{-}SiO_2$ melts to 1600 °C. Chem. Geol. 121, 155–176.

Freitas, D., Manthilake, G., Schiavi, F., Chantel, J., Bolfan-Casanova, N., Bouhifd, M.A., Andrault, D., 2017. Experimental evidence supporting a global melt layer at the base of the Earth's upper mantle. Nat. Commun. 8. http://dx.doi.org/10.1038/s41467-017-02275-9.

Frezzotti, M.L., Tecce, F., Casagli, A., 2012. Raman spectroscopy for fluid inclusion analysis. J. Geochem. Explor. 112, 1–20.

Fukumi, K., Hayakawa, J., Komiyama, T., 1990. Intensity of Raman band in silicate glasses. J. Non-Cryst. Solids 119, 297–302.

Furukawa, T., Fox, K.E., White, W.B., 1981. Raman spectroscopic investigation of the structure of silicate glasses. III. Raman intensities and structural units in sodium silicate glasses. J. Chem. Phys. 75, 3226.

Gómez-Ulla, A., Sigmarsson, O., Huertas, M.J., Devidal, J-L., Ancochea, E., 2018. Carbonated melts of heterogeneous mantle source inferred from historical basanite - alkali basalt - tholeiite suite at Lanzarote, Canary Islands. Chem. Geol (under review).

Grove, T.L., Parman, S.W., Bowring, S.A., Price, R.C., Baker, M.B., 2002. The role of an H_2O-rich fluid component in the generation of primitive basaltic andesites and andesites from the Mt. Shasta region, N California. Contrib. Mineral. Petrol. 142, 375–396.

Haddadi, B., 2016. Ascension et dégazage des magmas basaltiques: application aux volcans d'Islande et de la Chaîne des Puys (Ph.D. thesis). Univ. B. Pascal, Clermont-Ferrand, France.

Herzog, F., Zakaznova-Herzog, V.P., 2011. Quantitative Raman spectroscopy: challenges, shortfalls, and solutions – application to calcium silicate glasses. Am. Mineral. 96, 914–927.

Iacovino, K., Oppenheimer, C., Scaillet, B., Kyle, P., 2016. Storage and evolution of mafic and intermediate alkaline magmas beneath Ross Island, Antarctica. J. Petrol. 57, 93–118.

King, P.L., Vennemann, T.W., Holloway, J.R., Hervig, R.L., Lowenstern, J.B., Forneris, J.F., 2002. Analytical techniques for volatiles: a case study using intermediate (andesitic) glasses. Am. Mineral. 87, 1077–1089.
Le Losq, C., Neuville, D., Moretti, R., Roux, J., 2012. Determination of water content in silicate glasses using Raman spectrometry: implications for the study of explosive volcanism. Am. Mineral. 97, 779–790.
Long, D.A., 1977. Raman Spectroscopy. 276 pp.. MacGraw-Hill, New York.
Malfait, W.J., Sanchez-Valle, C., Ardia, P., Médard, E., Lerch, P., 2011. Compositional dependent compressibility of dissolved water in silicate glasses. Am. Mineral. 96, 1402–1409.
Mandeville, C.W., Webster, J.D., Rutherford, M.J., Taylor, B.E., Timbal, A., Faure, K., 2002. Determination of molar absorptivities for infrared absorption bands of H_2O in andesitic glasses. Am. Mineral. 87 (7), 813–821.
Maruyama, Y., Kanematsu, W., 2011. Confocal volume in laser Raman spectroscopy depth profiling. J. Appl. Phys. 110, 103107.
Matson, D.W., Sharma, S.K., Philpotts, J.A., 1983. The structure of high-silicate glasses. A Raman spectroscopic investigation. J. Non-Cryst. Solids 58, 323–352.
McMillan, P., 1984. Structural studies of silicate glasses and melts – applications and limitations of Raman spectroscopy. Am. Mineral. 69, 622–644.
McMillan, P.F., Remmele, R.L., 1986. Hydroxyl sites in SiO_2 glass: a note on infrared and Raman spectra. Am. Mineral. 71, 772–778.
McMillan, P.F., Wolf, G.H., Poe, B.T., 1992. Vibrational spectroscopy of silicate liquids and glasses. Chem. Geol. 96, 351–366.
Médard, E., Groove, T.L., 2008. The effect of H_2O on the olivine liquidus of basaltic melts: experiments and thermodynamic models. Contrib. Mineral. Petrol. 155, 417–432.
Mercier, M., Di Muro, A., Giordano, D., Métrich, N., Lesne, P., Pichavant, M., Scaillet, B., Clocchiatti, R., Montagnac, G., 2009. Influence of glass polymerisation and oxidation on micro-Raman water analysis in alumino-silicate glasses. Geochim. Cosmochim. Acta 73, 197–217.
Mercier, M., Di Muro, A., Métrich, N., Giordano, D., Belhadj, O., Mandeville, C.W., 2010. Spectroscopic analysis (FTIR, Raman) of water in mafic and intermediate glasses and glass inclusions. Geochim. Cosmochim. Acta 74 (19), 5641–5656.
Métrich, N., Wallace, P., 2008. Volatile abundances in basaltic magmas and their degassing paths tracked by melt inclusions. In: Putirka, K., Tepley, F. (Eds.), Minerals, Inclusions & Volcanic Processes. 69. Rev Mineral Geochem, pp. 363–402.
Morizet, Y., Brooker, R.A., Iacono-Marziano, G., Kjarsgaard, B.A., 2013. Quantification of dissolved CO_2 in silicate glasses using micro-Raman spectroscopy. Am. Mineral. 98, 1788–1802.
Mourtada-Bonnefoi, C.C., Laporte, D., 2002. Homogeneous bubble nucleation in rhyolitic magmas: an experimental study of the effect of H_2O and CO_2. J. Geophys. Res. 107. http://dx.doi.org/10.1029/2001JB000290.
Mysen, B.O., Virgo, D., 1986. Volatiles in silicate melts at high pressure and temperature: 1. Interaction between OH groups and Si^{4+}, Al^{3+}, Ca^{2+}, Na^{+} and H^{+}. Chem. Geol. 57, 303–331.
Mysen, B.O., Virgo, D., Harrison, W.J., Scarfe, C.M., 1980. Solubility mechanisms of H2O in silicate melts at high pressures and temperatures: a Raman spectroscopic study. Am. Mineral. 65, 900–914.
Neuville, D.R., Cormier, L., Massiot, D., 2004. Al environment in tectosilicate and peraluminous glasses: a ^{27}Al MQ-MAS NMR, Raman, and XANES investigation. Geochim. Cosmochim. Acta 68, 5071–5079.
Ohlhorst, S., Behrens, H., Holtz, F., 2001. Compositional dependence of molar absorptivities of near-infrared OH-and H_2O bands in rhyolitic to basaltic glasses. Chem. Geol. 174 (1), 5–20.
Rossano, S., Mysen, B., 2012. Raman spectroscopy of silicate glasses and melts in geological systems. In: Dubessy, J., Caumon, M.-C., Rull, F. (Eds.), Raman Spectroscopy Applied to Earth Sciences and Cultural Heritage, EMU Notes in Mineralogy. vol. 12. European Mineralogical Union, London, pp. 319–364.
Sanchez-Valle, C., Gaillard, F., Ghosh, S., Metzger, K., 2015. Fluids and melts in planetary interiors: from crust to core-mantle boundaries. Chem. Geol. 418, 1–5.
Schiavi, F., Provost, A., Schiano, P., Cluzel, N., 2016. P-V-T-X evolution of olivine-hosted melt inclusions during high-temperature homogenization treatment. Geochim. Cosmochim. Acta 172, 1–21.
Seifert, F.A., Mysen, B.O., Virgo, D., 1981. Structural similarity of glasses and melts relevant to petrological processes. Geochim. Cosmochim. Acta 45 (10), 1879–1884.
Severs, M.J., Azbej, T., Thomas, J.B., Mandeville, C.W., Bodnar, R.J., 2007. Experimental determination of H_2O loss from melt inclusions during laboratory heating: evidence from Raman spectroscopy. Chem. Geol. 237, 358–371.
Sharma, S.K., Mammone, J.F., Nicol, M.F., 1981. Raman investigation of ring configurations in vitreous silica. Nature 292, 140–141.
Shishkina, T., Botcharnikov, R.E., Holtz, F., Almeev, R.R., Jazwa, A.M., Jakubiak, A.A., 2014. Compositional and pressure effects on the solubility of H_2O and CO_2 in mafic melts. Chem. Geol. 388, 112–129.
Sigmarsson, O., Halldorsson, S.A., 2015. Delimiting Bárðarbunga and Askja volcanic systems with Sr- and Nd-isotope ratios. Jökull 65, 17–28.
Stolen, R.H., Walrafen, G.E., 1976. Water and its relation to broken bond defects in fused silica. J. Chem. Phys. 64, 2623–2631.
Stolper, E., 1982. Water in silicate glasses: an infrared spectroscopic study. Contrib. Mineral. Petrol. 81, 1–17.
Thomas, R., 2000. Determination of water contents of granite melt inclusions by confocal laser Raman microprobe spectroscopy. Am. Mineral. 85, 868–872.
Thomas, R., Kamenetsky, V.S., Davidson, P., 2006. Laser Raman spectroscopic measurements of water in unexposed glass inclusions. Am. Mineral. 91, 467–470.
Wang, Z., Cooney, T.F., Sharma, S.K., 1995. In situ structural investigation of iron-containing silicate liquids and glasses. Geochim. Cosmochim. Acta 59, 1571–1577.
Withers, A.C., Behrens, H., 1999. Temperature-induced changes in the NIR spectra of hydrous albitic and rhyolitic glasses between 300 and 100 K. Phys. Chem. Miner. 27 (2), 119–132.
Woelffel, W., Claireaux, C., Toplis, M.J., Burov, E., Barthel, E., Shukla, A., Biscaras, J., Chopinet, M.-H., Gouillart, E., 2015. Analysis of soda-lime glasses using non-negative matrix factor deconvolution of Raman spectra. J. Non-Cryst. Solids 428, 121–131.
Xue, X., Kanzaki, M., 2004. Dissolution mechanisms of water in depolymerized silicate melts: constraints from ^{1}H and ^{29}Si NMR spectroscopy and ab initio calculations. Geochim. Cosmochim. Acta 68, 5027–5057.
Zajacz, Z., Halter, W., Malfait, W.J., Bachmann, O., Bodnar, R.J., Hirschmann, M.M., Mandeville, C.W., Morizet, Y., Müntener, O., Ulmer, P., Webster, J.D., 2005. A composition-independent quantitative determination of the water content in silicate glasses and silicate melt inclusions by confocal Raman spectroscopy. Contrib. Mineral. Petrol. 150, 631–642.
Zotov, N., 2001. Effects of composition on the vibrational properties of sodium silicate glasses. J. Non-Cryst. Solids 287, 231–236.
Zotov, N., Keppler, H., 1998. The influence of water on the structure of hydrous sodium tetrasilicate glasses. Am. Mineral. 83, 823–834.
Zotov, N., Yanev, Y., Epelbaum, M., Konstantinov, L., 1992. Effect of water on the structure of rhyolite glasses – X-ray diffraction and Raman spectroscopy studies. J. Non-Cryst. Solids 142, 234–246.